SEPTEMBER 1956

A.I.Ch.E. JOURNAL

Published by the American Institute of Chemical Engineers

East Anglia Library

CONTENTS

Operating Characteristics of a Centrifugal Extractor	F. M. Jacobsen and G. H. Beyer
Viscosity of Liquids	Lyle F. Albright and John Lohrenz
Rate of Flow and Mechanics of Bubble Formation from Single Submerged Orifices	Irving Leibson, Eugene G. Holcomb, Anthony G. Cacoso, and John J. Jacmic
Structure and Performance of Filter Media	H. P. Grace
Formation of Gas Bubbles at Horizontal Orifices	Leon Davidson and Erwin H. Amick, Jr.
Enthalpy of Hydrocarbon Mixtures	Lawrence N. Canjar and Vernon J. Peterka
Vapor Pressures: The Saturated Aliphatic Hydrocarbons	Norman E. Sondak and George Thodos
Theorem of Corresponding States Applied to Saturated Liquids and Vapors	Merk Hobson and James H. Weber
Turbulent Exchange of Mass and Momentum with a Boundary	Thomas J. Hanratty
Fractionation During Condensation of Vapor Mixtures	Eric R. Kent and Robert L. Pigford
Turbulent Diffusion in Particulately Fluidized Beds of Particles	Thomas J. Hanratty, George Latinen, and Richard H. Wilhelm
Ferric Ion Removal from Dilute Acidic Solutions by Fixed-bed Cation Exchange	Brian W. Mar and M. M. David
Mechanism of Heat Transfer to Liquid Drops	R. V. McDowell and J. E. Myers
Differential Heats of Condensation and Enthalpies of Saturated Liquid Hydrocarbon Mixtures	J. G. Stiehl, Merk Hobson, and James H. Weber
Characteristics of Porous Beds and Structures	R. B. MacMullin and G. A. Muccini
Interpretation and Correlation of Ion Exchange Column Performance under Nonlinear Equilibria	Nevin K. Hiester, Shirley B. Radding, Richard L. Nelson, Jr., and Theodore Vermeulen
Mass Transfer Studies in an Agitated Vessel	A. I. Johnson and Chen-Jung Huang
Effect of Wall Proximity on the Rate of Rise of Single Air Bubbles in a Quiescent Liquid	Seiji Uno and R. C. Kintner

Did you ever think of using LITHIUM *as:*

AN ANTI-FREEZE OR DE-ICING COMPOUND—

Lithium chloride solutions freeze as low as -67° F. and are used for this reason in dry cells, fire extinguishers and as de-icers.

A CATALYST—

Synthetic rubber made from isoprene by using lithium as catalyst is remarkably similar to natural rubber in structure. The low cost of its use suggests it should be tried in other areas.

AN AIR CONDITIONER AND REFRIGERANT—

Lithium chloride is extremely hygroscopic, highly soluble at low temperature, and has good thermal stability. In contact with air will maintain relative humidities from 10% up, over a wide temperature range. Such solutions may be used as heat transfer media to heat or cool and dry conditioned air. Lithium bromide is used as an absorbent in sealed industrial cooling units.

A ROCKET PROPELLANT—

Lithium hydride is a most convenient raw material for production of other "active" hydrogen-containing possible fuels, since it gives smooth reactions with high yields. In solid propellants, lithium compounds provide the highest percentage of active ingredients.

A CORROSION INHIBITOR—

Lithium dichromate offers good corrosion inhibition in cooling systems. Its solubility in organic fluids should extend the usefulness of many organics.

A DEGASIFIER—

Lithium metal (as low as 50 ppm) is used to remove gases from copper and increase electrical conductivity.

A FLUX—

Lithium fluoride, chloride, etc. with other salts produce compositions with low, favorable surface tension characteristics and excellent fluxing and deoxidizing properties, useful in production and fabrication of such metals as aluminum, magnesium and titanium.

AN ELECTROLYTE ADDITIVE—

Lithium salts cause a pronounced increase in electrical conductivity, and lower melting temperatures when used in both aqueous and fused salt baths.

FOOTE CAN HELP PUT LITHIUM TO WORK IN YOUR PROCESS REQUIREMENTS

Want to explore further? **Just send this coupon to FOOTE.**

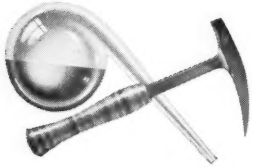

Foote
MINERAL COMPANY

448 Eighteen West Chelten Building,
Philadelphia 44, Pa.

RESEARCH LABORATORIES: Berwyn, Pa.

PLANTS: Exton, Pa.; Kings Mountain, N.C., Knoxville, Tenn.; Sunbright, Va.

FOOTE MINERAL COMPANY
448 Eighteen W. Chelten Bldg., Phila. 44, Pa.
I am interested in lithium for:

_____

_____

Name _____

Company _____

Address _____

A.I.Ch.E. JOURNAL

SEPTEMBER 1956 · VOL. 2, NO. 3

PUBLISHER
F. J. Van Antwerpen
EDITOR
Harding Bliss
ADVERTISING MANAGER
L. T. Dupree

ADVISORY BOARD

C. M. Cooper, O. E. Dwyer, W. C. Edmister, E. R. Gilliland, A. N. Hixson, W. R. Marshall, Jr., R. H. Newton, R. L. Pigford, J. M. Smith, Theodore Vermeulen, R. R. White, R. H. Wilhelm

The A.I.Ch.E. Journal, an official publication of the American Institute of Chemical Engineers, is devoted in the main to theoretical developments and research in chemical engineering and allied branches of engineering and science. Manuscripts should be submitted to the New York office.

Chemical Engineering Kinetics 281

Operating Characteristics of a Centrifugal Extractor . . . . . *F. M. Jacobsen and G. H. Beyer* 283

Viscosity of Liquids . . . . . *Lyle F. Albright and John Lohrenz* 290

Rate of Flow and Mechanics of Bubble Formation from Single Submerged Orifices
Irving Leibson, Eugene G. Holcomb, Anthony G. Cacoso, and John J. Jacmic 296

Structure and Performance of Filter Media . . . . . *H. P. Grace* 307

Formation of Gas Bubbles at Horizontal Orifices . . . . . *Leon Davidson and Erwin H. Amick, Jr.* 337

Enthalpy of Hydrocarbon Mixtures . . . . . *Lawrence N. Canjar and Vernon J. Peterka* 343

Vapor Pressures: The Saturated Aliphatic Hydrocarbons . . . . . *Norman E. Sondak and George Thodos* 347

Theorem of Corresponding States Applied to Saturated Liquids and Vapors
Merk Hobson and James H. Weber 354

Turbulent Exchange of Mass and Momentum with a Boundary . . . . . *Thomas J. Hanratty* 359

Fractionation During Condensation of Vapor Mixtures . . . . . *Eric R. Kent and Robert L. Pigford* 363

Turbulent Diffusion in Particulately Fluidized Beds of Particles
Thomas J. Hanratty, George Latinen, and Richard H. Wilhelm 372

Ferric Ion Removal from Dilute Acidic Solutions by Fixed-bed Cation Exchange
Brian W. Mar and M. M. David 381

Mechanism of Heat Transfer to Liquid Drops . . . . . *R. V. McDowell and J. E. Myers* 384

Differential Heats of Condensation and Enthalpies of Saturated Liquid Hydrocarbon Mixtures
J. G. Stiehl, Merk Hobson, and James H. Weber 389

Characteristics of Porous Beds and Structures . . . . . *R. B. MacMullin and G. A. Muccini* 393

Interpretation and Correlation of Ion Exchange Column Performance under Nonlinear Equilibria
Nevin K. Hiester, Shirley B. Radding, Richard L. Nelson, Jr., and Theodore Vermeulen 404

Mass Transfer Studies in an Agitated Vessel . . . . . *A. I. Johnson and Chen-Jung Huang* 412

Effect of Wall Proximity on the Rate of Rise of Single Air Bubbles in a Quiescent Liquid
Seiji Uno and R. C. Kintner 420

Communications to the Editor 426

Books 11S

Publication Office, Richmond, Virginia. Published quarterly in March, June, September, and December by the American Institute of Chemical Engineers, 25 West 45 Street, New York 36 New York. Manuscripts and other communications should be sent to the New York office. Correspondence with the editor may be addressed to him at Yale University, 225 Prospect Street, New Haven 11, Connecticut. Statements and opinions in the *A.I.Ch.E. Journal* are those of the contributors, and the American Institute of Chemical Engineers assumes no responsibility for them. Subscriptions: one year, member $4.50, nonmember $9.00; two years, member $7.50, nonmember $16.00; additional yearly postage, Canada 50 cents, Pan American Union $1.50, other foreign $2.00 (foreign subscriptions payable in advance). Single copies: $3.00. Second-class mail privileges authorized at Richmond, Virginia.

Copyright 1956 by the American Institute of Chemical Engineers.

National headquarters of A.I.Ch.E. is concerned about nondelivery of copies of the *A.I.Ch.E. Journal* and urgently requests subscribers to give prompt notification of any change of address. Sixty days must be allowed for changes to be made in the records.

HARSHAW

Tellerette

A NEW POLYETHYLENE TOWER PACKING BASED ON THE PRINCIPLE OF INTERSTITIAL HOLDUP

Increased Efficiency

Increased Capacity

Lighter Weight

Unbreakable Units

Tray Column Characteristics

Send for this folder. It contains more detailed explanation.

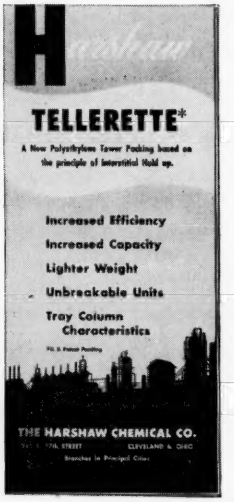

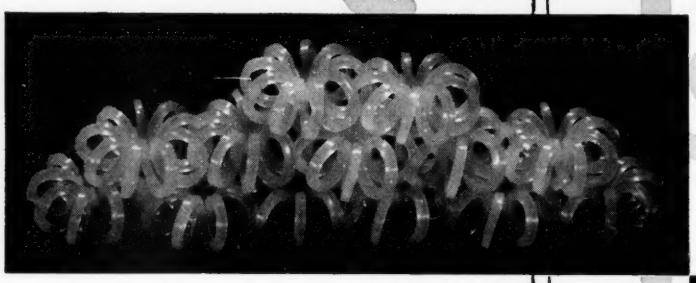

THE HARSHAW CHEMICAL CO.

1945 E. 97th Street Cleveland 6, Ohio

A.I.Ch.E. JOURNAL

Chemical Engineering Kinetics

It is a pleasure to welcome a new and important book, Professor Smith's "Chemical Engineering Kinetics," to the literature of chemical engineering. This book should increase the interest in this subject already generated by the well-known "Kinetics and Catalysis" of Hougen and Watson. In the past the appearance of certain books, such as Walker, Lewis, and McAdams's "Principles of Chemical Engineering" and Dodge's "Chemical Engineering Thermodynamics," has engendered in many readers a determination to explore more fully the corresponding fields. New and fruitful research ideas and programs have sprung up in many places as a direct consequence of these trail-blazing books.

Kinetics is a particularly promising field and one of such breadth and complexity that the opportunities for research are almost without limit. Theoreticians may engross themselves in mathematical problems just about as difficult as can be found in any field of endeavor. The measurement of phenomena, on the other hand, will occupy the experimentalist, safe in the realization that his results will be of immediate utility and also of ultimate value in bringing to fruition the mathematical and theoretical developments.

Kinetics as a branch of pure chemistry is old and extensively explored, although by no means exhausted. As a branch of chemical engineering, however, it is relatively new and bursting with vigor and opportunity. The difference between the purely scientific and engineering aspects of this field is not easy to establish, but it is probably largely one of the complexity of the systems. As an example, the chemical kinetics of a catalytic reaction may be established by relatively simple measurements under controlled conditions, of which the maintenance of isothermal operation is probably the most important. When one attempts to predict what will happen when this reaction is to be carried out in a full-scale catalytic converter, however, the problem is one of chemical engineering kinetics. The superimposition of heat transfer and mass transfer on the purely chemical rate consideration increases the difficulty enormously and invites the exercise of every kind of ingenuity and originality.

Another characteristic of chemical engineering kinetics is the growth and development of ideas always with the aim of complete understanding of a phenomenon. At first we may be content, though not satisfied, with a relatively simple "mechanism." This may leave certain observations unexplained, but, as time and thought progress, other ideas develop by which the original mechanism may be modified and improved. Typical of this progression is the problem of heat transfer or mass transfer in fixed beds. This was first explored theoretically and experimentally as a problem in which the resistance to transfer in the fluid phase was presumed to be governing. For many years this explanation of the behavior of fixed beds was considered reasonable and adequate. However, certain discrepancies disturbed workers in this field, and it was realized that the resistance in the solid phase could, in some cases at least, be important. A theoretical explanation of this problem was made with considerable success, and certain disagreements were clarified and resolved. Very recently, however, still another factor has come to the fore—that of longitudinal diffusion. It is now clear that certain anomalies probably can be explained only on the basis of the superimposition of longitudinal diffusion on the previously established fluid- and solid-diffusion problem. Thus another difficult problem begins to yield to the constant aim in chemical engineering for understanding as complete as is possible.

Chemical engineering kinetics is a subject of almost boundless promise for research, and it is to be hoped that Professor Smith's book will do much to excite further interest among all of us.

H. B.

NEW!

BOWEN CONICAL LABORATORY SPRAY DRYER

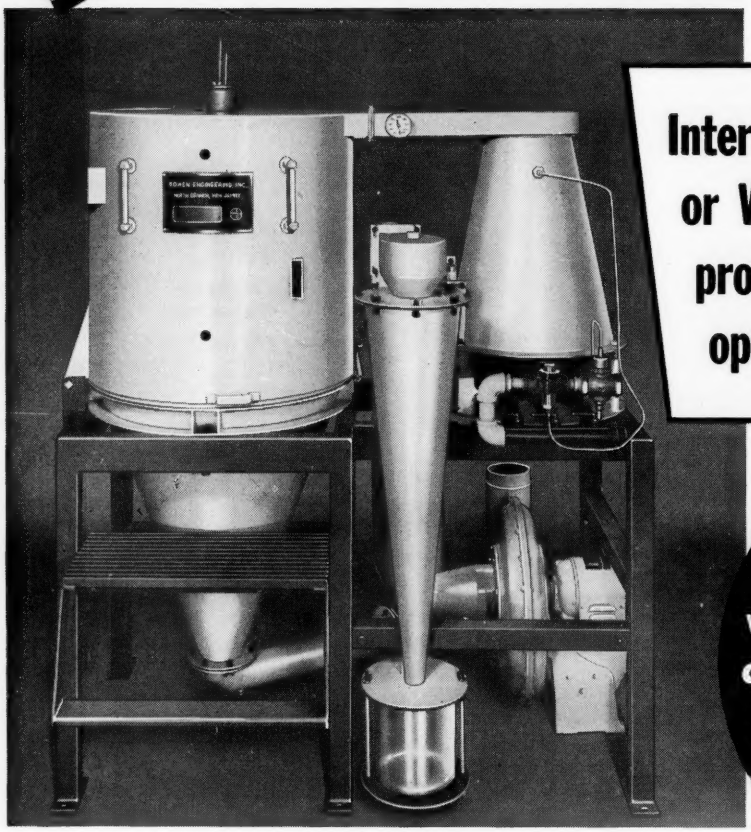

Interchangeable Nozzle or Wheel Atomization provides extreme operating flexibility

CAPACITY
15 to 80 lbs/hr water evaporation depending on inlet temperature and product drying rate

The New Bowen Conical Laboratory Spray Dryer has been especially designed for economical product evaluation and production of limited quantities of valuable materials. Particular attention has been given to operating features and ease of cleaning. Surfaces in contact with feed material and product are stainless steel throughout. Drying temperatures are variable up to 1000°F to accomodate a wide variety of materials.

The New unit can be seen in operation, by appointment, at the Bowen Laboratory in North Branch.

Write for Bulletin 34

Describes the Bowen Conical Laboratory Spray Dryer in detail and gives complete technical specifications.

BOWEN ENGINEERING, INC.
NORTH BRANCH 13, NEW JERSEY

BOWEN SPRAY DRYERS
Always Offer You More!

Recognized Leader in Spray Dryer Engineering Since 1926

Operating Characteristics of a Centrifugal Extractor

F. M. JACOBSEN and G. H. BEYER

Iowa State College, Ames, Iowa

The operating characteristics of a Podbielniak model 5,000 centrifugal extractor, having a combined-stream capacity of 450 cc./min. at 5,000 rev./min. and a rotor holdup of 529 cc., were investigated. Variables studied were density difference, rotor speed, light-liquid-out pressure, flow rates, holdup, and number of stages.

A technique for holdup determination that comprises displacing either phase in the extractor with the other phase is described and experimentally demonstrated. An equation useful in predicting flooding limits is verified. It is suggested that the effective values of the rotor dimensions in this equation be determined by the behavior of the extractor.

A relationship among number of stages, light-liquid-out pressure, and flow-rate ratio is demonstrated by extracting boric acid from isoamyl alcohol with water. With only a few runs this relationship should permit one to map in a family of curves for a particular system and thus rapidly to estimate optimum operating conditions.

A procedure is outlined for applying the methods to other systems using similar extractors. First the constants in an equation are estimated from holdup measurements in order to predict flooding limits. Then a few extraction runs are made to estimate optimum operating conditions.

The centrifugal extractor is a relatively new countercurrent liquid-liquid contacting device consisting of a series of concentric stages in which both mixing and settling are accelerated by a readily variable centrifugal-force field. The centrifugal-force field enables the extractor to handle systems of low density difference more efficiently than do conventional extractors. The low holdup and high throughput capacity of the centrifugal extractor lead to short contact times, which have proved useful in the pharmaceutical industry. Low holdup and rapid attainment of steady state operation may considerably reduce process- and feedstock-switching losses in petroleum refining. For comparable capacity the centrifugal extractor occupies a fraction of the volume required for conventional extractors. Additional stages beyond the extraction capacity of a particular unit are obtainable only by duplication of the unit.

The Podbielniak "Pup" model 5,000 laboratory extractor used in this study has been described previously (*1*). It is convenient for studying many systems in a relatively short time because of its low holdup, rapid attainment of steady state operation, and substantial capacity. The manufacturer claims to be able to extrapolate data obtained with this model to commercial-size units.

A literature review indicated few articles (*1, 5*) on the operating characteristics of centrifugal extractors. The first objective of this study, therefore, was to investigate these characteristics.

The literature review also led to an equation that would be useful in predicting operating limits if it could be experimentally verified. Inferences drawn from reported data (*2, 3, 4*) suggested a method of relating the number of stages with several operating variables. Additional objectives of this study, therefore, were to test the validity of an equation for predicting operating limits and to investigate the feasibility of relating stages and operating variables. Attainment of these objectives led to a procedure for rapidly predicting operating limits and for estimating optimum operating conditions.

DESCRIPTION OF EXTRACTOR

Operating Principles

The centrifugal extractor studied had a rotor approximately 18 in. in diam. and 2 in. thick. The rotor was constructed by machining concentric annuli in two mating disks and then bolting the disks together. The annuli were connected at 180° intervals by slots, with the slots in adjacent rings rotated 90° to assure radial flow in each annulus. Figure 1 is a photograph of one of these disks. Figure 2 is a schematic diagram of the extractor, showing for the sake of clarity only five of the annuli.

Figure 2 is useful in explaining the operation of the extractor. The heavy liquid is fed axially through a rotary seal at one side of the extractor so that it enters the contacting section of the rotor near the axis. The light liquid is fed axially through a similar seal at the opposite side of the extractor and then into a small radial channel leading from the axis to the periphery of the rotor so that it enters the contacting section near the periphery. Centrifugal force causes the heavy liquid to be thrown outward, thereby displacing the light liquid inward. The heavy liquid leaves the contacting section near the periphery and is channeled radially to the axis, where it leaves through a rotary seal. The light liquid leaves the contacting section near the axis and is discharged through a similar seal.

The light-liquid-in pressure is determined by the density difference of the light-liquid-in and heavy-liquid-out phases, the speed of rotation, and the rotor radius. The heavy-liquid-out pressure is atmospheric; the heavy-liquid-in pressure is essentially the same as the light-liquid-out pressure, which is adjusted by a back-pressure regulator.

Two important differences between the centrifugal and conventional tower extractors should be noted (*6*). The first is that the settling effect of density difference is multiplied by the centrifugal force. The product of these factors is sufficient to force the two phases past one another through the small slots shown in Figures 1 and 2. This procedure permits the extractor effectively to handle systems of very low density difference. The second difference is that the liquid is either accelerated or decelerated radially and the process of acquiring or losing energy creates turbulence.

Conditions in the contacting section during operation may be thought of in terms of

F. M. Jacobsen is at present with American Oil Company, Texas City, Texas, and G. H. Beyer at the University of Missouri, Columbia, Missouri.

a "principal" interface, to describe the behavior of liquids in the contacting section as a whole, and of a series of "minor" interfaces, to describe the behavior of liquids in the individual stages of the contacting section (*1*). Considering the entire contacting section, the heavy liquid will predominate radially outward from the principal interface to the periphery; whereas the light liquid will predominate radially inward from the principal interface to the axis. Within each annulus there is a minor interface because enough of the dispersed phase must build up to develop sufficient head to pass through the slots.

The minor interfaces in the annuli are one source of interfacial area through which mass transfer may take place. Another, and perhaps more important, source of interfacial area is provided by the dispersing action of the slots; for example, as the heavy liquid passes outward through a slot it forms droplets which are dispersed in the continuous light-liquid layer on the outer face of the annulus wall. These droplets continue radially until they coalesce on the inner face of the next annulus wall. The light-liquid droplets moving inward through the slots and heavy-liquid layers exhibit similar behavior. The net effect is the continuous creation of fresh mass transfer area. The principle is that of repeated mixing and settling, except that the settling is accelerated by centrifugal force and that the two layers must flow past each other radially until they escape into another annulus.

The position of the principal interface between the light and heavy liquid is controlled by the light-liquid-out pressure. Thus, changing this pressure is analogous to opening and closing the outlet valve in the exit line of a tower extractor. At low light-liquid-out pressures the heavy-liquid phase predominates in the contacting section; whereas at high light-liquid-out pressures the light-liquid phase predominates. Therefore, as the light-liquid-out pressure is varied, a change may be expected in both types of mass transfer area.

Flooding

Two types of flooding have been observed with this extractor. The first type, caused by too large a throughput, is fixed for centrifugal extractors by their design. The second type of flooding is analogous to level control in a tower extractor. It is caused by movement of the principal interface to either of the effluent stream take-offs. For a particular centrifugal extractor this type of flooding depends primarily on rotor-speed and phase-density difference. At a sufficiently low light-liquid-out pressure the rotor will be essentially full of heavy liquid, and so the principal interface will spill into the light-liquid-out line. This condition has been defined as flooding in the light liquid out. Likewise, at a sufficiently high light-liquid-out pressure, the rotor will be essentially full of light liquid, and so the principal interface will spill into the heavy-liquid-out line. This condition has been defined as flooding in the heavy liquid out. The useful operating range of the extractor for a particular system may be described by light-liquid-out pressures between flooding limits, because at and outside these limits stable operation is difficult.

Holdup

The liquid volume or holdup in this extractor is contained in two functional sections. One is the rotor or contacting section; the other comprises the seals and feed and product lines. If V_E is the total extractor volume and V_C the rotor volume, then the difference

$$V_E - V_C = V_S \qquad (1)$$

will be called the seal volume. The subscript L denotes the light-liquid phase and the subscript H the heavy-liquid phase. The following equations are then implied by Equation (1):

$$V_E = V_H + V_L \qquad (2)$$

$$V_C = V_{CH} + V_{CL} \qquad (3)$$

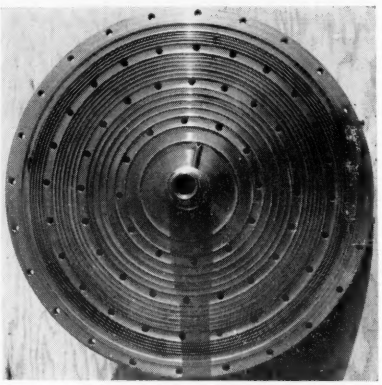

Fig. 1. Extractor disk.

$$V_S = V_{SH} + V_{SL} \qquad (4)$$

$$V_L = V_{CL} + V_{SL} \qquad (5)$$

$$V_H = V_{CH} + V_{SH} \qquad (6)$$

In these equations V_E, V_C, V_S, V_{SH}, and V_{SL} are constants; whereas V_L, V_H, V_{CL}, and V_{CH} are variables dependent upon experimental conditions.

Previous workers (*1, 5*) reported the extractor holdup as $V_E = 600$ cc., and the contacting section holdup as $V_C = 65$ cc. Values experimentally observed during this investigation were $V_E = 638$ and $V_C = 529$ cc.

EXPERIMENTAL INVESTIGATION

Morgenthaler *et al.* (*5*) derived the following equation for light-liquid pressure drop across the extractor:

$$P_{LI} - P_{LO} = \Delta\rho w^2 V_{CH}/2\pi b g_c \qquad (7)$$

Barson and Beyer (*1*) derived the following equation for light-liquid-in pressure:

$$P_{LI} = \Delta\rho w^2 r^2/2g_c \qquad (8)$$

and evaluated r as 7.71 in.

Eliminating P_{LI} from Equations (7) and (8) and solving for P_{LO}, one obtains

$$P_{LO} = \Delta\rho w^2(r^2 - V_{CH}/\pi b)/2g_c \qquad (9)$$

Equation (9) has two important uses. The first is to predict operating limits for any system. The second is to estimate optimum operating conditions in conjunction with a relationship between rotor inventory and number of stages that will be demonstrated below.

Before the validity of Equation (9) is tested, it seemed wise to check both Equation (8) and the effects of flow rates on the light-liquid-in and light-liquid-out pressures. Recent data (*4*), such as those shown in Figure 3, indicate that Equation (8) is an excellent approximation. It has

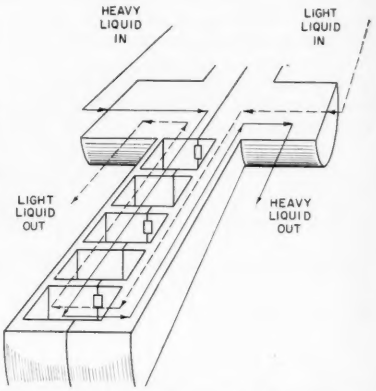

Fig. 2. Schematic diagram of flow through extractor.

also been shown (*4*) that the change in light-liquid-out pressure at either flooding limit with flow rates is small compared with the light-liquid-out pressure range between flooding limits. Data at incipient flooding in the light liquid out are shown in Figure 4. The light-liquid-out pressure between flooding limits is of course operationally independent of flow rates because one may choose it and the heavy- and light-liquid flow rates independently of one another.

Holdup Studies

If the two extractor parameters, r and b, in Equation (9) are known, that equation may be used to predict operating limits. Thus, specification of $\Delta\rho$ and w fixes P_{LO} at both flooding limits because V_{CH} is constant at either flooding limit. At flooding in the light liquid out, V_{CH}/V_C will be essentially unity, and at flooding in the heavy liquid out, V_{CH}/V_C will be

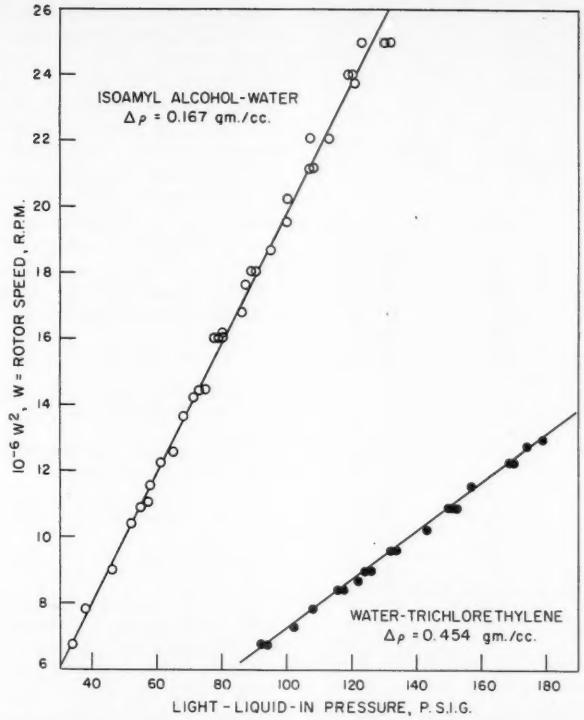

Fig. 3. Relation among rotor speed, density difference, and light-liquid-in pressure.

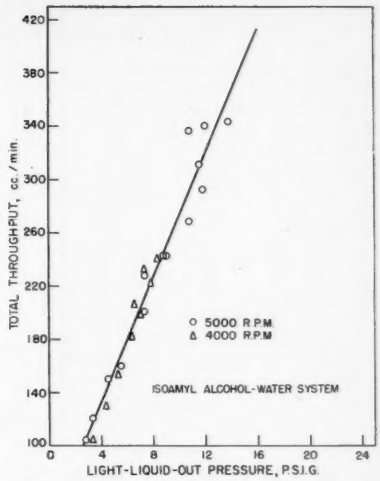

Fig. 4. Relation between total throughout and light-liquid-out pressure at incipient flooding in the light liquid out.

essentially zero. This section outlines methods by which the constants in Equation (9) were evaluated. The application of these methods to other centrifugal extractors is discussed in a later section.

The application of Equation (9) is not limited by a varying rotor width if b is defined as the effective rotor width and evaluated numerically from the behavior of the extractor rather than from its dimensions. Defining b in this manner should permit the application of Equation (9) independently of the internal arrangement of the contacting sections of similar extractors.

To test the validity of Equation (9) it was necessary to make direct holdup measurements. Previous workers (*1, 5*) attempted to measure holdup by valving off both the feed and effluent streams, stopping the rotor, and then draining it. The limitation of this method is evident from Figures 1 and 2, which indicate the tortuous path either liquid has to follow in leaving the rotor. A more promising approach appeared to be displacing either phase from the extractor with the other phase. Equation (2) could then be employed to check the consistency of the results since the sum of V_L and V_H must be constant at all operating conditions.

An aspect of Equation (9) useful in demonstrating its validity and evaluating the constants in Equations (1) through (6) is seen by solving Equation (9) for V_{CH}:

$$V_{CH} = \pi b(r^2 - 2g_cP_{LO}/\Delta\rho w^2) \quad (10)$$

and substituting into Equation (3) to obtain

$$V_{CL} = (V_C - \pi br^2) + 2\pi bg_cP_{LO}/\Delta\rho w^2 \quad (11)$$

Since r and b are defined as effective rotor dimensions and πbr^2 is therefore rotor holdup V_C, the first two terms on the right-hand side of Equation (11) vanish, giving

$$V_{CL} = 2\pi bg_cP_{LO}/\Delta\rho w^2 \quad (11a)$$

Substituting Equations (10) and (11*a*) into Equations (6) and (5), respectively, one obtains

$$V_H = (\pi br^2 + V_{SH}) - 2\pi bg_cP_{LO}/\Delta\rho w^2 \quad (12)$$

$$V_L = V_{SL} + 2\pi bg_cP_{LO}/\Delta\rho w^2 \quad (13)$$

Equations (12) and (13) are of the form

$$V_X = a_X \pm c_3P_{LO} \quad (14)$$

where the a_X's are constants and c_3 is constant at constant $\Delta\rho$ and w. Equations (12) and (13) predict that the volume of either phase in the extractor should vary linearly with P_{LO}.

Before the data used to verify these equations is discussed, however, two other points should be considered. The first point is concerned with the rotor inventory at either flooding limit. The second is concerned with the effect of rotor construction on holdup-determination technique.

It was observed earlier that when the principal interface spills into either effluent stream the rotor will be essentially full of one phase. At flooding in the light liquid out, for example, when the rotor is essentially full of heavy liquid, Equation (13) indicates that if the rotor were completely full of heavy liquid, V_L would be equal to V_{SL}, and P_{LO} would be zero. Experimentally, it was observed that the light-liquid-out pressure was not zero at flooding in the light liquid out. The amount of light liquid in the rotor under these conditions was therefore estimated to be the difference between V_L at flooding in the light liquid out and V_{SL}. The light-liquid seal volume V_{SL} was estimated from Equation (13) when P_{LO} was zero. Evaluating V_{SL} in this manner assumes that the rotor is full of heavy liquid when the light-liquid-out pressure is zero. Likewise, the heavy-liquid seal volume V_{SH} was estimated from Equation (12) on the assumption that at flooding in the heavy liquid out $V_H = V_{SH}$.

The second point is concerned with the effect of rotor construction on holdup-determination technique. This point will be discussed with reference first to heavy-liquid and then to light-liquid holdup.

Tabulated heavy-liquid holdups are actually the sum of two heavy-liquid volumes. The first of these volumes was displaced while the rotor was spinning. The extractor was permitted to attain stable operation at the desired values of the operating variables: w, $\Delta\rho$, and flow rates. Attainment of stable operation was judged by the constancy of these variables for a 10-min. interval. The heavy-liquid feed was then turned off and light

Table 1. Variation of Holdup with Light-liquid-out Pressure for Light-liquid-out Pressures Less Than 100 lb./sq. in.

Isoamyl alcohol–water system
Rotor speed = 4,950 to 5,000 rev./min.
H flow rate = 90 to 105 cc./min.
L flow rate = 125 to 150 cc./min.
Volumes = cc. at 25° C.
P_{LO} = lb./sq. in. gauge

Light-liquid holdup

Run H	P_{LO}	V_L	Run H	P_{LO}	V_L
56	9.3	123.55	84	59	392.16
57	8.7	121.01	86	59	395.59
58	8.6	127.91	79	77.7	479.03
92	23.8	203.10	81	79	473.30
93	23.8	210.65	75	98	573.67
68	39	287.41	78	98	573.76
69	39	283.67			

Heavy-liquid holdup

Run H	P_{LO}	V_H	Run H	P_{LO}	V_H
60	9	622.60	39	77	266.12
61	9	617.93	40	79	265.51
62	9	622.18	41	80	268.73
63	9	622.05	42	76	268.74
94	23.8	541.29	43	77	272.73
95	23.8	537.70	44	79	272.72
70	40	466.91	77	98	178.60
67	41	460.39	88	98	174.27
85	59	353.49	89	98	175.77
87	59	352.50			

liquid was introduced into both the heavy- and light-liquid-in lines. Closing a valve in the light-liquid-out line forced the total input to the extractor to leave through the heavy-liquid-out line, facilitating displacement of the heavy liquid. The rotor speed was not reduced while the heavy liquid was being displaced. The displaced heavy liquid was collected, separated from the light liquid, and weighed to determine its volume.

The second of these heavy-liquid volumes was obtained by stopping the rotor after no more heavy liquid was being displaced while it was spinning and by flushing the extractor with light liquid while the rotor was slowing down and after it had stopped. The origin of this volume of heavy liquid may be seen by observing in Figure 1 that centrifugal force will prevent displacement of the heavy liquid normally contained in the rotor at a radial distance from the center of the rotor greater than the radial distance of the heavy-liquid take-off. The average volume of heavy-liquid in the rotor that could not be displaced by a less dense liquid while the rotor was spinning was approximately 25 cc. This volume is the heavy-liquid rotor inventory at flooding in the heavy liquid out,

$$(V_{CH})_{FH} = 25 \text{ cc.} \qquad (15)$$

Similar considerations indicated that the rotor might contain light liquid that could not be displaced by heavy liquid while the rotor was spinning. Attempts to displace additional light liquid from the rotor while it was slowing down and after it had stopped, after the spinning rotor had been thoroughly flushed, were unsuccessful. This indicated that substantially all light liquid may be displaced from a spinning rotor by a denser liquid.

Table 2. Variation of Holdup with Light-liquid-out Pressure for Light-liquid-out Pressures Greater Than 96 lb./sq. in.

Isoamyl alcohol–water system
Rotor speed = 4,950 to 5,000 rev./min.
H flow rate = 90 to 105 cc./min.
L flow rate = 125 to 150 cc./min.
Volumes = cc. at 25° C.
P_{LO} = lb./sq. in. gauge

Light-liquid holdup

Run	P_{LO}	V_L	Run	P_{LO}	V_L
$H75$	98	573.67	$G6$	113	590.61
$H78$	98	573.76	$G8$	118	618.86
$G3$	104	580.70	$H53$	120	607.23
$G7$	111	591.21	$H55$	122	615.03
$G5$	113	590.02			

Heavy-liquid holdup

Run	P_{LO}	V_H	Run	P_{LO}	V_H
$H77$	98	178.60	$H50$	114	154.02
$H88$	98	174.27	$H49$	116	147.66
$H89$	98	175.77	$H51$	118	150.44

Selected data (*4*) indicating the volume by either phase in the extractor as a function of P_{LO} are given in Table 1 for $P_{LO} < 100$ lb./sq. in. gauge and in Table 2 for $P_{LO} > 96$ lb./sq. in. gauge. The following equations were obtained from these data by least squares:

$$V_H = 663.14 - 5.03P_{LO} \qquad (12a)$$

$$V_L = 84.38 + 5.04P_{LO} \qquad (13a)$$

for light-liquid-out pressures less than 96 lb./sq. in. gauge and

$$V_H = 314.53 - 1.41P_{LO} \qquad (12b)$$

$$V_L = 417.83 + 1.57P_{LO} \qquad (13b)$$

for light-liquid-out pressures greater than 96 lb./sq. in. gauge. The foregoing equations and the data from which they were obtained are plotted in Figure 5.

The reason two sets of equations are required for the light-liquid-out pressure is that the constant b is common to both the slope and intercept of Equation (10) and therefore of Equations (12), (12*a*), and (12*b*). The data in Figure 5 indicate that the effective rotor thickness probably changes sharply somewhere between the center and periphery, as at a horizontal heavy-liquid take-off.

By substituting Equations (12*a*) and (13*a*) and Equations (12*b*) and (13*b*) into Equation (2), one obtains, respectively,

$$V_E = 747.52 + 0.01P_{LO} \qquad (2a)$$

$$V_E = 732.36 + 0.16P_{LO} \qquad (2b)$$

These equations indicate that the experimentally determined sum of the heavy- and light-liquid volumes in the extractor is sufficiently constant to warrant placing considerable confidence in the methods used to determine holdup.

A comparison of the first terms of the right-hand sides of Equations (13) and (13*a*) shows that

$$V_{SL} = 84.38 \text{ cc.} \qquad (16)$$

This value is 46 cc. lower than the value of $V_L = 130$ cc. calculated from Equation (13*a*) at incipient flooding in the light liquid out, for which P_{LO} is about 9 lb./sq. in. gauge. This 46 cc. represents the light liquid in the rotor at incipient flooding in the light liquid out,

$$(V_{CL})_{FL} = 46 \text{ cc.} \qquad (17)$$

At flooding in the heavy liquid out, $P_{LO} = 128$ lb./sq. in. gauge for this system at 5,000 rev./min. Under these conditions the rotor contains essentially

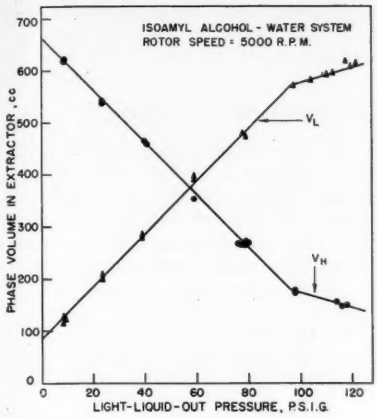

Fig. 5. Variation of rotor inventory with light-liquid-out pressure.

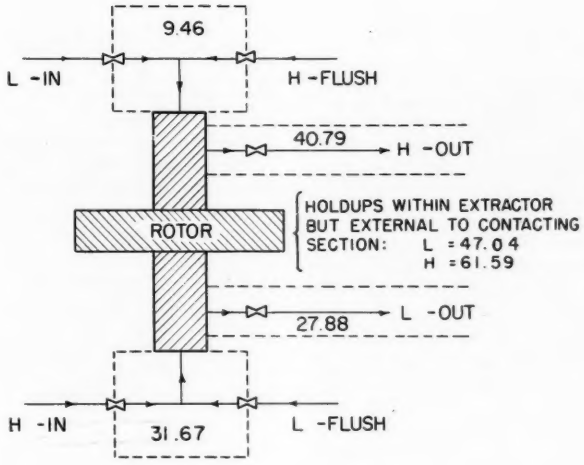

NOTE : ALL VOLUMES ARE IN CC

Fig. 6. Holdup of external extractor piping and internal lines and seals exclusive of contacting section.

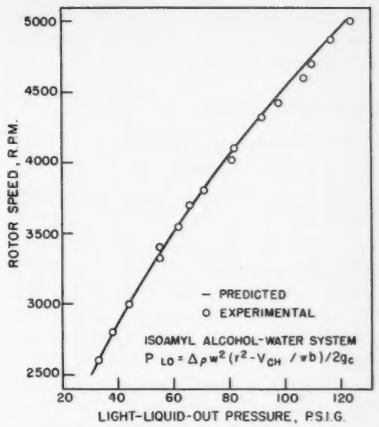

Fig. 7. Relation between rotor speed and light-liquid-out pressure at flooding in the heavy liquid out.

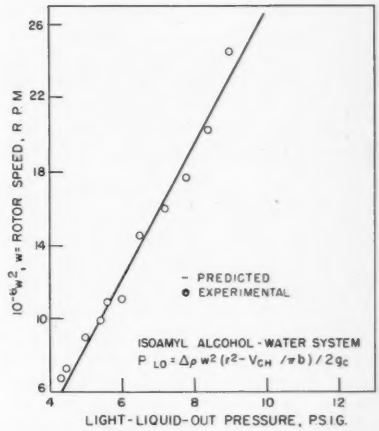
$10^{-6}w^2$, w= ROTOR SPEED, R.P.M.
LIGHT-LIQUID-OUT PRESSURE, P.S.I.G.
- PREDICTED
o EXPERIMENTAL
ISOAMYL ALCOHOL - WATER SYSTEM
$P_{LO} = \Delta\rho w^2 (r^2 - V_{CH}/\pi b)/2g_c$

Fig. 8. Relation between rotor speed and light-liquid-out pressure at flooding in the light liquid out.

no heavy liquid, and from Equation (12*b*)

$$V_H = V_{SH} = 134.05 \text{ cc.} \quad (18)$$

Substituting Equations (16) and (18) into Equation (4) gives

$$V_S = 84.38 + 134.05$$
$$= 218.43 \text{ cc.} \quad (4a)$$

Comparing Equation (18) and the first term on the right-hand side of Equations (12) and (12*a*), one obtains

$$V_C = 663.14 - 134.05$$
$$= 529.09 \text{ cc.} \quad (19)$$

Substituting Equations (4*a*) and (19) into Equation (1) gives

$$V_E = 529.09 + 218.43$$
$$= 747.52 \text{ cc.} \quad (1a)$$

The constants in Equations (1) through (6) have now been evaluated.

Since that portion of V_S outside the extractor was peculiar to the particular feed- and product-piping arrangement used in this investigation, it is of interest to report the portions of V_S both inside and outside the extractor. The quantities and locations of holdup in the piping external to the extractor are outlined by the broken lines in Figure 6. The volumes were obtained by measuring the liquid required to fill the particular lines. Holdup data are summarized in Table 3.

From Equation (19),

$$V_C = \pi b r^2 = 529 \text{ cc.} \quad (19)$$

and for $r = 7.71$ in., $b = 0.173$ in.

Prediction of Operating Limits

With numerical values of V_{CH} at either flooding limit and b, one may predict operating limits for various systems by substitution of the appropriate constants into Equation (9); for example, the rotor constants are $r = 7.71$ in. and $b = 0.173$ in., and the system constant is $\Delta\rho = 0.167$ g./cc. At flooding in the heavy liquid, $V_{CH} = 25$, and Equation (9) yields

$$(P_{LO})_{FH} = (4.86 \times 10^{-6} w^2)$$
lb.-force/sq. in. (20*a*)

At flooding in the light liquid, $V_{CH} = 529 - 46 = 483$ cc., and Equation (9) yields

$$(P_{LO})_{FL} = (0.447 \times 10^{-6} w^2)$$
lb.-force/sq. in. (20*b*)

where w is the rotor speed in revolutions per minute. These equations are plotted, in Figures 7 and 8, respectively, together with experimental data. The agreement between predicted and experimental val-

ues shown in Figures 7 and 8 indicates that Equation (9) predicts operating limits satisfactorily.

EXTRACTION STUDIES

Proposed Relation Among Stages, P_{LO}, and Flow-rate Ratio

The data of Barson (*2, 3*) at low light-liquid-out pressures and the data of Jacobsen (*4*) at high light-liquid-out pressures suggested Figure 9*A*, which shows lines of constant light-liquid flow rate R_L at constant heavy-liquid flow rate R_H on a plot of number of stages against P_{LO}. The relationship shown is based upon the idea that P_{LO} is an indication of mass transfer area. The curves shown are members of a family of curves, each representing a different operating line slope. Other systems might show an increase in number of stages with increasing light-liquid-out pressure. One may be able to estimate the qualitative effect of increasing light-liquid-out pressure from a knowledge of the relative resistances to mass transfer in the two phases. The useful feature of this relationship is that with a small number of laboratory runs one should be able to map in a family of curves for a particular system and thus rapidly determine optimum operating conditions.

Since the heavy-liquid rate is the same for both curves shown in Figure 9*A*, these curves are also lines of constant-flow-rate ratio. A cross plot of Figure 9*A* would give Figure 9*B*, which shows lines of constant P_{LO} (constant rotor inventory) at constant heavy-liquid flow rate on a plot of number of stages against flow-rate ratio. These curves are similar to those in Figure 8 of Barson and Beyer's paper (*1*) for conditions of incipient flooding in the light liquid out, as under these conditions the rotor inventory is essentially constant.

Materials and Methods

Each stream experiences a temperature rise of approximately 10°C. in passing through the extractor. Reagent-grade boric acid was used as a solute in the isoamyl alcohol–water system for all extraction studies because this system has a straight equilibrium curve independent of temperature between 15° and 45°C. The equilibrium data for this system were obtained from Barson's work (*2*).

The number of theoretical stages extracting boric acid from isoamyl alcohol with water was calculated from the expression

$$N = \frac{\log\left(1 - \frac{(y_2 - y_1)(m - a)}{a(y_1 - mx_1)}\right)}{\log\,(a/m)} \qquad (21)$$

Representative data are given in Table 4. A complete discussion of composition-analysis procedure, material-balance errors, and attainment of steady state is given in reference *4*.

Experimental Relation Among Stages, P_{LO}, and Flow-rate Ratio

Figure 10, a plot of number of stages against light-liquid-out pressure for several flow-rate ratios, supports the relationship proposed in Figure 9*A*. The following additional conclusions may be drawn from Figure 10. First, more stages are obtained with this system when extracting from alcohol to water at low light-liquid-out pressures than at high light-liquid-out pressures. Second, increasing the flow-rate ratio increases the number of stages at low light-liquid-out pressures but has little effect at high light-liquid-out pressures. Third, the effect of flow-rate ratio on the relationship between number of stages and light-liquid-out pressure becomes increasingly important at higher flow-rate ratios. The effect of total throughput on the relationship between number of stages and light-liquid-out pressure was found to be small experimentally. Although the rate of mass transfer should increase with increasing throughput because of greater turbulence, the contact time in any one stage would be correspondingly shorter so that stage efficiency might remain unchanged.

APPLICATION TO OTHER SYSTEMS

The procedure for applying the methods presented above to other systems using similar extractors involves two steps. First, the constants in an equation for predicting flooding limits are estimated from holdup measurements. Then a few extraction runs are made to estimate optimum operating conditions.

For an extractor having the same effective rotor dimensions and holdup as the

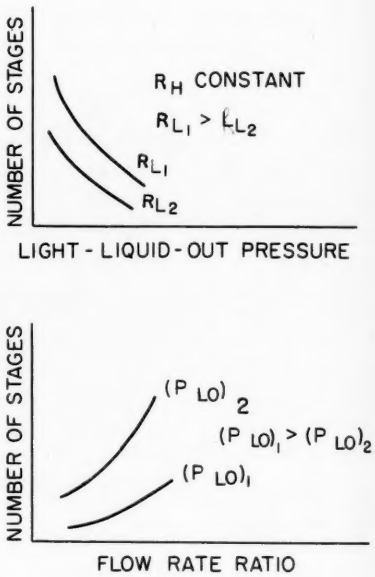

Fig. 9. Correlation among number of stages, flow-rate ratio, and light-liquid-out pressure.

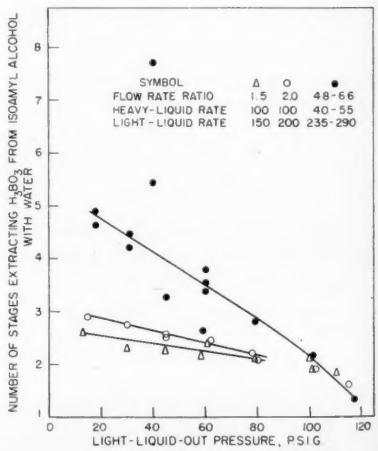

Fig. 10. Variation of number of stages with light-liquid-out pressure and flow-rate ratio.

TABLE 3. SUMMARY OF EXTRACTOR HOLDUP DATA

Source of holdup		Holdup, cc.
Rotor holdup, V_C		529.09
Internal LL line and seal volume	47.04	
Internal HL line and seal volume	61.59	
Total internal line holdup		108.63
Extractor holdup		637.72
External LL line holdup	37.34	
External HL line holdup	72.46	
Total external line holdup		109.80
Equipment holdup, V_E		747.52
L line holdup, V_{SL}	84.38	
H line holdup, V_{SH}	134.05	
Total line holdup, V_S		218.43
L in rotor at flooding in the light liquid out, $(V_{CL})_{F_L}$		46
H in rotor at flooding in the heavy liquid out, $(V_{CH})_{F_H}$		25

Table 4. Data from Representative Extraction Runs

All concentrations expressed as grams of H_3BO_3 per liter
Rotor speed: 4,950 to 5,000 rev./min.

Run	Feed conc.	Solvent conc.	Raffinate conc.	Extract conc.	Material balance, % error	H flow rate, cc./min.	L flow rate, cc./min.	Flow-rate ratio	P_{LO}, lb./sq.in. gauge	Number of stages
*A*9	7.628	0.096	1.164	13.64	10.6	103.5	193.9	1.873	116	2.36
*A*13	2.207	0.079	0.572	4.462	5.1	102.9	261.8	2.544	108	2.03
*A*20-1	8.037	0.083	0.153	4.291	0.6	106.2	57.0	0.537	120	2.13
*B*12	7.923	0.042	0.696	10.54	4.9	98.6	150.4	1.523	44	2.27
*B*17	7.878	0.063	0.981	13.51	5.3	99.1	203.6	2.054	62	2.49
*B*36	7.858	0.319	4.240	23.30	7.4	40.1	273.4	5.917	101	2.19
*B*40-1	7.845	0.288	3.683	25.17	2.1	46.5	283.7	6.101	61	3.48
*B*40-2	7.845	0.288	3.705	25.31	2.9	45.5	282.9	6.213	61	3.57
*B*40-3	7.845	0.288	3.627	25.45	4.7	45.9	286.7	6.252	61	3.78
*B*41-1	7.845	0.288	3.527	26.42	4.9	45.4	288.6	6.355	40	5.45
*B*41-2	7.845	0.288	3.503	26.83	3.7	45.1	286.1	6.343	40	7.71
*B*41-3	7.845	0.288	3.643	26.50	1.8	45.3	287.4	6.349	40	5.48

extractor used in this investigation, one may use $r = 7.71$ in., $b = 0.173$ in., $V_C = 529$ cc., $(V_{CL})_{FL} = 46$ cc., and $(V_{CH})_{FH} = 25$ cc. to calculate the maximum permissible rotor speed (within the pressure limitations of the equipment) from Equation (8) and to estimate both flooding limits as a function of rotor speed from Equation (9).

For an extractor having different rotor dimensions and holdup from those of the extractor in this investigation it is suggested that the procedure outlined below be followed, a two-phase system in which no extraction takes place being used. Working with such a simple two-phase system will provide a background of experience that will be useful in explaining and circumventing apparently anomalous behavior with more complex systems.

The procedure is as follows: the light-liquid-in pressure is measured at several rotor speeds; the light-liquid-out pressure is measured at both incipient flooding and flooding in the heavy liquid out at a single rotor speed; and the holdup of each phase is measured at this latter rotor speed and at least two rather high and two rather low light-liquid-out pressures, including incipient flooding in the light liquid out. These data are then used to estimate r, b, V_C, $(V_{CL})_{FL}$, $(V_{CH})_{FH}$ and the holdups of the various sections of the extractor.

The rotor radius r is estimated by substituting the data for light-liquid-in pressure as a function of rotor speed into Equation (8).

The equipment holdup V_E is estimated as the sum of V_L and V_H at each light-liquid-out pressure, according to Equation (2).

The light-liquid-holdup measurements as a function of light-liquid-out pressure are used to obtain the equation

$$V_L = a_1 + a_2 P_{LO} \qquad (14a)$$

for low light-liquid-out pressures and the equation

$$V_L = a_3 + a_4 P_{LO} \qquad (14b)$$

for high light-liquid-out pressures, where the a_i, $i = 1$ to 4, are estimated from the data when plotted as in Figure 5.

The light-liquid line volume is estimated as a_1. The light liquid in the rotor at flooding in the light liquid out $(V_{CL})_{FL}$ is estimated as $a_2 P_{LO}$ when P_{LO} is given its value at flooding in the light liquid out. The rotor holdup V_C is estimated as the difference between V_L at flooding in the heavy liquid out and V_{SL}, where V_L at flooding in the heavy liquid out is computed from the measured value of P_{LO} under these conditions and Equation (14*b*).

The effective rotor width b is estimated from $\pi br^2 = V_C$.

The heavy-liquid line volume is estimated as

$$V_{SH} = V_E - V_C - V_{SL} \qquad (22)$$

The heavy liquid in the rotor at incipient flooding in the heavy liquid out $(V_{CH})_{FH}$ is estimated as the heavy liquid flushed from the extractor while it is being stopped, after no more heavy liquid can be flushed from the spinning rotor. This step completes the estimation of constants required for the prediction of flooding limits.

The second part of the procedure for applying the methods presented above to other systems involves making at least nine extraction runs: at three flow-rate ratios and at low, intermediate, and high light-liquid-out pressures. Such data should permit one to map in a family of curves on a plot of stages against light-liquid-out pressure, such as shown in Figures 9 and 10.

It should be noted that the system studied was characterized by a small change in density difference between the inlet and effluent streams. When large changes in density occur as the result of solute transfer, the proper method for evaluating the $\Delta\rho$ term has not been established.

NOTATION

V_E = extractor holdup, cc.
V_C = rotor holdup, cc.
V_S = line and seal holdup, cc.
V_H = heavy-liquid holdup, cc.
V_L = light-liquid holdup, cc.
V_{CH} = heavy-liquid rotor holdup, cc.
V_{CL} = light-liquid rotor holdup, cc.
V_{SH} = heavy-liquid line and seal holdup, cc.
V_{SL} = light-liquid line and seal holdup, cc.
R_L = light-liquid flow rate, cc./min.
R_H = heavy-liquid flow rate, cc./min.
P_{LI} = light-liquid-in pressure, lb./sq. in. gauge
P_{LO} = light-liquid-out pressure, lb./sq. in. gauge
$\Delta\rho$ = density difference between two phases, g./cc.
w = rotor speed, rev./min.
r = rotor radius, in.
b = rotor width, in.
g_c = gravitational constant
N = number of theoretical stages
m = slope of equilibrium line
a = slope of operating line
y_2 = feed concentration, g./liter
x_1 = solvent concentration, g./liter
y_1 = raffinate concentration, g./liter
x_2 = extract concentration, g./liter

LITERATURE CITED

1. Barson, N., and G. H. Beyer, *Chem. Engr. Progr.*, **49**, 243 (1953).
2. ———, M.S. thesis, Iowa State College Library, Ames, Iowa (1952).
3. ———, personal communication, Institute for Atomic Research, Iowa State College, Ames (1953).
4. Jacobsen, F. M., Ph.D. thesis, Iowa State College Library, Ames, Iowa (1954).
5. Morgenthaler, J. H., G. T. Keene, W. L. Mann, and A. A. Wasserman, U. S. Atomic Energy Commission *Rept. KT-110* (1951).
6. Poffenberger, N., personal communication, Dow Chemical Company, Midland, Michigan (1955).

Presented at A.I.Ch.E. Houston meeting

Viscosity of Liquids

LYLE F. ALBRIGHT and JOHN LOHRENZ

University of Oklahoma, Norman, Oklahoma

Three viscosity correlations were tested for liquids at their boiling points. Compounds studied included normal paraffins, branched-chain hydrocarbons, aromatics, halogenated methanes and ethanes, water, and aliphatic alcohols. The correlations were tested for the most part with viscosity and thermodynamic data found in the literature. Some experimental viscosity measurements were made, however, for normal paraffins from pentane to octane at temperatures up to about 300°F., which is higher than has previously been reported.

Two correlations are based on Eyring's theory of absolute reaction rates. The third is based on the compressibility factor of the saturated liquid, and this correlation is unique, as all available data for normal paraffins with eight or more carbon atoms are represented by a single curve. The three correlations presented here can be used to extrapolate viscosity data over large temperature ranges up to the critical temperature. Logical predictions of the viscosities of related compounds are possible.

The theory of absolute reaction rates (*17*) was applied to the viscosity of liquids by Eyring and coworkers (*16, 18, 22, 27, 39*). It was postulated that before a molecule can flow (move) a "hole" must be available for it to move into. Energy is required to make this hole, and the following equation was developed to represent the relationship between the free energy of activation and the viscosity in centipoises:

$$\mu = \frac{hN}{V} e^{\Delta F_{vis}/RT} \qquad (1)$$

Since a flow process can be considered to be at constant volume, the energy required to make a hole the size of a molecule is the internal energy of vaporization. It was thought (*22, 39*) that the relationship between the internal energy of vaporization and the free energy of activation might be significant. The ratio of these two values has been designated the energy ratio n:

$$n = \frac{\Delta E_{vap}}{\Delta F_{vis}} \qquad (2)$$

This energy ratio was reported (*22, 39*) to be equal to approximately 2.45 for numerous liquids including water, alcohols, and hydrocarbons. The alcohols and hydrocarbons tested or the temperatures of any of the liquids however were not specified. Since at the critical temperature the internal energy of vaporization is zero and since the free energy of activation is still presumably finite, the energy ratio is also probably zero at this temperature. It appears, therefore, that the energy ratio is a function of temperature.

Another equation (22) based on the theory of absolute reaction rates is as follows:

$$\mu = \frac{N}{V} (2\pi mkT)^{1/2} v_f^{1/3} \cdot \exp\left[(\Delta E_{vap}/n' + PV/n'')/RT\right] \qquad (3)$$

The numerator of the exponent is equal to the internal energy of activation. It was shown that the viscosity data of several compounds, including hydrocarbons, could be correlated at a given temperature over a large pressure range within about 30% accuracy. As far as can be determined, however, the equation was tested for a given compound at only one temperature.

Viscosity data have been extrapolated frequently in the past by means of the following plots: (1) viscosity vs. temperature, (2) logarithm of viscosity vs. the reciprocal of absolute temperature, and (3) logarithm of viscosity vs. the logarithm of absolute temperature. All these plots approximate straight lines over relatively short temperature ranges, but it seems as if accurate extrapolations are not possible for wide ranges of conditions. The present investigation was made, as a result, to develop better correlations or extrapolation methods. Hydrocarbons, chlorofluoro derivatives of methane and ethane, aliphatic alcohols, and water were studied primarily. A search was made of the literature to find viscosity, thermodynamic, and physical-property data of these compounds. In addition, some experimental viscosity measurements were made for normal paraffin hydrocarbons from butane to octane. Part of these measurements were at temperatures higher than those previously reported. Correlations based on Eyring's theory of absolute reaction rates and on the compressibility factor of the liquid were developed. These correlations are useful in extrapolating viscosity data over a wide temperature range.

APPARATUS AND MATERIAL USED

Viscosity measurements were made in a Humble-type high-pressure (10,000 lb./sq. in.) rolling-ball viscometer manufactured by Engineering Products, Inc. No corrections

Lyle F. Albright is at Purdue University, West Lafayette, Indiana, and John Lohrenz at the University of Kansas, Lawrence, Kansas.

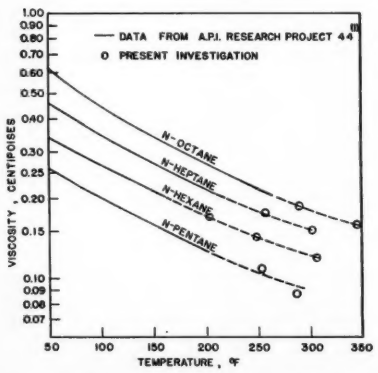

Fig. 1. Viscosity measurements of light-paraffin hydrocarbon liquids at their boiling points.

Table 1. Viscosity Data of This Investigation

Temp., °F.	μ, centipoises	n	T_r	ZZ_c
		n-pentane		
253.7	0.108	1.370	0.849	0.01110
286.0	0.086	1.216	0.883	0.01588
		n-hexane		
202.6	0.169	1.934	0.725	0.00289
248.1	0.142	1.703	0.774	0.00526
306.8	0.120	1.404	0.839	0.01002
		n-heptane		
256.6	0.175	1.864	0.737	0.00275
303.0	0.148	1.667	0.784	0.00500
		n-octane		
289.7	0.186	1.918	0.731	0.00238
347.2	0.158	1.661	0.787	0.00506

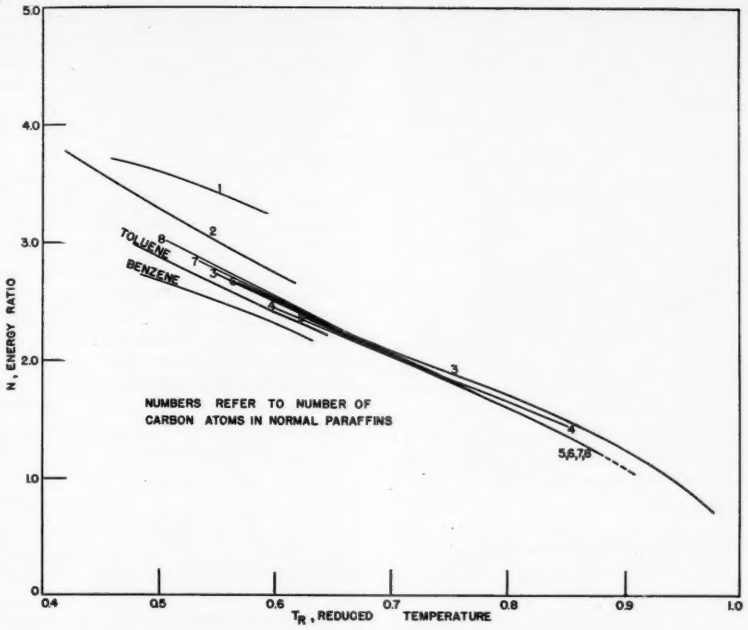

Fig. 2. Energy ratios of light normal paraffins and aromatics.

for pressure or temperature were required with the viscometer as the pressure was identical on each side of the sample chamber and because both the sample chamber and ball were constructed of steel. The steel ball was approximately ¼ in. in diameter, and the length of roll for the ball was about 7 in. A thyratron and sensitive ammeter were used to determine when the ball made contact at the bottom of the viscometer. A flexible high-pressure coil constructed of 1/16-in. O. D. tubing connected the viscometer to the auxiliary equipment, which included a calibrated pressure gauge, a vacuum pump, manometers, and connecting lines to the hydrocarbon cylinders. The viscometer and connections were immersed in a well-agitated oil bath. Bath temperatures were controlled manually with electric heaters to within 0.1°F. Calibrated mercury thermometers that could be read to within 0.1°F. were used for temperature measurements.

Research-grade *n*-butane, *n*-pentane, *n*-hexane, *n*-heptane, and *n*-octane were furnished by the Phillips Petroleum Company. The materials were reported to be at least 99% pure on a mole basis.

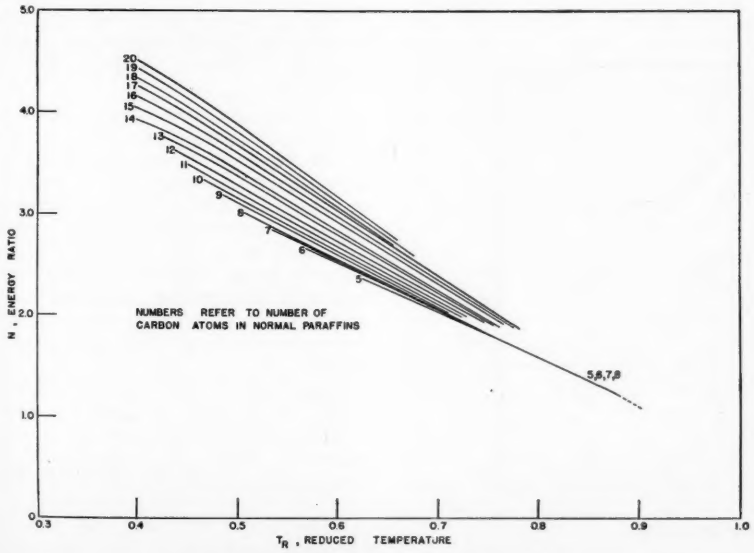

Fig. 3. Energy ratios of heavy normal paraffins.

OPERATION OF EQUIPMENT AND VISCOSITY RESULTS

After the viscometer was filled with a hydrocarbon sample, the apparatus was evacuated for several minutes to remove the air. The bath was then adjusted to a desired temperature, and the time of fall was measured with a stop watch until four or more readings reproducible within ± 0.15 sec. were obtained. The time of fall varied in this investigation from about 3 to 6 sec. The bath was then adjusted to other temperatures, and the procedure was repeated at each temperature. Data were obtained approximately every 50° from room temperature to about 300°F. for *n*-pentane to *n*-octane and up to 191°F. for *n*-butane.

Since viscosity information is available (*1*) for *n*-butane to *n*-octane at temperatures up to about 200°F., it was possible to construct a calibration curve for the viscometer, as suggested by Hubbard and Brown (*26*). The curve was a straight line except for slight curvature at low viscosities. The viscosity data of *American Petroleum Institute Project* 44 (*1*) agree within 5% of the "best" curve except for viscosity values of *n*-pentane from 120° to 160°F., which were about 8% low.

Using the calibration curve, one could determine the viscosities of *n*-pentane, *n*-hexane, *n*-heptane, and *n*-octane at temperatures up to approximately 100°F. above those previously reported. These results are shown in Table 1 and Figure 1. The viscosity data of this investigation produce "smooth" extensions of the curves, representing the results of *A.P.I. Project 44*.

CORRELATIONS BASED ON THE THEORY OF ABSOLUTE REACTION RATES

Viscosity data, in addition to those of this investigation, were obtained from the literature for paraffin and aromatic hydrocarbons (*1, 15, 21, 30, 34, 44, 45, 47*), chlorofluoro derivatives of methane and ethane (*5, 52, 53*), aliphatic alcohols (*51* through *54*), and water (*28, 33*). The free energy of activation for flow was calculated by means of Equation (1). Thermodynamic and physical information required for this equation was found in the literature for hydrocarbons (*1, 2, 4, 13, 19, 31, 35, 36, 43, 45, 46, 49, 50, 56*), halogenated hydrocarbons (*6* through *9, 11, 14, 20, 23, 56*), aliphatic alcohols (*3, 10* through *13, 24, 25, 29, 37, 38, 40* through *42, 48, 52, 55, 56*), and water (*28*). For most compounds it was necessary to calculate the internal energy of vaporization from the latent heat of vaporization as follows:

$$\Delta E_{vap} = \Delta H_{vap} - P\Delta V \qquad (4)$$

Typical values of the energy ratio n are shown in Table 1. Plots of the energy ratio vs. the reduced temperature for normal paraffin hydrocarbons, benzene, and toluene are shown in Figures 2 and 3. The energy ratio for these compounds decreases continuously with temperature. The correlations for all hydrocarbons are almost straight lines except at higher

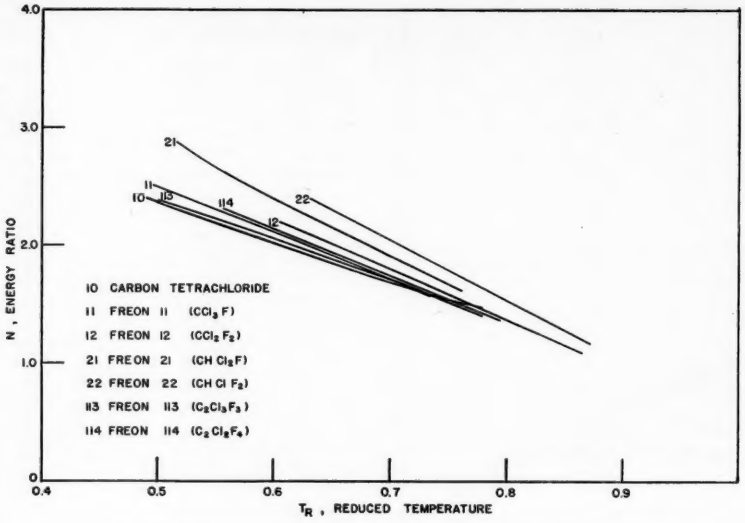

Fig. 4. Energy ratio of halogenated methanes and ethanes.

temperatures where all curve downward and tend to coincide as they approach zero at the critical temperature. Energy ratio values for a given reduced temperature, in general, decrease progressively from methane to pentane and then increase progressively from pentane to eicosane. For the most part, the curve for each hydrocarbon appears consistent. Possible exceptions may be the methane curve, the slope of which appears inconsistent with other hydrocarbons. The propane and butane correlations also seem rather inconsistent at high temperatures.

The energy-ratio curve of benzene is below that of toluene, and both lie below that of *n*-hexane. The viscosity and thermodynamic data for branch-chain saturated hydrocarbons are limited. As a result, it is impossible in most cases to calculate energy ratios over a large temperature range. Sufficient data are available though for these isomeric hydrocarbons with four to eight carbon atoms to indicate that the shapes of the energy-ratio curves are similar to those of normal and aromatic hydrocarbons. At a given reduced temperature the energy-ratio value of the isomeric hydrocarbon is always less than that of the comparable normal paraffin. Furthermore, the more branched the molecule is, the lower the energy ratio. The position of the branch chain apparently does not give any systematic trend of the energy-ratio values.

The halogenated hydrocarbon curves, as shown in Figure 4, are similar in shape to those of the regular hydrocarbons. The numerical values of the energy ratio for a given reduced temperature vary to a rather significant extent with the compound. The energy ratio is decreased with increased chlorine and simultaneous decreased fluorine content and with increased chlorine and decreased hydrogen content. The curves for both halogenated methanes and ethanes appear to be relatively consistent. A possible exception is the curve of carbon tetrachloride, the slope of which is rather different. Trichlorotrifluoroethane also seems to have a rather inconsistent curve at high temperatures.

The energy-ratio correlations for water and aliphatic alcohols are, in general, curved to a rather appreciable extent, as Figure 5 shows. In several cases the energy-ratio values pass through maxima at reduced temperatures from 0.5 to 0.7. As the number of carbon atoms increase and branched isomerization occurs, energy-ratio values decrease.

Efforts were also made to evaluate Equation (3) over a wide temperature range. The term pV/n'' was found to be insignificant at the relatively low pressures of saturated liquids if n' and n'' are of the same order of magnitude as previously indicated (*22*). Consequently, this term was dropped in the present study. The free volume v_f can be determined by use of velocity-of-sound data of both the gas and the liquid. Such data are apparently limited, but sufficient were found (*57*) to calculate free volumes of several compounds for, at least, one temperature. The following equation (*22*) was used to extrapolate values of the free volume:

$$v_f = c^3(v^{1/3} - d)^3 \qquad (5)$$

The term c depends on how the liquid molecules are packed, and it is reported to vary with temperature. It was assumed, however, that the molecules are packed cubically, for which c equals 2.0. By use of a known value of v_f, d was then computed for various compounds as shown in Table 2. Free volumes were determined over a wide temperature range.

Values for the free volume and viscosity at a given temperature were substituted into Equation (3), and n' was calculated. Values of n' determined in this manner are shown in Table 2. The viscosity was calculated over the temperature range comparable with that of the experimental data. The computed and experimental viscosity values of all

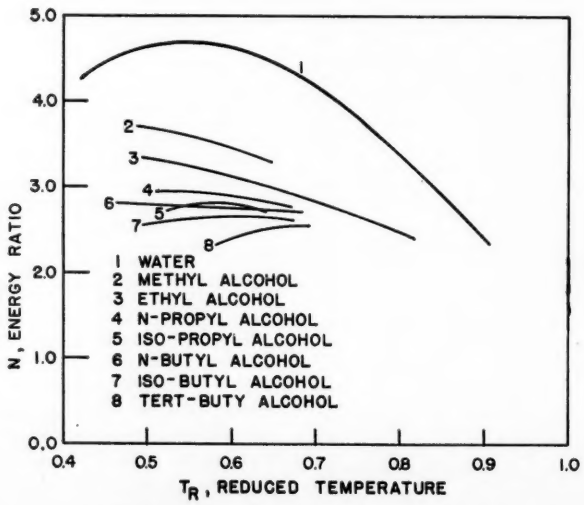

Fig. 5. Energy ratios of water and alcohols.

hydrocarbons tested agree within at least 10 to 30%. A typical comparison is shown in Table 3 for *n*-pentane. Other hydrocarbons studied include *n*-hexane, benzene, and toluene. Poorer agreement was found for carbon tetrachloride. In the case of water, Equation (3) is not applicable.

The free volume can also be calculated (*22*) by use of the internal energy of vaporization. Values calculated in this manner differ significantly and give poorer correlations of the viscosity than those determined from sonic data.

COMPRESSIBILITY-FACTOR-PRODUCT CORRELATION

The viscosity of the saturated liquid was correlated as a function of the compressibility factor product ZZ_c. This term is the product of the compressibility factor of the saturated liquid Z and the compressibility factor at the critical point Z_c. Typical values for ZZ_c are shown in Table 1. The correlation was tested for normal paraffins and freons by plotting the logarithm of viscosity in centipoises vs. the logarithm of ZZ_c as shown in Figures 6 and 7 respectively. The curve for each compound tested was found to be almost a straight line except, in some cases, at high values of ZZ_c, that is, at high temperatures. For a given value of ZZ_c viscosity values increase for paraffins from methane to octane. The unique feature of this correlation, however, is that all available viscosity data of normal paraffin hydrocarbons containing eight or more carbon atoms are represented within 3.0% by a single curve. Sufficient data are also available to test these correlations for branched-chain paraffins with up to eight carbon atoms. In general, for a given ZZ_c value isomerized hydrocarbons have higher viscosities than straight-chain hydrocarbons. Some of the less branched isomers of heptane and octane, however, have lower viscosity values. Although the ranges of data are limited, it appears as if the correlations for the isomerized compounds are relatively parallel to those of the normal paraffins.

The curves for the halogenated methanes and ethanes are also almost straight lines. For a given value of the compressibility-factor product, it was found that the viscosity increases with increased chlorine and decreased fluorine content, increased chlorine and decreased hydrogen content, and increased number of carbons in the atom. The carbon tetrachloride curve has a rather different slope from that of any of the other freons.

DISCUSSION OF RESULTS

The experimental viscosity measurements obtained from about 200° to 300°F. for *n*-pentane to *n*-octane appear to extend consistently the viscosity results of *A.P.I. Project* 44. This is to be expected as the viscometer was calibrated by use of the results of that study. It is estimated that the calibration curve used for the present viscometer was accurate to within 5%. Experimental inaccuracies of temperature measurements and the time of fall of the ball may cause, for any given viscosity measurement, errors as high as 5%. The total errors of the viscosity results of this investigation are probably less than 10%.

The graphical viscosity correlations (Figures 2 to 7) developed in this study were examined in regard to the position and slope of the various curves. In most cases, if a certain compound appears inconsistent on the graph based on the theory of absolute reaction rates, it is also inconsistent in the correlation of the compressibility-factor product. Compounds in this category are methane, carbon tetrachloride, and at high temperature both propane and *n*-butane. It is possible that the curves for these compounds as shown on the graphs are correct, but it seems more likely that the curves are somewhat incorrect because of inaccuracies of the viscosity and/or thermodynamic data. Since viscosity and saturated liquid volumes are the common factors of both correlations, these seem like the most questionable terms. Trichlorotrifluoroethane appears somewhat inconsistent at higher temperatures on Figure 4 only. Apparently values of the internal heat of vaporization for this compound are somewhat in error.

Earlier it was reported (*22, 39*) that the energy ratio n of Equation (2) was a constant equal to approximately 2.45 for many compounds. As determined here (*see* Figures 2 to 5), energy-ratio values vary, however, from at least 1.0 to 4.7. Even at the normal boiling points of the liquids, the values vary from about 1.9 to 4.7. On the basis of the present investigation, it must be concluded that the energy ratio is definitely a function of temperature and varies over a relatively wide range of values.

Although graphs such as Figures 2 to 5 are relatively complicated to construct, they are considered more accurate for extrapolation purposes than simpler plots of viscosity vs. some function of temperature. The energy-ratio curves were found not only to be relatively straight over most of the temperature range, but in addition to extrapolate to zero at a reduced temperature of one. As Figures 2 to 5 indicate, however, the curvatures of these correlations must be large at high temperatures. In addition, it was found that the energy-ratio values at high temperatures were sensitive to small changes of the values of viscosity, saturated liquid volume, and latent heat of vaporization. Near the critical temperature the energy-ratio extrapolation is, as a result, only an approximate guide for predicting viscosity values.

It was noted that several of the normal paraffin curves of the energy-ratio values tend to coincide at high temperatures, e.g., *n*-pentane to *n*-octane. If it is assumed that the curves of the heavier normal paraffins coincide at higher temperatures, it is possible to calculate viscosity values for several of the compounds at temperatures much higher than those reported in the literature. Viscosity values for *n*-octane were calculated at reduced temperatures of 0.85 and 0.90, as shown in Table 4, and the octane line of Figure 6 was extrapolated as shown by the dotted portion of the curve.

The correlation based on the compressibility-factor product is considered empirical in nature, but a single curve was found to represent all available viscosity data for normal paraffins from octane to eicosane. It seems logical to assume, therefore, that the paraffins higher than

Table 2. Values of n' and d for Compounds Studied

	$d \times 10^8$	n'
n-Pentane	5.22	4.16
n-Hexane	5.55	4.35
Benzene	4.90	2.11
Toluene	5.24	2.35
Carbon tetrachloride	5.03	3.48
Water	2.66	5.4

Table 3. Viscosity of Liquid *n*-Pentane

t, °F.	Experimental viscosity, centipoises	Viscosity calculated with Equation (3)	% Deviation
68	0.235*	0.235	0.0
95	0.207*	0.215	+ 4.0
160	0.150*	0.170	+13.3
200	0.126*	0.147	+16.7
253.7	0.108†	0.123	+13.9
286.0	0.086†	0.111	+29.0

A.P.I. Project 44.
†Present investigation.

Table 4. Extrapolation of *n*-Octane Viscosity Values

T_R	Temp., °F.	n	ΔE_{vap}, cal./g. mole	V_L, cc./g. mole	μ	ZZ_c
0.85	410	1.37	−10,310	225	0.137	0.00908
0.90	462	1.10	− 8,560	256	0.109	0.01609

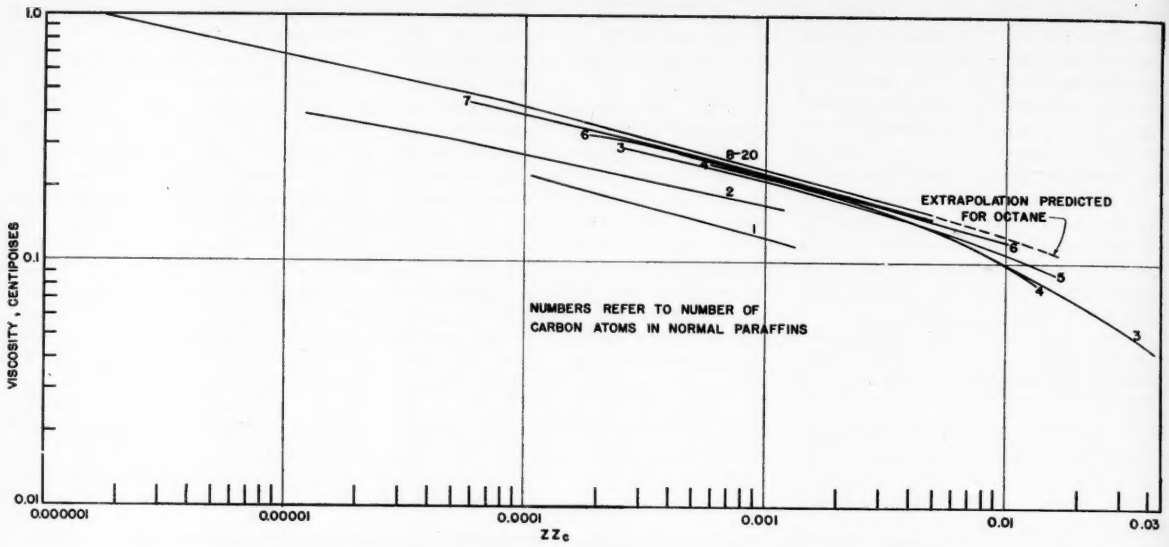

Fig. 6. Viscosity of normal paraffins as a function of compressibility-factor product.

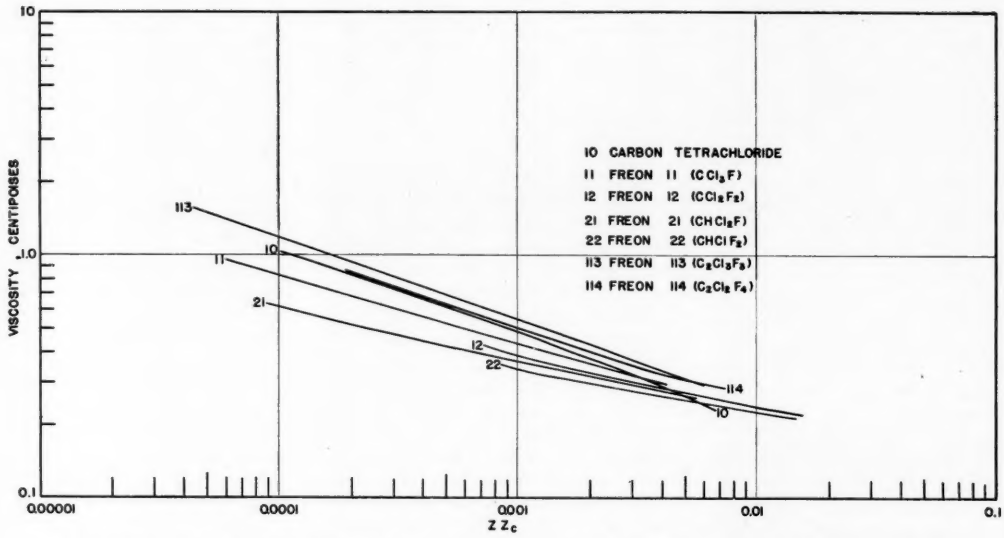

Fig. 7. Viscosity of halogenated methanes and ethanes as a function of compressibility-factor product.

eicosane are also represented by the same curve. This represents a useful method in estimating the viscosities of compounds for which the literature reports no data. It would be interesting, however, to check this theory by obtaining some viscosity data for a few such compounds. In addition, this single curve can be used to extrapolate the viscosity of the normal paraffins from octane to eicosane over the entire temperature range covered. In many cases this serves as a means for an extrapolation over an extremely large range of temperatures.

The available viscosity data for many branched-chain hydrocarbons are limited. Both graphical viscosity correlations are useful for extrapolation purposes if it is assumed, as seems likely, that the slopes of their curves are similar to those of related normal hydrocarbons. As more data become available for these compounds, it may be possible to establish systematic trends for predicting the energy ratio (and viscosity) of branched-chain compounds by comparison with normal hydrocarbons.

The two graphical correlations should be of value in predicting the viscosity of compounds similar to those studied here; for example, by comparison of the curves of Figures 4 and 7 for CCl_4, CCl_3F, and CCl_2F_2, it is probable that the approximate positions of the $CClF_3$ and possibly even the CF_4 curve could be estimated on each graph.

The energy-ratio curves for the associated liquids are unique primarily because some pass through a maximum. This abnormality is not surprising when it is considered that the internal energy of vaporization produces a "hole" the size of a simple molecule. It is known that associated liquids may be aggregrates of two or more simple molecules. It is possible that if the actual energy required to form a full-size molar hole were known, the energy-ratio curves would be similar in shape to those of unassociated molecules.

The results of this study indicate that Equation (3) can be used to correlate with at least fair accuracy the viscosity data of several hydrocarbon liquids over large temperature ranges. The method used for evaluating free volumes by means of some sonic data and Equation (4) was shown to be superior, at least for correlation purposes, to the method using the internal energy of vaporization. The method used here is considered, however, only an approximation. It is possible that when more accurate methods become available for calculating free volumes Equation (3) will correlate the viscosity data even better than the present results indicate. Although only four hydrocarbons were tested in regard to Equation (3), it is probable that other hydrocarbons and related compounds could be correlated when accurate free-volume data become available. Viscosity data for water could not, however, be correlated by this equation, and so it might be concluded that associated liquids could not be, either. Since it has been reported (*22*) that the equation correlates fairly well the viscosity data of liquid hydrocarbons at a given temperature over a large pressure range, it seems as if the equation will represent with fair accuracy the viscosity data of these liquids at all pressures and temperatures.

CONCLUSIONS

The viscosity correlations which were tested are useful for extending viscosity data over larger temperature ranges than was previously possible. In addition, it is frequently possible to predict the viscosities of compounds in homologous series.

ACKNOWLEDGMENT

The Dow Chemical Company gave generous financial aid in the form of a research fellowship. The Phillips Petroleum Company furnished the hydrocarbon samples for the viscosity study, and the Continental Oil Company furnished the oil for the bath.

NOTATION

c = packing coefficient
d = incompressible diameter of molecule
h = Planck's constant
k = Boltzmann constant
n, n', and n'' = energy ratios
N = Avogadro's number
m = reduced mass
P = vapor pressure
R = gas constant
T = absolute temperature
T_r = reduced temperature
v = molecular volume of saturated liquid
V = molar volume of saturated liquid
v_f = free volume
Z = compressibility factor of liquid, PV/RT
Z_c = compressibility factor at critical point, P_cV_c/RT_c
ΔE_{vap} = internal energy of vaporization
ΔH_{vap} = latent heat of vaporization
ΔF_{vis} = free energy of activation for flow
ΔV = volume change for vaporization
π = 3.1416
μ = viscosity, centipoises

LITERATURE CITED

1. *Am. Petroleum Inst. Research Proj.* 44, Carnegie Institute of Technology, Pittsburgh (1953).
2. Barkelew, C. H., J. L. Valentine, and C. O. Howard, *Chem. Eng. Progr.*, **43**, 25 (1947).
3. Bartoszewiszowna, E., *Roczniki Chem.*, **11**, 90 (1931).
4. Beall, I. N., *Refiner Natural Gasoline Mfr.*, **14**, 588 (1935).
5. Benning, A. F., and W. H. Markwood, Jr., *Refrig. Eng.*, **47**, 93 (1939).
6. Benning, A. F., and R. C. McHarkness, "The Thermodynamic Properties of Freon-11," E. I. duPont deNemours and Co., Inc., Wilmington, Del. (1938).
7. ———, "The Thermodynamic Properties of Freon-21," E. I. duPont deNemours and Co., Inc., Wilmington, Del. (1939).
8. ———, "The Thermodynamic Properties of Freon-113," E. I. duPont deNemours and Co., Inc., Wilmington, Del. (1938).
9. ———, "The Thermodynamic Properties of Freon-114," E. I. duPont deNemours and Co., Inc., Wilmington, Del. (1944).
10. Brown, J. C., *J. Chem. Soc.* (*London*), **89**, 311 (1906).
11. Buffington, R. M., and W. K. Gilkey, *Am. Soc. Refrig. Engrs. Circ.*, **12** (1931).
12. Centnerzwer, M., *Z. physik. Chem.*, **49**, 199 (1904).
13. Dreisbach, R. R., "Pressure—Volume—Temperature Relationship of Organic Materials," 3rd ed., Handbook Publishers, Inc., Sandusky, Ohio (1952).
14. Eiseman, B. J., Jr., *Refrig. Eng.*, **60**, 68 (1952).
15. Evans, E. B., *J. Inst. Petroleum Technol.*, **24**, 38, 321 (1938).
16. Ewell, R. H., and H. Eyring, *J. Phys. Chem.*, **41**, 240 (1937).
17. Eyring, H., *J. Chem. Phys.*, **3**, 107 (1935).
18. *Ibid.*, **4**, 283 (1936).
19. Fiock, E. F., D. C. Ginnings, and W. B. Holton, *J. Research Natl. Bur. Standards*, **6**, 881 (1931).
20. Fisher, R., and T. Reichel, *Mikrochemie ver. Michrochim. Acta*, **31**, 103 (1943).
21. Geist, J. M., and M. P. Cannon, *Ind. Eng. Chem., Anal. Ed.*, **18**, 611 (1946).
22. Glasstone, S., K. J. Laidler, and H. Eyring, "The Theory of Rate Processes," McGraw-Hill Book Company, Inc., New York (1941).
23. Graham, D. P., and R. C. McHarness, "The Thermodynamic Properties of Freon-22," E. I. duPont deNemours and Company, Inc., Wilmington, Del. (1945).
24. Herz, W., and E. Neukirch, *Z. physik. Chem.*, **110**, 23 (1924).
25. Hodgman, C. D., ed., "Handbook of Chemistry and Physics," 34th ed., Chemical Rubber Publishing Company, Cleveland, Ohio (1952).
26. Hubbard, R. M., and G. G. Brown, *Ind. Eng. Chem., Anal. Ed.*, **15**, 212 (1943).
27. Kincaid, J. F., H. Eyring, and A. F. Stearn, *Chem. Rev.*, **28**, 301 (1941).
28. Keenan, J. H., and F. G. Keyes, "Thermodynamic Properties of Steam," John Wiley and Sons, Inc., New York (1936).
29. Kohlbaum, G. W. A., *Z. physik. Chem.*, **13**, 14, 26, 577 (1898).
30. Lipkin, R. M., J. A. Davison, and S. S. Kurtz, Jr., *Ind. Eng. Chem.*, **34**, 976 (1942).
31. Matthews, C. S., and C. O. Hurd, *Trans. Am. Inst. Chem. Engrs.*, **42**, 55 (1946).
32. Maxwell, J. B., *Ind. Eng. Chem.*, **24**, 502 (1932).
33. Merrington, A. C., "Viscometry," Edward Arnold Company, London (1949).
34. Meyer, J., and B. Mylius, *Z. physik. Chem.*, **95**, 355 (1930).
35. O'Hara, J. B., and R. W. Fahien, Document 3327, Amer. Doc. Inst., Library of Congress, Washington 25, D. C.
36. Osborne, N. S., and D. C. Ginnings, *J. Res. Natl. Bur. Standards*, **39**, 453 (1947).
37. Parks, G. S., and B. Baron, *J. Am. Chem. Soc.*, **50**, 24 (1928).
38. Pitzer, K. S., *J. Am. Chem. Soc.*, **62**, 2413 (1941).
39. Powell, R. E., W. E. Roseveare, and H. Eyring, *Ind. Eng. Chem.*, **33**, 430 (1941).
40. Reid, R. C., and J. M. Smith, *Chem. Eng. Progr.*, **47**, 415 (1951).
41. Richardson, A., *J. Chem. Soc.* (*London*), **47**, 761 (1886).
42. Roland, M., *Bull. soc. chim. Belges*, **37**, 117 (1928).
43. Sage, B. H., and W. N. Lacey, "Thermodynamic Properties of Lighter Paraffin Hydrocarbons and Nitrogen," Am. Petroleum Inst., New York (1950).
44. ———, *Trans. Am. Inst. Mining Met. Engrs.*, **127**, 118 (1938).
45. ———, *Ind. Eng. Chem.*, **30**, 829 (1938).
46. Sage, B. H., D. C. Webster, and W. N. Lacey, *Ind. Eng. Chem.*, **29**, 1188 (1937).
47. Sage, B. H., W. D. Yale, and W. N. Lacey, *Ind. Eng. Chem.*, **31**, 223 (1939).
48. Smith, J. M., *Chem. Eng. Progr.*, **44**, 521 (1948).
49. Smits, A., and S. Connegeiter, *Z. physik. Chem.*, **A168**, 391 (1934).
50. Stearns, W. V., and E. J. George, *Ind. Eng. Chem.*, **35**, 602 (1943).
51. Thorpe, T. E., and J. W. Rodger, *Trans. Roy. Soc.* (*London*), **A185**, 397 (1894); **A186**, 397 (1895); **A189**, 71 (1897).
52. Timmermans, J., "Physico-Chemical Constants of Pure Organic Compounds," Elsevier Publishing Company, Inc., New York (1950).
53. Titani, T., *Bull. Inst. Research* (*Japan*), 671 (1927).
54. Tsakalatos, D. E., *Z. physik. Chem.*, **68**, 32 (1909).
55. Verkade, P. E., and J. Coops, Jr., *Rec. trav. chim.*, **46**, 903 (1927).
56. Young, S., *Sci. Pro. Soc. Dublin, N. S. XII*, 374 (1909–10).
57. "Landbolt-Bornstein Physikalisch- Chemische Tabellen," 5th ed., Julius Springer, Berlin (1923–1936).

Presented at A.I.Ch.E. Houston meeting

Rate of Flow and Mechanics of Bubble Formation from Single Submerged Orifices

IRVING LEIBSON, EUGENE G. HOLCOMB, ANTHONY G. CACOSO, and JOHN J. JACMIC

U. S. Army Chemical Corps, Camp Detrick, Maryland

A study has been made of the rate of flow and mechanics of bubble formation from single submerged orifices 1/64, 1/32, 1/16, and 1/8 in. in diameter installed in an 8-in. I.D. column operating in the air-water system. The coefficients of discharge obtained for sharp-edged orifices operating with this system indicate that the effective orifice discharge area for this type of operation is greater than that for an orifice of the same size and type operating at the same pressure ratio in the air-air system. The effective orifice discharge areas for a round-edged orifice operating in either the air-water or air-air systems appear to be identical at the same pressure ratio. The thick-plate orifice operating in the air-water system exhibits a constancy of discharge coefficient at ratios of the downstream to upstream pressures less than 0.33. Inasmuch as bubble formation occurring close to the downstream face of a sharp-edged orifice operating in the air-water system influences the effective orifice discharge area, liquid physical properties may be expected to be important in determining the rate of flow from this type of orifice for other gas-liquid systems.

In Part II photographic studies of bubble formation reveal that nonuniformity of bubble size is initiated by the onset of turbulence in the air stream flowing through the orifice. In the section of the laminar-flow range studied in this investigation ($200 < N_{Re} < 2{,}100$) the frequency of bubble formation is nearly constant with respect to Reynolds number. The bubble size is relatively uniform at a given Reynolds number and depends markedly upon orifice diameter. Stroboscopic examination reveals that as turbulence is fully developed for the air flow through the orifice, a counterclockwise spiraling, swirling motion of the air jet is initiated. In the turbulent-flow range the bubblesize–distribution data are fitted reasonably well by a logarithmic-normal-probability distribution. More data for bubble formation in other liquids (particularly liquids of low surface tension) are necessary before a general correlation for bubble size in gas-liquid systems can be developed.

I. Rate of Flow Studies

The introduction of a gas into a liquid through submerged orifices plays an important part in many gas-liquid contacting operations and processes. This investigation is concerned with bubble formation and behavior in the high-seal liquid-level systems encountered in the aeration of fermentation broths (*1* and *16*), gas reactions in liquids (*11*), foam flotation (*9*), and the air-lift pump (*6*). Previous workers (*7*, *10*, *14*, *15*, *21*, *22*, and *24*) have studied bubble formation as a function of flow rate in low-seal liquid-level systems analogous to bubble-cap and sieve-tray columns. In the majority of these investigations the rate of gas flow is small and the pressure drop across the orifice pulsates rapidly. Very few data are available in the literature for the rate of gas flow through a single submerged orifice discharging into a liquid. Part I of this investigation was undertaken to obtain data concerning the rate of air flow into water through single, submerged, sharp-edged orifices operating in both the subcritical and supercritical regions. A study of the mechanics of bubble formation at high rates of gas flow is reported in Part II.

Pressure ratio is defined in this paper as the ratio of the pressure downstream from the orifice to that upstream from the orifice. To review the concept of the critical pressure ratio, one may consider the case of an ideal nozzle operating in a gas-gas system. As the downstream pressure is decreased while a constant upstream pressure is maintained, the weight rate of discharge of the gas increases to a maximum (*8* and *18*) as the pressure ratio decreases to the critical pressure ratio. At the critical pressure ratio the linear velocity at the throat of the nozzle is equal to the velocity of sound in the gas at the throat temperature. The rate of discharge from an ideal nozzle is constant at all pressure ratios less than the critical pressure ratio. In the supercritical region the pressure at the throat of the nozzle (i.e., axial critical pressure) cannot decrease to a value less than the product of the upstream pressure and the critical pressure ratio. The ratio of this minimum pressure to the upstream pressure is constant for any given fluid. Values of the critical pressure ratio calculated at 15°C. are 0.49 for monatomic gases, 0.53 for diatomic gases, and slightly higher for gases of greater atomic complexity.

In the case of a sharp-edged orifice operating in a gas-gas system, the stream filaments of the orifice jet converge to a minimum section (*vena contracta*) downstream from the orifice and then diverge (*23*). The ratio of throat length to orifice diameter is 0.125 or less for a sharp-edged orifice and the cross section of the upstream edge of an orifice of this type is square (*2*). The upstream edge of a round-edged orifice is beveled to minimize the constriction of stream filaments at the throat of the orifice. In the supercritical region, as the pressure downstream from a sharp-edged orifice is decreased, the *vena contracta* moves toward the orifice and increases in diameter. Although the linear velocity at the *vena contracta* is constant at sonic velocity, since the *vena-contracta* diameter increases, the weight rate of discharge is also increased. Cox and Germano (*4*) have interpreted the data of Stanton (*23*) and Schiller (*20*)

Irving Leibson is with Humble Oil & Refining Company, Baytown, Texas, and Anthony Cacoso is with General Foods Corporation, Hoboken, New Jersey.

to show that a 12% maximum increase over flow at the critical pressure ratio is attained as the pressure downstream from a sharp-edged orifice is reduced while a constant pressure is maintained upstream from the orifice. Other investigators (*5, 12, 17, 19*) studying gas-gas systems in the supercritical region have noted similar increases over flow at the critical pressure ratio.

Grace and Lapple (*12*) present orifice discharge coefficients calculated from the critical-orifice-flow equation (*8*) for sharp-edged and round-edged orifices varying from 1/32 to ⅛ in. in diameter. Their work indicated that at a given pressure ratio the orifice discharge coefficient increases as the orifice diameter is decreased.

The behavior of a thick-plate orifice operating in a gas-gas system is somewhat similar to that noted above for a sharp-edged orifice. However, several important differences have been shown in previous work. Grace and Lapple (*12*) reported a data scatter as great as 30% for the flow of air through an orifice 1/32 in. in diameter with a ratio of throat length to diameter of unity. Reynolds (*19*) studied the flow of air through thick-plate orifices ranging from ⅛ to ½ in. in diameter in 1/16-in. increments. Although Reynolds reported his orifices as sharp edged, the ratio of throat length to diameter was greater than 0.125 in all cases. His results contradict those of Grace and Lapple, inasmuch as Reynolds' data are reproducible within ±2% throughout the entire range. In several runs with a ¼-in. orifice, varying the ratio of throat length to orifice diameter from 0.25 to 0.75 produced no change in the adiabatic coefficient of discharge. Reynolds found this coefficient to be substantially constant at pressure ratios less than 0.33. Blackshear (*3*) corroborated this result using a thick-plate orifice 0.04 in. in diameter with a ratio of throat length to orifice diameter of 0.25. The constancy of the orifice coefficient of discharge at pressure ratios less than 0.33 is also shown by the data of Grace and Lapple for a thick-plate orifice 1/16 in. in diameter with a ratio of throat length to diameter of unity.

In summary, studies of gas-gas systems have shown that a marked increase in the rate of discharge from a sharp-edged orifice occurs as the pressure ratio is decreased below the critical pressure ratio. This increase is less marked for flow through a round-edged orifice. For flow through a thick-plate orifice, the coefficient of discharge is relatively constant at pressure ratios less than 0.33. For orifices from 1/32 to ⅛ in. in diameter, at a constant pressure ratio, the discharge coefficient increases as the orifice diameter is decreased.

Compared with a gas-gas system, the mechanics of flow for a gas-liquid system are further complicated by bubble formation with resultant gas-liquid mixing occurring close to the downstream face of the orifice. Furthermore, one would expect liquid physical properties to be of some importance in determining the rate of discharge of gases from submerged orifices. In this study interest has been focused on determining the effect of orifice diameter and type on the rate of discharge from single submerged orifices operating in the air-water system only.

APPARATUS

A schematic flow diagram of the experimental equipment is presented in Figure 1. Air at pressures up to 115 lb./sq. in. abs. was supplied to the column by a reciprocating-piston compressor. The flow of air to the column was controlled by a ¾-in. Keckley pressure-regulating valve in series with a ¼-in. needle valve. All air lines were ½-in. black-iron pipe with the exception of a section of ¾-in. pipe from the compressor to the pressure-regulating valve. The orifice assembly tube was made from 2-in. stainless steel tubing. A 12-ft. section of ½-in. metallic hose was provided upstream from the orifice assembly tube to permit the introduction of air at either the bottom or the side of the column with a minimum of piping changes.

The experimental column, shown in detail in Figure 2, consisted of an 82-in. section of 8-in. standard black-iron pipe. Clear vision over the entire length of the column was provided by two sets of three Lucite windows located in parallel planes. The window frames were fabricated from ⅜-in. angle iron welded to the outside of the column. Rubber-sheet gaskets 1/16 in. thick were sealed to the angle-iron window frames with an adhesive cement. The Lucite windows were clamped into place over these rubber gaskets by steel frames fitted with sixteen ⅜-in. machine bolts per window.

Air entered through the orifice assembly tube located at either the bottom or the side of the column. Suitable packing glands were provided to permit the location of the orifice at any point desired. For the runs made with a side entry, the orifice assembly tube was pointed down at an angle of 15 degrees from the horizontal.

Three metering instruments were used to determine the rate of air flow in most of the experimental runs. A range of air-flow rates from 0.0400 to 11.0 std. cu. ft./min. was covered. A rotameter was located upstream from the orifice to meter the flow of air to the column. From 0.0400 to 0.500 std. cu. ft./min. the rate of air flow from the column was measured by several wet-test meters of suitable capacity. From 0.500 to 2.00 std. cu. ft./min. this flow rate was measured by a specially calibrated standard rotameter and a wet-test meter of suitable capacity in series. Another specially calibrated standard rotameter was used to measure flow rates in the remainder of the experimental range.

In order to obtain accurate rates of air flow as a function of pressure ratio, pressures and temperatures were measured at several points in the flow system. The pressure was measured immediately downstream from the pressure-regulating valves, at the orifice-assembly tube, at the top of the experimental column, at the inlet and exit of the specially calibrated standard rotameter, and at the wet-test meter. Temperatures were measured at the orifice-assembly tube, at the top of the column, and at the wet-test meter. Pressures less than 32 lb./sq. in. abs. at all points upstream from the orifice were measured with mercury manometers. Pressures greater than 32 lb./sq. in. abs. were measured with Bourdon gauges calibrated with a dead-weight gauge tester at frequent intervals during the experimental work. In most cases pressures downstream from the orifice were measured by use of water manometers. However, for air-flow rates greater than 2.00 std. cu. ft./min. pressures downstream from the orifice were measured by use of mercury manometers. Temperatures were measured by dial thermometers calibrated in degrees centigrade.

The investigation included four different orifice diameters, 1/64, 1/32, 1/16, and ⅛ in. The actual dimensions of the orifices and the velocity of approach factors are summarized in Table 1. The throat-length–to–diameter ratio of the sharp-edged orifices was less than 0.125 in all cases. The round-edged orifice 1/16 in. in diameter was machined with an included bevel angle of 90 deg. on the upstream edge. Two thick-plate orifices, ⅛ in. in diameter, were machined with throat-length–to–diameter ratios of 0.891 and 0.816. The machining of all orifices was observed with a low-powered optical microscope to ensure a minimum of variation in diameter and throat length. The upstream edge of each orifice was lapped by means of fine jeweler's rouge. Before use, the actual dimensions of each orifice were obtained with a sliding-stage microscope equipped with a micrometer, reticule micrometer, and a matching substage condensing lens. Each diameter was measured five times and the maximum variation encountered was ±0.0002 in. for the 1/64-in. orifice and ±0.0004 in. for the ⅛-in. orifice. The orifices were reexamined at intervals during the experimental work and no change in orifice diameter was detected.

A view of the orifice-assembly tube is shown in Figure 3. The tube inside diameter

Table 1. Orifice Dimensions

Series	Nominal diameter, in.	Actual diameter, in. D_o	Velocity of approach factor β	Orifice throat length, L_o	L_o/D_o
B	1/64	0.0165	0.00900	.....	< 0.125
C	1/32	0.0323	0.0176	.....	< 0.125
D	1/16	0.0635	0.0346	.....	< 0.125
D-R	1/16	0.0641	0.0350	.....	.....
A	1/8	0.1261	0.06879	.....	< 0.125
AT-11	1/8	0.1235	0.0674	0.110	0.891
AT-12	1/8	0.1311	0.0715	0.107	0.816

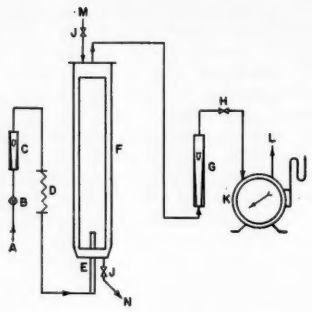

A = AIR INLET
G = STANDARD ROTAMETER
B = PRESSURE REGULATING VALVES
H = GLOBE VALVE
C = ROTAMETER
J = GATE VALVES
D = METALLIC HOSE
K = WET TEST METER
E = ORIFICE ASSEMBLY
L = AIR OUTLET
F = COLUMN
M = WATER INLET
N = DRAIN LINE

Fig. 1. Schematic flow diagram of equipment.

is 1.833 in. The velocity of approach factor varied from 0.00900 for the 1/64-in. orifice to 0.06879 for the ⅛-in. sharp-edged orifice. An undisturbed length equivalent to sixteen tube diameters was provided upstream from the orifice.

EXPERIMENTAL PROCEDURE

At the beginning of each data series the pressure upstream from the orifice was set at approximately 20 lb./sq. in. abs. The column was filled with liquid to a depth of 50 in. above the orifice in all experimental runs. By placing the orifice-assembly tube under pressure before the introduction of liquid to the column, the back-flow of liquid into the orifice-assembly tube was prevented. The level of the orifice was held at 12 in. above the bottom of the column in all the experimental runs. For the limited amount of data obtained with side entry, the orifice-assembly tube projected into the column a distance of approximately 2 in., as measured on the center line of the tube.

In operation the pressure-regulating valve was used for coarse adjustments in the air rate of flow, and fine adjustments were made with the needle valve. The air entered the column through the orifice, bubbled through the liquid, passed through the flow meters downstream from the column, and was discharged to the atmosphere. The globe valve located downstream from the column was adjusted to minimize pressure fluctuations. The absence of fluctuations in the readings of the manometers and flow meters was accepted as a criterion for equilibrium. Sufficient time was allowed for the liquid to become saturated with air before any readings were recorded.

RESULTS

Orifice discharge coefficients have been calculated for the rate of flow data of this

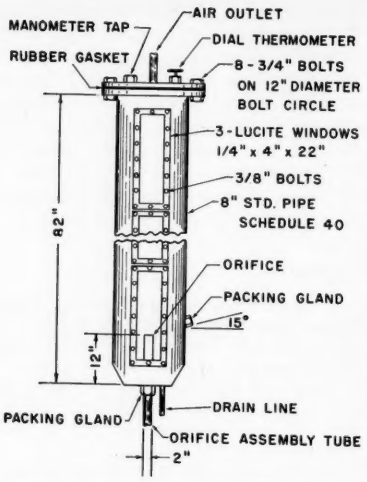

Fig. 2. Details of column design.

study by use of the critical orifice-flow equation:

$$C_n = \frac{w}{A_o P_1 \sqrt{\frac{g_c k M_W}{R T_1}\left(\frac{2}{k+1}\right)^{\frac{k+1}{k-1}}}} \quad (1)$$

The coefficient C_n is the ratio of the discharge obtained from an orifice to that from an ideal nozzle operating at pressure ratios less than 0.53. The coefficient C_n may also be regarded as the ratio of the effective orifice discharge area to the actual orifice cross-sectional area. Pressure ratio is the ratio of the pressure downstream from the orifice (taken as equivalent to the static head of the liquid plus the pressure at the top of the column) divided by the pressure upstream from the orifice.

In Figure 4 the orifice discharge coefficient is plotted vs. pressure ratio for the 1/64- through ⅛-in. sharp-edged orifices. Within the accuracy of the data, the results for the 1/64- and 1/32-in. orifices fall on one curve and those for the 1/16- and ⅛-in. orifices fall on another. There is a considerable increase in C_n as the pressure ratio decreases even in the supercritical flow region. Approximately a 12% maximum increase in the coefficient of discharge over that at the critical pressure ratio occurs for the 1/64- and 1/32-in. orifices and a 14% maximum increase occurs for the 1/16- and ⅛-in. sharp-edged orifices. The data fit the curves with an average deviation of approximately ±1.5%. The effect of orifice diameter on the coefficient of discharge is similar to that obtained by Grace and Lapple (*12*). The data show approximately a 6% increase in the coefficient of discharge for the 1/64- and 1/32-in. orifices compared with the 1/16- and ⅛-in. orifices. In the course of the experimental work, to obtain clearer vision of the bubble formation occurring at the orifice, the included angle of the bevel on the downstream face of each

Fig. 3. View of the orifice-assembly tube.

orifice was changed from 90 to approximately 160 deg. with no effect on the experimental results. A single point at the critical pressure ratio reported by Pattle (*16*) for bubble formation from a nozzle 0.0394 in. in diameter is shown in Figure 4 to be in close agreement with the present work.

The air-air-system data in the literature were obtained in most cases with the diameter of the tube upstream equal to that downstream from the orifice. In this study the orifice was mounted in the end of a 2-in. stainless steel tube which is placed inside an 8-in. column. It has been shown by Datta, Napier, and Newitt (*6*) that the principal effect of column diameter in the air-water system is the wall effect which results for bubble formation in equipment with a large ratio of orifice diameter to column diameter. The column diameter was not varied in this investigation; however, it is felt that for small values of the ratio of orifice diameter to column diameter the effect of column diameter may be neglected. The range of values for this ratio in the air-air-system data from the literature is from 0.03 to 0.12. In this paper the corresponding range for the air-water system is from 0.002 to 0.012.

In Figure 5 the data for the ⅛- and 1/16-in. submerged sharp-edged orifices discharging air into water are compared with the data in the literature for sharp-edged and round-edged orifices operating in an air-air system. In the subcritical region the data for the flow of air into water approximate the data in the literature for the air-air system. As the pressure ratio is decreased, however, the curve approaches that of Grace and Lapple (*12*) for a ⅛-in. round-edged orifice. Similar behavior is exhibited by the data for the 1/32- and 1/64-in. orifices, as shown in Figure 6. On the basis of the data obtained, the effective orifice discharge area for a sharp-edged orifice operating in the air-water system must be greater than that for an orifice of the same size and type operating at the same pressure ratio in the air-air system. This behavior may be attributed to the tendency of the bubble formation which occurs close to the downstream face of the orifice for the air-water system to inhibit the development of the *vena contracta* ob-

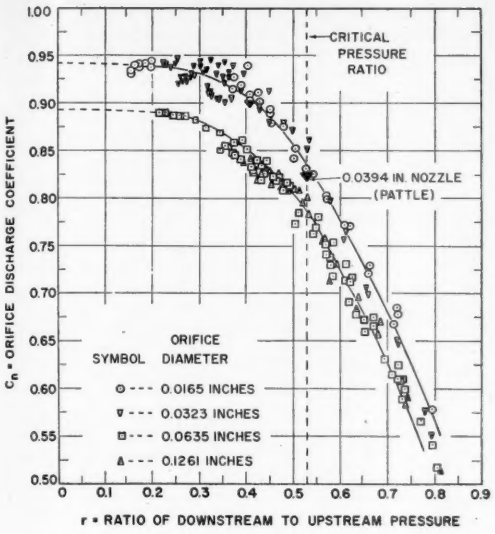

Fig. 4. Sharp-edged orifices.

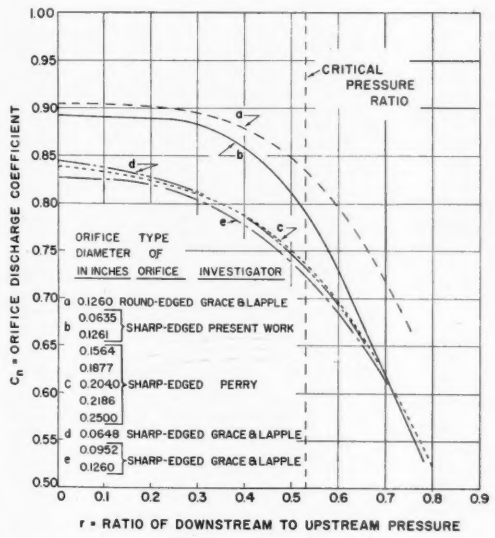
CRITICAL PRESSURE RATIO
ORIFICE DIAMETER IN INCHES
TYPE OF ORIFICE
INVESTIGATOR
a 0.1260 ROUND-EDGED GRACE & LAPPLE
b 0.0635, 0.1261 SHARP-EDGED PRESENT WORK
c 0.1564, 0.1877, 0.2040, 0.2186, 0.2500 SHARP-EDGED PERRY
d 0.0648 SHARP-EDGED GRACE & LAPPLE
e 0.0952, 0.1260 SHARP-EDGED GRACE & LAPPLE
C_n = ORIFICE DISCHARGE COEFFICIENT
r = RATIO OF DOWNSTREAM TO UPSTREAM PRESSURE

Fig. 5. Comparison with previous work.

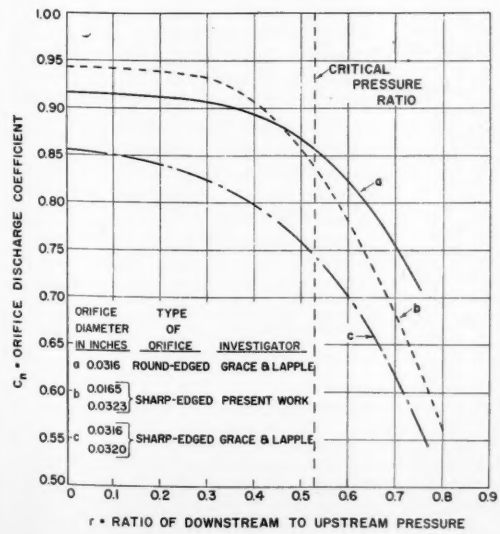
CRITICAL PRESSURE RATIO
ORIFICE DIAMETER IN INCHES
TYPE OF ORIFICE
INVESTIGATOR
a 0.0316 ROUND-EDGED GRACE & LAPPLE
b 0.0165, 0.0323 SHARP-EDGED PRESENT WORK
c 0.0316, 0.0320 SHARP-EDGED GRACE & LAPPLE
C_n = ORIFICE DISCHARGE COEFFICIENT
r = RATIO OF DOWNSTREAM TO UPSTREAM PRESSURE

Fig. 6. Comparison with previous work.

served for the air-air system. Attempts to verify this premise by making longitudinal pressure traverses downstream from the orifice with a specially constructed pressure probe were unsuccessful. In every case visual evidence was obtained that the presence of the probe disturbed the bubble formation. However, the pressure-probe measurements did indicate that at pressure ratios less than the critical pressure ratio the bubbles formed at the orifice possess an excess internal pressure compared with the pressure equivalent to the static head of the liquid at this point.

In Figure 7 the coefficients of discharge calculated from the data for the 1/16-in. submerged round-edged orifice are compared with data in the literature for a 1/32- and a ⅛-in. round-edged orifice operating in the air-air system. Close agreement is shown for the discharge coefficients for the round-edged orifice operating in the two systems. For a round-edged orifice operating in the air-air system the *vena contracta* is located at the throat of the orifice. Consequently, one might expect that for a round-edged orifice operating in the air-water system, bubble formation would have little or no effect on the effective orifice-discharge area.

Coefficients of discharge for two ⅛-in.-thick-plate orifices with ratios of throat length to diameter of 0.816 and 0.891, respectively, are shown in Figure 8. These data are reproducible within ±1.5%. In the supercritical region the curve is located approximately 8% above that given by Grace and Lapple (*12*) for a 1/16-in.-thick-plate orifice operating in the air-air system. As discussed in the introduction, the coefficient of discharge for a thick-plate orifice operating in the air-air system is relatively constant for values of the pressure ratio less than 0.33. For a ⅛-in. submerged thick-plate orifice discharging air into water there is only a 3% increase in the coefficient of discharge over that at the critical pressure ratio. Thus the coefficient of discharge for a submerged thick-plate orifice operating in the air-water system exhibits constancy similar to that shown by the coefficient for an ideal nozzle operating in the supercritical region.

SUMMARY

The coefficients of discharge obtained for sharp-edged orifices operating in the air-water system indicate that the effective orifice-discharge area for this type of operation is greater than that for an orifice of the same size operating at the same pressure ratio in the air-air system. The effective orifice-discharge areas for a round-edged orifice operating in either the air-water or air-air systems appear to be identical at the same pressure ratio. The thick-plate orifice operating in the air-water system exhibits a constancy of discharge coefficient at pressure ratios less

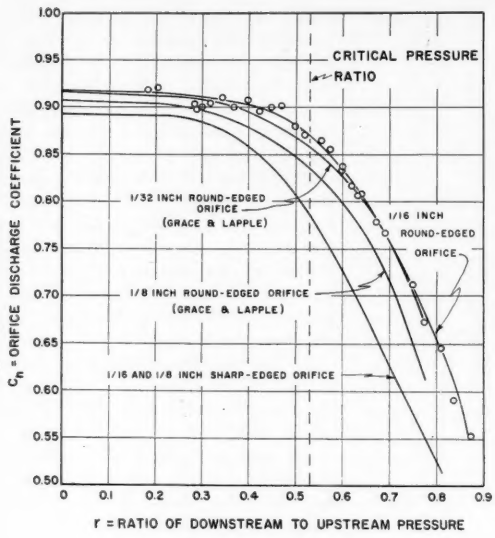
CRITICAL PRESSURE RATIO
1/32 INCH ROUND-EDGED ORIFICE (GRACE & LAPPLE)
1/16 INCH ROUND-EDGED ORIFICE
1/8 INCH ROUND-EDGED ORIFICE (GRACE & LAPPLE)
1/16 AND 1/8 INCH SHARP-EDGED ORIFICE
C_n = ORIFICE DISCHARGE COEFFICIENT
r = RATIO OF DOWNSTREAM TO UPSTREAM PRESSURE

Fig. 7. Round-edged orifice.

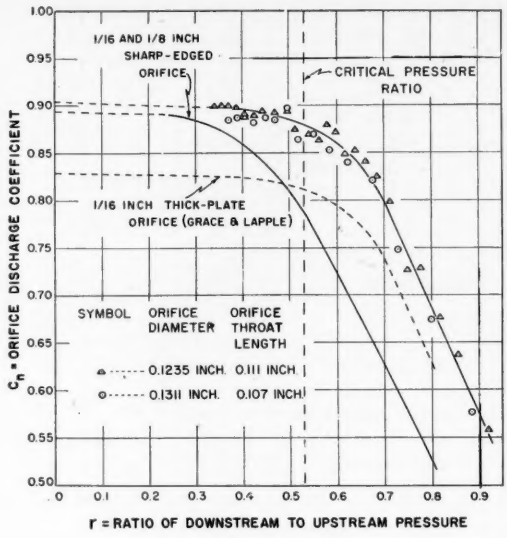
1/16 AND 1/8 INCH SHARP-EDGED ORIFICE
CRITICAL PRESSURE RATIO
1/16 INCH THICK-PLATE ORIFICE (GRACE & LAPPLE)
SYMBOL ORIFICE DIAMETER ORIFICE THROAT LENGTH
0.1235 INCH 0.111 INCH
0.1311 INCH 0.107 INCH
C_n = ORIFICE DISCHARGE COEFFICIENT
r = RATIO OF DOWNSTREAM TO UPSTREAM PRESSURE

Fig. 8. Thick-plate orifice.

than 0.33. Inasmuch as bubble formation occurring close to the downstream face of a sharp-edged orifice operating in the air-water system influences the effective orifice discharge area, liquid physical properties may be expected to be important in determining the rate of flow from this type of orifice for other gas-liquid systems. Before a generalized correlation can be developed for the flow of gases into liquids through single submerged orifices further data must be obtained for systems containing liquids other than water.

NOTATION

		Dimension
A_o	= orifice cross-sectional area	L^2
C_n	= orifice coefficient of discharge	
D_o	= orifice diameter	L
g_c	= conversion factor = 32.17 (lb./lb. force)(ft./sec.^{2})	$ML/F\theta^2$
k	= ratio of specific heat at constant pressure to specific heat at constant volume	
L_o	= orifice throat length	
M_W	= molecular weight, lb./lb. mole	
P_1	= absolute pressure upstream from the orifice	F/L^2
P_2	= absolute pressure downstream from the orifice	F/L^2
q	= volumetric rate of air flow at standard conditions, 32°F. and 14.7 lb. force/sq. in.	L^3/θ
R	= gas constant	LF/MT
r	= ratio of absolute pressure downstream from the orifice to the absolute pressure upstream from the orifice	
T_1	= absolute temperature upstream from the orifice	T
T_3	= temperature of the air flowing from the experimental column	T
w	= mass flow rate	M/θ
β	= ratio of orifice diameter to orifice-assembly-tube diameter	
ρ_1	= gas density upstream from the orifice	M/L^3

LITERATURE CITED

1. Achorn, G. B., and J. L. Schwab, *Science*, **107**, 377 (1948).
2. Am. Soc. Mech. Engrs., "Fluid Meters—Their Theory and Application," New York (1951).
3. Blackshear, P. L., *Trans. Am. Soc. Mech. Engrs.*, **75**, 51 (1953).
4. Cox, G. N., and F. J. Germano, "Fluid Mechanics," D. Van Nostrand Company, New York (1941).
5. Cunningham, R. G., *Trans. Am. Soc. Mech. Engrs.*, **73**, 625 (1951).
6. Datta, R. L., D. H. Napier, and D. M. Newitt, *Trans. Inst. Chem. Engrs.*, **28**, 14 (1950).
7. Davidson, L., Ph.D. thesis, Columbia Univ., New York (1951).
8. Dodge, B. F., "Chemical Engineering Thermodynamics," p. 331, McGraw-Hill Book Company, Inc., New York (1944).
9. Dzienisiewicz, J., Ph.D. thesis, Royal School of Mines, Univ. London (1951).
10. Eversole, W. G., G. H. Wagner, and E. Stackhouse, *Ind. Eng. Chem.*, **33**, 1459 (1941).
11. Fischer, F., and K. Peters, *Ges. Abhandl. Kenntnis Kohle*, **11**, 441 (1934).
12. Grace, H. P., and C. E. Lapple, *Trans. Am. Soc. Mech. Engrs.*, **73**, 639 (1951).
13. Hartshorn, L., *Proc. Roy. Soc. (London)*, **A94**, 155 (1918).
14. Hughes, R. R., A. E. Handlos, H. D. Evans, and R. L. Maycock, paper presented at San Francisco meeting, Am. Inst. Chem. Engrs. (Sept. 14, 1953).
15. Maier, G. G., *U. S. Bur. Mines Bull.* **260**, 62 (1927).
16. Pattle, R. E., *Trans. Inst. Chem. Engrs.*, **28**, 32 (1950).
17. Perry, J. A., *Trans. Am. Soc. Mech. Engrs.*, **71**, 757 (1949).
18. Prandtl, L., "Essentials of Fluid Mechanics," Hafner Publishing Company, New York (1952).
19. Reynolds, H., *Trans. Am. Soc. Mech. Engrs.*, **38**, 799 (1916).
20. Schiller, W., *Forsch. Gebiete Ingenieurw.*, **4**, 128 (1933).
21. Spells, K. E., and S. Bakowski, *Trans. Inst. Chem. Engrs.*, **28**, 38 (1950).
22. *Ibid.*, **30**, 189 (1952).
23. Stanton, T., *Proc. Roy. Soc. (London)*, **A111**, 306 (1926).
24. Van Krevelen, D. W., and P. J. Hoftijzer, *Chem. Eng. Progr.*, **46**, 29 (1950).

II. Mechanics of Bubble Formation

Very little information is available concerning bubble formation and behavior at the high rates of gas flow reported in Part 1. The purpose of this paper is to develop an understanding of the mechanics of formation and detachment of bubbles from single, submerged orifices operating at relatively high rates of air flow in a high-seal liquid-level system. Studies of these phenomena by use of orifices, nozzles, capillaries, and porous plates operating at low rates of gas flow have been made by many investigators (*5, 8, 9, 15, 28*) and were thoroughly reviewed by Jackson (*16*).

PREVIOUS WORK

Studies of bubble formation reported in the literature show that as the rate of gas flow through the orifice is increased, three regions of bubble formation are obtained. At very low rates of gas flow (below the

range covered in this paper) bubble formation is a static problem, bubble size being determined primarily by orifice diameter, surface tension, and fluid densities. In fact, the basis of the drop-volume (*13*) method of measuring surface tension is the formation of bubbles from fine capillaries at practically zero rate of gas flow. At low rates of gas flow previous work (*1, 7, 8*) has shown that for any given system and orifice diameter, bubble size is constant with respect to gas-flow rate. At intermediate rates of gas flow bubbles are formed at a constant frequency and the bubble size is uniform and depends primarily on the rate of gas flow, the orifice diameter, and the volume of the gas chamber upstream from the orifice. Van Krevelen and Hoftijzer (*29*) on the basis of studies using capillaries less than 0.02 in. in diameter claim that bubble size is independent of capillary-tip diameter. However, Davidson (*8*) shows that bubble size is approximately proportional to the square root of the orifice diameter for bubble formation at constant frequency. The effect of liquid physical properties such as surface tension, viscosity, and density is not clear (*12, 24*). Some authors (*5, 7, 11, 16, 21, 26, 29, 30*) have observed the formation of clouds of minute bubbles upon the addition to water of small amounts of acetic acid, alcohols, or surface-active agents. Davidson (*8*) showed that an increase in liquid viscosity tends to cause an increase in bubble size. At high rates of gas flow, the bubbles formed are not uniform in size and no data have been found in the literature to show the effects of rate of gas flow or orifice diameter on the bubble-size distribution.

APPARATUS

The experimental equipment used for this study was described in Part I. A Kodak 16-mm. high-speed motion picture camera, equipped with a Kodak Cine Ektar 63-mm. f/2 lens, was used to obtain motion pictures of the bubble formation. At full voltage of 115 volts this machine has a top film speed of 3,000 frames/sec. Illumination was provided by five G. E. 750-watt intermittent lamps. The number and position of these lamps were determined by trial and error. The optimum conditions were found to be two top lights (front and back), one center light (front), and two bottom lights (front and back). Kodak Super XX high-speed panchromatic reversal film type III, Class L-1, was used. The sharpest definition of the small bubbles was obtained by use of a black background.

Several hundred photographs of the bubbles were taken, both at the orifice and at a section approximately 3 ft. above the level of the orifice. A 4- by 5-in. Speed Graphic camera, equipped with a Kodak Ektar 127-mm. f/4.7 lens and Super panchromatic press type B film, was used. Lighting was provided by a No. 1 Strobonar Heiland Model HR3 lamp flashing for 1/2,000 sec. This lamp was held above the camera by hand and canted at a 45-deg. angle to the column. The distance from the focal plane of the camera to the column varied between 1 and 2 ft. The maximum depth of field was obtained with a lens aperture of f/22 with the camera focused on the center line of the column.

At intermediate rates of air flow, stroboscopic studies were performed to determine the frequency of bubble formation with a General Radio Company strobotac. Observations of bubble formation were limited to bubbles in the immediate proximity of the orifice. With the onset of turbulence in the air stream flowing through the orifice, shifting frequencies of formation were obtained and in some cases visibility was greatly reduced by the clouds of very small bubbles which were formed. Under these conditions the accurate determination of the frequency of bubble formation is also seriously handicapped by the surface irregularities in the bubbles of the air stream emerging from the orifice. The reproducibility of results was enhanced by attempting to "stop" the motion of the bubble forming at the orifice.

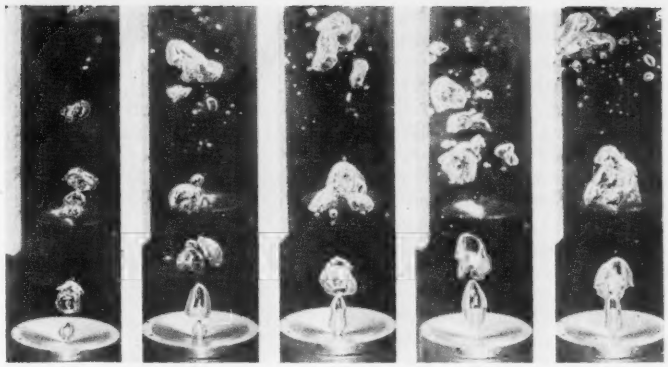

(1) (2) (3) (4) (5)

Fig. 1 through 5. Flow of air into water through 1/16-in. orifice; (1) $N_{Re} = 700$, (2) $N_{Re} = 1{,}088$, (3) $N_{Re} = 1{,}800$, (4) $N_{Re} = 2{,}050$, (5) $N_{Re} = 2{,}250$.

DESCRIPTION OF BUBBLE BEHAVIOR

To understand the mechanics of bubble formation at high rates of gas flow, a review of the mechanism of formation and detachment of bubbles at low flow rates is desirable. As a bubble forms, the surrounding liquid is accelerated away from the opening by viscous drag forces acting on the top surface of the bubble. If the volume of the gas chamber upstream from the orifice is small, the chamber pressure drops slightly because of this liquid motion, and the growth of the bubble is decelerated. Since the rate of gas flow to the chamber is steady, the pressure rises again and the growth of the bubble is accelerated. As liquid circulates inward at the level of the opening, the bubble is necked in and detached by a combination of buoyant forces and the motion of the liquid toward the opening. The detached bubble rises and the portion of its volume remaining at the orifice becomes the nucleus of the next bubble to form.

Turner (*28*) states that during bubble formation at low flow rates no significant cyclical pressure fluctuations occur in the gas chamber below the orifice if the chamber volume is greater than 10^4 times the volume of an individual bubble issuing from the orifice. Bubble formation then becomes dependent on dynamic effects in the liquid and in the gas but is surprisingly little different in the absence of the pressure surges described. Other investigators (*15*) clearly demonstrate the importance of the gas-chamber volume below the orifice as a factor influencing bubble formation and point out that if the chamber volume is much greater than $(A_o\rho_g c^2/g_c\Delta\rho)$ the chamber pressure is constant. Both these conditions are met throughout most of the range in the present investigation and the results obtained should be applicable to large-scale equipment.

Early in the present study it was realized that most of the phenomena occurring at very high air-flow rates (with the orifice operating near the critical pressure ratio) might be explained by a study of the effect of gas turbulence and liquid circulation on bubble formation at lower rates of gas flow. Previous investigators (*15, 19*) have suggested that the formation of bubbles nonuniform in size as they pass through the orifice may be closely connected with gas turbulence. Figures 1 through 9 are a series of photographs showing bubble formation in water from a 1/16-in. sharp-edged orifice at Reynolds numbers (for gas flow through the orifice) varying from approximately 700 to 10,450. The photographs shown in Figures 1 through 4 reveal that bubbles relatively uniform in size are produced for laminar flow of air through the orifice (i.e., at Reynolds numbers less than 2,100). In this range as a bubble is detached from the orifice some very small bubbles are formed by the rupture and collapse of the elongated bubble neck. This is illustrated in Figure 4 by the small bubble shown between the large detached bubble and the growing bubble at the orifice. In Figures 1 through 4 small bubbles are present between the large bubbles near the orifice. Thus in the laminar-flow range bubbles much smaller than the average bubble size may be formed by the rupture and collapse of the elongated bubble neck as liquid circulates inward at the level of the orifice.

As the flow rate is increased (Figures 1 to 4), the bubble formed at the orifice

changes from a smooth sharply defined ellipsoid (Figure 1) to a pear-shaped bubble (Figure 2), which becomes increasingly elongated at higher flow rates (Figures 3 and 4). Incipient coalescence, a condition in which one bubble is projected into, and may become totally enclosed by, the one immediately above, is shown by the second bubble above the orifice in Figures 3 and 4. In the laminar-flow range, high-speed motion pictures show that upon detachment the bubble is swept by a surface wave which initiates at the bottom of the bubble and films over the entire bubble with fresh liquid. At the conclusion of the surface wave the bubble appears to be helmet shaped with a flat bottom (Figure 2). Jakob and Fritz (*17*) have photographed bubbles of this shape near heat transfer surfaces during their study of bubble formation in boiling liquids. Yamagata (*32*) et al. have observed that single steam bubbles (both spherical and helmet shaped) are formed in boiling water in the free-convection region. In the forced-convection region steam-bubble formation was found to be a function of the degree of turbulence in the boundary layer near the heat transfer surface, and nonuniform steam bubbles were produced in this region of operation.

With the onset of turbulence for the gas flow through the orifice (Figures 5 through 9 for Reynolds numbers greater than 2,100), coalescence occurs very close to the orifice and the resultant large irregular bubble rises only a very small distance (3 to 4 in. above the opening) before it is shattered into many small bubbles of varying sizes. Many very small bubbles formed by this process are evident at a Reynolds number of 4,600 (Figure 8). As the Reynolds number increases to 10,000, the bubbles formed by the shattering process become smaller.

As gas turbulence becomes fully developed ($N_{Re} > 10{,}000$), stroboscopic examination and high-speed motion pictures show that what appears to the unaided eye to be a continuous jet of gas is actually a series of closely spaced, irregular bubbles rising with a very rapid counterclockwise swirling motion. A large number of very fine bubbles (Figure 9) are formed by being torn from the swirling air stream in a manner similar to that described for liquid sprays by Castelman (*2, 3*). Rough portions of the air-bubble surface (Figure 9) are pinched or torn off to form very minute bubbles. The formation of bubbles nonuniform in size is greatly accelerated by the virtual explosion of the large irregular bubbles at a point approximately 4 in. above the orifice. The jet of gas leaving the orifice is similar to a tornado or a waterspout. A combined vortex is formed composed of a forced vortex on an axis perpendicular to the plane of the orifice and a free vortex in the bulk of the liquid. Liquid circulates in a large eddy near the orifice, flowing toward the jet at the level of the orifice, rotating very rapidly around the central core of bubbles, and flowing away from the top of the forced vortex as gas-liquid mixing with the shattering of the large bubbles occurs. A series of photographs of bubble formation from orifices of other diameters corroborates the observations of bubble formation from the 1/16-in. sharp-edged orifice. Figures 10, 11, 12, and 13 for bubble formation from the 1/64-in. sharp-edged orifice submerged in water trace the development of turbulence in the air stream as the Reynolds number is increased from 621 to 9,470. Figure 10 shows that the bubbles produced for laminar flow of air through the 1/64-in. orifice are much smaller than those produced from the 1/16-in. orifice at a similar Reynolds number (Figure 1). As in Figure 1, the bubble forming at the orifice is a smooth, sharply defined ellipsoid. Figure 11 shows the bubble formation at a Reynolds number of 2,010. Some very small bubbles are apparent, and incipient coalescence occurs near the orifice. Figures 10 and 11 corroborate the relative

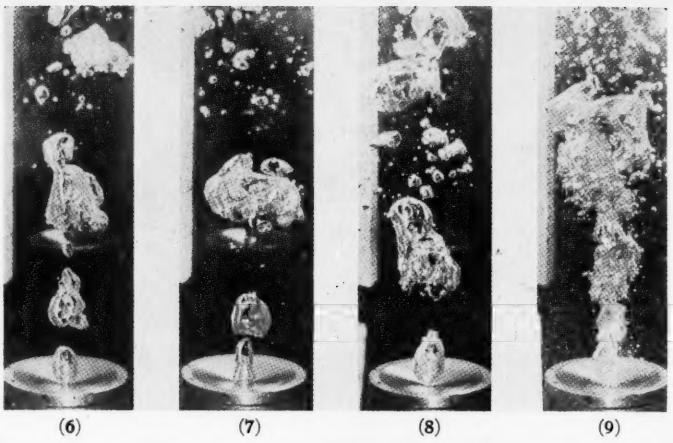

(6) (7) (8) (9)

Fig. 6 through 9. Flow of air into water through 1/16-in. orifice; (6) N_{Re} = 2,700, (7) N_{Re} = 3,680, (8) N_{Re} = 4,660, (9) N_{Re} = 10,450.

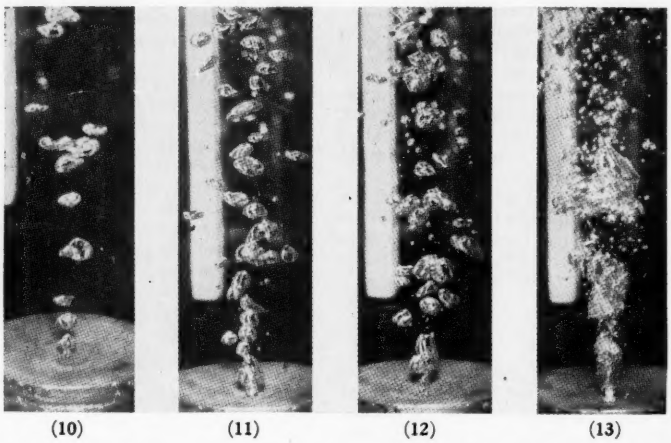

(10) (11) (12) (13)

Fig. 10 through 13. Flow of air into water through 1/64-in. orifice; (10) N_{Re} = 621, (11) N_{Re} = 2,010, (12) N_{Re} = 2,520, (13) N_{Re} = 9,470.

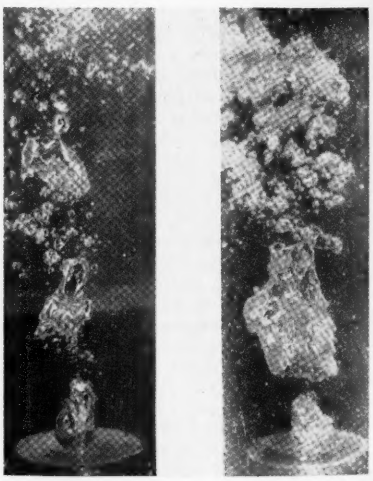

(14) (15)

Fig. 14 and 15. Flow of air into water: (14) N_{Re} = 7,760, 1/32-in. orifice; (15) N_{Re} = 9,460, 1/8-in. orifice.

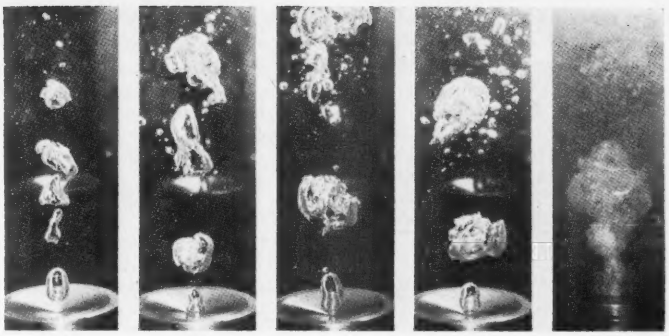

(16) (17) (18) (19) (20)

Fig. 16 through 20. Flow of air into 1.6% butanol solution through 1/16-in. orifice; (16) $N_{Re} = 730$, (17) $N_{Re} = 1{,}780$, (18) $N_{Re} = 2{,}000$, (19) $N_{Re} = 2{,}310$, (20) $N_{Re} = 8{,}550$.

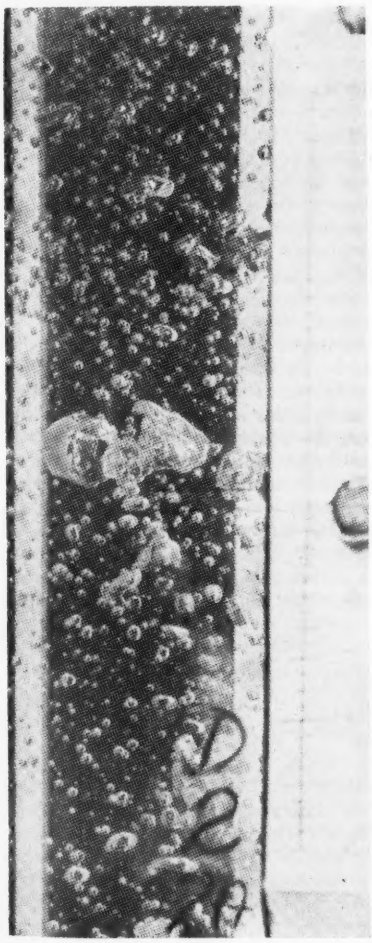

Fig. 21. 1/64-in. orifice; $N_{Re} = 14{,}000$, $D_{vs} = 0.187$.

uniformity of bubble size (shown by Figures 1 through 4) for the laminar flow of air through the orifice. Figure 12 shows the nonuniformity of bubble size characteristic of the onset of turbulent flow through the orifice. The mechanics of bubble formation for fully developed turbulence as shown in Figures 13, 14, and 15 for the 1/64-, 1/32-, and ⅛-in. orifices, respectively, are very similar to the bubble formation from the 1/16-in. orifice at a similar Reynolds number (Figure 9).

Several observations made from the high-speed motion pictures taken at high rates of gas flow through each of the orifices are of interest. At a Reynolds number of 20,000 many very small bubbles (smaller than 0.05 in. in diameter) are formed by being torn off the large swirling bubbles in the discontinuous jet. These fine bubbles rise with a relatively slow counterclockwise rotation about the discontinuous jet. Near the walls of the column the downward motion of the very small bubbles is indicative of liquid currents in the free vortex in the bulk of the liquid. Breakup of most of the large bubbles in the jet occurs approximately 3 to 4 in. above the orifice. At a Reynolds number of 30,000 the spiraling motion of the jet appears to be compressed and an intensified cloud of fine bubbles is present. For the orifice sizes larger than 1/64 in. a ring of fine bubbles appears very close to the orifice. These bubbles hang suspended with some motion of very small amplitude to and from the orifice. It is likely that the velocity of rise of the small bubbles near the orifice is of the same magnitude as the point velocity of the liquid circulating toward the orifice. Therefore the small bubbles of the ring are virtually trapped and can escape only when irregularities of flow occur. No ring of fine bubbles surrounding the orifice was observed for the 1/64-in. orifice until higher Reynolds numbers were reached. No marked changes in the flow regime were noted for any of the orifices as the pressure ratio decreased below 0.53 (the critical pressure ratio for air). The rapidly moving jet of bubbles appeared to be intermittently continuous in the motion pictures, an impression that stroboscopic examination of this jet suggests is a result of the superposition of discrete bubbles in different vertical and horizontal planes upon each other in such a manner that they overlap, giving the jet an appearance of continuity. At a Reynolds number of 40,000 the spiraling motion of the jet seemed to be compressed to an even greater extent. As the Reynolds number was increased, somewhat greater numbers of very small bubbles were formed by being torn off the very rapidly swirling core of large bubbles. At the greatest flow rates invesgitated, the visibility of phenomena at the orifice was very poor, inasmuch as the cloud of very fine bubbles formed rendered the liquid translucent.

Most of the phenomena described for bubble formation in the air-water system also occur for the formation of air bubbles in a 1.6% solution of butanol in water with a solution surface tension of 44.5 dynes/cm. Figures 16 through 20 are a series of photographs showing bubble formation from a 1/16-in. sharp-edged orifice submerged in an aqueous butanol solution for Reynolds numbers (for gas flow through the orifice) varying from approximately 730 to 8,550. Figures 16, 17, and 18 illustrate bubble behavior in the aqueous butanol solution in the laminar-flow range at approximately the same Reynolds numbers as Figures 1, 3, and 4, respectively. The most marked difference is the great increase in the number of very small bubbles formed in the butanol solution as the rate of air flow is increased. Figures 17 and 18 show several very small bubbles just above the bubble growing at the orifice. High-speed motion pictures and stroboscopic studies reveal that these small bubbles are produced by the collapse and rupture of the elongated bubble neck upon the detachment of a bubble from the orifice. Because of the low surface tension of the butanol solution, a larger number of small bubbles are formed in the butanol solution than in water at corresponding rates of air flow. Figure 19 shows the formation of bubbles nonuniform in size, resulting from the shattering of the rising bubble at a point approximately 4 in. above the orifice. As in Figure 5 (for water), the formation of bubbles of nonuniform size in the butanol solution is initiated with the onset of turbulence for the flow of the gas through the orifice. A comparison of Figures 19 and 5 shows that a much greater number of fine bubbles are formed in the butanol solution than in water. As the rate of air flow increases (Figure 20), a cloud of fine bubbles is formed which makes further observations difficult. However, stroboscopic examination reveals that as turbulence is fully developed for the air flow through the orifice, a counterclockwise spiraling, swirling motion of the air jet is initiated. Thus the major effect of lowering the surface tension of the seal liquid appears to be an increase in the formation of very small bubbles by a reduction in the amount of energy required to form a unit of interfacial area. The mechanisms by which very small bubbles are formed seem to be unaffected by changes in the surface tension of the seal liquid.

In summary, observation of bubble

Table 1. Laminar-flow Range

Point	Pressure ratio r	Flow rate q, cu. ft./min.	Reynolds number N_{Re}	Frequency f, bubbles/min.	Bubble diameter D_B, in.
Series B-15	Orifice diameter, D_0 = 0.0165 in. air-water system				
1	0.990	0.0061	630	1,110	0.275
2	0.983	0.0097	1,000	1,180	0.309
3	0.958	0.0161	1,660	1,200	0.364
4	0.952	0.0181	1,870	1,250	0.374
5	0.944	0.0197	2,030	1,300	0.379
Series B-17B	Orifice diameter, D_0 = 0.0165 in. air–aqueous butanol system				
1	0.994	0.0061	629	1,200	0.264
2	0.983	0.0102	1,050	1,270	0.308
3	0.965	0.0156	1,610	1,400	0.343
4	0.955	0.0177	1,820	1,350	0.362
5	0.948	0.0202	2,080	1,370	0.376
Series D-23	Orifice diameter, D_0 = 0.0635 in. air-water system				
1	0.996	0.0270	724	900	0.478
2	0.992	0.0415	1,110	1,000	0.532
3	0.989	0.0668	1,790	1,050	0.614
4	0.987	0.0759	2,030	1,050	0.614
Series D-24B	Orifice diameter, D_0 = 0.0635 in. air–aqueous butanol system				
1	0.996	0.0278	751	850	0.493
2	0.993	0.0393	1,040	920	0.535
3	0.989	0.0668	1,770	1,035	0.617
4	0.987	0.0758	2,040	1,040	0.642
Series A-17	Orifice diameter, D_0 = 0.1265 in. air-water system				
1	0.999	0.0234	314	650	0.507
2	0.980	0.0804	1,080	720	0.739
5	1.00	0.0048	64.2	202	0.440
6	0.999	0.0299	402	558	0.578
7	0.999	0.0294	395	795	0.511
8	0.984	0.0421	566	740	0.590

formation over a wide range of rates of air flow indicates that very small bubbles may be produced in three ways.

1. For laminar flow of the gas through the orifice, as a bubble is detached from the orifice, the rupture and collapse of the elongated bubble neck may produce several very small bubbles. This tendency is markedly increased for solutions of low surface tension.
2. For turbulent flow of the gas through the orifice, bubbles of nonuniform size, including some very small bubbles, are produced by the shattering of large bubbles at a point approximately 3 to 4 in. above the orifice.
3. As turbulence is fully established for the flow of the gas through the orifice (at Reynolds numbers greater than 10,000), a progressively larger number of very small bubbles is torn away from the large irregular bubbles of the swirling discontinuous jet.

A limited number of data were obtained for the 1/64- and 1/32-in. orifices with entry of the air through the orifice-assembly tube pointed down at a 15-deg. angle with the horizontal. High-speed motion pictures and stroboscopic study of this mode of operation revealed that the jet of gas leaving the orifice is composed of discrete bubbles being ejected with a very rapid counterclockwise spiraling motion referred to an axis perpendicular to the plane of the orifice. The bubbles formed at the orifice are similar in shape to those formed at comparable flow rates with bottom entry. However, a gradation in bubble size is set up with respect to distance from the orifice. The largest bubbles (formed by the coalescence of smaller ones issuing from the orifice) rise from the jet at points very close to the orifice. The very fine bubbles formed by being torn off larger bubbles rise from the jet at the points farthest from the orifice. Bubbles of intermediate sizes rise from the jet at all points between these extremities. As the Reynolds number increases from 2,000 to 20,000, the dicontinuous jet of gas increases in length from approximately 1 to 6 in. With the present experimental apparatus, no data could be obtained for side entry with orifices greater than 1/32 in. in diameter, because the jet of gas collided with the wall of the experimental column for the larger orifices.

LAMINAR-FLOW RANGE

The bubbles are relatively uniform in size for the laminar flow of air through the orifice. As shown in Figures 1, 2, 3, 4, 10, and 11, very few minute bubbles are formed in the laminar-flow region. The frequency of bubble formation in this range was determined by stroboscopic examination. The mean bubble volume was calculated by use of the following equation:

$$v_B = \frac{q'}{f} \qquad (1)$$

where v_B is the bubble volume, q' is the volumetric gas flow rate at the conditions of pressure and temperature downstream from the orifice, and f is the frequency of bubble formation. The average bubble diameter of a spherical bubble of equivalent bubble volume was calculated directly from average bubble volume obtained from Equation (1).

$$D_B = \left(\frac{6}{\pi} v_B\right)^{1/3} \qquad (2)$$

Within the experimental error of this work, the volume and surface contributions of the small number of minute bubbles formed in the laminar-flow range may be considered negligible. Table 1 presents the results for bottom entrance flow as calculated from the stroboscopic studies of bubble formation from the 1/64-, 1/16-, and ⅛-in. orifices, respectively. The frequency of bubble formation is relatively constant (for a given orifice) and increases very slightly as the Reynolds number is increased. The calculated bubble diameter increases markedly as the Reynolds number is increased in the laminar-flow range. The data show that the bubble diameter varies as a function of orifice diameter in the laminar-flow range (i.e., constant-frequency region). For the air-water system, the following equation correlates the bubble diameter as a function of orifice diameter and Reynolds number:

$$D_B = 0.18 D_o^{1/2} N_{Re}^{1/3} \qquad (3)$$

Davidson's results (*8*) for orifices ranging in diameter from approximately 0.04 to 0.40 in. may be expressed as

$$D_B = 0.19 D_o^{0.48} N_{Re}^{0.32} \qquad (4)$$

The close agreement between Equations (3) and (4) is interesting. The orifice used by Davidson was drilled in the bottom flange of his experimental column. However, in this investigation, for bottom entrance flow, the orifice projected 12 in. into the column. Thus the presence of liquid in the column below the level of the orifice-assembly tube appears to have very little influence on the mechanics of bubble formation. The data are plotted as bubble diameter vs. Reynolds number on logarithmic coordinates in Figure 23. Since the bubbles are relatively uniform in size in the laminar-flow region, the calculated bubble diameters are equivalent to mean bubble diameters based on either the bubble volume, surface, or specific surface per unit volume (*6*).

BUBBLE-SIZE DISTRIBUTION*

Formation of nonuniform bubbles is initiated with the onset of turbulence for the gas flowing through the orifice. As turbulence becomes fully developed (i.e., $2{,}100 < N_{Re} < 10{,}000$), a randomization of bubble sizes occurs (Figures 5 to 9, 12 to 15, 19, and 20). To determine the effect of Reynolds number on D_{vs}, photographs were taken of a section of the column approximately 3 ft. above the orifice. The 4- by 5-in. negatives obtained were enlarged to 8- by 10-in. prints and the number of bubbles in the various size classes were determined visually by use of a pair of dividers and a scale. Figure 21 is a typical photograph employed to determine the bubble-diameter distribution. For the purposes of bubble-size measurements, it was assumed that all bubbles were located in a plane passing through the center line of the column. With the exception of very large bubbles, most of the bubbles were spherical in shape. The larger bubbles appeared to rise as oblate spheroids. However, oscillation in shape is noticeable in the motion of very large bubbles. The actual bubble sizes were determined by multiplying relative-scale sizes by a scale factor determined separately for each photograph.

The bubble-size–distribution data are fitted reasonably well by a logarithmic normal-probability distribution. The use of this function to correlate the data has a semitheoretical basis in that a repeated random process such as the breakup and coalescence of particles with growth or diminution by constant factors leads to a logarithmic probability distribution. In this investigation the smallest bubble size which could be measured by the photographic method employed is approximately 0.014 in. Consequently a truncated distribution was obtained, and it was necessary to fit a logarithmic normal-probability distribution to the data by an approximation method. The problem was to estimate the geometric mean and standard deviation for a logarithmic normally distributed population from a truncated sample in the case when neither frequencies nor measurements of variates in the omitted portion of the sample are known. Cohen (*4*) has developed a method of successive approximations whereby certain special functions required in the solutions of this problem given by Pearson and Lee (*22*) and Fisher (*10*) may be readily evaluated with the aid of an ordinary table of the areas and ordinates of the normal-probability curve (*20*).

The geometric mean for a logarithmic normal-probability distribution is defined by

$$\log D_G = \frac{\sum (n \log D_B)}{\sum n} \qquad (5)$$

The standard deviation for a logarithmic normal-probability distribution is defined by

$$\sigma = \sqrt{\frac{\sum [n(\log D_B - \log D_G)^2]}{\sum n}} \qquad (6)$$

The logarithmic probability function may be written

$$\varphi(z) = \frac{1}{\sqrt{2\pi}} e^{-z^2/2} \qquad (7)$$

where z is defined by

$$z = \frac{\log D_B - \log D_G}{\sigma} \qquad (8)$$

Data for a sample bubble-size distribution are plotted on logarithmic vs. cumulative probability coordinates in Figure 22. To determine the reproducibility of the distribution data, bubble-frequency counts were made on duplicate photographs for most of the points investigated. The logarithm of the geometric mean diameter and the standard deviation for the logarithmic normal probability distribution of best fit were obtained by Cohen's method (*4*). A Remington Rand analogue computer was employed to carry out the necessary calculations. The reproducibility of the data is shown to be reasonable. Several points, each representative of a single large bubble, show some scatter compared with the remainder of the data. The line plotted was drawn on the basis of the geometric mean and the standard deviation obtained from Cohen's method. The geometric mean is the bubble diameter corresponding to the value of 50% on the probability scale. The bubble diameters corresponding to the 84.13 and 15.87% sizes were obtained from the following:

$$\sigma = \frac{84.13\%\text{ size}}{50\%\text{ size}} = \frac{50\%\text{ size}}{15.87\%\text{ size}} \qquad (9)$$

The total number of bubbles to be used in calculating the cumulative percentage greater than size from the frequency for each size range was obtained by an approximation method. By use of the line of best fit, the percentage greater than stated size was determined for each size range. The total number of bubbles was calculated from the frequency data for each size range as follows:

$$\sum n = \frac{n_1 + n_2 + \cdots + n_{size}}{\%\text{ greater than stated size}} \qquad (10)$$

The abscissae of Figure 22 were based on the arithmetic average of the total numbers of bubbles obtained by use of the frequency data for each size range.

The standard deviation and the logarithm of the geometric mean bubble diameter for each of the bubble-size distributions obtained for the 1/64-, 1/32-, and 1/16-in. orifices with bottom entrance flow were used to calculate D_{vs}, the diameter of the bubble whose ratio of volume to surface area is equal to that of the entire bubble-size distribution (*6*). The following equation, developed by Hatch and Choate (*14*), was used to calculate D_{vs}.

$$\log D_{vs} = \log D_G + 5.757\sigma^2 \qquad (11)$$

*Complete data on this section are filed as document 4958 with the American Documentation Institute, Photoduplication Service, Library of Congress, Washington 25, D. C., and may be obtained for $1.25 for photoprints or 35-mm. microfilm.

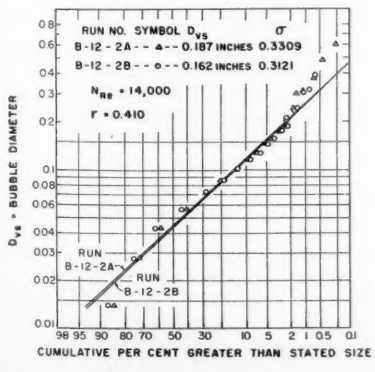
RUN NO. SYMBOL D_{VS} σ
B-12-2A - - ▲ - - 0.187 INCHES 0.3309
B-12-2B - - o - - 0.162 INCHES 0.3121
N_{Re} = 14,000
r = 0.410
RUN B-12-2A
RUN B-12-2B
D_{VS} = BUBBLE DIAMETER
CUMULATIVE PER CENT GREATER THAN STATED SIZE

Fig. 22. Typical bubble-size distribution.

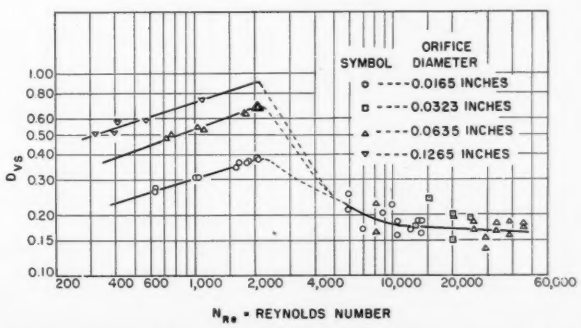

Fig. 23. Bottom-entrance-flow mean bubble diameter D_{vs} vs. Reynolds number.

TURBULENT-FLOW RANGE

The shattering of the large bubbles produced in turbulent flow with a resultant nonuniformity of bubble size has been discussed in a previous paragraph. The values of D_{vs} are plotted as a function of Reynolds number in Figure 23.

Only a very limited number of data are available for $2{,}100 < N_{Re} < 10{,}000$. With the onset of turbulence, the value of D_{vs} must be expected to drop very sharply, as shown by the dashed curves on Figure 23. This is reasonable, as the formation of very small bubbles is greatly increased as the discontinuous swirling jet is developed at the orifice. The data indicate that there is no noticeable effect of orifice diameter on D_{vs} in the turbulent-flow region. For the air-water system studied, the following equation fits the data for Reynolds numbers greater than 10,000:

$$D_{vs} = 0.28 N_{Re}^{-0.05} \qquad (12)$$

The data fit Equation (12) within the 95% confidence limits.

SUMMARY

Photographic studies of bubble formation reveal that nonuniformity of bubble size is initiated by the onset of turbulence in the air stream flowing through the orifice. In the section of the laminar-flow range studied in this investigation ($200 < N_{Re} < 2{,}100$) the frequency of bubble formation is nearly constant with respect to Reynolds number. The bubble size is relatively uniform at a given Reynolds number and depends markedly upon orifice diameter.

A normal distribution with respect to the logarithm of the bubble diameter is established for the turbulent flow of air through the orifice. As turbulence becomes fully developed, a marked decrease in D_{vs} occurs. For bottom entrance flow D_{vs} appears to be independent of the orifice diameter. The data indicate that a large increase of interfacial area may be effected in a gas-liquid contacting system by introducing the gas through orifices at Reynolds numbers greater than 10,000. The holdup of gas bubbles in a gas-liquid system was shown by Quigley (*23*) to be dependent on the 0.84 power of the gas rate of flow. Consequently, as the gas rate of flow is increased into the turbulent flow range, the resultant decrease in D_{vs} and the corresponding increase in gas holdup should greatly increase the gas-liquid interfacial contact area per unit volume.

It is important to note that the effects of liquid physical properties have not been studied in this investigation. The results obtained may be expected to apply qualitatively to similar systems. However, more data for bubble formation in other liquids (particularly of low surface tension) are necessary before a general correlation for bubble size in gas-liquid systems can be developed.

ACKNOWLEDGMENT

The authors wish to express their appreciation to S. T. Atkins, Jr., for his work in obtaining the photographs and motion pictures used in this investigation. The assistance of M. E. Ready and S. Chapman, E. Koval, and H. Cadolph in the statistical calculations involved in this study is gratefully acknowledged. The authors are indebted to G. B. Achorn, Jr., D. I. Dykstra, E. R. Dapper, and C. E. Cottrell, as well as many other staff members of Camp Detrick, for their suggestions and cooperation during the course of this study and to the U. S. Army Chemical Corps for permission to publish the paper.

NOTATION

		Dimension
A_o	= orifice cross-sectional area	L^2
c	= velocity of sound in the gas	L/θ
D_B	= bubble diameter	L
D_G	= geometric-mean bubble diameter	L
D_o	= orifice diameter	L
D_{vs}	= diameter of a bubble whose ratio of volume to surface is equivalent to that of the bubble-size distribution	L
f	= frequency of bubble formation	θ^{-1}
g_c	= conversion factor = 32.17 (lb./lb. force)(ft./sec.^{2})	$ML/F\theta^2$
n	= frequency of bubble-size class in bubble-size distribution	
N_{Re}	= Reynolds number = $4w/\pi D_o\mu$	
q	= volumetric rate of air flow at standard conditions 32°F. and 14.7 lb. force/sq. in.	L^3/θ
q'	= volumetric rate of air flow at the conditions of temperature and pressure downstream from the orifice	L^3/θ
r	= ratio of the absolute pressure downstream from the orifice to that upstream from the orifice	
V_B	= bubble volume	L^3
w	= mass rate of gas flow	M/θ
z	= logarithmic size variable, Equation (8)	
$\varphi(z)$	= probability function, Equation (7)	
ρ_g	= gas density	M/L^3
σ	= logarithmic standard deviation, Equation (6)	

LITERATURE CITED

1. Breitner, J. H., *Kolloid-Z.*, **100**, 335 (1942).
2. Castelman, R. A., *Natl. Advisory Comm. Aeronaut. Rept.* 440 (1932).
3. ———, *J. Research Natl. Bur. Standards*, **6**, 369 (1931).
4. Cohen, A. C., *J. Am. Statistical Assoc.*, **44**, 518 (1949).
5. Coppock, P. D., and G. T. Mieklejohn, *Trans. Inst. Chem. Engrs.*, **29**, 75 (1951).
6. DallaValle, J. M., "Micromeritics," Pitman Publishing Corp., New York (1948).
7. Datta, R. L., D. H. Napier, and D. M. Newitt, *Trans. Inst. Chem. Engrs.*, **28**, 14 (1950).
8. Davidson, L., Ph.D. thesis, Columbia Univ., New York (1951).
9. Eversole, W. G., G. H. Wagner, and E. Stackhouse, *Ind. Eng. Chem.*, **33**, 1459 (1941).
10. Fisher, R. A., "Mathematical Tables," Vol. 1, Brit. Soc. Advance. Sci. (1931).
11. Foulk, C. W., and J. N. Miller, *Ind. Eng. Chem.*, **23**, 1283 (1931).
12. Halberstadt, S., and P. H. Prausnitz, *Z. angew. Chem.*, **45**, 970 (1930).
13. Harkins, W. D., and F. E. Brown, *J. Am. Chem. Soc.*, **41**, 499 (1919).
14. Hatch, T., and S. P. Choate, *J. Franklin Inst.*, **207**, 369 (1929).
15. Hughes, R. R., A. E. Handlos, H. D. Evans, and R. L. Maycock, paper presented at the San Francisco meeting, Am. Inst. Chem. Engrs. (Sept. 14, 1953).
16. Jackson, R. W., *Ind. Chem.*, **28**, 346 (1952).
17. Jakob, Max, and W. Fritz, *Forsch. Gebiete Ingenieurw.*, **2**, 434 (1931).
18. Lee, A., *Biometrika*, **10**, 208 (1915).
19. Maier, C. G., *U. S. Bur. Mines Bull.* 260, 62 (1927).
20. Natl. Bur. Standards, "Tables of Normal Probability Functions," U. S. Govt. Printing Office, Washington, D. C. (1953).
21. Pattle, R. E., *Trans. Inst. Chem. Engrs.*, **28**, 32 (1950).
22. Pearson, K., and A. Lee, *Biometrika*, **6**, 59 (1908).
23. Quigley, C. J., *Chem. Eng. Progr., Symposium Series* No. 16, **51**, 31 (1955).
24. Schnurrmann, R., *Z. physik. Chem.*, **143A**, 456 (1929).
25. ———, *Kolloid-Z.*, **80**, 148 (1937).
26. *Ibid.*, **87**, 127 (1939).
27. Thomas, M. D., *Ind. Eng. Chem. (Anal. Ed.)*, **5**, 1939 (1935).
28. Turner, G. M., paper presented at the San Francisco meeting, Am. Inst. Chem. Engrs. (Sept. 14, 1953).
29. Van Krevelen, D. W., and P. J. Hoftijzer, *Chem. Eng. Progr.*, **46**, 29 (1950).
30. Verschoor, H. T., *Trans. Inst. Chem. Engrs.*, **28**, 52 (1950).
31. Wirth, H., *Arch. exp. Pathol. Pharmokol.*, **181**, 198 (1936).
32. Yamagata, K., F. Hirono, K. Nishikawa, and H. Matsuoka, *Japan Sci. Rev. Ser. II*, No. 4, 409 (1952).

Presented at A.I.Ch.E. Houston meeting

Structure and Performance of Filter Media

H. P. GRACE

E. I. du Pont de Nemours & Co., Wilmington, Delaware

I. The Internal Structure of Filter Media

The internal structure of various types of filter media and the nature of fluid flow through them are examined. Methods of characterizing the internal pore structure of filter media are reviewed, and the permeability, bubble-pressure, and mercury-intrusion methods are applied to ten typical media, with resulting values of average and maximum pore radius and pore-size distribution being reported. These data on internal pore structure are related to the construction variables characteristic of the media examined, in particular the effect of yarn construction, yarn twist, fabric weave, and fabric finish on textile-type filter media.

The filter medium is an essential and very critical component of every filtration step and can make or break it from either an economic or a performance standpoint. Commercial filter media have been developed through the trial of hundreds of textile fabrics and other porous materials. Most of these were originally intended for other purposes, but through experience some five hundred or more have been found useful for filtering liquids. New filter media continue to evolve by this means. Few engineering criteria exist for the selection of existing filter media or for the design and construction of new media for efficient performance in the various types of filtration service. This lack of a quantitative basis for both the design and selection of filter media is largely responsible for the wide and continually changing variety of filter media in general use.

Experimental procedures for correlating physical characteristics, internal structure, and performance are needed before any major improvement in this situation can be expected. A means of quantitatively relating these factors should result eventually in the design of the best filter media for particular types of service. The immediate objectives of the work reported in Parts I and II of this paper were the development and application of techniques for evaluating pore structure and functional performance of filter media and the correlation of these factors with each other and with other measured properties of filter media.

STRUCTURE OF FILTER MEDIA

Filter media can be divided into three general classes: (1) a wide variety of woven textile fabrics, (2) random-packed beds of a fibrous material (including compacted or mechanically bound beds such as pressed felts, paper, and nonwoven fabrics), and (3) random-packed beds of rigid particles (including pressed and/or sintered compacts of such materials). Media composed of random-packed beds exhibit a highly random distribution of pore volume, show a great tortuosity of interconnecting pore structure, and are probably composed of interconnecting pores which contract and expand continually along any path through the medium. By contrast, woven filter media exhibit a highly oriented structure and are composed of distinctly different inter-yarn and interfiber pores, many of which are probably less tortuous than those through a packed bed.

General experience has indicated that to be a practical filter medium, a packed bed must be composed of particles or fibers appreciably larger, in at least one dimension, than the particles to be removed and that the particles or fibers in the packed bed must be of such a size and shape distribution that the packed bed is of a high porosity even when subjected to normal filtration pressure drop. Only meager information is available on the use of packed beds (other than sand beds for water clarification, which is a special case) as the medium for liquid filtration. Filter aids have been studied by Carman (*7*), Cummins (*9*), and Hoffing and Lockhardt (*21*), but principally as additives to increase filter-cake permeability; their use in precoat form as the filter medium itself and the physical properties of such precoat beds have not been considered. The relationship between particle removal from a passing gas stream and the structure of filter

beds of fibers has been considered theoretically by Langmuir (*27*) and Davies (*11*), whose work has been well summarized by Thomas (*43*). However, their work does not consider the effect of bed structure on the rate of plugging even for gas filtration and may not be generally applicable to liquid clarification because of differences in the basic mechanism of particle collection and retention. Thus the need for information on the structure and performance of packed beds as filter media for liquids appears second only to the need for similar information on woven filter media.

While woven filter media are more widely used for liquid filtration than are packed-bed media, the weavers and vendors have little knowledge of internal pore structure and the effect of construction variables (such as filament or staple denier, number of filaments, yarn packing structure and twist, plying of yarns, type of weave structure, and various finishing operations) on either the pore structure or the functional performance of the medium. Recently Schwarz (*38*) considered the effect of yarn structure on fabric properties. He points out that only a few of the various types of possible fiber-packing arrangements are sufficiently stable for good results, and he presents micrographs of sections of single and plied yarns which show the nature of interfiber voids with various yarn structures and yarn twists. He concludes that, in general, decreasing filament denier, increasing the number of filaments per yarn, and increasing yarn twist, all tend toward producing a smaller and more uniform interfiber void, although a design yielding a stable packing arrangement is an essential first requirement. More recently Hoffman (*22*) has considered the effect of fabric design and construction on the density, or porosity, of both the yarns and the over-all fabric. He predicts that a range of filament denier in the yarn structure will result in greater yarn porosity and larger interfiber voids because of a "wedging-apart" action. Hoffman also emphasizes the practical importance of the flattened or elliptical cross section of yarns when considered in the actual fabric and shows section views of various fabrics to illustrate this important point. This elliptical shape is characteristic of tight fabrics such as filter media and is further promoted by fabric-finishing procedures such as calendering. According to Hoffman, increasing yarn twist alone results in a thicker fabric, a lower porosity yarn, a more open weave, and a more nearly circular yarn within the fabric.

Backer (*3*) has shown the general effect of interyarn geometry (i.e., weave construction) on shape and area of pores at various cross sections through the fabric and has related these to the permeability characteristics of certain fabrics. Smith (*42*) in a recent discussion of filter-media properties and performance emphasizes the role of high yarn twist in reducing the volume of interfiber pores and the importance of filtering through interyarn instead of interfiber pores to prevent cloth plugging in cake filtrations. Silverman (*41*) has emphasized the importance of fiber diameter and total specific surface of the filter medium in removing small dust particles from dilute-gas suspensions. These factors, however, merely form a method of expressing effective pore radius in terms of fiber properties but fail to take into account yarn and weave construction, which also influences pore radius.

FLOW THROUGH FILTER MEDIA

Initial considerations require a knowledge of the flow and flow resistance with unused media before any understanding can be achieved of flow during the blocking period of actual filtration. For packed beds of fibers or solid particles, a large amount of information is available on correlation of flow resistance with bed properties, and this was reviewed recently as applied to filtration (*19*). For woven-filter media the picture is complicated by the highly oriented nature of the fiber packing. The idealized case of a monofilament weave, as represented by screens, has been treated by several workers (*20, 32,* and *36*) and by a screen manufacturer (*1*). These treatments are all similar and are based on development of a correlation of discharge coefficient vs. Reynolds number and the fractional free area represented by interyarn pores.

Robertson (*36*) has attempted to extend this treatment to multifilament and staple yarn fabrics with only limited success. For plain weaves of rather open construction, correlation by this method was fairly satisfactory, but for more complex weaves and particularly for weaves of tightness approaching that of most woven filter media, the method failed badly. This probably results from the fact that as interyarn pores become smaller or more tortuous, an appreciable amount of fluid flows through the interfiber pores in parallel with the interyarn pores. Data on various filter media have shown that while values for air flow and liquid flow through monofilament media usually agreed, with multifilament and staple-yarn media the resistance to liquid flow is almost always considerably greater than would have been predicted from the air-flow resistance. In some cases this discrepancy results largely from swelling of the fibers in the liquid. In many cases with synthetic fibers, however, swelling is not a factor, and this discrepancy is believed to result from the division of flow between parallel interyarn and interfiber pores and from possible slip flow of air in the interfiber pores. Recent results of Cunningham et al. (*10*) have further confirmed this observed discrepancy and have suggested that wetting phenomena may also be involved.

No sound data are available on this division of flow with tightly woven media, and literature reports are conflicting. Robertson (*36*) reports that complete plugging of interfiber pores of such media decreased permeability only 10% and Smith (*42*) reports that complete plugging of interfiber pores reduced permeability 95 to 98% with similar low-twist fabrics. Probably the magnitude of the effect even with tightly woven fabrics is largely dependent on many factors involved in fabric construction. Backer (*3*) has considered the effect of many of these design factors on division of flow through interfiber and interyarn pores and over-all permeability. He concluded that more numerous interlacing of the yarn system (higher fabric count) reduces permeability by simultaneously reducing the size of both interyarn and interfiber pores, other factors remaining constant. On the other hand, Robertson (*36*) found that if all elements other than twist are held constant, the permeability increases as the twist is increased even though the interfiber pores decreased in size with increasing twist. An explanation of this may be that as the twist increases and interfiber pore size decreases, the interyarn pore size increases, and the division of flow shifts more to the interyarn pores.

Rainard (*35*), in correlating air-permeability data in textile fabrics, has taken a different approach from that of most other workers. On the basis of his data, he proposes an empirical equation of the form

$$(70.6)\ \frac{\Delta p_f}{q_f} = C_1 q_f + C_2 \qquad (1)$$

This is similar in form to equations proposed more recently by Durwez and Green (*15*) to describe flow through metal compacts and by Ergun (*17*) to describe flow through packed columns. Although Rainard's data were insufficient to define the exact nature of C_1 and C_2, he suggested on theoretical grounds that

$$C_1 = \frac{b\rho_f}{g_c \pi^2 r^4 N^2 A^2}\,(10)^{16} \qquad (2)$$

$$C_2 = \frac{8h\mu_f}{g_c \pi r^4 N A}\,(10)^{14} \qquad (3)$$

where b is a constant to account for the variation in velocity resulting from expansions and contractions along the length of the pores. Actually the empirically determined values of C_1 obtained by Rainard were probably also a function of the distribution of flow between interfiber and interyarn pores.

PORE-SIZE MEASUREMENT

The size distribution, shape, tortuosity, and volume of pores in a filter medium

are of prime importance to the retentiveness, flow resistance, and plugging rate in filtration service. Available information also indicates that a knowledge of these properties is an essential intermediate link between the performance properties of a medium and the construction of the medium. Initial work on this problem resulted in development and application of procedures for measuring average and maximum pore size of woven media. The values of average pore radius so obtained are calculated from liquid-permeability data for the viscous-flow range employing a modification of the Kozeny-Carman relationship. Thus for a circular pore of radius r, the hydraulic radius

$$m = r_p/2$$

and

$$r_p = \frac{2\epsilon}{(1-\epsilon)S_0}\,(10)^4 \qquad (4)$$

where S_0 can be calculated from the resistance coefficient of the medium by employing the Kozeny-Carman relationship in the form

$$S_0^2 = \frac{\epsilon^3}{(1-\epsilon)^2 K}\,\frac{(R_m')}{(L)}\,(1.075 \times 10^3) \qquad (5)$$

The resistance coefficient of the filter medium R_m' is calculated from liquid-permeability data in the viscous-flow range by use of the relationship

$$R_m' = (2.16 \times 10^5)\,\frac{A g_c \Delta p_w}{\mu_f q_f} \qquad (6)$$

The pore radius so obtained is probably an average falling between the radius of interfiber pores and that of interyarn pores, but on a comparative basis these values have proved very useful in selection of filter media. A similar method has been used recently by Schwertz (*39*) to determine average pore size and pore-population density of fritted-glass filter disks; however, gases were used instead of liquid and this necessitated use of a slip-flow correction of uncertain accuracy. Other methods of calculating an average pore radius from permeability data have been employed by many workers dealing with membranes (*16, 28, 29, 31*). This method assumes that pores are straight-through, parallel capillaries of length equal to the membrane thickness. With this assumption, Poiseuille's law can be transformed to yield a pore radius directly,

$$r_p = \frac{(8L)^{1/2}}{(\epsilon R_m')}\,(30.5 \times 10^4) \qquad (7)$$

Although this method has been applied to calculate pore sizes in sintered ceramic filters (*12*), such use is difficult to reconcile with the basic assumption of straight-through pores made in its derivation. Thus this method does not appear so applicable to either woven or packed-bed filter media as does the modified Kozeny-Carman relationship.

Measurement of size of maximum pore by the bubble-pressure method is not new and has been widely applied to membranes (*4* and *30*) and fine structure of porous ceramic bodies (*26* and *2*). More recently it has been applied to textile fabrics (*39*) in studies relating to their water repellency. The bubble method depends simply on equating forces at the entrance to a liquid-filled capillary. Thus if a circular pore cross section is assumed, the radius of maximum pore is calculated from

$$r_m = (0.1448)\,\frac{2\sigma \cos\theta}{\Delta p_b} \qquad (8)$$

where $\cos\theta = 1$ if a liquid which wets the medium is used to fill the pores initially and is displaced by a gas. For this special case the liquid which preferentially wets the solid prevents the interfacial surface between liquid and gas from ever touching the solid; thus one is dealing with a two-phase fluid system, and the porous material is important only insofar as it imposes dimensional limitations on the system. Combined with the value of average pore radius obtained from permeability measurements, the maximum pore radius has proved a useful tool in selection of filter media, the ratio of maximum to average giving some measure of uniformity of pore sizes present. The bubble method can be modified to measure the rate of gas flow at various increasing pressures after the critical pressure for bubbling is reached; by this means a form of pore-size distribution can be calculated as Bechhold (*5*), Grabar (*18*), and Ruemele (*37*) did. The theory and method of calculation involve numerous doubtful assumptions, although these have been clarified recently and the method of calculation has been improved upon by Ishkin and Kazaner (*24*).

PORE-SIZE DISTRIBUTION MEASUREMENT

For packed-bed and woven filter media, two other methods of pore-size measurement are possible which are potentially capable of yielding a complete pore-size distribution curve for almost any type of filter media. The first of these, which is based on physical adsorption of a gas by capillary condensation on the pore walls of the solid, utilizes a modified form of the Kelvin equation. Thus in a circular capillary of radius r, the saturation vapor pressure of a liquid is reduced from p_0 to p_1, where, with a zero angle of contact assumed, p_1/p_0 is given by

$$\ln \frac{p_0}{p_1} = \frac{2\sigma M}{rRT} \qquad (9)$$

For a given liquid at constant temperature, therefore, r is only a function of p_1, provided that σ and ρ_f are constant. It follows that if an adsorption isotherm for a porous medium is drawn as v against p, where v = milliliters of liquid adsorbate per gram of adsorbent, it is necessary only to convert values of p_1 to corresponding values of r to obtain the pore-size-distribution curve. The limitations and difficulties of this method are summarized by Carman (*8*), who has successfully applied it to porous powder plugs with pore radii of 5 to 40 Å., and by Pierce (*33*), who has more recently applied the method successfully over the pore-size range of 25 Å. to 0.1μ. As yet the method has not been successfully applied to the 0.1- to 200-μ pore-radius range, which is of most interest with normal filter media.

The second method capable of yielding a complete pore-size distribution is the liquid-intrusion method first suggested by Washburn (*45*). Because the liquid used must be nonwetting with respect to the porous solid, mercury has been most widely used and the method has become known as the mercury-intrusion method. The method was first successfully applied by Ritter and Drake (*13* and *34*) for the pore-size distribution of such materials as fritted glass, activated clays, diatomaceous earth, and silica gel, covering a pore-radius range from 0.01 to 1.0μ. Drake (*14*) later used the method for further work on the pore structure of catalyst supports. The method was first successfully applied to the textile fabrics by Burleigh and associates (*6*), and this application was more recently extended by Wakeham and Spicer (*44*), and Honold and Skau (*23*). Cotton apparel-type fabrics were examined and an effort was made to correlate interfiber pore volume or radius with air permeability.

The mercury-intrusion method is dependent both on the experimental measurement of the volume of mercury entering the pores of a submerged sample as the absolute pressure is increased and on the relationship between pore size and the pressure required to overcome surface-tension forces and to force mercury into the pores of the sample. When pores of circular cross section are assumed, the pressurizing equation takes the simple form

$$r = (0.1448)\,\frac{-2\sigma \cos\theta}{p} \qquad (10)$$

where r is radius of pore constriction at which the pressure forces are in equilibrium. When an evacuated sample of a porous material is submerged in a nonwetting fluid such as mercury and subjected to continuously increasing pressure, a unique pressurizing curve of cumulative mercury volume in the sample vs. pressure is obtained if it is assumed that contact angle and surface tension remain constant. On the basis that the volume

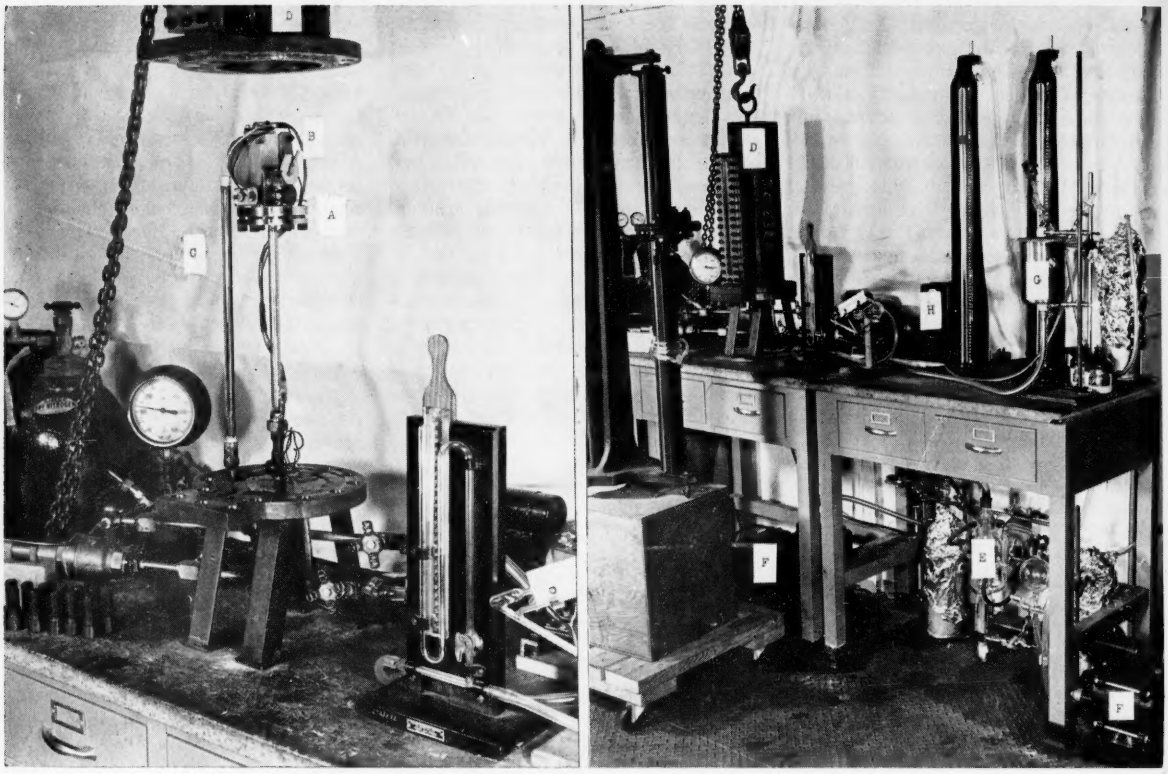

Fig. 1. Dilatometer apparatus for measurement of pore-size distribution: *A*, sample cell; *B*, electric valve; *C*, calibrated capillary, open leg; *D*, dilatometer casing; *E*, diffusion pump; *F*, mechanical forepumps; *G*, mercury reservoir; *H*, squeegee mercury-recirculating pump.

of liquid entering the pores is a function of the radius of the pores as the pressure is increased, a distribution function of pore size can be derived (*34*), and

$$D(r) = \frac{p}{r}\frac{d(\Delta V)}{V_0\, dp} \qquad (11)$$

where r is the radius of pores in equilibrium at absolute pressure p [calculated from Equation (10)] and $d(\Delta V)/V_0\, dp$ is the slope of the pressurizing curve at pressure p, this slope being determined by graphical differentiation.

The assumptions inherent in the application of Equation (11) are that the pore cross section is circular, that σ and θ remain constant during measurements on a single sample, and that satisfactory values of σ and θ are used for each sample. The assumption of circularity of pore cross section is the most likely source of error. If for noncircular pores the "true" pore radius is considered to be the radius of the largest possible inscribed circle, the constant 2 in Equation (10) can be shown to vary between 1.0 and 3.0 for extremes of noncircular pore shape and packing. Therefore, depending on pore shape, the distribution curve obtained from Equation (11), if circular pores are assumed, might be shifted toward either smaller or larger values of pore radius than the "true" pore radius for a noncircular pore. With woven filter media any error may be relatively constant as pore shapes probably do not change radically. Similarly, an error in contact angle or surface tension would have the effect of shifting the derived distribution function on the radius axis. In this work the I.C.T. value of surface tension of mercury in vacuum was used and contact angles between mercury drops and the samples were photographed and measured.

Nonrigidity of the pore system of a material such as a fabric might conceivably lead to compression of the sample during measurement and to distortion of the pore-size-distribution curve. However, with the materials examined, 50 to 90% of the pore volume of the samples were filled at absolute pressures of 10 lb./sq. in. or less, so that sample distortion over this major portion of the distribution curve was minimized. Also, this filling of the major portion of pore volume before the higher pressures were reached stabilized the samples so as to minimize further sample distortion during the remainder of the pressurizing curve. Interpretation of the results in the form

Fig. 2. Dilatometer sample cell with motor-driven valve.

of distribution curves must be tempered by a realization of the probable effect of expansions and contractions in the pore structure. Thus any point on the curves of $D(r)$ vs. r represents pore volume per micron size interval, which can be entered by the mercury only through a constriction of radius r. Thus the effect of such restrictions in either the open pore structure or in closed "ink-bottle" pores results in a hysteresis loop as pressure is released and mercury leaves the pores at the end of the run. This hysteresis effect is similar to that observed for the isotherms in physical-adsorptions measurements, and possible quantitative treatment of this hysteresis effect is discussed by Katz (*25*) and Drake (*14*).

lated through a similarly evacuated reservoir so as to remove air from the solution. After 4-hr. evacuation (absolute pressure usually 10 to 20μ), mercury from the reservoir was introduced into the U tube of the dilatometer until the mercury level rose to the valve level over the sample cell. The valves between the U tube and mercury reservoir were closed, as was the electrically operated valve at the top of the sample cell. Pressurizing of the casing was then started and continued in small increments every 2 to 3 min., a total of 40 to 50 pressurizing steps being included between 0.6 lb./sq. in. gauge and 350 lb./sq. in. abs. Descent of mercury in the open leg of the U tube was observed through the window by means of a cathetometer which allowed the level to be read to the nearest 0.005 cm. The capillary comprising the open leg of the U tube was calibrated against a certified microburette over its entire length of 50 cm., and was found to have a uniform bore capacity of 0.00357 ml./mm. $\pm$ 0.00002 ml./mm. over its length. Pressure in the dilatometer casing was raised by bleeding air until atmospheric pressure was reached and by introducing nitrogen at above atmospheric pressure. All pressures up to 15 lb./sq. in. gauge were measured by mercury manometers corrected for barometric pressure. Calibrated Bourdon tube gauges were used from 15 to 350 lb./sq. in. gauge.

Blank runs were made initially in order to correct for any slight expansion of the dilatometer piping during the pressurizing cycle as well as for slight mercury penetration of supporting screens during pressurizing. These blank runs were made with two and four supporting screens present, and

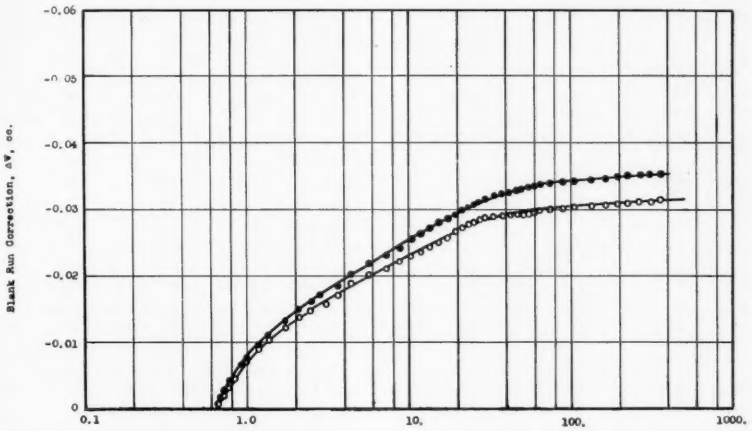

Fig. 3. Dilatometer calibration: blank-run correction curves, no sample; ○ two No. 8-mesh support screens; ● four No. 8-mesh support screens.

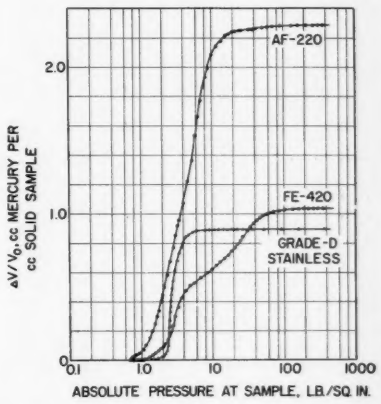

Fig. 4. Dilatometer pressurizing curves; $\Delta V/V_0$, cc. mercury/cc. solid sample.

EQUIPMENT AND EXPERIMENTAL METHODS

For the application of the mercury-intrusion method to most woven and packed-bed filter media, a pore-radius range of 0.3 to 180μ must be covered. This corresponds roughly to an absolute pressure range of 0.6 to 350 lb./sq. in. Such a range had not previously been covered by a single dilatometer, the only reported work over this range (*23*) requiring three separate dilatometers. In order to make uninterrupted pore-size measurements over this entire range by use of a single sample of filter medium, the U-tube dilatometer shown in Figures 1 and 2 was designed and constructed. This U-tube dilatometer (Figure 1*a*) has the sample cell and an electrically driven valve at the top of one leg and the other leg consists of the calibrated capillary with open end. The sample was held in a horizontal plane between 8-mesh stainless steel screens within the sample cell, which is shown disassembled in Figure 2. Before the mercury is introduced, the entire dilatometer casing (shown closed and assembled with accessory equipment in Figure 1*b*) was evacuated by a mechanical forepump and mercury-diffusion pump. Meanwhile the system mercury was circu-

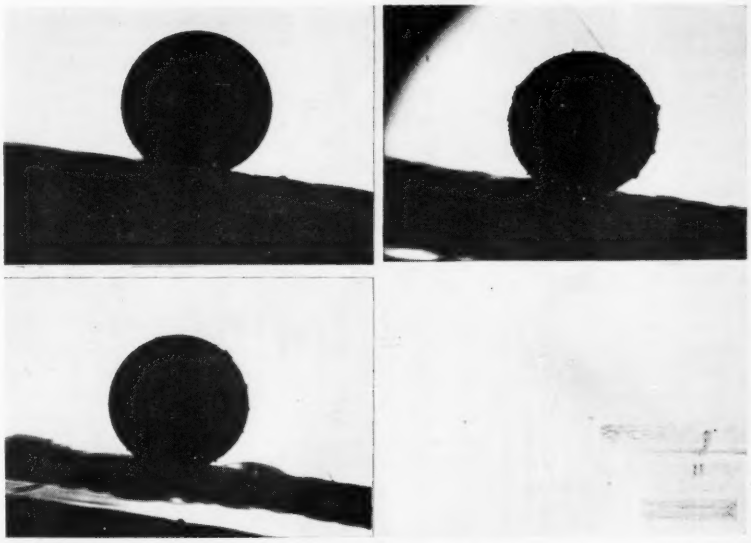

Fig. 5. Photomicrographs of contact angle between mercury and filter medium (filter medium inclined 10° from horizontal): top left, TF-5071-F Orlon, θ_A = 147°; top right, FE-420 Orlon, θ_A = 150°; bottom left, TF-5044 nylon, θ_A = 145°.

TABLE 1. DATA ON FILTER-MEDIA SAMPLES SUBJECTED TO MERCURY-INTRUSION MEASUREMENTS AND CLARIFICATION EVALUATIONS

Filter medium style or type	Yarn construction	Weave	Thread count/in. warp × fill	Wt., oz./sq. yd.	Thickness, in.	Porosity ϵ, void fraction	% Pore volume filled during measured portion of dilatometer run	Mercury-sample contact angle used	Modal pore sizes by mercury intrusion, μ		Permeability determined				
									Inter-fiber pore radius	Inter-yarn pore radius	Avg. pore radius*, μ	Radius of maximum pore†, μ	Liquid-resistance coefficient R_m, 1/ft.	Air-resistance coefficient R'_m, $\times 10^6$	Air Permeability** (cu. ft.)/(min.)/sq. ft.
Turner-Halsey 8 cotton duck	Spun staple	Plain	45 × 28	17.9	0.0350	0.537	95.9	140	2.9	55	0.90 (3.8)‡	12.4 (22.6)‡	13,600 (710)‡	413	1.0
National 33 (175-TW) cotton	Spun staple	Twill	37 × 25	17.9	0.0440	0.603	97.9	140	5.3	54	4.1 (9.9)‡	44 (44)‡	680 (116)‡	47	8.8
Wellington-Sears SN-23 nylon	Spun staple	Plain	50 × 29	14.9	0.0352	0.505	91.4	145	4.0	40	5.2	91	388	118	3.5
Feon 420 Orlon	Multifilament (moderate twist)	Satin	200 × 128	5.94	0.0140	0.517	96.4	150	3.9	42	8.0	83	72	34	12.3
Stehli 5044 nylon	Multifilament	Twill	220 × 125	3.55	0.0070	0.413	99.4	145	3.0	116	5.5	29	88	109	3.8
Stehli 5071-U Orlon (Edco HT-16-UF)	Multifilament, high-twist yarns	Taffeta	76 × 24	13.1	0.0320	0.528	69.8	150	3.8	29	14	71	44	26	16
Stehli 5071-F Orlon (Edco HT-16-F)	Multifilament, calendered, high-twist yarns	Taffeta	80 × 21	13.0	0.0210	0.296	92.8	150	2.2	25	5.4	39	380	243	1.7
Wellington-Sears SN-7 nylon	Multifilament (low twist)	Plain	60 × 42	6.32	0.0155	0.523	39.0	145	5.0	> 180	10.5	128	44	31	13.5
Albany 220 wool felt	Staple	Woven base felt	..	35.8	0.120	0.701	97.4	140	16.5	..	3.2 (15.0)‡	21 (24)‡	.. (118)‡	67	6.2
Micrometallic grade D, porous stainless steel	Pressed and sintered metallic powder	..	..	38.4	0.129	0.485	94.1	140	43.0	..	36.5	63			

*Calculated from water-permeability measurements by method of Equations (4) to (6).
†Calculated from maximum bubble-pressure measurements with air-water, by method of Equation (8).
‡Calculated as above, but from measurements with carbon tetrachloride instead of water.
**At $\Delta p = 0.5$ in. water and 70°F.

the correction curves of Figure 3 were obtained for subsequent use in correcting pressurizing curves obtained with various media. Size of samples of filter medium used in each run were chosen so as to yield a final mercury depression in the capillary of at least 25 cm., and size varied from 0.5 to 9 sq. in. depending on medium thickness. With very thin media, two or three layers of sample were used with screens between layers. The inside of the sample cell was 5.8 cm. diam. by 0.5 cm. in height, the samples being held at the desired vertical level by the screens.

In Figure 4 are shown typical pressurizing curves. For convenience, these curves were normally plotted on arithmetic paper and successive tangents taken. Thus values of $d(\Delta V)/V_0\, dp$, the slopes of the pressurizing curve, were obtained for various values of p, permitting calculation of the distribution function $D(r)$ from Equation (11). The values of contact angle θ, needed for application of Equations (10) and (11), were obtained directly from photographs of a mercury droplet resting on an inclined sample of each filter medium. The mercury droplet was 1.8 to 2.0 mm. in diameter in each case and was photographed resting on a clean piece of filter medium inclined at a 10° angle. The advancing contact angle was measured directly on these photographs, several of which are shown in Figure 5. The values obtained ranged from 136 to 152°. Values of 140° for cotton, wool, and stainless steel, 145° for nylon, and 150° for Orlon acrylic fiber were used in the calculations. The surface tension of mercury was taken as the I.C.T. value in a vacuum, the value at 25°C. being 475 dynes/cm.

The porosity or void fraction of all samples was determined independently with the gravimetric method, by use of the established density for the base fiber material. The air and liquid permeabilities of 2-in.-diam. samples were determined over a range of pressure drops representative of viscous-flow conditions, and the respective resistance coefficients were calculated by means of Equation (6). The effective specific surface of the medium and its average pore radius were calculated from this liquid resistance coefficient and the measured porosity, Equations (4) and (5) being employed. Liquid-saturated samples of 2-in. diam. were also subjected to the bubble-pressure test, and the results of five measurements of bubble pressure were averaged for use with Equation (8) in the calculation of maximum pore size.

DISCUSSION OF RESULTS

The ten types of filter media examined are listed in Table 1 together with various data on their physical properties, liquid resistance, air permeability, average pore size, and size of maximum pore. Table 1 also shows that with these samples 90 to 100% of the independently measured pore volume was filled with most media during the measured portion of the dilatometer run, although excessive surface roughness decreased this figure with two of the media. The pressurizing curves, as typified by those of Figure 4, show that in all cases the filling of the pores had practically ceased by the time 350 lb./sq.

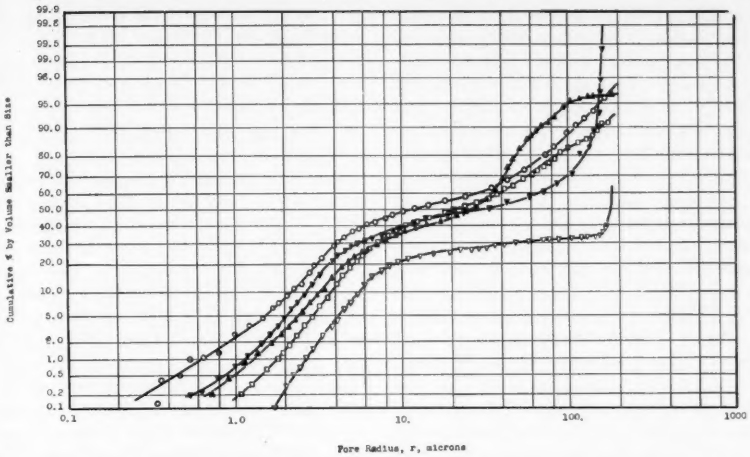

Fig. 6, Cumulative pore-size distribution curves: ○ No. 8 staple cotton duck; □ SN-23 staple nylon duck; ▲ FE-420 filament Orlon satin; ▽ SN-7 filament nylon duck; ▼ TF-5044 filament nylon twill.

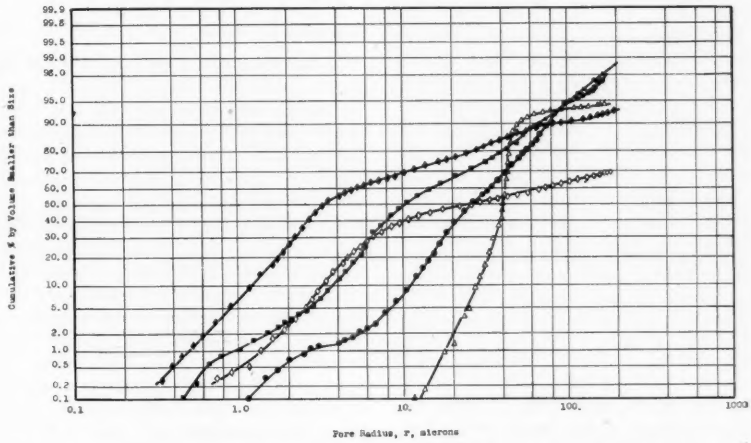

Fig. 7. Cumulative pore-size distribution curves: ● Albany No. 220 wool felt, ◇ Stehli TF-5071-U Orlon taffeta; ◆ Stehli TF-5071-F finished Orlon taffeta; △ Grade D porous stainless steel; ■ TW-175 staple cotton twill.

in. abs. pressure was reached, an indication of the existence of negligible pore volume not yet filled at this final pressure. Thus the major portion of the unfilled pore volume probably represents large surface pores of the medium which are filled by mercury at less than 0.6 lb./sq. in. abs. pressure. These large surface pores characterize the surface roughness of the medium.

Figures 6 and 7 show cumulative pore-radius-distribution curves, plotted according to particle size, for the ten media. These curves are based on the premise that essentially all pore volume is filled at 350 lb./sq. in. abs. pressure; thus pore volume not filled during the measured portion of the dilatometer run is assumed to be filled below 0.6 lb./sq. in. abs., which was the starting pressure. Curves of the pore-size-distribution function $D(r)$ are presented in Figures 8, 9, and 10. These curves were calculated directly from Equations (10) and (11), no assumptions concerning unfilled pore volume being involved.

Woven-fabric Media

In the woven-fabric media the measured pore volume was distributed between interyarn or interthread pores and interfiber pores within the yarn structure. The cumulative size-distribution curves of Figures 6 and 7 show that with all woven media 30 to 50% of the pore volume was measured at a radius of less than 10μ and probably represents mainly that portion of the pore volume existing as interfiber voids. This is confirmed by the curves of $D(r)$ vs. r of

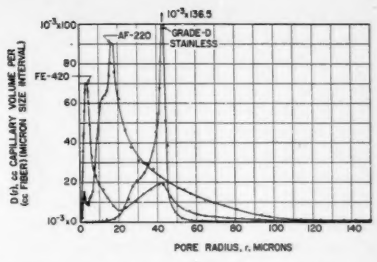

Fig. 8. Pore-size distribution: $D(r)$, cc. capillary volume/(cc. fiber) (micron size interval).

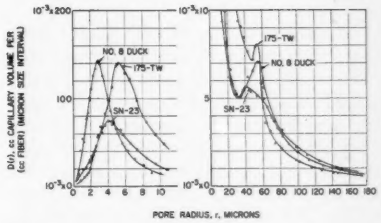

Fig. 9. Pore size distribution: $D(r)$, cc. capillary volume/(cc. fiber) (micron size interval).

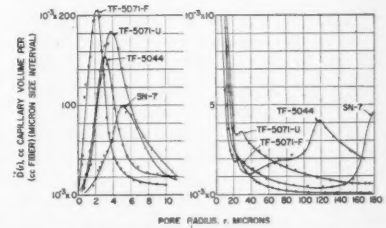

Fig. 10. Pore-size distribution: $D(r)$, cc. capillary volume/(cc. fiber) (micron size interval).

Figures 8 to 10, which for these same woven media show a sharp maximum at pore radius less than 10μ in each case, and a second less well defined maximum in the pore-radius range of 25 to 125μ. The sharp maximum below 10-μ radius appears to represent the "modal" interfiber pore radius; whereas the less distinct maximum above 25μ may represent the modal interyarn-pore radius. Actually the region over which the interyarn pores are filled is quite broad, extending from the radius of maximum pore, as measured by the bubble-pressure method, to a size approaching that of the largest interfiber pore. The sharpness of this secondary maximum appears to be much greater with a satin weave (FE-420 medium of Orlon acrylic fiber) than with the plain or taffeta weave. This may result from the fact that a satin weave embodies a greater tortuosity of interyarn pores than does a plain or taffeta weave. In some cases (Table 1) the modal value of the interyarn-pore radius was greater than the radius of maximum pore measured by the bubble-pressure method; the reason for this is not clear but probably involves complications of interyarn-pore shape which invalidate direct comparison of results.

In general the average pore radius calculated from independent permeability measurements (Table 1) falls between the modal value of interfiber pore radius and the modal value of interyarn pore radius. This would be expected if flow through the medium occurs by passage in parallel through both interyarn and interfiber pores. This is true even with the staple cotton media provided the average pore radius is calculated from permeability measurements with a liquid which does not swell the cotton fibers.

Although the Stehli 5071-U (Edco HT-16UF) and 5071-F (Edco HT-16-F) styles are constructed with unusually high-twist yarns (approximately 15 turns/in. on 600-denier yarn containing 400 filaments of 1.5 denier), Figure 7 shows that 40% of pore volume of the former style and 70% of pore volume of the latter measures smaller than 10μ and probably occurs as interfiber pores. This finding is in contrast to the views of Smith (*42*), who has stated that the yarns of such high-twist media are essentially impervious to flow and approach a monofilament in filtering action. Smith based his views on semiquantitative observation of comparative flow through media woven from ordinary yarns and from yarns which were intentionally loaded before weaving in an effort to saturate interfiber pores. It is likely that the yarn-loading process used by Smith may have been ineffective with the higher twist yarns, leading to the false conclusion that the absence of a decrease in permeability on loading meant that the original yarns were necessarily impervious. The effect on pore-size distribution of finishing by calendering and heat-treatment is shown by comparing the curves of Figures 7 and 10 for 5071-U and 5071-F, the latter being the same as the former except for finishing. Figure 7 shows little change in the shape of the size-distribution curve, but rather a shift of the entire curve. Figure 10 shows that much of the pore volume originally present as surface roughness and interyarn pores has been eliminated and that size of both interyarn and interfiber pores has been reduced. This is in general agreement with the findings by independent measurements of average and maximum pore radius in Table 1. In general these findings on high-twist media, in both the unfinished and finished conditions, indicate that the effectiveness of high-twist yarns in improving the performance of filter media does not result from elimination of flow through yarn structure by the forming of impervious yarns as reported by Smith (*42*). Rather it appears that the effectiveness of high-twist yarns depends only on reduction in size of the interfiber pores.

Thus, the size of interfiber pores is reduced below the size allowing particle penetration and plugging with a particular system, but yarns remain permeable and a large part of filtration continues to occur through the interfiber pores. In contrast, the effect of finishing appears to result from reduction in size of both interfiber and interyarn pores, with the predominant effect that of eliminating a large part of the interyarn pore volume. In fact these data indicate that when both high twist and finishing are combined, an abnormally high percentage of pore volume exists as interfiber voids and an even greater proportion of filtration action may occur through the yarn structure than occurs with low-twist media which are unfinished. This finding suggests that progressive plugging of a filter medium in cake-filtration service can be prevented only when a medium is selected with an interfiber pore radius sufficiently small to prevent penetration of the yarn structure by the smallest particles or particle agglomerates existing in the feed suspension. The value of a combination of high-twist yarns and the finishing method, which is employed by Stehli & Co. and by Edco as a means of reducing filter media plugging, therefore appears to accrue from (1) a reduction in interfiber pore size caused both by high-twist yarns and by finishing, and (2) a marked reduction in interyarn pore volume and size caused by the finishing operation alone.

Felt Media

Because of the more random orientation of fibers in felt media, a much higher porosity results and a much broader range of pore-size distribution might be expected. The single felt examined (Albany 220 of Table 1) is a woven-base felt. Such felts are made by weaving a loose base structure which is roughed and worked to form a felt surface on both sides of the base structure. The medium exhibited a much larger average pore size than the woven media, 90% of the pore volume being measured as above 10-μ radius (Figure 7). With this material the large peak at 10 to 20μ on the $D(r)$ curve of Figure 8 represents the modal size of interfiber pores in the bulk of the felted structure and the very slight inflection at 2- to 3-μ radius is indicative of modal size of interfiber pores in the woven-base structure. Average pore size calculated from permeability data agreed closely with the modal size of the interfiber pores in the bulk of the felted structure (Table 1) when a liquid was used which did not swell the fibers. The $D(r)$ curve of Figure 8 indicates that for felt media the interfiber pores in the bulk of the felt structure cover a greater range of size within a given medium than do interfiber pores of a woven-fabric type of medium.

Sintered-metal Media

Under this class a sample of grade *D* porous stainless steel (Table 1) was examined. Results showed the pore-size distribution of this type of medium to be much narrower than that of either woven fabrics or felt. Thus with the sample examined, 90% of the pore volume was measured as falling between 20 and 50μ of pore radius (Figure 7). The sharpness of the frequency distribution as compared with a fabric and a felt are shown by the $D(r)$ curves of Figure 8. The average pore radius of 36.5μ (Table 1) calculated from water-permeability data by means of Equations (4) and (6) appears in excellent agreement with the experimentally determined size distribution. This indicates that the porous stainless steel medium approximates a random-packed bed and that the assumptions of the Kozeny-Carman equation must be reasonably valid as applied to this particular material.

SUMMARY

It has been shown that the mercury-intrusion method can be successfully applied to determine the pore-size distribution of filter media. Following are the results of such measurements on typical filter media.

1. Pore-size distributions so obtained are compatible with pore-size information obtained by the permeability and bubble-pressure methods, but the pore-size distributions resulting from mercury-intrusion measurements are much more informative in regard to pore structure.

2. With woven filter media the pore volume is distributed between interyarn and interfiber pores, with 30 to 50% of the pore volume existing as interfiber pores even with media constructed of high-twist yarns.

3. The finishing of woven filter media by calendering and heat setting reduces the size of both interyarn and interfiber pores

while reducing the proportion of pore volume existing as interyarn pores.

4. With felt media the pore volume exists as interfiber pores which are distributed in size over a much wider range than are the interfiber pores of woven media.

5. With consolidated porous media the size distribution of pore volume is very narrow compared with that with woven or felt media.

Further application of the mercury-intrusion method to the study of the internal structure of filter media can be expected to define, with textile media, the effect of yarn packing, filament and yarn denier, staple length, yarn crimp and ply, and various finishing treatments. Similar application to consolidated porous media can be expected to define the effect of particle-size distribution, particle shape, consolidating pressure, and sintering conditions. However, the accumulation of such information on both types of filter media will lead to a more systematic design of filter media only if filtration studies can successfully correlate pore structure with particle size removed and rate of plugging of the medium.

NOTATION

A = superficial filtration area at surface of filter medium or cake deposited thereon, sq. cm.

b = empirical constant in Reinard's equation, dimensionless

C_1 = inertial coefficient in empirical equation, g.sec.^{2}/cm.^{3}

C_2 = viscous coefficient in empirical equation, g.sec./cm.^{5}

$D(r)$ = frequency-distribution function of pore volume in terms of pore size through which it is accessible to a penetrating fluid, (cc. pore volume)/(cc. solid)(μ size interval)

g_c = conversion factor in Newton's law of motion, 980 (g.)(cm.)/(g.force)(sec.)^2

h = effective pore length, cm.

K = constant of Kozeny-Carman relationship (5 $\pm$ 10%), dimensionless

L = thickness of filter medium, ft.

m = average hydraulic pore radius, cm. [$= r_p/2$ for circular pore; $= \epsilon/(1-\epsilon)S_0$ for packed bed]

M = molecular weight of liquid adsorbate used in capillary adsorption measurements, g./mole.

N = number of pores per unit area, 1/sq. cm.

p = absolute pressure at filter medium, lb./sq. in.

p_0 = saturation vapor pressure in bulk of a liquid absorbate, mm. Hg

p_1 = saturation vapor pressure of a liquid in capillary of radius r, mm. Hg

Δp_b = pressure drop across unused medium when first bubble of gas is passed in bubble-pressure method, lb./sq. in.

Δp_f = pressure drop across unused medium with single fluid phase flowing, lb./sq. in.

Δp_w = pressure drop across unused medium in liquid-permeability measurements, lb./sq. in.

q_f = rate of fluid passage through unused filter medium, cc./sec.

r = pore radius in medium, μ

r_p = average pore radius of filter medium calculated from liquid-permeability measurements, μ

r_m = radius of maximum size of pore calculated from bubble-pressure measurements, μ

r_f = modal value of interfiber pore radius as measured by mercury-intrusion method, μ

R = gas constant, calories/g. mole

R_m' = resistance of unused filter medium determined by liquid-permeability measurements in viscous range, 1/ft.

R_m'' = resistance of unused filter medium determined by air-permeability measurements, 1/ft.

S_0 = specific surface of filter medium, sq. cm./cc. fiber

T = absolute temperature, °Kelvin

v = volume of liquid adsorbate/unit solid absorbent, cc./g.

V_0 = volume of fiber solids in test specimen (mercury-intrusion method), cc.

$\frac{\Delta V/V_0}{V_0\, d_p}$ = cumulative volume of mercury having entered pores of filter medium under test (mercury-intrusion method) at absolute pressure p, cc./cc. fiber

$d(\Delta V)$ = slope of pressurizing curve at pressure p (mercury-intrusion method), (cc. pore volume)/(cc. fiber)(lb./sq. in.)

ϵ = porosity of filter medium, void fraction, dimensionless

ρ = density of liquid absorbate, g./cc.

ρ_f = density of flowing fluid, g./cc.

σ = surface tension, dynes./cm.

μ_f = viscosity of solution or filtrate, centipoises

θ = advancing contact angle, degrees

LITERATURE CITED

1. Anon., "Handbook of Technical Data on Wire Cloth and Filter Cloth," Catalog 50, Multi-Metal Wire Cloth Co., Inc., New York (1950).
2. Anon., "Physical Separation of Immiscible Fluids Through Porous Media by Means of Surface and Interfacial Tension," Selas Co., Philadelphia (1943).
3. Backer, S., *Textile Research J.*, **21**, 703 (1951).
4. Bechhold, H., *Z. physik. Chem.*, **64**, 328 (1908).
5. ———, *Kolloid-Z.*, **66**, 334 (1934).
6. Burleigh, E. G., Jr., H. Wakeham, E. Honold, and E. L. Skau, *Textile Research J.*, **19**, 547 (1949).
7. Carman, P. C., *Ind. Eng. Chem.*, **31**, 1047 (1939).
8. ———, *Proc. Roy. Soc. (London)*, **209A**, 69 (1951).
9. Cummins, A. B., *Ind. Eng. Chem.*, **34**, 403 (1942).
10. Cunningham, G. E., G. Broughton, and R. R. Kraybill, *Ind. Eng. Chem.*, **46**, 1196 (1954).
11. Davies, C. N., *Arhiv. Hi. Rada*, **1**, 4 (1950); *Proc. Inst. Mech. Engrs. (London)*, **1B**, 185 (1952).
12. Deadmore, D. L., *Ceram. Age*, **56**, 15, 23 (1951).
13. Drake, L. C., and H. L. Ritter, *Ind. Eng. Chem.*, **37**, 787 (1945).
14. Drake, L. C., *Ind. Eng. Chem.*, **41**, 780 (1949).
15. Durwez, P., and L. Green, *J. Appl. Mechanics*, **18**, 39 (1951).
16. Elford, W. J., *Proc. Roy. Soc. (London)*, **B112**, 384 (1933).
17. Ergun, S., *Chem. Eng. Progr.*, **48**, 89 (1952).
18. Grabar, P., and J. Nikitine, *J. chim. phys.*, **33**, 721 (1936).
19. Grace, H. P., *Chem. Eng. Progr.*, **49**, 303 (1953).
20. Hoerner, S. F., *Textile Research J.*, **22**, 274 (1952).
21. Hoffing, E. H., and F. J. Lockhardt, *Chem. Eng. Progr.*, **47**, 3 (1951).
22. Hoffman, R. M., *Textile Research J.*, **22**, 170 (1952).
23. Honold, E., and E. L. Skau, *Textile Research J.*, **21**, 419 (1951).
24. Ishkin, I. P., and M. G. Kazaner, *Zhur. Fiz. Khim.*, **24**, 943 (1950).
25. Katz, S. M., *J. Phys. & Colloid Chem.*, **53**, 1166 (1945).
26. Knoll, H., *Kolloid Zhur.*, **90**, 189 (1940).
27. Langmuir, I., "Smokes and Filters," No. 865, Part IV, U. S. Office Sci. Res. & Dev. (1942).
28. Madras, S., *Can. J. Research*, **27B**, 764 (1949).
29. Manegold, E., *Trans. Faraday Soc.*, **33**, 1088 (1937).
30. McBain, J. W., and S. S. Kistler, *loc. cit.*, **26**, 157 (1930).
31. Morton, T. H., *loc. cit.*, **31**, 267 (1935).
32. Penner, S. E., and A. F. Robertson, *Textile Research J.*, **21**, 775 (1951).
33. Pierce, C., *J. Phys. Chem.*, **57**, 149 (1953).
34. Ritter, H. L., and L. C. Drake, *Ind. Eng. Chem.*, **17**, 782 (1945).
35. Rainard, L. W., *Textile Res. J.*, **17**, 167 (1947).
36. Robertson, A. F., *loc. cit.*, **20**, 838, 844 (1950).
37. Ruemele, T., *Z. Anal. Chem.*, **119**, 360 (1940).
38. Schwarz, E. R., *Textile Research J.*, **21**, 125 (1951).
39. Schwertz, F. A., *J. Appl. Phys.*, **20**, 1070 (1949).
40. Segall, G. H., *Textile Res. J.*, **22**, 736 (1952).
41. Silverman, L., *Heating and Ventilating*, **47**, 68 (1950).
42. Smith, E. G., *Chem. Eng. Progr*, **47**, 545 (1951).
43. Thomas, D. J., *J. Inst. Heating, Ventilating Engrs. (London)*, **20**, 35 (1952).
44. Wakeham, H., and N. Spicer, *Textile Research J.*, **19**, 703 (1949).
45. Washburn, E. W., *Proc. Natl. Acad. Sci. U. S.*, **7**, 115 (1921).

II. Performance of Filter Media in Liquid Service

The performance of nine typical filter media of previously determined pore structure has been determined by the filtration of very dilute suspensions containing spherical particles of known size distribution. The mechanisms of filtration prior to the formation of a macroscopic cake are considered, and the applicability of various filtration laws proposed by Hermans and Bredée to describe these regions of filtration are examined. Regions of "standard-blocking" filtration are found to occur with each of the filter media examined. The clogging values for the various media over the region of standard blocking are shown to be related quantitatively to the modal value of interfiber pore radius of the media, as measured by the mercury-intrusion method.

Part I of this paper examined the internal structure of typical filter media commonly used for liquid filtration and presented data on the pore size and pore-size distribution of these media. In this second part the performance of these same filter media is determined quantitatively by a clarification technique, and the clogging values for the various media are correlated with the previously reported pore-size-distribution data.

FUNCTION OF FILTER MEDIUM

In Cake Filtration

Ideally a filter medium allows unrestricted passage of a fluid through its pore structure while retaining all suspended solid particles originally present in the fluid. The solid particles may be retained entirely at the surface of the filter medium if all particles are larger than the pores of the medium and the pore structure of the medium consists of simple, straight-through pores of nearly equal size. While this case may be approximated in a simple screening operation on a plain mesh screen or by filtration through colloidal membranes, the usual filtration case is much more complex. Most chemical suspensions as filtered contain ultimate particles of subsieve and often submicron size, which may be well dispersed or partially or highly flocculated depending on the solids concentration in the suspension and the chemical nature of the suspending solution. In almost all practical cases a fairly wide range of effective particle size exists in the feed, either as a result of a wide ultimate particle-size distribution and/or a condition of partial flocculation of the ultimate particles. Thus, in the usual case the pore structure of the filter medium must remove particles of over a hundredfold size range without unduly restricting fluid flow.

The problem is further complicated by the limitations placed on the pore structure of the medium by the method of construction. Woven fabrics used for cake filtration have relatively large inter-yarn pores in parallel with much smaller interfiber pores. Both types of pores tend to present a passage of greater tortuosity than a straight-through pore and both vary in size throughout their length. In packed beds of fibers (woven or pressed felts, fibrous filter aids, etc.) and in packed beds of rigid particles (sintered-

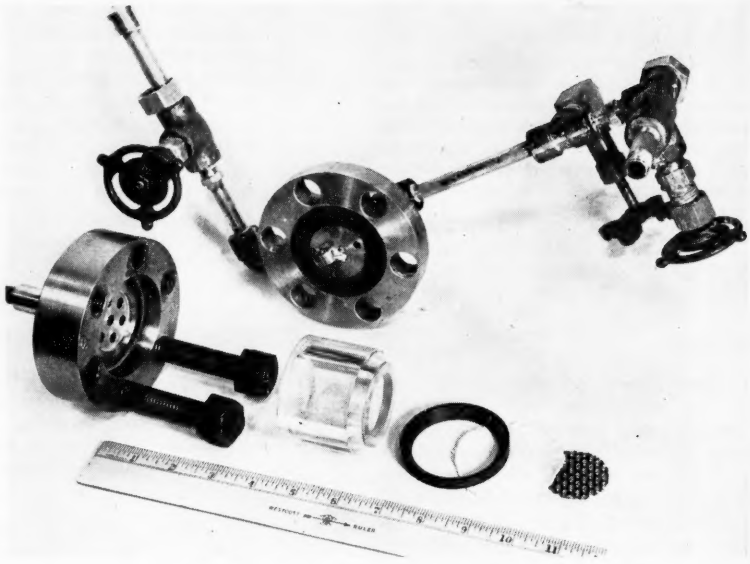

Fig. 1. Apparatus used to make filtration runs: top, pressure-filter cell; bottom, assembled filtration and recording apparatus.

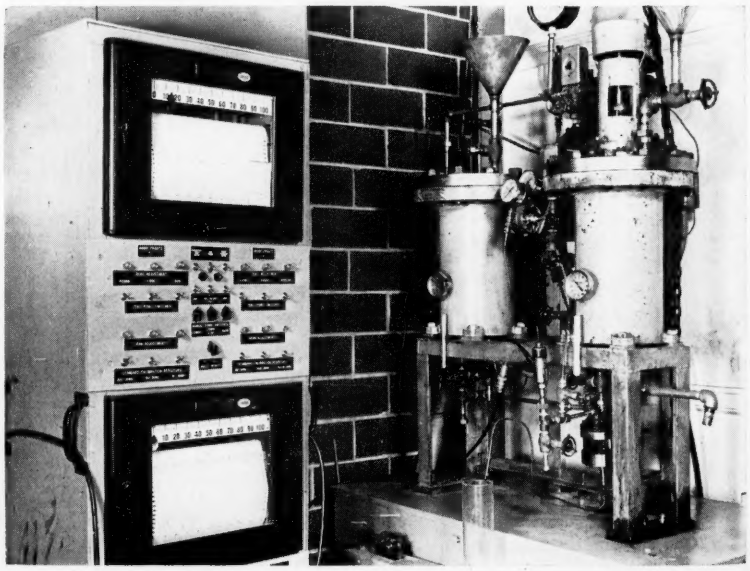

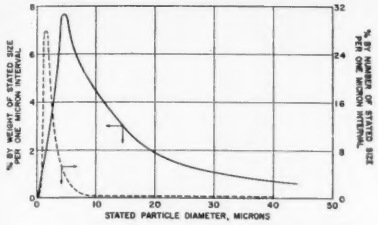
% BY WEIGHT OF STATED SIZE PER ONE MICRON INTERVAL
% BY NUMBER OF STATED SIZE PER ONE MICRON INTERVAL
STATED PARTICLE DIAMETER, MICRONS

Fig. 2. Particle-size distribution of spherical particles filtered.

Fig. 3A. Initial portion of filtration run with 175-TW cotton twill.

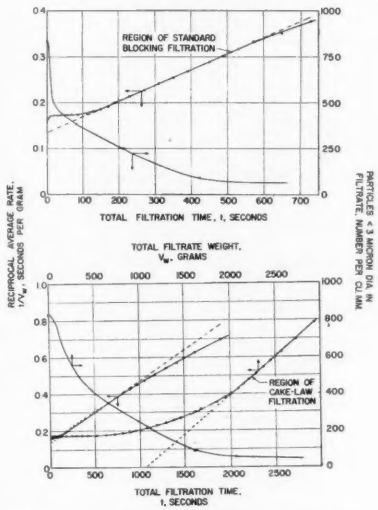
REGION OF STANDARD BLOCKING FILTRATION
TOTAL FILTRATION TIME, t, SECONDS
RECIPROCAL AVERAGE RATE, 1/V_w, SECONDS PER GRAM
PARTICLES < 3 MICRON DIA IN FILTRATE, NUMBER PER CU MM
TOTAL FILTRATE WEIGHT, V_w, GRAMS
REGION OF CAKE-LAW FILTRATION
TOTAL FILTRATION TIME, t, SECONDS

Fig. 3B. Over-all filtration run with 175-TW cotton twill.

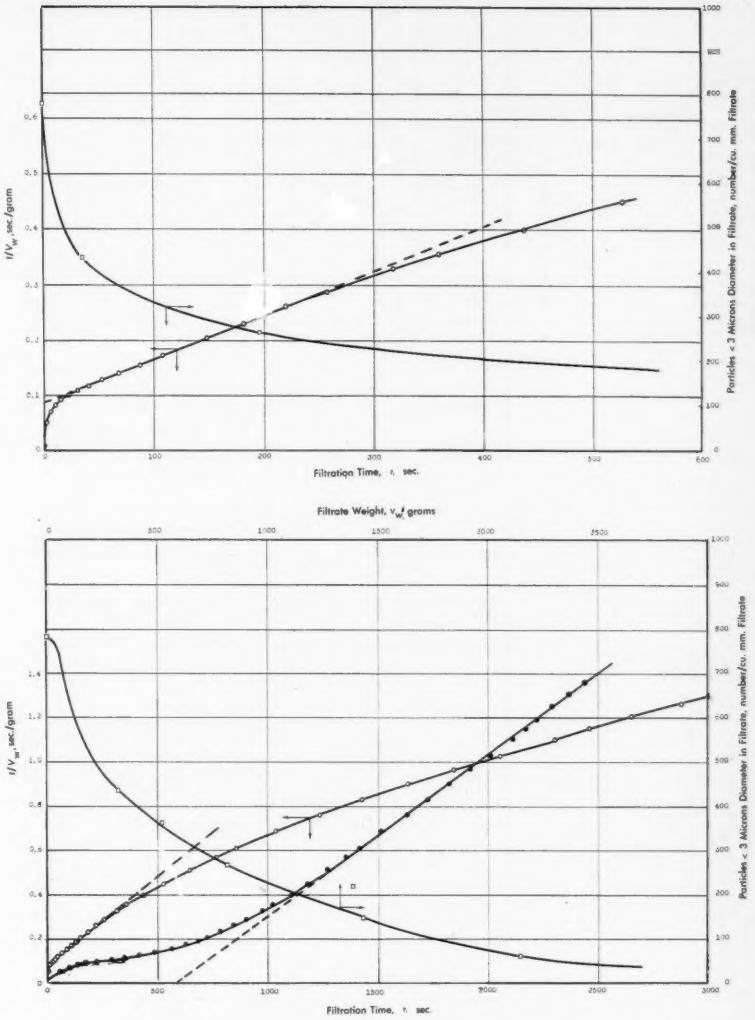
t/V_w, sec./gram
Particles < 3 Microns Diameter in Filtrate, number/cu. mm. Filtrate
Filtration Time, t, sec.
Filtrate Weight, V_w, grams

Fig. 4. Filtration performance curves FE-420 Orlon satin. Above: ○ t/V_w vs. t, □ particle count vs. t; below: ○ t/V_w vs. t, ● t/V_w vs. V_w, □ particle count vs. V_w.

metal or ceramic media, particulate filter aids, etc.) the tortuosity of pore structure is even greater, but a random distribution of pore volume exists throughout the medium although interconnecting pores probably contract and expand continually along any path through the medium.

When filtering suspensions contain more than 1% by volume solids (*cake filtration*), the pores block with cake in the first few seconds or fraction of a second and a continuous cake covers the surface of the filter medium. This cake immediately becomes the active filter surface, and particle passage through, or penetration of, the filter medium, which causes plugging of the medium, occurs for only a very short period at the start of each successive filtration cycle. Although of short duration, this repetitive plugging period eventually results in blinding of the filter medium, thus limiting its useful life. Very little is known concerning the mechanisms of this short plugging period or the initial stages of cake formation at the surface of the filter medium.

Many workers have demonstrated that the effective resistance of the filter medium during cake filtration is considerably greater than the resistance of the medium alone either before a filtration or after cake discharge at the end of a cycle; this work is well summarized by Ruth (*17*) and Carman (*1*). The effective filtration resistance is determined by extrapolation to $V/A = 0$ of the usual $\Delta t/\Delta(V/A)$ vs. V/A plot of constant-pressure data for cake filtration (*17*). Actually such a plot is no longer a straight line near $V/A = 0$, and mechanisms other than increasing resistance due to cake formation alone become controlling. Previously reported work (*6*) has shown that the effective resistance of a given medium in cake-filtration service depends on both the system and the filtration pressure but is generally equal to the resistance of a 0.01- to 0.06-in. thickness of cake under the same conditions. Many workers, including Ruth (*17*), Heertjes and Haas (*7*), and Hixson, Work, and Odell (*10*), have postulated the mechanism of particle bridging at the start of cake filtration. Although Hixson et al. were able experimentally to demonstrate bridging by means of glass capillaries and highly concentrated quartz suspension, there is no conclusive evidence that bridging is a major factor in most industrial filtrations involving cake formation. General expe-

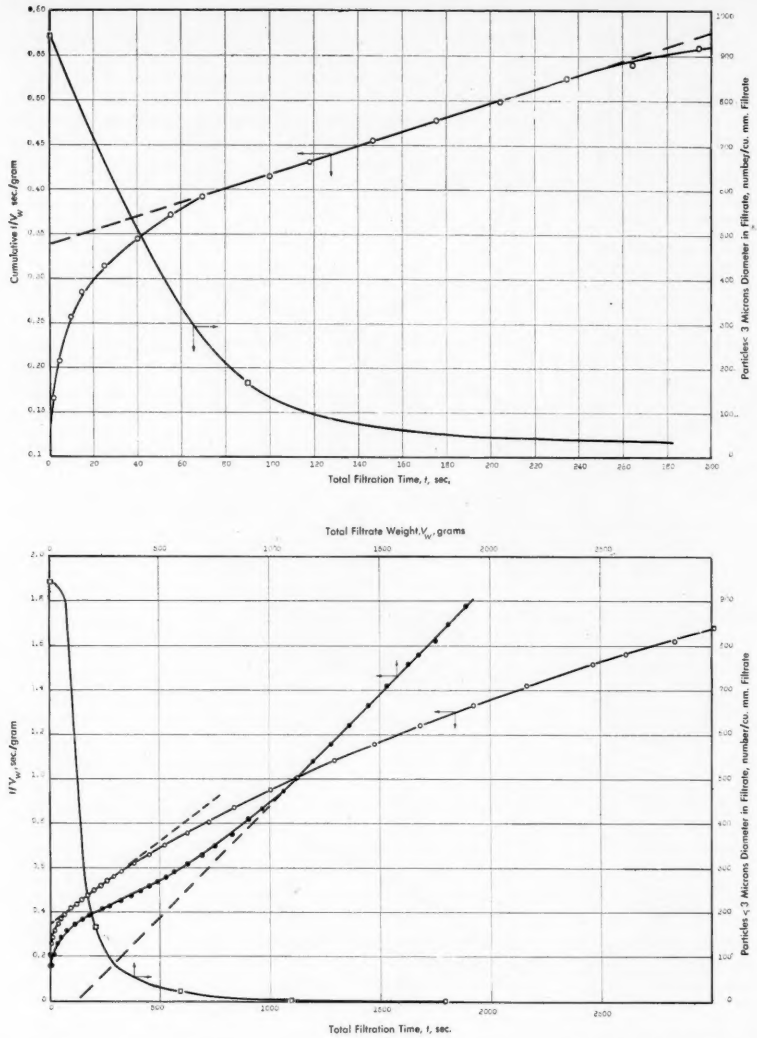
Cumulative t/V_w, sec./gram
Particles≥ 3 Microns Diameter in Filtrate, number/cu. mm. Filtrate
Total Filtration Time, t, sec.
Total Filtrate Weight, V_w, grams
t/V_w, sec./gram
Particles ≥ 3 Microns Diameter in Filtrate, number/cu. mm. Filtrate
Total Filtration Time, t, sec.

Fig. 5. Filtration performance curves SN-23 spun nylon. Above: ○ t/V_w vs. t, □ particle count vs. t; below: ● t/V_w vs. V_w, ○ t/V_w vs. t, □ particle count vs. V_w.

rience has shown that both initial filtration pressure and solids concentration have great influence on the effective resistance of the filter medium. Smith (*19*) has stated that for a given system and filter medium a critical pressure drop exists for each solids concentration and that if this is exceeded bridging fails to occur and severe plugging of the filter medium results. Although it is recognized that excessive filtration pressure drop can cause serious plugging of the medium at the start of filtration with certain highly compressible cakes, there is no direct experimental evidence that a critical pressure drop exists. The postulated failure of bridging may be correct; however, the plugging may just as likely be due to breakdown of floc structure (compressible cakes result from filtering of highly flocculated suspensions) at the surface of the filter medium under the intense shear at the pore openings; such breakdown of floc would result in increasing penetration and plugging of the filter medium by a smaller effective size of particle as the initial pressure drop is increased.

The lack of knowledge concerning the mechanisms occurring during the initial period of cake filtration results largely from the extremely short duration of this critical period. An important practical consequence is the difficulty of determining, on a laboratory scale, the relative-performance characteristics of several media for a particular cake filtration. The running of a protracted series of cake-filtration cycles has been recommended, but at best this method is laborious and yields data which have meaning only with the exact conditions and system employed. As the solids concentration in the feed suspension is decreased below 100 p.p.m. (0.01%) by volume, the duration of the initial period of filtration before formation of a cake is extended to such an extent that study of the mechanisms involved becomes practical. It seems very probable that essentially the same mechanisms may occur at higher solids concentrations with only the relative time duration of the mechanisms varying; this assumes that the effective particle size of the system is not changed by flocculation. An attempt to apply this approach was made by Heertjes and Haas (*7*); however, most of their work dealt with particles which were so large that they did not tend to penetrate and plug the filter media used.

In Solution Clarification

The filtration of dilute suspensions containing less than 100 p.p.m. by volume of solids is in its own right of great practical importance. For economical

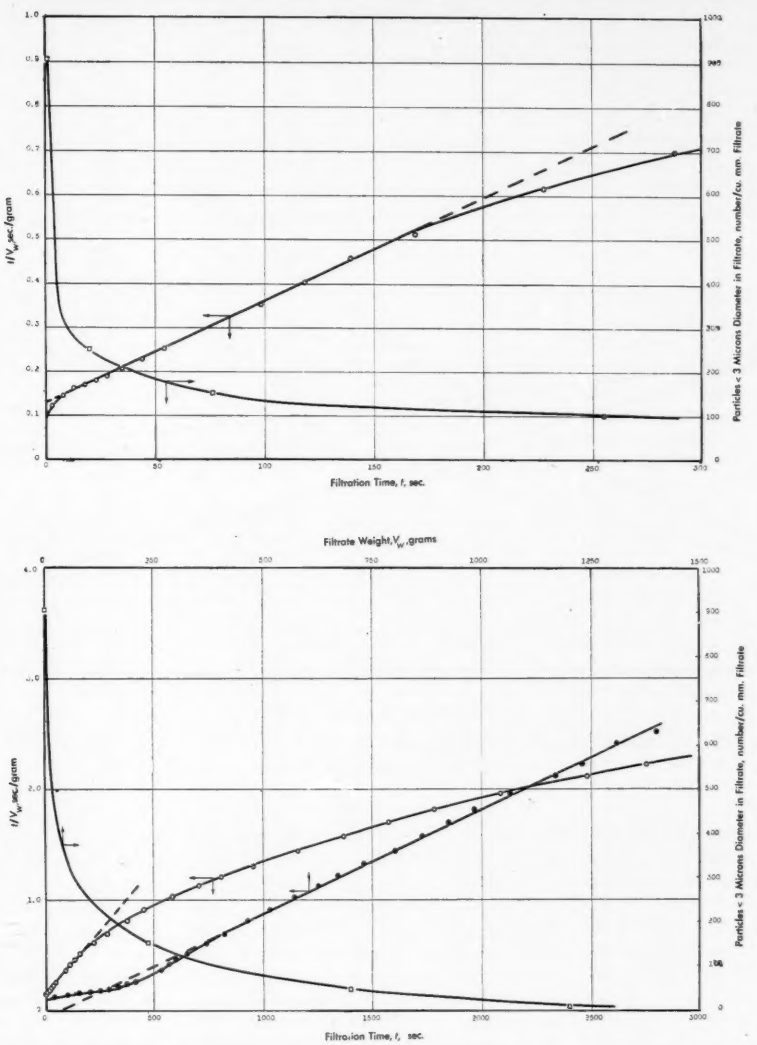
Filtration Time, t, sec.
Particles < 3 Microns Diameter in Filtrate, number/cu. mm. Filtrate
Filtrate Weight, V_w, grams
Filtration Time, t, sec.
Particles < 3 Microns Diameter in Filtrate, number/cu. mm. Filtrate

Fig. 6. Filtration performance curves TF-5044 filament nylon twill. Above: ○ t/V_w vs. t, □ particle count vs. t; below: ● t/V_w vs. V_w, ○ t/V_w vs. t, □ particle count vs. V_w.

reasons such filtrations normally include only that portion of the filtration cycle preceding cake formation. Operation into the region of cake filtration is usually impractical because of the very high resistance of the cake deposited. This results from the much better particle dispersion existing in such dilute suspensions and also, in several important cases, from the fact that the particles being removed are true gels having a very deformable structure. Thus in solution-clarification operations the purpose of the filter medium is to allow penetration but to trap individual particles within the structure of the medium with the least increase in medium resistance to flow per volume of particles trapped. Unlike the practice with cake filtration, stopping of particles at the surface of the medium is not desirable, and the objective is a long life during a single filtration cycle rather than a long life in terms of many cycles, as in cake filtration. Despite this basic difference in the over-all objective, the ultimate service life, as limited by plugging and increased resistance, depends in both cases on that portion of the filtration cycle preceding cake formation. It therefore appears that performance evaluation of filter media employing dilute suspensions may serve to characterize the performance of a filter medium in both cake-filtration and solution-clarification services.

MECHANISMS OF PARTICLE REMOVAL IN CLARIFICATION

In addition to (*a*) the direct-sieving action at constrictions in the pore structure, other possible mechanisms of particle collection within the filter medium are (*b*) gravity settling, (*c*) Brownian diffusion, (*d*) interception at the solid-liquid interfaces, (*e*) impingement, and (*f*) electrokinetic forces. Expressions for estimating the relative magnitudes of (*b*) to (*e*) under various conditions have been reported by Langmuir (*13*), Thomas (*20*), and Davies (*3*) and applied in gas filtration. Calculations employing these expressions and based on a range of filtration conditions for removal of 0.5- to 20-μ particles from liquids suggest that (*b*), (*c*), and (*e*) are negligible compared with (*d*), the direct interception of particles from liquid streamlines in contact with pore walls. In general, the relative importance of (*d*) with respect to (*b*), (*c*), and (*e*) increases as the liquid viscosity increases. The relative impor-

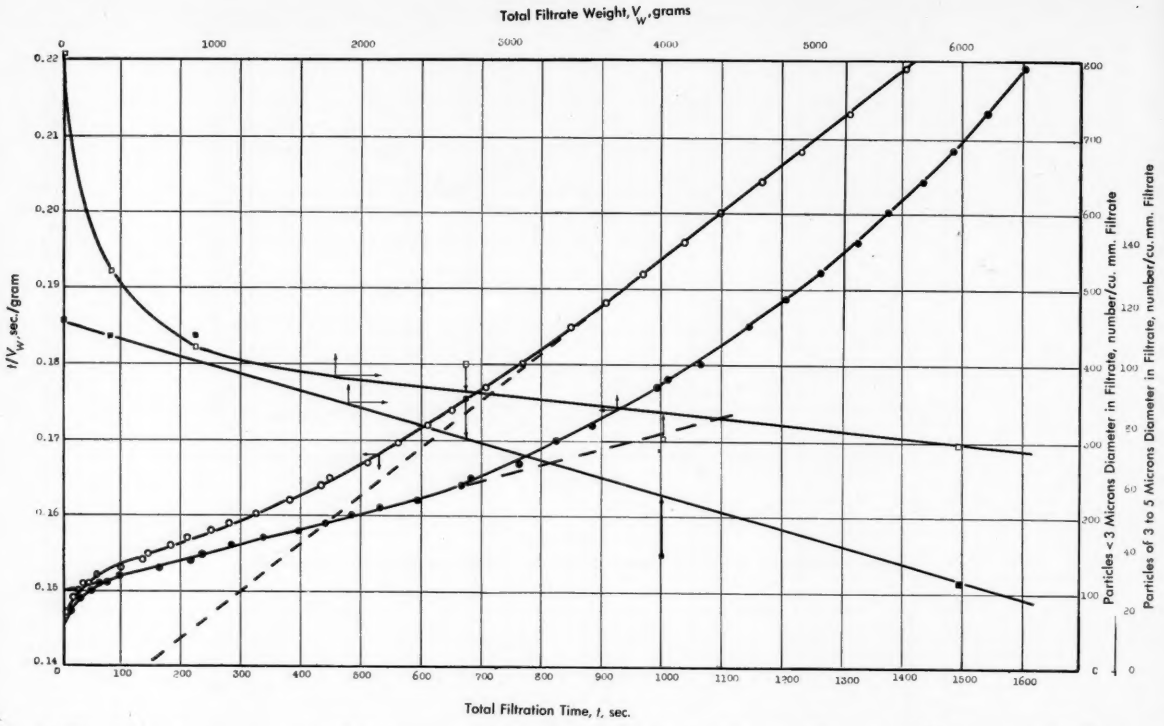

Fig. 7. Filtration performance curves AF-220 woven wool felt: ● t/V_w vs. V_w, ○ t/V_w vs. t, □ <3 μ particle count vs. V_w, ■ 3 to 5 μ particle count vs. V_w.

tance of this direct-interception mechanism to direct sieving action at constrictions in the pore structure and to electrokinetic forces cannot be estimated at this time. Also, the effectiveness of particle retention after collection has been accomplished is a factor which is little understood. Data for gas filtration (*20*) show that retention decreases as gas velocity (and also pressure drop) increases. Whether increased viscosity (with velocity constant and pressure drop increasing) will decrease retention has not been established for either gases or liquids.

The basic differences between the controlling mechanisms of particle collection in the clarification of gases and the clarification of liquids result either directly or indirectly from the much greater liquid viscosity. The direct effect of a higher filtrate viscosity on the relative importance of the several collection mechanisms has already been noted. Indirectly a higher filtrate viscosity results in the use of media of much lower porosity (0.30 to 0.70 void fraction for liquid clarification as compared with 0.90 to 0.99 void fraction for gas clarification). This comes about because media of higher porosity, such as packed beds of fibers, become so compressed by the resulting pressure drop when filtering liquids at practical rates that they are no longer high-porosity media under actual filtration conditions with liquids. Rodebush (*16*) has reported that for gases a decrease in medium porosity results in an increase in the collection coefficient, but that such an increase is accompanied by a correspondingly larger increase in flow resistance. On this basis the low porosities of media used for liquid filtration appear undesirable, but necessary until a completely rigid medium of very high porosity can be devised. On a theoretical basis an increase in collection efficiency with decreasing porosity cannot be accounted for on the basis of collection mechanisms (*b*) to (*e*) above, as the basic number of targets is not changed by compression of the medium. However, as compression occurs and porosity decreases, the filter appears less and less like a field of targets and more and more like a barrier with interconnecting pores or passages. As this occurs, collection by direct sieving at pore constrictions becomes increasingly important and probably accounts in part for the reported increase in collection coefficient with decreasing porosity. In any case most liquid clarifications are carried out with media having low enough porosities so that they can best be thought of as barriers with an interconnecting pore structure, rather than as an open field of targets as is the case in most gas clarifications.

LAWS AND MECHANISMS OF PORE PLUGGING DURING FILTRATION OF DILUTE SUSPENSIONS

Hermans and Bredée (*8*), and more recently Gonsalves (*4*), have analyzed the entire filtration cycle and proposed a series of laws to correlate the filtration-rate data for various parts of it. The mathematical expressions for these laws are summarized in various forms in Table 1. These filtration laws were derived by Hermans and Bredée on the assumption of separate physical mechanisms of pore plugging for complete blocking, standard blocking, intermediate blocking, and cake modes of filtration. However, Gonsalves (*4*) has shown that these same laws can also be derived on the assumption of quite different physical mechanisms for the blocking of pores within the medium; thus even though the mathematical expressions for these laws fit the experimental data for certain parts of the filtration cycle, there is no real evidence as to what the actual physical mechanism of pore blocking may be. The work of Hermans and Bredée and of Gonsalves has shown, however, that all the derived relationships stem from a common differential equation which can be adapted to any portion of the filtration cycle by adjusting the values of two constants. Thus, for constant-pressure filtration,

$$\frac{d^2t}{dV^2} = k\left(\frac{dt}{dV}\right)^n \qquad (1)$$

and for constant-rate filtration

$$\frac{d(\Delta p)}{dV} = k(\Delta p)^n \qquad (2)$$

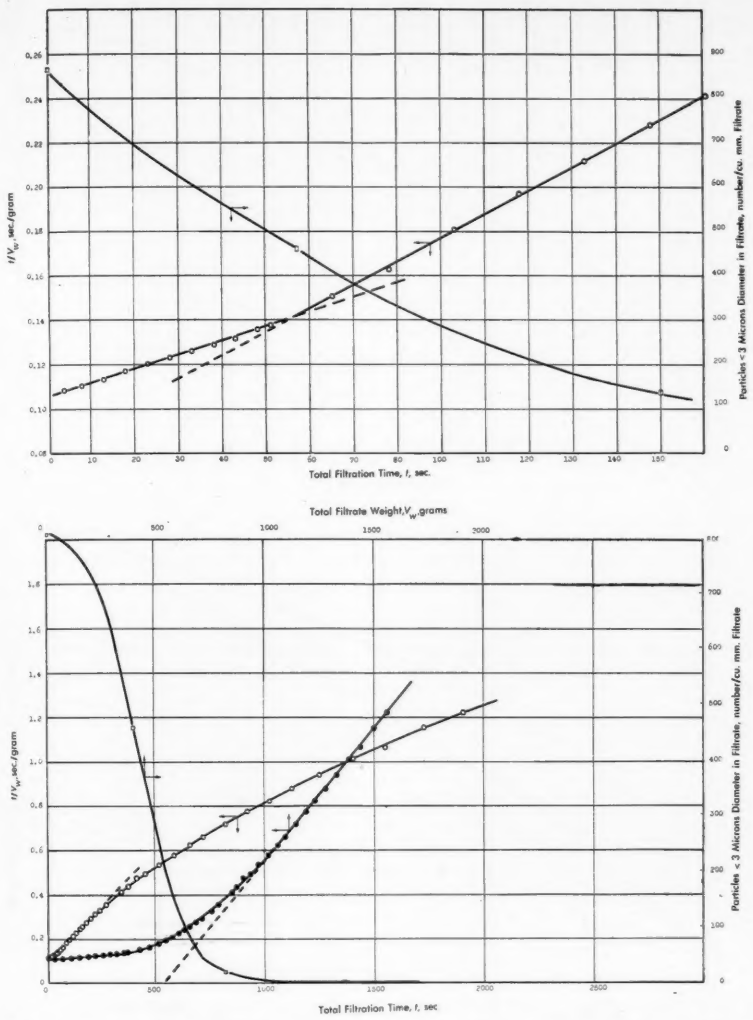
Total Filtration Time, t, sec.
Particles < 3 Microns Diameter in Filtrate, number/cc. mm. Filtrate
Total Filtrate Weight, V_w, grams
Total Filtration Time, t, sec

Fig. 8. Filtration performance curves TF-5071 Orlon taffeta, not calendered. Above: ○ t/V_w vs. t, □ particle count vs. t; below: ● t/V_w vs. V_w, ○ t/V_w vs. t, □ particle count vs. V_w.

where the value of n defines the mode of filtration occurring, and the value of k for a particular mode of filtration depends on the system, the filter medium, and the conditions of filtration. In simple terms, Equations (1) and (2) state that the rate of change of filter resistance is proportional to the instantaneous filtration resistance raised to a power which is dependent on the mode of filtration. The mode of cake filtration is well established, and for this case $n = 0$. Integration of Equation (1) at constant pressure drop for $n = 0$ gives

$$\frac{t}{V} = \frac{K_c V}{2} + \frac{1}{q_0} \qquad (3)$$

where

$$K_c = (1.56 \times 10^{-7}) \frac{\mu_f \alpha w}{A^2 g_c \Delta p_0} \qquad (4)$$

$$\frac{1}{q_0} = (4.74 \times 10^{-4}) \frac{\mu_f R_m}{A g_c \Delta p_0} \qquad (5)$$

The mode of standard blocking, although not so well established experimentally as cake filtration, has been found to fit the data for a significant portion of the filtration cycle with many dilute suspensions. Hermans and Bredée (*8*) cited examples of this mode of filtration as occurring in the filtration of polymer solutions, dispersed pigments, and cellulose solutions such as viscose and cellulose acetate. For this mode of filtration, $n = 3/2$ and integration of Equation (1) at constant pressure gives

$$t/V = \frac{K_s}{2} t + \frac{1}{q_0} \qquad (6)$$

The physical assumption made in the derivation of this relationship is that of particle retention at the walls of the pores and gradual build-up on pore walls with eventual plugging of the pores. Such a physical concept represents a constantly decreasing pore size in the filter medium and is in agreement with Kane's (*11*) more recent analysis of performance data on one commercial type of filter cartridge for clarifying liquids. The form of the standard-blocking relationship shown in Equation (6) has been widely used to correlate data for the filtration of viscose and cellulose acetate through various types of filter media which function by filtration in depth. As applied to the evaluation of viscose filterability in Europe, the German Standard Method assumes that Equation (6) applies from near the start of filtration for this particular case and K_s is solved for directly without plotting of t/V vs. t, by use of filtrate volumes collected after 20- and 60-min. filtration. Several European workers (*9*, *14*, *15*, and *21*) have recently recognized that Equation (6) does not apply for an initial period of filtration even with viscose and have recommended more care in the industrial use of Equation (6). Applying improved techniques, these same workers have investigated the effect of both viscose preparation and the filter medium used on the region over which Equation (6) applies. These workers suggested many reasons for the failure of Equation (6) at the start of the first stage of viscose filtration or when viscose is refiltered at later stages, but none have been satisfactorily verified. In plant practice such clarifications are often carried out at constant rate rather than constant pressure.

The constant-rate form of the standard-blocking law, as is needed to correlate such constant-rate filtration data, can be written in the form

$$\left(\frac{\Delta p_0}{\Delta p}\right)^{1/2} = 1 - \frac{(K_s)}{(2)} V \qquad (7)$$

Equation (7) has been observed to fail near the start of filtration, as has Equation (6).

The complete-blocking ($n = 2$) and intermediate-blocking ($n = 1$) modes of filtration as proposed by Hermans and Bredée have been found to have much more limited application. In general the regions of the filtration cycle to which these modes of filtration apply are ill-defined and of short duration, although a few systems involving only particles of size larger than the pores of the medium appear to follow the complete-blocking mode of filtration. The mathematical expressions for these modes, as derived by Hermans and Bredée for constant-pressure and constant-rate filtrations, are given in Table 1.

Recently both Gonsalves (*4*) and Vosters (*22*) have reanalyzed the work of Hermans and Bredée, raising the question as to whether several distinct

modes of filtration exist (as characterized by fixed values of n) before cake formation. Gonsalves has further questioned the physical mechanisms assumed in Hermans and Bredée's derivations, and has suggested trial-and-error solution of Equation (1) for simultaneous determinations of both k and n values which best fit a particular set of data for filtration before cake formation. This is a laborious process and the results are not particularly informative on a comparative basis because both k and n are generally different for filtrations under different conditions. Essentially what Gonsalves (*4*) has attempted is to find a single solution of Equation (1) over the entire filtration cycle preceding cake formation. On the other hand, Vosters (*22*), in an attempt to improve the reproducibility of the plugging-constant method of evaluating viscose, has resorted to calculation of a statistical straight line through the t/V vs. t values over a 50-min. period of constant-pressure filtration. For plant-control work, Vosters then uses the plugging constant as the tangent of the regression line, t/V on t. This approach ignores the real shape of the curve and is unsuited to interpretation of the real meaning of changes in the t/V vs. t curve. Although the filtration data of both Gonsalves and Vosters, like those of many other workers, do not follow the standard-blocking mode ($n = 3/2$) at the start of filtration, they, like those of most others, do so over a significant part of the remaining filtration cycle before cake formation. Thus, although Gonsalves' and Vosters' criticisms of indiscriminate application of the standard blocking mode ($n = 3/2$) as a means of analyzing filtration data from the very start of filtration are justified, complete discard of the idea that a definite standard-blocking mode ($n = 3/2$) exists does not yet appear justified.

The physical assumptions and derivation of the equations for the standard-blocking mode are presented in the Appendix. Derivation of the relationships has been carried a step beyond that of Hermans and Bredée (*8*). This has been done in an effort to express the relationships entirely in terms of the filter-medium properties. This has resulted, for constant-pressure filtration, in the form

$$t/V = (1.42 \times 10^{-4}) \frac{(8h)}{(\pi N r_0^4)} \frac{(\mu_f)}{(A g_c \Delta p)} + \left[\frac{c/(1-\epsilon_p)}{\pi N A h r_0^2}\right] t \quad (8)$$

and, for constant-rate filtration, in the form

$$\left(\frac{\Delta p_0}{\Delta p}\right)^{0.5} = 1 - \left[\frac{c/(1-\epsilon_p)}{\pi N A h r_0^2}\right] V \quad (9)$$

Thus, in either case a solution for the clogging value $\pi N h r_0^2$ should be possible from filtration data provided that the standard-blocking mode applies to a portion of the filtration cycle, resulting in a straight-line region for a t/V vs. t or a $(\Delta p_0/\Delta p)^{0.5}$ vs. V plot of the data. For such a straight-line region to exist, the degree of particle-size retention, or the value of c, must remain substantially constant, and unless the retention is essentially complete ($c = c_f$), the amount of bleed, $c_f - c$, must be known. This fact has been largely overlooked in the application of Equation (6) by most workers and may account for the generally reported failure of Equation (6) at the start of filtration. Solution of Equations (8) and (9) for comparative values of the clogging value $\pi N h r_0^2$ with various filter media, under similar filtration conditions and with the same suspension, offers a means of quantitatively comparing the plugging characteristics of various media. If the values of $\pi N h r_0^2$ so determined could be related to independently measured dimensions of the pores in the media, then a quantitative link might also be established between the plugging characteristics of a medium and its internal pore structure.

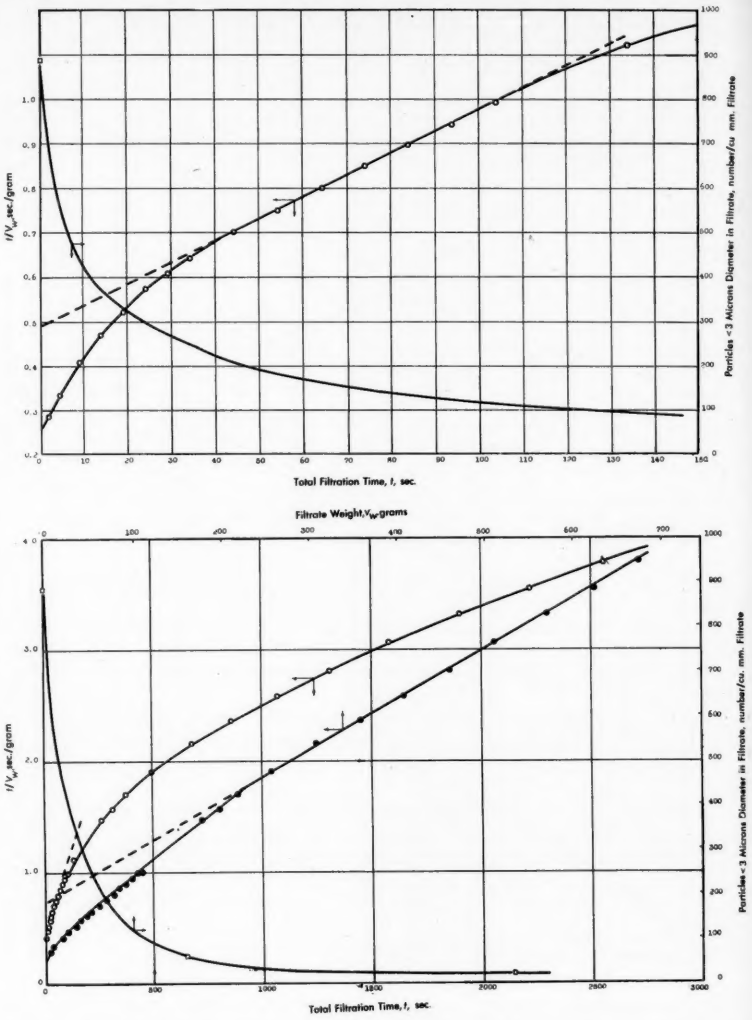
t/V_w, sec./gram
Particles < 3 Microns Diameter in Filtrate, number/cu. mm. Filtrate
Total Filtration Time, t, sec.
Filtrate Weight, V_w grams

Fig. 9. Filtration performance curves TF-5071-F Orlon taffeta, calendered. Above: ○ t/V_w vs. t; below: ● t/V_w vs. V_w, ○ t/V_w vs. t, □ particle count vs. V_w.

EXPERIMENTAL EQUIPMENT AND PROCEDURES

Equipment

The equipment shown in Figure 1 was used to obtain comparative filtration data for various filter media by use of a dilute suspension of known particle-size distribution. The filtration cell (Figure 1*a*) was of 11.35 sq. cm. filtration area. The filter medium was clamped over an 8-mesh

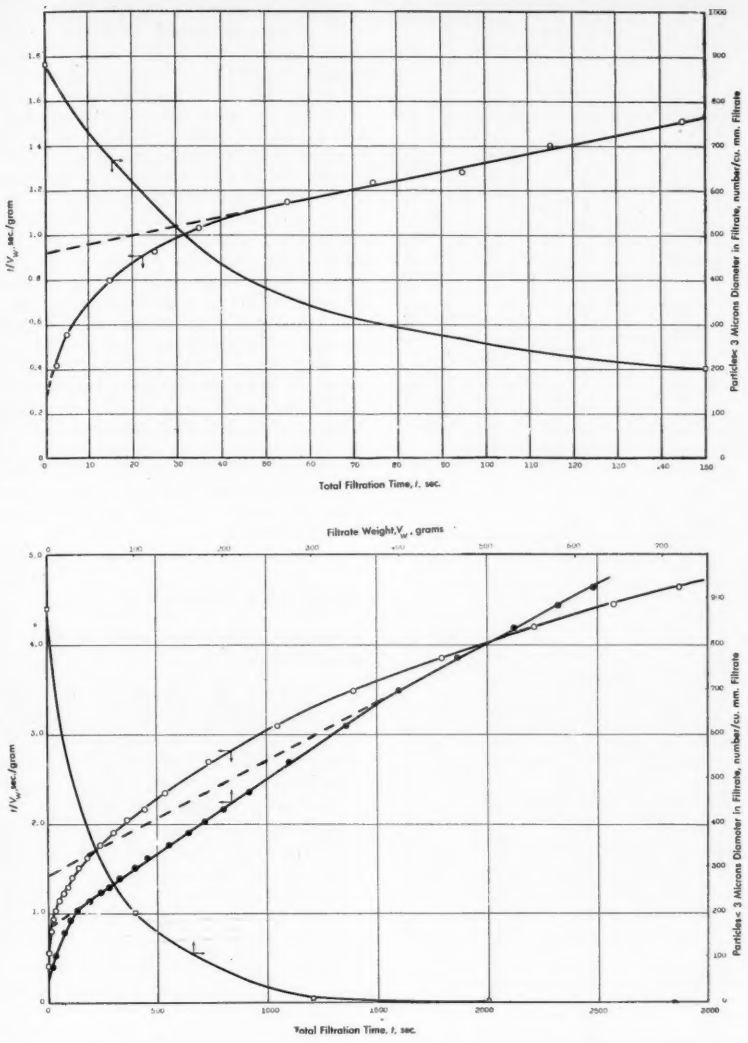

backing screen. The 20 p.p.m. by volume feed suspension was fed to the filtration cell from the agitated blow case (Figure 1*b*) at constant pressure drop. Filtrate weight, pressure drop, and filtrate temperature were recorded continuously by the automatic recording system. The all stainless steel piping and equipment were thoroughly cleaned before use and maintained uncontaminated by other than the feed suspension throughout the experimental program.

Filtration Runs

The suspension system used for the filtration runs consisted of an 80% glycerol–20% water solution containing approximately 0.18 g./liter (23 p.p.m. by volume) of spherical particles of carbonyl iron powder. The carbonyl iron powder used was a mixture of three commercial grades made by the Anatara Products Division of General Aniline & Film Corp. The particles were very nearly all of spherical shape, facilitating microscopic counting of size. The powder mixture was first dispersed in 0.01M $Na_4P_2O_7$ solution by 1-hr. agitation, following which C. P. white glycerol was added with agitation to make the final suspension. The particle-size-distribution function of the powder mixture is shown in Figure 2. The weight-frequency distribution curve was calculated from the sedimentation analysis of individual grades present in the mixture. The number-frequency-distribution curve was determined directly by microscopic count of suspension samples (Figure 2). Similar number-frequency-distribution curves have recently been reported

Fig. 10. Filtration performance curves No. 8 cotton duck. Above: ○ t/V_w vs. t, □ particle count vs. t; below: ● t/V_w vs. V_w, ○ t/V_w vs. t, □ particle count vs. V_w.

TABLE 1. FILTRATION LAWS OF HERMANS AND BREDÉE (8)

1. For constant-pressure filtration

Function	Complete blocking	Standard blocking	Intermediate blocking	Cake filtration
$\frac{d^2t}{dV^2} = k\left(\frac{dt}{dV}\right)^n$	$n = 2$	$n = 3/2$	$n = 1$	$n = 0$
$V = f(t)$	$V = q_0(1 - e^{-k_b t})$	$t/V = \frac{K_s}{2}t + \frac{1}{q_0}$	$K_i V = \ln(1 + K_i t q_0)$	$t/V = \frac{K_c}{2}V + \frac{1}{q_0}$
$q = f(t)$	$q = q_0 e^{-K_b t}$	$q = \frac{q_0}{\left(\frac{K_s}{2}V + 1\right)^2}$	$K_i t = \frac{1}{q} - \frac{1}{q_0}$	$q = \frac{q_0}{(1 + K_c q_0^2 t)^{1/2}}$
$q = f(V)$	$K_b V = q_0 - q$	$q = q_0\left(1 - \frac{K_s V}{2}\right)^2$	$q = q_0 e^{-K_i V}$	$K_c V = \frac{1}{q} - \frac{1}{q_0}$

2. For constant-rate filtration

$\frac{d(\Delta p)}{dV} = k(\Delta p)^n$	$n = 2$	$n = 3/2$	$n = 1$	$n = 0$
$\Delta p = f(V)$	$\frac{\Delta p_0}{\Delta p} = 1 - \frac{K_b V}{q_0}$	$\left(\frac{\Delta p_0}{\Delta p}\right)^{0.5} = 1 - \left(\frac{K_s}{2}\right)V$	$\ln\left(\frac{\Delta p}{\Delta p_0}\right) = K_i V$	$\frac{\Delta p}{\Delta p_0} = K_c q_0 V + 1$
$\Delta p = f(t)$	$\frac{\Delta p_0}{\Delta p} = 1 - K_b t$	$\frac{1}{q_0}\left(\frac{\Delta p_0}{\Delta p}\right)^{0.5} = \frac{1}{q_0} - \left(\frac{K_s}{2}\right)t$	$\frac{1}{q_0}\ln\left(\frac{\Delta p}{\Delta p_0}\right) = K_i t$	$\frac{\Delta p}{\Delta p_0} = K_c q_0^2 t + 1$

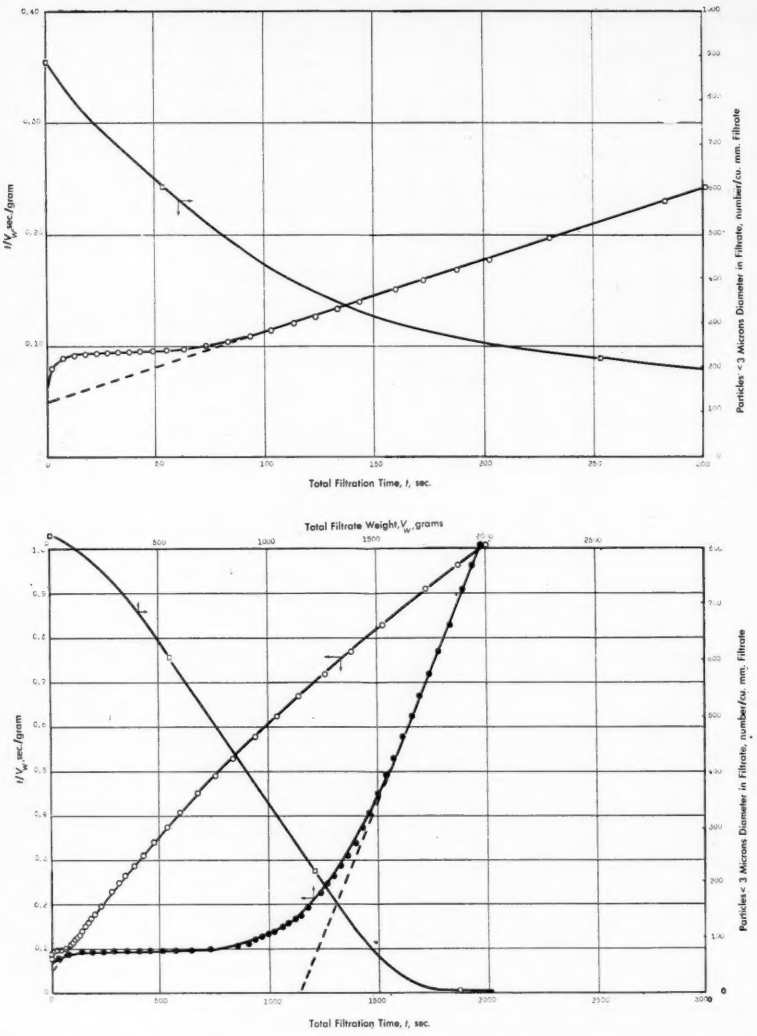

Fig. 11. Filtration performance curves WS SN-7 filament nylon duck. Above: ○ t/V_w vs. t, □ particle count vs. t; below: ○ t/V_w vs. t, ● t/V_w vs. V_w, □ particle count vs. V_w.

for individual grades of similar carbonyl iron powders by Kohl and Zentner (*12*).

Constant-pressure-filtration runs were made with nine of the filter media previously examined by the mercury-intrusion method (Part I of this paper). Pieces cut from the same filter-medium sample were used for both mercury-intrusion and filtration measurements. The filtration runs were made at room temperature by use of the feed suspension and equipment just described. A constant pressure drop in the range of 14 to 15 lb./sq. in. was maintained during each run. At the start of filtration, air was bled out the top of the filtration cell before filtration started. Filtrate holdup volume between the filter medium and the strain-gauge scale was 6 ml.; this volume was filled with solution before filtration started so that filtrate collection and filtration started simultaneously. Grab samples of filtrate of 50-ml. volume were taken periodically throughout the run for filtrate analysis. These samples were noted on the recorder chart and taken into account in analyzing the filtrate-weight vs. time data. The filtrate container on the strain-gauge scale was changed for every 500 to 1,000 g. of filtrate collected; these larger composite samples of filtrate were also analyzed for solids content, as was a sample of the feed suspension at the start of filtration. Filtrate viscosity at the run temperature was determined in each case by use of the Hoeppler falling-ball viscometer. Duration of the filtration runs was from 1,400 to 3,600 sec., depending on the filter medium employed. It was generally apparent that the $t - V_w$ data had begun to follow the cake-filtration law before each filtration was stopped. However, in the case of Albany 220 felt this condition was not achieved before the blow case was emptied. At the end of each run the filter medium was removed and examined microscopically on both cake and filtrate sides.

Filtrate Evaluation

The samples of suspension feed, grab samples of filtrate, and composite samples of filtrate taken during each filtration run were examined microscopically and particle counts made for the < 3, 3–5, 5–10, 10–15 and $> 15\mu$ size ranges. A Howard mold counting cell was used and provided a sample depth of 0.10 mm. Counts were made at 200 X magnification by use of binocular eyepieces and a calibrated counting grating. Counts were made about 10 min. after the sample was placed in the Howard mold counting cell; this provided time for iron particles to settle through the 0.10 mm. depth of cell and facilitated counting since all particles were in essentially the same plane and were at rest. In general, several scans were made across various diameters of the circular-mold counting cell (18.5 mm. diam.). For most samples the total number of particles counted was in the range of 100 to 1,000, with 85 to 100% of the particles being smaller than 3μ, for the various samples. The concentration of the various feed suspensions (Table 2) was determined gravimetrically by filtering on weighed Gooch crucibles with asbestos pads, the volumetric concentration being calculated from the particle density of 7.81 g./cc.

DISCUSSION OF RESULTS

Limitations Found in the Application of the Filtration Laws

Data from the filtration runs on the nine filter media are first analyzed in terms of the t/V_w vs. t and t/V_w vs. V_w curves of Figures 3 to 11. These curves are shown for the entire run and are also plotted on an expanded scale for the portion of the cycle preceding cake-law filtration. The straight-line portions of these curves fully define the regions of both standard blocking and cake filtration, in accordance with Equations (3) and (6). Also plotted on these same Figures 3 to 11 for the various filter media are curves of particle count in the filtrate vs. V_w or t.

In general, the data for all media exhibit an initial region of filtration during which neither the standard-blocking nor cake-filtration modes apply. Over this initial region a large number of feed particles appear in the filtrate, and this number decreases very rapidly as filtration proceeds. Following this, a transition into a region of standard blocking appears to occur with all media except the Albany 220 felt. The duration of this region of standard blocking varies depending on the character and tightness of the filter medium, being longest for loosely woven media of staple fibers such as 175-TW cotton twill (Figure 3) and shortest for tightly woven and calendered media of multifilament construction such as TF-5044 (Figure 6) or TF-5071-F (Figure 9). However, the standard-blocking period is also of short duration with a tightly woven medium of staple fibers, such as No. 8 cotton duck (Figure 10). With the other media of staple or multifilament construction the period of standard blocking was of intermediate duration. With the Albany 220 felt (Figure 7) the initial region of filtration

Table 2. Summary of Plugging Coefficients and Cake-Resistance Values Calculated from Filtration Runs

Region of cake filtration

TABLE 2. SUMMARY OF PLUGGING COEFFICIENTS AND CAKE-RESISTANCE VALUES CALCULATED FROM FILTRATION RUNS

Filter-media style	Pressure drop, Δp, lb./sq. in.	Filtrate viscosity, μ_f, centipoises	Solids concentration, c, p.p.m. by vol.	Region of standard blocking (From t/V_w vs. t data plots) Straight line Slope, $K_s/2$, 1/g.	Straight line Intercept, $1/q_0$ sec./g.	Clogging value $\pi N h r_0^2$, cc./sq. cm.	Pore resistance $8h/\pi N r_0^4$, 1/cm.	Region of cake filtration (From t/V_w vs. V_w data plots) Straight line Slope, sec./g.^{2}	Straight line Intercept, sec./g.	Avg. specific cake resistance, α, ft./lb.	$\Delta t/\Delta V_w$ at start of cake-filtration region, sec./g.	Effective cloth resistance at start of cake filtration R_m, 1/ft.
175-TW Cotton twill	14.85	35.9	20.8	0.333×10^{-3}	0.137	83×10^{-4}	5.4×10^6	0.41×10^{-3}	-0.298	4.0×10^{10}	1.18	1.4×10^9
FE-420 Orlon, satin	14.5	30.4	22.1	0.79×10^{-3}	0.085	37×10^{-4}	3.8×10^6	0.73×10^{-3}	-0.423	7.7×10^{10}	1.41	1.92×10^9
SN-23 Staple nylon, duck	14.4	30.5	22.8	0.78×10^{-3}	0.340	39×10^{-4}	15×10^6	1.01×10^{-3}	-0.131	10.2×10^{10}	1.69	2.28×10^9
TF-5044 Filament nylon, twill	14.6	38.4	23.1	2.56×10^{-3}	0.130	12×10^{-4}	4.6×10^6	1.90×10^{-3}	-0.070	15.2×10^{10}	1.43	1.55×10^9
AF-220 Woven wool felt	14.2	32.4	21.9	6.75×10^{-5}	0.130	430×10^{-4}	5.4×10^6					
TF-5071-U Filament Orlon, taffeta	14.6	29.1	23.3	0.625×10^{-3}	0.106	50×10^{-4}	5.0×10^6	1.225×10^{-3}	-0.662	12.0×10^{10}	2.04	2.92×10^9
			1.04	1.04×10^{-3}	0.083	30×10^{-4}	4.0×10^6					
SN-7 Filament nylon, duck	14.8	26.4	22.8	0.637×10^{-3}	0.050	48×10^{-4}	2.6×10^6	1.37×10^{-3}	-1.55	16.4×10^{10}	2.27	3.40×10^9
TF-5071-F, Filament Orlon, calendered taffeta	14.8	28.2	23.0	4.88×10^{-3}	0.485	6.3×10^{-4}	25×10^6	6.87×10^{-3}	0.25		0.59	
								4.50×10^{-3}	0.74	50×10^{10}	3.08	4.60×10^9
No. 8 Cotton duck	14.5	27.4	22.6	4.12×10^{-3}	0.91	7.3×10^{-4}	46×10^6	6.60×10^{-3}	0.86		1.43	
								5.25×10^{-3}	1.40	60×10^{10}	5.65	8.55×10^9

$$t/V_w = \left(\frac{8h}{\pi N r_0^4}\right)\left(\frac{\mu_f}{\pi A \rho_f g_c \Delta p}\right) + \left(\frac{c/1-\epsilon_p}{\rho_f A \pi N h r_0^2}\right) t$$

$$\pi N h r_0^2 = \frac{(c_f/1-\epsilon_p)}{\rho_f A(\text{slope})} = \left(\frac{1}{11.35 \text{ sq. cm.}}\right)\left(\frac{c_f}{1-0.45}, \frac{\text{cc.}}{10^6 \text{ cc.}}\right)\left(\frac{\text{cc.}}{1.2\text{g.}}\right)\left(\frac{1}{\text{slope}}, g\right) = \frac{1.33(10)^{-7} c_f}{\text{slope}}, \text{ cc./sq. cm.}$$

$$\left(\frac{8h}{\pi N r_0^4}\right) = \left(\frac{A \rho_f g_c \Delta p}{\mu_f}\right)(\text{intercept}) = 9.43(10)^7\left(\frac{\Delta_p, \text{ lb./in.}^2}{\mu_f, \text{ cp.}}\right)(\text{intercept, sec./g.}) = \frac{1}{\text{cm.}}$$

$$\alpha = \frac{2A^2 g_c \rho_f^2 \Delta_p}{\mu_f \rho_s c}(\text{slope}) = 4.88(10)^{15}\left(\frac{\Delta_p, \text{ lb./sq. in.}}{\mu_f, \text{ centipoises} \times c, \text{ p.p.m.}}\right)\left(\text{slope}, \frac{\text{sec.}}{\text{g.}^2}\right) = \text{ft./lb.}$$

$$R_m = \frac{A \rho_f g_c \Delta_p}{\mu_f}\left(\frac{\Delta t}{\Delta V_w} \text{ at start cake-filtration region}\right) = 28.6(10)^8\left(\frac{\Delta_p, \text{ lb./sq. in.}}{\mu_f, \text{ centipoises}}\right)\left(\frac{\text{sec.}}{\text{g.}}\right) = \frac{1}{\text{ft.}}$$

was followed by a brief region during which the cake-filtration law was apparently followed even though no cake existed on the surface of the felt. This in turn was followed by a prolonged period of standard-blocking behavior. This unusual behavior is similar to reported experiences in which the cake law may sometimes apply to the filtration of highly filtered solutions where no actual cake is formed and no apparent discoloration of the filter medium occurs. This unusual period of cake filtration was accompanied by passage through the filter medium of nearly half the number of particles originally present in the feed. With the Albany 220 felt (Figure 7) the period of standard blocking, which followed this pseudo cake filtration, continued until the end of the filtration run.

With all other media the period of standard blocking was followed by a transition region which yielded to a prolonged region of cake filtration; this continued until the end of the run. With very tight media such as the No. 8 cotton duck (Figure 10) and 5071-F calendered medium made from Orlon acrylic fiber, two regions of cake filtration occurred with an abrupt change in slope occurring at the transition from the first to the second. This transition resulted in a decrease in slope or a decrease in effective cake resistance. Only in the case of TF-5044 (Figure 6) was there any macroscopic evidence of cake formation at the end of the filtration run, although the surface of the filter medium was discolored in all cases. Figures 19 to 21 show photomicrographs of the filtrate side and cake side of the various filter media as removed at the end of the runs. It is evident that a true cake covering the entire surface of the filter medium was not formed in any case and that in most cases only a small part of the filter-medium surface is covered by a cake in even a microscopic sense. The successive regions of cake filtration with No. 8 cotton duck (Figure 10) and with TF-5071-F (Figure 9) may well result from changes in effective filtration area at the surface of the cake as the cake progressively covers a greater percentage of the filter-medium surface.

The data of Figures 3 to 11 on the media therefore show that the filtration cycle generally passes through a number of modes. In each case a portion of the cycle can be satisfactorily represented by the mode of standard blocking, while one or more regions appear to follow the mode of cake filtration even though a true cake does not exist in a macroscopic sense. Data for the region between the start of filtration and the region of standard blocking and between the region of standard blocking and that of cake filtration seem to represent transition zones. Attempts to apply the complete-blocking law (Table 1) to the initial region of filtration period failed in each case,

arithmetic plots of q_w vs. V_w resulting in smooth curves. It was found, however, that logarithmic plots of both q_w vs. V_w and q_w vs. t did give a straight line for this initial region (Figure 12). Consideration of this showed that as a result a simple logarithmic plot of V_w vs. t would be a straight line. This was verified for each medium (Figure 13) over this initial region of filtration. The resulting empirical relationship, $V_w = k't^m$, is not in agreement with any of the proposed filtration laws (Table 1). The value of m was very nearly 1.0 for four of the media and was near 0.7 for the other five examined. Vosters (*22*) has recently reported that filtration data for this initial region of filtration with viscose yield straight lines when plotted as log t vs. log t/V_w and has suggested an empirical relationship of the form $t/V_w = (t^{m'+1})/k''$. In general the data over the initial regions of filtration also correlate well by means of the method of Vosters. However, the direct exponential relationship between t and V_w appears to fit the data as well or better and is of a simpler form. Behavior during this initial period of filtration may be governed by the rapid change in the degree of particle retention occurring during this period. All the proposed filtration laws (Table 1) assume that the volume or number of particles removed per volume filtered remains constant. As this is far from true for this initial period of filtration even with very tight media, it is not surprising that all relationships of Table 1 fail for this period. Insufficient data were obtained over this period to describe adequately the rate of change of particle retention with volume filtered. Such data if taken into account in the derivation of the standard-blocking law may well result in a form similar to the empirical expression obtained. Attempts to apply the law of intermediate blocking to the transition region between standard blocking and cake filtration on the curves of Figures 3 to 11 were not successful. This region of filtration was of short duration in most cases and appears to be a true transition zone not amenable to any single relationship.

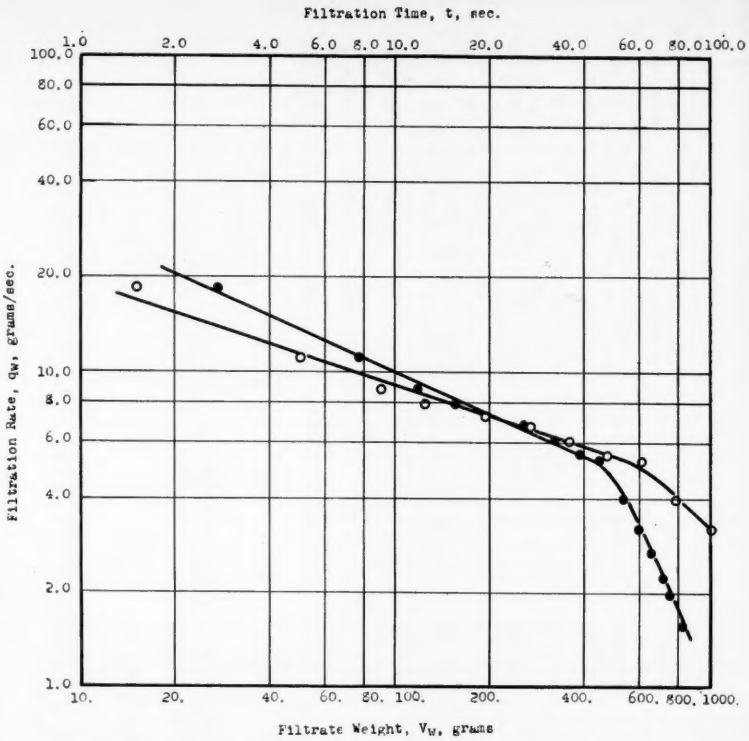

Fig. 12. Initial portion of clarification run FE-420 Orlon satin: ● q_w vs. V_w. ○ q_w vs. t.

Comparative Performance of Various Media

Plugging Characteristics. The comparative plugging rates of the various media can be judged best on the basis of the period of standard blocking. For this period the comparative slopes of the t/V_w vs. t curves (or the plugging constant K_s), as shown in Table 2, indicate directly the plugging rates expressed as the ratio of the packed volume of solids removed per gram of filtrate to the clogging value of pores within the filter medium. These values of K_s are all for very nearly the same conditions of pressure drop, solution viscosity, and initial solids concentration, as indicated in Table 2. The plugging constant K_s varied over a hundredfold range with the media examined, the value for Albany 220 felt being lowest, values for No. 8 cotton duck and TF-5071 being highest, and values for all others falling near the midpoint of these extremes. Although K_s is widely recognized as indicating the rate of plugging during the standard-blocking period, the present data indicate that K_s is also directly related to the volume of suspension which can be filtered through a medium before the end of the standard-blocking period is reached. Thus in Figure 14 a logarithmic plot of V_w/A at the end of standard-blocking period vs. $2/K_s$ results in a good approximation of a straight line. This indicates that capacity of a medium to the end of the standard-blocking period, V_w/A, is empirically related to K_s by

$$V_w/A = C\left(\frac{1}{K_s}\right)^{m''} \qquad (10)$$

at least for the system and conditions involved. This is of considerable significance, as filter media of widely different characteristics are involved. Thus it appears that K_s not only characterizes the rate of plugging of a medium for the standard-blocking period, but also the filtrate capacity of the medium before plugging, irrespective of the construction of the medium or the amount of bleed that occurs.

The straight-line intercepts obtained by extrapolation of the standard-blocking periods of Figures 3 to 11 to $t = 0$ also appear to bear a distinct relationship to the properties of the medium, despite the fact that the standard-blocking period is preceded by an initial period of filtration which establishes the actual $t = 0$ intercept. Thus the logarithmic plot of the intercept value (as given in Table 2) vs. the liquid resistance of the medium R_w' (as given in Table 1 of Part I of this paper) shows that a definite relationship exists (Figure 15). The indicated exponent is, however, less than the value of 1.0 which would be expected if no complicating factors were involved.

Particle-retention Characteristics and Relationship to Pore Structure. All clarification runs were characterized by a progressive decrease in the number of particles passing through the filter medium, as shown by the particle-count curves of Figures 3 to 11 for the $>$ 3-μ particles. A similar decrease in number of particles passed occurred for the 3 to 5, 5 to 10, 10 to 15 and $>$ 15-μ size ranges.* In general, the percentage by number of the $<$ 3-μ particles passing uncollected exceeded 50% with all the media for the initial period of filtration preceding the standard-blocking region. Over this region the number of $<$ 3-μ particles in the filtrate dropped very rapidly, indicating

*These data may be obtained as document 4956 from the American Documentation Institute, Photoduplication Service, Library of Congress, Washington 25, D. C., for $1.25 for photoprints or 35-mm. microfilm.

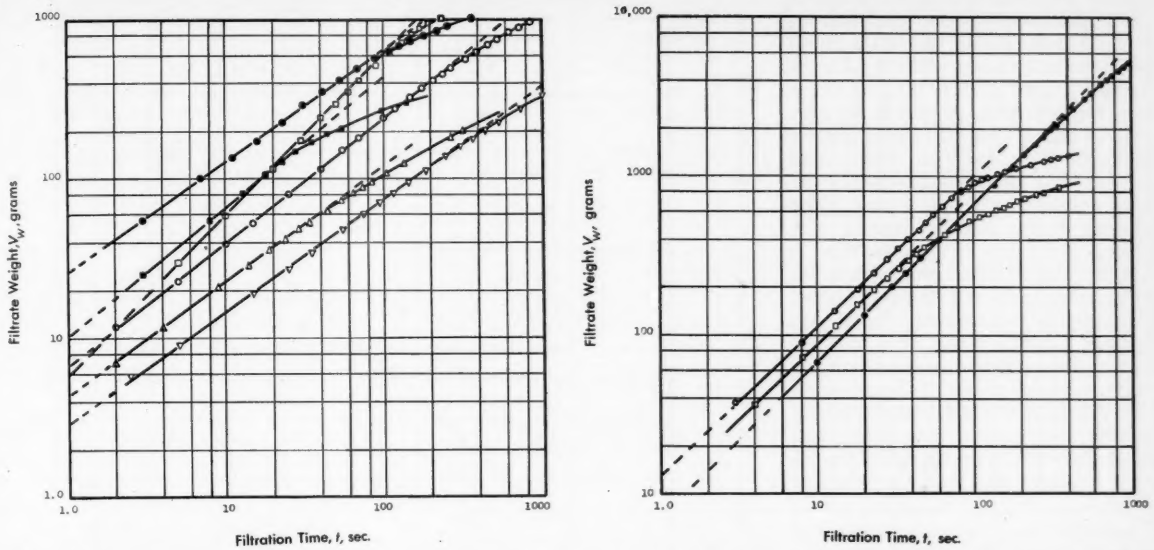

Fig. 13. (a) Initial portions of various clarification runs: ○ SN-23 staple nylon duck, ● FE-420 filament Orlon satin, □ 175-TW cotton twill, ■ TF-5044 filament nylon twill, △ TF-5071-F filament Orlon taffeta, calendered, ▽ No. 8 cotton duck; (b) initial portions of various clarification runs: ○ SN-7 filament nylon duck, ● AF-220 woven wool felt, □ TF-5071-U filament Orlon taffeta.

that during this initial region the large but relatively few interyarn or interthread pores became rapidly plugged to a degree which reduced their effective size to the same order of magnitude as the interfiber pores. At the start of the region of standard blocking, the percentage by number of < 3-μ particles passing uncollected ranged from 30 to 60% with the various media used. Similarly at the end of the region of standard blocking the percentage by number uncollected was from 10 to 30%. Over the observed regions of cake-law filtration with these media the percentage by number of < 3-μ particles uncollected was less than 10%.

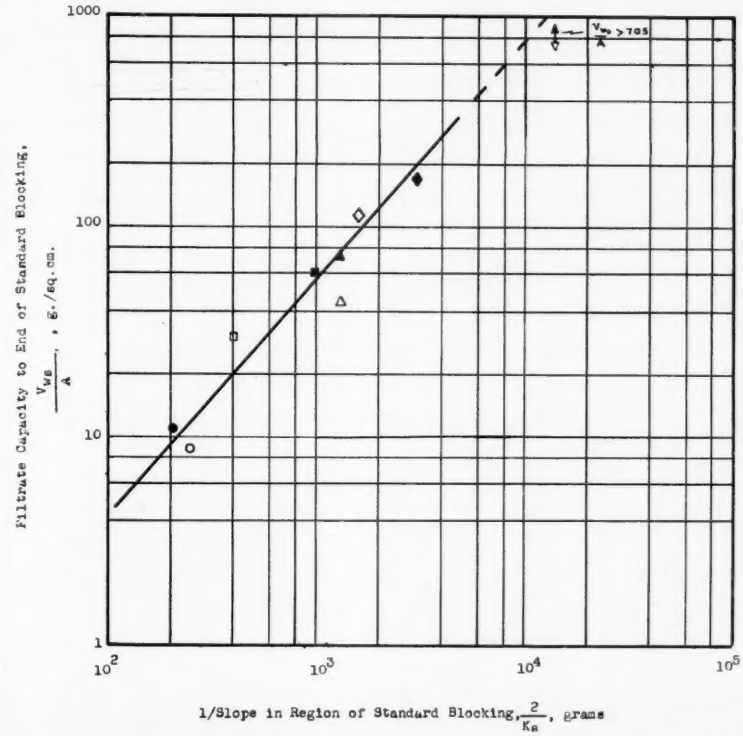

Fig. 14. Comparative capacity of various filter media to end of standard-blocking period: ○ No. 8 cotton duck, ● TF-5071-F, □ TF-5044, ■ TF-5071-U, △ SN-23, ▲ FE-420, ◇ SN-7, ◆ 175-TW, ▽ No. 220 felt.

As already discussed, at the solution viscosities and the filtration rates normally found in liquid filtrations, direct interception of particles from the streamlines of fluid adjacent to the pore walls is probably the major mechanism of collection. With this assumption the percentage of particles passing uncollected through a circular pore of radius r can be calculated on the basis that the particles are randomly distributed in the flowing liquid stream and that all within a distance of one particle radius of the wall will be collected. Since the < 3-μ particles as counted were all in the range of 1 to 3 μ diam., an average radius of 1 μ can be taken as representative of this fraction. If this particle radius, collection by the mechanisms of direct interception, and complete particle retention once collection occurs are assumed, the percentage of particles by number uncollected after passage through pores of various sizes would be as shown in the accompanying table:

Pore radius, μ	Predicted % < 3-μ particles uncollected
6.0	69.5
5.0	64
4.0	56.2
3.0	44.5
2.0	25
1.5	11.1

Since the modal values of the interfiber-pore radius for all but one of the media used were in the range of 2.2 to 5.3 μ, the observed values of 30 to 60% of < 3-μ particles passing uncollected at the start of the region of standard blocking agree well with these predicted values. This suggests that the standard-blocking region represents a region during which plugging of the interfiber pores is controlling and that the assumption of particle collection by direct interception is reasonably valid under these conditions. The passage uncollected during the standard-blocking region of a few particles of size equal to or greater than twice the modal value of interfiber-pore radius may reflect the actual distribution of interfiber-pore size or may result from the effective size of the plugged interyarn pores being greater than the interfiber pores.

Recently Cranston (*2*) developed a method whereby it should be possible at any instant in the filtration cycle to calculate the effective pore-size distribution of the medium if the particle-size distributions in both feed and filtrate are known at the same instant in the filtration cycle. The method has not actually been applied, however, because of the accurate particle-size-distribution data needed in the range of 0 to 5 μ for any worth-while calculations and because of the limited

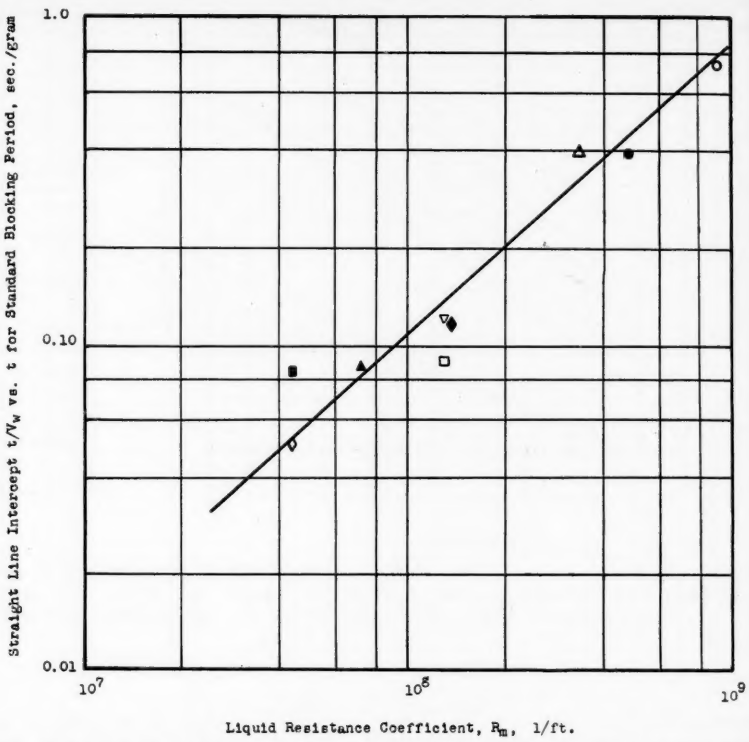

Fig. 15. Correlation of initial blocking resistance with liquid resistance of various filter media: ○ No. 8 cotton duck, ● TF-5071-F, □ TF-5044, ■ TF-5071-U, △ SN-23, ▲ FE-420, ◇ SN-7, ◆ 175-TW, ▽ 220 felt.

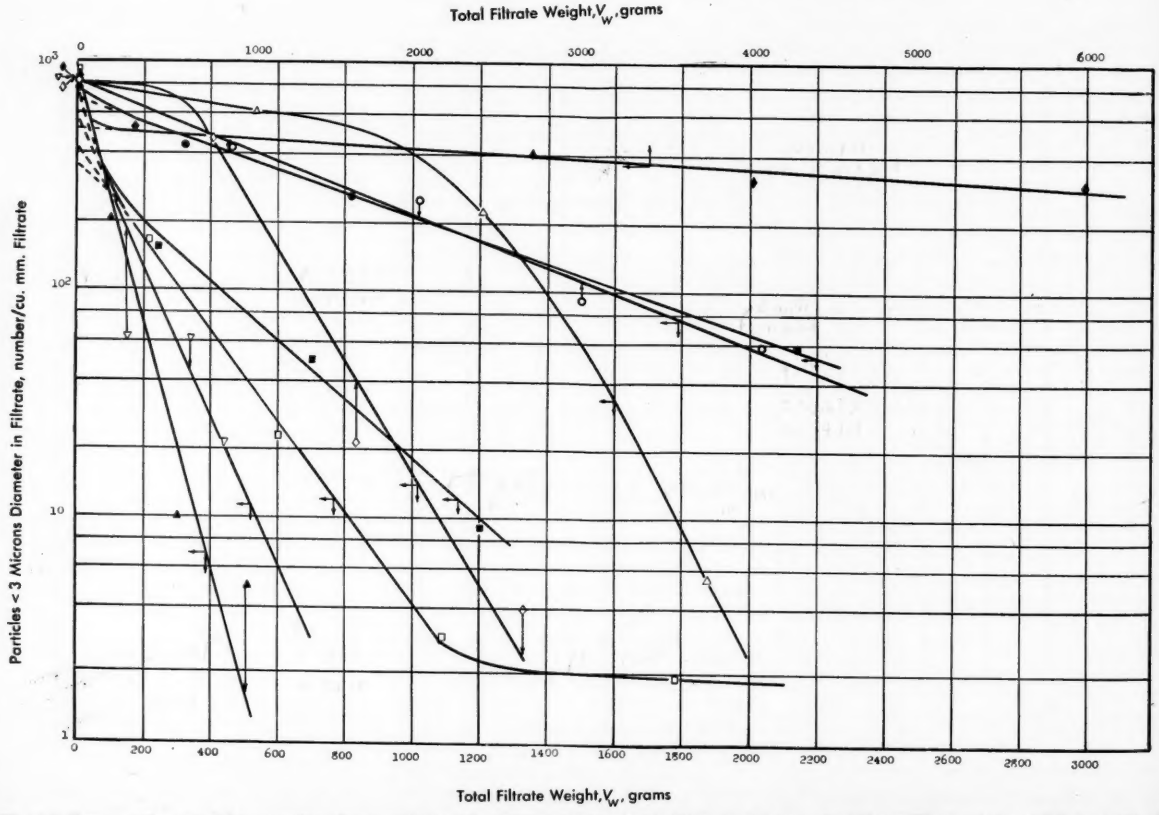

Fig. 16. Comparative particle-retention characteristics of various media: ○ 175-TW, ● FE-420, □ SN-23, ■ TF-5044, △ SN-7, ▲ No. 8 cotton duck, ◇ TF-5071-U, ◆ AF-220 felt, ▽ TF-5071-F.

utility of the results, as the effective pore-size distribution of the medium is changing continuously. The method, however, should also be applicable to the calculation of expected particle-size distribution in the filtrate at the start of a filtration provided that the particle-size distribution of feed and pore-size distribution of filter medium are known at the start of the filtration cycle. Since the mercury-intrusion method (Part I of the paper) provides an accurate pore-size distribution for a given medium, this reverse application of Cranston's method may have practical value but has not yet been applied to the data reported here. The particle-count data for < 3-μ particles passing uncollected with all media examined have been plotted vs. V_w on a semilogarithmic scale in Figure 16. For many of the media these plots approximate a straight line over most or all of the filtration cycle. This shows that the particle count in the filtrate decreases at a constant percentage rate throughout a significant portion of the filtration cycle. With the 175-TW cotton twill and the FE-420 satin medium made from Orlon acrylic fiber, this decrease in number continued at a constant percentage rate throughout the periods of initial blocking, standard blocking, and cake filtration. With very open cloths, such as 5071-U or SN-7, the percentage rate of decrease in particle number increased during the initial blocking period but remained constant throughout the standard-blocking and cake-filtration periods. With very tight cloths, such as No. 8 cotton duck, the percentage rate of decrease in particle number appeared to diminish during the initial blocking period but was constant throughout the remaining part of the filtration cycle. Thus, over the standard-blocking region and initial regions of cake-law filtration an empirical relationship of the form $C_0 = C_s e^{-BV}$ is indicated, where B is a constant which is related to the pore radius of the medium, C_s is the number of uncollected particles in the filtrate at the start of standard blocking, and C_0 is the number of uncollected particles in the filtrate at any time after the start of standard blocking. At any point in a filtration cycle the over-all collection number N_c has been defined (*13* and *3*) by the relationship $C_0 = C_f e^{-N_c}$, where C_f is the number of particles in the feed. When written for the start of the standard-blocking region, this expression becomes $C_s = C_f e^{-N_c'}$, where N_c' is the over-all collection number at the start of standard-blocking filtration. Combining yields the general relationship $C_0 = C_f e^{-(N_c' + BV)}$ for constant-pressure filtration over the standard-blocking and initial cake-law periods of filtration.

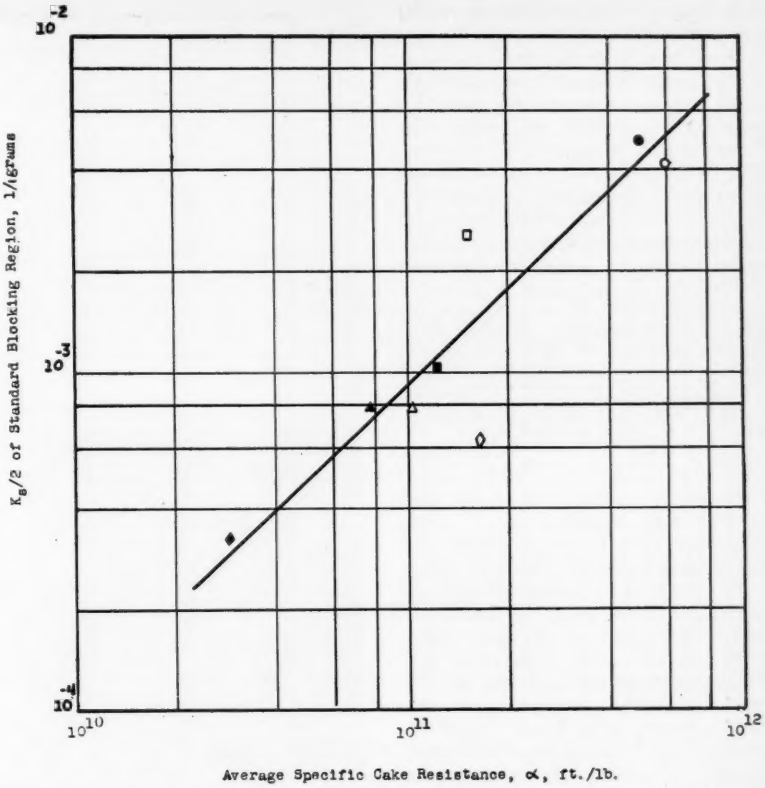

Fig. 17. Correlation between average specific cake resistance and standard-blocking performance: ○ No. 8 cotton duck, ● TF-5071-F, □ TF-5044, ■ TF-5071-U, △ SN-23, ▲ FE-420, ◇ SN-7, ◆ 175-TW.

Cake-filtration Characteristics. With all media except the AF-220 felt, one or more regions of cake-law filtration followed the region of standard blocking, as indicated by the straight-line portions of the t/V_w vs. V_w plots of Figures 3 to 11. In Table 2 are tabulated the values of the slope and intercept of the straight-line

Table 3. Comparison of Clogging Values with Total Pore Volume and Volume of Feed Solids

	(1)	(2)	(3)	(4)	(5)	(6)	(7)
			Packed volume* of feed solids				
Filter-medium style	Total pore vol. of medium $AL\epsilon/A$, cc./sq.cm.	Clogging value of medium $\pi N h r_0^2$, cc./sq.cm.	To end of standard blocking period, cc./sq.cm.	To start of cake law filtration, cc./sq.cm.	Ratio, column (2)/ column (1)	Ratio, column (3)/ column (2)	Ratio, column (4)/ column (2)
175-TW Cotton twill	68×10^{-3}	8.3×10^{-3}	5.7×10^{-3}	6.4×10^{-3}	0.12	0.69	0.77
FE-420 Filament Orlon satin	18.6×10^{-3}	3.7×10^{-3}	2.7×10^{-3}	4.0×10^{-3}	0.20	0.73	1.08
SN-23 Staple nylon duck	46×10^{-3}	3.9×10^{-3}	2.2×10^{-3}	3.3×10^{-3}	0.085	0.57	0.85
TF-5044 Filament nylon twill	7.5×10^{-3}	1.2×10^{-3}	0.80×10^{-3}	1.3×10^{-3}	0.16	0.67	1.08
AF-220 Woven wool felt	220×10^{-3}	43×10^{-3}	18×10^{-3}	....	0.20	0.42	
TF-5071-0 Filament Orlon taffeta	43×10^{-3}	3.0×10^{-3}	2.4×10^{-3}	3.1×10^{-3}	0.070	0.80	1.03
SN-7 Filament nylon duck	21×10^{-3}	4.8×10^{-3}	4.0×10^{-3}	4.9×10^{-3}	0.23	0.83	1.02
TF-5071-F Filament Orlon taffeta, calendered	16×10^{-3}	0.63×10^{-3}	0.35×10^{-3}	0.67×10^{-3}	0.040	0.56	1.06
No. 8 Cotton duck	48×10^{-3}	0.73×10^{-3}	0.38×10^{-3}	1.1×10^{-3}	0.015	0.52	1.51

*Packing porosity of particles within pore, $\epsilon_p = 0.45$.

(cake-law) portions of these curves for the various media. With all media except the very tight No. 8 duck and TF-5071-F, the intercept obtained by extrapolation to $V_w = 0$ was negative. Such a negative intercept is obtained in normal cake filtrations only when initial bleed occurs. The curves of Figures 3 to 11 are extreme examples of this and show in detail how particle bleed and initial regions of blocking filtration shift the cake-filtration region, resulting in a reduced or negative

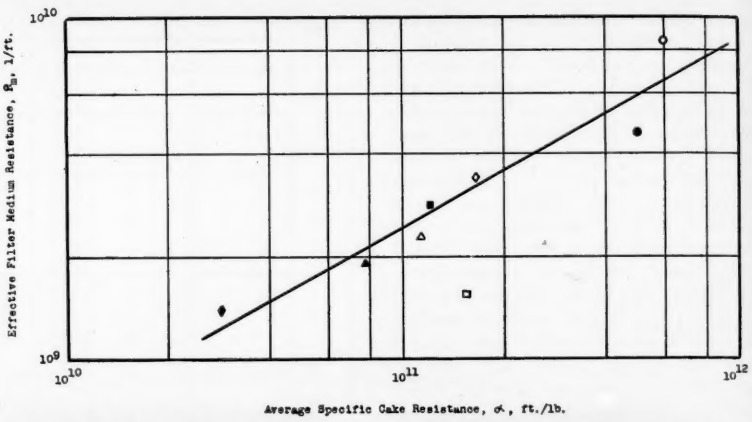

Fig. 18. Correlation of effective filter-medium resistance in cake filtration with average specific cake resistance: ○ No. 8 cotton duck, ● TF-5071-F, □ TF-5044, ■ TF-5071-U, △ SN-23, ▲ FE-420, ◇ SN-7, ◆ 175-TW.

intercept. In a qualitative sense the value of this extrapolated intercept is an indication of the amount of bleed which has occurred before cake filtration starts.

The values of α, corresponding to the regions of cake filtration for the various media, vary over a tenfold range (Table 2) despite the fact that the same well-dispersed suspension was used in each case. Also, with very tight media such as No. 8 cotton duck and TF-5071-F, two successive regions of cake filtration resulted, with the value of α decreasing for the second region. The absolute values of α are much higher than would be expected if they represented a true cake over the entire surface of the filter medium. Thus the value of α obtained by filtering a well-dispersed suspension of the same solids under identical filtration conditions except at a solids concentration of 6,100 p.p.m. by volume (48 g./liter) was constant at a value of $\alpha = 2.1\ (10)^{10}$ ft./lb., which was independent of the filter medium used. The values of α tabulated in Table 2 are two to thirty times this true value of α for a macroscopic cake. The photomicrographs of Figures 19 to 21 show the probable reason for this variation in the calculated value of α and for the high absolute values obtained. Thus, in general, no macroscopic cake was formed on the surface of the filter medium even at the end of the filtration cycle. Figures 19 to 21 show that only a microscopic cake had formed, both at each interyarn pore and at numerous isolated points on the surface of each yarn. Thus the effective filtration area at the cake surface was very much less than the surface area of the cloth. Also this effective surface area of the cake appears to vary for various media constructions during the regions of cake-law filtration involved. Since area enters as a squared term in the calculation of α, this lack of a macroscopic cake and variation in the points of forma-

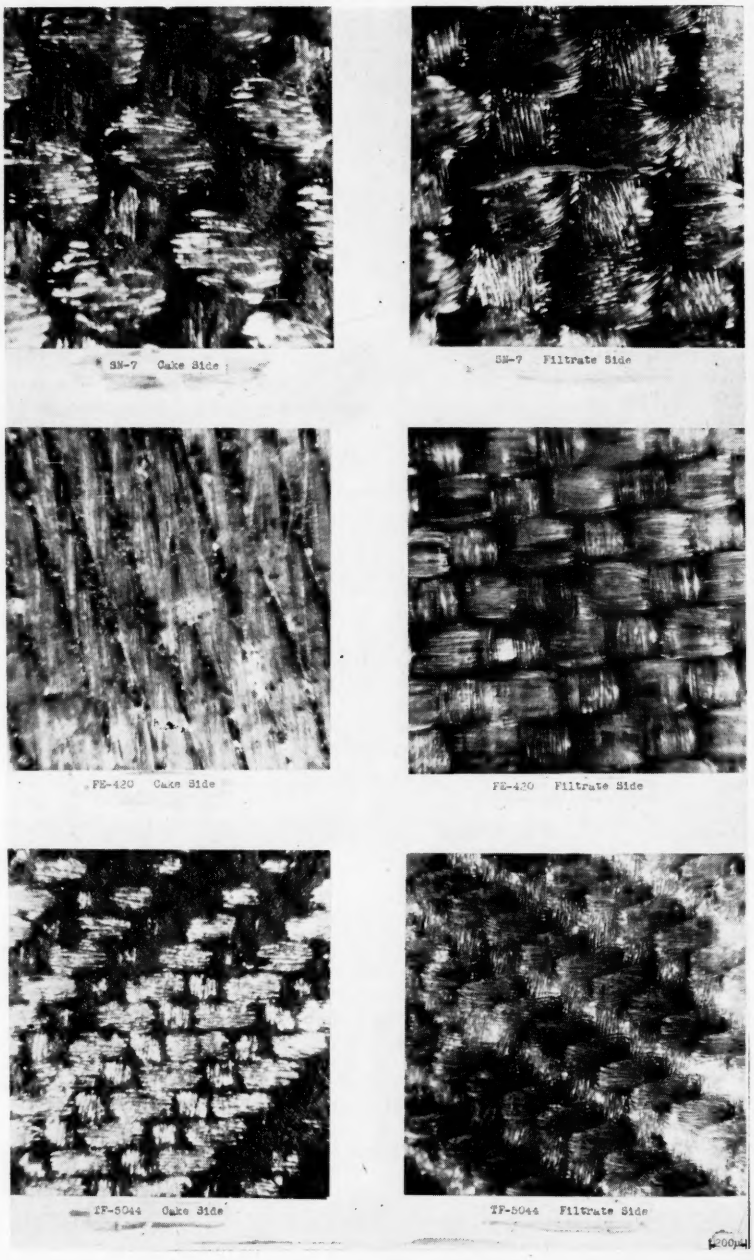

Fig. 19. Photomicrographs of filter-media surfaces at end of runs.

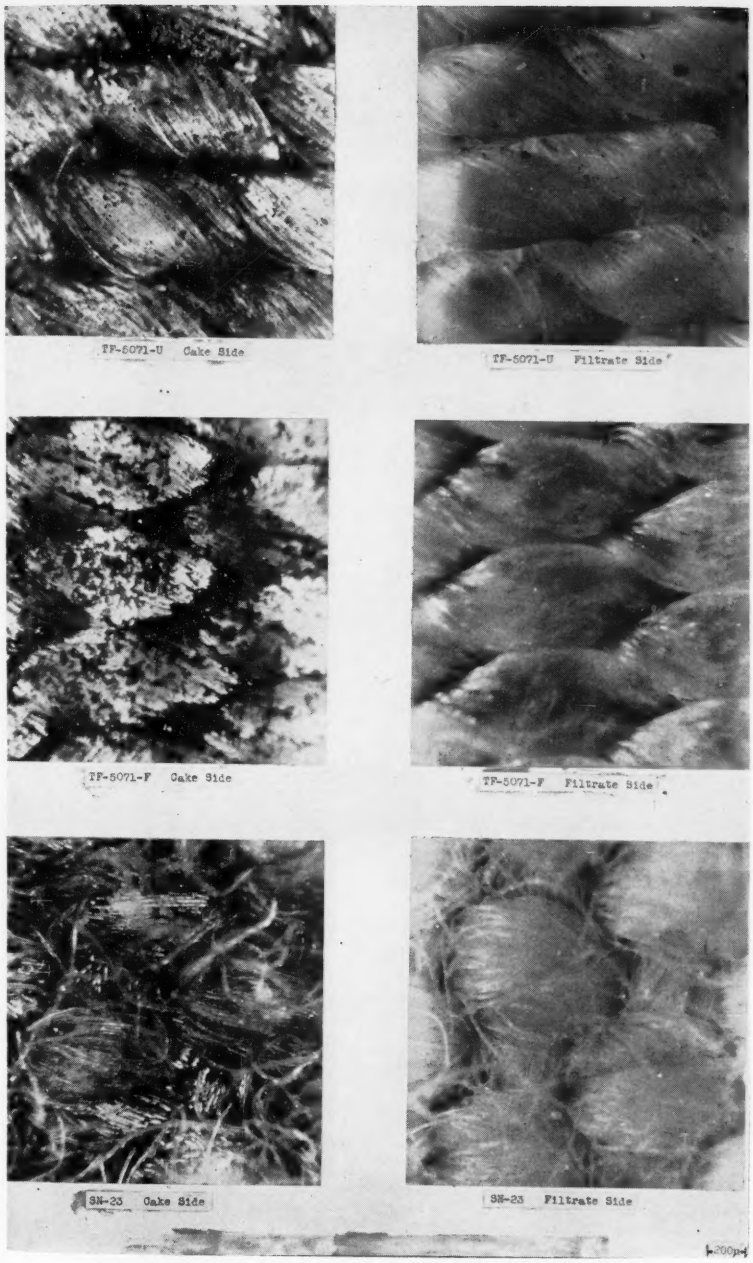

Fig. 20. Photomicrographs of filter-media surfaces at end of runs.

tion of the microscopic cake can easily account for the variability and the high absolute values of α. A changing cake-surface area during this period of cake filtration probably accounts for the successive regions of cake filtration encountered with the very tight media. This indicates that if the filtration cycle had been carried on until a macroscopic cake formed over the entire surface, a number of successive regions of cake filtration would result, with the values of α for successive regions decreasing to a final value which would be representative of a true macroscopic cake and thus independent of the filter medium. With rather loose cloths which tend to bleed particles even during the observed region of cake-law filtration, this particle bleed further complicates the picture. Thus final elimination of this bleed upon formation of a true macroscopic cake would have the opposite effect of tending to cause an increase in calculated α as a macroscopic cake forms.

In any case, Figures 19 to 21 show that the observed regions of cake-law filtration did not constitute true cake filtration with a macroscopic cake. These photomicrographs and the corresponding filtration data throw considerable light on how a cake forms on the surface of woven media. Despite the high yarn twist of the TF-5071-U and the TF-5071-F media, the photomicrographs of Figure 19 show that appreciable filtration is occurring through the yarn structure with cake formation at numerous isolated places on the surface of the yarn itself. In this respect, the photomicrographs show little difference between low and high yarn twist. However, the smaller interfiber pores resulting from both high-twist yarns and from calendering appear to minimize penetration of the yarns by particles and result in filtration with more rapid cake formation at the surface of the yarns.

The variability of the values of α obtained with various media appears to be closely related to the value of the plugging constant K_s obtained for the same medium during the standard blocking portion of the filtration cycle. Thus the plot of Figure 17 indicates an exponential relationship between $K_s/2$ and α. The apparent increase in observed α with increasing values of $K_s/2$ is related to the variation in the clogging value $\pi N h r_0^2$ from medium to medium, smaller clogging values causing higher values of plugging constant and a reduced area of pore constriction at which cake-law filtration starts. Thus the greater the plugging constant in these runs, the lower the true cake-forming area at the start of cake filtration and the greater the value of α computed for the initial region of cake-law filtration by use of the total filter-medium area. The effective resistance of the filter medium at the start of the region of cake-law filtration can be calculated from the instantaneous $\Delta t/\Delta V_w$ values at this point in the filtration cycle. Such values of R_m, as given in Table 2, appear unrelated to the liquid resistance of the unused medium. Rather, these values of R_m appear closely related to the value of α obtained from the region of cake-law filtration with each respective medium. This is shown by the logarithmic plot of Figure 18. With the more open media, the value of R_m was near a value equal numerically to 0.1α, which experience in true cake filtration (*6*) has shown to be the usual order of magnitude of R_m. However, as the media became tighter, the ratio of R_m/α decreased, with $R_m = 0.01\alpha$ for the very tight media. This low value of the R_m/α probably results from lack of a macroscopic cake in the observed region of cake-law filtration, which causes the calculated value of α to be too large.

Comparison of Filtration Performance with Pore Volume and Pore Size of the Filter Media. Clogging values $\pi N h r_0^2$ for the various filter media used are computed in Table 2 by use of Equation (8) and the slope of the corresponding t/V_w vs. t plot of the filtration data for the region of standard blocking. Based on previous measurements (*5*) a value of $\epsilon_p = 0.45$ was used for the packing porosity of the

particles retained on the pore walls. These clogging values represent the effective pore volume of the filter medium which plugs during this standard-blocking period of filtration. In Table 3 these clogging values are compared with the total pore volume of each filter medium. The clogging value of pore volume is seen to range from 1.5 to 23% of the total pore volume. The ratio of the clogging value to the total pore volume is smallest for the tightest media but otherwise seems independent of the construction of the filter medium. For media other than the tightly woven No. 8 cotton duck and 5071-F calendered Orlon the clogging value was from 7 to 23% of the total pore volume. This percentage of the pore volume can be interpreted to represent the volume of the pore constrictions which is controlling insofar as particle buildup and plugging are concerned.

Also shown in Table 3, for the various media, is a comparison of the clogging values with the total packed volume of solid particles fed to both the end of the standard-blocking region and the start of the region of cake-law filtration. The packed volume of the solids fed to the end of the standard-blocking region is seen to range from 52 to 83% of the clogging value of pore volume. The packed volume of the solids fed to the start of the region of cake-law filtration is seen to range from 77 to 151% of the clogging value of pore volume, with five of the media showing packed volume of feed solids to equal the clogging value ±10% at the start of cake-law filtration. These figures then support the interpretation of the clogging value as the volume of the pore constrictions which is controlling insofar as particle buildup and plugging are concerned. Failure of the standard-blocking relationship before 100% of the clogging value of pore volume is filled with packed particles, and the existence of a transition region between the regions of standard-blocking and cake-law filtration may result from at least two factors. First, as that portion of the pore volume represented by the clogging value becomes more than half filled with packed particles, an appreciable part of the flow may occur through the smaller pores between the packed particles along the pore wall, causing a combination of standard-blocking and cake-law filtration. Second, since the r_0 term of the clogging value, $\pi N h r_0^2$, is not a constant but rather a distribution of sizes, some of the pore constrictions representing the clogging value of pore volume may become plugged before others, resulting in cake-law filtration through some pore constrictions while filtration through other constrictions still follows the standard-blocking mode. This second factor can be expected to be more pronounced in constant-rate filtration than in constant-pressure filtration.

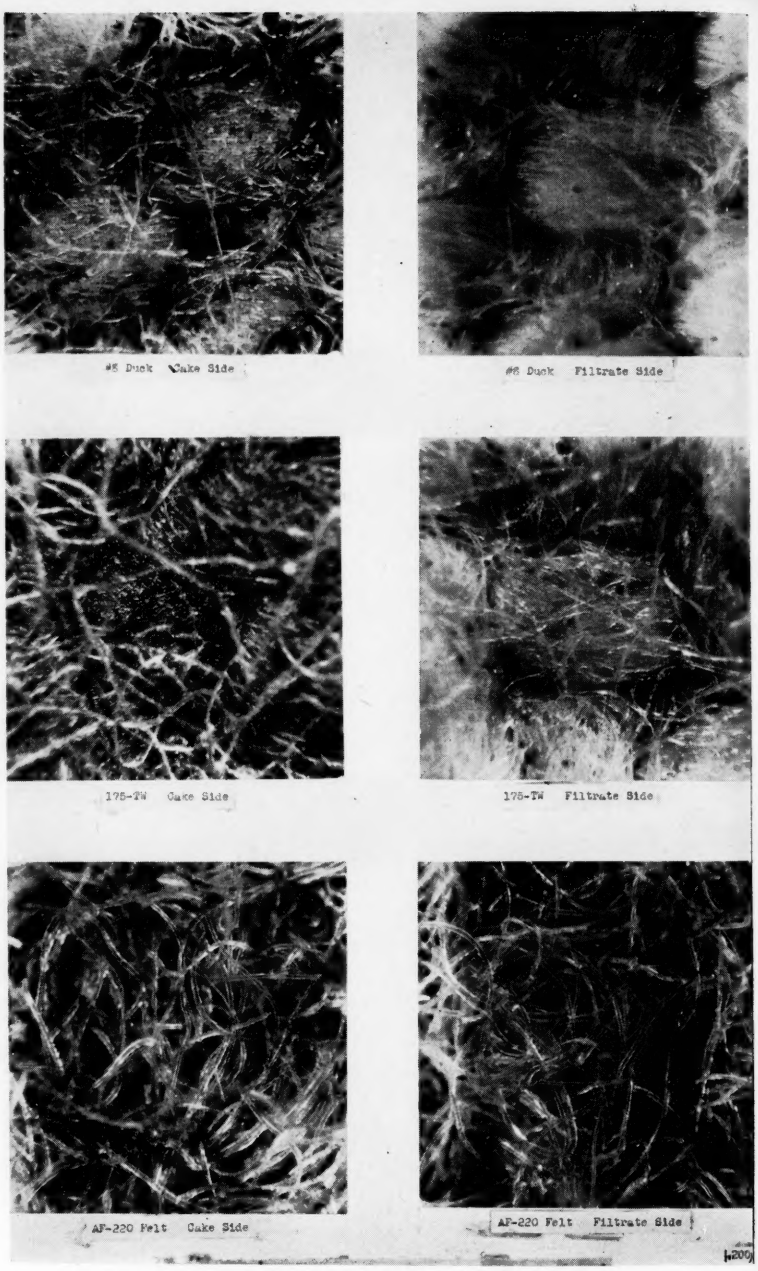

Fig. 21. Photomicrographs of filter-media surfaces at end of runs.

With the physical picture of buildup of packed particles on the walls of the pore constrictions represented by the clogging value of pore volume, a basic difference between constant-pressure and constant-rate filtration during the region of standard blocking becomes clear. Thus the shear stress at the walls of these constrictions is equal to either $r(\Delta p)/2h$ or $(\mu_f/g_c)\ (4q/\pi r^3)$, where $r = r_0$ at the start of standard-blocking filtration and r decreases as a packing of particles builds up on the walls. With flow through the packing of the particles neglected, the shear stress at the wall or surface of packed particles on the wall then decreases with constant-pressure filtration, but increases with constant-rate filtration. As already discussed, particle retention increased during the standard-blocking period of filtration for the constant-pressure filtrations reported here. Few data on particle retention for constant-rate filtration during the standard-blocking period have been reported, and it is not clear whether the degree of retention actually decreases short of breakthrough. The fact that particle collection by interception will tend to increase as the radius term of the clog-

TABLE 4. ANALYSIS OF CLOGGING VALUES IN TERMS OF CIRCULAR PORES OF MEASURED INTERFIBER PORE RADIUS

Filter-medium style	Filter-medium porosity, ϵ void fraction	Modal value of interfiber pore radius, r_f, cm.	Calculated values assuming $r_0 = r_f$				
			hN, 1/cm.	$\pi hN/b$,* cm.	Constriction-free area/ avg. pore-free area a, dimensionless	Population density of plugging pores, N, No./sq. cm.	Effective length of plugging pores, h, cm.	Ratio of h/L, dimensionless
175-TW Cotton twill	0.603	5.3×10^{-4}	9.5×10^{3}	6.3×10^{-4}	0.35	2.4×10^{5}	4.0×10^{-2}	0.36
FE-420 Filament Orlon satin	0.517	3.9×10^{-4}	7.8×10^{3}	5.2×10^{-4}	0.44	4.7×10^{5}	1.6×10^{-2}	0.46
SN-23 Staple nylon duck	0.505	4.0×10^{-4}	7.8×10^{3}	5.2×10^{-4}	0.23	2.3×10^{5}	3.4×10^{-2}	0.38
TF-5044 Filament nylon twill	0.413	3.0×10^{-4}	4.2×10^{3}	2.8×10^{-4}	0.37	5.5×10^{5}	0.79×10^{-2}	0.44
AF-220 Wool felt	0.701	16.5×10^{-4}	5.0×10^{3}	3.4×10^{-4}	0.22	0.18×10^{5}	27.6×10^{-2}	0.91
TF-5071-U Filament Orlon taffeta	0.528	3.8×10^{-4}	6.6×10^{3}	4.4×10^{-4}	0.38	4.5×10^{5}	1.5×10^{-2}	0.18
SN-7 Filament nylon duck	0.523	5.0×10^{-4}	6.2×10^{3}	4.1×10^{-4}	0.47	3.1×10^{5}	1.9×10^{-2}	0.49
TF-5071-F Filament Orlon taffeta, calendered	0.296	2.2×10^{-4}	4.1×10^{3}	2.7×10^{-4}	0.22	4.3×10^{5}	0.97×10^{-2}	0.18
No. 8 Cotton duck	0.537	2.9×10^{-4}	2.8×10^{3}	1.9×10^{-4}	0.073	1.5×10^{5}	1.9×10^{-2}	0.21

$$hN = \frac{(\text{measured clogging value})}{\pi r_0^2}$$

$$N = \frac{a\epsilon}{\pi r_0^2}$$

$$h = \frac{(\text{measured clogging value})}{a\epsilon} = \frac{(\text{measured pore resistance})(\pi N r_0^4)}{8}$$

$$a = \left(\frac{1}{\epsilon r_0}\right)\sqrt{\frac{(8)\ \text{measured clogging value}}{\text{measured pore resistance}}}$$

*$b = 4.7(10)^7$, determined from empirical correlation of Figure 22*a*

ging value decreases complicates the picture for the case of constant-rate filtration.

In Figure 22*a* is shown a logarithmic plot of the clogging, πNhr_0^2, vs. the modal value of interfiber pore radius, r_f, for the various media as determined by the mercury-intrusion method. A good correlation is indicated of the form

$$\pi Nhr_0^2 = br_f^n \qquad (11)$$

in which $n = 3.0$ and $b = 4.7(10)^7$ cm^{-2}. This is strong evidence of a definite relationship between the radius, r_0, of the pore constrictions at which plugging occurs and the measured value of interfiber pore radius, r_f. Further, the value of $n = 3.0$ suggest that the value of the product Nh may vary in direct proportion to the value of r_0, which would result in a direct relationship between r_0 and r_f. The fact that the particle retention, calculated on the basis of r_f and the assumed mechanism of collection by interception, is in the range of observed particle retention lends support to this hypothesis. When it is recognized that measurements by the mercury-intrusion method result in the distribution of pore size in terms of the pore volume which can be entered through constrictions of a certain size, the equality of r_f and r_0 appears to be a reasonable approximation.

The plotting of the clogging value vs. the average pore radius, as measured by the permeability method (Figure 22*b*), shows that a relationship similar to that of Figure 22*a* appears to exist. The slope is again 3 although the scatter of data is greater. However, this relationship is believed to be a secondary one which results from the primary relationship of Figure 22*a* and a direct relationship between the values of r_f measured by the mercury-intrusion method and the values of r_p measured by the permeability method. The fact that particle retention calculated on the basis of r_p is very much less than the observed values indicates that r_p and r_0 cannot be equivalent. Consideration of the permeability method of measuring r_p also indicates that r_p would be expected to be considerably larger than the pore constrictions and therefore not equivalent to r_0.

If r_f is assumed equivalent to r_0, values of the pore-population density, N, and effective pore length, h, can be calculated from the measured values of the clogging value, πNhr_0^2, and pore resistance, $8h/\pi Nr_0^4$, as discussed in the Appendix. In order to give additional meaning to this for an actual filter medium which has pores containing constrictions of radius r_0 rather than straight-through pores of uniform radius, use is made of the relationship

$$N = a\epsilon/\pi r_0^2 \qquad (12)$$

in which ϵ is the measured value of the average porosity of the medium, and a

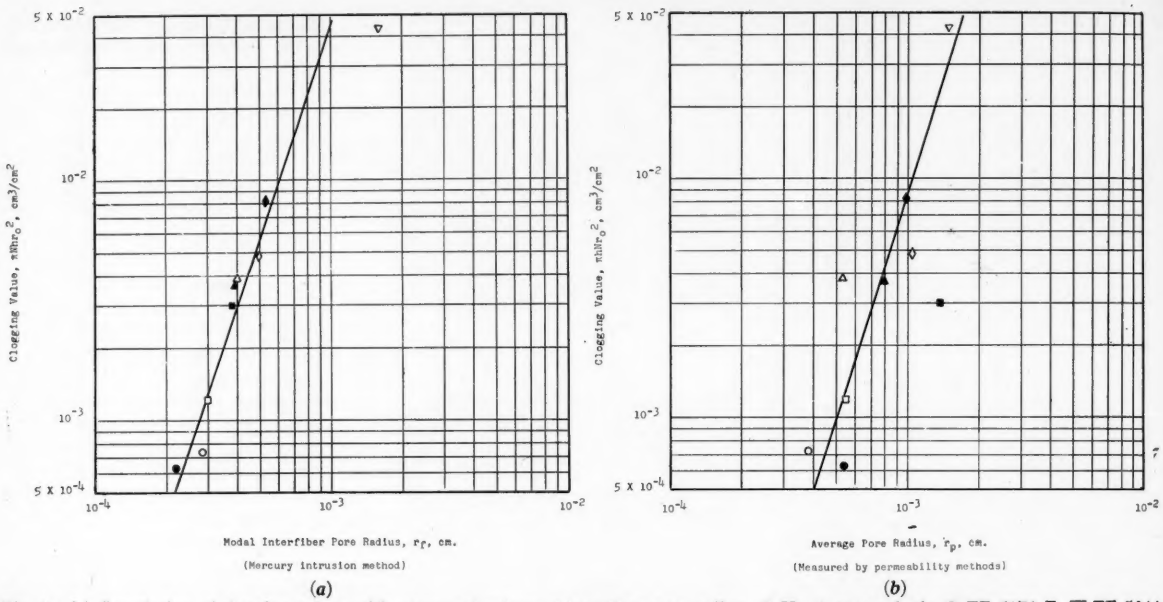

Fig. 22. (a) Correlation of clogging values with measured values of interfiber pore radius: ○ No. 8 cotton duck, ● TF-5071-F, □ TF-5044, ■ TF-5071-U, △ SN-23, ▲ FE-420, ◇ SN-7, ◆ 175-TW, ▽ 220 felt; (b) correlation of clogging values with measured average pore radius: ○ No. 8 cotton duck, ● TF-5071-F, □ TF-5044, ■ TF-5071-U, △ SN-23, ▲ FE-420, ◇ SN-7, ◆ 175-TW, ▽ 220 felt.

is the fraction of average cross-sectional area of the pores existing at the constriction of radius r_0. Thus, a can be thought of as the minimum free area represented by the constrictions of radius r_0 which become plugged during filtration. The values of N, h, and a, calculated on the assumption that $r_0 = r_f$, are given in Table 4. As expected, the values of the product hN are approximately proportional to the values of r_0. The scatter can be seen by comparing r_f numerically to the quantity $\pi hN/b$. Only the values for the AF-220 felt disagree badly, indicating that the assumption of $r_f = r_0$ is probably valid except for the felt. Permeability measurement of average pore size on this felt, as reported in Part I, showed that, because of swelling in aqueous solution, the pore size in this medium decreased markedly when water wet. Since the measured value of r_f was determined on the dry felt, while the solution filtered contained 20% water, it is not surprising that the measured value of r_f is indicated to be too large to fit the correlation.

The calculated values (Table 4) of a, the ratio of free area of pore constrictions to average free area of pores, ranged from 0.07 to 0.44 with the various media. This suggests that the radius, r_0, at the pore constrictions was in the range of 27 to 66% of the average radius of the pores. The ratios of the effective pore length, h, to the measured thickness of the medium (Table 4) was less than 1.0 in all cases and fell in the range of 0.18 to 0.44 for all media except the felt. The examination of many more media appears necessary before the real meaning of the calculated values of h, a, and N can be established; however, the values obtained for the media studied here appear consistent with the physical picture of medium structure and particle removal by the plugging of pore constrictions, as already discussed.

The empirical relationship of Figure 22*a* and Equation (11) may be of great practical significance. Since the values of interfiber pore radius and clogging values on which this relationship is based cover media of widely different construction, prediction of clogging values for other media should be possible based on measurement of pore-size distribution. Consideration of the nature of the clogging value leads to the conclusion that this value is a property of the filter medium which can be expected within limits to be independent of the concentration or size distribution of the particles in the feed suspension. Thus the variation in the over-all plugging constant, K_s, with such changes in feed suspension may in fact result only from variations in the numerator, $c/(1 - \epsilon_p)$, of the second term of Equation (9). If this can be verified, prediction of the changes in over-all plugging constant resulting from changes in feed suspension with a given medium will follow. The problem of predicting filtration performance from either measured or predicted clogging values is greatly complicated, however, if the filter medium is either compressible within the range of operating pressures to be encountered or is physically changed by absorption of the liquid being filtered. Either of these factors can greatly alter the clogging value of the medium, and these effects were purposely minimized by the conditions used in the work reported here.

SUMMARY

The application of a clarification technique to the evaluation of the performance of nine widely different filter media of previously determined pore structure has shown the following observations.

1. A region of standard-blocking filtration occurs with each medium, and thus a characteristic clogging value which is a measure of the volume of pore constrictions that plug during filtration can be determined.

2. The region of standard-blocking filtration ends when 50 to 80% of the clogging value of pore volume becomes filled with packed solids.

3. An initial region of cake-law filtration begins when the packed volume of solids removed becomes 80 to 150% of the clogging value of pore volume.

4. This initial region of cake-law filtration represents cake filtration on a microscopic rather than a macroscopic scale, such that the specific cake resistance computed on the basis of the superficial filtration area is two to thirty times the actual specific cake resistance and is dependent on the pore structure of the filter medium.

5. The degree of particle removal during the region of standard-blocking filtration is of the same magnitude as that calculated on the basis of particle removal by direct interception at the walls of pore constrictions of radius equal to the modal value of interfiber-pore radius.

6. A definite correlation exists between the clogging value, measured for the region of standard-blocking filtration, and the modal value of interfiber-pore radius of the medium.

7. This correlation strongly suggests equality between the radius of pore constrictions which plug during standard-blocking filtration and the modal value of interfiber-pore radius as measured by the mercury-intrusion method.

8. The work directed along the lines

initiated here may ultimately make possible prediction of filter-media performance on the basis of pore structure, but the limitations imposed by variables not considered here must first be evaluated.

NOTATION

a = fraction of average free area of pores existing as plugging restrictions, dimensionless

A = superficial filtration area at surface of filter medium or cake deposited thereon, sq. cm.

b = constant in empirical relationship, 1/sq. cm.

B = exponent in empirical equation $C_0 = C_s e^{-BV}$, dimensionless

c = volume of solid particles removed per volume of solution filtered, cc./cc.

c_f = volume of solid particles in feed suspension per volume of solution, cc./cc.

C = constant in empirical equation, 1/sq. cm.

C_f = number of particles per unit volume of feed suspension, 1/cc.

C_0 = number of particles per unit volume of filtrate at any time, 1/cc.

C_s = number of particles per unit volume of filtrate at start of standard-blocking region, 1/cc.

g_c = conversion factor in Newton's law of motion, 980 (g.) (cm.)/(g. force)(sec.)^2

h = pore length in standard-blocking equation, cm.

k = constant in general differential equation for filtration cycle (dimensions depend on value of exponent, n)

k', k'' = constants in empirical equation for initial portion of filtration cycle

K = constant of Kozeny-Carman relationship ($5 \pm 10\%$), dimensionless

K_b = plugging constant of complete-blocking law, 1/sec.

K_s = plugging constant of standard-blocking law, 1/cc. (1/g. when V_w is used)

K_i = plugging constant of intermediate-blocking law, 1/cc. (1/g. when V_w is used)

K_c = plugging constant of cake-filtration law, sec./cm.^{6} (sec./g.^{2} when V_w is used)

L = measured thickness of filter medium, cm.

m, m', m'' = exponents of empirical relationships

n = exponent of general differential equation for filtration process

N = number of pores per unit area, number/sq. cm.

N_c = collection number as defined by equation $C_0 = C_f e^{-N_c}$, dimensionless

N_c' = collection number at start of standard-blocking region, dimensionless

Δp = total pressure drop (across filter medium and cake if any) at time, t, during filtration, lb./sq. in.

Δp_0 = total pressure drop at start of filtration, lb./sq. in.

q = filtration rate at time, t, during filtration, cc./sec. (g./sec. when V_w is used)

q_0 = filtration rate at start of filtration, cc./sec. (g./sec. when V_w is used)

q_w = rate of liquid passage through unused filter medium in permeability measurements in viscous flow range, cc./sec.

r = effective pore radius in medium at any time, t, during filtration, μ

r_f = modal value of interfiber-pore radius as measured by mercury intrusion method, μ

r_0 = effective initial pore radius in standard-blocking equation, cm.

r_p = average pore radius of filter medium calculated from liquid permeability measurements, μ

R_m = effective resistance of filter medium during cake filtration, 1/ft.

t = time of filtration, sec.

V = cumulative volume of filtrate at time, t, cc.

V_w = cumulative weight of filtrate at time, t, g.

w = weight of suspended solids per unit volume of filtrate, lb./cu. ft.

α = average specific cake resistance, ft./lb.

ϵ = porosity of filter medium, void fraction, dimensionless

ϵ_p = packing porosity of particles deposited on pore walls, void fraction, dimensionless

ρ_f = density of solution, fluid, or filtrate, g./cc.

ρ_s = density of suspended solid, g./cc.

μ_f = viscosity of solution or filtrate, centipoises

LITERATURE CITED

1. Carman, P. C., *Trans. Inst. Chem. Engrs. (London)*, **16**, 168 (1938).
2. Cranston, R. W., *Aircraft Eng. (London)*, **24**, 154 (1952).
3. Davies, C. N., *Arhiv. Hi. Rada*, **1**, 4 (1950); *Proc. Inst. Mech. Engrs. (London)*, **1B**, 185 (1952).
4. Gonsalves, V. E., *Rec. trav. chim.*, **69**, 873 (1950).
5. Grace, H. P., *Chem. Eng. Progr.*, **49**, 303 (1953).
6. *Ibid.*, 367 (1953).
7. Heertjes, P. M., and H. v. d. Haas, *Rec. trav. chim.*, **68**, 361 (1949).
8. Hermans, P. H., and H. L. Bredée, *Rec. trav. chim.*, **54**, 680 (1935); *J. Soc. Chem. Ind.*, **55T**, 1 (1936.)
9. Herrent, P., A. Lunde, and G. Jnoff, *Svensk Papperstidn.* **54**, 153 (1951).
10. Hixson, A. W., L. T. Work, and I. H. Odell, *Trans. Am. Inst. Mining Met. Engrs.*, **73**, 225 (1927).
11. Kane, E. D., *Ind. Eng. Chem.*, **45**, 860 (1953).
12. Kohl, J., and R. D. Zentner, *J. Phys. Chem.*, **57**, 68 (1953).
13. Langmuir, I., "Smokes and Filters," No. 865, Part IV, U. S. Off. Sci. Res. & Dev. (1942).
14. Matthes, A. von, *Chem. Tech.*, **3**, 13 (1951).
15. Nicolaysen, V. B., and W. B. Borregard, *Norsk Skogind.*, **4**, 219 (1950), **6**, 338 (1952).
16. Rodebush, W. H., "Handbook on Aerosols," Chap. 9, U. S. Atomic Energy Commission, Washington, D. C. (1950).
17. Ruth, B. F., *Ind. Eng. Chem.*, **27**, 806 (1935).
18. Samuelson, O., *Svensk Papperstidn.*, **52**, 465 (1949).
19. Smith, E. G., *Chem. Eng. Progr.*, **47**, 545 (1951).
20. Thomas, D. J., *Inst. Heating Ventilating Engrs. (London)*, **20**, 35 (1952).
21. Vosters, H., *Svensk Papperstidn.*, **53**, 29, 613, 771 (1950).
22. *Ibid.*, **54**, 539 (1951).

APPENDIX

Modified Development of Standard-Blocking Relationships

The physical picture assumed in deriving the standard-blocking law of Hermans and Bredée is that the filter medium consists of parallel pores of equal length and radius. The mechanism assumed is one of direct interception of particles from streamlines adjacent to the pore walls and of particle retention on the walls of the pores in such a way that the volume of the major flow channel through the pores decreases in direct proportion to the volume of filtrate whch passes through the pore. This means that for standard blocking to occur over a period of considerable duration, the initial pore diameter of the medium must be at least several times the particle diameter even at very low solids concentration.

In a capillary of round cross section of radius r_0 and length h, through which passes a volume of liquid, dV, from which is removed a volume, c, of filterable particles per unit volume of liquid filtered, the reduction in volume of the original capillary channel will equal the packed volume of solids deposited, or

$$-2\pi NAhr\,dr = \left(\frac{c}{1-\epsilon_p}\right) dV \quad \text{(A1)}$$

where ϵ_p is the porosity of the layer of retained particles. Integrating between the limits of the start of filtration and the point where the volume filtered is V and the radius is r gives

$$-2\pi NAh \int_{r_0}^{r} r\,dr = \frac{c}{1-\epsilon_p} \int_0^V dV \quad \text{(A2)}$$

$$\pi NAh(r_0^2 - r^2) = cV/(1-\epsilon_p) \quad \text{(A3)}$$

From Poiseuille's law, the instantaneous time rate of flow, $q_0 = dV/dt$, can be related to the pressure drop, Δp; the number of capillaries per unit area, N; the filtration area, A; the diameter and length of capillaries, $2r_0$ and h; and the solution viscosity, μ_f, by the expression

$$q_0 = \frac{dV}{dt} = \frac{\pi NAr_0^4 g_c \Delta p_0}{8h\mu_f} \quad \text{(A4)}$$

and as the pores plug during filtration by

$$q = \frac{\pi NAr^4 g_c \Delta p}{8h\mu_f} \quad \text{(A5)}$$

provided that the flow through the packing voids of the layer of retained solids on the pore walls is negligible compared to flow

through the main channel of the pore. Rearrangement gives

$$r_0^2 = \left(\frac{q_0}{\frac{\pi N A g_c \Delta p_0}{8h\mu_f}}\right)^{0.5} \quad \text{(A6)}$$

$$r^2 = \left(\frac{q}{\frac{\pi N A g_c \Delta p}{8h\mu_f}}\right)^{0.5} \quad \text{(A7)}$$

Substitution of values from (A6) and (A7) in (A3) gives

$$\pi N A h\left[\left(\frac{q_0}{\frac{\pi N A g_c \Delta p_0}{8h\mu_f}}\right)^{0.5} - \left(\frac{q}{\frac{\pi N A g_c \Delta p}{8h\mu_f}}\right)^{0.5}\right] = \frac{cV}{1-\epsilon_p} \quad \text{(A8)}$$

or

$$\left(\frac{q_0/(g_c\Delta p_0)}{8\pi N A h^3 \mu_f}\right)^{0.5} - \left(\frac{q/(g_c\Delta p)}{8\pi N A h^3 \mu_f}\right)^{0.5} = \frac{cV}{1-\epsilon_p} \quad \text{(A9)}$$

setting

$$\left(\frac{g_c}{8\pi N A h^3 \mu_f}\right)^{0.5} = \beta \quad \text{(A10)}$$

Then

$$\left(\frac{q_0}{\Delta p_0}\right)^{0.5} - \left(\frac{q}{\Delta p}\right)^{0.5} = \left(\frac{c}{1-\epsilon_p}\right)\beta V \quad \text{(A11)}$$

which is the general differential form of the standard-blocking law.

For constant-pressure operation Equation (A11) becomes

$$\left(\frac{q_0}{\Delta p_0}\right)^{0.5} - \left(\frac{q}{\Delta p_0}\right)^{0.5} = \left(\frac{c}{1-\epsilon_p}\right)\beta V \quad \text{(A12)}$$

Rearranging gives

$$q = \frac{dV}{dt} = \Delta p_0\left[\left(\frac{q_0}{\Delta p_0}\right)^{0.5} - \frac{\beta c V}{(1-\epsilon_p)}\right]^2 \quad \text{(A13)}$$

Integrating gives

$$\int_0^V \frac{dV}{\left[\left(\frac{q_0}{\Delta p_0}\right)^{0.5} - \frac{\beta c V}{1-\epsilon_p}\right]^2} = \Delta p_0 \int_0^t dt \quad \text{(A14)}$$

$$\frac{V}{\left(\frac{q_0}{\Delta p_0}\right)^{0.5}\left[\left(\frac{q_0}{\Delta p_0}\right)^{0.5} - \frac{\beta c V}{(1-\epsilon_p)}\right]} = \Delta p_0 t \quad \text{(A15)}$$

Rearrangement of Equation (A15) yields the form

$$\frac{V}{t} = q_0 - \left(\frac{\beta c}{1-\epsilon_p}\right)(q_0^{0.5}\Delta p^{0.5})V \quad \text{(A16)}$$

or by further rearrangement, the form

$$\frac{t}{V} = \frac{1}{q_0} + \left(\frac{\beta c}{1-\epsilon_p}\right)\left(\frac{\Delta p_0}{q_0}\right)^{0.5} t \quad \text{(A17)}$$

where the K_s of the Hermans and Bredée equation equals

$$\left(\frac{2\beta c}{1-\epsilon_p}\right)\left(\frac{\Delta p_0}{q_0}\right)^{0.5}$$

Equation (A17) can be made more understandable and significant in terms of filter-medium behavior if the terms Δp_0, β, and q_0 are replaced by terms containing the filter-medium constants. This can be done by substituting Equations (A5) and (A10) in (A17) to give

$$\frac{t}{V} = \frac{8h\mu_f}{\pi N A r_0^4 g_c \Delta p} + \left(\frac{g_c}{\pi N A h^3 \mu_f}\right)^{0.5} \cdot \left(\frac{h\mu_f}{\pi N A r_0^4 g_c}\right)^{0.5}\left(\frac{c}{1-\epsilon_p}\right)t \quad \text{(A18)}$$

or, simplified,

$$\frac{t}{V} = \left(\frac{8h}{\pi N r_0^4}\right)\left(\frac{\mu_f}{A g_c \Delta p}\right) + \left(\frac{c/(1-\epsilon_p)}{\pi N A h r_0^2}\right)t \quad \text{(A19)}$$

This shows that the slope of a t/V vs. t plot during the period of standard blocking (the $K_s/2$ of Hermans and Bredée's equation) is equal to the packed volume of solids removed per volume of filtrate divided by the effective pore volume of the area of filter medium used. Thus, with $c = c_f$, the volume of solids per unit volume solution in the feed suspension, assumed and the probable value of ϵ_p known from independent measurements on the particulate solids, the clogging value of the medium, $\pi N h r_0^2$, can be solved for directly from the slope of the t/V vs. t plot over the standard-blocking region. The pore-resistance constant, $8h/\pi N r_0^4$, can also be calculated from the extrapolated intercept of the standard-blocking region. Solution for individual terms N, h, and r_0 is not possible by use of these values alone. If the filter medium were truly composed of straight-through circular pores of uniform radius, the relationship $N = \epsilon/\pi r_0^2$ becomes valid and a direct solution for values of N, h, and r_0 would become possible. However, since the actual pores of the filter medium are of nonuniform cross section along their length, the major areas of plugging are probably restricted to the constrictions within these pores. Although these constrictions will not all be at the same depth within the filter medium, it seems reasonable that under these conditions this plugging area or minimum free area will be less than ϵA and can be written as $a\epsilon A$, where a is the fractional free cross-sectional area represented by the pore constrictions which actually plug. For an actual filter medium, the population density of the pores can then be written as

$$N = \frac{a\epsilon}{\pi r_0^2} \quad \text{(A20)}$$

where r_0 is the radius of the pore constrictions which plug and a is the fractional free cross-sectional area represented by pore constrictions of this radius. This leads to four unknown terms, N, a, h, and r_0, and direct solution with the three independent relationships available is not possible. However, measurement of any one will allow calculation of the remainder. Measurement of pore-size distribution by the mercury-intrusion technique actually reflects the distribution of pore constriction and thereby offers a means of measuring one of these variables, thus permitting calculation of the remainder.

This same procedure can be applied to relate the characteristics of the filter medium to performance over the standard-blocking region for the case of constant-rate filtration. For constant-rate filtration $q = q_0$ and the general differential form of the standard-blocking equation [Equation (A11)] can be written as

$$\frac{1}{\Delta p^{0.5}} = \frac{1}{\Delta p_0^{0.5}} - \left(\frac{\beta}{q_0^{0.5}}\right)\left(\frac{c}{1-\epsilon_p}\right)V \quad \text{(A21)}$$

Substituting the values of β and q_0 given by Equations (A5) and (A10) gives

$$\frac{1}{\Delta p^{0.5}} = \frac{1}{\Delta p_0^{0.5}} - \left(\frac{g_c}{8\pi N A h^3 \mu_f}\right)^{0.5} \cdot \left(\frac{8h\mu_f}{\pi N A r_0^4 g_c \Delta p_0}\right)^{0.5}\left(\frac{cV}{1-\epsilon_p}\right) \quad \text{(A22)}$$

Simplifying and rearranging gives

$$\left(\frac{\Delta p_0}{\Delta p}\right)^{0.5} = 1 - \left(\frac{c/(1-\epsilon_p)}{\pi N A h r_0^2}\right)V \quad \text{(A23)}$$

Thus the slope of a plot of $(\Delta p_0/\Delta p)^{0.5}$ vs. V should allow direct calculation of the clogging value, $\pi N h r_0^2$, for the filter medium during constant-rate filtration. However, direct solution for N, a, h, and r_0 is again not possible if all are unknown.

Inspection of Equation (A19) for constant-pressure filtration shows that neither Δp nor μ_f should have any direct effect on the slope of the t/V vs. t plot during the period of standard blocking, but that both affect the intercept directly. However, changes in Δp can be expected to have considerable indirect effect by changing the values of c_f, ϵ_p, and r_0. The r_0 term of the clogging value will decrease with increasing Δp because of compression of the medium. Values of c_f and ϵ_p can be expected to decrease with increasing Δp because of the increasing shear stress, $r(\Delta p)/2h$, in the pores. If direct interception is the controlling mechanism of particle retention, changes in μ_f should have no effect on constant-pressure filtrations provided that the same Δp is used and shear stress within the pores is similar from run to run.

Similar consideration of Equation (A22) for a constant-rate filtration shows that changes in rate of filtration or the viscosity have no direct effect on the slope of the $(\Delta p_0/\Delta p)^{0.5}$ vs. V plots of such data. However, changes in either q_0 or μ_f can be expected to have a large indirect effect by changing the values of r_0, c_f, and ϵ_p. Thus, if either q_0 or μ_f is left constant and the other increased, the value of Δp_0 increases, causing increased initial compression of the medium and an increased shear stress, $(\mu_f/g_c)(4q/\pi r^3)$, in the pores at any point in the filtration cycle.

Presented at A.I.Ch.E. New York meeting

Formation of Gas Bubbles at Horizontal Orifices

LEON DAVIDSON and ERWIN H. AMICK, JR.

Columbia University, New York, New York

Air bubbles were formed in water and in mineral oil by use of single, circular, horizontal, square-edged orifices facing upward. Twenty orifices were tested, ranging from 0.017 to 0.79 cm. (0.0067 to 0.31 in.) in radius. Increasing the volume of the gas chamber below the orifice (over the range of 4 to 4,000 cc.) was found to increase the bubble size. The gas-chamber volume was minimized in most of the work in order to confine attention to the effects of orifice size and gas-flow rate. The liquid containers were large enough to eliminate significant wall effects, and operations were conducted at atmospheric pressure.

The gas-flow rate was varied from about 0.01 to about 250 cc./sec. over the course of the work. At relatively low flow rates, the orifices generally formed single "static" bubbles, the volumes of which were proportional to the surface tension and orifice radius and independent of the gas-flow rate. At high flow rates the bubble frequency became high and the bubble volume became proportional to the gas-flow rate and independent of the surface tension. The bubble frequency reached a maximum value for each orifice, this value being a function of the orifice radius. For air bubbles in water, the correlation of the maximum bubble frequency, n_m bubbles/sec., with the orifice radius, r cm., and the air-flow rate, q cc./sec., was found to be $n_m = 9.1q^{0.13}/r^{0.43}$. The maximum frequencies ranged from about 25 bubbles/sec. for the largest orifices to about 75 bubbles/sec. for the smallest orifices used.

It was found that consecutive bubbles paired or coalesced in definite ways in certain ranges of the gas-flow rate. A description is given of this bubble behavior, based on stroboscopic and photographic observation.

The interest of chemical engineers in studies of the formation of gas bubbles at orifices immersed in a liquid has grown tremendously since the 1946 paper of Geddes (*4*). Many recent papers include analytic treatment of the subject (*7, 9*) or correlate the phenomena involved (*11*). The present paper describes work done in 1949 at Columbia University in a series of bubble-formation experiments which covered a wide range of orifice diameters and gas-flow rates.

This study has been based on certain generally accepted simplifying assumptions and calculational procedures and has been limited to a reasonably small set of variables. The guiding principle has been that determinations of bubble volume and bubble frequency, as well as descriptions of bubble behavior, should be based on observations of a large number of consecutive bubbles formed under steady operating conditions. For convenience, the volumetric gas-flow rate (steady time-average value) was chosen as an independent variable, and the bubble volume and bubble frequency have been treated as dependent variables. Orifice radius has been a major variable in this study, covering a fortyfold range of values. As a linear measure of the "size" of a gas bubble, the radius of a sphere having an equal volume has been used.

The usual simplifying conditions, which were satisfied in the present work, are that there is no chemical reaction between the gas and the liquid and that the liquid container is wide enough to preclude wall effects. Procedures were simplified by operating at essentially atmospheric pressure and using air as the gas phase, since the physical properties of the gas are assumed to enter the theory in simple and readily calculable ways.

Single, circular, horizontal, square-edged orifices were used, generally mounted essentially flush with the bottom of the liquid container, facing upward. The volume of the gas chamber below the orifice is considered to include the entire gas volume in the piping extending back to the nearest effective restriction governing the air flow through the orifice.

In the present work it was found that container widths from 3 to 10 in. square had no effect and that orifice submergences from about 1 to about 10 in. usually had negligible effect. When the orifice projected above the container bottom (as for a capillary-type orifice), the bubble frequency was found to increase owing to the enhanced liquid circulation, in agreement with the results of Maier (*8*) and Sprague (*10*). No results for such a case will be discussed in this paper, but the effect of the orifice-chamber volume will be discussed.

The analysis of the bubble-formation problem by van Krevelen and Hoftijzer (*11*), otherwise similar to that followed in the present work, omitted the orifice radius as a factor in the high-bubble-frequency region. This probably resulted from the fact that those authors did not have available to them any high-frequency data for orifices larger than 0.025 cm. in radius.

APPARATUS AND TECHNIQUES

A constant-pressure air-supply system was of vital importance in enabling extremely reproducible data and photographs to be obtained. It consisted of a diaphragm-type pressure regulator (reducing the laboratory air supply from about 55 to about 25 lb./sq. in. gauge) followed by a sensitive needle valve for flow regulation (dropping the pressure from about 25 to about 2 lb./sq. in. gauge). A separate shut-off valve following the needle valve permitted the flow setting to remain undisturbed between parts of a run, if required. Despite fluctuating line pressure, this system gave extremely steady performance owing to the constant upstream pressure maintained on the critical-pressure-drop needle valve. (*See* the section Reproducibility of the Data below.)

A capillary flow meter was used, with two interchangeable capillaries providing a usable range from 3 to 250 cc./sec. It was operated at a constant upstream pressure of 880 mm. Hg absolute. At very low flow rates the bubble frequency, bubble volume, and air-flow rate were determined by collec-

Leon Davidson is at present with Nuclear Development Corporation of America, White Plains, New York.

Table 1. Inside Radii of the Orifices Used in the Present Work

Orifice	r, cm.	Orifice	r, cm.	Orifice	r, cm.	Orifice	r, cm.	Length, cm.*
A-1	0.35	*B*-1	0.48	*C*-2	0.79	*D*-1	0.20	0.32
A-2*a*	0.16	*B*-2	0.40	*C*-3	0.64	*D*-2	0.21	1.27
A-3*a*	0.08	*B*-3	0.32	*C*-4	0.56	*D*-3	0.21	2.54
A-4	0.048	*B*-4	0.16	*C*-61	0.05	*D*-4	0.05	0.32
A-5	0.017	*B*-5	0.05	*C*-71	0.017	*D*-5	0.40	7.6

*All orifices except the *D* series were holes drilled in brass plates 0.08 cm. thick. The *D* series were sections of tubing of the lengths listed.

tion of a counted number of bubbles in a graduated cylinder for a timed interval.

The liquid containers, made of cellulose acetate, had flat sides 1 ft. high and 3 to 10 in. wide, cemented to a brass base plate. Under the center of the plate a fitting was provided for mounting the orifices.

The orifices used are described in Table 1. The orifices of series *A*, *B*, and *C* were made by drilling single holes in thin brass sheets and soldering these over the ends of brass or copper tubes of somewhat larger diameter than the holes. Series *D* consisted simply of sections of brass or copper tubing having one end faced off squarely to act as the orifice. The orifice tubes were supplied with air through a tee which during certain runs allowed any liquid which dripped down through the orifice to be automatically siphoned off and measured, without affecting the air-flow rate or the chamber volume.

At higher frequencies than could be directly counted, a General Radio Company Strobotac was used, with the room darkened, to "stop" the motion of the bubbles. The Strobotac was also used to allow slow-motion studies of bubble behavior. A scale on this instrument gave the bubble frequency directly when the bubbles appeared to be "stopped" at the orifice. The steadiness of the air-supply system made this technique quite feasible and allowed readings to be made rapidly. Suitable means were utilized to assure that the correct frequency was determined. For example, since the true bubble frequency and the vertical spacing between single bubbles were essentially constant during a run, the apparent spacing between the bubbles would be halved when the Strobotac frequency was increased to twice the correct bubble frequency. The apparent spacing, however, would remain equal to the true spacing when the Strobotac frequency was decreased to one-half the true bubble frequency, but in the latter case the visual image was noticeably dimmer, as there were only half as many illumination periods per second.

In some runs electronic flash photographs were taken to record typical bubble behavior, but these were not used as a source of quantitative data. Data derived from the various instruments or techniques checked and overlapped quite well, and so there is a negligible possibility that breaks in the curves can be attributed to instrument errors.

TYPES OF BUBBLE FORMATION

As has been pointed out by van Krevelen and Hoftijzer (*11*), two distinct regimens of bubble formation are found to occur as the gas-flow rate through an orifice is increased. At very low flow rates (and with a reasonably small gas-chamber volume below the orifice) the bubble volume is predicted within a factor of two by the hydrostatic equation

$$v_e = \frac{2\pi r\sigma}{(\rho - \rho_g)g} \qquad (1)$$

The bubble volume remains constant at about the value given by Equation (1), independent of moderate changes in the gas-flow rate, and so the bubble frequency is proportional to the gas-flow rate in this range. This may be referred to as the region of *constant-volume* or *static* bubbles.

As the gas-flow rate increases sufficiently, it is found that the bubble frequency levels off at a constant value and that the bubble volume thereafter increases in proportion to the gas-flow rate. This may be called the region of *constant-frequency* bubbles. It is this region which will prove to be of most interest in this paper.

CONSTANT-VOLUME BUBBLE REGION

Possible refinements of Equation (1) might be considered to improve its imperfect fit to the experimental data. A factor might be included to allow for the increase in bubble volume with large chamber volumes below the orifice, as discussed by Hughes et al. (*7*). A factor might also be included to account for the deviation of the bubble profile from the true vertical, where it is attached to the orifice, since Equation (1) assumes a vertical profile. Wark (*12*) discussed the relationship for stationary bubbles between the angle of contact of the gas-water-solid interfaces and the bubble volume. His theoretically calculated profiles agree well with observations.

The relation between the radius of the detached "static" bubble and the orifice radius, which may be derived from Equation (1), is

$$\frac{a}{r} = \left(\frac{1.5\sigma}{r^2(\rho - \rho_g)g}\right)^{1/3} \qquad (2)$$

where a = radius of equivalent spherical bubble, cm. Thus, as the orifice size increases, the static-bubble radius will eventually become smaller than the orifice radius. The gas-liquid interface will then tend to be horizontal at the orifice perimeter, leading to instability. In this work stable stationary bubbles could not be formed at an orifice having a radius of 0.79 cm. (0.31 in.), but stable bubbles were formed at an orifice of 0.64-cm. radius (0.25 in.). It may be concluded that orifices larger than about 0.7-cm. radius (0.27 in.) cannot produce stable static bubbles in water.

It might be worth noting that for very viscous liquids [for example, the castor oil and olive oil of Guyer and Peterhans (*5*)] even such a low frequency as one bubble per second may be far above the static-bubble flow-rate range and may be well in the region where bubble volume is increasing with gas-flow rate.

EFFECT OF THE VOLUME OF THE ORIFICE CHAMBER

A series of runs was made to determine the effect of the volume of the gas space below the orifice (the "chamber volume"), using single orifices of 0.16-cm. (0.063 in.) radius over a wide range of flow rates. The data are shown in Figure 1. The chamber volume ranged from about 4 to about 4,000 cc., corresponding to values of the "capacitance number" N_c ranging from 0.033 to 33.0. N_c is a parameter developed by Hughes et al. (*7*) relating the acoustical properties of the gas-orifice system to the chamber volume, as follows:

$$N_c = \frac{g(\rho - \rho_g)V_b}{\pi r^2 \rho_g c^2} \qquad (3)$$

where

V_b = volume of chamber below orifice, including gas lines, cc.
c = velocity of sound in the gas, cm./sec.

In agreement with the results of Hughes, the bubble behavior was found to be independent of N_c for $N_c < 0.8$, at low flow rates. At higher flow rates the critical value of N_c decreased to about 0.2. In the bulk of the present work the chamber volume was minimized to eliminate its effect.

In the region of large chamber volumes, to the right of the dashed line on Figure 1, indicated by the word *pair*, the ordinate value plotted is the combined volume of the pair of bubbles released at one time. It is very important to note that this type of bubble pairing, which is characteristic of large chamber volumes, is definitely not the same type of bubble pairing as will be described below under Transition Region. The pairing now under discussion may occur even at very low flow rates for a given orifice, as Figure 1 shows, before the transition region is reached. This type of "pair creation" is caused by the surplus gas accumulated in the chamber volume between bubble-release times. It is more fully discussed, from the theoretical and experimental aspects, in Sections 2.6 and 7.7 of the original thesis (*2*). Hughes et al. (*7a*) also discuss this.

BUBBLE-BEHAVIOR DATA FOR A TYPICAL ORIFICE

Typical plots of bubble frequency and bubble volume vs. gas-flow rate for a flat-plate orifice are shown in Figures 2 and 3. The points represent results from four different arrangements using orifice *B*-4 over a period of several months. The orifice radius was 0.16 cm., and N_e was kept below 0.2. Data were obtained for both water and mineral oil. The letters on the plots indicate the regions in which certain phenomena occurred, to be described in the following paragraphs. This orifice was chosen for discussion because it demonstrated most of the interesting phenomena observed during the work. With other-size orifices some regions did not appear.

Static-bubbling Region

The value of v_s computed by Equation (1) is indicated on the bubble volume plot, Figure 3. While there is fair agreement, the bubble volume increases slightly with the flow rate, and the frequency is therefore slightly less than proportional to the flow rate.

Since the velocity of rise of bubbles is a function of their size (*11*), it is essentially constant in this region. Therefore for a given orifice the center-to-center spacing of the rising bubbles is inversely proportional to their frequency. At low frequencies the liquid at the orifice may be assumed to come to rest before each bubble escapes. The bubbles are identical at any given point early in their rising path. Although each bubble passes through violent symmetrical oscillations in shape as it rises, these are exactly copied by each succeeding bubble. Higher up, away from the stabilizing influence of the base plate, the bubbles move erratically sidewise and become irregular in shape.

Transition Region

At higher flow rates the bubble volume increases sharply as the frequency levels off. The spacing between bubbles has decreased, and each forming bubble is affected by the presence of the preceding bubble, perhaps through the mechanism of a liquid vortex ring at the orifice. The bubbles now start to form into pairs, although still forming individually at regular time intervals at the orifice. A bubble will appear to hover above the orifice until the next bubble emerges, and the two bubbles will then remain together as they rise. This pattern is repeated by the next two bubbles, and so on indefinitely.

In some cases pair formation as just described continues for only a fraction of a minute (during which time hundreds of bubbles form). The flow then suddenly reverts to single-bubble formation, at a bubble frequency about 5 to 30% higher than existed during the period of pair formation. These single bubbles are usually elongated and twisted, like candle flames, and show turbulence and erratic behavior even near the orifice. After a fraction of a minute pair formation begins again. The flow oscillates periodically between the two regimens. However, the bubble frequency in a given regimen returns to the same value each time that that regimen is restored. Gas-flow rate remains constant. (One might speculate that the two regimens correspond to two different states of liquid motion in the vicinity of the orifice, e.g., axially symmetrical pulsating flow in the case of pair formation and continuous rotation about the orifice axis in the case of the twisted single bubbles.)

Bubble frequencies reported in this transition region are averages for the two regimens. Scatter of the data in this region is due partly to persistence of one or the other regimen throughout certain runs, which introduces the frequency difference between the regimens into the results.

Incipient Coalescence

As the flow rate further increases, the members of a bubble pair touch each other. This condition may be called

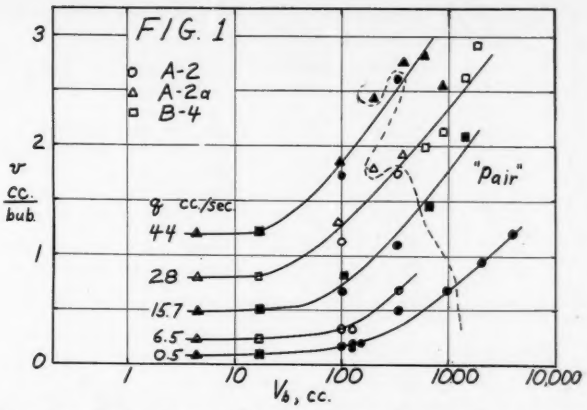

Fig. 1. Bubble volumes v vs. volume of chamber below orifice V_b at various air flow rates q for orifices having radii of 0.16 cm. (air-water data). In the region marked "pair" to the right of the dashed line, v is the combined volume of the pair of bubbles emitted at one time.

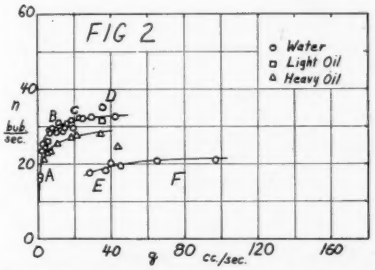

Fig. 2. Bubble frequency n vs. air flow rate q for orifice *B*-4; orifice radius 0.16 cm., container width 12 cm., liquid depth 5 to 10 cm., chamber volume 10 to 17 cc. (data for air-water and air-oil systems). The letters refer to regions of static bubbling (*A*), transition (*B*), incipient coalescence (*C*), coalescence (*D*), coalescence at the orifice (*E*), and double coalescence (*F*).

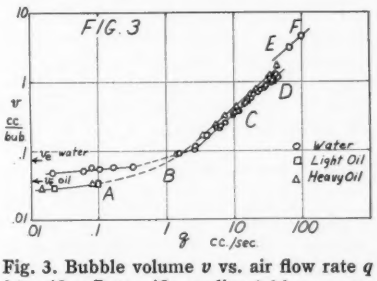

Fig. 3. Bubble volume v vs. air flow rate q for orifice *B*-4; orifice radius 0.16 cm., container width 12 cm., liquid depth 5 to 10 cm., chamber volume 10 to 17 cc. (data for air-water and air-oil systems). The letters refer to regions given under Figure 2.

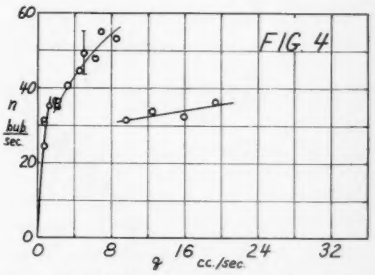

Fig. 4. Bubble frequency n vs. air flow rate q for orifice *C*-61; orifice radius 0.05 cm., container width 12 cm., liquid depth 10 cm., chamber volume 2.9 to 4.4 cc. (air-water data).

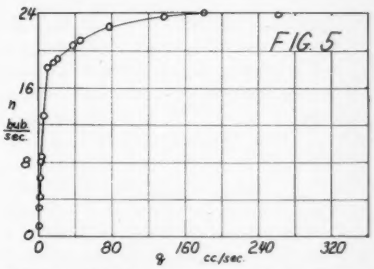

Fig. 5. Bubble frequency n vs. air flow rate q for orifice *B*-1; orifice radius 0.48 cm., container width 12 cm., liquid depth 10 cm., chamber volume 22 cc. (air-water data).

Table 2. Examples of Reproducibility of Data for Air Bubbles in Water
(With minimized volume of chamber below the orifice)

Orifice	Run	Air flow, cc./sec., q	Bubbles/sec., n	Actual Strobotac frequency readings during run, single bubbles/min.
A-2a	43–19	1.249	15.0	905, 898, 895, 900, 900
A-2a	43–20	1.246	14.9	895, 898, 885, 885, 892, 892
A-2a	43–21	1.238	14.9	898, 892, 895, 895, 894
A-2a	43–22	1.235	15.0	895, 899, 905, 895, 898
A-2a	43–23	1.260	15.0	897, 899, 910, 895, 897, 895
B-4	33–7	11.5	31.0	1,830*, 1,945, 1,765, 1,930*, 1,840*
B-4	33–13	11.5	30.4	1,800*, 1,780, 1,888, 1,900*, 1,750*

*These values are reported as exactly twice the actual value recorded experimentally, which corresponded to the frequency of doublet formation in these particular cases.

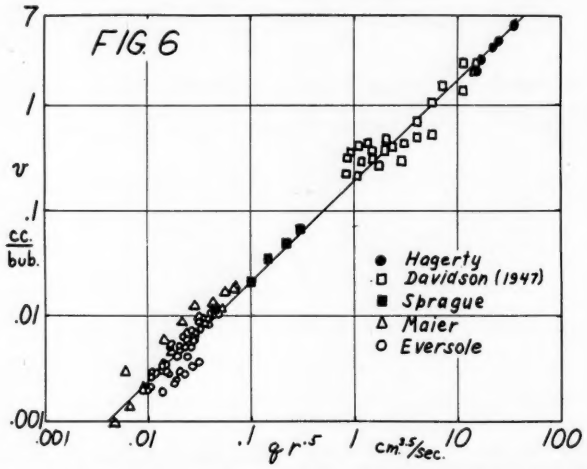

Fig. 6. Correlation of bubble volume v vs. (gas flow rate times square root of orifice radius) $qr^{0.5}$ for literature data in the constant-frequency region. The line drawn in has the equation $v = 0.19(qr^{0.5})^{0.95}$.

"doublet formation." The first member of the doublet usually assumes a hemispherical shape, and the second bubble is elongated vertically; the assembly resembles a mushroom. (The similarity between this behavior and the behavior of rising balls of fire, including atomic-bomb explosions, suggests that some common underlying principle is involved, since the fireball is merely a bubble of low-density gas in an atmosphere of higher density.)

With higher flow rates, the lower bubble often momentarily protrudes into the top bubble. This protrusion is facilitated by a column of liquid which rises inside the top bubble.

Coalescence

Further flow-rate increase causes the second bubble to penetrate the first one appreciably. Under some conditions the second bubble always shoots completely through the first bubble, rising through the inner column of liquid in the bubble and emerging on top. Under other conditions the first bubble absorbs part of the second and leaves the residue as a small satellite. In still other cases the second bubble is completely swallowed by the first, although their interface remains unruptured.

In most cases, however, the two bubbles completely coalesce at these flow rates, at some distance above the orifice, yielding a single large irregular bubble. At this point the frequency has usually reached a maximum value which remains essentially constant as the flow rate increases further. Liquid viscosity and orifice radius seem to have some effect on the value of the constant frequency.

Coalescence at the Orifice

Coalescence takes place closer and closer to the orifice as the flow rate increases. A flow rate is finally reached at which the bubbles coalesce right at the orifice, the first bubble having no time to rise before the second one emerges. Under these conditions it will appear that the frequency of bubbles rising from the orifice has suddenly been halved.

Double Coalescence

As the flow rate further increases, the large coalesced bubbles themselves undergo coalescence as they rise. This may be called "double coalescence." At this stage the fluid is usually quite turbulent and the gas seems to issue from the orifice as a continuous jet. The bubbles are erratic, and good data are hard to obtain. The liquid becomes filled with small circulating bubbles. At this point conditions of industrial interest are undoubtedly approached, but unfortunately this is the point at which laboratory experiments usually have to be terminated.

Curves for Other Orifices

In the original thesis describing this work (*2*) are complete plots of the data for about twenty orifices, as listed in Table 1. A few of these plots are reproduced here. In Figure 4 the point plotted at $q = 5$ cc./sec. indicates the actual extreme values assumed by the frequency at that flow rate (in the transition region) as the flow regimen fluctuated between pair and single-bubble formation. Figure 5 shows data for a large orifice of 0.48-cm. radius. It is apparent that the maximum bubble frequency varies somehow inversely with orifice radius.

Reproducibility of the Data

Table 2 illustrates the reproducibility of the data for five consecutive runs with orifice *A-2a* at a constant flow setting, each run lasting several minutes. The individual Strobotac frequency readings were taken in the order given, at approximately quarter-minute intervals, and no single reading deviates by more than about 1% of the mean value for its particular run. The average frequencies for each of the five runs lie within 1% of each other also. Table 2 also illustrates the reproducibility of nonconsecutive runs for orifice *B*-4 at a given flow rate, which happens to lie in the transition region of Figure 2. The preceding discussion of the transition region will explain the increased scatter (up to 5%) in these individual Strobotac readings for orifice *B*-4, although even here the average bubble frequency does not differ by more than 2% between the two runs listed.

Correlation of Bubble Volumes from Literature Data

Most of the data of Eversole et al. (*3*) are in the constant-frequency range, as are some data of Maier (*8*), Sprague (*10*), Hagerty (*6*), and Davidson (*1*). These data form lines of almost 45° inclination on logarithmic plots of bubble volume vs. flow rate for each orifice, but the various orifices do not line up well together on such plots. It was found empirically that by multiplying the flow rates by the square root of the orifice radius, a correlation could be obtained as shown in Figure 6, in which the data for a wide range of orifices line up well. No theoretical derivation of this correlating factor has been developed, but some ideas on the subject will be given later.

The relationship between bubble volume, flow rate, and orifice radius in the constant-frequency region appears from Figure 6 to be of the form

$$v = K(qr^{0.5})^w \qquad (4)$$

where

w = slope of straight line on a logarithmic plot

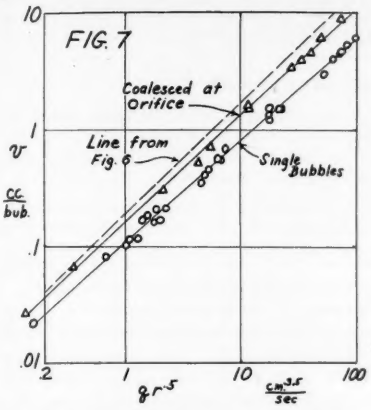

Fig. 7. Correlation of bubble volume v vs. (air flow rate times square root of orifice radius) $qr^{0.5}$ for present data in the constant-frequency region. The points plotted are the end points of the respective straight-line portions of the plots for the individual orifices.

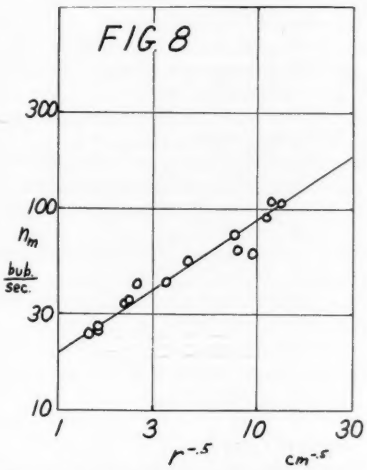

Fig. 8. Constant (maximum) bubble frequency n_m vs. reciprocal of square root of orifice radius $r^{-0.5}$ for the data of Table 3. The line drawn in has the equation $n_m = 19(r^{-0.5})^{0.66} = 19r^{-0.33}$.

K = value of ordinate of line at unity abscissa value

For the literature data plotted in Figure 6 the equation of the correlation line shown is

$$v = 0.189(qr^{0.5})^{0.953} \qquad (5)$$

CORRELATION OF THE BUBBLE-VOLUME DATA FROM THE PRESENT WORK

Data were available from the present work for thirteen orifices with radii from 0.0175 to 0.48 cm., with low values of N_c. Distilled water was the liquid chiefly used, but some data were obtained for light mineral oil ($\rho = 0.843$, $\sigma = 30.4$, viscosity = 0.224 poise) and for heavy mineral oil ($\rho = 0.861$, $\sigma = 31.2$, viscosity = 0.475 poise). The coordinates of the end points of the straight-line 45° portions of the individual orifice plots of bubble volume (similar to Figure 3) were read off and replotted on Figure 7 as bubble volume vs. $qr^{0.5}$. The correlation seems to be as good as that in Figure 6 for the literature data. The equation of the line marked *single bubbles* is

$$v = 0.110(qr^{0.5})^{0.867} \qquad (6)$$

For those orifices for which the halved bubble frequency was recorded, owing to coalescence at the orifice, the individual orifice plots show two parallel 45° lines at high flow rates, as in Figure 3 (where line EF is parallel to line CD but shows twice the bubble volume). In Figure 7 the end points of these upper lines from the individual orifice plots have been plotted as triangles. They form another correlation line roughly parallel to the main line but lying above it at about twice the bubble volume for a given abscissa value. The equation of this line, which is marked *coalesced at orifice*, is

$$v = 0.163(qr^{0.5})^{0.914} \qquad (7)$$

The literature-correlation line of Figure 6, copied onto Figure 7 as indicated, lies quite close to the line for the present data on bubbles which are coalesced at orifice. This suggests that the values given in the literature are chiefly for such coalesced bubbles. It is indeed found that the data of Maier (*8*) and Eversole (*3*) contain examples of bubble frequencies which are twice the usual values reported by those investigators. Probably these high frequencies correspond to the maximum single-bubble frequency, as in region D of Figure 2, and the remainder of the literature-data frequencies correspond to the halved frequency, as in the region of coalescence at the orifice.

CORRELATION OF THE MAXIMUM BUBBLE FREQUENCY

By dividing each side of Equation 4 into q, the flow rate, one obtains an expression for the constant (maximum) bubble frequency

$$n_m = \frac{q^{(1-w)}}{Kr^{0.5w}} \qquad (8)$$

For the data of this research for single bubbles, the corresponding expression, derived from the correlation of experimental data represented by Equation (6), is

$$n_m = \frac{9.09q^{0.133}}{r^{0.434}} \qquad (9)$$

It is evident that the maximum frequency, n_m, is not entirely a function of the orifice radius alone, but tends to increase slightly at the higher flow rates.

To shed further light on this, approximate values of q_m, the flow rate at which the maximum frequency first occurs for each orifice, were read off from plots of n vs. q (similar to Figures 2, 4, and 5). These q_m values are listed in Table 3, for orifices both from the literature and from the present work. It is seen that q_m increases substantially as r increases. Examination of Equation (9) indicates that if n_m were to be studied as a function of r only, the exponent of r would be effectively decreased in absolute value because of the offsetting nature of this variation in q_m.

This is illustrated in Figure 8, in which the constant-frequency data of Table 3 are plotted as a function of r only, the function chosen for the abscissa being the reciprocal square root of r. (Four cases in Table 3 were adjusted as indicated in the table to convert "coalesced-bubble" frequencies to single-bubble frequencies, as discussed previously.) The equation of the line drawn through the points on Figure 8 is

$$n_m = \frac{19}{(r^{0.5})^{0.67}} = \frac{19}{r^{0.33}} \qquad (10)$$

In agreement with the conclusion of the preceding paragraph, the exponent of r in

TABLE 3. CONSTANT (MAXIMUM)-BUBBLE-FREQUENCY DATA FOR WATER

Reference or orifice	Orifice radius r, cm.	Bubble radius a, cm.	$\frac{a}{r}$	Capacitance number N_c	Maximum frequency, bubbles/sec. Obs.	Doubled	Calc. by Eq. (13)	q_m
Maier	0.00591	0.052	8.8	——	107	—	—	0.06
Maier	0.0075	0.092	12.2	——	54	108	—	≈0.2
Eversole*	0.0085	0.077	9.1	54	90	—	—	0.17
Maier	0.01125	0.105	9.3	——	30	60	—	0.2
Sprague	0.016	0.111	7.0	——	31	62	—	0.4
C-71	0.0175	0.159	9.1	2.1	74	—	60	1.0
D-4	0.050	0.166	3.3	0.39	55	—	36	9.
C-61	0.050	0.153	3.1	0.38	55	—	36	8.
A-3*a*	0.082	0.464	5.7	0.14	43	—	28	18.
A-2*a*	0.16	0.640	4.0	0.036	42	—	20	60.
D-1	0.20	0.701	3.5	0.057	35	—	18	60.
D-3	0.21	0.695	3.2	0.047	33	—	17	≈50.
Hagerty	0.395	0.683	1.7	0.15	13	26	—	60.
D-5	0.40	1.016	2.6	0.015	25	—	13	120.
B-1	0.48	1.020	2.1	0.02	24	—	12	160

*This was Eversole's point for 70% ethanol in water.

Equation (10) is smaller in absolute value than it is in Equation (9).

It must be considered therefore that although the maximum bubble frequency is a function of the orifice radius, it is not a function of that alone. However, for practical purposes it may be considered to be only a function of r (for liquids with comparable kinematic viscosities) because of the small exponent of q in Equation (9), and because q_m is a function of r. It is therefore believed that Equation (10) may be used to estimate the maximum individual bubble frequency for orifices in the range of 0.01- to 0.50-cm. radius for liquids with kinematic viscosities about the same as the viscosity of water. [*See* Section 8.7 of the original thesis (*2*) for a discussion of the effect of liquid viscosity.] The frequency given by Equation (10) should be halved to allow for the coalescence of bubbles at the orifice when that is expected to occur.

DISCUSSION OF THE MAXIMUM-FREQUENCY CORRELATION

By use of van Krevelen's working hypothesis (*11*) that at the maximum frequency bubbles are spheres which just touch each other in a vertical line above the orifice and of his correlation for the rising velocity of bubbles in series, which reduces to

$$V = (ag)^{0.5} \tag{11}$$

where V = velocity of rise of bubbles in series, cm./sec., an equation relating orifice size and maximum frequency may be derived. From the data of Table 3 it is seen that at the maximum frequency the bubble radius is very roughly four times the orifice radius, over a wide range of orifice radii. Then, since by van Krevelen's hypothesis

$$V = 2an_m \tag{12}$$

it follows that

$$n_m \approx \frac{8}{r^{0.5}} \tag{13}$$

Values of n_m computed by Equation (13) are given in Table 3. The agreement with experiment is not good, because the real bubbles are far from being perfect spheres which just touch each other in a vertical line. Hence Equation (13) should not be used for predictions; it merely serves to illustrate a possible semitheoretical derivation of a correlation based on the square root of the orifice radius.

The relation of the maximum bubble frequency to the orifice radius should be tested by other investigators. The orifice radius was omitted as a factor in the analysis of van Krevelen (*11*). Equation (11) in his paper, for the critical gas flow rate, reduces to

$$n_m = \frac{36.5}{q^{0.2}} \tag{14}$$

This equation, which indicates that the constant frequency is independent of the orifice size, does not agree with the data for large orifices and should not be used.

DIMENSIONAL CONSIDERATIONS

The correlation function, $qr^{0.5}$, which appears in Equation (4), was found empirically, but it appears to hold some promise of having theoretical significance. Dimensionally, Equation (4) is badly unbalanced, but it may be greatly improved by the reasonable assumption that an appropriate factor, having a practically constant numerical value, is concealed in the numerical constant K. The expression $g^{0.5}$ is just such a factor, where g is the local acceleration of gravity. Support for the choice of this factor, and an indication of the possible role it may play in the theoretical development, is found in the simple equation for the velocity of a freely falling body, which contains the same factor $g^{0.5}$:

$$u = (2gh)^{0.5} \tag{15}$$

where

u = velocity of falling body, cm./sec.
h = distance through which body has fallen from rest, cm.

Writing the factor $g^{0.5}$ explicitly into Equation (4) (actually the more convenient and almost equal factor $g^{0.5w}$ is used) leads to the following equation:

$$v = K'\left(\frac{qr^{0.5}}{g^{0.5}}\right)^w \tag{16}$$

where K' = changed numerical value of the constant K of Equation (4). The dimensions of the left member of Equation (16) are [length]^3, while on the right the dimensions are now [length]^{3w}. Since w is not quite equal to unity, although almost so, there remains a slight discrepancy in the dimensional balance of Equation (16). Probably, since Equation (4) was derived from an empirical study of the data, one or more other factors remain hidden in K' and contribute to the discrepancy. This remains to be determined from further work along these lines. (It is of course unnecessary to take specific account of this factor $g^{0.5}$ in the numerical calculations and plots, as it has a constant value for all practical purposes and is covered by the numerical constants in the equations.)

OUTLOOK

This paper has presented some interesting aspects of bubble-formation phenomena and has, it is hoped, pointed out some areas in which theoretical analysis might be fruitful. It would seem that the study of the liquid behavior at the orifice, including the creation of vortex rings and currents of liquid by the emerging bubbles, might hold the key to greater understanding of the curious phenomena associated with the formation of gas bubbles at orifices.

ACKNOWLEDGMENT

The work reported in this paper was made possible through the generosity of the donor of the Samuel Willard Bridgham Fellowship at Columbia University.

NOTATION

a = bubble radius (radius of spherical bubble of equal volume), cm.
c = speed of sound, cm./sec.
g = local acceleration of gravity, cm./sec.^{2}
h = distance through which a body has fallen from rest, cm.
K = constant coefficient in Equation (4)
K' = numerical constant
n = bubble frequency, bubbles/sec.
n_m = maximum bubble frequency, bubbles/sec.
N_c = "capacitance number" of orifice chamber, defined by Equation (3)
q = average gas-flow rate through orifice, cc./sec.
q_m = value of q at which maximum bubble frequency is reached, cc./sec.
r = orifice radius, cm.
u = velocity of a falling body, cm./sec.
v = bubble volume, cc.
v_e = theoretical hydrostatic bubble volume, based on Equation (1), cc.
V = rising velocity of bubbles in liquid, cm./sec.
V_b = volume of gas chamber below orifice, including piping, cc.
w = exponent as used in Equation (4)
ρ = density of liquid, g./cc.
ρ_g = density of gas, g./cc.
σ = surface tension of gas-liquid interface, dynes/cm.

LITERATURE CITED

1. Davidson, Leon, M.S. thesis, Columbia University, New York (1947).
2. ———, Ph.D. thesis, Columbia University, New York (1951); publication 3678, University Microfilms, Ann Arbor, Mich.
3. Eversole, W. G., G. H. Wagner, and Eunice Stackhouse, *Ind. Eng. Chem.*, **33**, 1459 (1941).
4. Geddes, R. L., *Trans. Am. Inst. Chem. Engrs.*, **42**, 79 (1946).
5. Guyer, August, and E. Peterhans, *Helv. Chim. Acta*, **26**, 1099 (1943).
6. Hagerty, P. F., II, M.S. thesis, Mass. Inst. Technol., Cambridge (1947).
7. Hughes, R. R., A. E. Handlos, H. D. Evans, and R. L. Maycock, *Chem. Eng. Progr.*, **51**, 557 (1955).

7a. *Ibid.*, p. 559.

8. Maier, C. G., *U. S. Bur. Mines Bull.* 260 (1927).
9. Peebles, F. N., and H. J. Garber, paper presented at Am. Inst. Chem. Engrs., Atlanta meeting (March, 1952).
10. Sprague, R. O., M.S. thesis, Columbia University, New York (1948).
11. van Krevelen, D. W., and P. J. Hoftijzer, *Chem. Eng. Progr.*, **46**, 29 (1950).
12. Wark, I. W., *J. Phys. Chem.*, **37**, 623 (1933).

Enthalpy of Hydrocarbon Mixtures

LAWRENCE N. CANJAR and VERNON J. PETERKA

Carnegie Institute of Technology, Pittsburgh, Pennsylvania

A method of estimating enthalpies of mixtures of light hydrocarbons is presented. Enthalpies so obtained are consistent with equilibrium-vaporization constants that have been correlated with the composition characterization factor, the molal average boiling point (M.A.B.P.).

Values of the isothermal-pressure corrections to the enthalpy of ideal gas mixtures ($H° - H$) are presented on three plots with parameters of temperature, pressure, and molal-average boiling point. Pressures range from zero to 1,500 lb./sq. in. abs., temperatures from −200° to 500°F., and M.A.B.P. from −200° to 150°F.

Process-design engineers need a rapid and reliable method for estimating the enthalpies of complex hydrocarbon systems. Of the past work devoted to the general solution of this problem, undoubtedly the greatest contribution has been made by Benedict, Webb, Rubin, and Friend (*2*), who formulated an equation of state that could not only predict the pressure-volume-temperature relationships, but also describe the two-phase regions, of pure components and mixtures. They correlated fugacity coefficients for paraffins and olefins in hydrocarbon mixtures by use of this equation and suggested that enthalpy data may be calculated in the same way. More specific work followed the lead of Benedict and coworkers in the form of isothermal-pressure corrections to the partial-molal enthalpies of hydrocarbons in the ideal gas state. Two independent investigations carried on at the same time started with the original work of Benedict and coworkers but proceeded along different lines. Papadopoulos, Pigford, and Friend (*11*), using the same mixtures, densities, and temperatures that were used in the original work on fugacity coefficients, differentiated the Benedict-Webb-Rubin equation of state and calculated the isothermal-pressure corrections to the ideal gas partial-molal enthalpy. However the analytical equation which resulted from the differentiation of the B.W.R. equation of state was so complicated that the investigators finally presented partial-molal enthalpies only for methane, ethane, and propane in solution with other hydrocarbons.

At the same time Canjar and Edmister (*4*), starting with the fugacity coefficients which had already been calculated by Benedict and coworkers, differentiated these numerically and arrived at isothermal-pressure correction to the ideal-gas-state partial-molal quantities. They extended the study to methane, ethene, ethane, propene, propane, and *n*-butane but did not cover the pressure range covered by Papadopoulos et al. (*11*).

Being limited in scope, neither of these papers presented enthalpy data in a convenient form for process-design engineers. Consequently there existed a need for a method of estimating enthalpy data for hydrocarbon mixtures which was not only easy to use but comprehensive.

THE M.A.B.P. CONCEPT

The very heart of all the work discussed above is the molal-average-boiling-point (M.A.B.P.) concept, which is described by Equation (1).

$$\text{M.A.P.B} = \sum x_i B_i \qquad (1)$$

Benedict and coworkers (*2*) demonstrated that the fugacity coefficients calculated from their equation of state could be correlated by the simple composition-characterization factor, the M.A.B.P. Specifically, they found that at a given temperature and pressure the fugacity coefficient of a pure paraffin or olefin was a function only of the M.A.B.P. of the mixture regardless of what components made up the mixture or how they were distributed. Of course this is only approximately true and holds only for mixtures of the lighter hydrocarbons.

Papadopoulos et al. (*11*) demonstrated the same thing to be true of isothermal-pressure corrections to ideal-gas-state partial-molal enthalpies. Canjar and Edmister (*4*), on the other hand, assumed that if the M.A.B.P. correlation held for the fugacity coefficients then it must also be valid for the partial-molal-enthalpy–pressure corrections which were derived thermodynamically from them. It is obvious that if the M.A.B.P. successfully correlates the fugacity coefficients and isothermal-pressure corrections to the ideal gas partial-molal enthalpies at a given temperature and pressure, then the pressure-volume-temperature and all the derived thermodynamic properties of the mixtures must also be a function of the M.A.B.P. at a given temperature and pressure.

A much more convenient way to present enthalpy data therefore is not in the form of partial-molal quantities but as isothermal-pressure corrections to the total enthalpy of the ideal gas mixture.

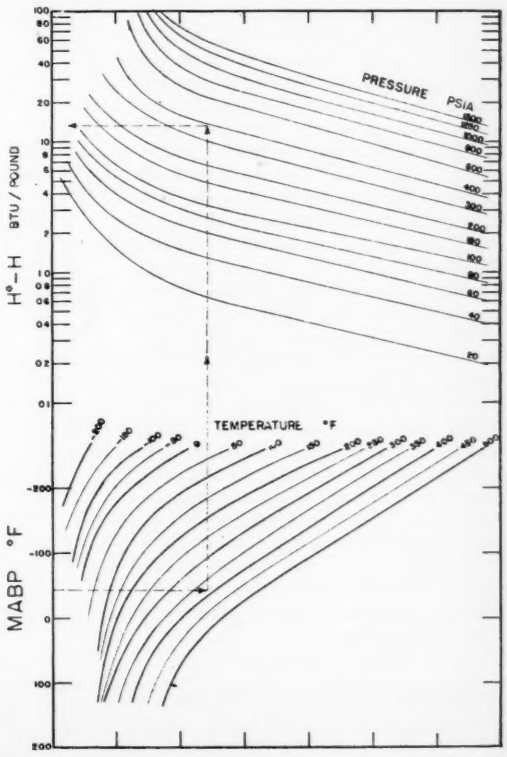

Fig. 1. Pressure correction to enthalpies of hydrocarbon mixtures in ideal gas state, vapor phase.

A direct method for computing these pressure corrections would be to use the equation for enthalpy derived from the B.W.R. equation of state. There are, however, two major disadvantages to this approach. The equation presents the enthalpy of the mixture as a function of temperature and density which involves considerable plotting and cross plotting in order to obtain the more convenient variables temperature and pressure. Second, the B.W.R. equation is inaccurate in the high-density, low-temperature regions unless suitable corrections are made, and consequently it is not convenient for the calculation of enthalpies in the liquid phase.

It is also obvious upon examination of the M.A.B.P. concept that when a mixture has the same M.A.B.P. as the normal boiling point of some pure hydrocarbon, pressure-volume-temperature as well as the derived thermodynamic relationships for the mixture are identical with those of the pure compound. This is borne out by the work done previously on fugacity coefficients and partial-molal enthalpies. Since this is true, a plot of isothermal-pressure corrections to the total enthalpy of an ideal gas mixture vs. the M.A.B.P. of the mixture at constant temperature and pressure coincides with a plot of isothermal-pressure corrections to the total enthalpy of pure compounds in the ideal gas state vs. the normal boiling points of the pure compounds. Or, in other words, such a correlation of isothermal-pressure corrections to the enthalpy of an ideal gas mixture will also hold for the limiting case of a mixture consisting of one component.

It follows then that to find such a correlation it is sufficient to plot the isothermal-pressure corrections to the ideal-gas-state enthalpy of pure components, which are already known to a high degree of accuracy, vs. their normal boiling points. This has been done with the normal paraffins by means of the data of the following investigators: Matthews and Hurd (*9*) for methane; Barkelew, Valentine, and Hurd (*1*) for ethane; Hoover (*8*) for propane; Prengle, Greenhaus, and York (*12*) for normal butane below 40 atm. pressure and Sage and Lacey (*14*) for the liquid region and higher pressures; and Brydon, Walen, and Canjar (*3*) for normal pentane. In addition to these a set of unpublished thermodynamic charts prepared by the Kamerlingh-Onnes laboratory at Leiden were also used particularly in the liquid region where other investigators failed to estimate thermodynamic properties. Plots of all these data vs. the normal boiling points of the pure compounds at constant pressure and temperature formed the basis for this work.

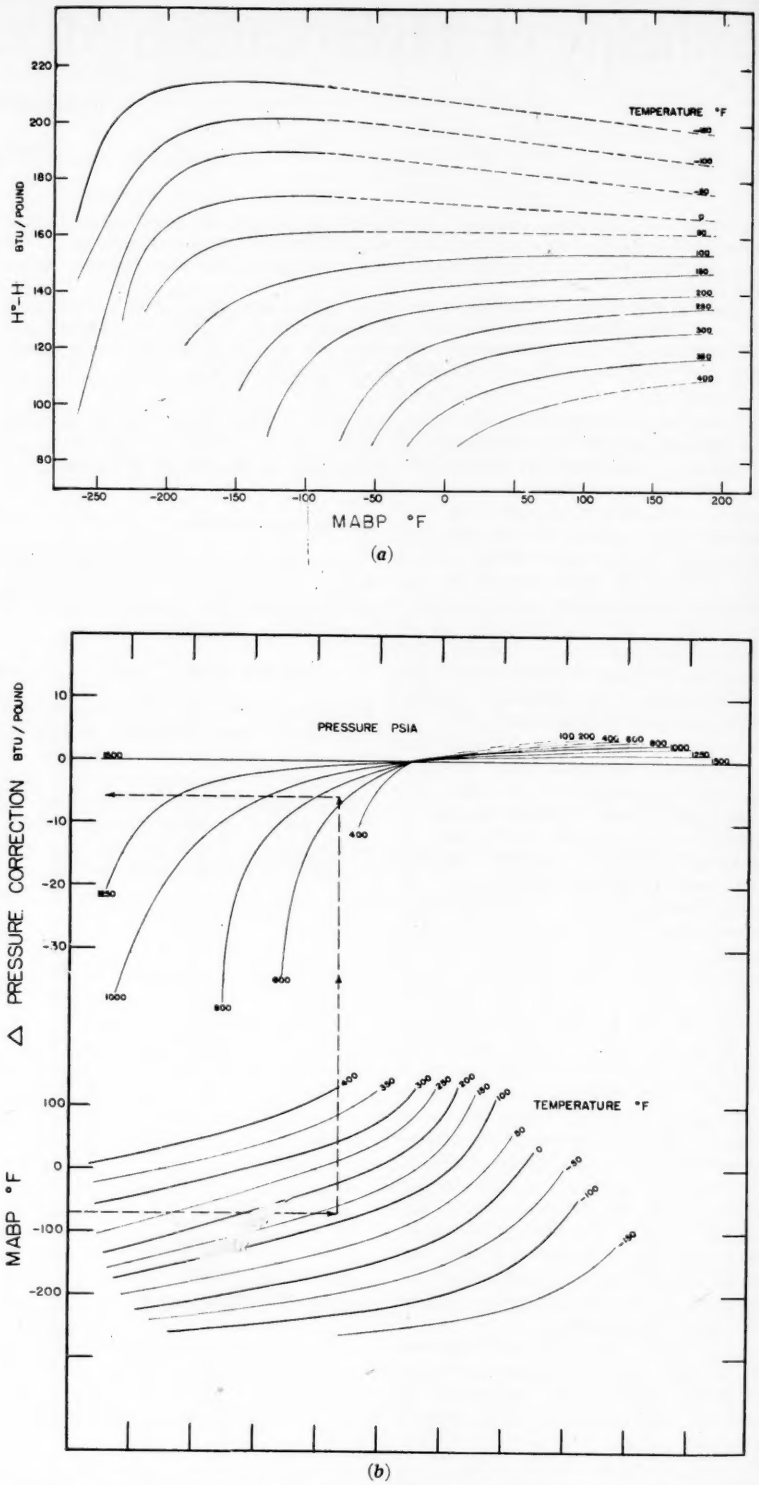

Fig. 2.(*a*) Pressure correction of 1,500 lb./sq. in. abs. to enthalpies of hydrocarbon mixtures in ideal gas state, liquid phase; (*b*) pressure correction to *a*.

DEVELOPMENT OF THERMODYNAMIC PLOTS

The major criticism of the previous works on hydrocarbon-mixture enthalpies is the inconvenient form of presentation. In order to apply the reported values to process-design calculations a considerable amount of interpolation is necessary. To avoid this it is necessary either to present

an enormous number of charts and tables reporting enthalpy data at many closely spaced intervals of pressure, temperature, and M.A.B.P. or to consolidate all the data on one or two charts in such a way that interpolation may be readily accomplished in any of the variables mentioned above. DePriester (*5*) was successful in consolidating all the data reported by Benedict and coworkers in their many plots of equilibrium vaporization constants, known more commonly as the Kellogg charts, on two plots for each of the hydrocarbons discussed. The success of DePriester with fugacity coefficients prompted a similar attempt in this work.

Figures 1 and 2* represent the consolidation of all the isothermal-pressure corrections to the enthalpy of the light normal paraffins in the ideal gas state taken from the authors mentioned above. Figure 1 deals exclusively with the vapor phase. Figure 2*a* is a plot of the liquid-phase–pressure corrections for systems at 1,500 lb./sq. in. abs. only. Inclusion of the other isobars complicated the plot to such an extent that it was deemed desirable to prepare an auxiliary plot, Figure 2*b*. If a system is in the liquid region at a pressure other than 1,500 lb./sq. in. abs., its isothermal-pressure correction to the ideal gas enthalpy is first determined for 1,500 lb./sq. in. abs. from Figure 2*a* and then corrected to the desired pressure by the algebraic addition of the delta correction plotted in Figure 2*b*.

$$(H^0 - H)^L = (H^0 - H)^L_{1,500 lb./sq.in.abs.} + \Delta \quad (2)$$

The isothermal-pressure corrections to the ideal-gas-state enthalpy are given in British thermal units per pound. It would be more convenient to present this information in British thermal units per pound mole since process calculations are carried out on molal basis; however, this would entail a much smaller scale for the high-molecular-weight mixtures with a corresponding loss in accuracy in the values for the lighter mixtures plotted on the same scale. The information obtained from these plots can be converted to a molal basis by multiplication by the average molecular weight of the mixture.

IDEAL-GAS-STATE ENTHALPIES

In order to calculate the enthalpy of a hydrocarbon mixture it is necessary first to calculate the enthalpy of the mixture in the ideal gas state. As ideal gases, or real gases at very low pressure, do not exhibit thermal effects upon mixing, the enthalpy of the mixture is simply the molal average of the enthalpies of the pure components in the mixture.

$$H^0_{mixture} = \sum x_i H_i^0 \quad (3)$$

or if one prefers to use heat capacities,

$$C_{p\,mixture}^0 = \sum x_i C_{pi}^0 \quad (4)$$

The most reliable tabulation of these ideal gas properties is the American Petroleum Institute Research Project 44 compilation (*13*). However, any compilation of ideal gas or zero-pressure properties that one is accustomed to using is suitable for this work. These properties will vary depending on individual preferences for the datum plane from which enthalpies for process calculations are computed.

COMPARISON WITH EXPERIMENTAL DATA

It is extremely difficult to evaluate a correlation such as the one presented here because of the lack of accurate experimental data for mixtures. One source of data, which was calculated from experimental P.V.T. data and therefore might be considered experimental data, is the work done by Sage and Lacey on hydrocarbon mixtures (*14*). They have reported isothermal-pressure corrections to the ideal gas partial-molal enthalpies of methane, ethane, *n*-butane, and *n*-pentane in binary mixtures of these four hydrocarbons. From these values the enthalpies of mixtures of methane-ethane, methane-butane, and methane-pentane can be determined. This was done, and on Figure 3 the values obtained from the Sage and Lacey work are compared with values obtained from the correlation presented here. It can be seen that there is excellent agreement for the methane-ethane system but rather poor agreement for the methane-butane and methane-pentane systems. This does not invalidate the correlation since the systems methane-butane and methane-pentane are a very stringent test for the correlation. The systems represent a mixture of two extremely different molecules. It would be just as reasonable to check this correlation with a mixture of pentane and some nonhydrocarbon. Further, it is very unlikely that one would be concerned with such a mixture in a practical process-design calculation. Normally mixtures which are encountered contain small amounts of light and heavy components with the major portion consisting of similar molecules.

Another source of experimental data is the investigation of Nelson and Holcomb (*10*) on three ternaries made up of propane, *n*-butane, and *n*-pentane. A comparison of these data with the correlation presented here is given in Figure 4. Surprisingly enough, the poorer agreement is in the vapor region, with excellent agreement in the liquid region. This can

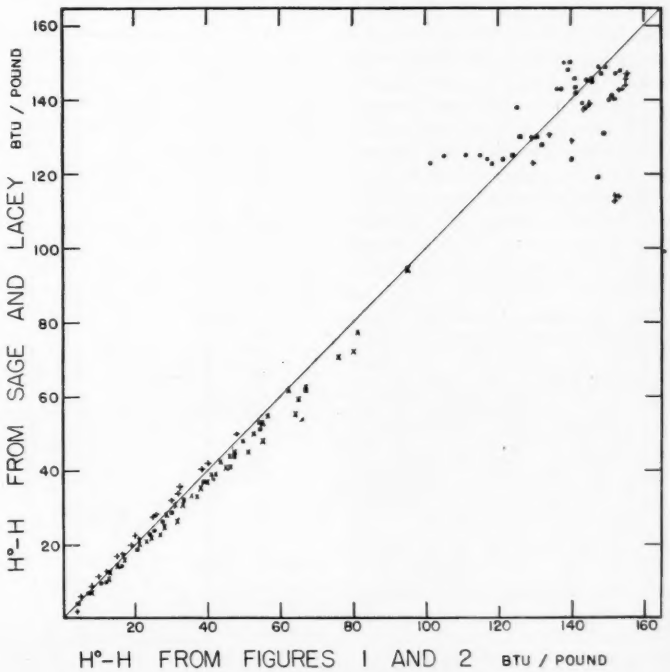

Fig. 3. Comparison of enthalpies of hydrocarbon mixtures calculated by Sage and Lacey with this work; × methane-ethane mixtures, ■ methane-butane mixtures, + methane-pentane mixtures.

*The plots presented with this article are solely for the purpose of showing the form the correlation takes. Working plots with fine-line backgrounds are obtainable free of charge upon request from the Department of Chemical Engineering, Carnegie Institute of Technology, Pittsburgh 13, Pennsylvania.

be explained by pointing out that all the vapor data reported by Nelson and Holcomb fall in the lower left-hand corner of Figure 1, which is undoubtedly the least accurate portion of the chart. In spite of this the maximum difference between the data of Nelson and Holcomb in the vapor region and this correlation is about 10 B.t.u./lb. According to the original paper by Nelson and Holcomb this seems to be the same order of magnitude as the agreement they report for the correlations of Scheibel and Jenny (*15*) and Holcomb and Brown (*7*). It might be pointed out here that differences of this order of magnitude were encountered when the thermodynamic properties reported by different investigators for the same compound were compared.

A very recent paper by Edmister (*6*) dealing with isobaric integral heats of vaporization contains a sample calculation which might serve as a comparison of the different methods of calculating the isobaric integral heat of vaporization. Edminster considers a hypothetical mixture containing 5 lb. moles of methane, 15 lb. moles of ethane, 30 lb. moles of propane, and 50 lb. moles of normal butane. This corresponds to a hydrocarbon mixture having an M.A.B.P. of −30°F. and an average molecular weight of 47.5. Using the DePriester charts (*5*), he obtains a bubble point of 95°F. and a dew point of 185°F. for this mixture at 300 lb./sq. in. abs. In order to calculate the isobaric integral heat of vaporization for this mixture it is necessary to subtract the enthalpy of the liquid at 95°F. and 300 lb./sq. in. abs. from the enthalpy of the vapor at 185°F. and 300 lb./sq. in. abs. Edmister presents detailed calculations using the method described in his paper and the earlier partial-molal enthalpy paper by Canjar and Edmister (*4*). Using the Canjar-Edmister partial-molal enthalpies he finds the isobaric integral heat of vaporization for the above-mentioned mixture to be 8,079 B.t.u./lb. mole of mixture compared with 7,953 B.t.u./lb. mole of mixture found by use of the Edmister K-value method.

In the way of a comparison and sample calculation, the same calculation is presented here by means of Figures 1 and 2 of this work. From Figure 1 it can be seen that the pressure correction at 300 lb./sq. in abs. to the enthalpy of an ideal gas mixture with an M.A.B.P. of −30°F. at 185°F. is 22 B.t.u./lb., or 1,045 B.t.u./lb. mole (average molecular weight of 47.5). Figure 2*a* gives a pressure correction for a liquid at 1,500 lb./sq. in. abs. and 95°F. of 152 B.t.u./lb. To adjust this to 300 lb./sq. in. abs., Figure 2*b* is employed. The adjustment is found to be about +1 B.t.u./lb., giving a value of $H° - H$ for the liquid at 300 lb./sq. in. abs. of 153 B.t.u./lb., or 7,268 B.t.u./lb. mole. To find the enthalpy of the liquid and vapor it is simply a matter of determining the ideal gas enthalpies. Edmister interpolated these values from the A.P.I. tables (*6*). They are shown in the accompanying table.

Component	Mole fraction	$H°$ (B.t.u./lb. mole)* 185°F.	95°F.
Methane	0.05	5,266	4,466
Ethane	0.15	6,593	5,367
Propane	0.30	8,375	6,643
Butane	0.50	11,073	8,783
$H°_{mixture} = \Sigma x_i H_i° =$		9,301	7,413

* Reference: ideal gas at 0°R.

$$H^V = H° - (H° - H)^V = 9{,}301 - 1{,}045 = 8{,}256 \text{ B.t.u./lb. mole}$$
$$H^L = H° - (H° - H)^L = 7{,}413 - 7{,}268 = 145 \text{ B.t.u./lb. mole}$$
$$H^V - H^L = 8{,}256 - 145 = 8{,}111 \text{ B.t.u./lb. mole}$$

In summary:

	B.t.u./lb. mole
Edmister K-value method	7,953
Canjar-Edmister partial-enthalpy method	8,079
Present method	8,111

The agreement with the partial-enthalpy method is excellent in view of the fact that the partial enthalpies were derived from Kellogg K values, which are essentially mixture data, and that Figures 1 and 2 are based on pure-component data only. The agreement with the Edmister K-value method is poorer although still good, owing to the fact that in the derivations of the equations used in the Edmister method some approximate assumptions were made about the constancy of partial molal heat of vaporization over a wide temperature range.

CONCLUSIONS

An enthalpy correlation has been presented which can be expected to predict hydrocarbon-mixture enthalpies with a fair degree of accuracy. Strictly speaking, the correlation should be used only with the Kellogg (*2*) and DePriester (*5*) equilibrium-vaporization constants. There is a thermodynamic consistency in these K values with the enthalpies presented here through the M.A.B.P. concept. For this reason the correlation is strictly valid for hydrocarbon mixtures containing the lighter paraffins and olefins. In the absence of better methods for estimating enthalpies of mixture, however, this method can be extended with caution to

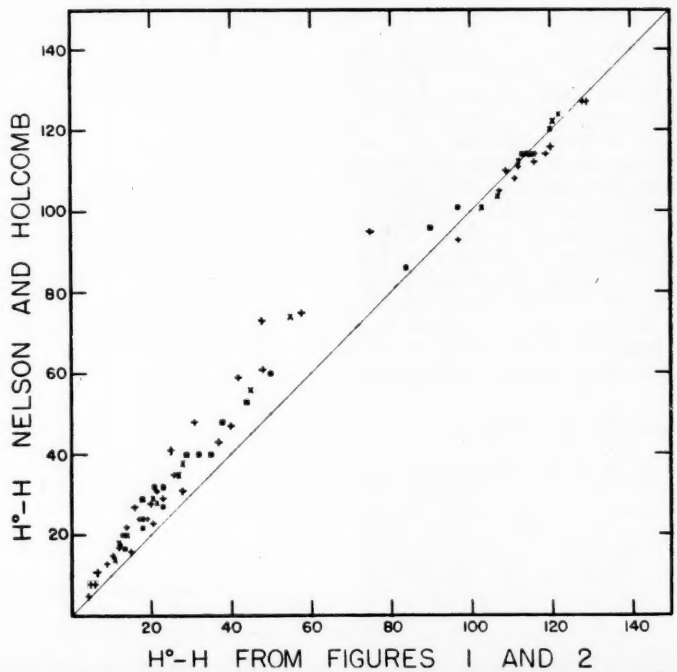

Fig. 4. Comparison of enthalpies of hydrocarbon mixtures determined by Nelson and Holcomb with this work; + mixture *A*, × mixture *B*, ■ mixture *C*.

mixtures containing other types of compounds such as aromatics and nonhydrocarbons. The correlation will fail completely if these other types of compounds are present in major amounts in the mixture.

It is impossible to estimate the accuracy of a correlation such as this because of the scarcity of good experimental data. The regions of greatest uncertainty in Figures 1 and 2 are those corresponding to high M.A.B.P.–low temperatures and the critical point of the region of high pressure–low temperature on Figure 1. The uncertainty in this latter region is due to uncertainty in PVT measurements on pure compounds in the vicinity of the critical point.

NOTATION

B = normal boiling point, °F.
C_p° = molal heat capacity for ideal gas state, B.t.u./(lb. mole)(°R.)
H = enthalpy of a real gas or liquid, B.t.u./lb. or B.t.u./lb. mole
H° = enthalpy of an ideal gas, B.t.u./lb. or B.t.u./lb. mole
M.A.B.P. = molal average boiling point, °F. ($\sum x_i B_i$)
P = pressure, lb./sq. in. abs.
T = temperature, °F.
x = mole fraction

Superscripts

L = liquid phase
V = vapor phase

Subscript

i = ith component in a mixture

LITERATURE CITED

1. Barkelew, C. H., J. L. Valentine, and C. O. Hurd, *Trans. Am. Inst. Chem. Engrs.*, **43**, 25 (1947).
2. Benedict, Manson, G. B. Webb, L. C. Rubin, and Leo Friend, *Chem. Eng. Progr.*, **47**, 419, 449, 571, 609 (1951).
3. Brydon, J. W., Nicholas Walen, and L. N. Canjar, *Chem. Eng. Progr. Symposium Series* No. 7, **49**, 151 (1953).
4. Canjar, L. N., and W. C. Edmister, *loc. cit.*, p. 73.
5. DePriester, C. L., *loc. cit.*, p. 1.
6. Edmister, W. C., *A.I.Ch.E. Journal*, **1**, 38 (1955).
7. Holcomb, D. E., and G. G. Brown, *Ind. Eng. Chem.*, **34**, 590 (1942), **36**, 384 (1944).
8. Hoover, H. G., M.S. thesis, Carnegie Inst. Technol., Pittsburgh (1947).
9. Matthews, C. S., and C. O. Hurd, *Trans. Am. Inst. Chem. Engrs.*, **42**, 55 (1946).
10. Nelson, J. M., and D. E. Holcomb, *Chem. Eng. Progr. Symposium Series* No. 7, **49**, 93 (1953).
11. Papadopoulos, A., R. L. Pigford, and Leo Friend, *Chem. Eng. Progr. Symposium Series* No. 7, **49**, 119 (1953).
12. Prengle, H. W., L. R. Greenhaus, and R. York, *Chem. Eng. Progr.*, **44**, 863 (1948).
13. Rossini, F. D., Am. Petroleum Inst. *Research Proj.* 44, Carnegie Inst. Technol., Pittsburgh.
14. Sage, B. H., and W. N. Lacey, "Thermodynamic Properties of the Lighter Paraffin Hydrocarbons and Nitrogen," Am. Petroleum Inst., New York (1950).
15. Scheibel, E. G., and F. J. Jenny, *Ind. Eng. Chem.*, **37**, 990 (1945).

Presented at A.I.Ch.E. Detroit meeting

Vapor Pressures: The Saturated Aliphatic Hydrocarbons

NORMAN E. SONDAK and GEORGE THODOS

Northwestern Technological Institute, Evanston, Illinois

A rigorous analysis of the available data presented in the literature for all the saturated aliphatic hydrocarbons from methane through *n*-eicosane was conducted to establish the constants *A*, *B*, *C*, and *D* of the vapor-pressure equation developed by Frost and Kalkwarf (21). With all the constants determined, vapor pressures can be calculated accurately from the triple to the critical point. The actual constants *A*, *B*, *C*, and *D* have been calculated from the available reported vapor-pressure data of eighty-seven saturated aliphatic hydrocarbons and include all the normal paraffins through eicosane and all the isomeric paraffins through the nonanes.

In order to ascertain the validity of calculated-vapor-pressure constants, values of *A*, *B*, *C*, and *D* were produced from the molecular structure and normal boiling point for all the normal paraffins through eicosane and all the thirty-four isomeric nonanes. The normal paraffins were selected to cover the range of the saturated aliphatic hydrocarbons; whereas the nonanes were chosen because they represent the most complex structures for which reported vapor pressures are available.

With the calculated constants, vapor pressures were evaluated from the equation at several representative points and were compared with reported values to produce an overall absolute average percentage of deviation of 0.58 for the normal paraffins and 0.73 for the isomeric nonanes, or 0.68 for these fifty-four saturated aliphatic hydrocarbons.

In order to obtain information on the vapor-pressure behavior of substances for which experimental data are available in limited ranges, extrapolations and interpolations are necessary. The resulting degree of accuracy will depend upon the reliability of the methods used to extend the experimental data. To facilitate these extensions, several vapor-pressure expressions have been proposed. The familiar Clausius-Clapeyron vapor-pressure equation

$$\log P = A + \frac{B}{T} \qquad (1)$$

possesses considerable simplicity because of the assumptions used in its development from the rigorous thermodynamic relationship of Clapeyron and has been applied to define satisfactorily the vapor pressures of metals (*5*, *41*). However, Equation (1) fails to represent properly the complete vapor-pressure behavior of many substances and must be applied over limited temperature ranges (*34*). Modifications of Equation (1) have been proposed by Antoine (*1*) and Cox (*16*).

Rankine (*44*), Kirchhoff (*31*), and Dupré (*18*) empirically proposed a refinement to Equation (1) with the introduction of a third constant to define the vapor-pressure equation as

$$\log P = A + \frac{B}{T} + C \log T \qquad (2)$$

Equation (2) can be developed from the Clapeyron equation by assuming the molar heat of vaporization to vary linearly with temperature. Although Equation (2) expresses the vapor-pressure behavior over wider ranges of temperature, still it fails generally to define satisfactorily the complete vapor-pressure function included between the triple and critical points. Modifications of Equation (2) have been proposed by van Laar (*56*), Riedel (*45*), and Gamson and Watson (*22*). Thodos (*53*) points out that a plot of precise experimental vapor pressures between the critical and triple points for normal paraffins produces an elongated *S*-shaped curve as presented in Figure 1. To retain the characteristics of the actual vapor-

pressure function, Frost and Kalkwarf (*21*), beginning with the Clapeyron equation and assuming van der Waals' equation to apply, developed the semi-theoretical expression

$$\log P = A + \frac{B}{T} + C \log T + D \frac{P}{T^2} \quad (3)$$

The shapes of curves resulting from Equations (1), (2), and (3) are presented in Figure 1.

VAPOR PRESSURES OF THE SATURATED ALIPHATIC HYDROCARBONS

In the past, considerable effort has been expended toward predicting the vapor pressures of organic substances. Owing to the industrial importance of the lighter hydrocarbons and the increasing importance of the heavier hydrocarbons, much of the recent work has dealt with the procurement of precise experimental vapor pressures in this field. Although considerable valuable experimental background has been established in the last 10 years for hydrocarbons, particularly by the exacting work of the Bureau of Standards group (*46*, *57*), the results produced are specific to the compounds studied for the pressure ranges investigated. The information provided should prove valuable in the development of a possible generalized pattern capable of handling hydrocarbons for which no experimental data are available and which can produce accurate calculated vapor-pressure values over extended pressure ranges.

The vapor-pressure function can be defined through Equation (3) over the pressure range included between the triple and critical points. To utilize this equation, the values of the four vapor-pressure constants, A, B, C, and D, which are specific to each substance, are required. The substitution of four reliable experimental vapor-pressure points in Equation (3) will produce four linear equations, the simultaneous solution of which yields the four vapor-pressure constants. Perry and Thodos (*42*) following this procedure established these constants for the normal paraffins through n-dodecane and were able to produce calculated vapor-pressure values of which the percentage of deviation was 0.27. Although this approach yields constants capable of producing precise vapor pressures, frequently the necessary experimental data to evaluate these constants may not be available.

In the general vapor-pressure equation the constant D is defined as equal to $a/2.303R^2$, where a represents the pressure van der Waals' constant. Therefore, knowledge of the value of a necessarily establishes the constant D. Both pressure and volume van der Waals' constants a and b, respectively, can be calculated from the critical point through the relationships

$$a = \frac{27R^2T_c^{\,2}}{64P_c} \quad (4)$$

$$b = \frac{RT_c}{8P_c} \quad (5)$$

and therefore the critical point can be utilized to establish the constant D.

Whenever experimental critical constants are not available, the methods proposed by Lydersen (*38*), Michaels and Thodos (*40*), and Thodos (*54*) may be applied. All these methods require the use of group contributions for the calculation of the critical temperature and pressure from the molecular structure of the compound. For the saturated aliphatic hydrocarbons presented in this investigation the values of constant D were established from the calculated van der Waals' constants a evaluated by Thodos (*54*). These calculated values of D are presented in Table 1.* This particular method was used because of the lack of experimental critical points for the majority of hydrocarbons studied and also because this approach produced more precise critical temperatures and pressures than were possible by the other two methods.

With constant D established, constants B and C can be evaluated from experimental vapor-pressure values by a reference-point procedure applied to the general vapor-pressure equation. This procedure consists of referring all the reported vapor-pressure points to a particular reliable reference value and rearranging the resultant expression to define constants B and C as the slope and intercept of a straight-line function.

Any point on the vapor-pressure function can be represented by Equation (3) as

$$\log P = A + \frac{B}{T} + C \log T + D \frac{P}{T^2} \quad (3)$$

For the reference point, this equation becomes

$$\log P_b = A + \frac{B}{T_b} + C \log T_b + D \frac{P_b}{T_b^{\,2}} \quad (6)$$

where P_b and T_b represent a selected vapor-pressure point. Subtracting Equation (6) from Equation (3) yields

$$\log \frac{P}{P_b} = B\left[\frac{1}{T} - \frac{1}{T_b}\right] + C \log \frac{T}{T_b} + D\left[\frac{P}{T^2} - \frac{P_b}{T_b^{\,2}}\right] \quad (7)$$

which when rearranged and divided through by $\log T/T_b$ produces

$$\frac{\log P/P_b - D[P/T^2 - P_b/T_b^{\,2}]}{\log T/T_b} = B\,\frac{[1/T - 1/T_b]}{\log T/T_b} + C \quad (8)$$

Equation (8) should be linear when

$$Y = \frac{\log P/P_b - D[P/T^2 - P_b/T_b^{\,2}]}{\log T/T_b}$$

is plotted against

$$X = \frac{[1/T - 1/T_b]}{\log T/T_b}$$

if Equation (3) properly represents the vapor-pressure function and the constant D has been evaluated correctly. Figure 2 presents a plot of Y vs. X for n-heptane that is linear through the range included between the lowest experimental value of Willingham et al. (*57*), 47.66 mm. of mercury, and the experimental critical value of Beattie and Kay (*9*). The resulting linearity of Figure 2 strongly implies that Equation (3) properly represents the vapor-pressure function and that constant D has been correctly determined.

The constants B and C are discrete values for a particular substance, and therefore a plot of Y-vs.-X values resulting from any experimental investigation should produce a single straight line of slope B and intercept C, regardless of the choice of the reference point. This fact makes it possible to treat experimental points of various investigations whose range may be limited to certain pressure regions by the selection of a reliable value

*Complete tables are available from the American Documentation Institute, Photoduplication Service, Library of Congress, Washington 25, D. C., as document 4951, obtainable for $1.25 for microfilm or photoprints.

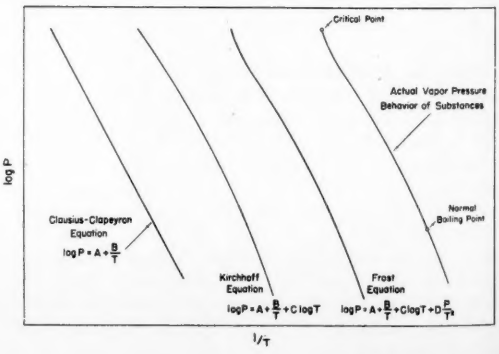
Critical Point
Actual Vapor Pressure Behavior of Substances
Normal Boiling Point
Clausius-Clapeyron Equation
log P = A + B/T
Kirchhoff Equation
logP = A + B/T + C logT
Frost Equation
logP = A + B/T + ClogT + D P/T²
log P
1/T

Fig. 1. Graphical representation of some vapor-pressure equations.

TABLE 1. CONSTANTS OF THE VAPOR-PRESSURE EQUATION LOG $P = A + B/T + C \log T + D(P/T^2)$ ESTABLISHED FROM A COMPREHENSIVE ANALYSIS OF VAPOR-PRESSURE DATA OF THE SATURATED ALIPHATIC HYDROCARBONS

	T_b, °K.	A	B	C	D	References
Methane	111.49	13.49190	−567.59	−2.70212	0.19212	*20, 29, 32, 54*
Ethane	184.466	16.85324	−1,070.59	−3.60963	0.46665	*8, 13, 25, 30, 32, 33, 36, 37, 43, 54*
Propane	231.105	19.07337	−1,427.41	−4.24329	0.78564	*11, 15, 17, 23, 28, 32, 47, 52, 54*
n-Butane	272.666	21.05182	−1,768.05	−4.80311	1.16463	*4, 12, 14, 26, 32, 48, 54*
n-Pentane	309.238	22.94265	−2,098.87	−5.33564	1.59674	*10, 32, 39, 54, 57, 61*
2,2-Dimethylpropane	282.665	21.68978	−1,838.01	−5.02604	1.43534	*3, 6, 32, 54*
n-Hexane	341.905	24.93410	−2,428.98	−5.90492	2.07790	*27, 32, 54, 55, 57*
2,3-Dimethylbutane	331.153	22.98513	−2,227.62	−5.31367	1.89817	*32,54, 57, 60*
n-Heptane	371.591	26.88236	−2,753.17	−6.46159	2.60489	*9, 25, 32, 49, 51, 54, 57, 58*
3-Methylhexane	365.015	25.94237	−2,642.58	−6.18037	2.47344	*32, 46, 54*
2,4-Dimethylpentane	353.665	25.47550	−2,515.62	−6.08036	2.40996	*19, 32, 54*
2,2,3-Trimethylbutane	354.037	22.86290	−2,360.79	−5.22840	2.23608	*19, 32, 50, 54*
n-Octane	398.830	29.23812	−3,099.36	−7.15220	3.17549	*32, 35, 54, 57, 59*
4-Methylheptane	390.874	27.64799	−2,936.97	−6.66209	3.03352	*32, 54, 57*
2,5-Dimethylhexane	382.268	26.82104	−2,812.77	−6.42726	2.96504	*32, 54, 57, 60*
3-Methyl-3-ethylpentane	391.424	24.13358	−2,702.61	−5.53952	2.78530	*32, 54, 57*
2,2,3,3-Tetramethylbutane	379.635	20.27060	−2,393.67	−4.30131	2.57544	*32, 46, 54*
n-Nonane	423.961	30.83077	−3,400.33	−7.59158	3.78666	*54, 57*
3-Methyloctane	417.345	30.60717	−3,312.44	−7.55782	3.63527	*46, 54*
4-Ethylheptane	414.365	30.29260	−3,258.78	−7.47429	3.57001	*46, 54*
2,5-Dimethylheptane	409.165	30.24904	−3,216.74	−7.47445	3.52393	*46, 54*
4,4-Dimethylheptane	408.365	26.81228	−2,994.56	−6.36295	3.41140	*46, 54*
2-Methyl-4-ethylhexane	406.965	28.49224	−3,072.73	−6.92721	3.45960	*46, 54*
2,2,4-Trimethylhexane	399.705	28.55469	−3,012.88	−6.97689	3.34912	*46, 54*
2,3,4-Trimethylhexane	412.165	26.79522	−3,017.34	−6.35117	3.35624	*46, 54*
3,3-Diethylpentane	419.333	25.24652	−2,961.91	−5.84034	3.31169	*46, 54*
2,3,3,4-Tetramethylpentane	414.716	25.15949	−2,920.50	−5.82578	3.15114	*46, 54*
n-Dodecane	489.443	38.36512	−4,465.27	−9.80767	5.85175	*54, 57*
n-Hexadecane	559.958	44.36486	−5,608.40	−11.45869	9.09708	*46, 54*
n-Eicosane	615.865	58.46119	−7,304.73	−15.68214	12.84792	*46, 54*

The dimensions of constants A, B, C and D presented in this table are consistent and produce, with absolute temperatures in degrees Kelvin, vapor pressures in millimeters of mercury.

within the particular set for a reference point. This analysis permits the examination of the consistency of a particular set of values within themselves to produce straight lines, which should coincide for all experimental investigations.

The results of this procedure are illustrated for *n*-heptane in Figure 2, in which the experimental data of Kay (*25*) are referred to his value of 521.055°K. and 15,510 mm.; those of Willingham et al. (*57*) are referred to their value of 345.095°K. and 324.97 mm. The results for *n*-heptane of six separate experimental investigations, each using its own reference point, produced straight lines which coincide and appear in Figure 2 as the single line of slope $B = -2{,}753.17$ and intercept $C = -6.46159$.

The use of an incorrect value of D with good experimental vapor-pressure values will yield curved lines of Y vs. X; whereas a correct value of D with inaccurate experimental vapor-pressure values will produce scattered points of correlation. In this investigation the values of B and C were determined by the selection of two points which fixed the best straight line that represented the reported data for a particular compound. With this procedure constants B and C were evaluated from the reported vapor-pressure

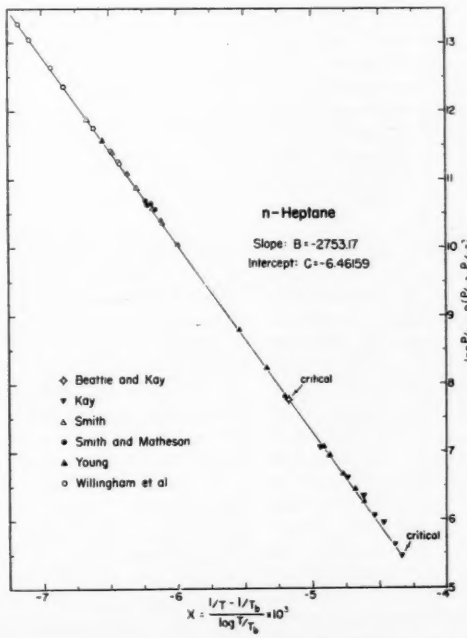

Fig. 2. Vapor-pressure–temperature reference moduli Y and X for *n*-heptane.

data of eighty-seven saturated aliphatic hydrocarbons, including all the normal paraffins through eicosane and all the isomeric paraffins through the nonanes. Both values B and C for these hydrocarbons appear in Table 1.

With the three constants B, C, and D established, the constant A can be evaluated by substituting a single reliable vapor-pressure value in Equation (3). By use of the normal boiling point as the reliable value, constant A was also calculated for these saturated aliphatic hydrocarbons and is included along with the other three constants in Table 1.

These constants calculated from reported vapor-pressure values are useful for producing exacting vapor pressures over the complete range, as illustrated in Table 5 for ethane and 2, 2, 4-trimethylhexane. However, their application is limited to the eighty-seven saturated aliphatic hydrocarbons appearing in Table 1. To facilitate the evaluation of these constants for the saturated aliphatic hydrocarbons, where no experimental vapor-pressure data are presently available, correlation procedures were undertaken to devise methods for their prediction.

Type	1
Structure	$-CH_3$

RELATIONSHIP OF CONSTANT B AND MOLECULAR STRUCTURE

Attempts were made to correlate empirically the constants B and C with the normal boiling point and with each other, the normal boiling point being used as the property capable of differentiating between the isomeric paraffins. No reasonable correlation was found to exist between constants B and C and the normal boiling point or with each other and the normal boiling point. Therefore, a study for the prediction of either constant B or C from the molecular structure was undertaken. A procedure analogous to that proposed by Thodos (*54*) for the evaluation of the van der Waals' constants was adopted. This method produced B values, which were consistent with the slopes B resulting from the analysis of reported vapor-pressure data. On the other hand, no correlation was found for constant C.

This analysis revealed that the constant B for the saturated aliphatic hydrocarbons varies linearly with the number of carbon atoms in the molecule and may be defined through the expression

$$B = -[B_0 + \Sigma\Delta(B)] \qquad (9)$$

where B_0 represents the constant B for the base group, methane, and $\Delta(B)$ the group contribution required in the successive substitution of hydrogen atoms by methyl groups. The numerical magnitude of the group contributions, $\Delta(B)$, depends primarily on the nature of the carbon atom on which the methyl substitution is made and second on the nature of the surrounding carbon atoms. The types of carbon atoms involved in this study were associated with the number of carbon-to-carbon linkages and may be defined as

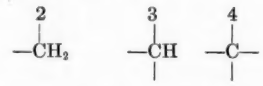

The numerical values of the different group contributions, $\Delta(B)$, presented in Table 2 are the results of average values obtained as differences between B values for hydrocarbons having similar structures but differing in molecular dimensions by a single methyl group. From Table 1, for example, the actual B values for 3,3-diethylpentane and 3-methyl-3-ethylpentane are $-2{,}961.91$ and $-2{,}702.61$, respectively. Thus the subtraction of a methyl group from 3,3-diethylpentane to produce 3-methyl-3-ethyl-pentane

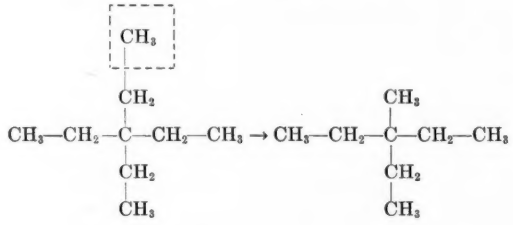

yields a group contribution value, $\Delta(B)$, of $-[-2{,}961.91 - (-2{,}702.61)] = 259.30$. This contribution value, $\Delta(B)$, must be associated with the replacement of a hydrogen atom by a methyl group on a type-1 carbon atom adjoined to a type-4 carbon atom and designated as a $4 \leftarrow 1$ group contribution value. The average value for this type of substitution was found to be 262.96 and appears in Table 2.

In Table 2 the type of carbon atom from which the arrows originate is the carbon atom involved in the replacement of a hydrogen atom by a methyl group; the adjacent carbon atoms are those to which the arrows are directed. Therefore the designation $1 \leftarrow \underset{\downarrow}{3} \rightarrow 2$ con-
$\quad\quad\quad

Table 3. Constants A, B, C, and D Calculated from Molecular Structure and the Normal Boiling Point of the Normal Paraffins and Average Absolute Percentage of Deviation Resulting from Them

	Critical constants		Calculated constants				Average percentage of deviation*
	T_c, °K.	P_c, atm.	A	B	C	D	
Methane	191.065	45.8	13.47611	−567.59	−2.69441	0.19212	0.22
Ethane	305.465	48.2	16.82808	−1,070.59	−3.59870	0.46665	0.08
Propane	369.965	42.0	19.07662	−1,427.41	−4.24333	0.78564	0.51
n-Butane	425.165	37.5	20.87990	−1,761.80	−4.74193	1.16463	0.16
n-Hexane	507.865	29.9	25.01175	−2,430.58	−5.93372	2.07790	0.36
n-Octane	569.365	24.6	29.22028	−3,099.36	−7.14534	3.17549	0.21
n-Decane	619.4	20.84	33.56699	−3,768.14	−8.40515	4.43771	0.06
n-Pentadecane	716.2	15.02	44.73939	−5,440.09	−11,65290	8.23591	0.29
n-Eicosane	789.5	11.69	56.54187	−7,112.04	−15.10625	12.84792	2.24
							0.58

The critical temperatures and pressures through *n*-octane represent screened literature values; whereas those for *n*-nonane to *n*-eicosane, inclusive, are calculated values presented by Thodos (*54*).
*Percentage of deviation $= [(P_{calc} - P_{lit})/P_{lit}] \times 100$
The dimensions of constants A, B, C, and D presented in this table are consistent and produce, with absolute temperatures in degrees Kelvin, vapor pressures in millimeters of mercury.

notes the replacement of a hydrogen atom by a methyl group on a type-3 carbon atom ($-\overset{|}{C}H$) surrounded by two type-1 carbon atoms ($-CH_3$) and a single type-2 carbon atom ($-CH_2-$). An illustration of this mode of methylation is the formation of 2,2-dimethylbutane from 2-methylbutane as follows:

$$CH_3-\overset{CH_3}{\overset{|}{C}}H-CH_2-CH_3 \rightarrow CH_3-\overset{CH_3}{\overset{|}{\underset{CH_3}{\underset{|}{C}}}}-CH_2-CH_3$$

To avoid ambiguities in the order of construction of complex branched chain paraffins, the following procedures were adopted:

1. The longest normal carbon chain of the hydrocarbon is constructed initially.
2. Only single-methyl-group substitutions are made on the normal carbon chain, the substitutions beginning from the left end and proceeding always in a clockwise direction. Should side chains of greater lengths be required, this process is continued with the introduction of methyl groups on the side chains already established by continuing these substitutions in the same clockwise manner until the complete molecular structure is obtained.

The results of this study permit the evaluation of constant B from a knowledge of the molecular structure of a saturated aliphatic hydrocarbon. Furthermore, both van der Waals' constants a and b can be predicted from the molecular structure (*54*) and the critical temperature and pressure established through the relationships

$$T_c = \frac{8a}{27Rb} \qquad (10)$$

$$P_c = \frac{a}{27b^2} \qquad (11)$$

In addition, the pressure van der Waals' constant a permits the evaluation of the constant D through the relationship already developed (*21*),

$$D = \frac{a}{2.303R^2} \qquad (12)$$

Therefore, for the saturated aliphatic hydrocarbons a knowledge of the molecular structure and a single experimental vapor-pressure point make possible the evaluation of all the constants of the general vapor-pressure equation, Equation (3). The accuracy of vapor pressures resulting with constants obtained from the molecular structure and a single vapor-pressure point was investigated for two comprehensive cases.

The constants A, B, C, and D of the normal paraffins through eicosane were calculated from the molecular structure and normal boiling point to cover the molecular dimension range of the saturated aliphatic hydrocarbons, for which reported vapor-pressure data are available. Vapor pressures at representative

Table 4. Constants A, B, C, and D Calculated from Molecular Structure and the Normal Boiling Point of the Isomeric Nonanes and Average Absolute Percentage of Deviation Resulting from Them

	Calculated critical values (*54*)		Calculated constants				Average percentage of deviation*
	T_c, °K.	P_c, atm.	A	B	C	D	
n-Nonane	595.4	22.57	31.37706	−3,433.75	−7.76950	3.78666	0.24
4-Methyloctane	593.9	23.38	30.57686	−3,287.27	−7.56217	3.63527	0.43
2,2-Dimethylheptane	582.5	23.39	29.24181	−3,114.64	−7.17033	3.49610	0.58
2,5-Dimethylheptane	584.7	23.39	29.30943	−3,153.27	−7.17410	3.52393	1.25
3,5-Dimethylheptane	592.4	24.27	29.33793	−3,140.79	−7.19662	3.48591	0.58
2-Methyl-4-ethylhexane	588.2	24.10	29.11430	−3,112.95	−7.12771	3.45960	0.24
2,2,4-Trimethylhexane	580.8	24.28	27.88253	−2,968.16	−6.76154	3.34912	0.18
2,3,4-Trimethylhexane	598.2	25.70	26.94831	−3,019.69	−6.40753	3.35624	0.62
3,3-Diethylpentane	621.8	28.01	24.68934	−2,899.91	−5.68426	3.31169	0.71
2,2-Dimethyl-3-ethylpentane	595.7	26.31	26.12492	−2,918.77	−6.16477	3.25076	0.15
2,2,3,3-Tetramethylpentane	593.9	27.84	21.18043	−2,698.95	−4.50432	3.05363	1.08
2,3,3,4-Tetramethylpentane	602.1	27.73	24.61675	−2,911.38	−5.62685	3.15114	2.40
							0.73

*Percentage of deviation $= [(P_{calc} - P_{lit})/P_{lit}] \times 100$
The dimension of constants A, B, C, and D presented in this table are consistent and produce, with absolute temperatures in degrees Kelvin, vapor pressures in millimeters of mercury.

points were evaluated by utilizing these calculated constants in Equation (3). Table 3* contains the calculated constants A, B, C, and D, along with the critical points evaluated by Thodos (*54*) and the average absolute percentage of deviation existing between calculated and reported vapor pressures for each normal paraffin. The over-all average absolute percentage of deviation obtained for all the normal paraffins investigated was 0.58 with a minimum for n-decane of 0.06 and a maximum for n-eicosane of 2.24.

The constants of all the isomeric nonanes were similarly determined to cover the case involving the highest molecular complexity for which reported vapor pressures are available. Again vapor pressures were calculated and compared with reported values to produce an average absolute percentage of deviation of 0.73 for all the thirty-four isomeric nonanes with a minimum of 0.15 for 2,2-dimethyl-3-ethylpentane and a maximum of 2.4 for 2,3,3,4-tetramethylpentane. The calculated constants for all the isomeric nonanes along with the calculated critical constants used and average absolute percentage of deviations obtained appear in Table 4.*

The vapor pressures produced by the use of calculated constants in Equation (3) for all the normal paraffins and all isomeric nonanes resulted in an over-all average percentage of deviation of 0.68 for the fifty-four hydrocarbons studied.

The vapor pressure of any substance can be calculated by the use of Equation (3), in which the constants A, B, C, and D may be established by treating experimental data according to the methods previously presented. If for this substance the van der Waals' constant a is not available, the constant D can be obtained by assuming various values of D until a linear plot of Y vs. X results from the experimental data as illustrated in Figure 3 for n-heptane when D is permitted to vary from zero to four.

If the substance for which vapor-pressure values are desired is a saturated aliphatic hydrocarbon presented in Table 1, the constants presented in this table can be used to calculate precise vapor-pressure values over the entire range from the triple to the critical point. However, if the saturated aliphatic hydrocarbon is an isomer of greater molecular weight than nonane, the constants of the vapor-pressure equation can be evaluated by the methods developed in this investigation.

Example

To illustrate the application of the methods developed in this investigation, the calculation of constants A, B, C, and D of the general vapor-pressure equation is presented for 2, 2, 4-trimethylhexane, the normal boiling point of which is reported as 399.705°K. (*46*).

*See footnote on page 348.

Table 5. Comparison of Vapor Pressures Produced from the Equation $\log P = A + B/T + C \log T + D(P/T^2)$ Employing Actual and Calculated Constants

	T, °K.	Vapor pressures, mm. Hg: Reported		Actual constants	Calculated constants	Percentage of deviation: Actual constants	Calculated constants
				Ethane			
	135.736	18.62	(*36*)	18.54	18.46	−0.42	−0.30
	193.415	1,200.8	(*30*)	1,201.3	1,200.8	+0.04	0.00
	252.065	10,366	(*33*)	10,304	10,335	−0.60	−0.03
crit.	305.465	36,632	(*13*)	36,343	36,632	−0.79	0.00
						0.32	0.08
				2,2,4-Trimethylhexane			
	348.165	150.0	(*46*)	148.42	149.86	−1.06	−0.09
	417.665	1,200.0	(*46*)	1,199.1	1,197.1	−0.75	−0.24
						0.84	0.18

Calculation of Constant B. In order to establish constant B for this compound,

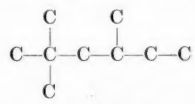

it is necessary to produce n-hexane from methane by the successive substitution of methyl groups for hydrogen atoms. Following the outlined procedure, successive methyl-group substitutions are made to form 2-methyl-hexane, 2, 4-dimethylhexane, and the desired compound, 2, 2, 4-trimethylhexane. From Table 2:

A. Base group–methane	567.59
B. Primary methyl substitution	503.00
C. Secondary methyl substitutions:	
$1 \leftarrow 1$	356.82
$2 \leftarrow 1$	334.39
$2 \leftarrow 1$	334.39
$2 \leftarrow 1$	334.39
$1 \leftarrow 2 \rightarrow 2$	200.39
$2 \leftarrow 2 \rightarrow 2$	187.91
$1 \leftarrow 3 \rightarrow 2$	149.28
$\downarrow$	
1	2,968.16

$B_{calc} = -2{,}968.16$
$B_{act} = -3{,}012.88$ (Table 1)

Calculation of the Critical Point. Following a procedure similar to that used to calculate constant B, Thodos (*54*) evaluated the van der Waals' constants for this compound to be $a = 39.466 \times 10^6$ (cc./g. mole)^2 atm. and $b = 245.38$ cc./g. mole. Therefore

$$T_c = \frac{8a}{27Rb}$$

$$= \frac{8(39.466 \times 10^6)}{27(82.055)(245.38)} = 580.8°\text{K.}$$

$$P_c = \frac{a}{27b^2} = \frac{39.466 \times 10^6}{27(245.38)^2}$$

$$= 24.28 \text{ atm. } (18{,}453 \text{ mm.})$$

For 2, 2, 4-trimethylhexane no critical constants are available.

Calculation of Constant D. With the pressure van der Waals' constant a established, by the method of Thodos (*54*), the constant D is calculated as

$$D = \frac{a}{2.303R^2} = \frac{29.466 \times 10^6}{2.303(62{,}360)^2}$$

$$= 3.34912 \text{ (°K.)}^2/\text{mm.}$$

where $R = 62{,}360$ (cc.)(mm.)/(g. mole)(°K.)

Calculation of Constants A *and* C. With constants B and D calculated and the critical point established from the molecular structure of this compound, a single vapor-pressure point permits the evaluation of constants A and C. Substitution of the normal boiling point and calculated critical point, in conjunction with the calculated constants B and C, produces two equations linear in A and C.
Thus

$$\log 760 = A - \frac{2{,}968.16}{399.705} + C \log 399.705 + 3.34912 \frac{760}{(399.705)^3}$$

$$\log 18{,}453 = A - \frac{2{,}968.16}{580.8} + C \log 580.8 + 3.34912 \frac{18{,}453}{(580.8)^2}$$

which can be solved simultaneously to yield

$$A = 27.88253$$

$$C = -6.76154$$

Therefore the general vapor-pressure equation for 2, 2, 4-trimethylhexane becomes

$$\log P = 27.88253 - \frac{2{,}968.16}{T}$$

$$- 6.76154 \log T + 3.34912 \frac{P}{T^2} \quad (13)$$

Comparison of Calculated and Reported Vapor Pressures. Vapor pressures calculated by the use of Equation (13) were compared with the only available literature values and appear in Table 5* for 2, 2, 4-trimethylhexane. Since the reported values (*46*) for this compound are limited to pressures below 2 atm., the calculated vapor pressures above this pressure cannot be compared with any literature values. To illustrate the accuracy of vapor pressures obtained with the use of calculated constants, the vapor pressures of ethane were calculated from 18.62 mm. to the critical pressure, 36,632 mm., and appear with the reported literature values (*13*, *25*, *30*, *33*, *36*, *43*) in Table 5. The actual constants presented in Table 1 have also been used to calculate vapor pressures for ethane and 2, 2, 4-trimethylhexane. The vapor-pressure values resulting from them are also presented in Table 5 and, when compared with reported values, show an average percentage of deviation of 0.32 for ethane and 0.84 for 2, 2, 4-trimethylhexane. Table 5 also illustrates, to some extent, the validity of the averaging process used to obtain ΔB values, as the calculated constants produce more accurate vapor-pressure values than those obtained from actual constants.

COMMENTS ON THE FROST-KALKWARF EQUATION

The Frost-Kalkwarf equation studied extensively in this investigation is transcendental in nature; solution of it for the vapor pressure P necessitates successive approximations, but, owing to the relatively small value of the term DP/T^2, only three to four repetitions are necessary to obtain essentially balanced values. Kalkwarf (*24*) claims an accuracy of less than ½% with not more than four repetitions for the most unfavorable case near the critical temperature. The term DP/T^2, because of its unusual nature, contributes significantly toward the reversal of curvature near the critical point. Equation (3) is continuous and requires four constants for the calculation of vapor pressures over the complete range between the triple and critical points.

NOTATION

a = pressure van der Waals' constant, (cc./g. mole)^2 atm.
b = volume van der Waals' constant, cc./g. mole
A, B, C, D = constants for vapor-pressure equations
P = vapor pressure
R = gas constant
T = 273.165 + t °C., absolute temperature in degrees Kelvin

$$X = \frac{\frac{1}{T} - \frac{1}{T_b}}{\log \frac{T}{T_b}},$$

temperature modulus

$$Y = \frac{\log \frac{P}{P_b} - D\left(\frac{P}{T^2} - \frac{P_b}{T_b^2}\right)}{\log \frac{T}{T_b}},$$

vapor-pressure-temperature modulus

Subscripts

b = reference point or normal boiling point
c = critical

LITERATURE CITED

1. Antoine, C., *Compt. rend.*, **107**, 681 (1888).
2. Aston, J. G., R. M. Kennedy, and S. C. Schumann, *J. Am. Chem. Soc.*, **62**, 2059 (1940).
3. Aston, J. G., and G. H. Messerly, *loc. cit.*, **58**, 2354 (1936).
4. *Ibid.*, **62**, 1917 (1940).
5. Baur, E., and R. Brunner, *Helv. Chim. Acta*, **17**, 958 (1934).
6. Beattie, J. A., D. R. Douslin, and S. W. Levine, *J. Chem. Phys.*, **19**, 948 (1951).
7. Beattie, J. A., D. G. Edwards, and S. Marple, Jr., *loc. cit.*, **17**, 576 (1949).
8. Beattie, J. A., C. Hadlock, and N. Poffenberger, *loc. cit.*, **3**, 93 (1935).
9. Beattie, J. A., and W. C. Kay, *J. Am. Chem. Soc.*, **59**, 1586 (1937).
10. Beattie, J. A., S. W. Levine, and D. R. Douslin, *loc. cit.*, **73**, 4431 (1951).
11. Beattie, J. A., N. Poffenberger, and C. Hadlock, *J. Chem. Phys.*, **3**, 96 (1935).
12. Beattie, J. A., G. L. Simard, and G. J. Su, *J. Am. Chem. Soc.*, **61**, 24 (1939).
13. *Ibid.*, **61**, 924 (1939).
14. Calingaert, George, and L. B. Hitchcock, *loc. cit.*, **49**, 750 (1927).
15. Cherney, B. J., Henry Marchman, and Robert York, Jr., *Ind. Eng. Chem.*, **41**, 2653 (1949).
16. Cox, E. R., *Ind. Eng. Chem.*, **28**, 613 (1936).
17. Deschner, W. W., and G. G. Brown, *loc. cit.*, **32**, 836 (1940).
18. Dupré, M. A., *Ann. Chim.*, **2**, 185 (1864).
19. Fawcett, F. S., *Ind. Eng. Chem.*, **38**, 338 (1946).
20. Freeth, F. A., and T. T. H. Verschoyle, *Proc. Roy. Soc.* (London), **130A**, 453 (1931).
21. Frost, A. A., and D. R. Kalkwarf, *J. Chem. Phys.*, **21**, 264 (1953).
22. Gamson, B. W., and K. M. Watson, *Natl. Petroleum News*, **36**, R-258 (May 3, 1944).
23. Harteck, P., and R. Edse, *Z. physik. Chem.*, **182A**, 220-4 (1938).
24. Kalkwarf, D. R., Ph.D. thesis, Northwestern Univ., Evanston, Ill. (1951).
25. Kay, W. B., *Ind. Eng. Chem.*, **30**, 459 (1938).
26. *Ibid.*, **32**, 358 (1940).
27. ———, *J. Am. Chem. Soc.*, **68**, 1336 (1946).
28. Kemp, J. D., and C. J. Egan, *loc. cit.*, **60**, 1521 (1938).
29. Keyes, F. G., R. S. Taylor, and L. B. Smith, *J. Math. Phys.*, **1**, 211 (1922).
30. Kharakorin, F. F., *J. Tech. Phys.* (*U.S.S.R.*), **11**, 1133 (1941)
31. Kirchhoff, G., *Ann. phys.*, **104**, 612 (1858).
32. Kobe, K. A., and R. E. Lynn, Jr., *Chem. Revs.*, **52**, 117 (1953).
33. Kuenen, J. P., and W. G. Robson, *Phil. Mag.*, **3**, No. 6, 149 (1902).
34. Lange, N. A., "Handbook of Chemistry," 7 ed., p. 1434, Handbook Publishers, Inc., Sandusky, Ohio (1949).
35. Linder, E. G., *J. Phys. Chem.*, **35**, 531 (1931).
36. Loomis, A. G., and J. E. Walters, *J. Am. Chem. Soc.*, **48**, 2051 (1926).
37. Lu, H., D. M. Newitt, and M. Ruhemann, *Proc. Roy. Soc.* (*London*), **178A**, 506–25 (1941).
38. Hougen, O. A., K. M. Watson, and R. A. Ragatz, "Chemical Process Principles," pp. 87–95, John Wiley and Sons, New York (1954).
39. Messerly, G. H., and R. M. Kennedy, *J. Am. Chem. Soc.*, **62**, 2988 (1940).
40. Michael, G. V., and George Thodos, *Chem. Eng. Progr. Symposium Series* No. 7, **49**, 131 (1953).
41. Partington, J. R., "An Advanced Treatise on Physical Chemistry," Vol. II, p. 239, Longmans, Green and Co., London (1951).
42. Perry, R. E., and George Thodos, *Ind. Eng. Chem.*, **44**, 1649 (1952).
43. Porter, F., *J. Am. Chem. Soc.*, **48**, 2055 (1926).
44. Rankine, W. J. M., *Phil. Mag.*, **31**, 199 (1866).
45. Riedel, L., *Chem. Ing. Tech.*, **26**, 83 (1954).
46. Rossini, F. D., K. S. Pitzer, R. L. Arnett, R. M. Braun, and G. C. Pimental, *Am. Petroleum Inst. Proj.* 44, Carnegie Press, Pittsburgh (1953).
47. Sage, B. H., and W. N. Lacey, *Ind. Eng. Chem.*, **32**, 992 (1940).
48. Sage, B. H., D. C. Webster, and W. N. Lacey, *Ind. Eng. Chem.*, **29**, 1188 (1937).
49. Smith, E. R., *J. Research Natl. Bur. Standards*, **24**, 229 (1940).
50. *Ibid.*, **26**, 129 (1941).
51. ———, and H. Matheson, *J. Research Natl. Bur. Standards*, **20**, 641 (1938).
52. Stearns, W. V., and E. T. George, *Ind. Eng. Chem.*, **35**, 602 (1943).
53. Thodos, George, *Ind. Eng. Chem.*, **42**, 1514 (1950).
54. ———, *A.I.Ch.E. Journal*, **1**, 168 (1955).
55. Thomas, G. L., and Sydney Young, *Trans. Chem. Soc.*, **67**, 1071 (1895).
56. van Laar, J. J., "Die Zustandgleichung von Gasen und Flussigkeiten," Leipzig (1924).
57. Willingham, C. B., W. J. Taylor, J. M. Pignocco, and F. D. Rossini, *J. Research Natl. Bur. Standards*, **35**, 219 (1945).
58. Young, Sydney, *J. Chem. Soc.*, **73**, 675 (1898).
59. *Ibid.*, **77**, 1145 (1900).
60. ———, *Proc. Roy. Soc.* (*Dublin*), **12**, 374 (1910).
61. ———, and G. L. Thomas, *J. Chem. Soc.*, **71**, 440 (1897).

*See footnote on page 348.

Theorem of Corresponding States Applied to Saturated Liquids and Vapors

MERK HOBSON and JAMES H. WEBER

University of Nebraska, Lincoln, Nebraska

The existence of a single generalized compressibility-factor relationship for univariant systems has long been denied because reduced variables do not provide a generalized vapor-pressure relationship. The present study demonstrates that a saturation curve depends on the ability of the theorem of corresponding states to correlate the reduced temperature as a function of reduced pressure and the critical compressibility factor. Saturation curves for both the liquid and the vapor phases are established from compressibility data on a variety of systems, substantiating this conclusion.

The compressibility factors of saturated mixtures are correlated with pseudoreduced properties based upon Kay's pseudocritical concept. The results indicate that the compressibility factors of saturated liquid mixtures can be predicted with reasonable precision over the entire two-phase region. For pseudoreduced isotherms of unity and above, the same isotherms apply to both phases and are approximately consistent with published compressibility charts for pure gases.

The theorem of corresponding states has been discussed many times in connection with the generalized correlation of PVT data for gases (*6, 7, 22,* for example). The correlation of compressibility-factor data for the univariant states along the vapor-liquid phase boundary for pure substances has, however, received a relatively small amount of emphasis.

Cope, Lewis, and Weber (*6*) denied the existence of a simple general reduced equation of state along the saturation curve despite the fact that a single independent variable is sufficient to define the state of a pure substance under these conditions. This argument was based upon conclusive experimental evidence indicating that reduced vapor pressures are not a unique generalized function of reduced temperature. As a result, two reduced-state variables have been used to define the univariant state (*8, 20*).

The present work studies the significance of the critical compressibility factor as a correlating parameter for the two-phase boundary. The problem of predicting compressibility factors for the saturated vapor and liquid phases is considered for both pure compounds and mixtures.

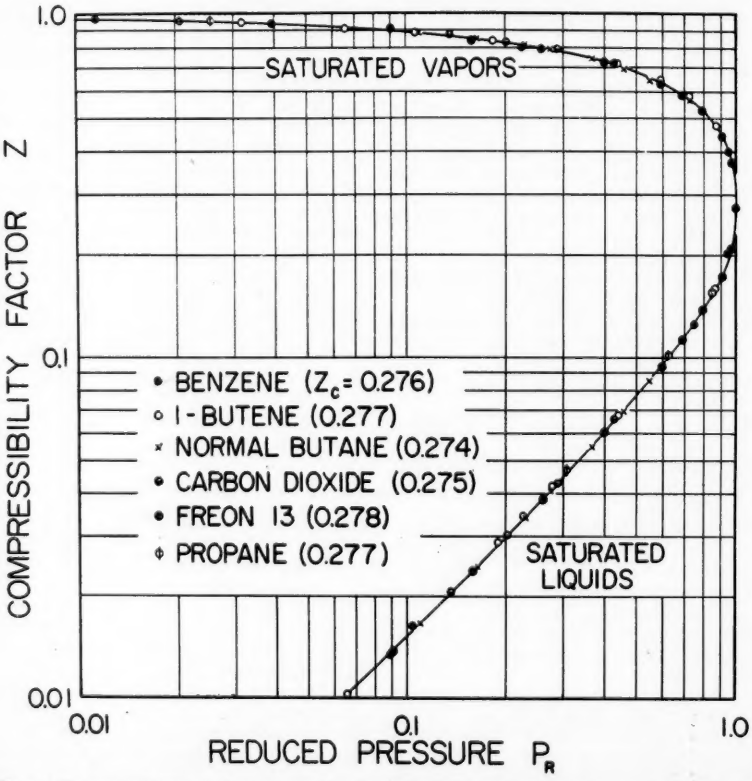

Fig. 1. Compressibility factors vs. reduced pressure for saturated pure compounds with Z_c values of approximately 0.275.

COMPRESSIBILITY FACTORS UNDER SATURATED CONDITIONS

Pure Compounds

The compressibility factor, defined by the equation

$$Z = \frac{PV}{RT} \tag{1}$$

is a state property of the system. Equation (1) may also be expressed in reduced form,

$$Z = \frac{P_r V_r Z_c}{T_r} \tag{2}$$

without affecting the exactness of the functional relationship between Z and the independent variables.

With discussion limited to the boundary of a two-phase region, specification of any one of the state variables is sufficient to define the state of the system. If P_r is arbitrarily selected as the independent variable, it follows from the principles of phase behavior that

$$V_r = f_1(P_r) \tag{3}$$

$$T_r = f_2(P_r) \tag{4}$$

Combining these relationships with Equation (2) gives

$$Z = f_3(P_r)Z_c \tag{5}$$

Equation (5) is of interest because it demonstrates the restriction imposed upon the theorem of corresponding states for successful correlation of the compressibility factor under saturated conditions, namely, that the same function of reduced pressure can apply only to those substances which have the same critical compressibility factor. Although Equation (5) applies specifically to univariant states, an analogous expression exists regardless of the number of independent variables required to define the state. This fact has long been recognized and several methods have been suggested for improving the generalized correlation for gases by compensating for the variations in Z_c. Su (*37*), following the principle of Onnes (*24*), has combined Z_c and V_r,

Meissner and Seferian (*21*) use Z_c as an additional variable to establish correction factors for the generalized chart based upon an average value of Z_c. Nelson and Obert (*22*), however, contend that differences in molecular structure may impair the correlation for substances with identical critical compressibility factors, and they suggest a molecular theorem of corresponding states as the more fundamental approach.

Cope, Lewis, and Weber (*6*) emphasized that f_2 is not a generalized function applicable to all compounds. In view of the restriction imposed by Equation (5), it is reasonable to assume that a similar restriction applies to the other state properties and that Equation (4) should be expressed in the form

$$T_r = f_2(P_r)_{constant\,Z_c} \qquad (6)$$

or, more generally,

$$T_r = f_4(P_r, Z_c) \qquad (7)$$

The general expression for the compressibility factor under saturated conditions would then include Z_c as an independent variable.

$$Z = f_5(P_r, Z_c) \qquad (8)$$

Equation (8) is fundamentally equivalent to Meissner and Seferian's procedure in establishing correction factors for the generalized chart for gases. In the current study, however, Z_c is considered as a unique property of the system which will justify the use of a single reduced-state variable to define the vapor-liquid equilibrium state for all substances with the same critical behavior.

Equation (7) is consistent with the work of Riedel (*29*), which presents a generalized reduced vapor-pressure equation in terms of an additional variable, α_c, defined as the slope of the logarithmic vapor-pressure curve at the critical point. In the present work the critical compressibility factor, Z_c, is considered analogous to Riedel's variable, α_c. Hougen and coworkers (*12*) have shown that the constant, A, in the reduced form of the Gamson and Watson (*9*) vapor-pressure relationship can be expressed as a unique function of the critical compressibility factor, lending additional support for the validity of Equations (7) and (8).

Correlation of Compressibility—Factor Data for Saturated Pure Compounds. The critical compressibility factors for most substances fall within the range of approximately 0.2 to 0.33. A large number of these show near constancy in their behavior at the critical point with a Z_c value of about 0.270. The various light-hydrocarbon series exhibit this property. While emphasizing the lack of any theoretical justification for a general reduced equation of state along the saturation curve, Cope, Lewis, and Weber (*6*) noted the excellent correlation between the compressibility factors for a number of saturated hydrocarbon vapors and the ratio P_r/T_r. Since the majority of these compounds have similar critical compressibility factors, and the use of P_r/T_r is equivalent to a single independent variable, $1/V_r$, their correlation is consistent with Equation (8). Equation (8), however, represents a more practical form for the graphical presentation of the same data.

The experimental volumetric data for the substances listed in Table 1 were considered in both the saturated vapor and liquid phases. The compressibility factors for six compounds having essentially similar values of Z_c are presented in Figure 1 to demonstrate the consistency of the data. The result is a single saturation curve expressed as a function of reduced pressure. The average absolute deviation is probably about 1% and the maximum deviation approximately 2%. The compressibility factors for the balance of the substances listed in Table 1 were found to deviate in a regular manner from the curve in Figure 1 in accordance

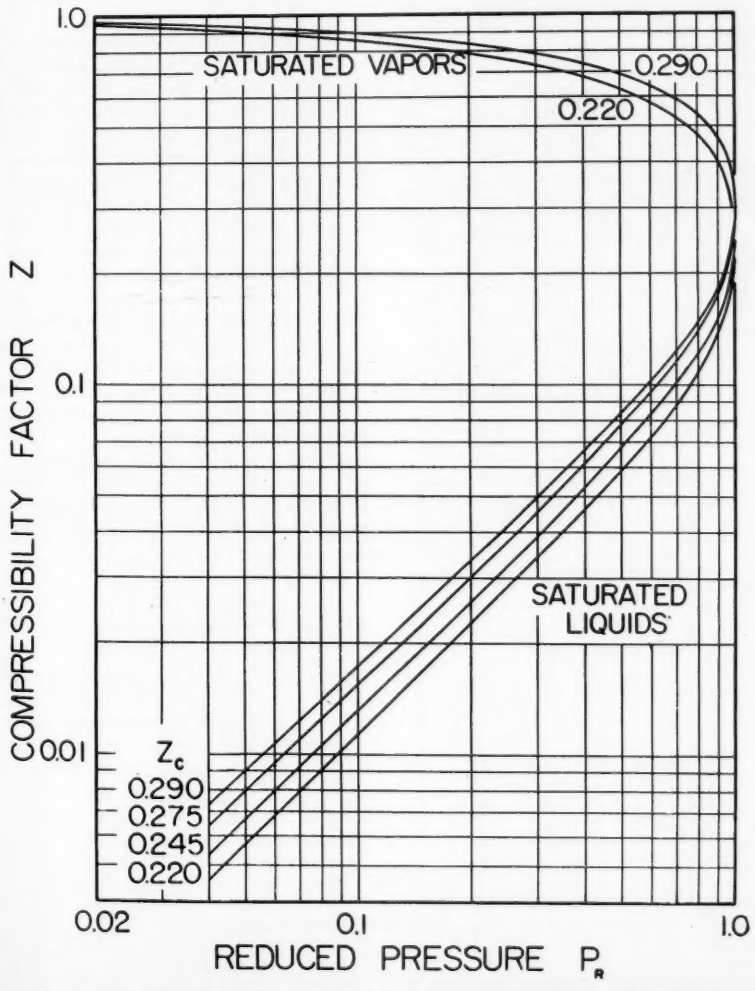

Fig. 2. Effect of Z_c on the compressibility factors for saturated pure compounds.

Table 1. Summary of Volumetric Data for Saturated Pure Compounds

Compound	Z_c	Literature reference
1-Butene	0.277	*24a*
Benzene	0.276	*25a*
Normal butane	0.274	*26*
Carbon dioxide	0.275	*30*
Ethane	0.285	*3*
Ethanol	0.248	*30a*
Ethylene	0.27	*42*
Freon 13	0.278	*1*
Normal heptane	0.260	*37*
Hydrogen sulfide	0.283	*27*
Methane	0.290	*19*
Methanol	0.220	*35a*
Nitrogen	0.291	*3a*
Normal pentane	0.269	*4*
Propane	0.277	*36*
Propylene	0.274	*5*
Sulfur dioxide	0.269	*31*
Water	0.230	*17a*

with the value of Z_c. Compounds with values of Z_c above 0.275 showed progressively higher compressibility factors over the entire range of reduced pressures consistent with the increased values of Z_c. A similar trend was noted below the curve.

The variation of the compressibility factors with Z_c is shown in Figure 2. Unique saturation curves are established for various values of the critical compressibility factor. The consistency between data for compounds having essentially the same value of Z_c was excellent over the entire range. Some inconsistencies were noted for water vapor, however, which would tend to substantiate Nelson and Obert's suggestion that differences in molecular structure may impair the correlation. The agreement in the liquid phase was found to be even better than in the vapor phase. This is of particular interest since the theorem has not been successfully applied to the correlation of liquid compressibility factors up to the present time. Watson (*40*) pointed out that deviations in the compressibility factors of liquids may vary as much as 20% at the same reduced conditions. The differences in critical compressibility factor may well account for these variations. It may be concluded from Figures 1 and 2 that a simple reduced equation of state for the vapor-liquid phase boundary is supported by the experimental volumetric data for any specific value of the critical compressibility factor. Theoretically, there would seem to be as much justification for a saturation curve based upon an average value of Z_c as there is for a generalized-compressibility-factor chart for the gas phase based upon an average value of Z_c. There is little question but that the accuracy of the compressibility-factor correlation under all conditions can be greatly improved by consideration of various values of Z_c. Under these conditions a unique saturation curve may be included.

Mixtures

Kay's empirical pseudocritical concept (*14*) has been widely used as a means of estimating the volumetric behavior of mixtures from the compressibility factors of the pure components. The method is based upon the concept of a hypothetical pure material the critical properties of which are so defined as to produce isometrics which coincide with those for the mixture. The critical constants of the hypothetical substance have been termed the *pseudocritical* properties of the mixture. In the following discussion reduced conditions for mixtures have been evaluated by use of pseudocritical properties rather than the actual critical properties of the mixture. This procedure permits direct comparison of the compressibility factors for mixtures with those of pure substances under the same reduced conditions.

Kay found that a simple summation of the products of the mole fractions and critical properties of the pure components provided a reasonable estimate of the pseudocritical constants. These summations may be expressed in the form of equations:

$$T_{pc} = \sum X_i T_{ci} \qquad (9)$$

$$P_{pc} = \sum X_i P_{ci} \qquad (10)$$

Kay's method is analogous to combining the equation-of-state constants for pure materials to obtain constants for the mixture.

Several other procedures, such as the one proposed by Joffe (*13*), have been suggested for estimating the pseudocritical properties of mixtures with a greater degree of precision. These relationships are much more complex than the simple linear molal average suggested by Kay, and since the latter method produces results close to the correct average, its use has continued.

The importance of the critical compressibility factor in correlating the volumetric behavior of saturated pure compounds suggests the need for an average value of Z_c for the mixture. Since most of the experimental volumetric data available for mixtures are for binary hydrocarbon systems, however, the present study was restricted to the use of Kay's method for predicting the volumetric behavior of saturated mixtures with an average critical compressibility factor of approximately 0.270.

Saturated Vapor Mixtures. The volumetric data for various mixtures of the ten systems listed in Table 2 were considered over a range of vapor pressures from approximately 1 atm. up to the actual critical point of the mixture. Cross plotting the experimental data for the saturated vapors of each mixture established eight reduced isotherms between 0.85 and 1.2. Each reduced isotherm was then plotted and compared with the compressibility factors published by Watson and Smith (*41* and *11*). Two typical isotherms have been illustrated in Figure 3. The saturation curve for pure compounds which was developed in the previous section is also included in Figure 3 for comparison.

A number of general conclusions may be reached on the basis of these comparisons. The data for reduced isotherms between 0.85 and 1.00, inclusive, show rather poor consistency. Deviations of more than 20% from the Watson and Smith curves were not uncommon and the errors in estimating the compressibility factors for saturated vapors are much larger than those normally encountered with the use of Kay's method in the superheated region. It was concluded, however, that the Watson and Smith relationships represent the data about as well as they can be represented at reduced pressures above 0.3 and reduced temperatures up to and including 1.0. Below

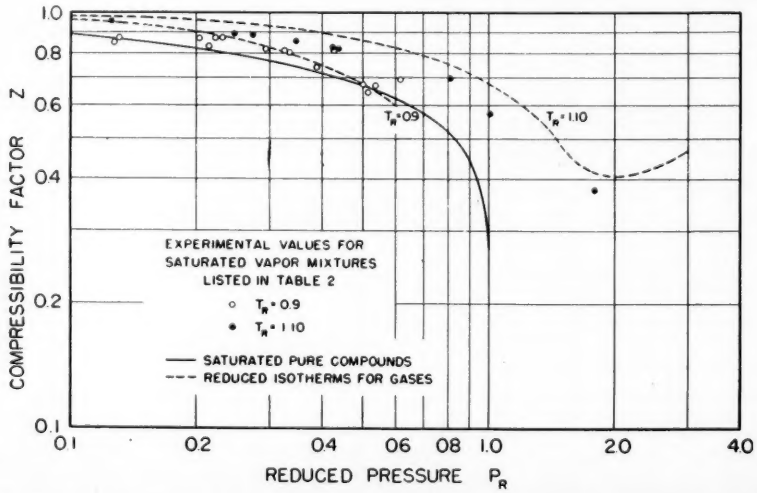

Fig. 3. Comparison of compressibility data for saturated vapor mixtures correlated by Kay's method (*14*) with reduced isotherms for pure gases (*41*).

TABLE 2. SUMMARY OF VOLUMETRIC DATA FOR SATURATED MIXTURES

Components	Number of compositions used	Literature reference
Methane—normal butane	3	*34*
Methane—normal pentane	4	*35*
Methane—decane	3	*33*
Methane—carbon dioxide	4	*24*
Methane—hydrogen sulfide	3	*27*
Ethylene—normal heptane	3	*17*
Ethane—normal butane	5	*16*
Ethane—normal heptane	5	*15*
Propane—normal butane	4	*23*
Propane—normal pentane	5	*32*
Propane—benzene	3	*10*

0.3 P_r the experimental compressibility factors are consistently lower than those which would be predicted by the curves.

Above 1.0 T_r the experimental compressibility factors show excellent internal consistency, as indicated by the data in Figure 3 for 1.1 T_r. The experimental data, however, fall below the Watson and Smith curves. This was generally true for all the reduced isotherms greater than unity. The difference is probably due to the approximate nature of Kay's method for estimating the pseudocritical properties of mixtures. The experimental data show much the same configuration as the existing gas-phase parameters, and it is reasonable to assume that a more accurate estimate of the pseudocritical point might bring the curves together. In this connection it would be interesting to study the effectiveness of Joffe's relationships; however this was not attempted in the present study.

Saturated Liquid Mixtures. The experimental data for saturated liquid mixtures were analyzed by the methods reported in the previous section. The binary systems indicated in Table 2 were also used as sources for liquid compressibility factors.

The results of the study are presented in Figure 4. Below a reduced temperature of 0.9 the compressibility factors for saturated liquid mixtures appear to be directly proportional to the reduced pressure and are independent of reduced temperature. This corresponds to the behavior of an incompressible fluid, and so the conclusion is undoubtedly an approximation. Over a wide range of reduced pressures, however, the compressibility factors for saturated liquid mixtures may be estimated by the relationship

$$Z = (0.153)P_r \qquad (11)$$

with reasonable accuracy. At lower reduced pressures the data for mixtures are superimposed on the relationship established for pure saturated liquids with a critical compressibility factor of 0.27. It will be noted that for mixtures the direct proportionality extends above a pseudoreduced pressure of 1.0. The effect of pseudoreduced temperature becomes significant above 0.9 T_r.

To illustrate the high degree of reproducibility of the data the experimental compressibility factors have been plotted for pseudoreduced isotherms of 0.9, 0.95, 1.0, 1.05, and 1.1. The pseudoreduced isotherms for saturated liquid mixtures show the same general configuration as the curves given by Watson and Smith for pure gases. The 1.0 T_r curve from their generalized chart is a satisfactory representation of the liquid data along the same reduced isotherm. Above 1.0 T_r the same displacement of the reduced isotherms that was noted for saturated vapors is also apparent in the liquid phase. The data for saturated vapors

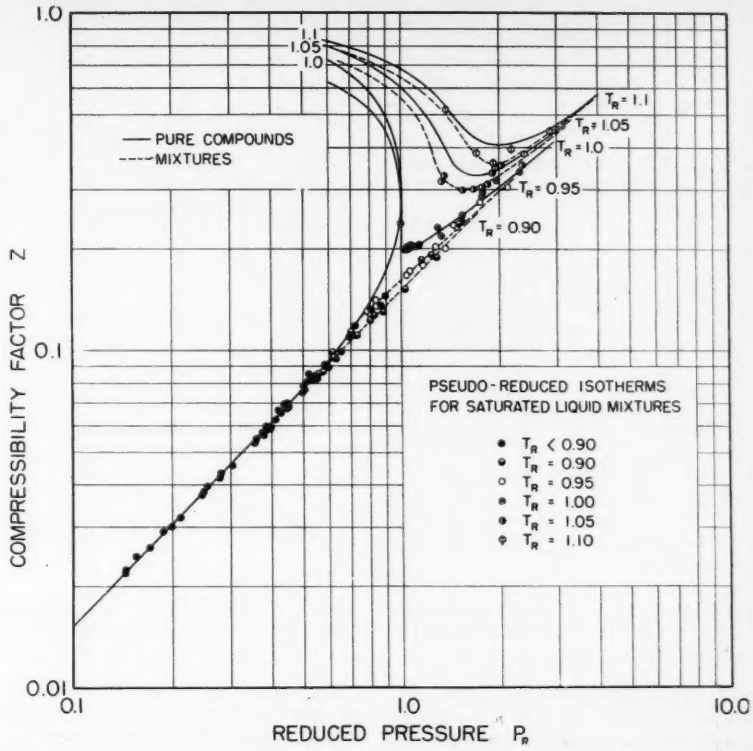

Fig. 4. Comparison of compressibility data for saturated liquid mixtures correlated by Kay's method (*14*) with the compressibility factors of pure compounds

overlapped the liquid compressibility factors, and the curves representing the liquid data are extensions of those previously established for the vapor phase. The compressibility factors show their greatest sensitivity in this range and a relatively small error in estimating the pseudocritical properties of the mixture might well account for the differences between the curves for pure gases and the data for mixtures.

Figure 4 demonstrates that it is possible to estimate the compressibility factors for saturated liquid mixtures from a generalized correlation extending over the entire two-phase region. The precision of the correlation for the liquid phase appears to be as good as if not better than that for the vapor phase.

SUMMARY AND CONCLUSIONS

A study of the compressibility factors for pure substances under saturated conditions indicated that a unique saturation curve can be expressed as a function of reduced pressure for compounds with the same critical compressibility factor. Saturation curves for various values of Z_c are presented in Figure 2.

TABLE 3. EFFECT OF Z_c ON THE COMPRESSIBILITY FACTORS OF PURE SATURATED VAPORS AND LIQUIDS

	Vapor phase			Liquid phase			
Z_c	0.290	0.275	0.220	0.290	0.275	0.245	0.220
				Z, Compressibility factor			
P_R							
0.02	—	—	—	0.00374	0.00329	0.00270	0.00223
0.04	0.947	0.940	0.922	0.00725	0.00636	0.00534	0.00451
0.07	0.920	0.915	0.886	0.0123	0.0109	0.00920	0.00793
0.10	0.898	0.892	0.856	0.0173	0.0152	0.0131	0.0113
0.20	0.838	0.830	0.785	0.0332	0.0299	0.0256	0.0226
0.30	0.786	0.780	0.734	0.0492	0.0450	0.0388	0.0341
0.40	0.746	0.730	0.683	0.0660	0.0613	0.0527	0.0459
0.50	0.688	0.680	0.633	0.0835	0.0780	0.0677	0.0585
0.70	0.591	0.582	0.529	0.118	0.116	0.102	0.0883
0.80	0.536	0.526	0.478	0.148	0.140	0.123	0.109
0.90	0.469	0.453	0.406	0.182	0.175	0.149	0.138
0.95	0.416	0.405	0.344	0.216	0.202	0.176	0.163
1.00	0.290	0.275	0.220	0.290	0.275	0.245	0.220

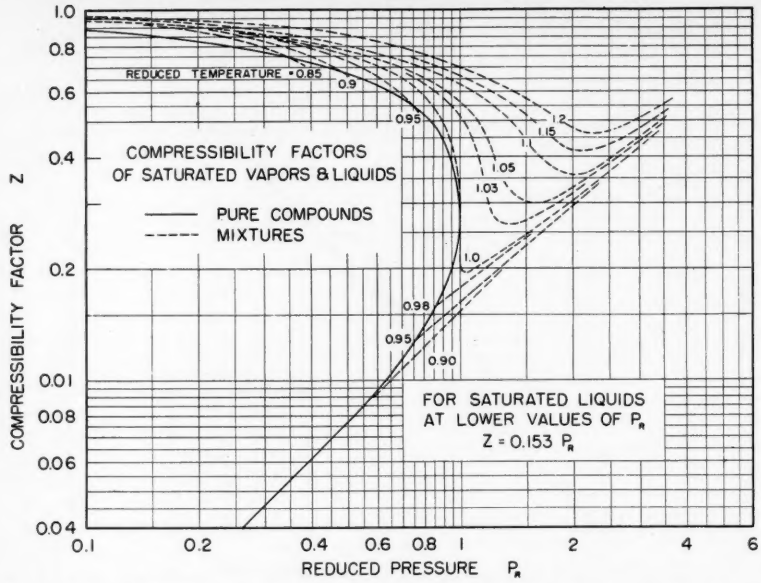

Fig. 5. Compressibility factors for saturated liquids and vapors of pure compounds and of mixtures based upon pseudoreduced properties estimated by Kay's method (*14*).

Compressibility factors for saturated mixtures in both the vapor and liquid phases were correlated over the entire two-phase region by means of pseudoreduced variables based upon Kay's pseudocritical concept (*14*). These data were then compared with Watson and Smith's (*41*) average-compressibility-factor chart for pure gases and with a saturation curve applicable to pure substances with a critical compressibility factor of 0.27. The comparisons are presented in Figures 3 and 4. The pseudoreduced isotherms for mixtures provide excellent correlation above 1.0 T_r, but fall below the corresponding isotherms for pure gases. The agreement between the vapor and liquid compressibility factors along a given pseudoreduced isotherm is also excellent.

Figure 5 summarizes the results of the study on mixtures and provides a graphical presentation of the pseudoreduced equations of state for both saturated vapors and liquids. Figure 5 applies specifically to Kay's method for estimating the pseudocritical properties of the mixture and differs from the average-generalized-compressibility-factor chart for pure gases. It is reasonable to assume that a more accurate method of determining the pseudocritical properties might produce better agreement. In view of the simplicity of Kay's method, however, the new relationships presented in Figure 5 would seem to be justified. Although this procedure may not be the most satisfactory one from the technical standpoint, it offers a practical method for estimating the compressibility factors of multicomponent hydrocarbon systems with a reasonable degree of precision. The absolute errors resulting from the use of Figure 5 are reported in Table 4 for a number of systems.

TABLE 4. REPRESENTATIVE ERRORS RESULTING FROM THE USE OF FIGURE 5 FOR ESTIMATING COMPRESSIBILITY FACTORS OF SATURATED MIXTURES

System	Range of compositions, mole %	Number of mixtures	Number of datum points	Average absolute error, %	Maximum error, %
		Saturated liquids			
Methane—normal butane	20.0 –60.0 methane	3	14	3.4	6.7
Ethane—normal butane	17.49–94.72 ethane	5	39	2.2	5.9
Ethane—normal heptane	26.54–96.85 ethane	4	41	2.7	10.0
Carbon dioxide—methane	33.3 –82.7 methane	4	12	15.0	27.0
Methane—normal pentane	10.0 –60.0 methane	3	12	3.7	14.9
Hydrogen sulfide—methane	10.0 –40.0 methane	3	8	10.7	21.8
Propane—benzene	12.1 –81.0 propane	4	20	2.4	10.9
		Saturated vapors			
Methane—normal butane	17.49–82.18 methane	2	9	4.0	8.2
Ethane—normal heptane	58.7 –88.71 ethane	2	14	6.3	10.6
Ethylene—normal heptane	28.57–89.31 ethane	3	12	2.6	6.8
Methane—normal pentane	20.0 –90.0 methane	6	20	4.3	9.8
Propane—normal pentane	14.68–85.50 *n*-pentane	5	21	2.7	4.3

LITERATURE CITED

1. Albright, L. F., and J. J. Martin, *Ind. Eng. Chem.*, **44**, 188 (1952).
2. *Am. Petroleum Inst. Research Proj.* 44, Table 21, Carnegie Inst. Technol., Pittsburgh (1953).
3. Barkelew, C. H., J. L. Valentine, and C. O. Hurd, *Trans. Am. Inst. Chem. Engrs.*, **43**, 25 (1947).

3a. Bloomer, O. T., and K. N. Rao, *Inst. Gas Technol. Research Bull.* 18 (1952).

4. Brydon, J. W., Nicholas Walen, and L. N. Canjar, *Chem. Eng. Progr. Symposium* Series No. 7, **49**, 151 (1953).
5. Canjar, L. N., Max Goldman, and Henry Marchman, *Ind. Eng. Chem.*, **43**, 1186 (1951).
6. Cope, J. Q., W. K. Lewis, and H. C. Weber, *loc. cit.*, **23**, 887 (1931).
7. Dodge, B. F., *loc. cit.*, **24**, 1353 (1932).
8. Edmister, W. C., *Petroleum Refiner*, **27**, No. 11, 656 (1948).
9. Gamson, B. W., and K. M. Watson, *Natl. Petroleum News* (Sept. 6, 1944).
10. Glanville, J. W., B. H. Sage, and W. N. Lacey, *Ind. Eng. Chem.*, **42**, 508 (1950).
11. Hougen, O. A., and K. H. Watson, "Chemical Process Principles: Part II, Thermodynamics," John Wiley and Sons, Inc., New York (1947).
12. Hougen, O. A., private communication (1955).
13. Joffe, J., *Ind. Eng. Chem.*, **39**, 837 (1947).
14. Kay, W. B., *Ind. Eng. Chem.*, **28**, 1014 (1936).
15. *Ibid.*, **30**, 459 (1938).
16. *Ibid.*, **32**, 353 (1940).
17. *Ibid.*, **40**, 1459 (1948).

17a. Keenan, J. H., and F. G. Keyes, "Thermodynamic Properties of Steam," John Wiley and Sons, Inc., New York (1936).

18. Lorentz, H. A., *Wied. Ann.*, **12**, 127, 660 (1881).
19. Matthews, C. S., and C. O. Hurd, *Trans. Am. Inst. Chem. Engrs.*, **42**, 55 (1946).
20. Meissner, H. P., *Ind. Eng. Chem.*, **33**, 1440 (1941).
21. ———, and Ralph Seferian, *Chem. Eng. Progr.*, **47**, 579 (1951).
22. Nelson, L. G., and E. F. Obert, *A.I.Ch.E. Journal*, **1**, 74 (1955).
23. Nysewander, C. N., B. H. Sage, and W. N. Lacey, *Ind. Eng. Chem.*, **32**, 118 (1940).

24. Olds, R. H., H. H. Reamer, B. H. Sage, and W. N. Lacey, *loc. cit.*, **41**, 475 (1949).
24a. Olds, R. H., B. F. Sage, and W. N. Lacey, *Ind. Eng. Chem.*, **38**, 301 (1946).
25. Onnes, H. Kamerlingh, *Commun. Phys. Lab. Univ. Leiden*, **11**, Suppl. 23, 115 (1912).
25a. Organick, E. I., and W. R. Studhalter, *Chem. Eng. Progr.*, **44**, 847 (1948).
26. Prengle, H. W., L. R. Greenhaus, and Robert York, Jr., *Chem. Eng. Progr.*, **44**, 863 (1948).
27. Reamer, H. H., B. H. Sage, and W. N. Lacey, *Ind. Eng. Chem.*, **42**, 140 (1950).
28. *Ibid.*, **43**, 976 (1951).
29. Riedel, L., *Chem. Ing. Tech.*, **26**, 83 (1954).
30. "Refrigerating Data Book," 5 ed., Am. Soc. Refrigerating Engrs., New York (1942).
30a. Reid, R. C., and J. M. Smith, *loc. cit.*, **47**, 415 (1951).
31. Rynning, D. F., and C. O. Hurd, *Trans. Am. Inst. Chem. Engrs.*, **41**, 265 (1945).
32. Sage, B. H., and W. N. Lacey, *Ind. Eng. Chem.*, **32**, 992 (1940).
33. Sage, B. H., H. M. Lavender, and W. N. Lacey, *loc. cit.*, p. 743.
34. Sage, B. H., B. L. Hicks, and W. N. Lacey, *loc. cit.*, p. 1085.
35. Sage, B. H., H. H. Reamer, R. H. Olds, and W. N. Lacey, *loc. cit.*, **34**, 1108 (1942).
35a. Smith, J. M., *loc. cit.*, **44**, 521 (1948).
36. Streans, W. V., and E. J. George, *loc. cit.*, **35**, 602 (1943).
37. Stuart, E. B., K. T. Yu, and J. Coull, *Chem. Eng. Progr.*, **46**, 311 (1950).
38. Su, G. J., *Ind. Eng. Chem.*, **38**, 803 (1946).
39. van der Waals, J. D., "Die Continuität des gasförmigen und flüssigen Zustandes," Part II, Barth, Leipzig (1900).
40. Watson, K. M., *Ind. Eng. Chem.*, **35**, 398 (1943).
41. ———, and R. L. Smith, *Natl. Petroleum News* (July, 1936).
42. York, Robert, Jr., and E. R. White, Jr., *Trans. Am. Inst. Chem. Engrs.*, **40**, 227 (1944).

Presented at A.I.Ch.E. Detroit meeting

Turbulent Exchange of Mass and Momentum with a Boundary

THOMAS J. HANRATTY

University of Illinois, Urbana, Illinois

Visual observations by Fage and Townend of the behavior of a turbulent-flow stream near a boundary and experimental data by Lin, Moulton, and Putnam of concentration profiles near a boundary contradict the commonly held concept of the "laminar sublayer." A model developed by Higbie and Danckwerts which is consistent with the visual observations of Fage and Townend is used to describe the exchange of mass and heat between a turbulent fluid and a solid surface. It is postulated that masses of fluid are continuously moving to and from the wall. The exchange process then depends on the average contact time of these fluid masses with the wall.

The agreement of the concentration profile predicted on the basis of the proposed model with experimental mass transfer data where the exchange process is rate controlling lends support to the usefulness of the model. No equivalent data are available for velocity profiles. Velocity data represent a condition where the transport process within the fluid is playing an important role; however, in the immediate vicinity of the wall the proposed model might serve as a rough approximation of the profile. Such an approximation is made in this paper, and the agreement obtained is much better than should be expected.

That rates of momentum, heat, and mass transfer in a turbulent field are very much smaller in the vicinity of a surface than in the main body of a fluid has been recognized for a long time. In order to explain this phenomenon it has been postulated that there exists a thin nonturbulent layer of fluid adjacent to the wall. In this "laminar sublayer" momentum, heat, and mass are transported by random motion of the molecules rather than motion of macroscopic masses. As would be predicted by such a model, velocity-profile data extrapolate to a linear relationship between the velocity and distance in the vicinity of the wall. If, as is commonly assumed, the edge of the laminar sublayer is at the point where the velocity data deviate from linearity, its thickness may be calculated from the following empirical equation:

$$\frac{\delta_b}{d} = \frac{5}{Re}\sqrt{\frac{8}{f}} \qquad (1)$$

Fage and Townend (*1*) studied the behavior of fluid in the immediate vicinity of the wall by examining under the ultramicroscope the motion of dust particles in turbulently flowing water. The conditions of their experiments were such that the laminar-sublayer thickness as calculated by Equation (1) was about 0.03 in. Their experiments gave no evidence of the existence of a region possessing rectilinear motion. The following is a description of the flow very near the boundary given by Fage and Townend:

> With this magnification particles with a distance of 0.001 inch (0.0023*s*) from the surface were in focus. The view obtained showed a large number of particles moving in sinuous paths, and a few very slow particles which in the absence of a hairline in the eyepiece appeared to be moving in rectilinear paths.... The slowest particles seen were therefore moving with a mean velocity of about 0.006 feet per second, and since the gradient $\partial(V/V_0)/\partial(n/s)$ at the surface was roughly 14, the distance of these particles from the surface was of the order of 1/40,000 inch. Attention could therefore be confined to the motion of particles at this distance from the boundary.
>
> It was first thought that these particles were moving in rectilinear paths, but it was noticed that their axial motions were frequently jerky (u, comparable with V, see later), and that sometimes they almost came to rest. A hairline was then inserted in the eyepiece of the microscope, and it subsequently appeared that all such particles moving near the hairline usually crossed and recrossed it several times. A considerable time was spent in observing these particles and the impression formed was that no particle was ever seen about which it could be said with conviction that its motion was rectilinear. In addition to these very slowly moving particles other faster particles could be observed at the same time on account of the finite thickness of fluid (0.001 inch) within the focus of the microscope. It occasionally happened that a group of

these particles made unusually large lateral excursions, and it was always observed that on these occasions the slowly moving particles would appear to shift laterally to other paths slightly removed from their previous ones. Sometimes two or more slowly moving particles, often widely separated, were observed to shift in step, and the whole appearance suggested that the violent motion in the faster moving fluid dragged the whole surface layer bodily sideways. It should follow that smaller lateral motions would also drag the surface layer sideways, but might do so to an extent too small to be observed, with the result that the flow during the intervals between these excursions would appear to be in rectilinear motion. It should also follow that below the critical speed, where no fluctuations in the motion were observed, the flow at the surface should be rectilinear. In turbulent flow v (velocity perpendicular to the boundary) is small but presumably finite near the boundary (except of course at the boundary), and the jerkiness of the axial motion due to the large fluctuations in u will be associated with the combined effect of very small changes in v and the large velocity gradient $(\partial U/\partial y)$ at the boundary.

Further evidence that in turbulent flow the fluid near the surface moves in relatively large masses was obtained during the experiments with the rotating objective now to be described.

Another contradiction of the commonly accepted concept of the laminar sublayer is reflected in a recent correlation by Lin, Moulton, and Putnam (*2*) of mass transfer data and of concentration profiles near the surface of concentration-polarized electrodes. The authors carried out experiments on the deposition of cadmium metal from cadmium sulfate solution onto a thin layer of fresh mercury supported on a smooth silver plate. The concentration distribution near the surface of the electrode was measured by means of light interference with a Mach-Zehnder type of interferometer. Measurements were carried out in a rectangular chamber under conditions such that the Reynolds number varied from 4,000 to 12,400. The Schmidt number was 900. Owing to the high Schmidt number the concentration of cadmium ions was essentially constant throughout the fluid and dropped from its main-stream value to zero at the wall within a space of less than 1 mm. The concentration profile was thus greatly dependent on conditions in the region described by Equation (1). The authors, finding it impossible to explain these measurements on the basis of a sublayer in laminar motion, assumed that turbulence existed in the laminar sublayer in which the eddy diffusion coefficient could be described approximately by the expression

$$\frac{\epsilon}{\mu} = \left(\frac{y^+}{14.5}\right)^3 \qquad (2)$$

Likewise in the correlation of mass transfer data over a wide range of Schmidt numbers Lin, Moulton, and Putnam (*2*), as well as Deissler (*3*), had to introduce turbulence into the laminar sublayer.

Visual observations of fluid behavior near a boundary and experimental data on rates of turbulent mass transfer and on concentration profiles, therefore, indicate either that the laminar sublayer is much thinner than has commonly been assumed or that it is nonexistent. If the first alternative be true, change of temperature, concentration, and velocity through it would be small and the sublayer would be unimportant as a transfer resistance.

In either case it appears as if it might be profitable to examine other models for explaining the turbulent exchange of heat, mass, and momentum with a solid surface or for describing the resistance to transfer in the region commonly ascribed to the laminar sublayer.

One such model which is consistent with the visual observation of Fage and Townend has been formulated by Danckwerts (*4*). It was first proposed by Higbie (*5*) to explain mass transfer in two-phase systems. According to this theory, the fluid in the immediate vicinity of the wall is not a continuous laminar layer but is discontinuous. Masses of fluid are pictured as moving to and from the wall, causing a continual change of the fluid in contact with the wall. The exchange of heat, mass, and momentum with the wall may then be visualized as occurring in the following manner. A mass of fluid comes in contact with the wall and its surface layer immediately assumes an equilibrium condition with the wall (same temperature, equilibrium concentration, zero velocity). Exchange of momentum, heat, and mass with the wall occurs. Just as with the unsteady heating or cooling of a block of metal, the rate of exchange between this fluid mass and the wall decreases with time. Eventually the mass of fluid is replaced and the whole process repeated. The contact time of these masses of fluid with the wall will vary. The smaller the average contact time of all masses of fluid coming in contact with the wall, the larger will be the measured exchange rate with the wall.

This paper has been written to show how such a model might be used to describe the measured concentration profiles of Lin, Moulton, and Putnam. It will also be shown that measured velocity profiles are not contradictory to the model. However, much more stringent assumptions must be made in the treatment of the velocity-profile data.

DISCONTINUOUS-FILM MODEL

Mathematical Formulation

Mathematical formulation of the discontinuous-film model will be accomplished by first considering the history of the surface layers of a fluid mass which comes in contact with the wall and then averaging the effect of all masses which will come in contact with the wall to calculate the exchange rate between the fluid and the surface.

If there is very little motion in surface layers of the fluid contacting the wall, then mass will be transferred through these layers by molecular diffusion and Fick's law will be applicable:

$$\frac{\partial C}{\partial \theta} = D\,\frac{\partial^2 C}{\partial y^2} \qquad (3)$$

For the data of Lin, Moulton, and Putnam the Schmidt number was high. Momentum is therefore transported much more rapidly than mass and the foregoing assumption is probably valid.

At high Schmidt numbers the concentration changes from the midstream value to an equilibrium value with the wall in a very short distance. For the experiments of Lin, Moulton, and Putnam, this was less than 1 mm. Therefore it will be assumed that the concentration of diffusing substance in a fluid mass approaching the wall will be uniform and equal to the midstream concentration. If the contact time is small enough, then the extent of the fluid mass in the y direction will not be important. Solutions for a semiinfinite medium may be used. With the following boundary conditions assumed

$$y = 0 \qquad C = C_W$$

$$y = \infty \qquad C = C_L$$

$$\theta = 0 \qquad C = C_L$$

Equation (3) may be solved for the concentration distribution and the rate of mass transfer (*6*):

$$\left(\frac{C - C_W}{C_L - C_W}\right) = \text{erf}\left(\frac{y}{2\sqrt{D\theta}}\right) \qquad (4)$$

$$(N_A) = (C_L - C_W)\sqrt{\frac{D}{\pi\theta}} \qquad (5)$$

Equations (4) and (5) give the concentration distribution and the instantaneous rate of mass transfer for a fluid mass which has been in contact with the wall for a time θ. For fluid masses having total contact lifetimes with the wall equal to θ_c, the probability for a contact time between θ and $\theta + d\theta$ is

$$\psi(\theta)\,d\theta = \frac{d\theta}{\theta_c} \qquad (6)$$

If all fluid masses had a contact lifetime of θ_c, then the measured concentration profile and rate of mass transfer would be

$$\left(\frac{C - C_W}{C_L - C_W}\right)_{\theta_c} = \int_0^{\theta_c} \text{erf}\left(\frac{y}{2\sqrt{D\theta}}\right)\frac{d\theta}{\theta_c} \qquad (7)$$

$$(N_A)_{\theta_c} = \int_0^{\theta_c} (C_L - C_W)\sqrt{\frac{D}{\pi\theta}}\,\frac{d\theta}{\theta_c}$$

$$= 2(C_L - C_W)\sqrt{\frac{D}{\pi\theta_c}} \qquad (8)$$

Actually, however, there will be a variation in the contact lifetime which must be taken into account. If the probability that a fluid mass possesses a lifetime between θ_c and $\theta_c + d\theta_c$ be defined as $\phi\, d\theta_c$, Equations (7) and (8) may be summed to give the actual measured average concentration distribution and transfer rate.

$$\frac{C - C_W}{C_L - C_W} \qquad (9)$$

$$= \int_0^\infty \phi(\theta_c)\left[\frac{1}{\theta_c}\int_0^{\theta_c} \operatorname{erf}\left(\frac{y}{2\sqrt{D\theta}}\right)d\theta\right]d\theta_c$$

$$N_A = \frac{2(C_L - C_W)}{\sqrt{\pi}} \int_0^\infty \phi(\theta_c)\sqrt{\frac{D}{\theta_c}}\,d\theta_c \qquad (10)$$

A mass transfer coefficient may be defined in the following manner:

$$K = \frac{N_A}{C_L - C_W}$$

$$= \frac{2}{\sqrt{\pi}} \int_0^\infty \phi(\theta_c)\sqrt{\frac{D}{\theta_c}}\,d\theta_c \qquad (11)$$

Application to Measured Concentration Profiles

Use of Equations (9), (10), and (11) depends upon the evaluation of the probability function, $\phi(\theta_c)$, which has been assumed to have the form

$$\phi(\theta_c) = Ae^{-(\theta_c/\tau)^n} \qquad (12)$$

where A and τ are constants. The constant A may be evaluated in terms of τ from the relation

$$\int_0^\infty \phi(\theta_c)\, d\theta_c = 1 \qquad (13)$$

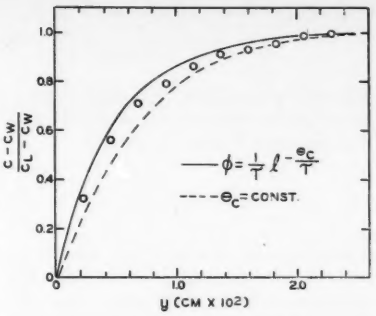

Fig. 1. Comparison of theory with measured concentration profiles.

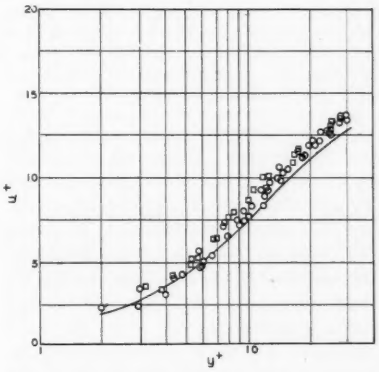

Fig. 2. Comparison of theory with measured velocity profiles.

The constant τ may be evaluated from experimental measurements of the mass transfer coefficient K. Table 1 presents the final form of a number of assumed probability functions for the age of the fluid masses. Form 1 represents the case in which the contact times of the fluid masses coming to the wall are of such a small range that their effect can be calculated by considering all these masses to have the same θ_c. For this case the concentration profile may be calculated by Equation (7). The contact time θ_c may be evaluated from data on K by the equation presented in Table 1.

Table 1. Probability Functions Representing the Distribution of Eddy Ages

Probability function	From Equation (26)	From Equation (21)	
1. θ_c = constant		$K = 2\sqrt{\frac{D}{\theta_c\pi}}$	$\theta_c = \frac{4D}{\pi K^2}$
2. $Ae^{-\theta_c/\tau}$	$A = \frac{1}{\tau}$	$K = \sqrt{\frac{D}{\tau}}$	$\tau = \frac{D}{K^2}$
3. $Ae^{-(\theta_c/\tau)^2}$	$A = \frac{2}{\sqrt{\pi}\,\tau}$	$K = \frac{\Gamma(1/4)}{\pi}\sqrt{\frac{D}{\tau}}$	$\tau = \frac{D}{K^2}\left[\frac{\Gamma(1/4)}{\pi}\right]^2$
4. $Ae^{-(\theta_c/\tau)^3}$	$A = \frac{3}{\tau\Gamma(1/3)}$	$K = \frac{\Gamma(1/6)}{\Gamma(1/3)}\sqrt{\frac{D}{\pi\tau}}$	$\tau = \frac{D}{\pi K^2}\left[\frac{\Gamma(1/6)}{\Gamma(1/3)}\right]^2$
5. $Ae^{-(\theta_c/\tau)^4}$	$A = \frac{4}{\tau\Gamma(1/4)}$	$K = \frac{\Gamma(1/8)}{\Gamma(1/4)}\sqrt{\frac{D}{\pi\tau}}$	$\tau = \frac{D}{\pi K^2}\left[\frac{\Gamma(1/8)}{\Gamma(1/4)}\right]^2$

Table 2. Effect of Assumed Probability Function Upon Calculation of $(C - C_W)/(C_L - C_W)$

Measured $(C - C_W)/(C_L - C_W) = 0.59$ (1) $y = 0.50 \times 10^{-2}$ cm.

Probability function	Calculated $\frac{C - C_W}{C_L - C_W}$
Constant Age	0.50
$Ae^{-\theta_c/\tau}$	0.64
$Ae^{-(\theta_c/\tau)^2}$	0.66
$Ae^{-(\theta_c/\tau)^3}$	0.66
$Ae^{-(\theta_c/\tau)^4}$	0.67

Equation (9) was used to calculate the concentration profile for test 87 of Lin et al. Data for K presented by Deissler (3) were used. The calculations and experimental measurements are presented in Figure 1. Only the probability functions represented by forms 1 and 2 of Table 1 were used in the graph. The particular probability function used did not appear greatly to affect the calculated profile. This is illustrated in Table 2 where calculated values of $(C - C_W)/(C_L - C_W)$ at $y = 0.50 \times 10^{-2}$ cm. are presented for different assumed-probability functions.

The agreement between the predicted and measured values, as presented in Figure 1, indicates that the discontinuous-film model supplies a satisfactory representation of these data. The agreement, in fact, is quite gratifying, as no arbitrary constants were used in the calculation. The profiles were predicted entirely from experimental values of K. This, of course, does not prove that the discontinuous-film model is a description of actuality. It shows only that it is a model which gives a better description than the laminar sublayer of the data of Lin, Moulton, and Putnam (2) and which is not in contradiction to the visual observations of Fage and Townend (1).

Since one of the arguments in support of the laminar-sublayer concept is the prediction of velocity data, it would be desirable to examine the reasonableness of the discontinuous-film model in light of these data. Such an examination presents difficulties which cannot be entirely overcome, but after some simplifying assumptions are made it may be attempted. The results of the comparison will be presented not to support the discontinuous-film model but only to show that velocity-profile data are not in contradiction to it.

COMPARISON OF VELOCITY DATA

The prediction of velocity data in the immediate vicinity of the wall on the

basis of the discontinuous-film model is handicapped for the following reasons.

1. Under the conditions under which all the velocity data have been obtained, the rate of transport of momentum to the vicinity of the wall is important. The exchange of momentum with the wall is not controlling. The velocity does not increase to the free-stream velocity in the region commonly ascribed to the laminar sublayer. It is therefore difficult to ascribe an average velocity to the fluid masses arriving at the wall.

2. The average velocity measured at any point in a turbulent field represents contributions of eddies of different frequencies. The probability of any individual eddy having a particular velocity will depend on its frequency. Consequently, the velocity of a mass of fluid arriving at the wall will probably be dependent upon the amount of time during which the mass will be in contact with the wall. This presents a degree of complication over the description of the mass and heat transfer processes, as to describe the phenomenon accurately a double probability function would be needed, expressing the probability that a mass of fluid will have a velocity between $u_L + du_L$ and a contact time between θ_c and $\theta_c + d\theta_c$.

3. The model proposes only to describe the exchange of momentum with the wall. The diffusion of momentum to the wall is probably governed by a more complex process than is represented by the model. Consequently predicted velocity profiles in the vicinity of the wall should be regarded only as a first approximation.

In order to circumvent these difficulties the following assumptions will be made.

1. The wall exchange process on the average can be represented by the motion of masses of fluid possessing a fixed velocity u_L and a fixed wall-contact time θ_c.

2. The transport of momentum within any one of these masses can be represented by the equation

$$\frac{\partial u}{\partial \theta} = \frac{\mu}{\rho}\left(\frac{\partial^2 u}{\partial y^2}\right) \tag{14}$$

By use of the boundary conditions

$$y = 0 \qquad u = 0$$

$$y = \infty \qquad u = u_L$$

$$\theta = 0 \qquad u = u_L$$

Equation (14) may be solved to give the velocity distribution and the instantaneous rate of momentum transfer with the wall for a fluid mass which has been in contact with the wall for a time θ (*6*).

$$u = u_L \operatorname{erf}\left(\frac{y}{2\sqrt{\frac{\mu}{\rho}\theta}}\right) \tag{15}$$

$$\tau_0 g_c = \rho u_L \sqrt{\frac{\mu}{\rho \pi \theta}} \tag{16}$$

Now the probability for a fluid mass to have been in contact with the wall for a time between θ and $\theta + d\theta$ is

$$\psi(\theta)\, d\theta = \frac{d\theta}{\theta_c} \tag{6}$$

Averaging the effect of all masses in contact with the wall gives the predicted measured velocity distribution and the predicted measured rate of momentum transfer to the wall

$$u = \frac{u_L}{\theta_c}\int_0^{\theta_c} \operatorname{erf}\left(\frac{y}{2\sqrt{\frac{\mu}{\rho}\theta}}\right) d\theta \tag{17}$$

$$\tau_0 g_c = \int_0^{\theta_c} \rho u_L \sqrt{\frac{\mu}{\rho \pi \theta}}\,\frac{d\theta}{\theta_c}$$

$$= 2\rho u_L \sqrt{\frac{\mu}{\rho \pi \theta_c}} \tag{18}$$

By use of Equation (18), the expression for the velocity distribution, Equation (17), may be put into a form which can be compared with experimental data:

$$\frac{u}{\sqrt{\tau_0/\rho}} = \frac{u_L}{\sqrt{\tau_0/\rho}} \cdot \int_0^1 \operatorname{erf}\left(\frac{y^+\sqrt{\tau_0/\rho}\,\sqrt{\pi}}{u_L 4\sqrt{\theta/\theta_c}}\right) d\left(\frac{\theta}{\theta_c}\right) \tag{19}$$

Equation (19) gives a first approximation of the velocity profile in the vicinity of the wall based on the discontinuous-film model using the assumptions outlined in this section. Essentially it embodies one arbitrary constant, $u_L/\sqrt{\tau_0/\rho}$.

In order to carry out a comparison with experimental data it has been assumed that

$$\frac{u_L}{\sqrt{\tau_0/\rho}} = 13.5 \tag{20}$$

This expression arises from a consideration of measurements of velocity profiles (*2* and *3*). When these data are plotted on semilog paper two distinct regions are noted. The major portion of the data fall on a straight line. However, very close to the wall there is a break from this linearity. The portion of the field represented by the straight line has usually been referred to as the *turbulent core* and the nonlinear region has been referred to as the *buffer layer* and the *laminar sublayer*. It seems reasonable to assume that the latter region is the one over which the influence of the wall is felt. Therefore the fluid masses moving against the wall have been assumed to possess a velocity equal to that at the break point. This break point occurs at $y^+ = 30$ and the value of $u/\sqrt{\tau_0/\rho}$ represented by Equation (20).

Substituting Equation (20) into Equation (19) results in the following relation between $u^+ = u/\sqrt{\tau_0/\rho}$ and y^+.

$$\frac{u}{\sqrt{\tau_0/\rho}} = 13.5 \cdot \int_0^1 \operatorname{erf}\left(\frac{y^+\sqrt{\pi}}{13.5 \times 4 \times \sqrt{\theta/\theta_c}}\right) d\left(\frac{\theta}{\theta_c}\right) \tag{21}$$

Owing to the boundary conditions selected, $u = u_L$ at $y = \infty$, one would expect the foregoing expression to hold only for values of y^+ much less than 30.

Equation (21) has been plotted in Figure 2 along with experimental data presented by Deissler (*3*). The agreement is far better than would be suspected. Actually even better agreement would have been obtained by use of a larger value of $u_L/\sqrt{\tau_0/\rho}$ in Equation (19).

NOTATION

C = concentration
C_L = concentration of diffusing material in fluid mass before contact with the wall
C_W = concentration at the wall
d = pipe diameter
D = molecular diffusion coefficient
f = Fanning friction factor = $4\tau_0/(\frac{1}{2}\rho U_0^2)$
K = mass transfer coefficient = $N_A/(C_L - C_W)$
N_A = rate of mass transfer per unit area
Re = Reynolds number = $(dU_0\rho)/\mu$
$2s$ = length of side of square pipe
u, U = velocity in axial direction
U_0 = average fluid velocity
u_L = velocity in axial direction of fluid mass before contact with the wall
u^+ = $u/\sqrt{(\tau_0 g_c)/\rho}$
y = perpendicular distance from the wall
y^+ = $y\sqrt{(\tau_0 g_c)/\rho}\,\rho/\mu$
δ_b = thickness of laminar sublayer
θ = time
θ_c = total time for which a fluid mass had been in contact with the wall
μ = fluid viscosity
ρ = fluid density
τ = constant appearing in distribution function
τ_0 = shear stress at the wall

LITERATURE CITED

1. Fage, A., and H. C. H. Townend, *Proc. Roy. Soc. London*, **135A**, 656 (1932).
2. Lin, C. S., R. W. Moulton, and G. L. Putnam, *Ind. Eng. Chem.*, **45**, 636, 640 (1953).
3. Deissler, R. G., *Natl. Advisory Comm. Aeronaut. Tech. Note* 3145 (May, 1954).
4. Danckwerts, P. V., *Ind. Eng. Chem.*, **43**, 1460 (1951).
5. Higbie, R., *Trans. Am. Inst. Chem. Eng.* vs. **31**, 65 (1935).
6. Carslaw, H. S., and J. C. Jaeger, "Conduction of Heat in Solids," Oxford University Press, London (1947).

Fractionation During Condensation of Vapor Mixtures

ERIC R. KENT and ROBERT L. PIGFORD

University of Delaware, Newark, Delaware

Partial condensers of the reflux type are capable of producing substantial fractionation of vapor mixtures. For vapor products having low dew points they may be preferred to conventional equipment for adiabatic distillation plus total condensation.

Experimental studies of a condenser used to fractionate mixtures of ethylene dichloride and toluene show that observed mass transfer effects are in agreement with the Colburn-Drew film theory, which accounts for the influence of the net mass exchange on the relative mass transfer rates of the components. In an adaptation of the transfer-unit concept to partial condensation, new equations are derived relating the number of transfer units to liquid- and gas-phase resistances, surface area, and amount of condensation. Observed resistances to mass transfer agree qualitatively with values independently measured; the diffusional resistance of the liquid phase has a pronounced effect on the fractionation, which does not conform to the Rayleigh theory of equilibrium differential condensation.

Partial condensers appear to require more interfacial area than adiabatic distillation equipment in order to produce the same fractionation at the same heat load; for the same interfacial area condensers require more heat removal.

Although only the system ethylene dichloride–toluene was investigated here, the results of this work are believed pertinent to other binary liquid mixtures also. Knowledge of the vapor-liquid equilibrium relationship of the new system and of the liquid and vapor-phase transfer coefficients is required in order to employ the calculation methods introduced here.

Design of heat transfer equipment for the condensation of vapors is carried out according to well-established procedures in two extreme cases. In the first, the vapor phase is composed of a pure component, and only heat transfer considerations are involved, all the thermal resistance on the vapor side of the heat transfer surface being in a liquid condensate film that covers the surface. Here the problem is essentially that of estimating the thickness of this film and its effective thermal conductivity (*12*). In the second case the vapor is a mixture of components, one of which does not condense and is not soluble in the condensed phase. The problem still involves the estimation of the thermal resistance of the condensate layer, though the really important step in the design procedure is the estimation of the diffusional resistance offered by the gas phase to the mass transfer of the condensing component to the vapor-liquid interface. When only a single component condenses, the diffusion calculations are simple in principle (*2, 9, 10, 11*).

If more than one component condenses —a case intermediate between the two extreme cases—two new rate processes need to be considered carefully: the influence of the net flux of mass through the vapor phase on its diffusional resistance must be included, particularly when large concentrations of inert components are not present, and the diffusional resistance of the liquid mixture composing the condensate layer must be estimated and allowed for. Although the extended calculations are not expected to be difficult in principle, the necessary studies of diffusional mechanism having been partially worked out in previous investigations (*1*), no data on condensers have been available to determine whether computations made according to logical procedures would agree with observed performance.

The use of partial condensers in conjunction with distillation apparatus is not new. When the overhead product is composed of light and heavier components, reflux is provided for the fractionator by condensing mainly the heavier components, the distilled product being kept in the vapor state. In such concurrent-flow operations the vapor product and the condensed liquid leave the condenser together and even the apparatus that is most efficient in promoting mass transfer can do no better than cause the exit streams to reach phase equilibrium with each other. Thus the enrichment accomplished in such a device cannot exceed that equivalent to a single theoretical plate or equilibrium contact.

There are process situations, however, in which it may be advantageous to provide for as large a composition change in the condenser as can be achieved. This may occur, for example, if the condensation of even a portion of the vapor leaving a distillation column would require a refrigerated coolant. In this event it might be desirable to feed vapor containing appreciable quantities of heavy components to the bottom of a countercurrent partial condenser, sometimes referred to as a *backward-return* type of unit because the vapor and liquid products leave at opposite ends of the heat transfer surface. Under these conditions a very efficient condenser can produce a liquid stream that may be nearly at equilibrium with the entering vapor and the exit vapor may be much more concentrated in the volatile components. A substantial part of the heat removed from the condensing phase may be transferred to the coolant at a higher temperature than would be possible if the fractionation were done in a conventional adiabatic distillation unit producing the same light-distillate stream.

When a partial condenser of this type is to be designed to provide for efficient fractionation of components having comparable volatilities, presently available design procedures are incapable of determining the heat load or reflux requirements. Furthermore, the estimation of the required condensate surface appears difficult, as it depends both on the required heat load and on the specified composition change. What is apparently needed is a method of combining heat transfer and mass transfer computations in an extended version of the separate procedures that have been devised previously for the two extremes of condensers for pure components and for single condensable components mixed with inert gases.

THEORY

In the condensation of both components simultaneously from a binary vapor mixture there is a net flux of mass toward the interface which transports both types of molecules, assisting the diffusion of the less volatile component through the laminar fluid near the interface and hindering that of the more volatile component. The net rate of mass transport is of course proportional to the rate of heat transfer, and the problem under discussion is essentially that of describing the influence of the heat flux at the

E. R. Kent is at present with Socony Mobil Oil Company, Paulsboro, New Jersey.

interface on the diffusional resistance of the liquid and vapor phases. The problem is not a new one. It was considered first by Colburn and Drew (*1*) in a paper on the condensation of binary vapor mixtures. Although this early work provided the mathematical methods needed to subdivide the total local mass flux into the portions due to the two kinds of molecules, no attempt was made by these authors to apply their equations to heat transfer surfaces of finite extent and no data were available from which the mass-transfer resistance of the liquid phase could be determined.

Using y to represent the local mole fraction of component A at a distance s and z for that in the net condensate stream, Colburn and Drew wrote the following equation for the total rate of transfer of component A owing to diffusion and to net mass flux:

$$N_A \equiv wz = -k_G(dy/d\eta) + wy \quad (1)$$

where k_G is equal to $D_V\pi/RTB_G$ and $\eta = s/B_G$, in which D_V is the diffusion coefficient and B_G is the equivalent laminar-film thickness.

The composition of the net condensate stream is

$$z \equiv N_A/(N_A + N_B) = N_A/w \quad (2)$$

in which N_A and N_B refer to the constant mass fluxes of A and B components, respectively. The solution of Equation (1) can be represented as

$$y - y_i \exp(-w/k_G) = z[1 - \exp(-w/k_G)] \quad (3)$$

in which y now refers to the mole fraction of component A in the bulk of the gas phase and y_i is the value at the interface.

Equation (3) can be put in a familiar form either when w is zero (no mass exchange) or when N_B is zero (no mass transfer of B, the "inert-gas component" when $N_B = 0$).

$$wz = N_A = k_G z \ln\left[\frac{z - y_i}{z - y}\right] \quad (4)$$

$$\lim_{z\to\infty} N_A = k_G(y - y_i) \quad (5)$$

$$\lim_{z\to 1} N_A = k_G \ln\frac{1 - y_i}{1 - y} = k_G\left(\frac{y - y_i}{1 - y}\right)_{log\ mean} \quad (6)$$

Equation (1) and the results derived from it do not appear to depend on the assumption of a stagnant film which offers the sole resistance to mass transfer; the equation would seem to remain unchanged when applied to turbulent diffusion in the core of the vapor stream. However, under some circumstances, such as those leading to the progressive development of a boundary layer, the problem is more complex. It has been solved, however, by Eckert and Lieblein (*4*) and discussed by Mickley et al. (*10a*); the results are qualitatively similar to those given here.

On the assumption that the diffusion process in the liquid layer is also that of steady state mass transfer of two components through a condensed phase the velocity of which is not disturbed by the mass exchange, the same equations should apply to the liquid mass transfer resistance.

$$x_i - x \exp(-w/k_L) = z[1 - \exp(-w/k_L)] \quad (7)$$

$$wz = N_A = k_L z \ln\frac{z - x}{z - x_i} \quad (8)$$

where k_L is the liquid-phase mass transfer coefficient.

A somewhat more reasonable model of the liquid phase is that of a liquid layer that flows under the influence of gravity and on which incremental liquid condensate is deposited, the interface gradually moving toward the gas phase. The influence of molecular diffusion on the mass transfer rate in this situation can be estimated if it is assumed that the fluid motion is laminar (*8*). The results are somewhat involved but show that Equations (7) and (8) are very nearly correct, the deviations being a function of the ratio of the velocity of interface movement toward gas to the velocity of diffusion. For very wide limits of this ratio the deviations from the equations given are not more than a few per cent.

By use of Equations (4) and (8) the interfacial compositions y_i and x_i can be found if it is assumed that interfacial resistance is absent. For binary mixtures forming ideal solutions,

$$y_i = \frac{\alpha x_i}{1 + (\alpha - 1)x_i} \quad (9)$$

Equating the right sides of Equations (4) and (8) gives

$$\frac{z - x}{z - x_i} = \left[\frac{z - y_i}{z - y}\right]^{k_G/k_L} \quad (10)$$

which has to be solved simultaneously with Equation (9).

The procedure used for calculating the composition changes in liquid and vapor phases occurring as these fluids move past the heat transfer surface in a condenser involves the use of Equations (4), (8), (9), and (10) at each point on the surface, followed by differential energy and material balances to compute the changes in bulk composition. In principle such computations are simple, though they may be very time-consuming unless carried out by machine. If V and L represent the molar mass flow rates of vapor and liquid, respectively,

$$wz = -d(yV)/dA = -d(xL)/dA$$

or

$$w(z - y) = -V(dy/dA) \quad (11)$$

where dA represents a differential element of heat transfer area ($w = -dV/dA$).

Although Equations (4), (8), (9), (10), and (11) would be used in step-by-step computations for designing equipment, for understanding the principal features of the condensation phenomenon it is helpful to integrate the rate equations and the differential material balances approximately. This is done to determine how finite composition changes owing to fractionation in a condenser may be influenced by the rate of condensation. First an idealized unit is considered in which there is no liquid-phase resistance to mass transfer; i.e., k_L = infinity. Under these conditions Equations (4) and (11) give

$$V\,dy = (y_i - y)\frac{dV}{1 - \exp(w/k_G)} \quad (12)$$

or

$$\int_{y_1}^{y_2}\frac{dy}{y_i - y} = \int_{V_1}^{V_2}\frac{d\ln(V)}{1 - \exp(w/k_G)} \quad (13)$$

In view of the assumed absence of interfacial and liquid-phase resistance to diffusion $x - x_i$ and $y_i - y^* = \alpha x/[1 + (\alpha - 1)x]$. The integral on the left of Equation (13) is frequently referred to as the *number of transfer units* because its numerical value is a measure of the amount of composition change accomplished in a binary system, regardless of its particular phase-equilibrium characteristics. Numerical evaluation of the integral on the right shows the influence of partial condensation on the enrichment. In order to evaluate it precisely the functional dependence of k_G on the local value of V should be allowed for. Although exact numerical values can be found, it is sufficiently precise to assume that k_G is proportional to V and to use the logarithmic-mean value of k_G in the denominator of the integral.

$$\left[\frac{w}{k_G}\right]_{avg} \doteq \frac{(G_{M_1} - G_{M_2})(\pi D^2/4\pi Dh)}{(k_G)_{l.m.}} = \frac{(G_{M_1} - G_{M_2})}{\dfrac{(k_{G_1} - k_{G_2})ah}{\ln(k_{G_1}/k_{G_2})}} = \frac{(G_{M_1} - G_{M_2})}{ah\dfrac{k_{G_1}}{G_{M_1}}\dfrac{(G_{M_1} - G_{M_2})}{\ln(G_{M_1}/G_{M_2})}} = \frac{H_G}{h}\ln\left(\frac{G_{M_1}}{G_{M_2}}\right) = \frac{H_G}{h}\ln\left(\frac{V_1}{V_2}\right)$$

where $H_G = V_1/k_{G_1}a$ and a = interfacial area per unit volume of apparatus. With these approximations

$$N_G = \int_{y_1}^{y_2} \frac{dy}{y_i - y}$$

$$\doteq \frac{\ln (V_1/V_2)}{1 - [V_1/V_2]^{(-H_G/h)}} \quad (14)$$

Figure 1 shows a plot of N_G vs. V_1/V_2 according to Equation (14). It is interesting to notice that the normal value (h/H_G) of the number of transfer units is in the limit when V_1/V_2 approaches unity or when the rate of condensation is negligible. When V_1/V_2 is large, the number of transfer units is independent of the mass transfer resistance, as expressed by H_G, and can be computed from the Rayleigh equation, which assumes that the vapor stream is differentially condensed, each incremental quantity of condensate having a composition x^* at local equilibrium with the vapor stream. Diffusional mass transfer is assumed absent, each incremental condensate being isolated from the vapor as soon as it has been formed. The Colburn-Drew expressions thus are seen to provide the connecting link between the conventional expressions for the composition changes accomplished in adiabatic distillation and those calculated without regard for diffusional effects, according to the Rayleigh procedure.

In order to obtain a useful approximate expression showing the effect of condensation on mass transfer when liquid-phase resistance is allowed for, it is helpful to approximate the true, curvilinear relationship expressed by Equation (9) by means of a straight equilibrium line,

$$y_i = mx_i \quad (15)$$

Substituting this into Equation (10) and assuming that the operation is at total reflux, so that $V = L$ at all points, the following equation can be derived in a form similar to Equation (14), as shown in the appendix:

$$N_{0L} \equiv \int_{x_1}^{x_2} \frac{dx}{x - x^*} \doteq \frac{\ln (V_1/V_2)}{m^{-1}[(V_1/V_2)^{(H_G/h)} - 1] + [1 - (V_2/V_1)^{(H_L/h)}]} \quad (16)$$

where $H_L = L/k_L aS$.

Figure 2 is a plot of this equation; it shows that in the limit when the condensation rate is negligible $(V_1/V_2 \rightarrow 1)$ the number of transfer units according to Equation (16) agrees with the well-known expression,

$$N_{0L} = \frac{h}{(H_G/m) + H_L} \quad (17)$$

In contrast with Figure 1 and Equation (14), however, the Rayleigh line is no longer significant in the limit when the condensation is rapid unless gas-phase resistance is absent $(h/H_G = \infty)$. In the extreme case of rapid condensation the liquid-phase resistance has a large effect and is capable of causing the enrichment to be much smaller than that given by the equation of equilibrium differential condensation.

The Rayleigh equation is derived on the assumption that the composition of the incremental condensate, z, is that in equilibrium with the bulk of the vapor, x^*; that is,

$$z = x^* = \frac{y}{\alpha - (\alpha - 1)y}$$

Figure 2 shows that the condensate is in equilibrium with the vapor from which it is produced only if the resistance of the vapor phase is negligible, i.e. $h/H_G = \infty$, and if the resistance of the liquid is large, i.e. $h/H_L = 0$.

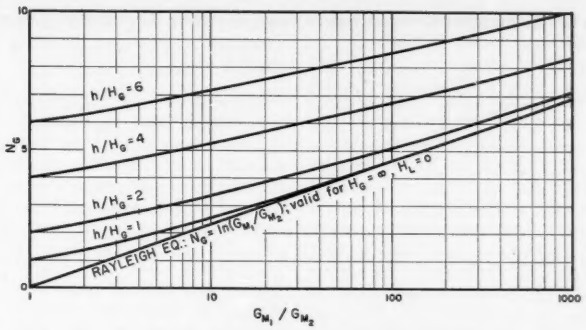

Fig. 1. Partial condensation in countercurrent column: gas-film resistance only.

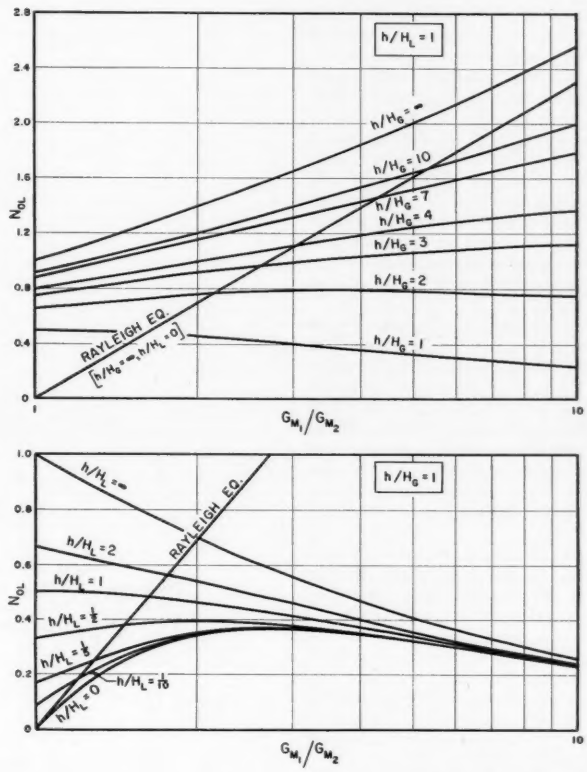

Fig. 2. Partial condensation in countercurrent column: gas- and liquid-film resistances ($m = 1.0$).

APPARATUS

The apparatus used in this investigation is shown in Figure 3; it consisted essentially of a wetted-wall distillation column equipped with an annular jacket through which water could be circulated under carefully controlled conditions so as to produce known, nearly uniform rates of condensation. External reflux could be supplied from a total condenser operating on the exit vapor stream from the test section, so that the column could be operated as an adiabatic

countercurrent distillation unit or as a partial condenser.

The wetted-wall section of the column was 1.063 in. I.D. and 6 ft. long. It was made from a piece of brass pipe of 1.315 in. O.D. around which a spiral of heavy copper wire was wound with a spacing of ½ in. between adjacent turns. Surrounding the copper spiral was a piece of 1⅝-in., 15-B.W.G. brass tubing which fitted snugly and formed a spiral channel for the passage of cooling water. This construction was used so that both a measurable temperature rise of the water and a high water velocity might be obtained. The temperature of the water in the annular space was measured by thermocouples located at 1-ft. intervals, and local values of the heat flux were computed from the known mass flow rate of the coolant and the slope of the experimentally observed plot of water temperature vs. position.

The column was wrapped with ⅝-in. asbestos rope on the outside of which thermocouples were mounted at three levels. When the readings of these thermocouples were compared with those of three similar thermocouples mounted outside a second layer of asbestos rope flow of heat through the insulation could be detected. Adiabatic conditions were achieved by adjusting the current through electrical resistance windings which were applied outside a third layer of asbestos rope.

Provision was made for withdrawing samples of the vapor stream at the center line of the wetted-wall section and at 1-ft. intervals along the axis. Short lengths of hypodermic tubing were inserted into the vapor space through the annular jacket. These tubes had their inner ends pointed upward so that any condensate formed inside the tubes could not drop out into the gas stream. The small copper tubes led to water-cooled condensers.

The test section was provided with electrically heated upper and lower calming sections. The external reflux was heated to its boiling point before being returned to the column and was distributed evenly to the wetted wall by means of a fine-mesh screen. The liquid stream was sent through a calcium-chloride drier before being returned to the column. Flow rates of external reflux and liquid returned to the boiler were measured with calibrated rotameters.

Only the system ethylene dichloride–toluene was distilled. Its composition was determined from measurements of refractive index made with an Abbé refractometer. Technical-grade materials were purified carefully by distillation before use. The refractive indexes (n_D) of the purified pure components were 1.4427 ± 0.0001 and 1.4941 ± 0.0001 at 25°C. for ethylene dichloride and toluene, respectively.

range of vapor Reynolds numbers extending approximately from 9,000 to 25,000.

The still pot, having a capacity of 4.9 gal., was charged with approximately 3 gal. of the liquid mixture; it was found that this amount was sufficient completely to cover the electrical immersion heaters during a run and at the same time to avoid bumping and carryover of liquid from the still pot into the column. The power input to the immersion heaters was adjusted to give the desired vaporization rate, and after about 30 min. the material in the still pot began to boil and the vapors started to flow through the lower calming section.

Adiabatic conditions were established and maintained by regulating the electrical input to three insulation heaters along the column until each pair of thermocouples at any one of the three levels along the column showed the same temperature inside and outside the insulation.

As soon as the reflux was flowing at a fairly uniform rate, the reflux heater was turned on and adjusted to assure the return of liquid reflux at its boiling point.

It was found that approximate equilibrium was established about 2 hr. after the reflux began to flow through the reflux rotameter. During this time the various heaters had to be adjusted frequently to keep pace with the warming of the column. After this time another hour of running followed during which no further adjustments were made on the column, and then the first set of four samples was taken, consisting of liquid and vapor samples from the top and the bottom of the wetted-wall section of the column.

Without any adjustments on the column, operation was continued for another hour. Then the second set of samples was taken at the same four points. These generally agreed very closely with the first set. Each run was made individually, always starting with cold equipment.

All analyses were made by determining the refractive index of a sample, by use of an Abbé refractometer. The time lapse between sample taking and analysis was usually less than 10 min. and in no case exceeded 15.

With the height of the column, the relative volatility, and the compositions of the vapor and liquid streams at the top and at the bottom of the column known, the overall height of a gas-phase transfer unit was computed by use of standard relationships. A series of about ten runs each was made at total reflux for three conditions representing

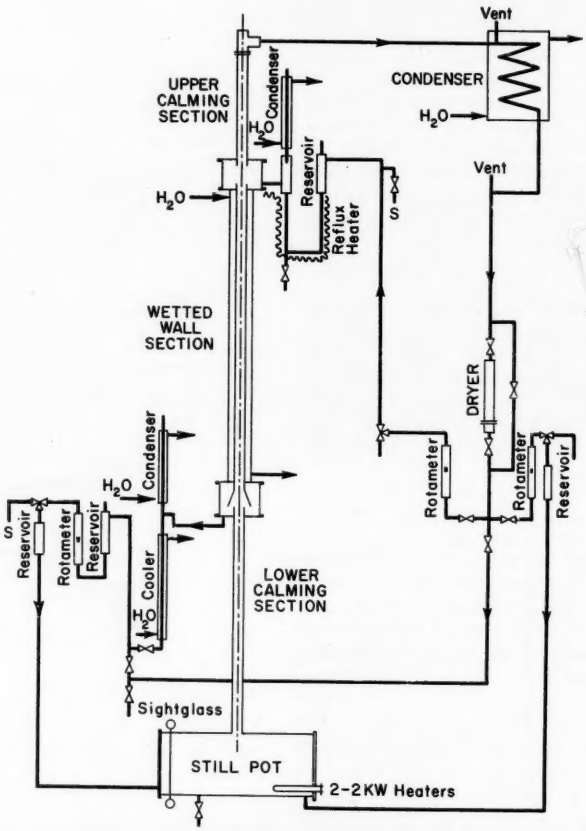

Fig. 3. Schematic drawing of distillation apparatus.

RESULTS*

Adiabatic Distillation Experiments

Ordinary distillation tests were carried out at total and at finite reflux by use of three different average levels of liquid composition, in each case covering a

*A complete description of the experimental procedure is given in reference (8). Tables of original data are on file as document number 4954 with the American Documentation Institute, Photoduplication Service, Library of Congress, Washington 25, D. C., and may be obtained for $5.00 for photoprints or $2.25 for 35-mm. microfilm.

high, medium, and low ethylene dichloride concentration; similar series of runs were made for adiabatic operation at finite reflux and for the condensation experiments.

Material and energy balances were computed for the adiabatic runs as well as for those in which condensation occurred. In the adiabatic runs the average of the absolute deviations from perfect balances were 0.2 and 1.2%, respectively, expressed in each case as the error divided by the net mass or energy transported into the column. For operation as a condenser the corresponding figures were 0.3 and 8.1%, respectively.

Since the principal object of these runs was to determine the extent of the liquid-phase resistance, it was necessary to estimate the vapor-phase diffusional resistance and to calculate the liquid-phase value by difference. By use of a vapor Reynolds number computed from the vapor velocity relative to the falling interface, the friction factor for a smooth tube was calculated from the empirical equation of Drew, Koo, and McAdams (*3*). Next this was corrected for the roughness of the liquid-vapor interface, on which ripples were invariably present, by use of an empirical equation due to Kamei (*7*),

$$\frac{f_r}{f_0} = 1 + 0.00397(Re_L)^{0.476}\left(\frac{\mu_L}{\mu_G}\right)^{0.271} \qquad (18)$$

in which the Reynolds number of the liquid layer is expressed as

$$Re_L = 4\Gamma/\mu_L \qquad (19)$$

where Γ = liquid-mass flow rate, lb./(hr.)(ft. wetted perimeter) and μ_L = liquid viscosity, lb. mass/(hr.)(ft.). Kamei's result is based on careful measurements of interfacial friction in wetted-wall columns of various diameters, water and aqueous solutions having a wide range of viscosities being used. The values of the ratio of friction factors estimated for the conditions of these experiments were in the range $1.1 < f_r/f_0 < 1.25$. In estimating H_G it was assumed that

$$j_M = f_r/2 \qquad (20)$$

and the usual relationship between j factor and the height of a transfer unit was employed.

$$H_G = (D/4j_M)(Sc_V)^{2/3} \qquad (21)$$

The Schmidt number of the vapor phase was calculated from a diffusivity that had been estimated from the empirical equation of Gilliland (*6*). The numerical values of other physical properties were interpolated from experimental data reported in standard references. In the standard equation for the addition of individual resistances of the phases,

$$H_{OG} = H_G + (mV/L)H_L \qquad (22)$$

from which H_L was computed, the average value of the slope of the equilibrium curve, m, was calculated for the particular range of compositions encountered in each experiment following the procedure suggested by Sherwood and Pigford (*13*).

Figure 4 shows the values of H_L derived from the over-all composition changes in distillation plotted against the Reynolds number of the liquid phase. The drawing of the line in Figure 4 requires some explanation: It has been observed visually that when the liquid Reynolds number fell below approximately 250, uniform wetting along the entire length of the column no longer occurred. Operation of the column with dry spots along its wetted wall gave

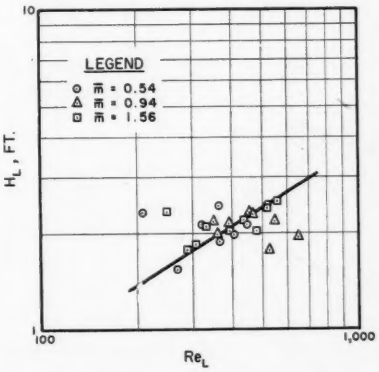

Fig. 4. H_L as function of liquid Reynolds number.

erratic results and the two points at the lowest Reynolds numbers must therefore be ignored.

The trend toward higher values of H_L with increasing Reynolds numbers is normal, the general direction of the line following the diffusion theory for falling liquid films. Previous data obtained by Emmert and Pigford (*5*) and shown on Figure 9 also indicate an upward trend with increasing Reynolds number.

The H_L values shown on Figure 4 are more accurate and reliable than previous values obtained by Johnstone and Pigford (*13*), who published the only previous information on H_L values in adiabatic distillation.

On Figure 4 the H_L line for the high and low concentration ($\bar{m}$ = 0.54 and $\bar{m}$ = 1.56, respectively) is rather clearly defined, and it was thought unlikely that a line at intermediate concentration ($\bar{m}$ = 0.94) would show any drastic change in direction from the other two. It is interesting to observe that a single line could be drawn for the values at the three different concentration levels.

In a preliminary attempt to calculate H_L values from estimates of H_G based on friction factors for smooth tubes, a large variation of H_L with liquid composition appeared to be present. These variations were eliminated when Kamei's roughness correction was introduced according to Equation (18). Whether the true values of the friction factor have been used and whether Equation (20) is valid for the rippling interface cannot be determined with certainty, though it would appear significant that the H_L values given on the figure show approximately the same small influence of composition that would have been expected from the liquid physical properties.

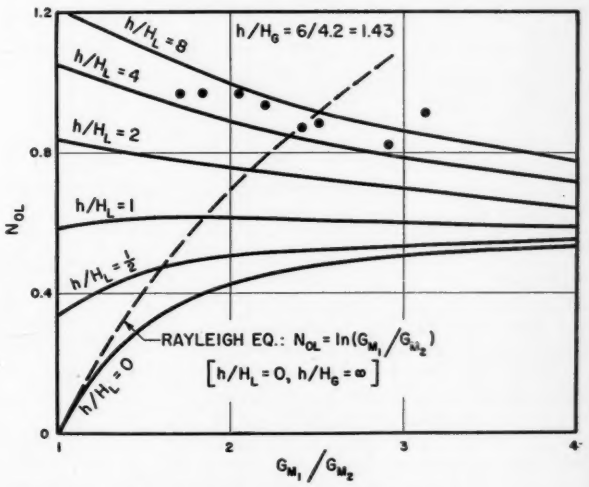

Fig. 5. Comparison between experimental and theoretical results.

Condensation Experiments

Figure 5 compares the effect of condensation on the apparent number of transfer units computed from the terminal compositions with the theory in its approximately integrated form according

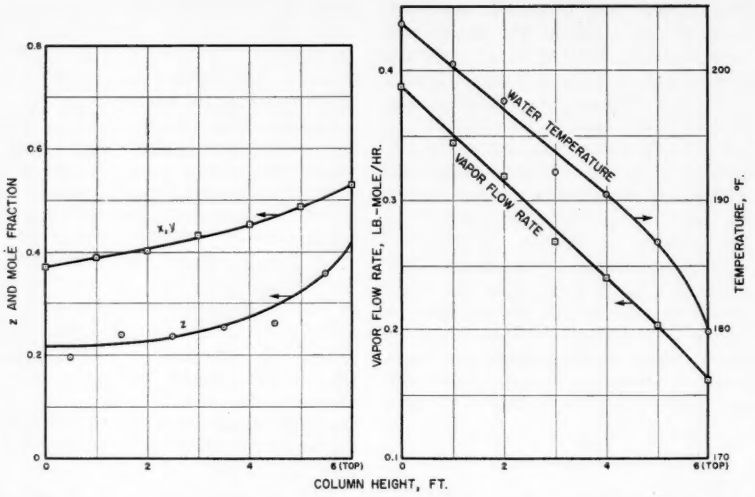

↑ Fig. 6. Point conditions in column (for run 105).

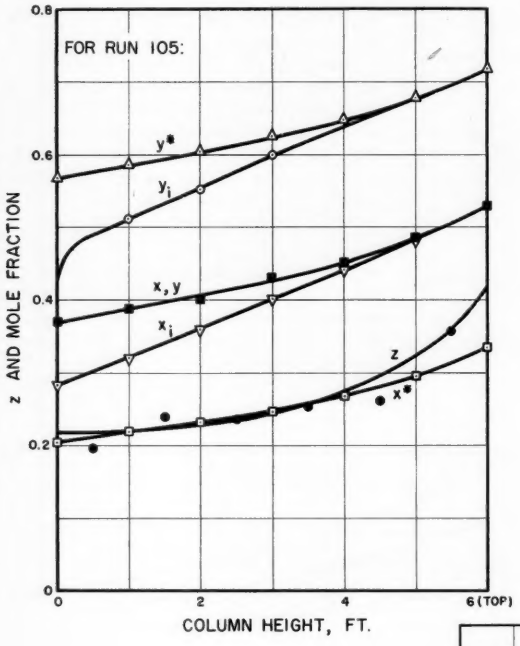

← Fig. 7. Interfacial compositions.

↓ Fig. 8. Local values of k_L.

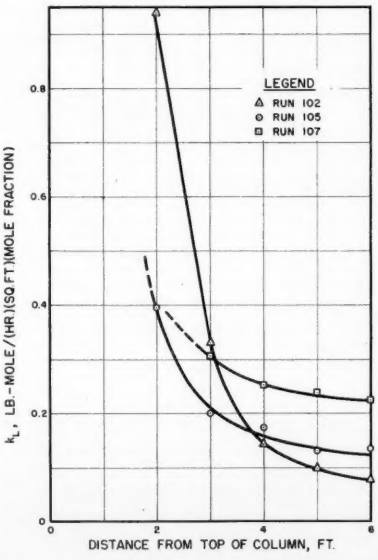

to Equation (16). The theoretical lines on the figure are similar to those on the lower part of Figure 2; they apply to a different value of the h/H_G parameter, however, this time corresponding to the height of the experimental column and the value of H_G expected at the vapor flow rate used in the condensation runs. Like Figure 2, Figure 5 shows lines corresponding to various assumed values of the h/H_L parameter, though only a single value of this parameter applied to the condensation experiments.

As may be seen on the figure, the observed influence of the rate of condensation is the same as that expected from the theory, and it is significant that the points fall approximately along a line of constant h/H_L. When this line is extrapolated backward to the left-hand margin of the figure, it intersects the vertical axis at a value of N_{OG} equal to the value expected from the adiabatic-distillation tests. Apparently, as expected from the theory, the liquid-phase resistance has a large influence and causes the experimental points to cross the Rayleigh differential-distillation line, which is often used (incorrectly) for the estimation of fractionation that can be accomplished in a partial condenser.

As far as the quantitative use of the Colburn-Drew theory is concerned, it is of greater interest to study the effect of condensation on the local changes in composition within the column. Figure 6 is a plot of the observed local vapor compositions and cooling water temperatures at 1-ft. intervals along the condenser. The figure also shows other quantities, such as the vapor rate V and the composition of the incremental condensate z derived from the experimental observations. The values of V were computed from the following equation expressing a differential energy balance:

$$(dV/dh) = (Wc_P/\lambda)(dT/dh) \quad (23)$$

where W = cooling-water rate, lb./hr.; c_p = specific heat of water; T = local water temperature at position h; and λ = latent heat of condensation, B.t.u./lb. The composition of the incremental condensate was computed from the differential material balance, as expressed by Equation (11) and written in the form

$$z = y + V(dy/dV)$$

$$= y + (V\lambda/Wc_P)\frac{(dy/dh)}{(dT/dh)} \quad (24)$$

The differential quotients in Equation (23) and (24) were evaluated by means of a least-squares procedure based on five equally spaced points.

The fact that z is everywhere smaller than y, as shown in Figure 6, corresponds to the enrichment of the vapor stream as it flows upward. Thus the less volatile component, toluene, is condensed relatively faster than the more volatile one, ethylene dichloride.

Having available values of y and z at each point in the condenser makes it possible to compute the interfacial compositions y_i and x_i from Equations (3) and (9) if k_G/w is known. It was assumed that in spite of the progressive change in vapor velocity the local Reynolds number could be used to compute k_G from Equations (18), (20), and (21) and the smooth-tube friction factors. (This computation also neglects the probable distortion of the normal turbulent-velocity profile in the vapor phase owing to the transport of momentum to the interface by the condensing vapor.) The resulting values of interfacial composi-

tions are shown by Figure 7. It is interesting to observe that at the top of the column, where the liquid layer is freshly formed, the values of x and x_i are very nearly equal. Thus only a very small concentration across the liquid phase is capable of producing a finite rate of mass transfer of each component. Doubtless this is due to the sudden creation of a sharp concentration gradient in a relatively quiet liquid mass; a similar end effect probably is present in the vapor phase at the bottom of the column, where the vapor stream is first exposed to the liquid layer and where the local gas-phase mass transfer coefficient is probably very large. In all probability, however, this end effect in the gas phase disappears very quickly, and so the steady state values of k_g computed from Equation (20) should be nearly equal to the local ones throughout most of the test section.

Figure 8 shows local values of k_L computed from the estimated interfacial compositions by means of Equation (8). It is evident that, in agreement with the discussion just given, the value of k_L is very large at the top of the column and undergoes a progressive decrease as the liquid flows down the column.

In order to compare the values of k_L computed from the condensation data with the values previously obtained in the adiabatic distillation runs it is necessary to compute an average of the local values of k_L. This was done by means of the following equation, which is suggested by theoretical relations for mass transfer into purely laminar liquid layers.

$$(k_L)_{avg} = \int_0^1 k_L \, d(t/\theta)$$

$$= 2 \int_0^1 k_L (t/\theta)^{1/2} \, d(t/\theta)^{1/2} \quad (25)$$

in which (t/θ) refers to the ratio of time of exposure of the liquid surface at any point to the total time of flow of surface layers down the column, as computed from the well known relations for laminar, gravitational flow of liquid layers. Figure 9 shows values of H_L [$= L_{avg}/(k_L)_{avg}aS$] from three of the condensation runs. The agreement with the adiabatic data is considered to be good in view of the uncertainties in the estimation of local conditions.

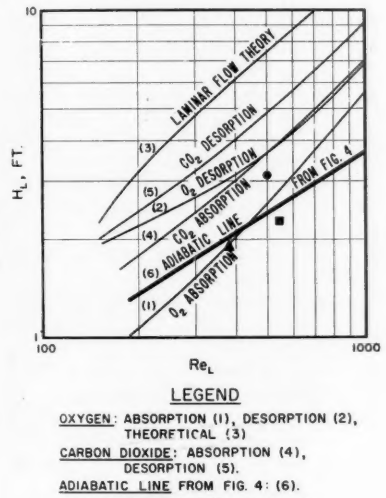

Fig. 9. H_L for distillation, condensation, and absorption. Curves (1) and (5) are from reference 5.

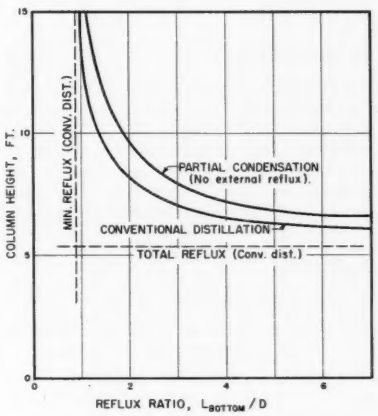

Fig. 10. Comparison between condensation and distillation.

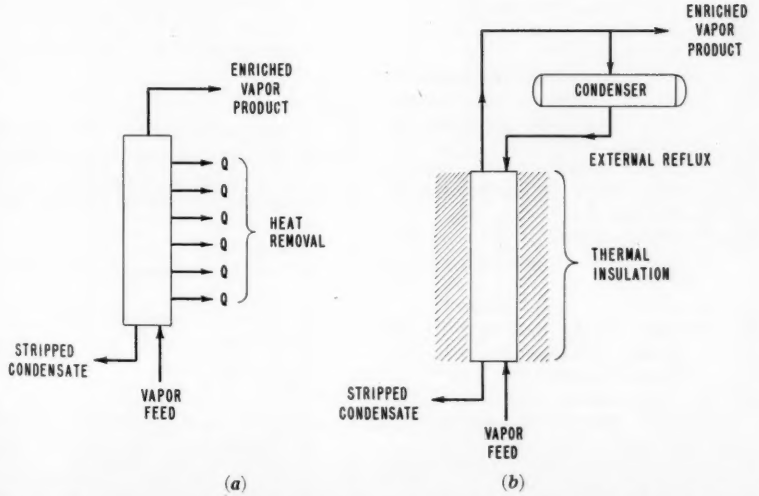

Fig. 11. Flow sheet for fractionation (a) with partial condenser, (b) with adiabatic distillation column plus ordinary condenser.

DISCUSSION OF RESULTS

The agreement shown on Figure 9 between values of H_L measured independently in distillation and in condensation experiments suggests that the Colburn-Drew analysis of mass transfer during condensation can be applied successfully by point-to-point calculation, by use of diffusional-resistance parameters evaluated from experiments in which condensation did not occur. This conclusion is further borne out when the H_L values are compared with data from gas-absorption studies. Figure 9 also shows a line representing the data of Emmert and Pigford (5) for liquid-phase resistances in the absorption and desorption of oxygen and carbon dioxide in water at room temperature, a wetted-wall column being used which is somewhat smaller than that employed in the condensation work. When it is remembered that H_L should decrease with increasing temperature, owing to the increase in the diffusion coefficient, the comparison appears to be a good one. A further explanation of the differences between the two sets of data may be the influence of interfacial resistance, which probably contributed to the total resistance to transfer of the slightly soluble gases in water but may have had less effect in the hydrocarbon system.

With the data just described it is possible to carry out a numerical design calculation for a reflux type of condenser and for an adiabatic-distillation column so that the two operation may be compared at equal capacities or at equal rates of heat removal. At equal values of the ratio of the liquid rate at the bottom of the apparatus, L_{bottom}, to the vapor-product rate at the top, D, the total heat transferred in fractionator or auxiliary condenser is the same, as indicated by Figure 11. The conditions assumed for an illustrative calculation are as follows:

System: ethylene dichloride–toluene

Bottom vapor rate: 0.400 lb.-mole/hr. at dew point

Vapor composition given: 0.400 mole fraction ethylene dichloride at bottom of column
Vapor composition desired: 0.550 mole fraction ethylene dichloride at top of column
Inside diameter of condenser tube: 1 in.
Coolant liquid: water, introduced at top of condenser, single pass on shell side

It is desired to determine the height of the tubes or the surface required. The calculations are made solely from the point of view of mass transfer, the assumption being that the correct heat transfer rate will be obtained by adjusting the cooling-water temperature.

For conventional distillation without heat transfer from the column, the required tube height is computed in the customary way by use of the values of H_G and H_L found in this work. The influence of the reflux ratio on the height is indicated in Figure 10.

For partial condensation a trial-and-error computation is required. A tube length is assumed so as to get a value of condensation rate (w, assumed constant here) and the Colburn-Drew equations are applied stepwise starting at one end until the composition at the other end of the column is reached. If it does not agree with the composition desired, another length is assumed and the calculations are repeated. After the extent of the surface is known, the required cooling-water temperatures are found from conventional heat transfer calculations. If these temperatures cannot be obtained, the specified vapor compositions must be altered. Thus it is not possible to specify fractionation, heat requirements and coolant temperatures independently; only two of the three can be fixed independently.

Under finite reflux in partial condensation the condenser operates in such a fashion that all condensation takes place inside the column, and no external reflux is returned to it. Thus the overhead product is all the vapor leaving at the top. For example, at a reflux ratio of $(L_{bottom}/D) = 1.50$, the first trial, with a column height of 8 ft. assumed and Equations (4), (8), (9), (10), and (11) applied for a stepwise integration over eight 1-ft. increments, gave $y_1 = 0.432$ (which compares with the given value of $y_1 = 0.400$); a second trial, with a column height of 11 ft. assumed, gave $y_1 = 0.405$. A detailed sample calculation for the design of a reflux condenser is given in reference *8*.

Figure 10 shows the computed results in the illustrative example. It is seen that at a given ratio of the liquid flow rate from the bottom of the tube to the rate of flow of the vapor product from the top of the tube the partial condenser requires slightly greater transfer surface in the fractionator to accomplish the same enrichment. To produce reflux in conventional distillation, on the other hand, heat transfer surface is required in an external condenser, which is not needed for the partial condenser, as shown by Figure 11. Conversely, for the same surface and the same enrichment conventional distillation requires a smaller reflux ratio, i.e., a smaller heat load per unit of product. Though an exact statement cannot be made, it appears from the numerical work that the minimum reflux ratio in a partial condenser is the same as that in ordinary distillation or that the same amount of liquid must be condensed to provide reflux whether the condensation takes place in a separate condenser or in the condenser fractionator.

In spite of the disadvantages in heat consumption and in required transfer surface the partial condenser does of course have the advantages of eliminating the need of a separate condenser when a vapor product is acceptable and of permitting heat removal partly at a higher temperature.

ACKNOWLEDGMENT

The financial assistance of the Research Corporation of New York, New York, is gratefully acknowledged. N. A. Copeland and R. D. Rice contributed valuable assistance and preliminary data. One of the authors received a generous fellowship award from the Socony Mobil Oil Company.

NOTATION

A = interfacial area, sq. ft.
a = interfacial area per unit volume of apparatus, sq. ft./cu. ft.
B_G = equivalent film thickness, ft.
c_P = specific heat at constant pressure, B.t.u./(lb.)(°F.)
D = diameter of column, ft.
D_V = diffusion coefficient of vapor, sq. ft./hr.
f_0 = friction factor for smooth tube, dimensionless
f_r = friction factor corrected for roughness, dimensionless
G_M = molar rate of gas flow, lb.-mole/(hr.)(sq. ft.)
h = height of wetted-wall column, ft.
H_G = height equivalent to a transfer unit, based on gas-phase resistance, ft.
H_L = height equivalent to a transfer unit, based on liquid-phase resistance, ft.
H_{OG} = height equivalent to a transfer unit, based on over-all gas-phase resistance, ft.
j_M = j factor for mass transfer
k_G = mass transfer coefficient for gas phase, lb.-mole/(hr.)(sq. ft.)(mole fraction)
k_L = mass transfer coefficient for liquid phase, lb.-mole/(hr.)(sq. ft.)(mole fraction)
L = molar mass flow rate of liquid, lb.-mole/hr.
L_M = molar rate of liquid flow, lb.-mole/(hr.)(sq. ft.)
m = slope of equilibrium curve, dy^*/dx
N_A = rate of diffusion of component A, lb.-mole/(hr.)(sq. ft.), taken positive when A diffuses from gas toward interface
N_B = rate of diffusion of component B, lb.-mole/(hr.)(sq. ft.), taken positive when B diffuses from gas toward interface
N_G = number of transfer units based on gas-phase driving force, dimensionless
N_{OG} = number of transfer units based on over-all gas-phase driving force, dimensionless
N_{OL} = number of transfer units based on over-all liquid-phase driving force, dimensionless
n_D = refractive index, dimensionless
R = universal gas constant, 1,544 (ft.)(lb.-force)/(lb.-mole)(°F.)
Re = Reynolds number, dimensionless
S = cross section of vapor channel, sq. ft.
s = distance, ft., measured positively from gas phase toward the interface; $s = 0$ at gas side of equivalent laminar film
Sc = Schmidt number, dimensionless
T = absolute temperature, °R.
t = time, hr.
V = molar mass flow rate of vapor, lb.-mole/hr.
w = total molal rate of condensation on unit area, lb.-mole/(sq. ft.)(hr.)
x = mole fraction of more volatile component in liquid phase
x^* = mole fraction of more volatile component in liquid phase existing in equilibrium with vapor of mole fraction y
y = mole fraction of more volatile component in vapor phase
y^* = mole fraction of more volatile component in vapor phase existing in equilibrium with liquid of mole fraction x
z = ratio of the rate of condensation of the more volatile component to the net rate of condensation

Greek Letters

α = relative volatility, dimensionless
Γ = liquid mass flow rate, lb./(hr.)(ft. wetted perimenter)
η = fractional distance through film, $= s/B_G$
θ = time, hr.
λ = latent heat of vaporization, B.t.u./lb.-mole
μ = viscosity, lb.-mass/(ft.)(hr.)
π = 3.14159

Subscripts

G = gas
i = interface
L = liquid
V = vapor
1 = the bottom of the column
2 = the top of the column

LITERATURE CITED

1. Colburn, A. P., and T. B. Drew, *Trans. Am. Inst. Chem. Engrs.*, **33**, 197 (1937).
2. Colburn, A. P., and O. A. Hougen, *Ind. Eng. Chem.*, **26**, 1178 (1934).
3. Drew, T. B., E. C. Koo, and W. H. McAdams, *Trans. Am. Inst. Chem. Engrs.*, **28**, 56 (1932).
4. Eckert, E. R. G., and V. Lieblein, *Forschung*, **16**, 33 (1949).
5. Emmert, R. E., and R. L. Pigford, *Chem. Eng. Progr.*, **50**, 87 (1954).
6. Gilliland, E. R., *Ind. Eng. Chem.*, **26**, 681 (1934).
7. Kamei, Saburo, and J. Oishi, *Chem. Eng. (Japan)*, **18**, 421 (1954).
8. Kent, E. R., Ph.D. thesis, Univ. Delaware, Newark (1953).
9. Lewis, J. G., and R. R. White, *Ind. Eng. Chem.*, **45**, 486 (1953).
10. Mickley, H. S., *Chem. Eng. Progr.*, **45**, 739 (1949).

10a. ———, R. C. Ross, A. L. Squyers, and W. E. Stewart, *Nat. Advisory Comm. Aeronaut., Tech. Note* 3208 (July, 1954).

11. Mizushina, Takuro, and T. Kotoo, *Chem. Eng. (Japan)*, **13**, 75 (1949).
12. Nusselt, Wilhelm, *Z. Ver. Deut. Ing.*, **60**, 541, 569 (1916).
13. Sherwood, T. K., and R. L. Pigford, "Absorption and Extraction," 2 ed., McGraw-Hill Book Company, Inc., New York (1952).

APPENDIX

Partial Condensation for Gas- and Liquid-film Resistances

In the derivation of Equation (14) it was shown that

$$\left[\frac{w}{k_G}\right]_{avg} \doteq \frac{H_G}{h} \ln\left[\frac{V_1}{V_2}\right] \quad (1A)$$

Similarly,

$$\left[\frac{w}{k_L}\right]_{avg} \doteq \frac{H_L}{h} \ln\left[\frac{L_1}{L_2}\right] \quad (2A)$$

Since by definition $h/H_G = N_G$ and $h/H_L = N_L$, Equations (1A) and (2A) may be written as

$$\frac{w}{k_G} = \ln\left[\left(\frac{V_1}{V_2}\right)^{N_G^{-1}}\right] \quad (3A)$$

and

$$\frac{w}{k_L} = \ln\left[\left(\frac{L_1}{L_2}\right)^{N_L^{-1}}\right] \quad (4A)$$

Let

$$G = e^{w/k_G} = (V_1/V_2)^{N_G^{-1}} \quad (5A)$$

and let

$$\pounds = e^{w/k_L} = (L_1/L_2)^{N_L^{-1}} \quad (6A)$$

Solving the Colburn-Drew equation—Equation (3)—for z in terms of both the liquid and vapor phase gives

$$z = \frac{\pounds x_i - x}{\pounds - 1} = \frac{Gy - y_i}{G - 1} \quad (7A)$$

and replacing y_i by mx_i results in

$$x_i = \frac{G(\pounds - 1)y + (G - 1)x}{\pounds(G - 1) + m(\pounds - 1)} \quad (8A)$$

and

$$x_i - x \quad (9A)$$

$$= (\pounds - 1)\frac{Gy - (G - 1 + m)x}{\pounds(G - 1) + m(\pounds - 1)}$$

or

$$\frac{x_i - x}{x^* - x}$$

$$= \frac{[Gy - (G - 1 + m)x](\pounds - 1)}{[\pounds(G - 1) + m(\pounds - 1)](y/m - x)}$$

$$= \frac{m(\pounds - 1)}{\pounds(G - 1) + m(\pounds - 1)} \cdot \frac{G(y - x) - (m - 1)x}{(y - mx)} \quad (10A)$$

From Equation (7A)

$$z - x = \frac{\pounds}{\pounds - 1}(x_i - x)$$

or

$$\frac{dx}{z - x} = \frac{\pounds - 1}{\pounds}\frac{dx}{x_i - x} \quad (11A)$$

but $dx/(z - x) = dL/L$; therefore, according to Equation (11A)

$$\frac{dx}{x_i - x} = \frac{\pounds}{\pounds - 1} d \ln L \quad (12A)$$

For the over-all resistance

$$\frac{dx}{x - x^*} = \frac{x_i - x}{x^* - x}\cdot\frac{dx}{x - x_i}$$

which upon substitution by Equations (10A) and (12A) gives

$$dN_{OL} = \frac{dx}{x - x^*} = \left[\frac{1}{\frac{G - 1}{m} + \frac{\pounds - 1}{\pounds}}\right][-d \ln L]$$

$$= \frac{-d \ln L}{\frac{1}{m}[(V_1/V_2)^{N_G^{-1}} - 1] + [1 - (L_1/L_2)^{-N_L^{-1}}]}$$

Upon integration this becomes Equation (16) in the text, i.e.

$$N_{OL} \equiv \int_{x_1}^{x_2} \frac{dx}{x - x^*} = \frac{\ln(V_1/V_2)}{m^{-1}[(V_1/V_2)^{(H_G/h)} - 1] + [1 - (V_2/V_1)^{(H_L/h)}]}$$

Presented at A.I.Ch.E. Louisville meeting

ERRATA

Below is the list of references cited in John W. Delaplaine's paper "Forces Acting in Flowing Beds of Solids," which appeared in the March, 1956, issue of the *Journal* on page 127. The list was omitted from the published paper.

LITERATURE CITED

1. Adams, B. F., M.S. thesis, Univ. Delaware (1951).
2. Bowden, F. P., and D. Tabor, "The Friction and Lubrication of Solids," Clarenden Press, Oxford (1948).
3. Brinn, M. S., S. J. Friedman, F. A. Gluckert, and R. L. Pigford, *Ind. Eng. Chem.*, **40**, 1052 (1948).
4. Caquot, A., and J. Karisel, "Traité de Mécanique des Sols," Gautier Villars, Paris (1949).
5. Jaky, J., "Proc. Second Intl. Conf. on Soil Mechanics and Foundation Engineering," Rotterdam (1948).
6. Janssen, H. A., *Z. Ver. Deut. Ing.*, 1045 (1895).
7. Ketchum, M. S., "The Design of Walls, Bins, and Grain Elevators," McGraw-Hill Book Company, Inc., New York (1919).
8. Kirk, R. E., and D. F. Othmer, ed., "Encyclopedia of Chemical Technology," vol. 6, pp. 614—656, The Interscience Encyclopedia, Inc., New York (1951).
9. Pleissner, J., *Z. Ver. Deut. Ing.*, **976** (1906).
10. Rausch, J. M., Ph.D. thesis, Princeton Univ. (1948).
11. Schwartz, C. E., and J. M. Smith, *Ind. Eng. Chem.*, **45**, 1209 (1953).
12. Sechler, E. E., "Elasticity in Engineering," John Wiley and Sons, New York (1952).
13. Shaffer, M. R., M.S. thesis, Purdue Univ. (1953).
14. Shaxby, J. H., and J. C. Evans, *Trans. Faraday Soc.*, **19**, 60 (1923).
15. Taylor, D., "Fundamentals of Soil Mechanics," John Wiley and Sons, New York (1948).
16. Tschebotarioff, G., "Soil Mechanics, Foundations, and Earth Structures," McGraw-Hill Book Company, Inc., New York (1951).
17. Westergaard, H. M., "Theory of Elasticity and Plasticity," John Wiley and Sons, New York (1952).
18. Zhavoronkov, N. M., et al., *Zhur. Fiz. Khim.*, **23**, 342 (1949).

In the paper "Entrainment Removal by a Wire-mesh Separator" by C. LeRoy Carpenter and Donald F. Othmer, which appeared in the December, 1955, issue of the *Journal*, on page 554 the equation

$$k = \frac{36{,}856 \times 9.4167 \times 10^{-4/3}}{3.2739} = 10.601$$

should be

$$k = \frac{36{,}856 \times 9.4167 \times 10^{-4}}{3.2739} = 10.601$$

and Equation (8) on page 556, which appeared as $E_s = 1 - (1 - (E_M/c))^N$, should be $E'_s = 1 - [1 - (E_M/c)]^N$.

Turbulent Diffusion in Particulately Fluidized Beds of Particles

THOMAS J. HANRATTY, GEORGE LATINEN, and RICHARD H. WILHELM

Princeton University, Princeton, New Jersey

Measuring the spreading of a tracer dye from a point source yields information on diffusion in glass-sphere beds fluidized in water. Particulately fluidized beds, which are here formed, are well described by the statistical turbulence equations of Taylor. Mixing parameters—eddy diffusivity, scale, and intensity of turbulence—are established. Transition of these variables is traced from fixed beds through fluidized beds in different degrees of bed expansion.

Mixing characteristics of these "ideal" types of fluidization may provide a frame of reference for consideration of more complex systems.

A study of diffusion in the continuous phase of a particulately fluidized bed of particles is of interest for two reasons. Particulate fluidization is suggested to represent, among the various possible modes of fluidization behavior, the smoothest or most "ideal" type. Knowledge gained about mechanisms of mixing through diffusional studies in this kind of system therefore may provide a frame of reference for consideration of more complex types of fluidization, such as are encountered in fluid-powder technology. Particulately fluidized beds are of interest also because they furnish an experimental illustration of aspects of the statistical formulation of diffusion in a turbulent field, proposed by Taylor (*14*) in 1921.

In particulate fluidization, individual particles have random motion and appear to be uniformly dispersed. There is little correlation between the fluctuating motions of adjacent particles. A counterpart is suggested in the molecular motions of an ideal gas. Particulate fluidization is achieved in high-density fluids with small density difference between particle and fluid, as in glass beads suspended in a rising stream of water.

Turbulence theory has been applied to various physical arrangements, commonly with the assumptions of homogeneity, i.e., independence of the translation of reference coordinates and isotropy, or independence of the rotation of the coordinates. An important application has been to steady-state turbulence in the central portion of a tube or duct for which a relatively flat velocity profile may be assumed. The decay of turbulence produced by flow through a stationary grid also has been a major topic of theoretical and experimental investigation. The effect on lateral diffusion of the presence of a fixed bed of particles in a fluid stream has been reported (*2, 12*). A fluidized bed, in turn, may be considered a transition system between unpacked and packed ducts. This is an arrangement for generating steady-state, fluid-phase turbulence through the presence of randomly spaced and randomly moving particles. The particle-population density is capable of being varied between the limits of a packed bed and of a duct in which the fluid stream is devoid of particles.

This paper sets forth particulate fluidization as an example of a turbulent system and establishes parameters such as eddy diffusivity, scale, and intensity of turbulence. The paper is based upon studies (*5, 12*) which may be consulted for details beyond those here presented.

THEORY

A turbulent field usually is considered to be a distribution of eddies ranging in size from dimensions that are too small to be measured to the dimensions of the container. Eddies are continually forming and disappearing within the field. Hence there exists a random motion of large masses of material, which is responsible for turbulent diffusion. Large-scale mixing results from the movement of larger eddies, whereas the small eddies are responsible for fine-grained mixing. This paper is concerned with averaged properties resulting from gross mixing.

It is instructive to compare molecular- and turbulent-diffusional processes between which two elements of dissimilarity have been noted. In molecular diffusion, experimental distances are large compared with the molecular mean free path. In turbulent diffusion such simplification may not be counted on. Experimental measurements can well be made within a turbulent "mean free path" or scale. As a result, for diffusion from a fixed-point source, the size of the turbulent-diffusion coefficient ($\overline{X^2}/2t$) is found to depend upon the time of diffusion, reaching constancy only after a long time interval has elapsed in a given experiment. A second difference between molecular and turbulent diffusion relates to the elementary mechanism steps. The former may be represented as consisting of discrete motions of single particles. By contrast, turbulent diffusion must be thought to involve continuous variation of properties because masses of material move about and continuously change their identity. These elements of difference were recognized by Taylor (*14*) and were given quantitative expression in his equation for turbulent diffusion. Confirmation of Taylor's formulation rests upon a limited number of experimental investigations to date: behind a grid in a wind tunnel (*15, 18, 19*), in a circular duct (*16*), and in a channel (*8, 9*).

To serve in interpreting diffusion measurements in the continuous phase of a fluidized mass of particles, Taylor's equations and other pertinent theoretical background are summarized herewith.

A fixed-point source located at $x = 0$ in a homogeneous isotropic turbulent field is assumed.* Assumed also is the x component of motion of a diffusing particle of fluid. If the velocity component in this direction is u, the displacement of a single particle after a time t is

$$X = \int_0^t u\,dt \qquad (1)$$

Because of the random nature of turbulent motion a plus or minus value for X is equally probable. Therefore, averaged for a large number of particles, $\overline{X} = 0$. However, if the value X^2 be averaged, a finite value will result, $\overline{X^2} \neq 0$. $\overline{X^2}$ will be a measure of the spread which may be expected in a given diffusion time.

The quantity $\overline{X^2}$ may be expressed as a function of the diffusional dispersion time, t, the root-mean-square fluctuating-velocity component, $\overline{u^2}$, and a correlation coefficient,

$$R = \frac{\overline{u_{t_1} u_{t_2}}}{\overline{u^2}}.$$

The covariance $\overline{u_{t_1} u_{t_2}}$ represents the average for a large number of particles of the product of the velocity of a particle at time t_1 and its velocity after a time, $s = t_2 - t_1$. For very large values of s there is no correlation between u_{t_1} and u_{t_2}; i.e., the product can be plus as often as minus $\overline{u_{t_1} u_{t_2}} = 0$. For the case of a small s, the motion of the particle at time t_1 will resemble motion at t_2. If u_{t_1} is negative, then it is probable that u_{t_2} will be negative. Likewise if u_{t_1} is positive, it is probable that u_{t_2} will be positive. Therefore, it is likely that $u_{t_1} \cdot u_{t_2}$ will be positive for a large number of particles; $\overline{u_{t_1} u_{t_2}}$ = positive value.

G. I. Taylor was the first to use these concepts to describe diffusion from a fixed-point source in a homogeneous isotropic field. Kampe de Feriet (*4, 10*) has also considered this problem, and the

*In the present work diffusion measurements were performed only in two dimensions and generally under such conditions that diffusion in the third dimension may be neglected. Present work has therefore been proved to be isotropic in two dimensions. Isotropy in three dimensions is assumed in the present development.

*T. J. Hanratty is at present at the University of Illinois, Urbana, Illinois, and George Latinen with Monsanto Chemical Company, Springfield, Massachusetts.

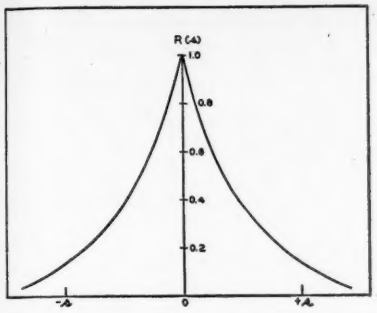

Fig. 1. Typical form of Taylor-de Feriet correlation $R(s)$ for turbulent-velocity fluctuations at time intervals, s.

expression for $\overline{X^2}$, derived by the latter author, is presented below:

$$\overline{X^2} = \int_0^t \int_0^t \overline{u_{t_1} u_{t_2}}\, dt_1\, dt_2$$

$$\overline{u_{t_1} u_{t_2}} = \overline{u^2} R(t_2, t_1)$$

If the field is steady, i.e., $\overline{u_{t_1} u_{t_2}}$ is a function only of $t_2 - t_1$ and not of t_2 or t_1, then

$$\overline{u_{t_1} u_{t_2}} = \overline{u^2} R(t_2 - t_1) = \overline{u^2} R(s)$$

$$\overline{X^2} = \int_0^t \int_0^t \overline{u^2} R(s)\, dt_1\, dt_2$$

Since $R(s)$ is an even function,

$$\overline{X^2} = 2 \int_0^t (t - s) \overline{u^2} R(s)\, ds \quad (2)$$

Because of the nature of the turbulent field, $R(s)$ will vary continuously from 1 to 0 as s varies from 0 to ∞ in a form similar to that shown in Figure 1. The $\overline{X^2}$ vs. t curve has a form depicted in Figure 2. The behavior of the Taylor-de Feriet equation in the limits may be obtained by integration. For t very small, $t \to 0$, $R_s \to 1$:

$$\overline{X^2} = 2\overline{u^2} \int_0^t (t - s)\, ds = \overline{u^2} t^2; \quad (3)$$

$$\sqrt{\overline{X^2}} = \sqrt{\overline{u^2}}\, t$$

For t very large:

$$\overline{X^2} = 2\overline{u^2} \int_0^t tR(s)\, ds - 2\overline{u^2} \int_0^t sR(s)\, ds \quad (4)$$

$$\int_0^t R(s)\, ds \to \text{const.} = \tau = \int_0^\infty R(s)\, ds$$

$$\int_5^t sR(s)\, ds \to \text{const.} = \int_0^\infty sR(s)\, ds$$

since $R(s)$ approaches zero in an exponential manner for large t,

$$\overline{X^2} = 2\overline{u^2}\tau t - 2\overline{u^2}(\text{const.}) \quad (5)$$

For the calculation of the root-mean-square displacement $\overline{X^2}$ at intermediate times, the dependence of R upon the time interval s must be known. It is convenient to assume the exponential relation

$$R(s) = e^{-s/\tau} \quad (6)$$

in which τ is a constant which is a property of the field and may be looked upon as the average lifetime of eddies responsible for diffusion. Turbulent-diffusion studies by Kalinske and Pien (*9*) are satisfactorily approximated by this relation, as are also the results of the present work.

The integrals in Equation (4) may now be evaluated as follows:

$$\int_0^\infty R(s)\, ds = \int_0^\infty e^{-s/\tau}\, ds = \tau \quad (7)$$

$$\int_0^\infty sR(s)\, ds = \int_0^\infty se^{-s/\tau}\, ds = \tau^2 \quad (8)$$

Equation (4) thus becomes

$$\overline{X^2} = 2\overline{u^2}\tau t - 2\overline{u^2}\tau^2 \quad (9)$$

As shown in Figure 2, the intercept of this relation on the t axis occurs at $t = \tau$.

Employing Equation (6) one may write a general expression for $\overline{X^2}$:

$$\overline{X^2} = 2\overline{u^2}\tau^2 \left[\frac{t}{T} - (1 - e^{-t/\tau})\right] \quad (10)$$

Therefore $\overline{X^2}/2\overline{u^2}\tau^2$ is a unique function of t/τ. Kalinske and Pien (*9*) correlated diffusion data by means of these variables.

HOMOGENEOUS ISOTROPIC SYSTEMS INVOLVING TURBULENT DIFFUSION

The variation of $\overline{X^2}$ with time for molecular diffusion from a fixed point has been shown by Einstein (*3*) to be

$$\frac{\overline{X^2}}{2t} = D = \text{constant} \quad (11)$$

where D = molecular diffusivity. Systems involving molecular diffusion may be described by the Fick's law differential equation using appropriate boundary conditions:

$$\frac{\partial c}{\partial t} = \nabla \cdot (D \nabla C) \quad (12)$$

The use of this equation implicitly involves the assumption that the diffusion characteristics of particles contained in a differential volume are independent of their previous history, i.e., the length of time they have been in the field. This independence is not encountered in turbulent diffusion, i.e., $\overline{X^2}/2t$ is a function of time. Therefore Fick's law may not be used to describe the diffusion of particles which have been in the field for different lengths of time. The description of turbulent systems must be accomplished by defining the diffusion behavior of a single source or sink of heat or mass

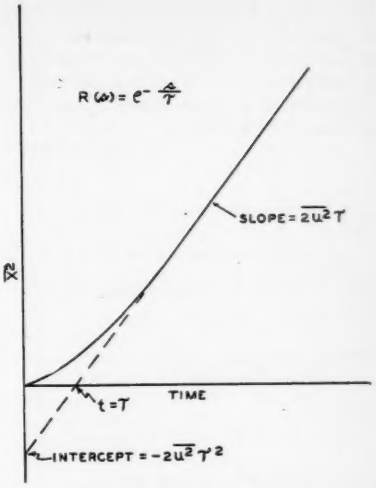

Fig. 2. Relation between $\overline{X^2}$ for diffusion from a point source with time when the correlation for turbulent-velocity fluctuations is approximated by $R(s) = e^{-s/\tau}$

and then representing the system as consisting of a number of distributed sources and sinks.

Batchelor (*1*) and Hanratty (*6*) have shown that Equation (12) with a diffusion coefficient which varies with time can be used to describe the behavior of a single instantaneous source or sink

$$\frac{\partial C}{\partial t} = \phi(t) \nabla^2 C \quad (13)$$

provided that (1) the diffusion coefficient be defined as

$$\phi(t) = \frac{1}{2} \frac{d\overline{X^2}}{dt} \quad (14)$$

and (2) the distribution describing $\overline{X^2}$ be Gaussian:

$$P\, dx\, dy\, dz = \frac{1}{(2\pi \overline{X^2})^{3/2}} \cdot \exp\left[-\frac{x^2 + y^2 + z^2}{2\overline{X^2}}\right] dx\, dy\, dz \quad (15)$$

$P\, dx\, dy\, dz$ = probability of finding a particle between x and $x + dx$, y and $y + dy$, z and $z + dz$.

For the description of the experiments described in this paper it is convenient to consider the solution to Equation (13) for a cylindrical polar-coordinate system for radial symmetry for the case in which diffusion in the z direction is important and also for the case in which it is negligible. The equations to be solved are then as follows:

$$\frac{\partial C}{\partial t} = \phi(t)\left[\frac{\partial^2 C}{\partial r^2} + \frac{1}{r}\frac{\partial C}{\partial r} + \frac{\partial^2 C}{\partial z^2}\right] \quad (16)$$

$$\frac{\partial C}{\partial t} = \phi(t)\left[\frac{\partial^2 C}{\partial r^2} + \frac{1}{r}\frac{\partial C}{\partial r}\right] \quad (17)$$

If N units of material, or N units per unit length for the two-dimensional case, emitted into the field at zero time from a position $r = 0$, $z = 0$, are considered, the solutions of Equations (16) and (17) for boundary conditions

$$t > 0$$

$$C \to 0 \quad \text{as} \quad r \to \infty$$

$$C \to 0 \quad \text{as} \quad z \to \infty$$

are respectively longitudinal diffusion important:

$$C = \frac{N}{(2\pi)^{3/2}[\int_0^t 2\phi\, dt]^{3/2}} \cdot \exp\left\{-\frac{r^2 + z^2}{2\int_0^t 2\phi\, dt}\right\} \quad (18)$$

negligible longitudinal diffusion:

$$C = \frac{N}{(2\pi)[\int_0^t 2\phi\, dt]} \exp\left\{-\frac{r^2}{2\int_0^t 2\phi\, dt}\right\} \quad (19)$$

When the diffusing time is long enough so that material reaches the container walls, the boundary conditions become for $t > 0$

$$z = +\infty \qquad C = C_A$$

$$z = -\infty \qquad C = 0$$

$$r = a \qquad \frac{\partial C}{\partial r} = 0$$

The solutions of Equations (16) and (17) are then longitudinal diffusion important:

$$C = \frac{N \exp\left\{-\frac{z^2}{4\int_0^t \phi\, dt}\right\}}{\pi a^2 \sqrt{2\pi}\,[\int_0^t 2\phi\, dt]^{1/2}} \cdot \sum_0^\infty \exp\left\{-\beta_n{}^2 \int_0^t \phi\, dt\right\} \frac{J_0(\beta_n r)}{J_0{}^2(\beta_n a)} \quad (20)$$

longitudinal diffusion unimportant:

$$C = \frac{N}{\pi a^2} \sum_0^\infty \exp\left\{-\beta_n{}^2 \int_0^t \phi\, dt\right\} \cdot \frac{J_0(r\beta_n)}{J_0{}^2(a\beta_n)} \quad (21)$$

where β_n is defined by the equation below:

$$J_1(\beta_n a) = 0 \quad (23)$$

The validity of the preceding four solutions [Equations (18) to (21)] can be seen by substituting back into Equations (16) and (17). These solutions are identical with those that would be obtained by solving Equation (12) if it is assumed that D = constant if one substitutes in the final expression

$$Dt = \int_0^t \phi\, dt$$

Hence a turbulent diffusivity, E, analogous to D may be defined as

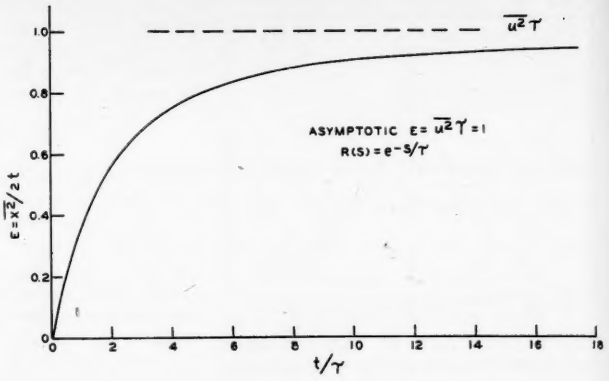

Fig. 3 Graph showing that eddy diffusivity varies with time of diffusion in a turbulent field and ultimately reaches a constant value.

$$E = \frac{1}{t}\int_0^t \phi\, dt = \frac{\overline{X^2}}{2t} \quad (24)$$

Unlike molecular diffusion from a fixed-point source, E will vary with time. If Equation (2) is used, an expression may be written for E for a homogeneous isotropic field:

$$E = \frac{\overline{X^2}}{2t}\int_0^t (t - s)R(s)\, ds$$

If Equation (6) is valid the foregoing expression may be integrated to yield

$$E = \overline{u^2}\tau\left[1 - \frac{\tau}{t}(e^{-t/\tau} - 1)\right] \quad (25)$$

This function is plotted in Figure 3. Only for large times of diffusion does E level out to a constant value.

TURBULENT FLOW SYSTEM INVOLVING DIFFUSION FROM A CONTINUOUS SOURCE

Theory presented up to this point has been for isotropic, homogeneous turbulence, conditions which at best can be only approximated. Flow in ducts, for example, may deviate from ideal conditions because of the effect of walls on the flow profile and on turbulence isotropy and homogeneity. Even if a uniform flow existed, the condition of isotropy might not be satisfied as diffusion in the direction of flow might be different from that in other directions. If turbulence is caused by a grid, there will be a continuous state of decay of the turbulence in the stream. The experimental system used in this research consisted of diffusion from a continuous source of material located in the center of a "particulate" fluid bed through which fluid is flowing in the z direction. The fluid velocity is substantially uniform in the cross section of the container, and, although there must necessarily be a decay of turbulence, continuous concurrent replenishment proceeds from the suspended particles. It has been assumed therefore that the field may be considered homogeneous and isotropic in the radial direction. Turbulence is probably not the same in the r as in the z direction.

The equations developed in the theory section may be used if the system is represented as a number of instantaneous sources which are carried downstream with the fluid. Each one of these sources will spread out equally in all directions and thus consists of a spherical cloud of the material which increases in radius as it is transported downstream. The case in which longitudinal diffusion is neglected is represented by a number of sources which spread out only in the radial direction and therefore is represented by a series of expanding disks.

At $r = 0$ and at a distance z' from the injection point is a source which has been in the field a time $t = z'/U$. The concentration profile in a cross section at a given value of z will result from contributions of sources that have been in the field for times ranging from 0 to ∞. When longitudinal diffusion is neglected, only a source which has been in the field a time $t = z/U$ will contribute to the concentration profile at a longitudinal distance z from the injector.

Equations (18) and (20) may be used to describe the contribution of a single source if the quantity $(Ut - z)$ is substituted for z. The sum of the effect of all the sources is obtained in the following manner:

wall effect unimportant:

$$C = \int_0^\infty \frac{Q\, dt}{[2\pi\int_0^t 2\phi\, dt]^{3/2}} \cdot \exp\left\{-\frac{r^2 + (Ut - z)^2}{4\int_0^t \phi\, dt}\right\} \quad (26)$$

wall effects important:

$$C = \int_0^\infty \frac{Q\, dt \exp\left\{-\frac{(Ut - z)^2}{4\int_0^t \phi\, dt}\right\}}{\pi a^2[2\pi\int_0^t 2\phi\, dt]^{1/2}} \cdot \sum_0^\infty \exp\left\{-\beta_n{}^2 \int_0^t \phi\, dt\right\} \frac{J_0(\beta_n r)}{J_0{}^2(\beta_n a)} \quad (27)$$

Q = rate of flow of material from the injector

Equations (19) and (21) may be used to describe a continuous source by substituting $t = z/U$.

wall effects unimportant:

$$C = \frac{N}{(2\pi)\left[\int_0^{z/U} 2\phi\, dt\right]} \cdot \exp\left\{-\frac{r^2}{2\int_0^{z/U} 2\phi\, dt}\right\} \quad (28)$$

wall effects important:

$$C = \frac{N}{\pi a^2} \sum_0^{\infty} \exp\left\{-\beta_n{}^2 \int_0^{z/U} \phi\, dt\right\} \cdot \frac{J_0(r\beta n)}{J_0{}^2(a\beta_n)} \quad (29)$$

Equation (28) is the Gaussian error curve.

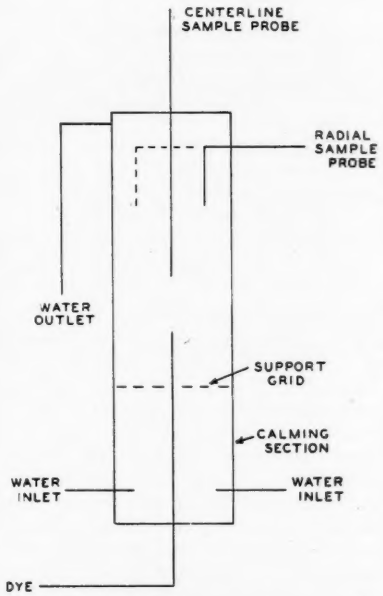

Fig. 4. Elements of apparatus for measuring diffusion of tracer from a point source into a fluidized bed.

EXPERIMENTAL

As noted above, turbulent diffusion may be characterized by two of the following parameters: an asymptotic value of E, an intensity $\sqrt{\overline{u^2}}/U$, and a scale factor τ. The measure of spread of a tracer material from a fixed-point source into the turbulent field (as determined in the present work) served as a convenient technique for finding these properties. The particulately fluidized bed here used consisted of uniformly sized spherical glass beads suspended in an upward stream of water flowing in a 5.4-cm. tube. The size of bead, 3 mm. in diameter, was carefully chosen to give a representative "ideal" system, i.e., one that is described by a Taylor $\overline{X^2}$ vs. t function. When glass beads of smaller size were employed, the scale of turbulence was found to be very small, leading to precision difficulties in measuring this relation. Larger glass spheres were not used because of possible wall effects with large particle-to-tube-diameter ratios. Heavier particles of lead 3-mm. spheres lead to "nonideal" behavior (*5*), in which the Taylor $\overline{X^2}$ function does not hold, a system which is not included in the present discussion.

Fluidized glass beads are in random motion which from observation appears to lack strong correlation in the motion of neighboring particles except for an over-all net movement up one side of the tube and down the other, an action which is slow compared with movements of individual particles relative to each other. Diffusion measurements were restricted to the central section of the tube, away from the upper and lower ends, at which there is lateral motion of particles.

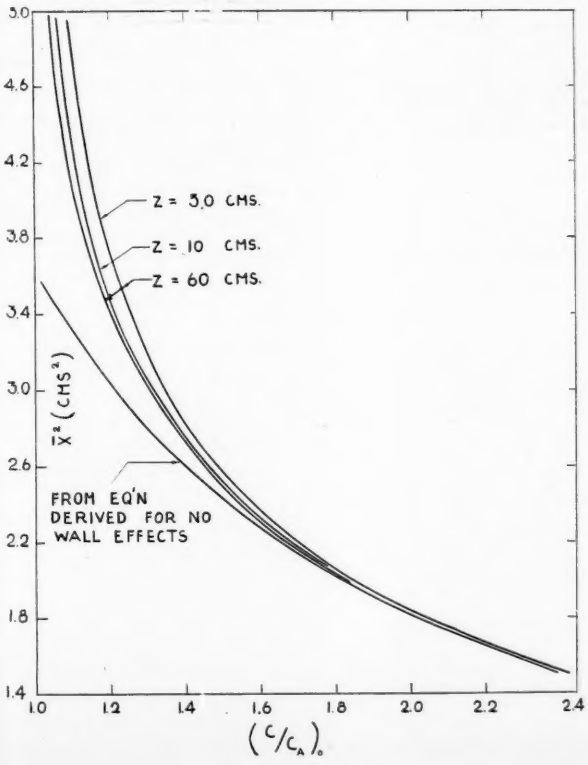

Fig. 5. Computed relationships between $\overline{X^2}$ and center-line compositions (C/C_A) at different coordinate distances between source and sampling taps. $\overline{X^2}$ is a measure of tracer spreading under the condition of $U_{AVG}/U = 1$ and the hypothetical condition of no containing walls and zero fluid velocity.

Apparatus

The equipment was substantially that used by Bernard and Wilhelm (*2*) and Latinen (*12*). A line sketch is shown in Figure 4. Features of the design are as follows:

The column was a Lucite tube 5.40 cm. I.D., 25.1 cm. long. Methylene blue dye, concentration 4 g./1,000 ml. of water, was admitted to the fluidized bed of particles from a centrally located stainless tube entering from the bottom. The tracer-tube position could be varied vertically from a position flush with the support plate to an elevation of 9.2 cm. from the plate. The tracer tube was 1/16 in. I.D., ⅛ in. O.D., and was tapered to 3/32 in. at the point of injection. Dye was introduced from a storage tank pressurized with nitrogen.

The main water stream was pumped to a distributor and thence through eight equally spaced radial arms to a turret at the base of the column. This design ensured a symmetrical feed to the column.

A calming section preceded the column proper to ensure a uniform-flow profile and to break up any large-scale eddies which might have formed. The calming section consisted of a 12 in. length of piping packed with 1-mm. glass spheres.

The support plate for the bed was a grid made by milling 0.020-in. grooves 0.020 in. apart into each face of a 1.6-in. brass disk. The two series of grooves were at right angles to one another so that the net effect was of a plate having uniformly sized and spaced 0.020-in. square holes. The plate was covered with a fine-mesh screen to prevent small particles from being jammed in the openings.

Water flow rates were measured by means of rotameters, and the tracer-dye flow rate was determined from the known water flow rate and the average concentration in the column effluent. The temperature of the water was measured.

Two types of sampling traverses were made, radial and center line. The radial sampling probe consisted of a horizontal leg of ⅛-in. stainless steel tubing which entered at a position about 10 cm. above the top level of the fluid bed. A length of similar tubing with a 2-in. piece of 3/64-in. hypodermic tubing soldered into the end constituted the vertical segment. By using probes having vertical legs of different length, one could vary the longitudinal position of the traverse.

The center-line probe consisted of a length of ⅛-in. stainless steel tubing which was tapered to an outside diameter of 3/32 in. at the sampling position. It entered through the top of the column and was held in a central position by three 1/16-in.-diam. brass rods which were soldered to the probe at a position 2¾ in. from its tip. A vernier was etched on the surface of the tubing so that its position might be determined directly.

Probe samples were analyzed with a Fisher electrophotometer having a red filter.

Procedure

Data may be obtained over a range of fluidized-bed properties depending on the flow rates, bed heights, and fractions void. In all runs except two, a constant bed height of 20.3 cm. was maintained. Fractions void and flow rates were varied by changing the amount of solids in the bed.

The operating procedure was as follows. After the lines were flushed, water was admitted to the column which contained a known weight of spheres. The bed was expanded to the standard height. After an initial flushing of lines, the dye rate was adjusted to a velocity slightly less than that of the surrounding water stream. Time-average tracer samples were secured by a slow, uniform withdrawal over a period ranging from 1½ to 2½ min. It was determined that sample compositions do not depend upon withdrawal rates at these low withdrawal velocities.

REDUCTION OF DATA

Two types of data were obtained: radial traverses in a plane at a fixed longitudinal distance from the plane of the source and center-line traverses. Radial traverses were measured to examine the validity of the equations developed in preceding sections of this paper and to obtain information about the nature of the distribution describing $\overline{X^2}$.

In order to evaluate the parameters intensity $\sqrt{\overline{u^2}/U}$ and scale τ, it is necessary to obtain the $\overline{X^2}$ vs. t relation that one of the single instantaneous sources would possess under the hypothetical condition of zero flow and no confining boundaries. Experimentally the relationship is conveniently obtained from the longitudinal traverse.

The experiments described in this paper were such that diffusion in the flow direction could not be measured. Therefore the equations developed for a two-dimensional source were used in examining the data. Throughout most of the field concentration gradients in the flow direction were much smaller than in the radial direction and the foregoing simplification was a valid one. However, close to the source this is not true and longitudinal diffusion will affect the measured concentration profiles.

The amount of material flowing from the injector per unit time may be calculated from the mixed average concentration of the column effluent, C_A, and the average velocity over the tube cross section within the fluidized bed.

$$Q = C_A \pi a^2 U_{AVG} \qquad (30)$$

The flux of diffusing material at any point in the tube is UC where U is the velocity of the fluid at that point. The quantity $UC/(\pi a^2 U_{AVG} C_A)(2\pi r\, dr)$ then represents the probability of finding a particle of the diffusing material in the differential area $2\pi r\, dr$. In terms of the nomenclature used in Equations (28) and (29) this is equal to $(C/N)2\pi r\, dr$.

These equations may be rewritten in the following form:

$$\frac{C}{C_A} = \left(\frac{U_{AVG}}{U}\right) \frac{a^2}{2[\overline{X^2}]} \cdot \exp\left\{-\frac{r^2}{2\overline{X^2}}\right\} \qquad (31)$$

$$\frac{C}{C_A} = \left(\frac{U_{AVG}}{U}\right) \sum_0^\infty \exp\left\{-\frac{\beta_n^2}{2}\overline{X^2}\right\} \cdot \frac{J_0(r\beta_n)}{J_0^2(a\beta_n)} \qquad (32)$$

The term U_{AVG}/U is the ratio of the average fluid velocity in the bed to the velocity of the diffusing material. Thus if the field were such that the fluid velocity were larger in the center than in other portions and if diffusion measurements were made only in this region then (U_{AVG}/U) would be less than unity. The parameter U_{AVG}/U can be evaluated directly from a concentration profile for cases in which longitudinal diffusion is negligible through the relation

$$U_{AVG}/U = \overline{C/C_A} \qquad (33)$$

The validity of this equation can be proved by considering the case in which C/C_A is negligible at the wall:

$$\overline{C/C_A} = \int_0^a \frac{(C/C_A)\, d(r^2)}{a^2}$$

Substituting from Equation (31) for C/C_A gives

$$\overline{C/C_A} = \frac{\left(\frac{U_{AVG}}{U}\right)\frac{a^2}{2[\overline{X^2}]}\int_0^a \exp\left\{-\frac{r^2}{2\overline{X^2}}\right\} d(r^2)}{a^2}$$

Since C/C_A is negligible at the wall

$$\left(\frac{U_{AVG}}{U}\right)\frac{a^2}{2\overline{X^2}} \exp\left\{-\frac{r^2}{\overline{X^2}}\right\} \to 0$$

integration of the equation for $\overline{C/C_A}$ results in Equation (33).

Relations for center-line concentrations can be obtained from Equations (31) and (32) by setting $r = 0$:

wall reflections unimportant:

$$(C/C_A)_0 = \left(\frac{U_{AVG}}{U}\right)\frac{a^2}{2\overline{X^2}} \qquad (34)$$

wall reflections important:

$$(C/C_A)_0 = \left(\frac{U_{AVG}}{U}\right)\sum_0^\infty \frac{1}{J_0^2(a\beta_n)} \cdot \exp\left\{-\frac{\beta_n^2}{2}\overline{X^2}\right\} \qquad (35)$$

Therefore, for cases in which U_{AVG}/U is known, $\overline{X^2}$ may be obtained as a function of z from center-line traverses provided Equations (31) and (32) are valid in describing radial-concentration profiles. This is shown to be true for distances far from the source. Close to the source Equation (31) does not describe the entire profile, owing to longitudinal diffusion. However, the effects of longitudinal diffusion are confined to the outer regions and Equation (31) may still be used to calculate the center-line concentrations. Frenkiel (5) has calculated concentration profiles for the asymptotic case of $t \to 0$ and $R(s) \to 1$. These show

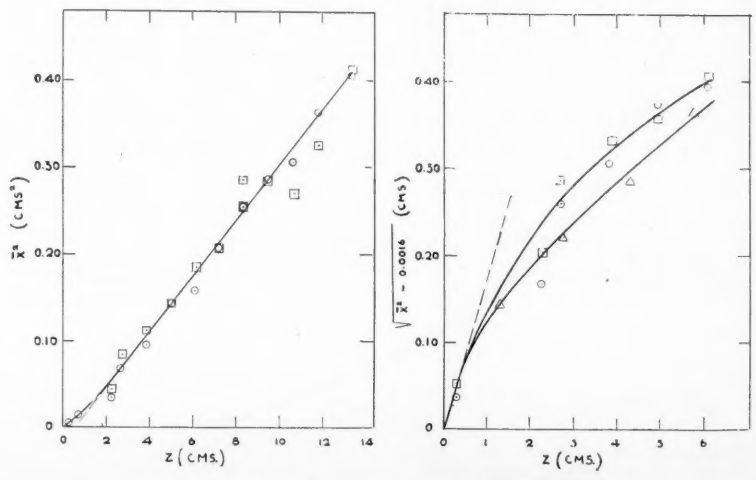

Fig. 6. Empty-tube data. $\overline{X^2}$ vs. z and $\sqrt{\overline{X^2} - 0.0016}$ vs. z.

that for small intensities, $\sqrt{\overline{u^2}}/U$, Equation (31) is valid. As the intensity approaches a value of about 0.1, however, the concentration profile digresses from the Gaussian distribution at large values of r. As the intensity increases, this effect extends itself to smaller r. However, the concentration at $r = 0$ is not affected until the intensity reaches a value larger than 0.5.

The relation between $\overline{X^2}$ and $(C/C_A)_0$ as calculated from Equations (34) and (35) for the case of $U_{AVG}/U = 1$ are presented in Figure 5. It can be seen from this graph that reflections of tracer substance from the wall do not affect these calculations until C/C_A at the tube center drops to a value of about 2.2. Values of $\overline{X^2}$ obtained from this graph are not the actual mean square displacement of the material at the level under consideration but are values describing the spread under the hypothetical condition of no confining walls and mean velocity of zero. The mean square displacement so computed may be used directly to secure turbulence parameters of interest.

Limiting Value of E

With Equations (5) and (24), corrected for flow, applied to the limiting slope of $\overline{X^2}$ vs. z at large values of z, the slope is shown to be the limiting value of E/U. Since this equals $U\tau(\sqrt{\overline{u^2}}/U)^2$, evaluation of the scale τ or the intensity $\sqrt{\overline{u^2}}/U$ will completely define the system, provided that U of the tracer is the same as the mixed average fluid velocity, i.e., $U = U_{AVG}$, or that U/U_{AVG} is known.

Intensity, $\sqrt{\overline{u^2}}/U$

Application of Equation (3) in a flow system to the initial slope of an $\sqrt{\overline{X^2}}$ vs. t curve results in a slope with a numerical value of the intensity. Extraction of turbulence intensity by this route presents difficulties because (1) the source is finite and therefore at $z = 0$, $\overline{X^2} \neq 0$ and (2) it is not possible to make measurements very close to the source without altering the system between the injector and sampling probe.

In order to estimate the effect of the initial displacement of tracer due to the finite source, the data were treated in the relationship $\sqrt{\overline{X^2} - \overline{X_0^2}}$ vs. z. $\overline{X_0^2}$ is the initial displacement at the source, which may be derived as follows:

$$\overline{R_0^2} = \overline{X_0^2} + \overline{Y_0^2} = 2\overline{X_0^2}$$

$$\overline{R_0^2} = \frac{\int_0^b r^2 2\pi r\, dr}{\pi b^2} = \frac{b^2}{2}$$

$$\overline{X_0^2} = \frac{b^2}{4}$$

For the tracer tube used, $\overline{X_0^2}$ has a value of 0.0016 sq. cm.

The variable $\sqrt{\overline{X^2} - \overline{X_0^2}}$ should extra-

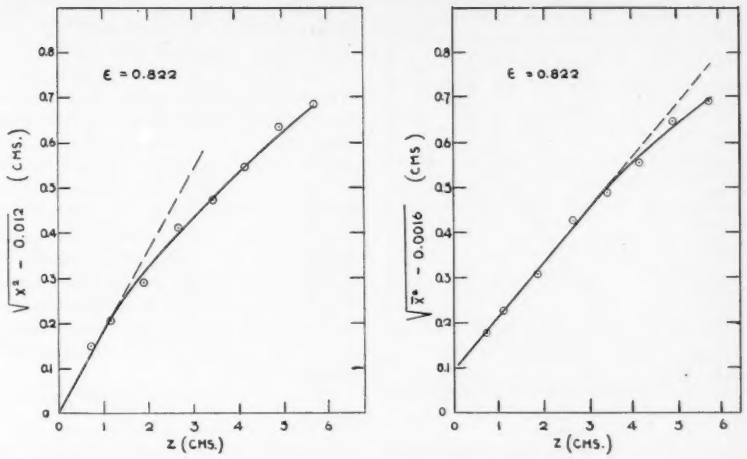

Fig. 7. Typical fluidized-bed data showing the effect of selecting values for X_0^2 in the ordinate, $\sqrt{\overline{X^2} - \overline{X_0^2}}$.

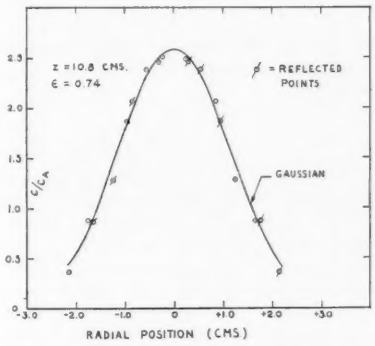

Fig. 8. Typical Gaussian distribution of tracer substance in particulately fluidized bed at substantial distance from source.

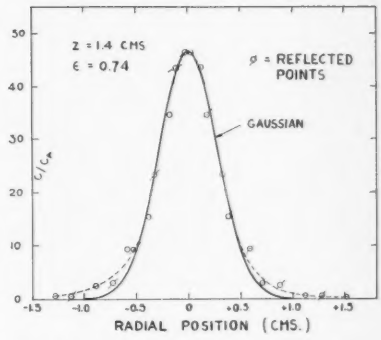

Fig. 9. Typical distribution of tracer substance in a particulately fluidized bed at a level close to the source, showing deviation from a Gaussian distribution at the larger radial positions.

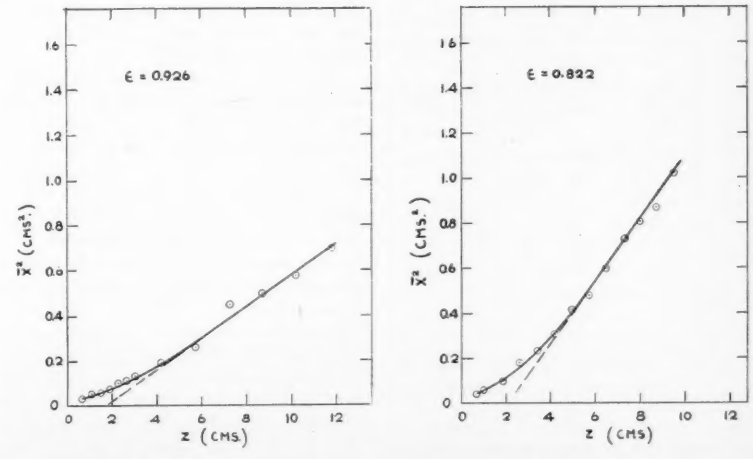

Fig. 10. Typical $\overline{X^2}$ vs. z curves obtained from axial traverses of tracer composition.

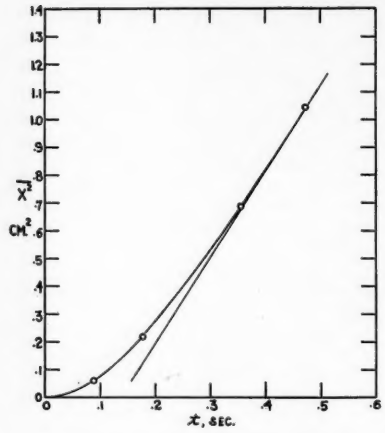

Fig. 11. $\overline{X^2}$ vs. t for 3.4-mm. glass beads fluidized in water at $\epsilon = 0.80$; experimental points determined by full radial traverses at different z positions.

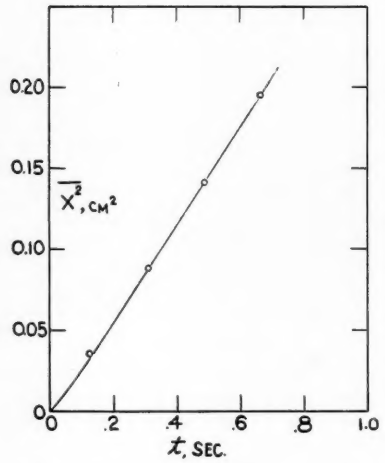

Fig. 12. $\overline{X^2}$ vs. t for 1.8-mm. glass beads fluidized in water at $\epsilon = 0.90$; experimental points determined through full radial traverses at different z positions.

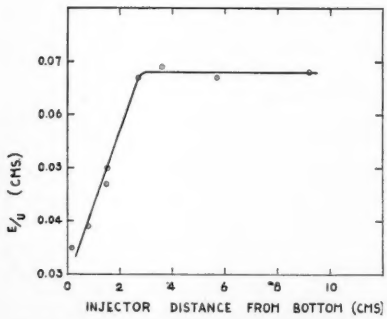

Fig. 13. Asymptotic values of E/U related to the distance of the tracer injector from the grid-bed support.

polate to a value of zero at $z = 0$ as a gross test of the relationship. Data from empty-tube measurements (Figure 6) conform quite well when $\overline{X_0^2}$ is taken at the aforementioned value. However, in the case of all fluidization runs with glass spheres the value of $\overline{X_0^2}$ had to be adjusted to an empirical value of 0.012 sq. cm. This single value sufficed for all fluidization experiments (Figure 7). It would appear that the effective diameter of the injector during fluidization is approximately three times the internal diameter of the tube. It is possible that collisions of particles with the injector tip serve to spread the emerging dye stream.

Scale, τ

The most convenient route to the scale is first to assume the function $R(s) = \exp(-s/\tau)$, which validates Equation (9). When this equation for the limiting asymptote of the $\overline{X^2}$ vs. t curve is rewritten in the form below,

$$\overline{X^2} = \frac{2\overline{u^2}\tau z}{U} - 2\overline{u^2}\tau^2 \qquad (36)$$

it can be seen that the scale τ can be evaluated from the intercept on the z axis, z_0.

$$z_0 = U\tau \qquad (37)$$

A judgment of the validity of the assumptions may be achieved through comparison of the complete experimental $\overline{X^2}$ vs. curve, especially in the curvilinear section, with the same complete function [Equation (10)] computed from the assumed relation for R. An alternative procedure to evaluate τ(*9, 14, 15*) involves double differentiation of $\overline{X^2}$ vs. t data in the nonlinear section, where $R > 0$. Because of questionable precision, this latter method was not chosen in the present work.

RESULTS

Experiments were conducted over the gross linear velocity range from 4 to 26 cm./sec. encompassing fractions void between 0.47 and 0.93.

Typical radial-concentration profiles are shown in Figures 8 and 9. Individual experimental points are used twice, as original points and as reflected points on the other lobe of the curve. At substantial distances from the source (Figure 8) diffusion is described by a Gaussian type of curve [Equation (31)]. However, close to the source, as in Figure 9, profiles diverge from a Gaussian distribution at large values of r, probably because of longitudinal diffusion. Application of Equation (26) gives a similar divergence. As shown in Figure 9, however, the data diverge much more than would be predicted by Equation (26). This could be due to nonhomogeneities in the field caused by the presence of the injector or to the nonisotropic nature of the field. Equation (26) assumes that diffusion in the direction of mean flow is the same as in the radial direction. This assumption, as was pointed out in the theory section, is probably not true. A similar divergence between experimental and predicted results on the basis of a homogeneous isotropic field was obtained by Hinze and van der Hegge (*7*) on the spread of heat in a gas stream close to the source.

Values of U_{AVG}/U were determined through the use of Equation (33) applied to radial-concentration profiles. The results, presented in Table 1, indicate that

Table 1. Summary of U_{AVG}/U Values from Radial Traverses

$\frac{U_{AVG}}{U}$	U, cm./sec.	ϵ	z, cm.
1.0	16.0	0.737	1.4
1.0	16.0	0.737	1.9
0.7	16.0	0.737	0.95
1.0	16.0	0.737	10.8
0.7	16.9	0.816	1.5
0.8	16.9	0.816	3.0
1.1	16.9	0.816	6.0
1.0	16.9	0.816	8.0
0.9	23.6	0.914	1.4

$U_{AVG}/U \approx 1$ at all levels in the tube. Fluid velocity is apparently quite uniformly distributed in the tube. It should be noted that calculation of the ratio is highly sensitive to a displacement of the center of the concentration traverse from the center of the tube.

$\overline{X^2}$ vs. z curves were determined, in the main, from center-line traverses, a typical set being illustrated in Figure 10. Figures 11 and 12 present similar data, but plotted against time rather than distance. This particular pair of curves was determined from full radial traverses at each z level, Figure 11 being for fluidization of 3.4-mm. glass beads and Figure 12 for 1.8-mm. beads, the former being at a void fraction of 0.80 and the latter, 0.90. Notable was the high visual uniformity of the bed with the smaller particles and the relatively small $\overline{X^2}$ and scale as indicated in Figure 12.

End effects are depicted in Figure 13, which presents asymptotic values of E/U (at large spacings between injector and sampling tubes) as a function of the distance of the injector from the bottom grid plate. A uniform field is not obtained until the injector is placed about 2.5 cm. from the support plate. In all axial traverses, therefore, the injector was placed at the safe distance of 4.6 cm. from the bottom. Taking traverse data in the upper few centimeters of the fluidized bed was also avoided.

All $\overline{X^2}$ vs. z results in this work are correlated in Figure 14 by the dimensionless variables $\overline{X^2}/2(E/U)_{1.v.}z_0$ and z/z_0. These variables are derived by a combination of Equations (9), (10), and (24). Clearly, the type of relation predicted by

Taylor for homogeneous, isotropic turbulence is achieved in a particulately fluidized bed.

A comparison is afforded in Figure 15 to show the closely similar characteristics of turbulence in the present water-fluidized beds and turbulence as measured in an open channel by Kalinske and Pien (*9*). The "calculated curve" is computed by means of Equation (10) and represents the form of the correlation function R as given in Equation (6). It appears that this function may be considered only as a convenient first approximation to a correlation function that completely expresses fluid-bed turbulence properties.

Turbulence intensities were computed from center-line traverses by two alternate methods. The first method involved determination of the time scale τ through the intercept of $\overline{X^2}$ vs. z curves and computation of $\sqrt{\overline{u^2}}/U$ from Equations (36), (13), and (17) as discussed under Reduction of Data. The second method secured the intensity from the initial slope of a $\sqrt{\overline{X^2} - \overline{X_0^2}}$ vs. z plot. Figure 7 gives a typical plot of the latter function and illustrates the effect of choosing different values of $\overline{X_0^2}$, the value of 0.0016 stemming directly from the dimensions of the injector tip, the value of 0.012 being an empirically chosen value such that the function passes through the origin. Table 2 presents a comparison of intensities computed by the two methods. The agreement between the two is considered satisfactory.

FLUID-BED PROPERTIES

The mixing properties of a fluidized bed are observed to vary in an interesting manner as, with increasing fluid velocity, the particle population is varied over the full possible range, from a fixed bed to a tube containing no particles. The mixing properties include the Peclet number, $D_p U/(E_{l.v.})$, turbulence intensity, $\sqrt{\overline{u^2}}/U$, a measure of the life of a turbulent eddy, τ, and a length, l, representing the scale of turbulence. The latter variable is defined through the equation

$$E_{l.v.} = l\sqrt{\overline{u^2}} \qquad (38)$$

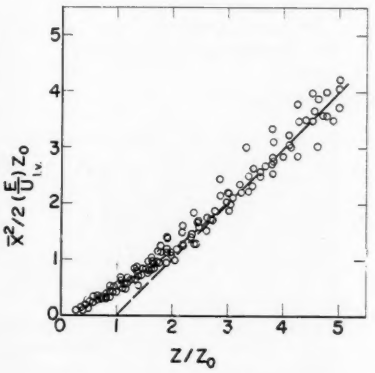

Fig. 14. Generalized plot of all 3-mm. glass-bead fluidization data, $\overline{X^2}/2(E/U)z_0$ vs. z/z_0.

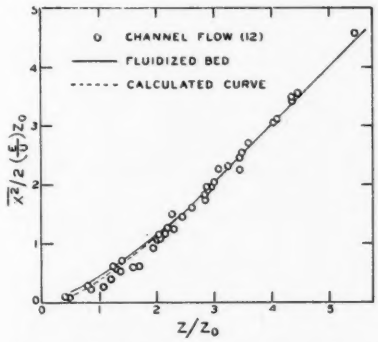

Fig. 15. Generalized plot of fluidization and channel-flow turbulent spreading of tracer substance. A calculated curve also is presented, based upon the form of the correlation function, $R(s) = \exp(-s/\tau)$.

Table 2. Comparison of Turbulence Intensities Calculated by Intercept of $\overline{X^2}$ vs. z Curve and by the Initial Slope of the $\sqrt{\overline{X^2} - \overline{X_0^2}}$ vs. z Curve

$\sqrt{\overline{u^2}}/U$

ϵ	Intercept	Initial slope
0.93	0.14	0.16
0.90	0.15	0.15
0.89	0.16	0.17
0.88	0.16	0.17
0.85	0.16	0.15
0.77	0.19	0.18
0.74	0.20	0.19
0.71	0.19	0.18
0.69	0.23	0.18
0.65	0.24	0.25
0.61	0.32	0.25
0.57	0.28	0.22
0.54	0.23	0.21
0.47	0.30	0.23
0.82	0.17	0.19
0.82	0.19	0.21
0.82	0.16	0.19
0.82	0.18	0.18

PECLET NUMBER DURING FLUIDIZATION

The change of the Peclet group during fluidization as fluid velocity (Reynolds number) is increased and as the particle population simultaneously is decreased is shown in Figure 16 for three different sizes of particles. A minimum Peclet number (maximum E) is found for each particle size to correspond to a fraction void of about 0.70. Mixing in a packed bed was found (*12*) to be explainable in terms of a random-walk model, and it is suggested that a dense fluidized bed retains elements of this mechanism. The distance a fluid element must side step in order to pass around a particle increases as the bed is expanded. Eventually, at a fraction void of 0.70, a fluid element may begin to flow past solid particles without the necessity at each level of flowing laterally in order to evade a particle. Beyond the critical fraction void, in dilute beds, the turbulence is particle generated and the eddy diffusivity then is a direct function of particle population, leading to an increase in Pe as Re is increased (and the population is thereby decreased between the tracer source and sample probe).

The manner in which the limits of a fluid bed are approached in the case of 3-mm. beads when the Peclet number is

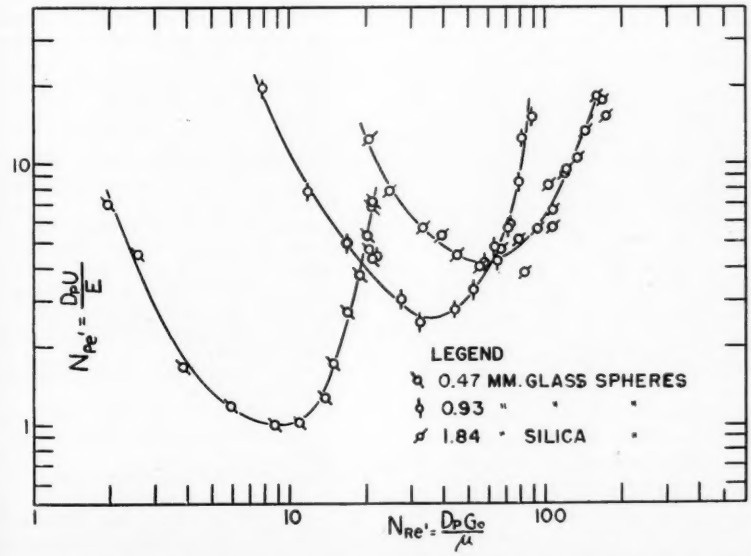

Fig. 16. Variation of Peclet number with Reynolds number during the fluidization in water of three different sizes of particles.

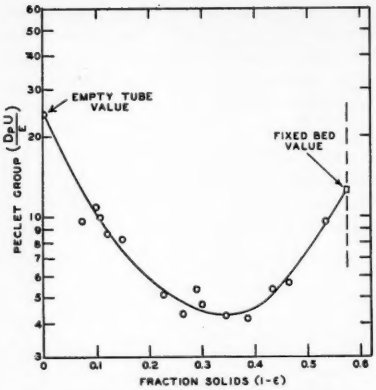

Fig. 17. Peclet-number variation with fraction solids during expansion of fluid bed of 3-mm. particles in water between the limits of an empty tube and a fixed bed.

related to fractions solid is shown in Figure 17. The Peclet number for a fixed bed was determined in a separate tracer-diffusion study (*12*).

SCALE AND INTENSITY

The variation of scale and intensity with fraction solids for a fluidized bed of 3-mm. particles is presented in Figure 18. Consistent with the model presented above for variation of Pe, the scale is observed to achieve a maximum value at a fraction void of about 0.70. The intensity is noted to vary directly with particle population although there are uncertainties at the limits. Fixed-bed values for scale and intensity were estimated through a calculation based upon the random-walk model (*5*).

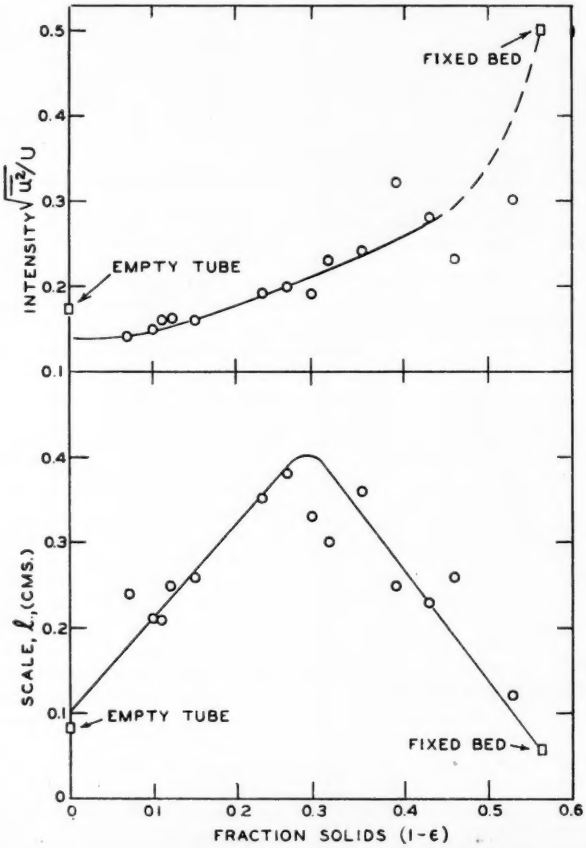

Fig. 18. Scale and intensity of turbulence in water-fluidized bed of 3-mm. glass spheres as function of fraction solids; empty-tube values by experiment, fixed-bed values through calculation based on random-walk model.

NOTATION

a = fluid-bed radius
b = tracer-tube internal radius
C = concentration of diffusing material
C_A = mixed average concentration in column effluent
D_p = particle diameter
D_t = tube diameter
E = eddy diffusion coefficient = $\overline{X^2}/2t$
$E_{l.v.}$ = limiting value of eddy diffusion coefficient
$J_0(\ )$ = Bessel function of first kind, zero order
Q = source strength
r = radial distance
Re = Reynolds number
R_0 = correlation coefficient

$$\frac{\overline{u_{t1}u_{t2}}}{\sqrt{\overline{u^2}_{t1}}\sqrt{\overline{u^2}_{t2}}}$$

S = $x^2 + y^2 + z^2$
s = increment of time = $t_2 - t_1$
t = time
U = fluid velocity associated with tracer material within fluidized bed
U_{AVG} = average velocity over the tube cross section within fluidized bed
u = velocity component in x direction
v = velocity component in y direction
w = velocity component in z direction
X = displacement in x direction
x = distance along x coordinate
y = distance along y coordinate
z = distance in the direction of flow
z_0 = intercept of $\overline{X^2}$ vs. z limiting slope on z axis
ϵ = fractions void
$(\beta_n a)$ = positive roots of Bessel function of first kind, first order. Dividing roots by a gives values of β_n.
τ = constant characteristic of a particular turbulent system

LITERATURE CITED

1. Batchelor, G. K., *Australian J. Sci. Research*, **A2**, 437 (1949).
2. Bernard, R. A., and R. H. Wilhelm, *Chem. Eng. Progr.*, **46**, 233, (1950).
3. Einstein, Albert, *Ann. Physik*, **17**, 549 (1905); **19**, 371, (1906).
4. Frenkiel, F. N., "Advances in Applied Mechanics," vol. 3, Academic Press, Inc., New York (1953).
5. Hanratty, T. J., Ph.D. thesis, Princeton Univ., Princeton, N. J. (September, 1953).
6. ———, *A.I.Ch.E. Journal*, **2**, 42 (1956).
7. Hinze, J. O., and B. G. van der Hegge Zijnen, paper presented at the Institute of Mechanical Engineers General Discussion on Heat Transfer, London (September, 1951).
8. Kalinske, A. A., and E. R. Van Driest, "Fifth International Congress for Applied Mechanics," John Wiley and Sons, New York (1938).
9. Kalinske, A. A., and C. L. Pien, *Ind. Eng. Chem.*, **36**, 220 (1944).
10. Kampe de Feriet, *Ann. Soc. Sci. Bruxelles*, **159**, 145 (1939).
11. Klinkenberg, Adriaan, R. J. Krajenbrink, and H. A. Lauwerier, *Ind. Eng. Chem.*, **45**, 1202 (1953).
12. Latinen, G. A., Ph.D. thesis, Princeton Univ., Princeton, N. J., (December, 1951).
13. Schubauer, G. B., *Natl. Advisory Comm. Aeronaut., Rept.* 524 (1935).
14. Taylor, G. I., *Proc. London Math. Soc.*, **20A**, 196 (1921).
15. ———, *Proc. Roy. Soc.* (*London*), **151A**, 421 (1935).
16. Towle, W. L., T. K. Sherwood, and L. A. Seder, *Ind. Eng. Chem.*, **31**, 457 (1939).
17. Townsend, A. A., *Proc. Cambridge Phil. Soc.*, **A43**, 560 (1947).
18. ———, *Proc. Roy. Soc.* (*London*), **A209**, 418 (1951); **A224**, 487 (1954).
19. Uberoi, M. S., and Stanley Corrsin, *Natl. Advisory Comm. Aeronaut. Rept.* 1142 (1953).

Ferric Ion Removal from Dilute Acidic Solutions by Fixed-bed Cation Exchange

BRIAN W. MAR and M. M. DAVID

University of Washington, Seattle

The removal of a trivalent ion (Fe^{+++}) from acidic nitrate solutions by a fixed bed of Dowex-50 cation-exchange resin was studied at entering iron concentrations from 14 to 84 meq./liter, flow rates of 0.073 to 1.20 liters/(hr.)(sq. cm.), and bed sizes from 3.7 to 15.4 g. of dry resin/sq. cm. Acid strengths were below 0.45 *N*. The results were correlated by a relatively simple break-through equation based on the assumptions of an equilibrium extremely favorable to iron adsorption and liquid-film diffusion being the rate-controlling factor. The capacity of the resin for iron was dependent upon the acid concentration of the solution.

The results provide a design equation requiring a minimum of experimental work.

The application of cation exchange resins for the recovery or removal of metallic cations from dilute wastes and other solutions is becoming of increasing importance. Accompanying this is an interest in fundamental ion exchange studies which will aid the development of generalized design methods requiring a minimum of experimental work. Such studies are lacking for trivalent–monovalent ion exchange, although many industrial wastes of importance contain trivalent ions (*5* and *6*). The purpose of the present study was to obtain performance data for trivalent–monovalent exchange and to develop a design equation if possible.

Cation exchange resin is usually employed in fixed beds, and a generalized design method for such units preferably includes a break-through–curve equation which relates solution flow rate, bed dimensions, initial bed condition, resin characteristics, and the composition of the treated effluent as a function of time and of the influent composition. Equations of this type have been developed for equi-valent ion exchange and unidivalent exchange (*8, 11, 13*). In the present work dilute acidic solutions of a noncomplexing trivalent ion, Fe^{+++}, were passed through fixed beds of hydrogen-form resin, and the experimental break-through data were correlated with a suitable equation.

THEORY

Break-through–curve equations are obtained by combining a material balance on a differential length of bed with a rate-of-exchange equation and an equilibrium equation. The resulting differential equation is integrated in accordance with the boundary conditions furnished by the initial bed condition and the influent composition. The final form of the break-through equation depends largely on the rate and equilibrium equations used.

Boyd and coworkers (*3*) have found that for cation exchange resin in contact with dilute solutions, the equilibrium is highly in favor of polyvalent ions replacing monovalent ions on the resin. The higher the valence of the polyvalent ion, the more favorable is the equilibrium for its "adsorption." Bauman (*1*) and Selke and Bliss (*13*) have found that in dilute solutions a divalent ion will replace virtually all the hydrogen or sodium ions on the resin, except when the divalent-monovalent ion ratio in the solution is very close to zero. Preliminary equilibrium experiments in the present study with ferric ion–hydrogen ion solutions showed the same situation to exist with trivalent-monovalent ion exchange.

Boyd and coworkers (*4*) and others (*10* and *13*) have also established that in fixed-bed ion exchange at or near commercially used flow rates, the rate-controlling resistance for cation exchange in dilute solutions is diffusion through the liquid film surrounding the resin particles. This leads to a rate-of-exchange equation in which the rate is proportional to the difference between the concentration of the exchanging ion in solution and the concentration of that ion in equilibrium with the resin composition. The proportionality "constant" is a function of the usual factors affecting the rate of diffusion through a liquid film.

Selke and Bliss have shown that for ion exchange systems where the types of equilibrium and rate equations described above are valid, the break-through curves may be correlated by an equation originally presented by Drew (*7*) for irreversible adsorption on fixed beds:

$$\frac{C}{C_0} = \exp\left\{\frac{k_D S}{V}\left(\frac{C_0 Y}{Aa} - x\right) - 1\right\} \quad (1)^*$$

where

C_0 = influent concentration of polyvalent ion, meq./liter
C = instantaneous effluent concentration of polyvalent ion, meq./liter
$k_D S$ = mass transfer coefficient, liters/(g.)(hr.)
V = volumetric flow rate, liters/(hr.)(sq. cm.)
Y = volume of effluent at a given time, corrected for the initial volume of liquid in the bed, liters
a = available resin capacity, meq./g.
x = bed length, g. of resin/sq. cm. of bed cross section
A = bed cross-sectional area, sq. cm.

Other consistent sets of units may be used.

If the experimental data conform to this equation, a plot of C/C_0 vs. Y on semilog paper should produce a straight line for a major portion of the break-through curve. The slope of the line is $(k_D S C_0)/(AVa)$, and the intercept is $-[1 + (k_D S x/V)]$. These terms permit evaluation of $k_D S$ and a, or a may be evaluated by the use of

$$a = \frac{C_0 Y}{Ax}$$

at the value of Y for

$$\frac{C}{C_0} = 0.368.$$

EXPERIMENTAL APPARATUS AND PROCEDURE

Ferric nitrate solutions were chosen for study, as the ferric ion of this salt is noncomplexing in the solutions used. The solutions were prepared by dissolving the desired amount of analytical-grade iron wire in a solution containing one part of concentrated nitric acid to three parts of water. The resulting solution was boiled to remove oxides of nitrogen and diluted to the desired compositions. Because of the method of preparation and the need for a low *p*H to prevent iron hydrolysis, all solutions used contained large quantities of acid relative to the iron content. Dowex-50 X-8, hydrogen form 20- to 50-mesh particle size, was used as the cation exchange material. The initial water content of the material used in the beds was determined by drying samples for 24 hr. at 105°C. so that all data might be reported on a standard basis of dry resin. Before data were collected from any bed the resin was pretreated by three to four preliminary saturation runs.

The ion exchange column was made of 12-mm.-I.D. glass tubing 30 in. long, closed at the lower end by a rubber stopper through which one side of a glass T was inserted. Glass wool was placed in the bottom of the column and wedged tightly around the stopper. The glass wool supported a layer of glass beads, which in turn supported the resin. Liquids could be supplied to either the top or the bottom of the column by gravity feed. Flow rates were controlled by a stopcock on the outlet line, and flow variation was minimized by a simple constant-head arrangement in the storage reservoirs.

*This equation may also be obtained as a special case of a more general equation presented in reference *17*.

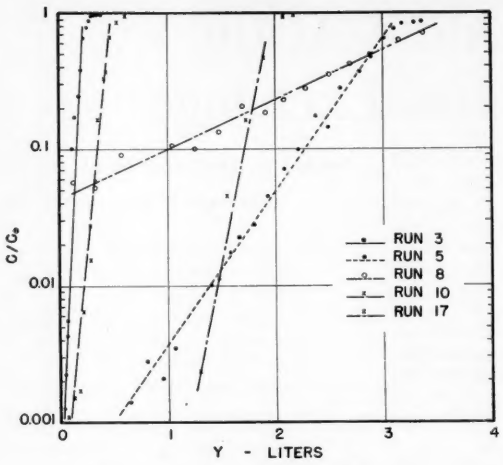

Fig. 1. Typical break-through curves.

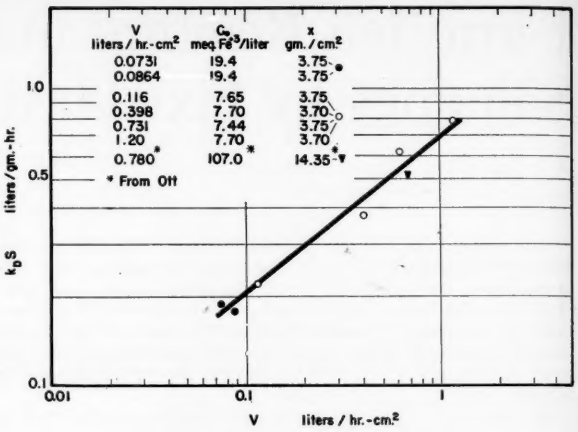

Fig. 2. Effect of velocity on k_DS.

For runs exceeding 10 hr. duration, a circular rotating collection table driven by an electric timer and motor was used.

In each run ferric nitrate solution was passed down through the bed at the desired flow rate until the bed was saturated. All effluent was collected in samples of suitable size, which were later analyzed for iron. After saturation the bed was washed, regenerated with an excess of 10% sulfuric acid (chosen as a typical industrial regenerent), backwashed, and reclassified before reuse. The regenerent was usually analyzed for iron content as a material-balance check. Iron concentrations were determined colorimetrically with KCNS.

Runs were made with solutions containing from 7.4 to 82.5 meq. Fe^{+++}/liter, flow rates from 0.073 to 1.20 liters/(hr.)(sq. cm.), and bed sizes from 3.7 to 15.4 g. of dry resin/sq. cm. of bed–cross-sectional area. All runs were downward at room temperature (substantially 70°F.). The operating conditions of the various runs are given in Table 1.

The break-through data from the runs were analyzed by plotting C/C_0 vs. Y on semilog paper, determining k_DS and a and studying the results for consistency with theory and other experimental data.

DISCUSSSION OF RESULTS

Figure 1 shows examples of the semilog plots of break-through data obtained in the study,* and Table 1 lists values of the mass transfer coefficients and bed capacities computed by Equation (1). The completeness of iron removal possible with proper operating conditions and the satisfactory representation of the break-through data by a straight line for the major portion of the break-through period may be noted in Figure 1.

Figure 2 and Tables 2 and 3 show the effects of velocity, influent concentration, and bed size on k_DS. Figure 2 is a log-log plot of k_DS vs. flow rate. Included is a pertinent data point from the work of Ott (*12*), which correlates well with the data of the present study though it is for a considerably higher iron concentration and larger bed size than other points on the figure. The mass transfer coefficient varies approximately as the 0.5 power of the flow rate. The data of Tables 2 and 3 show k_DS to be independent of influent composition and concentration and bed size. All three results are in agreement with the hypothesis of a liquid-film diffusion-controlled process (*2*, *13*, and *14*) and substantiate the use of Equation (1) to represent the data. The effect of velocity noted above would not exist were chemical-reaction rate the controlling step and would be different if diffusion in the resin particles were the rate-limiting process (*2* and *15*).

In Table 1 both the computed and the experimentally determined values of resin capacity a are listed. The agreement between these sets of values is further validation of Equation (1). The work of Ott (*12*) at higher iron concentrations, where diffusion within the particles plays an important part as the rate-determining

Table 1. Summary of Operating Conditions and Calculated Results

Run	C_0, meq. Fe^{+++}/liter	HNO_3 normality	V, liters/(hr.)(sq.cm.)	Bed size, x, g./sq.cm.	k_DS, liters/(g.)(hr.)	Bed capacity, a, meq. Fe^{+++}/g. Computed	Observed
2	47.4	0.21	0.112	3.75	0.194	4.45	4.65
3	82.5	0.45	0.114	3.75	0.206	4.00	4.02
4	14.1	0.15	0.107	3.70	0.192	3.00	3.06
5	7.65	0.019	0.116	3.75	0.221	4.95	5.20
6	7.70	0.0375	0.398	3.70	0.389	4.90	4.74
7	7.44	0.0375	0.731	3.75	0.628	4.57	4.77
8	7.70	0.0375	1.20	3.70	0.785	4.81	4.88
9	82.5	0.45	0.108	3.70	0.198	4.17	4.12
10	46.3	0.15	0.104	3.75	0.238	4.45	4.50
13	13.75	0.225	0.110	——	0.197	2.89	3.00
14	19.4	0.15	0.0731	3.75	0.189	4.64	4.70
15	19.4	0.225	0.0864	——	0.176	3.84	3.90
17	23.9	0.225	0.121	12.05	0.219	3.56	
18	23.9	0.23	0.112	17.45	0.228	3.56	
19	23.9	0.23	0.118	3.90	0.210	3.60	

Runs 1, 11, 12, and 16 were discarded because of experimental difficulties.

Table 2. Effect of Fe^{+++} Concentration on k_DS

Run	C_0, meq. Fe^{+++}/liter	HNO_3 normality	V, liters/(hr.)(sq.cm.)	Bed size, g./sq.cm.	k_DS, liters/(g.)(hr.)
5	7.65	0.019	0.116	3.75	0.221
13	13.75	0.225	0.110	3.70	0.197
4	14.1	0.15	0.107	3.70	0.192
19	23.9	0.23	0.118	3.90	0.210
2	47.4	0.21	0.112	3.75	0.194
10	46.3	0.15	0.104	3.75	0.238
3	82.5	0.45	0.114	3.75	0.206
9	82.5	0.45	0.108	3.70	0.198

*A complete tabulation of the original data is obtainable as document 4952 from the American Documentation Institute, Photoduplication Service, Library of Congress, Washington 25, D. C., for $1.25 for photoprints or microfilm.

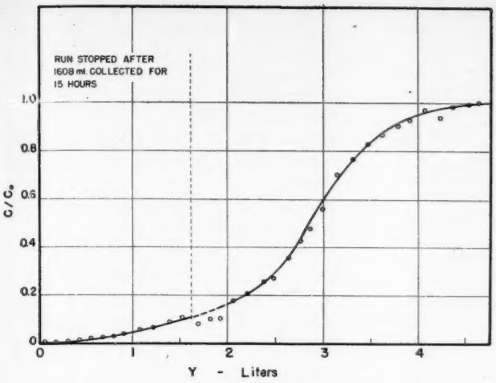

Fig. 3. Break-through data for interrupted run.

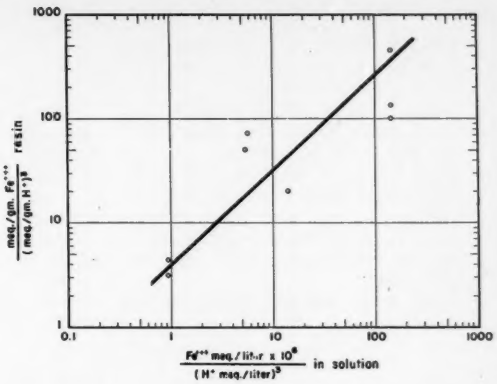

Fig. 4. Effect of solution composition on resin capacity.

process, shows that when Equation (1) is applied to such data, the computed and observed values of a differ considerably.

The results described above, indicating that diffusion through the liquid film surrounding the resin particles is the rate-controlling factor for total-solution molarities as high as nearly 0.5 M, are in contrast with the results of other workers for univalent exchange (*2* and *4*). Boyd et al. (*4*) found that diffusion within the particle pores became the rate-controlling step at total-solution molarities above 0.1 M and was important at total-solution molarities above 0.003 M. Bieber, Steidler, and Selke (*2*) report diffusion within the solid and through the liquid film to be of equal importance with 0.003 to 0.06 M solutions. Both groups used cation pairs the diffusion rates of which in solution were much nearer each other than would be expected for Fe^{+++} and H^+ ions, even though both the latter are probably in hydrated forms. In the present study it is probable that the diffusion of the Fe^{+++} ion, either inside the pores or through the liquid film, would be the rate-controlling diffusional step; and the maximum concentration of this ion was 0.0275 M (0.034 M for the data point used from Ott). Boyd points out that strong adsorption of an ion favors a film-controlled rate, and Selke and Bliss (*13*) found that liquid-film diffusion was the rate-controlling step for copper-hydrogen exchange up to at least 0.05 M copper concentration. That solid diffusion does play some part in the present study is indicated both by the curvature at the upper end of the graphs in Figure 1 and by the results shown in Figure 3. Run 7, plotted in Figure 3, was interrupted for a 15-hr. period, following which it was resumed as before. Immediately after the second startup, the first samples of effluent showed Fe^{+++} concentrations lower than the sample taken just before shutdown, an indication of a probable redistribution of iron in the resin previously partially saturated. However, this effect was transitory, and the break-through curve soon resumed its original shape. Hence the effects of solid diffusion, though present, are probably of minor importance in determining the break-through curve under the conditions of this study.

Examination of Table 1 reveals wide variation in the values of resin capacity found in the various runs. For Run 4 the low value was found to be caused by incomplete regeneration after the preceding run. (*See* below.) Runs 13, 15, 17, 18, and 19 were performed with new batches of resin, and the low capacities are attributed to the break-in treatment. In other work (*15*) it has been found that the working capacity of the resin for Fe^{+++} is reduced unless extreme care is taken during resin pretreatment. The variation of a in the remaining runs is in general accord with the equilibrium relationship $(Fe^{+++})_r/(H^+)_r^3 = K[(Fe^{+++})_s/(H^+)_s^3]$, as shown by the graph of log $(Fe^{+++})_r/(H^+)_r^3$ vs. log $(Fe^{+++})_s/(H^+)_s^3$ in Figure 4. $(Fe^{+++})_r$ and $(H^+)_r$ are respectively the milliequivalents of iron and hydrogen on a gram of dry resin and $(Fe^{+++})_s$ and $(H^+)_s$ are the milliequivalents per liter of these ions in the solution. The total capacity of the resin, $(Fe^{+++})_r + (H^+)_r$, was taken as 5.1 meq./g.

Although 10% sulfuric acid was successfully used as a regenerant in much of this study, the relative insolubility of ferric sulfate can lead to clogging of the resin pores. This is believed responsible for the decreased capacity of run 4, as treatment with hydrochloric acid restored the full resin capacity. For industrial operation, the use of an initial portion of more dilute sulfuric acid is recommended. This is similar to the procedure used for regeneration of resin containing appreciable amounts of calcium.

CONCLUSIONS

For noncomplexing solutions of ferric ion up to 0.01 N in Fe^{+++} and 0.45 N in acid, the exchange of the Fe^{+++} ion for the H^+ ion is highly favored on Dowex-50 exchange resin, and complete removal of Fe^{+++} from relatively acidic solutions is possible in fixed beds. At flow rates from 0.073 to 1.2 liters/(hr.)(sq. cm.) [1 to 15 gal./(min.)(cu. ft.) of bed], through the bed, diffusion through the liquid film surrounding the resin particles is the rate-controlling step in the exchange process. The value of the mass transfer coefficient is 0.50 liter/(g.)(hr.) at a flow rate of 0.60 liter/(hr.)(sq. cm.) and varies as the flow rate to the 0.5 power. The break-through data for the system can be represented by Equation (1). The capacity of the resin for iron is related to the solution composition as indicated in Figure 4.

Equation (1) may be used to design units for the removal of ferric ions from acidic solutions. Values of k_DS may be computed from the data presented in this paper, and the proper value of a may be determined from Figure 4 or from a simple equilibrium experiment. In addition to iron, Equation (1) should also be satisfactory for other noncomplexing trivalent ions within the same concentration ranges as above, since the equilibria and diffusion rates of such ions relative to the hydrogen ion will be similar to those of the ferric ion. The data from unpublished studies with trivalent chromium have been found to confirm the general validity of Equation (1) (*9*). For ions other than iron, or resins other than Dowex-50, 20- to 50- mesh size, at least one experimental fixed-bed run is necessary to determine k_DS and a.

Table 3. Effect of Bed Size on k_DS

Run	Bed size, g./sq.cm.	C_0, meq. Fe^{+++}/liter	HNO_3 normality	V, liters/(hr.)(sq.cm.)	k_DS, liters/(g.)(hr.)
19	3.90	23.9	0.23	0.118	0.210
17	12.05	23.9	0.225	0.121	0.219
18	17.45	23.9	0.23	0.112	0.228

LITERATURE CITED

1. Bauman, W. C., J. R. Skidmore, and R. H. Osmun, *Ind. Eng. Chem.*, **40**, 1350 (1948).
2. Bieber, Herman, F. E. Steidler, and W. A. Selke, *Chem. Eng. Progr. Sym. Ser.* No. 14, **50**, 17 (1954).
3. Boyd, G. E., J. Schubert, and A. W. Adamson, *J. Amer. Chem. Soc.*, **69**, 2818 (1947).
4. Boyd, G. E., A. W. Adamson, and L. S. Meyers, Jr., *J. Amer. Chem. Soc.*, **69**, 2836 (1947).
5. Costa, R. L., *Ind. Eng. Chem.*, **42**, 308 (1950).
6. David, M. M., and Harding Bliss, *Trans. Indian Inst. of Chem. Eng.*, **5**, 1 (1952–3).
7. Drew, T. B., F. M. Spooner, and J. Douglas (1944), reported by I. M. Klotz, *Chem. Revs.*, **39**, 241 (1946).
8. Gilliland, E. R., and R. F. Baddour, *Ind. Eng. Chem.*, **45**, 330 (1953).
9. Gross, P. L., personal communication on research at Yale University (1949).
10. Hagerty, P. F., and Harding Bliss, *Ind. Eng. Chem.*, **45**, 1253 (1953).
11. Hiester, N. K., and Theodore Vermeulen, *Chem. Eng. Progr.*, **48**, 505 (1952).
12. Ott, A. F., B.S. thesis, Univ. Washington, Seattle (1955).
13. Selke, W. A., and Harding Bliss, *Chem. Eng. Progr.*, **46**, 509 (1950).
14. Sherwood, T. K., and R. L. Pigford, "Absorption and Extraction," 2 ed., McGraw-Hill Book Company, Inc., New York (1952).
15. Sujata, A. D., J. T. Banchero, and R. R. White, *Ind. Eng. Chem.*, **47**, 2193 (1955).
16. Vasishth, R. C., research memo, Univ. Washington, Seattle (1955).
17. Vermeulen, Theodore, and N. K. Hiester, *J. Chem. Phys.*, **22**, 96 (1954).

Presented at A.I.Ch.E. Los Angeles meeting.

Mechanism of Heat Transfer to Liquid Drops

R. V. McDOWELL and J. E. MYERS

Purdue University, West Lafayette, Indiana

The purpose of this investigation was to study the process of heat transfer to a liquid drop rising through another liquid. In experimental runs various-sized drops of S.A.E.-10 lubricating oil, kerosene, and xylene were heated with water; also, water drops were heated with various organic liquids. Theoretical calculations of temperature change were made, various mechanisms of heat transfer being assumed. The temperature change predicted with each mechanism was compared with the experimental results and the controlling mechanism thus determined for each system studied.

A number of chemical engineering operations involve the transfer of heat and mass between a continuous fluid phase and a second phase such as a gas bubble, liquid drop, or solid sphere moving relative to the continuous phase. A thorough understanding of all the factors which govern this type of process has not been attained; however, a considerable amount of work has been done in recent years on segments of the over-all problem, and the present work on heat transfer to liquid drops is an attempt to fill in another portion of the picture.

No information was found in the literature concerning experimental measurements of heat transfer rates to liquid drops from other liquids. In the field of mass transfer, however, several investigators have studied the mechanism of solute extraction from drops (*6* and *14*). The apparatus used for these experiments was similar to the equipment employed in the present study of heat transfer. In the mass transfer apparatus a solute was extracted from the drops as they moved through a continuous liquid phase. The average concentration of the solute in the drops was measured before and after the extraction period. This procedure is analogous to measuring the heat transferred to a drop from a surrounding liquid by determining the average inlet and outlet drop temperatures.

Several factors could affect the heat transfer rate to a drop. A film of liquid surrounding the moving drop could cause appreciable resistance to heat transfer. If the liquid in the drop were stagnant, radial conduction would control the rate of heat transfer beneath the drop surface, but if there were circulation within the drop, the heat transfer rate would increase; consequently, the outside film coefficient, the thermal diffusivity of the liquid in the drop, and the extent of internal circulation appear to be the most important factors in the heat transfer process.

Kramers (*11*) developed an empirical equation for the film coefficient of a fluid flowing past steel spheres heated by high-frequency induction and maintained at a constant, uniform temperature. He used various sphere diameters from 0.70 to 1.27 cm. and correlated the experimental data as follows:

$$Nu = 2.0 + 1.3(Pr)^{0.15} + 0.66(Pr)^{0.31}(Re)^{0.50} \quad (1)$$

Film coefficients calculated from this equation are probably applicable to heat transfer between continuous fluid and a stagnant drop. When the equation was used to calculate an outside water-film coefficient, values were obtained between 550 and 800 B.t.u./(hr.)(sq. ft./°F.). Organic liquid-film coefficients were between 130 and 170 B.t.u./(hr./sq. ft.)(°F.). However, in the case of a circulating drop such a coefficient would serve only as an approximation.

Equation (2) has been developed for calculating the temperature change of a sphere being heated by the mechanism of pure radial conduction (*10*). In the development of this equation it was assumed that there was no outside film resistance and that the temperature of the drop surface was the same as the average

R. V. McDowell is at Union Oil Company of California, Rodeo, California.

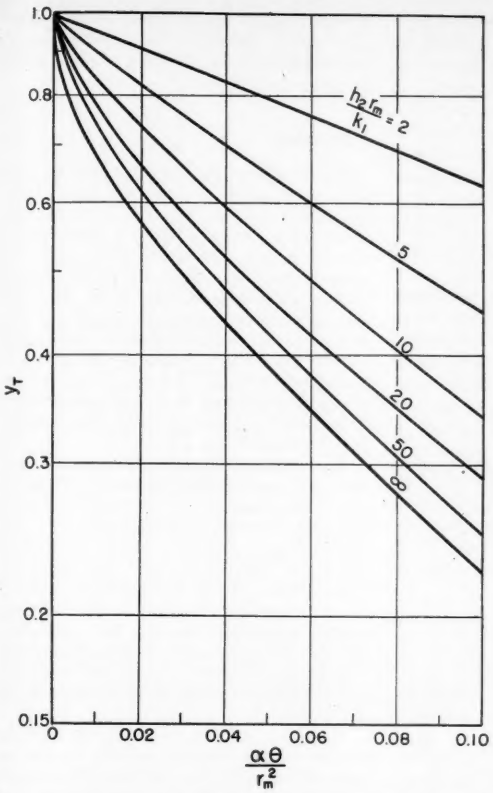

Fig. 1. Temperature change of a noncirculating drop with varying outside resistance.

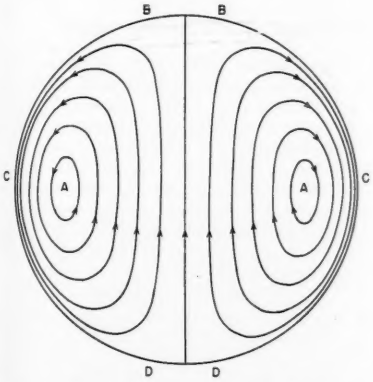

Fig. 2. Circulation pattern for rising drop.

temperature of the surrounding medium.

$$Y_T = \frac{6}{\pi^2}\left[\exp\frac{-\alpha\pi^2\theta}{r_m^2} + \frac{1}{4}\exp\frac{-4\alpha\pi^2\theta}{r_m^2} + \cdots\right] \quad (2)$$

Jakob (*10*) gives an equation for the case in which the outside film coefficient becomes small enough so that the outside resistance is an appreciable part of the over-all resistance to heat transfer. Charts are given in his book from which the temperature rise of a noncirculating drop with an outside film resistance can be predicted. A modified version of these charts is reproduced in Figure 1.

If a drop circulates internally, the heat transfer rate may be greatly increased. The hydrodynamics of falling drops undergoing viscous circulation was investigated by Hadamard (*7*). Using his results Kronig and Brink (*12*) developed a mathematical expression for the amount of solvent extracted from a drop which has internal circulation and negligible outside film resistance to mass transfer. The circulation pattern for a rising drop is shown by the streamlines in Figure 2. The liquid near the outside of the drop flows downward as a result of the drag forces exerted by the surrounding liquid. In order to calculate the amount of diffusion that would occur, Kronig and Brink assumed that the concentration of solvent in the drop was the same at any position on a given streamline. The analogous assumption for the heat transfer case is that all the streamlines are isotherms. If each streamline is to be at the same temperature throughout its length, the time required for the liquid to circulate must be small compared with the time required for the drop to cool. The critical ratio of these times is obviously not a definite value. However, it can be seen that the faster the drop circulates the more nearly constant the temperature becomes along any streamline.

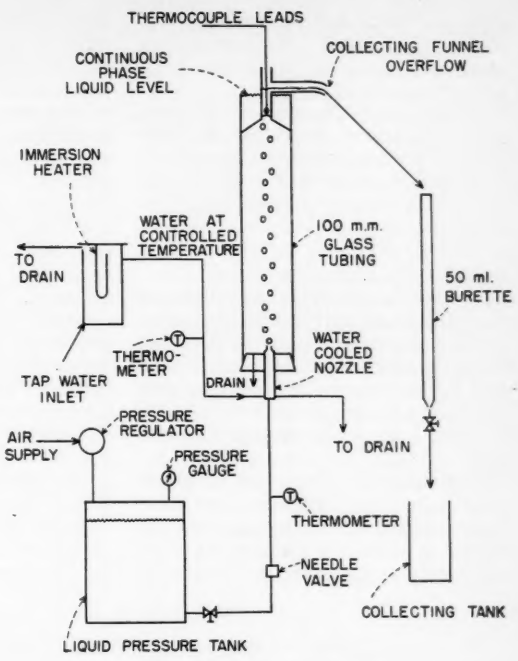

Fig. 3. Diagrammatic sketch of equipment.

The equation given by Kronig and Brink for solvent extraction can be written as an expression for the unaccomplished temperature change of a drop as follows:

$$Y_T = 0.653\exp\left[\frac{-26.84\alpha\theta}{r_m^2}\right] + 0.200\exp\left[\frac{-157.2\alpha\theta}{r_m^2}\right] + \cdots \quad (3)$$

The fact that the type of circulation described by Kronig and Brink actually does occur has been shown in several ways. Spells (*16*) photographed the striae in glycerine-water drops and his pictures show the circulation pattern clearly. In the studies of mass transfer (*6* and *14*) the rapid extraction rates measured experimentally were difficult to explain unless circulation within the drop was assumed. Another proof of internal circulation was shown by Heertjes (*8*) in his studies of mass transfer in an isobutanol–water system. Drops of isobutanol were allowed to rise through water, and the amount of isobutanol transferred to the continuous water phase was measured. In this case the fact that the liquid in the drop circulated was shown by a color change which occurred when the concentration of isobutanol in the drop reached a certain value. Heertjes found that the last remaining portion of the original color had the shape of a ring at position *A*, as

shown in Figure 2. If no circulation had occurred in the drop, the original color would have been expected to remain longest in the center of the drop.

Hughes and Gilliland (*9*) have studied the mechanics of drops and discussed much of the theory that has been developed in the past to explain the mechanisms of circulation. Garner (*2*) has published similar work which includes pictures of drops showing the movements of fluids in and around a drop.

Kronig, Van der Veen, and Ijzerman (*13*) have considered the transition region in which circulation is slow enough so that the streamlines are not isotherms. For this case the heat transfer rate is faster than for a stagnant drop, but slower than in a drop with more fully developed circulation.

In a circulating drop, new surface is continually being formed at point B, as shown in Figure 2. At the same time the surface at point D is disappearing. Once circulation has started, the energy required to form new surface at point B is offset by the energy added to the drop by the disappearing surface at D. According to Bond and Newton (*1*), the interfacial tension must be overcome to start the circulation. They developed a relation which defined a critical radius below which no circulation would occur. It was based on experimental data in the streamline region with Reynolds numbers less than unity and is therefore not generally applicable.

Garner and Hammerton (*4*) have checked Bond and Newton's theory with additional experimental work. The actual radius at which circulation started was usually much smaller than would be predicted by Bond and Newton. Garner and Skelland (*5*) investigated circulation at higher Reynolds numbers and found that as the interfacial tension increased from 1 to 5 dynes/cm. the Reynolds number corresponding to the critical radius increased from 70 to 120. Garner and Hale (*3*) have studied the effect of surface-active agents on circulation and found that small traces of the agents form an adsorbed layer on the drop surface which hinders circulation.

Table 1. Physical Properties of Liquids at 100°F.

	k, B.t.u./(hr.)(ft. °F.)	ρ, lb./cu.ft.	C_p, B.t.u./(lb.)(°F.)	α, sq.ft./hr.	μ, centipoises
Water	0.363	62.0	1.0	0.00585	0.69
Kerosene	0.084	50.5	0.49	0.00339	1.8
S.A.E.-10 lubricating oil	0.071	56.5	0.45	0.00280	30.0
Xylene	0.090	54.3	0.42	0.00395	0.55
Trichloroethylene	0.080	90.9	0.23	0.00380	0.54
1 part trichloroethylene* 1 part kerosene (by volume)	0.082	70.7	0.32	0.0036	1.2
2 parts trichloroethylene* 1 part kerosene (by volume)	0.081	77.4	0.29	0.0036	0.96
90% xylene* 10% trichloroethylene (by volume)	0.089	58.0	0.39	0.039	0.55

*Physical properties were determined by interpolation between properties of pure substances.

Table 2. Sample of Experimental Data

Run 14
System: continuous phase–water, drops–oil
Depth of liquid: 44 in.
Rate of drop formation: 105 to 125 drops/min.

Water temp., °F.	Inlet oil temp., °F.	Outlet oil temp., °F.	Time of rise, sec.	Volume of drops, ml.	Unaccomplished temp. change, dimensionless
190	74	129	8.9	0.433	0.525
185	74	129	8.6	0.450	0.505
176	74	127	8.6	0.440	0.480
174	74	123	8.6	0.443	0.510
170	74	119	8.5	0.446	0.531
167	74	118	8.5	0.447	0.527
165	74	117	8.5	0.446	0.528
162	74	116	8.5	0.437	0.523
157	74	116	8.5	0.430	0.495
154	74	116	8.5	0.429	0.475
152	74	113	8.5	0.426	0.500
148	74	110	8.5	0.434	0.514
143	74	105	8.5	0.426	0.550
141	74	104	8.5	0.411	0.552
136	74	102	8.5	0.417	0.548

EQUIPMENT

Figure 3 is a diagrammatic sketch of the equipment used in this experiment. The equipment for the formation of drops consisted of a pressure tank, a water-cooled circular nozzle, and an electric heater. The pressure tank was used as a supply storage vessel for the drop-forming liquid. The tank was fitted with a pressure gauge and connected to a pressure-regulated air supply. During runs the pressure in the tank was maintained between 1.5 and 2.0 lb./sq. in. gauge. With this pressure, the desired drop-formation rate could be obtained by adjusting the needle valve.

Three different water-cooled nozzles were used, all constructed as shown in Figure 4. The inside diameters of the nozzles were 2.5, 3.0, and 4.5 mm. A baffle, shown by the dotted line in Figure 4, forced the cooling water to circulate around the incoming stream. The cooling water was maintained at the same temperature as the incoming stream to prevent heating by conduction through the nozzle prior to drop formation. The immersion heater was used to control the temperature of the water flowing around the nozzle.

A rubber stopper was used to seal the column at the bottom. Various lengths of glass tubing were used to vary the time of contact of the drops. The column was filled to the top for each run and the drops were collected and drained off with a special glass funnel, shown in Figure 5. The liquid from this funnel ran into a burette which drained to a collecting tank.

EXPERIMENTAL DATA AND PROCEDURE

Experimental data were obtained for twenty-nine runs and have been reported by McDowell (*15*). Table 1 shows the physical properties of the systems used and Table 2 the data from one experimental run.

The data required to calculate the unaccomplished temperature change were as follows: (1) inlet-drop-liquid temperature t_i (°F.); (2) outlet drop-liquid temperature t_0 (°F.); and (3) continuous-phase liquid temperature t_c (°F.).

The data required to calculate the theoretical temperature rise of the drop were as follows: (1) radius of drop r_m (ft.); (2) time of rise for each drop θ (hr.); (3) velocity of rise u (ft./hr.); (4) physical properties of both liquids.

The inlet-liquid temperature was measured by a thermometer placed in the inlet-liquid stream. The outlet-liquid temperature was measured by a copper-constantan thermocouple placed just above the liquid-liquid interface. The height of this thermocouple was kept as close as possible to the interface between the two liquids. This procedure gave an average temperature of the liquid in the drop just after it broke through the interface. The temperature of the liquid in the column was measured at various heights and radial distances from the axis. At any time during a run the temperatures throughout the continuous liquid phase varied by less than 1°F.

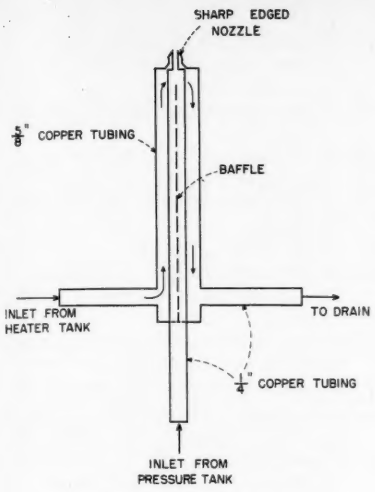

Fig. 4. Water-cooled nozzle.

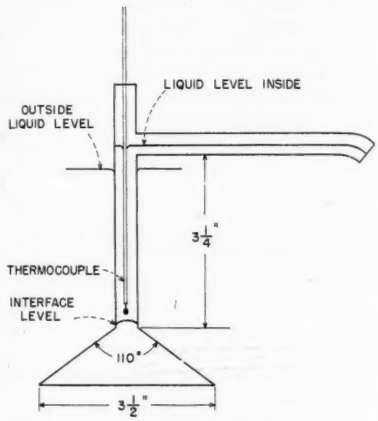

Fig. 5. Collecting funnel.

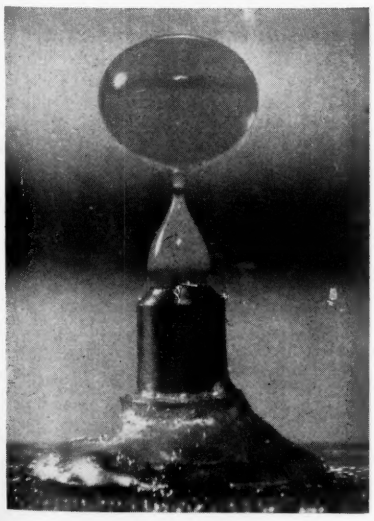

Fig. 6. Oil drop leaving nozzle.

The radius of each drop was calculated from measurements of the drop-formation and volumetric-flow rates. The drop-formation rate was measured in two ways. At slow rates the time required for twenty-five drops to form was measured by a stop watch. At fast rates a Strobotac was used. Drop rates varied from about 100 to 400 drops/min. The volumetric-flow rate was calculated from measurements of the time required to collect 25 ml. of fluid in the burette. From these two measurements the volume of each drop could be calculated. The radius was calculated on the assumption that each drop was a sphere.

The time of rise of the drops was measured directly with a stop watch, the average velocity of rise being calculated from the time of rise and column height.

Figure 6 is a picture of an oil drop just as it is separating from the nozzle. The photograph has been enlarged about four times. Actually the drop is not so flat as it appears in the picture, as the optics involved in photographing through a cylindrical column of water tend to make the drop appear flattened. If the drop was assumed to be an oblate spheroid with an eccentricity of two, instead of a sphere, the increase in surface area would be only 10%. This fact combined with the experimental results helps to justify the assumption for purposes of heat transfer calculations that the drops behaved as spheres.

RESULTS

If a drop were allowed to remain in contact with the continuous-phase liquid long enough, its temperature would change from some initial value to the temperature of the continuous-phase liquid. The actual average temperature change of the drop may be expressed as the ratio of the unaccomplished temperature change to the total possible temperature change. Thus, if the drop were allowed to heat to the temperature of the bulk fluid this ratio, Y_e, would be zero.

Table 3. Results

System	Column height, ft.	Average time of rise, sec.	Drop radius, ft.	Run	Y_e	Y_t I	Y_t II	Y_t III
K-W	3.67	7.0	0.0113	5	0.15–0.19	0.38	0.39	*0.16*
K-W	3.67	6.8	0.0128	4	0.21–0.25	0.45	0.46	*0.23*
K-W	3.67	7.6	0.0144	3	0.24–0.32	0.48	0.49	*0.26*
K-W	1.17	2.5	0.0118	19	0.42–0.46	0.62	0.64	*0.44*
K-W	1.17	2.6	0.0138	17	0.48–0.50	0.66	0.68	*0.50*
K-W	1.17	2.3	0.0140	18	0.50–0.53	0.68	0.70	*0.52*
K-W	0.71	1.6	0.0111	8	0.46–0.52	0.66	0.68	*0.50*
K-W	0.71	1.6	0.0128	6	0.51–0.54	0.71	0.73	*0.56*
K-W	0.71	1.6	0.0143	7	0.56–0.62	0.73	0.75	*0.60*
O-W	3.67	8.9	0.0146	10	0.49–0.56	0.49	*0.50*	0.28
O-W	3.67	8.5	0.0154	14	0.48–0.55	0.52	*0.53*	0.31
O-W	3.67	8.6	0.0177	11	0.61–0.73	0.57	*0.59*	0.38
O-W	3.67	8.9	0.0181	15	0.56–0.60	0.57	*0.59*	0.38
O-W	3.67	8.6	0.0186	13	0.58–0.66	0.59	*0.61*	0.40
O-W	1.17	3.1	0.0178	16	0.75–0.80	0.71	*0.73*	0.57
O-W	0.71	1.9	0.0144	9	0.71–0.82	0.72	*0.74*	0.58
O-W	0.71	2.1	0.0178	12	0.85–0.87	0.77	*0.80*	0.65
X-W	3.67	8.3	0.0156	23	0.15–0.19	0.46	0.48	*0.24*
X-W	1.17	2.5	0.0117	22	0.28–0.30	0.58	0.60	*0.39*
X-W	1.17	2.9	0.0143	20	0.30–0.34	0.62	0.64	*0.44*
X-W	1.17	2.8	0.0158	21	0.40–0.45	0.67	0.69	*0.51*
X-W	0.71	2.0	0.0124	24	0.45–0.47	0.63	0.65	*0.46*
X-W	0.71	1.9	0.0146	26	0.47–0.50	0.69	0.71	*0.54*
X-W	0.71	1.9	0.0152	25	0.53–0.55	0.71	0.73	*0.56*
0.9*X-W*	0.71	3.5	0.0199	27	0.48–0.53	0.70	0.72	*0.55*
W-2,1	2.67	6.2	0.0115	29	0.37–0.44	0.29	0.52	0.08
W-2,1	2.67	6.2	0.0134	28	0.48–0.55	0.37	0.59	0.14
W-1,1	2.67	7.2	0.0143	31	0.50–0.57	0.36	0.59	0.14
W-1,1	2.67	7.4	0.0160	30	0.51–0.57	0.41	0.64	0.19

System
- *K–W* = kerosene drops in water
- *O–W* = S.A.E.-10-lubricating-oil drops in water
- *X–W* = xylene drops in water
- 0.9*X–W* = 90% xylene–10% trichloroethylene (by volume) drops in water
- *W*–2, 1 = water drops in solution of two parts trichloroethylene and one part kerosene by volume
- *W*–1, 1 = water drops in solution of half trichloroethylene and half kerosene by volume

Column height = distance between nozzle and interface in collecting funnel, ft.

Drop radius (r_m) = radius of a sphere of the same volume as the drop, ft.
Y_e = experimental value of unaccomplished temperature-change ratio
Y_t = theoretical value of unaccomplished temperature-change ratio
Italicized numbers in columns II and III indicate the values of Y_t that agree with those of Y_e.

Mechanism
- I = internal radial conduction with no outside film resistance
- II = internal radial conduction plus outside film resistance
- III = internal circulation with no outside film resistance

The smaller the value of Y_e the greater the heat transfer for a given drop in a bulk fluid at a given temperature.

In Table 3 these experimental values for each run are tabulated and compared with the values of Y_t, the calculated theoretical-temperature-difference ratios.

DISCUSSION OF RESULTS

Three different mechanisms of heat transfer were assumed in calculating values of Y_t, as shown in columns I, II, and III of Table 3. Column I contains the theoretical Y_t value for drops with radial conduction inside and no outside film resistance. Column II is for drops with internal radial conduction plus an outside film resistance. Column III contains the Y_t values for drops with internal circulation and no outside film resistance. The Y_t values were obtained from Equations (2) and (3) and Figure 1.

Internal Radial Conduction with No Outside Film Resistance

When the flow of heat inside a drop is by radial conduction alone, its resistance is higher than if there were circulation within the drop. The numerical values of Y_t shown in column I are generally higher than the experimental values, indicating that some mechanism such as circulation must have decreased the resistance of the drops to heat transfer. In the oil–water systems, however, the Y_t values in column I are close to the experimental values, an indication that there was negligible circulation inside the high-viscosity oil drops.

Internal Radial Conduction Plus Outside Film Resistance

The figures in column II were calculated with the outside film resistance as determined from Equation (1) taken into account. Where water was used as the continuous-phase liquid, this additional factor did not increase the Y_t values more than 4%. However, the Y_t values in column II are slightly closer to the experimental Y_e values for the oil–water runs than are those in column I.

The close check confirms the assumption that heat transfer is by radial conduction internally with an outside film offering a small additional resistance.

Internal Circulation with No Outside Film Resistance

The Y_t values in column III calculated with this mechanism assumed agree fairly well with the experimental values for the runs in which kerosene, xylene, and organic-liquid drops were heated with water. This agreement indicates that there was circulation within these drops and that any outside resistance was negligible. Circulation would be expected in these cases as the viscosities involved were much lower than in the oil drops.

Internal Circulation with Appreciable Outside Film Resistance

In the last four runs using water drops heated with mixed organic liquids, this was undoubtedly the mechanism involved. Water has a low enough viscosity so that, on the basis of previous runs, water drops would be expected to circulate. As organic liquids were used in the continuous phase, the film resistance would be much higher than for water films. The experimental values of Y_e were between the Y_t values in columns II and III. This is to be expected, as any circulation within the drop would lower the Y_t values shown in column II and any outside film resistance would tend to increase the values shown in column III.

Those values of Y_t which agree with the experimental values Y_e are italicized in Table 1, to indicate what appears to be the controlling mechanism. For these cases agreement between experimental and calculated values was fairly satisfactory. The last four runs involved circulating drops with what appeared to be appreciable outside film resistance. As no method for calculating Y_t for this mechanism was available, comparison of theoretical calculations with experimental results was not possible.

No specific investigation was made of end effects. It might be expected that if end effects were significant they would show up in the form of deviations of experimental results from the theoretical values for the shortest column (0.71 ft.); however, from Table 1 it can be seen that the results for this column are as good as those for the longer columns. Furthermore, it was noted by McDowell (*15*) that variations of 35% in drop-formation rate produced no change in exit-drop temperature. It is likely that systems involving much higher velocities and shorter liquid columns would be necessary before end effects would contribute appreciably to the heat transfer.

CONCLUSIONS

The following conclusions were drawn from this investigation.

1. If the viscosity of the liquid in the drop is low enough compared with the viscosity of the continuous-phase fluid, the liquid in the drop will circulate. Circulation lowers the resistance to heat transfer.

2. If the thermal conductivity of the continuous-phase liquid surrounding the drop is low compared with that of the liquid in the drop and there is no circulation within the drop, an appreciable part of the resistance to heat transfer will be in the film outside the drop.

3. Theoretical calculations of temperature rise enable the prediction of values that are in good agreement with experimental results.

NOTATION

C_p = specific heat, B.t.u./(lb.)(°F.)
h = heat transfer coefficient, B.t.u./(hr.)(sq. ft./°F.)
k = thermal conductivity, B.t.u./(hr.)(ft./°F.)
Nu = Nusselt number = $2r_mh/k$, dimensionless
Pr = Prandtl number = $C_p\mu/k$, dimensionless
r = spherical radius, ft.
Re = Reynolds number = $2r_mu\rho/\mu$
r_m = outside radius of drop or sphere, ft.
t_c = temperature of continuous-phase liquid in column, °F.
t_i = temperature of inlet-drop fluid, °F.
t_0 = average temperature of drop as it leaves at the top of the column, °F.
u = average drop velocity, ft./hr.
v = volume of drop, ml. or cu. ft.
Y_e = experimental ratio of unaccomplished temperature change to total possible temperature change $(t_c - t_0)/(t_c - t_i)$, dimensionless
Y_t = theoretical temperature difference ratio $(t_c - t_0)/(t_c - t_i)$, dimensionless
α = thermal diffusivity, sq. ft./hr.
θ = time, hr.
μ = viscosity, lb./(ft.)(hr.)
ρ = density, lb./cu. ft.

Subscripts

1 = drops
2 = continuous-phase liquid

LITERATURE CITED

1. Bond, N. W., and D. A. Newton, *Phil. Mag.*, **5**, 794 (1928).
2. Garner, F. H., *Trans. Inst. Chem. Engrs. (London)*, **28**, 88 (1950).
3. ——— and A. R. Hale, *Chem. Eng. Sci.*, **2**, 157 (1953).
4. Garner, F. H., and D. Hammerton, *loc. cit.*, **3**, 1 (1953).
5. Garner, F. H., and A. H. P. Skelland, *Trans. Inst. Chem. Engrs. (London)*, **29**, 315 (1951).
6. Garner, F. H. and A. H. P. Skelland, *Ind. Eng. Chem.*, **46**, 1255 (1954).
7. Hadamard, J. C. R., *Acad. Sci. (Paris)*, **152**, 1735 (1911).
8. Heertjes, P. M., W. N. Holve, and H. Talsma, *Chem. Eng. Sci.*, **3**, 122 (1954).
9. Hughes, R. R., and E. R. Gilliland, *Chem. Eng. Progr.*, **48**, 497 (1952).
10. Jakob, Max, "Heat Transfer," John Wiley and Sons, Inc., New York (1949).
11. Kramers, H., *Physica*, **12**, 61 (1946).
12. Kronig, R., and J. C. Brink, *Appl. Sci. Res.*, **A2**, 142 (1950).
13. Kronig, R., B. Van der Veen, and P. Ijzerman, *loc. cit.*, **A3**, 103 (1951).
14. Licht, W., and W. F. Pansing, *Ind. Eng. Chem.*, **45**, 1885 (1953).
15. McDowell, R. V., M.S. thesis, Purdue Univ., West Lafayette, Ind. (1955).
16. Spells, K. E., *Proc. Phys. Soc. (London)*, **65B**, 541 (1952).

Presented at A.I.Ch.E. Detroit meeting.

Differential Heats of Condensation and Enthalpies of Saturated Liquid Hydrocarbon Mixtures

J. G. STIEHL, MERK HOBSON, and JAMES H. WEBER

University of Nebraska, Lincoln, Nebraska

By use of saturated-vapor enthalpies determined by accepted procedures in conjunction with differential latent heats of condensation, the saturated-liquid enthalpies are established for the system methane–ethane at 200, 400, and 600 lb./sq. in. abs. and for the systems ethane–*n*-butane and propane–*n*-butane at the two lower pressures. Where comparison is possible, the liquid-enthalpy values obtained by this method are in general agreement with those previously determined by Edmister and Canjar. The procedure used is thermodynamically rigorous and may be applied to any binary mixture, provided the Benedict-Rubin-Webb equation of state is valid in the vapor phase and *P-V-T-x* data are available.

As operating pressures in the petroleum and related industries increase, the heat effects and the vapor-liquid equilibrium relationships become difficult to predict. Designs for conditions of elevated pressures are often reduced to questionable estimates and the design engineer is frequently confronted with inconsistencies between the vapor-liquid equilibrium data and the enthalpy data. The Kellogg equilibrium-vaporization ratios (*13*), based on the Benedict-Rubin-Webb equation of state (*4*), have helped immeasurably in the prediction of accurate y/x data over wide pressure ranges; however, the determination of the heat effects has remained a problem.

At the present time the partial-enthalpy approach used in conjunction with the Benedict-Rubin-Webb equation appears to be the most promising method for obtaining precise thermal data on mixtures which will also be consistent with the equilibrium information. This approach has been used by Papadopoulos, Pigford, and Friend (*16*) and Edmister and Canjar (*11*). Although the Benedict-Rubin-Webb equation holds with a high degree of precision in the vapor phase, its applicability to the liquid phase, particularly when the liquid density is greater than 125% of the critical density, is open to some question. Hence it is desirable to determine the enthalpy of saturated-liquid mixtures by some other method which would provide the same degree of accuracy as can be obtained in the vapor phase. This accuracy can be achieved either by calculating the latent heat of condensation of the mixture and subtracting it from the vapor-phase enthalpy or by determining the liquid-phase enthalpy directly.

As no exact equation of state exists for liquid mixtures, the prediction of the latent heat of condensation offers the better prospect. With mixtures either of two latent heats may be considered, the integral heat and the differential heat. The integral heat of condensation may be determined under isothermal or isobaric conditions, and the isothermal integral heat of condensation may be calculated by the method of Bahlke and Kay (*2*). The isobaric integral heat is the heat emitted under constant pressure when a given amount of a mixture at its dew point is completely converted to a liquid at its bubble point. It may also be calculated rigorously, although this is not often done because of the large amount of experimental data required. Edmister (*10*) developed an expression by which the isobaric integral heat of vaporization may be approximated.

As an alternate approach, it is suggested that the enthalpy differences between the saturated liquid and vapor phases be obtained through the differential latent heat of condensation. These enthalpy differences are of great value, for they are the heat effects involved in many distillation operations. Further, the differential heat of condensation and, in turn, the enthalpy difference between the two saturated phases may be calculated from rigorous thermodynamic relationships which require considerably fewer experimental data than are needed for the exact determination of either of the integral heats of vaporization.

The differential heat of condensation on a molal basis is the heat given up when a mole of vapor is condensed from a gaseous mixture containing N moles, where N is so large that the composition of the gaseous mixture remains unchanged. The composition of the liquid formed is governed by the equilibrium relationship, and the temperature and pressure of the process are constant. This case is analogous to the one developed by Dodge (*7*). As the process occurs under isobaric and isothermal conditions and without change of composition of the vapor phase, the Clapeyron equation

$$\left(\frac{\partial P}{\partial T}\right)_y = \frac{\Delta H_c}{T\Delta V} \qquad (1)$$

may be applied. This is pointed out by Dodge (*8*).

In Equation (1) $(\partial P/\partial T)_y$ is the slope of the dew-point pressure-temperature curve of the mixture; T, the absolute temperature of condensation; and ΔH_c, the differential heat of condensation. Not only does the volume change ΔV involve the difference between the saturated vapor and liquid volumes, as is the case for a pure material, but the change in the volume of the vapor due to the condensation of 1 mole must also be taken into account. As shown by Dodge (*7*), the net volume change for the process is expressed by

$$\Delta V = V_b - V_d + (y - x)\left(\frac{\partial V_G}{\partial y}\right)_{T,P} \qquad (2)$$

From Equations (1) and (2), it is apparent that precise dew-point pressure-temperature, volumetric, and equilibrium data are required to evaluate the differential heat of condensation. Such data have been reported for a number of binary systems, particularly those containing hydrocarbons.

The partial differential $(\partial V_G/\partial y)_{T,P}$ is the most difficult term in the equation to evaluate. To determine this quantity, an isotherm must be constructed on a plot of V_G vs. y, the pressure being held constant. The slope of the isotherm at its point of intersection with the saturated vapor curve must then be measured. It is apparent that volumetric data in the superheated vapor region, as well as the saturated vapor volume, are necessary to determine the value of $(\partial V_G/\partial y)_{T,P}$. The required volumetric data were calculated by the Benedict-Rubin-Webb equation of state,

$$P = RTd + (B_0RT - A_0 - C_0/T^2)d^2 + (bRT - a)d^3 + a\alpha d^6 + cd^3/T^2[(1 + \gamma d^2)e^{-\gamma d^2}] \qquad (3)$$

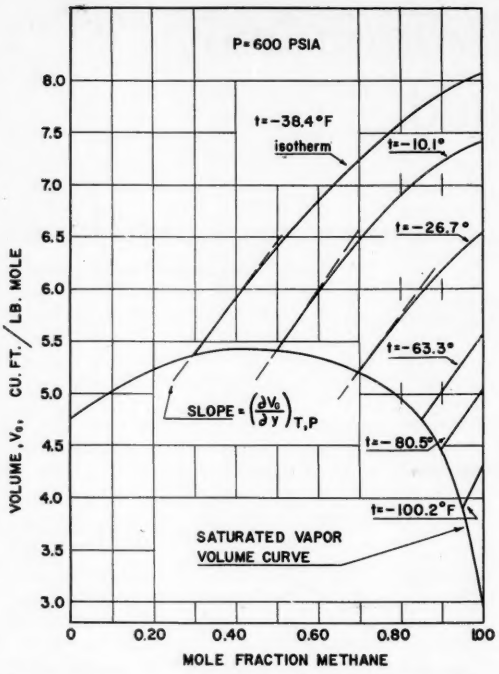

Fig. 1. Volume-composition diagram for methane-ethane system showing isotherms with slope equal to $(\partial V_G/\partial y)_{T,P}$.

For the systems investigated, sufficient experimental data are available to define the saturated vapor volume curves. The validity of the Benedict-Rubin-Webb equation of state was established by calculating saturated vapor volumes and comparing them with the experimental values. In no case did the two values differ by more than 1%. In most instances the calculated value agreed with the experimental value within 0.75%. As the Benedict-Rubin-Webb equation predicted the volumetric behavior of the saturated-vapor mixtures with such precision, it was felt that the equation could safely be used to predict the behavior of the superheated vapor mixtures.

To help illustrate the procedure used, the V_G vs. y plot for the methane-ethane system at 600 lb./sq. in. abs. is included as Figure 1. A number of isotherms were constructed on the plot to evaluate the quantity $(\partial V_G/\partial y)_{T,P}$ over the complete range of vapor composition.

With the term $(\partial V_G/\partial y)_{T,P}$ evaluated, the differential heat of condensation can be determined without difficulty through the use of Equations (1) and (2). The relationship between the differential latent heat of condensation and the saturated-vapor and -liquid enthalpies, as given by Dodge (*9*), is

$$\Delta H_c = H_b - H_d + (y - x)\left(\frac{\partial H_G}{\partial y}\right)_{T,P} \quad (4)$$

The term $(\partial H_G/\partial y)_{T,P}$ can be evaluated by a procedure similar to that outlined for the calculation of the term $(\partial V_G/\partial y)_{T,P}$. The Benedict-Rubin-Webb equation in the form

$$H = \sum_i x_i H_i^0 + (B_0RT - 2A_0 - 4C_0/T^2)d + (2bRT - 3a)d^2/2 + 6a\alpha d^5/5 + cd^2/T^2\left[3\frac{1 - \exp(-\gamma d^2)}{\gamma d^2} - \frac{\exp(-\gamma d^2)}{2} + \gamma d^2 \exp(-\gamma d^2)\right] \quad (5)$$

and the enthalpies in the ideal gas state obtained (*1*) were used to calculate enthalpies of the saturated and superheated vapors. Equation (4) can readily be solved for the single unknown, the saturated-liquid enthalpy.

The method of calculation outlined above was applied to three binary hydrocarbon systems, methane-ethane, ethane–*n*-butane, and propane–*n*-butane. These systems were used because the validity of

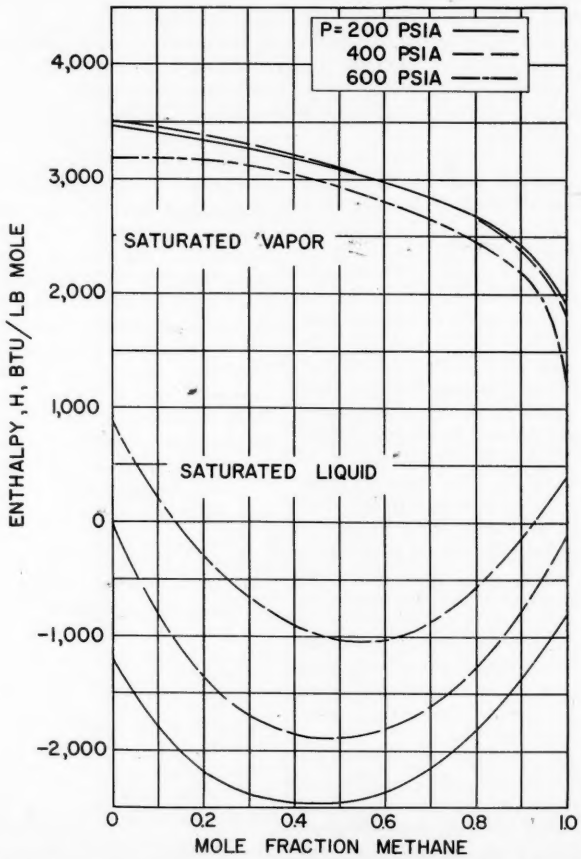

Fig. 2. Enthalpy-composition diagram for methane-ethane system. $H = 0$ for the pure components in the ideal gas state at unit fugacity and 0°R.

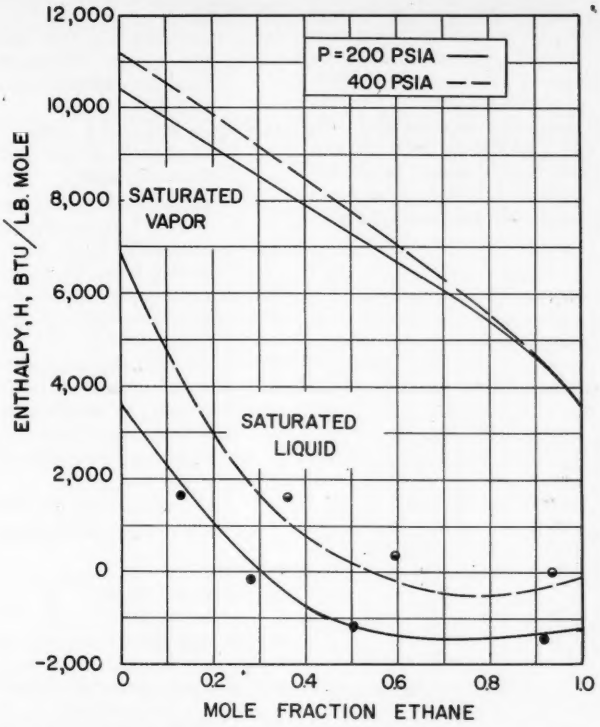

Fig. 3. Enthalpy-composition diagram for ethane–*n*-butane system. $H = 0$ for the pure components in the ideal gas state at unit fugacity and 0°R. Points represent data of Edmister and Canjar (*11*).

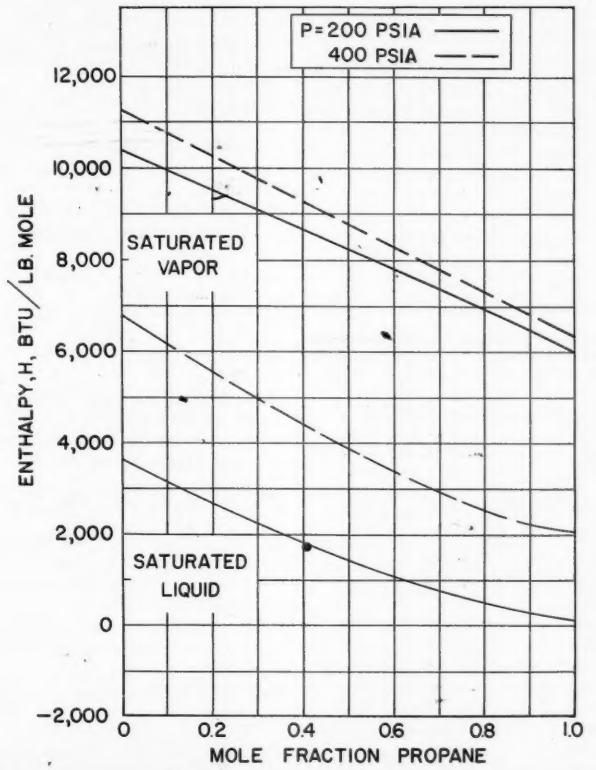

Fig. 4. Enthalpy-composition diagram for propane–*n*-butane system. $H = 0$ for the pure components in the ideal gas state at unit fugacity and 0°R. Point represents datum of Edmister and Canjar (*11*).

the Benedict-Rubin-Webb equation of state has been established for them and accurate equilibrium and volumetric data are available. The empirical constants of the various mixtures for the equation of state were calculated by the method outlined by Benedict-Rubin-Webb (*5*) with the exception of the A_0 for the methane-ethane system, which was calculated by the method of Bloomer, Gami, and Parent (*6*). The values of the constants for the pure materials used in the calculations were those given by Benedict-Rubin-Webb (*5*). The methane-ethane system was investigated at three pressures, 200, 400, and 600 lb./sq. in. abs., and the systems ethane–*n*-butane and propane–*n*-butane were investigated at the two lower pressures only.

The results are presented in graphical form in Figures 2 through 4 and in tabular form in Tables 1 through 3*. The tabulated data are reported to four significant figures, in order to keep the results consistent. The expected error in the enthalpy differences reported is approximately 3%, possible sources of error being in the inaccuracy of the Benedict-Rubin-Webb equation of state and the determination of the slopes of the numerous curves. The calculated-enthalpy differences were very sensitive to the values used for the slope of the dew-point pressure-vs.-temperature curve; hence it was necessary to determine these slopes with the highest possible degree of accuracy.

The ethane–*n*-butane system is the only one in which the liquid-phase enthalpies calculated in this work can be compared with those of Edmister and Canjar (*11*). The enthalpy values obtained by the two independent methods agree very well at 200 lb./sq. in. abs., but not so well at 400 lb./sq. in. abs. At these conditions the values of Edmister and Canjar tend to be above the values presented in this work. Their values represent a maximum disagreement of 10% in enthalpy difference between the saturated liquid and vapor conditions. The disagreements are only in the liquid-phase enthalpies, as the vapor-phase enthalpies presented by Edmister and Canjar (*11*) agree very well with those calculated in this work.

SUMMARY AND CONCLUSIONS

Differential latent heats of condensation and saturated-liquid enthalpies have been calculated by a rigorous thermodynamic relationship for the system methane-ethane at 200, 400, and 600 lb./sq. in. abs. and for the systems ethane–*n*-butane and propane–*n*-butane at the two lower pressures, experimental

*Complete tabular data may be obtained as document 4964 from an American Documentation Institute, Photoduplication Service, Library of Congress, Washington 25, D. C., for $1.25 for photoprints or 35-mm. microfilm.

P-V-T-x data and the Benedict-Rubin-Webb equation of state being used. Enthalpy-concentration diagrams for the three systems at the various pressures involved have been presented. For the ethane–n-butane system, where a number of comparisons were possible, the saturated-liquid enthalpies presented are in fair-to-excellent agreement with previously determined values.

When accurate P-V-T-x relationships are available, the method of calculation presented offers a thermodynamically rigorous means to obtain accurate enthalpy data of saturated-liquid mixtures. As more extensive experimental volumetric and equilibrium data become available, this method should be of considerable value in establishing accurate partial enthalpies for the liquid phase.

Table 1. Enthalpy Values for Saturated Hydrocarbon Mixtures

Methane-ethane system

Pressure = 200 lb./sq. in. abs.

Saturation temperature, °F.	Mole fraction methane (6) x	y	Enthalpy,* B.t.u./lb. mole H_b	H_d	
−6.2	0	0	−1,230	3,463	(3)
−51.2	0.10	0.526	−1,808	3,040	
−85.5	0.20	0.764	−2,200	2,723	
−112.0	0.30	0.882	−2,392	2,477	
−130.7	0.40	0.935	−2,468	2,291	
−143.9	0.50	0.959	−2,472	2,171	
−153.8	0.60	0.975	−2,375	2,076	
−161.2	0.70	0.983	−2,165	2,018	
−167.1	0.80	0.990	−1,836	1,962	
−172.7	0.90	0.994	−1,378	1,926	
−178.5	1.00	1.00	− 812	1,867	(14)

*H = 0 for the pure components in the ideal-gas state at unit fugacity and 0°R. The vapor- and liquid-phase enthalpies of the pure components, obtained from the literature sources cited, were in all instances adjusted to this reference state.

Table 2. Enthalpy Values for Saturated Hydrocarbon Mixtures

Ethane–n-Butane system

Pressure = 200 lb./sq. in. abs.

Saturation temperature, °F.	Mole fraction ethane (12) x	y	Enthalpy*, B.t.u./lb. mole H_b	H_d	
202.7	0	0	3,616	10,487	(17)
159.5	0.10	0.393	2,252	7,939	
122.5	0.20	0.640	1,008	6,421	
93.0	0.30	0.784	+ 10	5,480	
69.0	0.40	0.866	− 757	4,902	
49.5	0.50	0.918	−1,170	4,478	
34.0	0.60	0.949	−1,368	4,158	
21.0	0.70	0.969	−1,445	3,936	
10.0	0.80	0.984	−1,440	3,751	
1.0	0.90	0.995	−1,355	3,620	
−6.2	1.00	1.00	−1,243	3,560	(3)

*H = 0 for the pure components in the ideal-gas state at unit fugacity and 0°R. The vapor- and liquid-phase enthalpies of the pure components, obtained from the literature sources cited, were in all instances adjusted to this reference state.

Table 3. Enthalpy Values for Saturated Hydrocarbon Mixtures

Propane–n-butane system

Pressure = 200 lb./sq. in. abs.

Saturation temperature, °F.	Mole fraction propane (15) x	y	Enthalpy*, B.t.u./lb. mole H_b	H_d	
202.7	0	0	3,648	10,440	(17)
188.0	0.10	0.198	3,148	9,338	
174.3	0.20	0.387	2,665	8,719	
161.8	0.30	0.536	2,225	8,092	
150.8	0.40	0.649	1,803	7,603	
141.3	0.50	0.738	1,409	7,208	
132.5	0.60	0.814	1,062	6,854	
124.6	0.70	0.874	755	6,572	
116.6	0.80	0.930	497	6,305	
109.9	0.90	0.974	258	6,091	
105.0	1.00	1.00	85	5,962	(18)

*H = 0 for the pure components in the ideal-gas state at unit fugacity and 0°R. The vapor- and liquid-phase enthalpies of the pure components, obtained from the literature sources cited, were in all instances adjusted to this reference state.

NOTATION

H = enthalpy, B.t.u./lb. mole. $H = 0$ for a pure component in the ideal-gas state at unit fugacity and 0°R.

H° = enthalpy of a component in the ideal-gas state and unit fugacity, B.t.u./lb. mole

$\overline{\Delta H}$ = partial-enthalpy difference, $H - H^\circ$, B.t.u./lb. mole

ΔH_c = differential latent heat of vaporization, B.t.u./lb. mole

P = pressure, lb./sq. in. abs.

R = gas-law constant, 1.987 B.t.u./(lb. mole)(°R.)

T = absolute temperature, °R.

V = molal volume, cu. ft./lb. mole

d = density, lb. mole/cu. ft.

x = mole fraction in the liquid phase

y = mole fraction in the vapor phase

A_0, B_0, C_0, a, b, c, α, and γ = empirical constants of the Benedict-Rubin-Webb equation of state

Subscripts

G = vapor phase

b = bubble point

d = dew point

i = a component

j = total number of components

LITERATURE CITED

1. *Am. Petroleum Inst. Research Proj. 44*, Table 24u-E, Carnegie Institute of Technology, Pittsburgh, Pa. (1953).
2. Bahlke, W. H., and W. B. Kay, *Ind. Eng. Chem.*, **24**, 291 (1932).
3. Barkelew, C. H., J. L. Valentine, and C. O. Hurd, *Trans. Am. Inst. Chem. Engrs.*, **43**, 25 (1947).
4. Benedict, Manson, G. B. Webb, and L. C. Rubin, *J. Chem. Phys.*, **8**, 334 (1940); **10**, 747 (1942).
5. ———, *Chem. Eng. Progr.*, **47**, 419, 449 (1951).
6. Bloomer, O. T., D. C. Gami, and J. D. Parent, *Inst. of Gas Technol. Research Bull.*, **22** (1953).
7. Dodge, B. F., "Chemical Engineering Thermodynamics," p. 130, McGraw-Hill Book Company, Inc., New York (1944).
8. *Ibid.*, p. 134.
9. *Ibid.*, p. 131.
10. Edmister, W. C., *A.I.Ch.E. Journal*, **1**, 38 (1955).
11. ———, and Lawrence Canjar, *Chem. Eng. Progr. Symp. Ser.*, **49**, No. 7, 73 (1953).
12. Kay, W. B., *Ind. Eng. Chem.*, **32**, 353 (1940).
13. *Chem. Eng. Progr.*, **46**, 20 (1950).
14. Matthews, C. S., and C. O. Hurd, *Trans. Am. Inst. Chem. Engrs.*, **42**, 55 (1946).
15. Nysewander, C. N., B. H. Sage, and W. N. Lacey, *Ind. Eng. Chem.*, **32**, 118 (1940).
16. Papadopoulos, A., R. L. Pigford, and Leo Friend, *Chem. Eng. Progr. Symp. Ser.*, No. 7, **49**, 119 (1953).
17. Prengle, H. W., Robert York, Jr., and L. R. Greenhaus, *Chem. Eng. Progr.*, **44**, 863 (1948).
18. Stearns, W. V., and E. J. George, *Ind. Eng. Chem.*, **25**, 602 (1943).

Characteristics of Porous Beds and Structures

R. B. MACMULLIN and G. A. MUCCINI

The structure of a porous body can be characterized by three parameters, each of which can be directly measured by simple experimental procedures. These parameters are hydraulic radius m, viscous-flow permeability P, and electrical-resistivity ratio R/R_0, which are shown to be related by the simple equation

$$m^2 = k \cdot P \cdot R/R_0 \qquad (1)$$

or, in dimensionless terms,

$$\frac{m^2}{P} = k \cdot \frac{R}{R_0} \qquad (1a)$$

For beds of loose particles of known size and shapes, the hydraulic radius m may be calculated from the relation $m = \epsilon/s$, where ϵ is the void fraction and s the specific surface of the bed. Since this method is not usually applicable to consolidated beds, an experimental procedure based on surface-tension phenomena has been tested. This method, known as the *break point* for granular beds, or *bubble point* for consolidated beds, gives m directly by the relation $m = \gamma/(\Delta p \cdot g)$ where γ is the surface tension of the liquid employed and Δp the pressure required to break through the film of sealing liquid. The sealing liquid must easily wet the porous medium.

The permeability coefficient P is a property of the porous medium only and is evaluated by measuring the resistance to viscous fluid flow by means of a fluid of known viscosity; that is, $P = (u \cdot L \cdot \eta)/(\Delta p \cdot g)$, where u is the superficial fluid velocity, η is the viscosity, and $\Delta p/L$ the pressure gradient.

The resistivity ratio R/R_0 is measured by saturating the specimen with an electrically conducting fluid. R is the resistance in ohms, and R_0 is the resistance of the fluid occupying the same bounds of space as the specimen.

The correlation was tested on a great variety of porous media, including beds of glass beads; sand; and such materials as bonded alumina, porcelain, carbon and graphite, fritted glass, sandstone, and polyvinyl chloride sheet. The mean value of k was found to be 3.666 ± 0.098. The probable error of a single set was found to be 0.65, or 17.6%. Covering a thousand-fold range of hydraulic radius (a million-fold range in permeability), the correlation applies to a wide range of porous media, including packed granular beds and both rigid and flexible consolidated media. The correlation is independent of the porosity, which covers the range of $\epsilon = 0.1$ to 0.85. These are advantages which appear to be lacking in previous correlations by others.

Beyond the viscous-flow range of permeability the following modified forms of the Reynolds number Re and friction factor f are suggested:

$$Re = \frac{m \cdot u_e \cdot \rho}{\eta} = \frac{m \cdot u \cdot \rho}{\eta}\left(\frac{R/R_0}{\epsilon}\right)^{1/2} \qquad (28)$$

$$f = \frac{m \cdot \Delta p \cdot g}{u^2 \cdot L \cdot \rho} \cdot \frac{\epsilon^{1/2}}{(R/R_0)^{3/2}} \qquad (37)$$

The critical Reynolds number Re_{crit}, beyond which the fluid flow cannot be considered as 100% viscous, is approximately $Re_{crit} = 5.5$.

Table A. Fields of Interest in Porous Media

Civil engineering
- Permeability of earth and sand structures, such as dams, subsoil drainage systems
- Flow of wells from water-bearing formations
- Intrusion of sea water in coastal areas
- Filter beds for water supply and sewage purification
- Aeration media for sewage

Geological and mining engineering
- Fluid flow in gas- and petroleum-bearing formations
- Geophysical prospecting by electrical conductivity method
- Leaching of ores and concentrates

Chemical engineering
- Filtration of gases and liquids
- Fluid flow through packed beds
- Gas diffusion and dispersion

Electrochemical engineering
- Permeable and semipermeable diaphragms for electrolytic cells

Medicine and biochemistry
- Biochemical filters
- Mechanical devices to simulate natural organs of the body with respect to fluid flow and electrical response
- Electro osmosis

Miscellaneous
- All industries engaged in manufacture of porous media, such as ceramic, metallic, plastic, rubber, leather, textile, etc.
- Agriculture, as in porous character of soil

R. B. MacMullin is with R. B. MacMullin Associates, Niagara Falls, New York, G. A. Muccini, formerly at Niagara University, Niagara Falls, New York, is now at the University of Notre Dame, South Bend, Indiana.

THEORY

This paper is concerned with the correlation of viscous-flow permeability and electrical conductivity of porous media. It is believed that such a correlation would be of interest and importance in many fields of technology, as listed in Table A.

Permeability Alone

The most generally accepted concepts of fluid flow through porous beds are based on the Kozeny-Carman (*6* to *9*) equations, which relate the pressure gradient dp/dL of a fluid of density ρ, viscosity η, and superficial (approach) velocity u to the porosity ϵ and specific surface s of a bed of granular, nonconsolidated particles. Various forms of these equations are

$$\frac{dp}{dL} = \frac{fs\rho u^2}{g\epsilon^3} \qquad (2)$$

$$Re = \frac{\rho u}{\eta s} \qquad (3)$$

In terms of average-particle diameter and sphericity ϕ,

$$\frac{dp}{dL} = \frac{6f\rho u^2(1-\epsilon)}{g\phi D\epsilon^3} \qquad (4)$$

$$Re = \frac{\phi D u \rho}{6\eta(1-\epsilon)} \qquad (5)$$

In the viscous-flow region, with $P = (u \cdot L \cdot \eta)/(\Delta p \cdot g)$

$$f = \frac{k_c}{Re} = \frac{5}{Re} \qquad (6)$$

$$m^2 = k_c \frac{P}{\epsilon} \qquad (7)$$

The coefficient k_c is variously reported as from 5 to 5.5.

Useful as these equations may be, their limitations are often overlooked. For example, the porosity ϵ is an important factor. In loose beds of solid particles of known density, ϵ may be calculated readily enough from the apparent density of the porous bed. In consolidated bodies of such materials as porous ceramics, porous carbon, or sandstone, there are complications. One must distinguish between pores that are open, semiclosed, and closed and between the microporosity contributed by the porous nature of the particles themselves and the macroporosity of the interstitial space around the

particles. The porosity to be used in the Kozeny-Carman equations, therefore, is frequently in doubt and sometimes immeasurable.

Likewise, the specific surface s is an important factor. Obviously, the internal surface of microporous particles contributes little or nothing to the resistance to fluid flow, as compared with the external surface of the particles. Even in beds of irregular but nonporous granules the external surfaces sometimes mate, and these surfaces are "blind" to the flow of fluid. The total surface of a porous bed may be determined by the gas-absorption method, but obviously this is not necessarily the specific surface called for in the Kozeny-Carman equations.

The hydraulic radius m of Equation (7) is defined, for a porous body, as the ratio ϵ/s. It is therefore subject to the same sources of error as ϵ and s separately. There is, fortunately, a method that can be used to measure hydraulic radius directly. If a porous body is saturated with a liquid which easily wets the body, the liquid is locked into the pores by surface tension forces. In the well-known bubble-pressure method, and also the new break-point method described later, the force required to break through this sealing liquid is measured. At the saturation level in the bed, the following forces are in balance over a unit area of bed:

Force supported = open area $\cdot \Delta p \cdot g$

Supporting force = wetted perimeter of grains $\cdot \gamma \cdot \cos\theta$

The ratio, open area/wetted perimeter = hydraulic radius m

$$\therefore\ m = \frac{\gamma \cos\theta}{\Delta p \cdot g} \qquad (8)$$

If this is true for any section of the bed, it is true for all sections of the bed, provided that (a) the structure of the bed is reasonably (or better, statistically) uniform and (b) the unit area chosen is much larger than the areas of the open pores. By proper choice of sealing fluid, $\cos\theta$ may be taken as unity. Hence

$$m = \frac{\text{open area} \times L}{\text{wetted perimeter} \times L} = \frac{\epsilon}{s} \qquad (9)$$

Equation (8) is also used as the basis for determining "pore-size" distribution in a porous body, sometimes by use of mercury or some nonwetting liquid. Opinion varies as to whether m, given by Equation (8) by the bubble-point method, is identical with the reciprocal average value of m as calculated from the distribution curve or with the value of m calculated from independent measurement of ϵ and s. In the experiments here reported, the equivalence is quite good. The break-point method is believed to selectively exclude closed and semiclosed pores from the numerator of Equation (9), as well as to exclude the blinded surfaces from the denominator. If this is true, the break-point method should give the desired value of m to be used in the Kozeny-Carman equation (7). On the other hand, the reciprocal average m calculated from the distribution curve is likely to give undue weight to the very small values of m, which results from forcing the sealing liquid (mercury) into semiclosed pores and micropores.

Entirely aside from the question of what values of m, ϵ, and s to use in the Kozeny-Carman equations is that of the organization of the network of pores, the effective velocity u_e of the fluid in the pores, and the effective length of path L_e of a parcel of fluid. These factors may be lumped under the general heading of *tortuosity*, a term which conceals a great deal of ignorance. If the tortuosity is universal, then the Kozeny-Carman coefficient k_c should be a natural constant. For an illuminating discussion of this point, the reader is referred to a recent article by Scheidegger (*24*), who concludes that the tortuosity can have values in an extremely wide range and that it is not surprising that the Kozeny-Carman relation is frequently in poor agreement with actual experimental results. This emphasizes the danger of extending the very useful Kozeny-Carman equations into regions of application where they were not intended. For treating permeability in consolidated porous bodies, one must therefore search for a key to tortuosity.

It is recognized that much important work in this field has been published since the classical paper of Carman. For granular beds, Brownell and Katz (*2, 3, 4*) introduced arbitrary correction factors in the form of exponents of the porosity. Leva and coworkers (*17*) used the Kozeny-Carman relation to estimate surface of tower packings. Ergun (*14*) considered the problem of mixed flow, partly viscous and partly turbulent, in packed columns, and Wagstaff and Nirmaier (*30*) further verified the Ergun equation. Brownell (*5*) deduced a modification of the Kozeny-Carman equation which applies to beds of spheres consolidated with resin. Tiller (*27, 28*) and Grace (*15*) have applied the Kozeny-Carman relation to the unit operation of filtration, and Whitney (*31*) to the dewatering of wood pulp and fibrous materials. Hatfield (*16*) studied the permeability of porous carbon and graphite. Much information is to be found in books by Dallavalle (*13*), Muskat (*19*), and Terzaghi (*26*). It has become clear that no single general equation based only on the variables used by Kozeny-Carman has yet been proposed that is adequate for such an extensive range of application.

Before leaving this subject, the authors wish to point out an approach that could give permeability solely in terms of porosity and specific surface, provided that the fine structure of the bed is known. This can be done by evaluating the point-to-point variation of the hydraulic radius within the porous structure. Application of the method to certain geometrically predetermined beds is given in the appendix.*

Electrical Resistivity Alone

Electrical-resistivity measurements have been made on many porous nonconducting bodies, the pores being filled with a conducting medium (*1, 10, 11, 17, 18, 21, 22, 29, 32* to *35*). At first one might be tempted to reason that if such a body were, say, 40% porous, then it would conduct 40% as well as if the body were 100% porous (i.e., no solids present at all). This is far from the truth; the resistance always is much higher. The first record that could be found of this discovery was made by Velisek and Vasicek (*29*). To explain this result, they reasoned as follows: Since the pore structure resembles a three-dimensional network, only one of the three dimensions is in a position to conduct, namely, the one coinciding with the direction of the potential gradient. On this basis, $\epsilon\ R/R_0 = 3$. For porous bodies consisting chiefly of fissures, two dimensions conduct, and so $\epsilon\ R/R_0 = 1.5$. These authors were qualitatively correct in their reasoning. In the present work $\epsilon\ R/R_0$ ranged from 1.5 minimum to 3.0 maximum. In some recent work by Cornell and Katz (*11*), $\epsilon\ R/R_0$ ranged from 1.8 to 5.9 for sixteen samples of sandstone, and from 6.1 to 10.7 for eight samples of dolomite and limestone. De LaRue and Tobias (*12*) have recently determined the influence of suspended nonconducting particles on the conductivity of a liquid. The equation that they evolved will be discussed later in relation to the present work.

When a porous body is itself an electrical conductor, the mechanism of conduction is more complicated, as shown by Sauer et al. (*23*). The conductivity of the pore structure, however, can be independently measured by the use of direct current, as will be explained under Experimental Methods. There are other disturbing factors that can influence the measurement of resistivity ratio unless proper conditions are chosen to avoid them. The phenomena of superconductivity at low electrolyte concentration, doubly ionized layers, internal reactance, and such are dealt with in the cited references.

Permeability and Electrical Resistivity Together

A very early attempt to correlate permeability with resistivity ratio was made by Wirth (*32*), who presented an equation that reduces to $m^2 = 2P \cdot R/R_0$. The form of this equation is believed to be correct, but the coefficient 2 derives from the assumption of Poiseuille's law for capillary flow. This is known to give an erroneous result for porous beds.

*Complete data may be obtained as document 4955 from the American Documentation Institute, Photoduplication Service, Library of Congress, Washington 25, D. C., for $2.50 for photoprints or $1.75 for 35-mm. microfilm.

Much work has been done by Wyllie and Gregory (*33*, *34*) and by Cornell and Katz (*11*), all of whom introduce the resistivity ratio as a correction factor for various permeability equations. Cornell and Katz, for example, identify $(L_e/L)^2$ with $\epsilon \cdot R/R_0$ in the ideal form of the Kozeny-Carman equation

$$\frac{dp}{dL} = \frac{k_0 u\eta}{m^2 g\epsilon} \cdot \left(\frac{L_e}{L}\right)^2 \qquad (10)$$

which reduces to

$$m^2 = k_0 PR/R_0 \qquad (11)$$

Two problems remain: (1) the theoretical justification of an equation of the foregoing type and (2) the determination of the coefficient over a wide range of conditions. The present authors have undertaken to solve both problems.

Theoretical Basis for Relating Permeability to Resistivity Ratio

Since fluid velocity in the 100% viscous flow region is characterized by the relation

$$u\eta \sim \epsilon m^2 \chi \text{ grad } p \qquad (12)$$

and electrical current density by the relation

$$I_0(r) \sim \epsilon\chi \text{ grad } E \qquad (13)$$

it can be seen that the phenomena are analogous.

Equation (12) states that the velocity of a fluid of unit viscosity is proportional to the pressure gradient and three determining structural dimensions of the network. These dimensions are porosity ϵ, hydraulic radius squared m^2 (which produces the drag in viscous flow), and tortuosity χ, which is the "fudge" factor introduced to make Darcy's law hold. This equation may be recast into the more familiar form,

$$k \frac{u\eta L}{g\,\Delta p} = kP = \epsilon m^2 \chi \qquad (12a)$$

Equation (13) states that the current flowing through unit area of a specimen the pores of which are filled with a conductor of unit resistivity is proportional to the potential gradient and two determining structural dimensions of the network. These dimensions are porosity ϵ and tortuosity χ, which is precisely the same "fudge" factor used in Equation (31), here introduced to make Ohm's law hold. This equation may be recast into the more familiar form,

$$(r)L = R_0 = \epsilon\chi \frac{E}{I} = \epsilon\chi R \qquad (13a)$$

or

$$R_0/R = \epsilon\chi$$

Combining (31*a*) and (32*a*) so as to

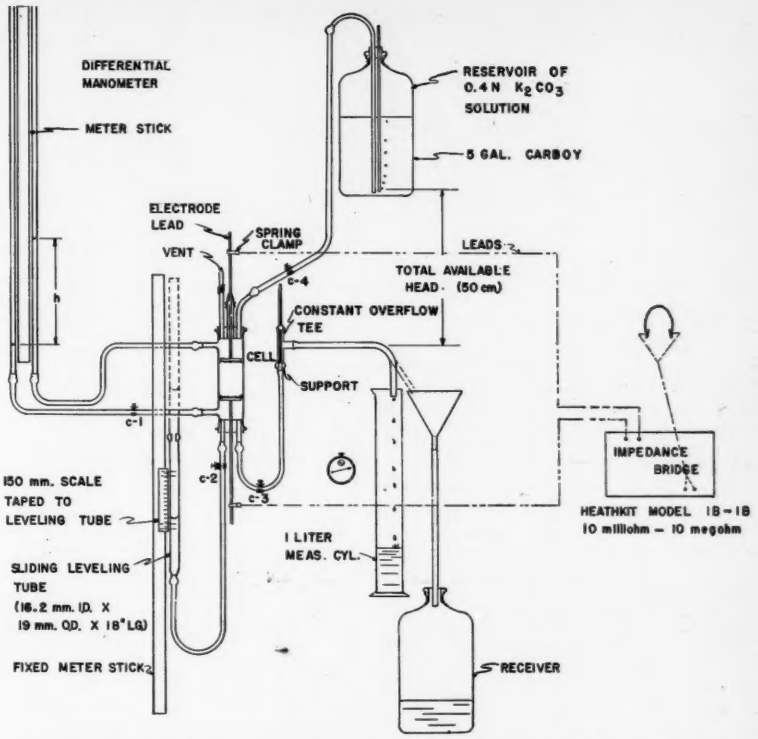

Fig. 1. Assembly for simultaneous measurement of permeability, electrical resistivity, and hydraulic radius of packed beds of unconsolidated particles.

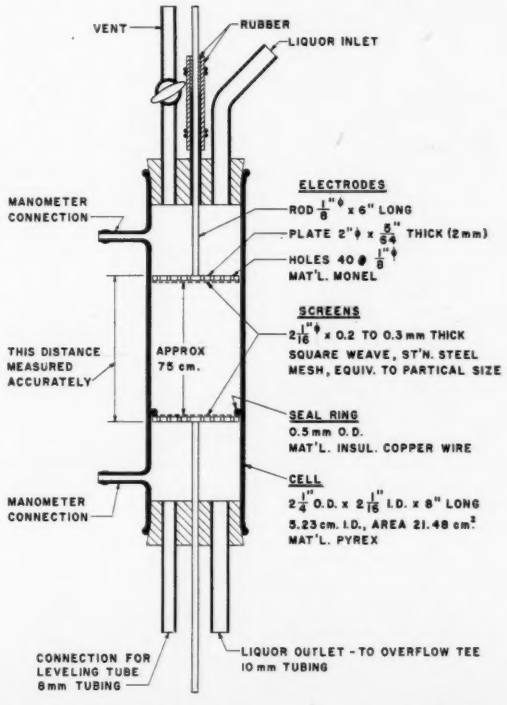
VENT
RUBBER
LIQUOR INLET
ELECTRODES
ROD 1/8" ϕ x 6" LONG
PLATE 2" ϕ x 5/64" THICK (2 mm)
HOLES 40 @ 1/8" ϕ
MAT'L. MONEL
MANOMETER CONNECTION
SCREENS
2 1/16" ϕ x 0.2 TO 0.3 mm THICK
SQUARE WEAVE, ST'N. STEEL MESH, EQUIV. TO PARTICAL SIZE
THIS DISTANCE MEASURED ACCURATELY
APPROX 75 cm.
SEAL RING
0.5 mm O.D.
MAT'L. INSUL. COPPER WIRE
CELL
2 1/4" O.D. x 2 1/16" I.D. x 8" LONG
5.23 cm. I.D., AREA 21.48 cm²
MAT'L. PYREX
MANOMETER CONNECTION
CONNECTION FOR LEVELING TUBE 8 mm TUBING
LIQUOR OUTLET - TO OVERFLOW TEE 10 mm TUBING

Fig. 2. Details of cell shown in Figure 1 (for unconsolidated beds).

eliminate ϵ and χ, one obtains the simple relation

$$m^2 = kPR/R_0 \qquad (1)$$

To prove this relation is the object of this paper, and therefore, independent measurements of hydraulic radius, permeability, and resistivity ratio have been made.

EXPERIMENTAL METHODS

Unconsolidated Packed Beds

It is of prime importance that the packed bed, once formed, must not in any way be disturbed during the course of the several measurements made upon it. The assembled equipment for accomplishing this is shown in Figure 1. Cell details are shown in Figure 2.

The solution used for the tests was 0.4*N* K_2CO_3, prepared from Baker's analyzed $K_2CO_3 \cdot H_2O$ crystal and distilled water. This solution was analyzed frequently. This particular electrolyte was chosen for the following reasons: (1) it is available in highly pure form; (2) it is stable to atmospheric air; (3) it has no effect on cell parts, such as pyrex glass, rubber, Tygon, Monel, electrodes, stainless steel screens; (4) it has no effect on the materials tested, glass beads, silica sand; and (5) all the necessary physical properties, such as density, viscosity, surface tension, and electrical resistivity, are accurately known as a function of concentration and temperature within the range of the work. These physical properties are listed in Table 13.*

Materials Tested. Superbrite glass beads were obtained from Minnesota Mining & Minerals Co. in four graded sizes as follows:

Grade No.	U.S. sieve size Through	On
108	40	45
109	50	60
110	60	80
111	100	120

Particle size† 1	2	3	Avg.
392	390	410	397
271	290	325	295
228	200	214	214
136	150	157	148

†1. Reciprocal average of screen opening.
2. Data from company (presumably micrometered).
3. Measured by authors. Average of fifty beads from random sample, measured under microscope with filar micrometer. Over 95% of the beads were perfect spheres, the balance somewhat ellipsoidal.

The glass beads were found to be free of extraneous material. A water extract was substantially as nonconducting as the water used. The specific gravity of the beads was measured and found to be 2.572.

A bag of clean, dry, washed, sized quartz sand of very light color was obtained. A screen analysis on new U. S. standard screens gave the results shown in Figure 12.* This sand was then carefully and exhaustively sized, and two ranges, 40 to 60 and 60 to 80, were selected for testing. Since the plot of accumulative weight fraction against $6/D$ (Figure 12) gave practically a straight line, it follows that the reciprocal average diameter for the chosen cuts truly represents the diameter for which specific surface and sphericity can be calculated. The hydraulic radius and porosity of six different beds were measured by the break-point method and yielded specific surface by the relation

$$s' = \frac{\epsilon}{(1-\epsilon)m}, \text{ sq. cm./cc. of sand} \qquad (14)$$

The specific surface of true spheres of diameter D_{ra} would be $s_0' = 6/D_{ra}$, where D_{ra} is the reciprocal average diameter for the cut. Sphericity is then defined as $\phi = s_0'/s'$.

Five beds of sand gave the accompanying results. The specific gravity of the sand was measured and found to be 2.640.

Preparation of Bed. With the lower electrode, screen, and wire seal ring in place, the cell was partly filled with potash solution, enough to cover the added beads or sand. An accurately weighed amount (approximately 200 to 250 g.) of particles was added slowly through a funnel, the stem of which was swirled above the surface of the liquid. In this way a uniform and level bed is formed, free from trapped air bubbles. The cell is then vibrated to pack the bed, and during that time the upper screen and electrode are placed and pressed down firmly. The cell is then filled and connected to the constant-level feed tank. All air is carefully vented from feed lines and cell. Clamps c-1 and c-3 are opened, and c-2 is closed. The flow of electrolyte is controlled by c-4.

The depth of bed is measured by taking a series of ten readings around the cell. Since the outer edges of the electrodes are clearly visible, this distance is actually measured; from the average value, the calipered thickness of the two electrodes and two screens is subtracted. The inside diameter of the cell is, of course, known.

Permeability. After steady state conditions are reached at any particular flow rate, the overflow is diverted to the liter-measuring cylinder, and the time to fill is measured with a stop watch. At regular intervals the loss in head is taken on the manometer, and the outlet temperature is recorded. Several flow rates are tried, and the proportionality of flow rate to head is checked immediately. Any deviation from proportionality would be cause for rejection of the data as not representing viscous-flow conditions. The correction for pressure drop through the screens has been shown to be negligible.

Permeability is calculated from the equation

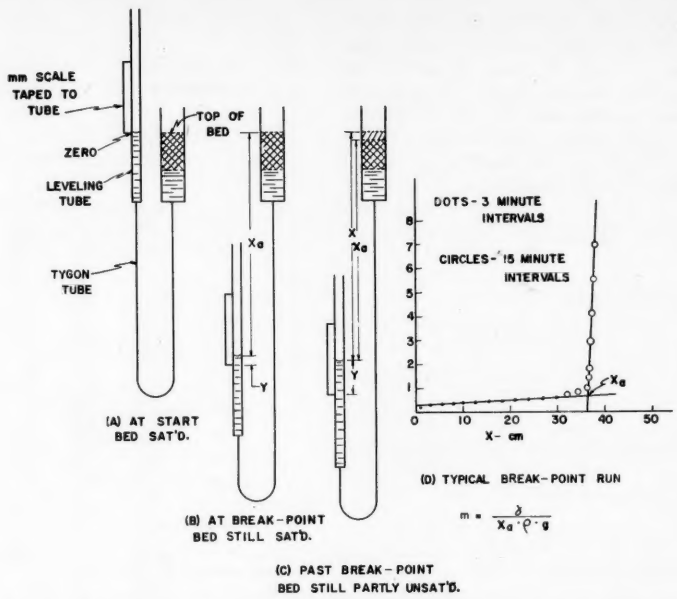
mm SCALE TAPED TO TUBE
TOP OF BED
ZERO
LEVELING TUBE
TYGON TUBE
(A) AT START BED SAT'D.
(B) AT BREAK-POINT BED STILL SAT'D.
(C) PAST BREAK-POINT BED STILL PARTLY UNSAT'D.
DOTS - 3 MINUTE INTERVALS
CIRCLES - 15 MINUTE INTERVALS
X - cm
(D) TYPICAL BREAK-POINT RUN

Fig. 3. Principle of break-point method for determining hydraulic radius of packed beds.

Results on Five Beds of Sand

Mesh through/on	D_{ra}, μ	m, μ	ϵ	s' cm.$^{-1}$	s_0' cm.$^{-1}$	ϕ
40/60	315	26.5	0.4423	300	190	0.634
40/60	316	26.8	0.4470	302	190	0.634
40/60	316	27.35	0.4325	281	190	0.677
60/80	207	19.25	0.4450	416.6	290	0.696
60/80	207	18.67	0.4570	450	290	0.645
					Average	0.657

*See footnote on page 394.

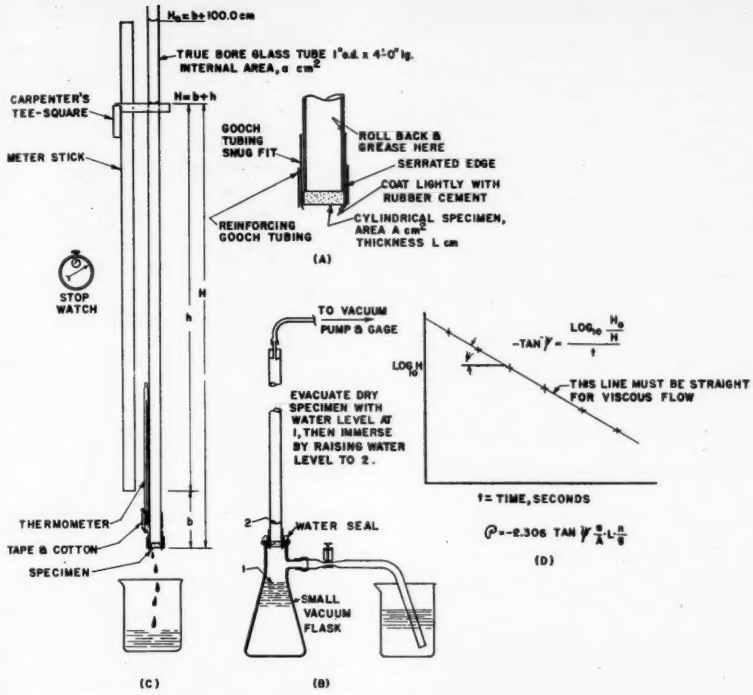

Fig. 4. Water-permeability test, falling-column method.

$$P = \frac{uL\eta}{\rho\, \Delta h\, g}\ , \text{cm}^2 \qquad (15)$$

Resistivity. Simultaneously with the foregoing permeability tests, the resistance R of the bed is taken on the impedance bridge. Sharp null points are obtained, by use of 1,000-cycle current and telephone detection. R_0 is calculated from the dimensions of the bed and the specific resistivity of the solution, on the basis of Ohm's law. The resistance of the electrodes, screens, and leads was measured and found to be negligible.

Hydraulic Radius. At the conclusion of the above-mentioned measurements of permeability and resistivity, and without any disturbance to the bed, the liquid level is dropped to the top of the bed (with the vent open). Clamps c-1, c-3, and c-4 are tightly closed, and c-2 is opened. The leveling tube is then adjusted to the top of the bed. The celluloid millimeter scale is then taped to the leveling tube, with the zero mark at the level of the water.

The leveling tube is then lowered 2 cm. at a time, at 3-min. intervals, and two readings are taken: the position of the zero mark of the millimeter scale with reference to the stationary meter stick and the level of the water in the leveling tube with reference to the millimeter scale. The top of the bed, with reference to the meter stick, is, of course, noted and remains constant.

The distance x and y are calculated and plotted immediately, in the manner shown in Figure 3 (D). As the breakpoint is approached, the increment $\Delta y/\Delta x$ starts to increase. At this point the leveling tube is lowered 1 cm. at a time at 15-min. intervals. Past the breakpoint, $\Delta y/\Delta x$ increases rapidly. Sufficient points are recorded to fix the slope of the new line accurately. The unsaturation line in the bed is usually clearly visible, because air has been drawn into the bed. It has been found impossible to reverse the procedure and to drive the air out of the bed by raising the leveling tube. It is, therefore, considered impractical to repeat the break-point tests, and it is preferable to start all over.

The intersection of the two lines, as shown in Figure 3(D) is considered to be the breakpoint, and x_a gives the effective head of liquid supported by the sand owing to surface tension. Neglecting the angle of contact θ gives

$$m = \frac{\gamma}{x_a \rho g}\ , \text{cm.} \qquad (16)$$

Density of Particles. Density was determined by comparing the weight in air and in water by use of a 200-g. sample and taking care to avoid errors due to entrapped air.

Rigid Porous Materials

The testing of rigid materials has the intrinsic advantage that the same specimens may be tested over and over again. It is necessary only to take the following precautions: (1) only clear liquids or clean gases may be used, to prevent clogging of the pores with fines; (2) the faces of specimens, particularly the fine ones, must not be handled with the fingers, as grease or wax may seal off some of the pores and give erroneous results; (3) specimens must be thoroughly dry before testing for gas permeability; (4) specimens must be freed of entrapped air (by evacuation) in order to obtain 100% saturation with liquid before testing for liquid permeability or resistivity; (5) specimens must be carefully sealed at the edges to prevent by-passing of fluid; and (6) when the bubble-point test is made for hydraulic radius, the fluid chosen should easily wet (have an affinity for) the specimen.

The specimens were prepared in the form of true cylindrical disks, approximately 1 in. in diameter and ¼ in. thick, with faces strictly parallel. All specimens were then accurately calipered.

Materials Tested. Porous porcelain filter disks from the Selas Corporation are made, it is understood, by incorporating carbon in the ceramic mix, so that, on firing, the carbon burns out, leaving a porous structure. The following grades were tested: XF, XFF, 10, 01, 015, 02, and 03.

Grades PC 40 and 60 and PG 40 and 60 of porous carbon and graphite from National Carbon Company were tested. For an estimate of m, based on grain size, distribution, and other data, the results shown in Table 4 should be consulted.

Of fritted-glass filter tubes made by Corning Glass Works and supplied by Will Corporation, three grades were tested, coarse, medium, and fine.

Water Permeability, Falling-column Method. In this method, also known as the method of Terzaghi (*26*), the specimen is

Fig. 5. Apparatus for measuring gas permeability of rigid specimens (*a*) by use of rotameters, (*b*) by use of water displacement.

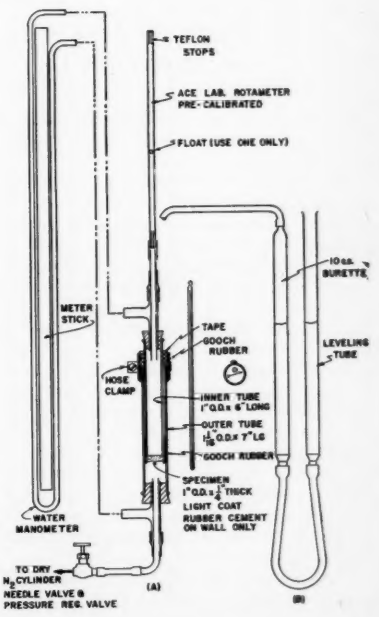

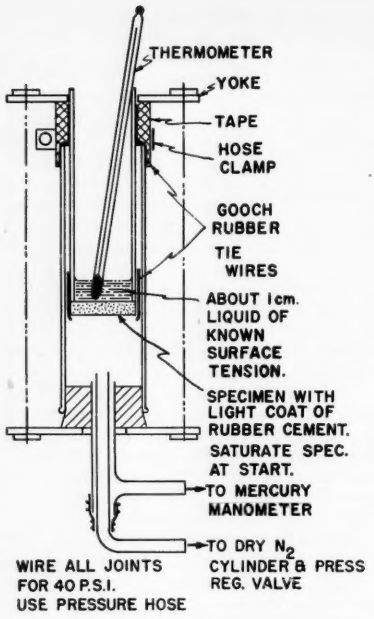
THERMOMETER
YOKE
TAPE
HOSE CLAMP
GOOCH RUBBER
TIE WIRES
ABOUT 1 cm. LIQUID OF KNOWN SURFACE TENSION.
SPECIMEN WITH LIGHT COAT OF RUBBER CEMENT.
SATURATE SPEC. AT START.
TO MERCURY MANOMETER
TO DRY N_2 CYLINDER & PRESS REG. VALVE
WIRE ALL JOINTS FOR 40 P.S.I. USE PRESSURE HOSE

Fig. 6. Apparatus for measuring bubble-point pressure of rigid specimens.

mounted below a column of water, and the height of the water column is measured against time. The inside area of the tube being known, the permeability can be calculated. The apparatus used is shown in Figure 4. Cut *A* shows how the specimen is mounted, cut *B* shows how the specimen is evacuated and saturated with water, cut *C* shows the assembly during test, and cut *D* shows the method of plotting the data.

If a = area water column, sq. cm.
A = area specimen, sq. cm.
L = thickness of specimen, cm.
H = head of water, cm., at time t, sec.
$\tan \psi$ = slope of line, $\Delta \log_{10} H/\Delta t$

Then $P = -2.306 \tan \psi \, (aL\eta/Ag)$, sq. cm. (17)

For viscous-flow conditions the plot of $\log H$ vs. t must be straight; otherwise, the experiment must be rejected.

Gas Permeability. In this test dry nitrogen gas from a cylinder equipped with a sensitive gas-pressure regulator is passed through the specimen. Pressure drop is measured by water manometer. Gas flow is measured either by a precalibrated Brooks laboratory flow meter (supplied by Ace Glass Company) or by the time required for water displacement from a calibrated pipette. The apparatus is shown in Figure 5. In use of the Brooks flow meter only one float is used, not two, as suggested by the manufacturer. The instruments were recalibrated before use. Moreover, the ball must be handled with care. If it is dropped on the floor, the calibration will change. The usual temperature and pressure corrections are applied to reduce readings to the temperature of the experiment.

For each specimen, several flow rates are used, covering a threefold range. Proportionality between flow rate and pressure drop is proof that the flow is in the viscous range; otherwise the experiment is useless.

If the pressure drop is only a matter of 10 to 40 cm. H_2O head, then the correction for expansion of the gas in the specimen is negligible. Where the pressure drop through the specimen is appreciable, the following correction factor must be applied to each different flow rate, after which the true permeability may be calculated:

$$\text{correction factor } C = \frac{2p_2}{p_1 + p_2} = \frac{2p_2}{2p_2 + \Delta p} \quad (18)$$

where

p_1 is the upstream absolute pressure (cm. of H_2O)
p_2 is the downstream absolute pressure (cm. of H_2O)

$$\Delta p = p_1 - p_2, \text{ cm. of } H_2O$$

$$P = \frac{CuL\eta}{\Delta p \, g}, \text{ sq. cm.} \quad (19)$$

Hydraulic Radius, Bubble-point Method. The specimen is mounted as shown in Figure 6. When mounted, the specimen is covered with about 1 cm. of a liquid of known surface tension which is allowed to permeate. It is not necessary to evacuate the specimen and saturate, as this procedure gives the same result as the simple permeation procedure.

The cell is connected to a dry nitrogen cylinder through a sensitive pressure regulator. The pressure is slowly increased until a slow but steady stream of bubbles is seen rising through the sealing liquid. Any bubbles from the edge do not count, only those arising from some part of the upper surface of the specimen. The bubble pressure is read on a mercury gauge or water gauge as applicable. If the pressure is too high for the mercury gauge, for example 40 cm. of greater, the Bourdon gauge on the low-pressure side of the regulator may be read. The gas pressure is then reduced and the procedure repeated to give a series of readings, which are averaged. Increasing the flow rate through the specimen until gas evolves all over the surface does not increase the bubble-point pressure appreciably. Above a certain point, however, the pressure increases owing to pressure drop through the specimen. With a little practice, the bubble point is reproducible.

It is important to use a sealing fluid that wets the porous body. Water is excellent for glass, porcelain, sandstone and, most ceramic bodies but is useless for porous carbon and graphite. For these materials CCl_4 or C_6H_6 may be used.

The hydraulic radius is calculated from the equation

$$m = \frac{\gamma}{\Delta p \, g}, \text{ cm.}$$

where

γ = surface tension of liquid at temperature of experiment
Δp = bubble-point pressure, cm. H_2O
g = 980.6 cm.sec.$^{-2}$

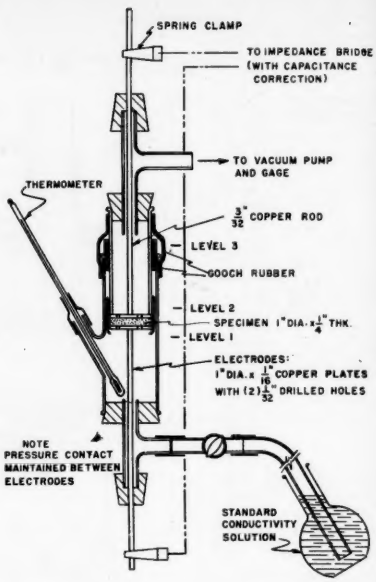

Fig. 7. Resistivity cell for porous solid specimens.

The hydraulic radiuses for fritted glass, with both water and CCl_4, are compared below:

	Coarse	Medium	Fine
m, (H_2O), μ	16.3	2.76	1.52
m, (CCl_4), μ	18.1	2.08	1.28

This indicates that CCl_4 tends to give a low reading on glass, probably because of a small angle of contact which is ignored in the equation above.

Electrical-resistivity Ratio. For nonconducting porous bodies made from such materials as ceramics and plastics, the apparatus shown in Figure 7 was used. The specimen is mounted between copper electrodes (satisfactory for K_2CO_3 solution) at the end of a 1-in. O.D. glass tube. The assembly is held together with Gooch rubber, and the electrodes are pressed tightly against the specimen. Each electrode is perforated with two small holes to permit evacuation of the specimen and saturation with an electrolyte of known electrical resistivity.

The cell is connected first to a Hyvac pump and the air exhausted. Then the electrolyte is slowly introduced until the specimen is just immersed. The water will boil a little until all the air is displaced. Then the vacuum is partially released (until boiling stops), and additional electrolyte is sucked through to sweep out any partly concentrated electrolyte present in the specimen. The vacuum is finally released altogether, the tightness of contact of electrodes is checked, and the resistance is then measured. The temperature is recorded, and the electrolyte analyzed.

For this work the Heath-Kit Model BI-Bl was used with 1,000-cycle alternating current and telephone detection. Frequently a poor null point was encountered, which was somewhat improved by use of a weaker electrolyte, i.e., about 0.1*N*. The capacitance

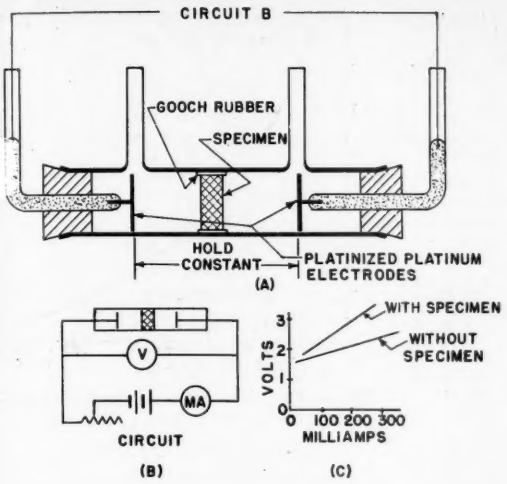

Fig. 8. Direct-current resistivity cell.

effect in the cell was then balanced out, and although this sharpened the null point, it did not appreciably affect the value of the resistance. This means that the reactance of the circuit was small, certainly under 5%.

The specific resistivity of the solution was read from the charts, the applicable concentration and temperature being used. Independent checks of the resistivity were made, and these generally checked the estimated value to within ±1 or 2%. If (r) = specific resistivity of the electrolyte, $R_0 = (r)L/A$, and from this R/R_0 is calculated.

For electrically conducting porous bodies, such as porous carbon and graphite or porous metallic membranes, a different technique is required. The porous body itself would conduct alternating current, so much more than the electrolyte that the resistance of the latter could be estimated only by subtracting two large quantities of almost equal magnitude. Therefore direct current is used, and as long as the potential difference across the membrane is appreciably less than the decomposition potential of the solution, the membrane itself provides no path for the direct current (except for a small leakage current at very low current density).

The apparatus used is shown in Figure 8. The electrodes must not be placed in contact with the specimen. Provision must be made to vent gases (H_2 and O_2) evolved at the cathode and anode. The specimen can be evacuated and saturated either before it is mounted or while it is in place. The authors favor the latter procedure. In principle, the total polarization of the cell is measured with and without the specimen in the path. During the measurements the current (a matter of milliamperes) is kept constant. Voltages are read at various currents, and the slope of the volt-ampere curve is established. A comparison of these slopes, with and without the specimen in the path, permits calculation of the R/R_0 value.

If R_1 = resistance of electrolyte with specimen in path, R_2 = resistance of electrolyte without specimen in path, and $R_0 = (r)L/A$, then

$$R/R_0 = \frac{R_1 - R_2}{R_0} + 1 \qquad (20)$$

This method for R/R_0 is not so accurate as the a.c. method previously described. The thicker the specimen in relation to the electrode spacing, the greater the precision. When both methods have been used on ceramic bodies, a comparison indicates that in most cases the d.c. method gives a somewhat lower value for R/R_0. The agreement is generally within 10%.

Nonrigid Porous Sheets

Porous sheets of polyvinyl chloride, rubber, or woven fabrics are easily tested in the apparatus shown in Figures 13* (permeability and bubble-point tests) and 14* (resistivity test). Some physically weak materials have to be supported by coarse screens to prevent bending. The sheets are sealed at the edges where clamped between the faces of the glass-spool pieces.

No new principles are involved, but a word of caution is offered in dealing with hydrophobic materials, such as polyvinyl chloride. In the resistivity measurement a wetting agent had to be added to the electrolyte to achieve 100% saturation of the pores during the evacuation and saturation procedures. Obviously the specific resistivity of solution used had to be measured, rather than calculated. In the bubble-point test no wetting agent should be used, as this would lower the surface tension of water to some indefinite value. The correct bubble-point pressure is obtained, because the same pressure is required to force water into a hydrophobic specimen, as to force the water out of a hydrophilic specimen.

EXPERIMENTAL RESULTS

The range of this experimental work is summarized in Table B. Also shown is the work of other investigators for which sufficient information is at hand to test the proposed relation. Individual points will be found plotted in Figure 10. Tables

*See footnote on page 394.

Table B. Summary of Results Shown in Tables 1 to 9*

(Individual points are plotted in Figure 10.)

Reference table	1	2	3	4	5	6	7	8	9	Ensemble
Experimenters	(1)	(1)	(1)	(1)	(1)	(1)	(2), (3)	(4)	(5)	
Material tested	Glass beads	Quartz sand	Porcelain	Carbon	Glass frit	PVC sheet	Glass beads	Bonded alumina	Sandstone	
Structure	Packed bed	Packed bed	Rigid	Rigid	Rigid	Flexible	Packed bed	Rigid	Rigid	
Number of sets of data	6	6	7	3	3	3	14	6	4	52
Range of properties										
Particle size, $D_p(\mu)$	148–397	207–316					156–6,100			
Sphericity, ϕ	1.00	0.63–0.70					1.00			
Porosity (macro), ϵ	0.38–0.43	0.43–0.46	0.22–0.57	0.34–0.35		0.85	0.33–0.41	0.30–0.47	0.11–0.23	
Hydraulic radius†, $m(\mu)$	20.7–41.6	18.7–27.4	0.35–25.7	8.0–17.2	1.5–16.3	1.65–4.52	15.6–706	15.5–109.2	0.50–4.45	
Permeability, $P(\mu^2)$	23.4–106.8	40.6–57.7	0.007–20.4	5.0–23.8	0.05–5.62	0.13–1.94	4.6–39,041	81–226	0.002–0.42	
Resistivity ratio, R/R_0	3.87–4.08	3.73–4.27	4.19–12.89	4.19–4.60	8.23–14.49	2.78–3.47	3.80–5.30	4.87–15.40	12.10–36.20	
Derived functions										
$k = m^2P^{-1}(R/R_0)^{-1}$										
Range	3.45–4.51	2.31–3.47	2.44–4.22	2.70–3.10	2.97–5.75	3.68–6.06	2.42–4.87	2.75–6.28	2.08–6.64	
Avg.	4.10	3.15	3.31	2.96	4.79	4.51	3.44	3.59	4.37	3.666
$\sum k$	24.62	18.90	23.14	8.86	14.38	13.53	48.19	21.53	17.47	190.62
$\sum \Delta k$	3.08	3.12	3.67	2.35	4.77	2.52	7.47	5.71	6.95	39.64
$\sum \Delta^2 k$	2.206	2.615	3.243	2.067	8.775	5.714	6.654	9.125	15.080	55.479
$k_c = \epsilon m^2 P^{-1}$ Range	5.70–10.52	3.92–6.64	5.00–11.40	4.35–7.19	7.20–13.10	8.90–19.50	3.83–7.86	9.00–16.00	6.40–18.00	
Avg.	7.20	5.63	7.76	5.85	10.64	12.60	5.41	12.40	13.10	8.100
$\sum k$	43.22	33.80	54.35	17.54	31.90	37.80	75.84	74.38	52.40	421.23

Experimenters: (1) MacMullin and Muccini; (2) Plain and Morrison; (3) LaRue and Tobias; (4) A. D. Little, Inc.; (5) Cornell and Katz
*See footnote on page 394.
†Hydraulic radius by surface-tension method throughout except for columns 7 and 8.

TABLE C. COMPARISON OF R/R_0 AS MEASURED BY PRESENT AUTHORS, WITH R/R_0 CALCULATED FROM THE EQUATION OF DE LARUE AND TOBIAS

R/R_0 as measured, for packed beds. R/R_0 as calculated from Equation (21), which applies to random dispersions of floating particles.

Col.	ϵ	R/R_0 calc.	R/R_0 meas.	% Dev.
Glass beads (*See* Table 1)				
1	0.3835	4.20	3.993	+ 5.3
2	0.4183	3.70	4.000	− 7.5
3	0.4268	3.56	3.900	− 6.1
4	0.4247	3.60	3.876	− 7.1
5	0.3975	3.98	4.085	− 2.6
6	0.4056	3.88	4.083	− 5.0
			Average	− 3.8
Sand (*See* Table 2)				
8	0.4470	3.32	4.050	−18.0
9	0.4470	3.32	4.275	−22.3
10	0.4325	3.50	3.992	−12.3
11	0.4356	3.47	3.920	−11.5
12	0.4570	3.21	3.730	−13.9
			Average	−15.6

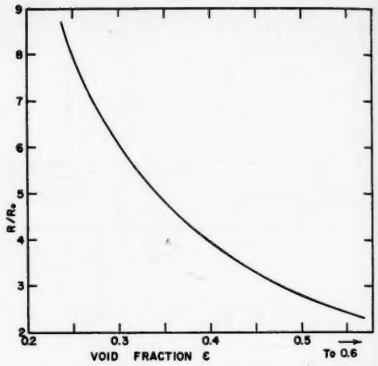

Fig. 9. Resistivity ratios of random dispersions; plot of De LaRue-Tobias equation $R/R_0 = \epsilon^{-3/2}$.

1 to 9* contain the results of individual sets of data.

ADDITIONAL EVIDENCE

Resistivity Ratio as a Function of Void Fraction

De LaRue and Tobias (*12*) have measured the fractional decrease in conductivity of a fluid medium resulting from random suspensions of various nonconducting particles in the fluid. The particles tested include glass spheres, polystyrene cylinders, and sand, of varying sizes. These were suspended in an aqueous solution of $ZnBr_2$ of approximately the same density as the particles, the slurry then being agitated to give random dispersions. The volume fraction of dispersed phase ranged from zero to a value approaching that for loosely packed beds. The authors found the following relation to hold, to a high degree of precision:

$$R/R_0 = \epsilon^{-3/2} \qquad (21)$$

The relation is plotted in Figure 9.

Now arises the question of whether this equation has validity when extrapolated to the region corresponding to packed beds, where all the particles are more or less in intimate contact with surrounding particles. The answer is seen in the data presented in Table C. One concludes that the De LaRue-Tobias equation gives consistently low values for R/R_0 but is good to about 4% for packed beds of glass spheres. For packed beds of irregular grains, the equation can not be depended upon, even as an approximation. The equation cannot be used at all for consolidated porous bodies.

Glass Beads

Plain and Morrison (*20*) measured the flow permeability of fourteen media composed of packed spherical glass beads, using the Terzaghi method. By using three fluids of widely different viscosity, they were able to determine the limits of viscous flow in terms of a critical Reynolds number.

In their Table I porosity ϵ and sphere diameter D are given from which has been calculated hydraulic radius by the relation $m = D\epsilon\phi/6(1 - \epsilon)$. Several values for permeability P are given, and those values demonstrably within the viscous-flow range were selected. Since Plain and Morrison did not measure the resistivity ratio R/R_0, the present authors have estimated it, using the De LaRue-Tobias relation, Equation (12), which has just been shown to be applicable to unconsolidated packed beds of spheres. This information is detailed in Table 7, summarized in Table B, and plotted in Figure 10.

The results support the proposed Equation (1) very well and give a mean value of $k = 3.44$.

Bonded Porous Alumina

A series of measurements on porous materials was carried out by A. D. Little, Inc. (*18*). Among the properties measured were porosity, air permeability, and electrical-resistivity ratio. No attempt was made to measure hydraulic radius directly. However, among the materials tested were six samples of porous bonded 85% alumina bodies, for which the manufacturer (Norton Company) supplies accurate data as to grain size before bonding. The grain size had been determined by microscope, with the average results given in Table 8. The manufacturer also estimated sphericity of grains (before bonding) as $\phi = 0.80$. During firing, the bond spreads and tends to round off the grains and broaden the points of contact, thus causing cementation. This increases the sphericity to an estimated $\phi = 0.90$. The hydraulic radius m of the bonded specimen can then be estimated. Sufficient data were available to calculate P and R/R_0.

This information is detailed in Table 7, summarized in Table B, and plotted in Figure 10. The results support the proposed Equation (1) very well and give a mean value of $k = 3.59$.

Sandstone

Cornell and Katz (*11*) measured the porosity, gas permeability, and resistivity ratio for twenty-four different samples of sandstone, dolomite, and limestone. The samples covered a wide range of these properties. Gas flow was in most cases in the viscous-turbulent region, and the pressure drop through the specimens was of considerable magnitude. Equations were developed to segregate the viscous-flow contribution α from the turbulent flow contribution β to the total permeability. Suitable corrections were made for gas expansion within the sample.

Only a few specimens were tested for equivalent pore size (diameter of circular capillary having same viscous-flow permeability). In their Figure I they show distribution of equivalent pore size vs. accumulative percentage of the total voids smaller than this size. No details of the method are given, other than that it was based on the water displaced from saturated specimens as air pressure was applied to the specimen.

The authors did not make any direct measurements of hydraulic radius m or equivalent pore size. In handling their data, they used a modified form of the Kozeny-Carman relation, given in their Equation (10).

Noting that $D_E = 4m$ for a circular capillary of uniform crosssection and that the authors arbitrarily take $k_1 = 0.50$, one finds that this equation reduces to

$$m^2 = \frac{4uL\eta}{\Delta p\, g} \cdot \frac{R}{R_0} = 4PR/R_0 \qquad (22)$$

This is identical with Equation (1) save for the numerical coefficient. Thus Cornell and Katz assumed a coefficient of 4 as being of the right order of magnitude (a very close approximation), whereas the

*See footnote on page 394.

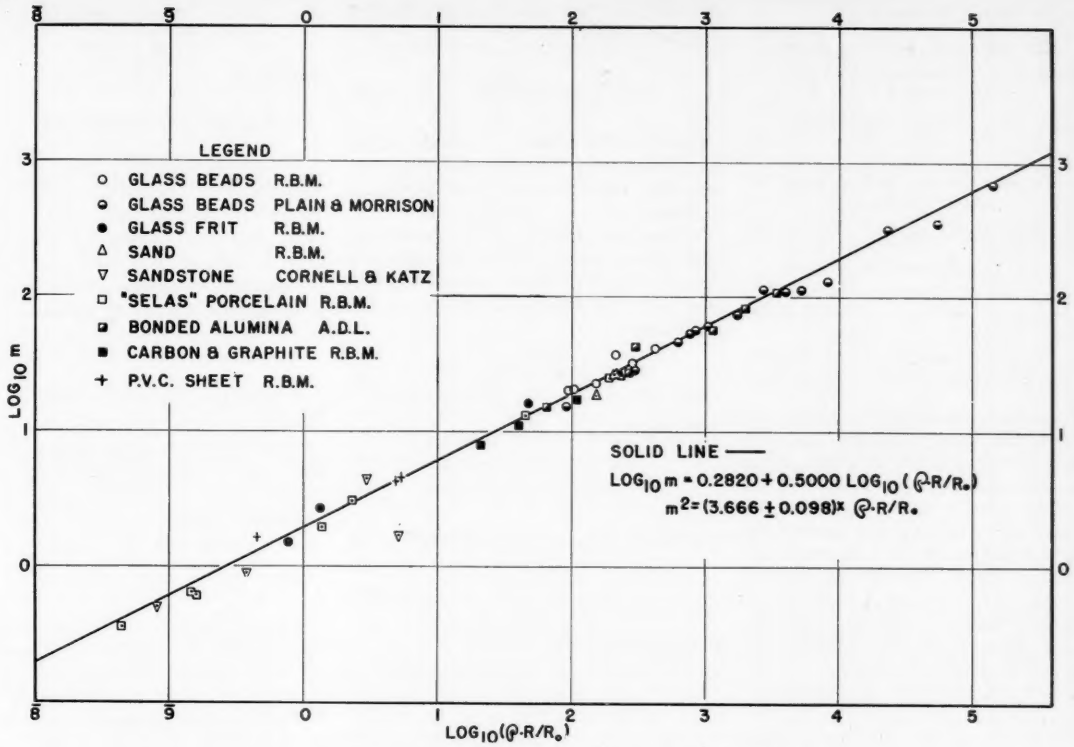

Fig. 10. Correlation plot for MacMullin equation $m^2 = kPR/R_0$.

present authors have experimentally determined this coefficient as being 3.666 ± 0.098. The results given by Cornell and Katz in their Table III all fall exactly on the curve represented by Equation (22) since D_E (or m) was calculated by means of this relation.

MacMullin and Muccini have calculated m from the pore size distribution curves in Cornell and Katz's Figure I, for the four samples of sandstone for which this was measured. Since fine pores contribute more to m than do coarse pores, the effective hydraulic radius must be the reciprocal average value of m. For equal increments of total void fraction,

$$m(\text{recip. avg.}) = \frac{1}{\Sigma(1/m)} \quad (23)$$

The method of calculation is detailed in Table 10.

The results are detailed in Table 9, summarized in Table B, and plotted in Figure 10. The data deviate widely (both plus and minus) from the expected values, although the average value of $k = 4.37$ is not far from the expected value, $k = 3.67$. This fact emphasizes the desirability of direct experimental determination of hydraulic radius by reliable methods.

DISCUSSION OF RESULTS

It was first necessary to establish the validity of the break-point and bubble-point methods for the measurement of hydraulic radius. The data on glass beads, Table 1, indicate an approximate concordance between m (breakpoint) and m (D and ϵ). Agreement is closest for uniformly sized beds, but m (breakpoint) gives high results for beds of mixed sizes.

MacMullin and Muccini believe that their experimentally determined values of m have real meaning with respect to permeability. These values of m may not always be strictly the same as those based on true values for total specific voids and total specific surface, but they reflect the fact that some of the surface may be blanked off, contributing nothing to support of the sealing liquid in the break-point method or to drag in permeability measurement.

The justification for use of surface-tension methods of determining hydraulic radius rests on the demonstration that these methods can be applied to all manner of porous media with reasonably consistent results.

The work on sand, Table 2, was preceded by many measurements on break-point only, to arrive at the effective specific surface of each cut of sand and thus to arrive at the sphericity ϕ of the sand in the permeability measurements. Independent measurements of sphericity all checked closely, and the average value was used to check the m values found in the flow experiments. The close checks in all cases merely indicate the reproducibility of the break-point method and are not any inherent check on the "true" value of m.

All the rest of the work was done on consolidated porous media, such as Selas porcelain, Table 3; carbon and graphite, Table 4; fritted glass, Table 5; and polyvinyl chloride sheet, Table 6.

To these experimental results are added the calculated results based on the work of others, as for example, glass beads, Table 7; bonded alumina, Table 8; and sandstone, Table 9. Thus one is able to double the number of experimental data which can be used to test the validity of the proposed relation, $m^2 = kPR/R_0$. Out of a total of fifty-two sets of data, twenty-eight are contributed by MacMullin and Muccini.

The authors wish to point out that in their work each set of results represents the average of several independent checks on m, P, and R/R_0, alternative fluids and methods being frequently used for these tests. They are sure that in all cases the permeability measurements that they made were in the viscous-flow range, well below the critical Reynolds number.

The entire fifty-two sets of results are plotted in Figure 10, $\log m$ vs. $\log PR/R_0$. To be dimensionally consistent, the straight line through these points must have a slope of 0.50. The position of the line was determined by least square methods.

In each column of each table is recorded the constant k of the equation, $m^2 = kPR/R_0$, the deviation from the mean $k = 3.666$, and the square of the deviation. Using the relations

probable error of the mean

$$E(k) = \frac{0.6745}{\sqrt{(n(n-1)}} \sqrt{\Sigma \Delta^2 k}$$

probable error of single observation,

$$e(k) = \frac{0.6745}{\sqrt{n-1}} \sqrt{\Sigma \Delta^2 k}$$

one finds the following:

	Experimental work columns 1–26	Whole array columns 1–52
k (mean)	3.690	3.666
$E(k)$	0.122 (3.3%)	0.098 (2.7%)
$e(k)$	0.646 (17.6%)	0.703 (19.2%)

The authors are satisfied with the accuracy of the mean value of k, although the probable error of any single set, when their technique is used, is as high as 0.646, or 17.6%. The expected error therefore in calculating any one of the three parameters m^2, P, R/R_0 from the other two is 17.6%. The expected error in calculating m from P and R/R_0, however, is only half this, or 8.8%. The expected error in estimating effective specific surface ($s = \epsilon/m$) is about 10%.

To test the alternative correlation of Kozeny-Carman, they have listed $k_c = \epsilon m^2 P^{-1}$ in the tables. For packed beds only,

	Experimental work columns 1–12	Plain and Morrison columns 29–42	Whole array (26 points)
k_c	6.15	5.42	5.76

Carman himself recommended the value $k_c = 5$, although many other workers seem to prefer a value of $k_c = 5.5$. Thus, the Kozeny-Carman correlation for packed beds is verified. However, inspection of the tables for consolidated porous media reveals a wide deviation, k_c reaching values as high as 18 on some samples of sandstone.

The new correlation does not hold for straight-walled capillaries, for which $R/R_0 = 1$, and $m^2 = k_0 P$. In such cases $k_0 = 2.0$ for round capillaries (Poiseuille's law) and may range from 1.2 to 3.0 for other than round cross sections. For porous media the constant $k = 3.666$ appears to be outside this range.

The new correlation covers a thousandfold range of hydraulic radius and a millionfold range in permeability; it covers a wide range of types of porous media, including packed granular beds and both rigid and flexible consolidated media, and the correlation is independent of the porosity, which covers a range of $\epsilon = 0.1$ to $\epsilon = 0.85$. This would seem to justify the use of this correlation, even though it lacks some desired precision.

Reynolds Number

Since *pore diameter* has no meaning within a porous body, the Reynolds number can be written in terms of the effective hydraulic radius m,

$$Re = \frac{m u_e \rho}{\eta} \tag{24}$$

where u_e is the "effective" velocity within the porous body. One recognizes that this velocity varies from point to point, just as m does.

It has been pointed out by Carman (*6*) and others that if L_e = the effective length of path of fluid through the bed and u = the superficial velocity of the fluid then

$$u_e = \frac{u}{\epsilon} \cdot \frac{L_e}{L} \tag{25}$$

Likewise it can be shown that

$$\frac{R}{R_0} = \frac{1}{\epsilon} \left(\frac{L_e}{L}\right)^2 \tag{26}$$

Combining Equations (25) and (26) gives

$$u_e = u \left(\frac{R/R_0}{\epsilon}\right)^{1/2} \tag{27}$$

Substituting in (24) yields

$$Re = \frac{mu\rho}{\eta} \cdot \left(\frac{R/R_0}{\epsilon}\right)^{1/2} \tag{28}$$

Plain and Morrison (20) defined their Reynolds number differently:

$$Re' = \frac{D_p u_e \rho}{\eta} \tag{29}$$

In their experiments on glass beads they arbitrarily take

$$L_e/L = \sqrt{2.5} = 1.58,$$

so that

$$u_e' = \frac{u}{\epsilon} \cdot 1.58$$

Also,

$$m = \frac{\epsilon}{1-\epsilon} \frac{D_e}{6} \text{ (for beds of spheres)}$$

and one can use the LaRue-Tobias realtion

$$R/R_0 = \epsilon^{-3/2} \text{ (for beds of spheres)}$$

Combining yields

$$Re = \frac{\epsilon}{1-\epsilon} \cdot \frac{1}{6} D_p \cdot u_e' \cdot \frac{\epsilon}{1.58} \cdot \frac{\rho}{\eta} \cdot \left(\frac{\epsilon^{-3/2}}{\epsilon}\right)^{1/2}$$

$$= \frac{1}{9.48} \cdot \frac{\epsilon^{3/4}}{1-\epsilon} \cdot Re' \tag{30}$$

As Plain and Morrison reached a critical Reynolds number, $Re' = 75$ in their bed 9, for which ϵ was 0.35,

$$Re_{crit} = \frac{1}{9.48} \cdot \frac{(0.35)^{3/4}}{0.65} \cdot 75 = 5.54$$

Carman (*6*) defines the Reynolds number

$$Re'' = \frac{\rho u}{\eta s} = \frac{mu\rho}{\epsilon\eta} \tag{31}$$

Therefore

$$Re = (\epsilon R/R_0)^{1/2} \cdot Re'' \tag{32}$$

For random-packed beds, where ϵ approximates 0.40 and R/R_0 approximates 4.0, then

$$Re = (0.4 \times 4)^{1/2} Re'' = 1.265\, Re''$$

Carman gives the critical Reynolds number as $Re''_{crit} = 2$; hence

$$Re_{crit} = 1.265 \times 2 = 2.53$$

Chilton (*10*) defines the Reynolds number as

$$Re''' = \frac{D_p u \rho}{\eta} = \frac{6m(1-\epsilon)}{\phi\epsilon} \cdot \frac{u\rho}{\eta} \tag{33}$$

Thus

$$Re = \frac{\phi\epsilon}{6(1-\epsilon)} \cdot \left(\frac{R/R_0}{\epsilon}\right)^{1/2} Re''' \tag{34}$$

For random-packed spheres ϵ will average 0.4, R/R_0 4.0, and $\phi = 1.0$, and so

$$Re = \frac{0.4}{6(0.6)} \left(\frac{4}{0.4}\right)^{1/2} \cdot Re'''$$

$$= 0.325\, Re'''$$

Chilton gives the critical Reynolds number as $Re'''_{crit} = 20$. Hence, $Re_{crit} = 0.325 \times 20 = 6.50$.

Summing up, MacMullin and Muccini prefer to use the Plain and Morrison data on critical Reynolds number, as they were aimed specifically at determining its value; that is, $Re_{crit} = 5.5$, and below this value 100% viscous flow prevails.

Friction Factor

In the viscous-flow region the product of the friction factor and the Reynolds number must be a constant, in order that u be proportional to Δp; that is,

$$f \times Re = \frac{m^2}{PR/R_0} = 3.666 \tag{35}$$

Substituting the value of Re [Equation (28)],

$$f = \frac{m\eta\epsilon^{1/2}}{Pu\rho(R/R_0)^{3/2}} \tag{36}$$

and breaking down P into its components yields

$$f = \frac{m\, \Delta p\, g}{u^2 L \rho} \cdot \frac{\epsilon^{1/2}}{(R/R_0)^{3/2}} \tag{37}$$

This form of the friction factor differs from that of Carman, who gives

$$f'' = \frac{m\, \Delta p\, g}{u^2 L \rho} \cdot \epsilon^2 \tag{38}$$

As a special case, for packed beds of spheres, one may apply the LaRue-Tobias

relation $(R/R_0) = \epsilon^{-3/2}$, and Equation (37) takes the form

$$f = \frac{m\,\Delta p\,g}{u^2 L \rho} \cdot \epsilon^{9/4} \qquad (37a)$$

which is practically identical with Equation (38).

The subject of this paper is limited to flow in the viscous region. It is suggested, however, that a new plot of f vs. Re, as defined by Equations (28) and (37), would yield rewarding results. In this paper the proper location of the plot in the viscous-flow region and the approximate point of departure where turbulent flow begins to take over have been established. In order for the new equations to be valid, it is recognized that the hydraulic radius, as defined, is an experimentally determined property, based on surface-tension phenomena. Where it has been possible to check m from particle size, sphericity, and porosity measurements, the agreement has been tolerably good.

NOTATION

		Dimensions
A	= cross-sectional area of specimen	l^2
a	= cross-sectional area of liquid column in the Terzaghi method for liquid permeability	l^2
C	= pressure-correction factor in measurement of permeability to gas flow	0
D	= particle diameter	l
D_{ra}	= reciprocal average particle diameter	l
d	= density of solid part of specimen	ml^{-3}
E	= voltage drop through specimen	volts
$E(k)$	= probable error of the mean value of k	0
$e(k)$	= probable error of a single determination of k	0
f	= friction factor	0
g	= acceleration of gravity	lt^{-2}
h	= static head of fluid	l
H	= hydraulic head in Terzaghi's method for permeability	l
I	electric current	amp.
I_0	= current density on superficial area of specmen	amp. l^{-2}
k	= coefficient in MacMullin equation for permeability	0
k_c	= coefficient in Kozeny-Carman equation for permeability	0
L	= thickness of specimen in direction of gradient	l
L_e	= effective length of path of fluid in traversing specimen	l
m	= hydraulic radius of specimen, ratio of specific voids to specific surface ϵ/s	l
$\bar{m}$	= mean effective value of m for permeability	l
N	= normality, gram equivalents per liter	ml^{-3}
P	= permeability coefficient of specimen	l^2
p	= pressure	ml^{-2}
R	= electrical resistance	ohms
R/R_0	= electrical-resistivity ratio, a property of the specimen	0
Re	= Reynolds number	0
(r)	= specific electrical resistance	ohms l
s	= specific surface (macroscopic) of porous bed	l^{-1}
s'	= specific surface of (nonporous) particles in bed	l^{-1}
t	= time	t
u	= velocity; unless otherwise noted, the superficial fluid velocity through a unit cross section of specimen in direction of gradient	lt^{-1}
u_e	= effective, or local, velocity of fluid in pores of specimen	lt^{-1}
V	= gross volume of porous specimen	l^3
w	= weight of specimen	m
x	= distance in specimen, measured in direction of gradient	l
x_a	= head of liquid supported in break-point method	l
y	= liquid removed from bed, as measured in level tube, in break-point method	l
z	= specific viscosity relative to water	0
γ	= surface tension	mt^{-2}
Δk	= deviation from the mean value of k	0
ϵ	= void fraction of specimen (total voids)	0
ϵ_{ma}	= macrovoid fraction (exterior to particles of bed)	0
ϵ_{mi}	= microvoid fraction (interior of particle of bed)	0
η	= viscosity of fluid	$ml^{-1}t^{-1}$
θ	= angle of contact of fluid with solid part of specimen	degrees
κ	= specific electrical conductance	ohm$^{-1}l^{-1}$
μ	= microns, 10^{-4} cm.	l
Π	= permeability to a particular fluid, where $\Pi = uL\Delta p^{-1}$	$m^{-1}l^4t^{-1}$
ρ	= density of fluid	ml^{-3}
ϕ	= sphericity of particle, $6/(Ds')$	0
χ	= tortuosity function	0

LITERATURE CITED

1. Archie, G. E., *Trans. Am. Inst. Mining Met. Engrs.*, **146**, 54 (1942).
2. Brownell, L. E., and D. L. Katz, *Chem. Engr. Progr.*, **43**, 537 (1947).
3. *Ibid.*, **43**, 601 (1947).
4. *Ibid.*, p. 703.
5. Brownell, L. E., D. C. Gami, R. A. Miller, and W. F. Nekarvis, *A.I.Ch.E. Journal*, **2**, No. 1, 79 (1956).
6. Carman, P. C., *Trans. Inst. Chem. Engrs. (London)*, **15**, 150 (1937).
7. *Ibid.*, **16**, 168 (1938).
8. *Ibid.*, **27**, 237 (1949).
9. Carman, P. C., *J. Soc. Chem. Ind.*, **69**, 134 (1950).
10. Chilton, T. H., and A. P. Colburn, *Trans. Am. Inst. Chem. Engrs.*, **26**, 178 (1931).
11. Cornell, D., and D. L. Katz, *Ind. Eng. Chem.*, **45**, 2145 (1953).
12. De LaRue, R. E., and C. W. Tobias, Paper 181, presented at Cincinnati meeting of Electrochem. Soc. (May 1–5, 1955).
13. Dallavalle, J. M., "Micromeritics," 2 ed., Pitman Publishing Corp., Chicago (1948).
14. Ergun, S. K., *Chem. Eng. Progr.*, **48**, 89 (1952).
15. Grace, H. P., *loc. cit.*, **49**, 303 (1953).
16. Hatfield, M. R., *Ind. Eng. Chem.*, **31**, 1419 (1939).
17. Leva, Max et al., *U.S. Bur. Mines Bull.* 504 (1951).
18. Little, Arthur D., Inc., *Rept. C-58493* (1953); private communication to R. B. MacMullin.
19. Muskat, Irving, "Flow of Homogeneous Fluids Through Porous Media," McGraw-Hill Book Company, Inc., New York (1937).
20. Plain, G. J., and H. L. Morrison, *Am. J. Phys.*, **22**, 143 (1954).
21. Rudolph, Hans, *Kolloid Z.*, **67**, 93 (1934).
22. Samartsev, A. G., and V. V. Ostroumov, *Kolloid Zhur.*, **12**, 136 (1950).
23. Sauer, M. C., P. F. Southwick, K. S. Spiegler, and M. R. Wyllie, *Ind. Eng. Chem.*, **47**, 2187 (1955).
24. Scheidegger, A. E., *J. Appl. Phys.*, **25**, 994 (1954).
25. Slawinsky, A., *J. Chim. Phys.*, **23**, 710 (1926).
26. Terzaghi, Karl, and R. B. Peck, "Soil Mechanics," John Wiley & Sons, Inc., New York (1948).
27. Tiller, F. M., *Chem. Eng. Progr.*, **49**, 467 (1953).
28. *Ibid.*, **51**, 282 (1955).
29. Velisek, von J., and A. Vasicek, *Kolloid Z.*, **71**, Heft. 1, 36 (1935).
30. Wagstaff, J. B., and E. A. Nirmaier, *Ind. Eng. Chem.*, **47**, 1129 (1955).
31. Whitney, R. P., W. L. Ingmanson, and S. T. Han, *Trans. Am. Paper Pulp Inst.*, **38**, 157 (1955).
32. Wirth, J. K., *Kolloid Z.*, **116**, 47 (1950).
33. Wyllie, M. R., and A. R. Gregory, *Trans. Am. Inst. Mining Met. Engr.*, **198**, 103 (1953).
34. ———, *Ind. Eng. Chem.*, **47**, 1379 (1955).
35. Zhukov, I. I., and D. A. Fridrikhsberg, *Kolloid Zhur.*, **11**, 163 (1949).

Interpretation and Correlation of Ion Exchange Column Performance Under Nonlinear Equilibria

NEVIN K. HIESTER and SHIRLEY B. RADDING

Stanford Research Institute, Menlo Park, California

RICHARD L. NELSON, JR., and THEODORE VERMEULEN

University of California, Berkeley, California

Various methods are known for interpreting experimental data for linear-equilibrium cases or constant-pattern break-through curves where either external or internal diffusion alone controls the rate in the ion exchange column. The present paper provides interpretive techniques for nonlinear equilibrium cases where the rate is controlled by a combined diffusion mechanism. The techniques can be applied whether or not the value of the equilibrium constant is known.

A completely general correlational method is derived for adding the mass transfer resistances under conditions of nonlinear equilibrium. Published break-through results from numerous sources and from new measurements, evaluated by the techniques described, are used to determine the numerical constants for the general correlation.

The fundamental design of fixed-bed ion exchange columns rests upon three separate steps: first, experimental data from the laboratory or pilot plant must be evaluated to determine the rate, equilibrium, and stoichiometric-capacity coefficients for the ion exchange system of interest; second, since it is impractical to do laboratory studies under all the conditions that might be encountered in full-scale operations, a means must be available for relating these coefficients to the operating variables; and, third, rate information must be introduced into design methods for predicting the break-through behavior as outlined by other investigators (*3, 12, 22, 27, 28*) and by some of the present authors (*16, 30, 31, 32*).

It is now well known that the break-through behavior or concentration history of an ion exchange column depends upon the mass-action equilibrium constant for the exchange reaction as well as upon the rate of exchange and other measurable factors. The break-through curve becomes less sharp if either the rate coefficient or the equilibrium constant is diminished. Moreover, the break-through curve does not have the same shape when external diffusion controls as when internal diffusion controls or as when a combination of these two rate-determining mechanisms is involved. For the interpretation of data, the choice of procedures will be seen to depend upon whether the equilibrium constant and the rate-controlling mechanism are both known.

The methods by which rate and other parameters are obtained from column–break-through measurements include matching of experimental and theoretical concentration histories, fitting of the curves to derived equations, and calculation from the slope of the curve at its midpoint. One or another of these techniques has been used for external diffusion controlling (*3, 11, 14, 16, 22, 27, 28*), internal diffusion controlling (*13, 16, 30*), and a reaction-kinetic representation (*4, 5, 7, 8, 12, 16, 23, 29, 31*). The midpoint slope has been used in an approximate reaction-kinetic calculation by Gilliland and Baddour (*12*) to treat a combination of internal and external diffusion mechanisms.

This paper will provide both a more rigorous treatment of the situation where external- and internal-diffusion resistances are combined and also a method for predicting in advance which mechanism is controlling. Part I indicates the evaluation techniques available for either a known or an unknown equilibrium constant and presents some new procedures. Part II gives the exact relationship between the reaction-kinetic rate constant obtained from the midpoint slope and the individual diffusion coefficients. This information is used to correlate break-through data for twelve different ion systems and a variety of operating conditions into a general equation.

I. MIDPOINT-SLOPE INTERPRETATION OF EXPERIMENTS WITH NONLINEAR EQUILIBRIUM

An algebraic criterion will be derived for determining whether external or internal diffusion controls or whether a column operation is in the intermediate region. This criterion is applicable both for interpreting experimental results and for making design predictions. Its numerical coefficients are obtained from the correlation to be developed in Part II. Use of the midpoint-slope method for evaluating the rate parameters is facilitated by two new plots which are presented. One plot is more applicable to combined mechanisms, and a second may be preferred when a single diffusional mechanism controls. Either plot can be used when the equilibrium constant for exchange is known and also with certain types of run data when the equilibrium is not known.

Basic Definitions for Various Transfer Mechanisms

The rate relations for the diffusion mechanisms have been stated in three earlier papers (*16, 30, 31*). This paper is based especially upon reference *16*, and the results derived therein will be applied here without further proof. In terms of the individual coefficients and the interfacial concentrations, the rate equation for external (fluid-film) diffusion is [*16*, Eq. (34)]

$$\frac{dq_A}{d\tau} = (k_f)_A a_p \frac{\epsilon}{\rho_b} [c_A - (c_A)_i] \quad (1)$$

and, as a first approximation, for internal (particle) diffusion [*16*, Eq. (42) and *30*]

$$\frac{dq_A}{d\tau} = (k_p)_A a_p [(q_A)_i - q_A] \quad (2)$$

Here q_A and c_A are the concentrations of component A on the coexisting solid and fluid phases; $(k_f)_A$ and $(k_p)_A$ are the mass transfer coefficients for external and internal diffusion controlling, respectively; a_p is the transfer area per unit of volume of bed, which is given by the external-surface area of the particles; ϵ is the fraction of voids in the column, external to the particles; ρ_b is the bulk density of the resin as packed; and τ is time.

These rate equations are applied to a typical exchange reaction involving ions of equal valence. In this case the equi-

R. L. Nelson, Jr., is at present with the Procter and Gamble Manufacturing Company, Ivorydale, Ohio.

librium resin concentration, q_A^*, is given by the explicit relation [*16*, Eq. (43)]

$$q_A^* = \frac{K_A Q c_A}{(K_A - 1)c_A + C_0} \qquad (3)$$

where K_A is the equilibrium mass-action constant;* the total ultimate exchange capacity of the resin, Q, is equal to $(q_A + q_B)$ or $(q_A^* + q_B^*)$; and the total ionic level of the solution, C_0, is equal to $(c_A + c_B)$.

If $c_A = (c_A)_i$, then $q_A^* = (q_A)_i$ in Equation (3). because equilibrium is maintained at the particle interface. Equation (3) can also be used to relate c_A^* and q_A.

Combined Diffusional Resistances. By equating the diffusional rates given by Equations (1) and (2), rearranging, and multiplying both sides of the new relation by $(q_A)_0^*/(c_A)_0$, two equivalent ratios result which are defined as a mechanism parameter ζ:

$$\zeta = \frac{\mathbf{D}_A(k_p)_A}{(k_f)_A} = \frac{(q_A)_0^*[c_A - (c_A)_i]}{(c_A)_0[(q_A)_i - q_A]} \qquad (4)$$

where

$$\mathbf{D}_A = (q_A)_0^* \rho_b/(c_A)_0 \epsilon \qquad (5)$$

and $(q_A)_0^*$ is the equilibrium exchange capacity of the resin corresponding to complete saturation with a fluid of entering composition $(c_A)_0$. [When the feed contains only one of the exchanging ions, $(q_A)_0^* = Q$ and $(c_A)_0 = C_0$.] It is noted that ζ will range from zero to infinity during the transition from internal [$(k_p)_A$ small] to external [$(k_f)_A$ small] diffusion controlling.

As will be shown later, Equation (16), the ratio of the mass transfer coefficients, leads to

$$\zeta = \mathbf{D}_A \frac{\beta_1 (D_p)_A}{\beta_2 (D_f)_A N_{Re}^{\ m} N_{Sc}^{\ n}} \qquad (6)$$

Here $(D_f)_A$ and $(D_p)_A$ are the diffusivities of ion A against the exchanged ion in the fluid and particle, respectively; and β_1, β_2, m, and n are dimensionless constants. The Reynolds number is as given by Ergun (*9*):

$$N_{Re} = \frac{d_p R \rho}{6(1 - \epsilon) S \mu} \qquad (7)$$

with d_p the resin particle diameter, R/S the superficial solution velocity through the column, and μ/ρ the kinematic viscosity. The Schmidt number is

$$N_{Sc} = \mu/\rho(D_f)_A \qquad (8)$$

Prediction of Controlling Resistance. As developed in the correlation section to follow, $\beta_1 = 0.29$, $\beta_2 = 0.060$, and $m = n = 0.50$ in the ambient temperature range of 70° to 80°F. Hence

*If the exchanging ions do not have the same valence, the true equilibrium constant must be replaced by an apparent second-order equilibrium constant $K_A{}^{11}$ as defined previously [*16*, Eq. (55)].

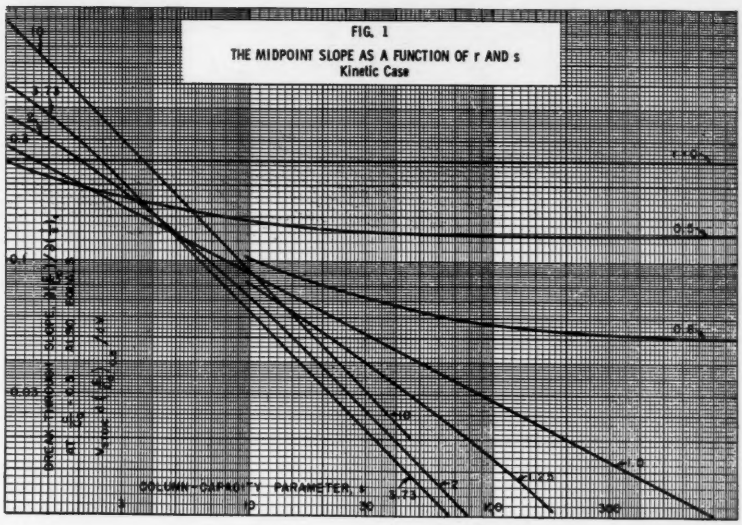

$$\zeta = 4.8\mathbf{D}_A(N'_{Pe})^{-0.5}\frac{(D_p)_A}{(D_f)_A} \qquad (9)$$

since $N'_{Pe} = (N_{Re})(N_{Sc})$. This equation conforms to the well-known fact (*4*, *31*) that the transition from internal to external diffusion controlling will occur at low total ionic concentrations (high $\mathbf{D}$ values) and at low flow rates (low Peclet or Reynolds numbers). If ζ is less than 0.30, the exchange may be considered to be controlled entirely by internal diffusion; and if greater than 3.0, by external diffusion alone. A value of ζ between 0.30 and 3.0 indicates that the combined effect of the two mechanisms must be considered. Typical values of D_p and D_f will be given in Part II.

This evaluation of the mechanism parameter is based on the assumption that only internal and external diffusion contribute to the rate. Therefore caution must be taken that longitudinal diffusion (*1*, *19*, *21*, *28*), which can occur at low flow rates and high diffusivities, does not enter into the picture. This mechanism becomes significant at Peclet numbers of 25 or less (*31*, Figure 6), but has been ignored by some investigators.

Intermediate cases with a combined effect of internal and external diffusion will be discussed in a following section, in terms of an over-all rate coefficient, $(\kappa_{kin})_A$, which is based on a reaction-kinetic mechanism. The transfer coefficient can be replaced by a dimensionless *column-capacity parameter* derived from it, analogous to the N.T.U. (*6*), as shown previously (*16*). This parameter takes the following form:

for external diffusion controlling [*16*, Eq. (59)],

$$(\Sigma_f)_A^{'} = (k_f)_A a_p h S\epsilon/R \qquad (10)$$

for internal diffusion controlling [*16*, Eq. (60)],

$$(\Sigma_p)_A = (k_p)_A a_p \mathbf{D}_A h S\epsilon/R \qquad (11)$$

For the combined-mechanism case the reaction-kinetic result [*16*, Eq. (18)] is applicable:

$$s_A = (\kappa_{kin})_A h S\epsilon/R \qquad (12)$$

Here h is the height of the resin-packed section of the column, and S is its cross-sectional area.

Regardless of the mechanism, the break-through curve will be a function of a throughput ratio which depends upon solution volume or upon elapsed time:

$$\frac{t}{s} = \frac{\theta}{\Sigma} = \frac{R\tau - v\epsilon}{\mathbf{D}v\epsilon} \qquad (13)$$

where v is the column volume of resin $(= hS)$ and t or θ is a dimensionless *solution-capacity parameter*. The steepness of a break-through curve depends also upon the equilibrium parameter:

$$r_A = \frac{1}{K_A} = \frac{c_A(Q - q_A^*)}{q_A^*(C_0 - c_A)} \qquad (14)$$

Evaluation If the Equilibrium Constant Is Known

Matching to Master Curves. This method was first used by Furnas (*10*) on problems of regenerative heat transfer and by others for ion exchange (*3*, *5*). For the curve-fitting method one first has to plot a family of theoretical break-through curves, with c/C_0 as ordinate, as obtained from cross plots of the earlier paper (*16*) for the proper controlling mechanism as indicated by Equation (9) and the appropriate value of r. With scales similar to those of the master curves, the experimental data for c/C_0 are plotted against log $(\tau - v\epsilon/R)$ or log $(V - v\epsilon)$; here $V(= R\tau)$ is the total volume of feed solution that has entered the column up to the time of measurement τ. The experimental curve is then compared with the reference family, horizontal displacement only being used, in order to find the prepared curve which best fits it and characterizes its Σ or s value.

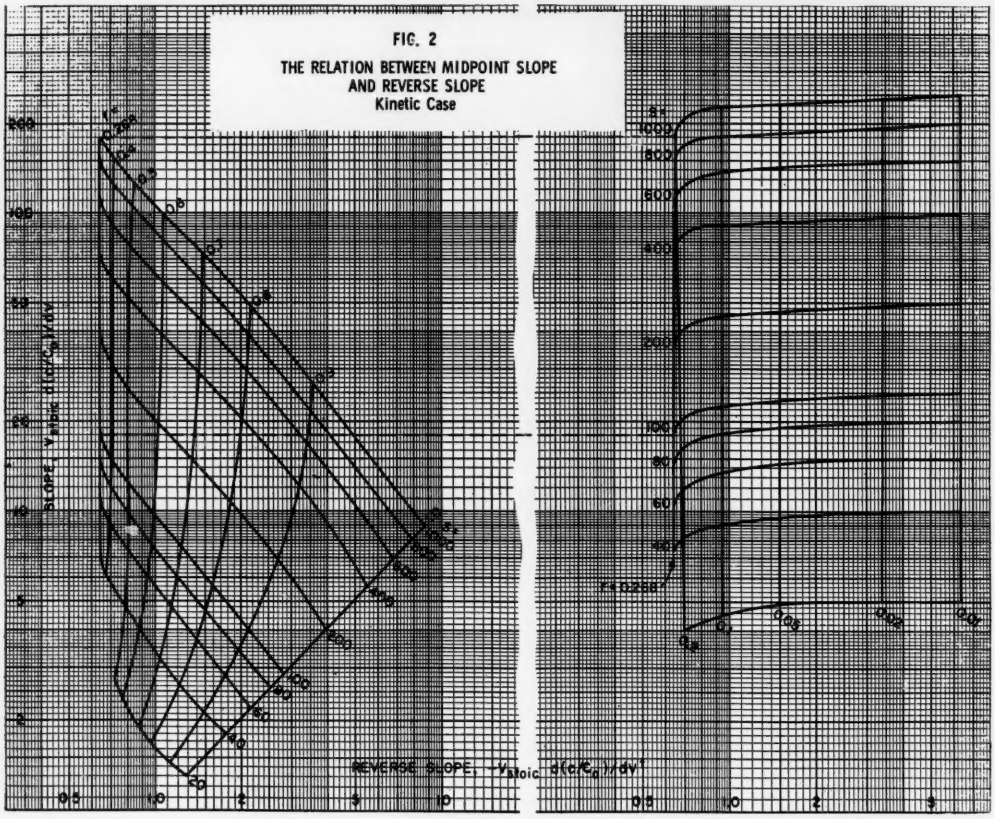

Fitting of Equations in the Constant-pattern Region. If the equilibrium constant K for the exchange is substantially greater than unity, and break-through curves therefore exhibit constant-pattern behavior, the experimental data can be interpreted through the use of analytic relations. For an intermediate mechanism, the kinetic relation [*8*, *28*, or *16*, Eq. (69)] can be applied; similar relations are available for external [*11*, *22*, or *16*, Eq. (70)] and internal diffusion [*30*, Eq. (35)]. This relation permits the determination of s or Σ from two values of the concentration ratio c/C_0, each at a different elapsed time.

To estimate the reliability of rate coefficients calculated in this manner, it is necessary to determine whether constant-pattern conditions are fulfilled. The technique for predicting limits of this type is shown in reference *24* [Eq. (43) and Figure 3, which is based on 1% accuracy].

Fitting of Midpoint Slopes. Thomas (*29*) and Gilliland and Baddour (*12*) have given special attention to the determination of the experimental slope at the "midpoint" ($c/C_0 = 0.5$). The slope, $[d(c/C_0)/d\tau]/R$ or $d(c/C_0)/dV$, is usually measured graphically on a linear plot of the concentration history. The present paper gives for the first time a single master plot for diffusional mechanisms and a single plot for the reaction-kinetic treatment, each of which shows all possible values of the calculated slopes, $d(c/C_0)/d(t/s)$ or $d(c/C_0)/d(\theta/\Sigma)$, as functions of the column-capacity parameter and the equilibrium parameter.

Through the use of Equation (13), the measured slope can be converted to a dimensionless form by multiplying it by $\mathbf{D}v\epsilon$:

$$\mathbf{D}v\epsilon \frac{d(c/C_0)}{dV} = \frac{d(c/C_0)}{d(t/s)} \text{ or } \frac{d(c/C_0)}{d(\theta/\Sigma)} \quad (15)$$

The term $\mathbf{D}v\epsilon$ gives the volume of solution that contains just as much ion A as the column will eventually take up, that is, the stoichiometric volume $V_{stoic.}$

The midpoint slopes for the kinetic case will illustrate the behavior. Figure 1 is a plot of $V_{stoic}\,[d(c/C_0)/dV]_{0.5}$ against s, as a function of r. The subscript 0.5 indicates that the functions are evaluated at the midpoint concentration. For a known slope and a known r, Figure 1 is seen to give directly a unique value of s.

The construction of Figure 1 has been based upon slopes determined graphically from numerical solutions for c/C_0 and upon slopes calculated by differentiation of the break-through relation [*16*, Eq. (29), and A.D.I. document 4953].

The authors have replotted the kinetic case data of Figure 1 in another form, Figure 2, which serves an additional use, to be described below. Figure 3 is an analogous plot for the cases where either external or internal diffusion solely controls.

Evaluation If the Equilibrium Constant Is Unknown

Use of Data for Two Bed Lengths at Equal Flow Velocity. Runs on beds of two different lengths with a particular resin and solution will sometimes be found to give break-through curves having the same (constant) pattern. For such curves r is known to fall between zero and unity and usually between zero and 0.5. Although unique values of r and s cannot be obtained from such curves, the product $(1 - r)s$ or $(1 - r)\Sigma$ can be calculated analytically as shown by Ekedahl and Sillén (*8*), and may then be used directly in design calculations for other columns.

It is found more often that two bed lengths give break-through curves of different shapes, each with c/C_0 practically zero during the early part of the run, even though the other operating conditions are equal. In this situation the following procedure may prove useful. For each curve, several values of r are assumed; the values of s (or Σ) are determined from the shapes of the theoretical curves corresponding to these values of r (by matching curves or midpoint slopes), and the apparent values of s are calculated *per unit length*. If these values are plotted against the assumed r on a single graph, the curves for the two runs will be found to intersect at the true value of r.

The use of differential beds, in which the effluent c/C_0 is very close to unity,

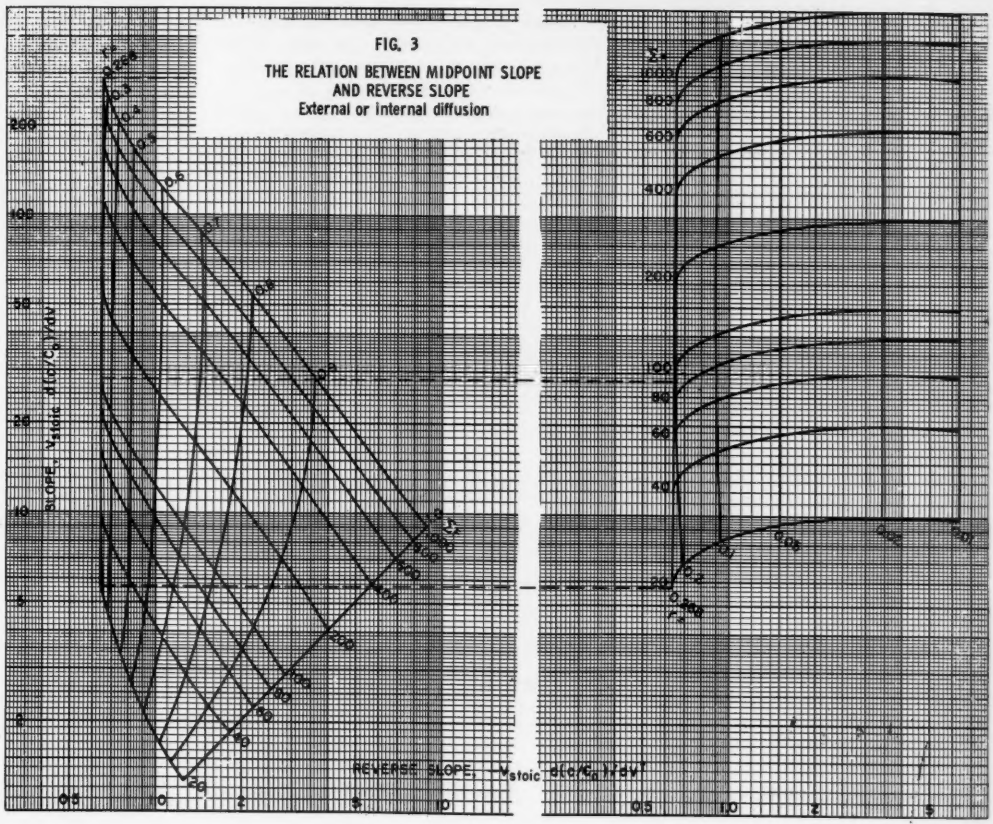

is well known from the work of DuDomaine, Swain, and Hougen (*7*) and Boyd, Adamson, and Myers (*4*) to be a means of obtaining the rate constants without consideration of the equilibria.

Saturation and Elution Curves from a Single Column at Equal Concentrations and Flow Rates. The mass-action equilibrium constant for a reverse exchange is evidently the reciprocal of the constant for exchange in the forward direction, as discussed by Thomas (*29*) and expanded by the present authors (*31*). Hence, if $r\dagger$ denotes the equilibrium parameter for elution, $r\dagger = 1/r$ where r applies to the saturation step. Since r and $r\dagger$ are not equal unless they are both unity, the break-through curves for saturation and elution will usually differ in shape and slope. In the kinetic case it is noted that $s\dagger = rs$ and $s = r\dagger s\dagger$; in the diffusion-controlled cases, $\Sigma\dagger = \Sigma$.

The equilibrium parameter can be determined readily on an exchange system by continuing the saturation-step break-through run to a concentration ratio approaching complete exchange ($c/C_0 \sim 1.0$). The column is then regenerated by a solution of the ion initially present on the resin, at the same concentration level C_0 and at the same flow rate as used in the saturating run.

If the saturation data are fitted against one of the standard curves for a given r value and the elution data are likewise fitted on the related $r\dagger$ chart, apparent values of s and $s\dagger$ will be obtained. This procedure can be repeated for other r values. Then, if $s\dagger/s$ is plotted against the assumed r, intersection of the curve with a line $s\dagger/s = r$ will indicate the correct value of r.

The midpoint-slope method is even more efficient when applied to such data. Because the designations of saturation and elution refer to process requirements rather than to the special problem of column performance, it will be convenient to designate the exchange with favorable equilibrium as the A step ($r_A < 1$; $K_A > 1$) and the reverse exchange as the B (or $A\dagger$) step. Each value of r_A and s_A then corresponds both to a particular value of slope $[d(c_A/C_0)/d(t_A/s_A)]_{0.5}$ for the A step as indicated by Figure 1 and to a particular value of $-[d(c_A/C_0)/d(t_A\dagger/s_A\dagger)]_{0.5}$, termed the reverse slope, for the B step. In Figure 2 the slope and the reverse slope are used as ordinate and abscissa on log-log coordinates, and the values of r_A and s_A are used as contours. Use of this plot involves calculating the dimensionless slopes [*cf.* Equation (15)] from the experimental data for both A and B steps, locating the corresponding point on Figure 3, and reading off both the r_A and s_A values.

The minimum slope which occurs at $r_A = 3.73$ produces a double plot in Figure 2. The left side corresponds to r_A values between 0.268 (= 1/3.73) and 1.0, and the right side to r_A between zero and

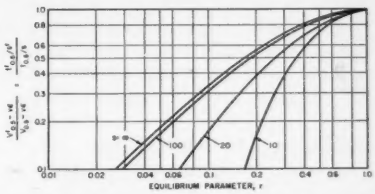

Fig. 4. The ratio of throughput volumes at the midpoint.

0.268. A choice may be made between these two ranges by comparing the experimental throughput volumes $(V\dagger - v\epsilon)_{0.5}$ and $(V - v\epsilon)_{0.5}$ for the two steps. Normally the latter will approach V_{stoic}, and the former may be appreciably smaller. Figure 4 shows the dimensionless ratio of these two corrected volumes, which is also the ratio of $(t\dagger/s\dagger)_{0.5}$ to $(t/s)_{0.5}$ as a function of r_A and s_A. With this chart the observed ratio of volumes will usually serve as a criterion for determining whether r_A is greater or less than 0.268. Similar considerations apply to Figure 3.

II. THEORY AND CORRELATION FOR COMBINED FLUID- AND PARTICLE-PHASE RESISTANCES

Definitions

As was pointed out above, the correlation now to be derived involves both

internal and external diffusion as rate-controlling mechanisms and thus permits a continuous transition from one region to the other. The rate relations for these two mechanisms have been stated above in Equations (1) and (2).

The mass transfer coefficients in these equations can be related to the operating variables and characteristics of the resin-ion system as shown previously (*15*). Combining Equations (24 to 26), (29), and (30) of that reference gives the film coefficients as

$$(k_f)_A a_p = \frac{6(1-\epsilon)(D_f)_A}{\beta_1 d_p^{\,2}} N_{Re}^{\,m} N_{Sc}^{\,n} \quad (16)$$

$$(k_p)_A a_p = \frac{6(1-\epsilon)(D_p)_A}{\beta_2 d_p^{\,2}} \quad (16a)$$

The interrelationship of these coefficients with the measured over-all rate constant will then enable the mass transfer data to be correlated with the system variables.*

Interrelation of Transfer Coefficients

In terms of the reaction-kinetic coefficient the rate of exchange can be expressed [*16*, Eq. (2) and (13)] as

$$\frac{dq}{d\tau} = \frac{(\kappa_{kin})_A \epsilon}{Q\rho_b}\left[c_A(Q - q_A) - \frac{1}{K_A} q_A(C_0 - c_A)\right] \quad (17)$$

The basic relation between the individual film coefficients is obtained by equating the rates given in Equations (1), (2), and (17).

$$\frac{dq}{d\tau} = \frac{c_A - (c_A)_i}{\left[\frac{\rho_b}{(k_f)_A a_p \epsilon}\right]} = \frac{(q_A)_i - q_A}{\left[\frac{1}{(k_p)_A a_p}\right]} = \frac{c_A(Q - q_A) - q_A(C_0 - c_A)/K_A}{\left[\frac{Q\rho_b}{(\kappa_{kin})_A \epsilon}\right]} \quad (18)$$

One of the useful algebraic properties of equal fractions is that the sum of the numerators divided by the sum of the denominators is the same fraction. Application of this principle, along with a conversion of solution concentrations to dimensions of q through multiplication by $(q_A)_0^*/(c_A)_0$ in both numerator and denominator, leads to

$$\frac{dq}{d\tau} = \frac{[c_A - (c_A)_i][(q_A)_0^*/(c_A)_0] + [(q_A)_i - q_A]}{[(q_A)_0^* \rho_b/\epsilon(c_A)_0(k_f)_A a_p] + [1/(k_p)a_p]} = \frac{[(q_A)_0^*/(c_A)_0][c_A(Q - q_A) - q_A(C_0 - c_A)/K_A]}{[Q(q_A)_0^* \rho_b/(c_A)_0(\kappa_{kin})_A \epsilon]} \quad (19)$$

Rearrangement leads to the usual reciprocal form, but modified by a correction term **b**:

$$\frac{\mathbf{b}_A}{(\kappa_{kin})_A} = \frac{1}{(k_f)_A a_p} + \frac{1}{\mathbf{D}_A (k_p)_A a_p} \quad (20)^*$$

where

$$\mathbf{b}_A = \frac{\{c_A - (c_A)_i + [(q_A)_i - q_A](c_A)_0/(q_A)_0^*\}Q}{c_A(Q - q_A) - q_A(C_0 - c_A)/K_A} \quad (21)$$

Equation (20) leads, with substitution of Equations (16) and (16*a*), to

$$\frac{\mathbf{b}}{(\kappa_{kin})_A} = \frac{\beta_1 d_p^{\,2} N_{Re}^{\,-m} N_{Sc}^{\,-n}}{6(1-\epsilon)(D_f)_A} + \frac{1}{\mathbf{D}} \cdot \frac{\beta_2 d_p^{\,2}}{6(1-\epsilon)(D_p)_A} \quad (22)$$

The following rearranged form of Equation (22) provides a more convenient basis for the final correlation

$$\mathbf{b}\mathbf{D} \frac{(D_p)_A}{(D_f)_A} \cdot \frac{6(1-\epsilon)(D_f)_A}{d_p^{\,2}(\kappa_{kin})_A} = \beta_1 \mathbf{D} \frac{(D_p)_A}{(D_f)_A} N_{Re}^{\,-m} N_{Sc}^{\,-n} + \beta_2 \quad (23)$$

As pointed out earlier, the term involving β_1 (external diffusion) will predominate over β_2 (internal diffusion) at low solution concentrations (high **D**) and at low flow rates (low N_{Re}).

Effect of Exchange Conditions. Before β_1 and β_2 in the correlation can be determined from experimental data **b** must be evaluated from theoretical considerations. Likewise, when the correlation is used, the applicable value of **b** must be calculated.

Inspection of Equation (21) indicates that a range of **b** values will occur as $(c_A)_i$ varies between c_A (for internal diffusion controlling) and c_A^* (for external diffusion controlling). For each intermediate value of $(c_A)_i$, the ratio of the controlling resistances, ζ, can also be calculated from Equation (4). It follows that **b** and ζ will be related in a manner that depends upon the particular values of c_A/C_0 (usually 0.5, since most interpretive methods emphasize the data at the midpoint) and q_A/Q at which **b** is to be evaluated and upon their equilibrium relations.

For a single ion in the feed, Equation (21) becomes

$$\mathbf{b} = \frac{[c_A - (c_A)_i]Q + [(q_A)_i - q_A]C_0}{c_A(Q - q_A) - q_A(C_0 - c_A)/K_A} \quad (24)$$

since then $(c_A)_0/(q_A)_0^* = C_0/Q$. Further simplification can be achieved by replacing the resin driving force by that of the solution through Equation (4) and the resin concentration by the concentrations of the solution through Equation (3). Thus

$$\mathbf{b} = \frac{K_A C_0(\zeta + 1)[(K_A - 1)c_A^* + C_0]}{K_A C_0^{\,2}\zeta + [(K_A - 1)c_A^* + C_0][(K_A - 1)(c_A)_i + C_0]} \quad (25)$$

Evaluation of Special Terms

Among the terms contained in Equation (23), **D**, d_p, and N_{Re} can be determined from the known resin properties and the operating conditions used experimentally (or specified for design purposes). $(\kappa_{kin})_A$ is determined by the methods already given (or is the final result of the correlation as computed for design). The liquid-phase diffusivity $(D_f)_A$—or, strictly, $(D_f)_{AB}$—is estimated from physico-chemical tabulations as the mean of the self-diffusion coefficients for the salt pairs *A*- and *B*-anion that are involved.

Only the correction term **b** and the diffusivity ratio $(D_p)_A/(D_f)_A$ impose a real difficulty of evaluation. These will be discussed in the following paragraphs.

Correction Term. As stated above, the value of **b** depends upon the values of c_A and q_A and the applicable equilibrium constant. The resin concentration q_A can be determined exactly by extensive trial-and-error calculations; however, for most purposes it will suffice to assume two types of limiting behavior. At $r < 1$ ($K > 1$), the limit of constant-pattern behavior [*16*, Eq. (67)] will be assumed. Likewise, at $r > 1$ ($K < 1$), the limit of equilibrium-limited exchange [*16*, Eq. (31*a*)] will be used.

For $K > 1$, $q_A/Q \approx 0.5$. The value of c_A^* can be obtained through Equation (3) and equals $C_0/(1 + K_A)$; this plus Equation (25) leads to

$$\mathbf{b} = \frac{2K_A C_0(\zeta + 1)}{(K_A + 1)C_0\zeta + 2[(K_A - 1)(c_A)_i + C_0]} \quad (26)$$

Assumption of a value of $(c_A)_i$ between c_A and c_A^* permits calculation of $(q_A)_i$ through Equation (3) and thus ζ from

*The ratio $(d_w/d_p)^{1/3}$ was introduced previously (*31*) to account empirically for the apparent effect of channeling flow in wide beds. Although this correction may possibly be necessary when longitudinal diffusion is involved, further study has shown that it does not improve the correlation of the present data in the regions where external or internal diffusion controls.

*Equation (48), reference *16*, which was derived by inference, is seen to be in error in omitting the term analogous to **b**.

Equation (4). Then Equation (26) is used to obtain **b**.

For the limit at which $(c_A)_i = c_A$, $(q_A)_i$ must equal q_A^*; internal diffusion controls, $\zeta = 0$, and in this case $\mathbf{b} = 2K_A/(K_A + 1)$. For the limit at which $(c_A)_i = c_A^*$, q_A must equal $(q_A)_i$; external diffusion controls, $\zeta = \infty$, and $\mathbf{b} = 2K_A/(K_A + 1)$.

Slightly higher values of **b** will occur under intermediate rate-controlling conditions. Figure 5 shows some typical values of ζ and **b** for $K > 1$, $c_A/C_0 = 0.5$, and s large, calculated from Equation (26). These may also be used as approximate values when s_A is too small to fall within the constant-pattern region.

For $K < 1$, in the equilibrium-limited region, $c_A^* = (c_A)_i = c_A = 0.5C_0$ and so Equation (25) becomes

$$\mathbf{b} = \frac{2K_A(K_A + 1)(\zeta + 1)}{4K_A\zeta + (K_A + 1)^2} \quad (27)$$

and only the mechanism parameter affects **b** for a given K_A. When external diffusion only controls, $\zeta = \infty$ and $\mathbf{b} = (K_A + 1)/2$, and for internal diffusion $\zeta = 0$, and so $\mathbf{b} = 2K_A/(1 + K_A)$. Values in the range of $K < 1$ are also shown in Figure 5.

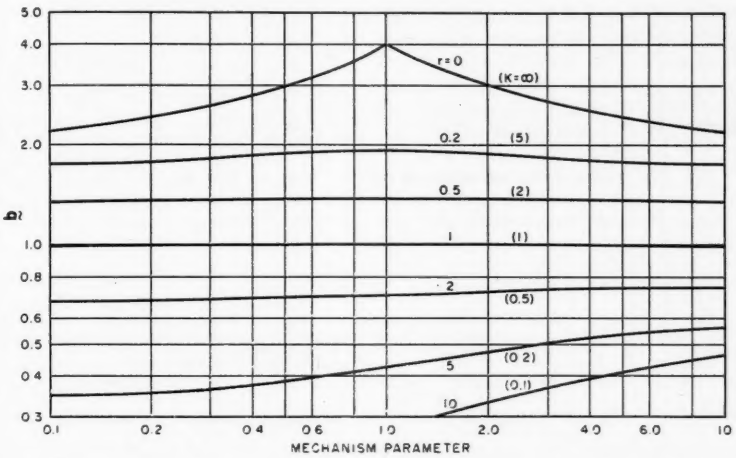

Fig. 5. Correction term b for combining diffusion resistances, as a function of the mechanism parameter ζ.

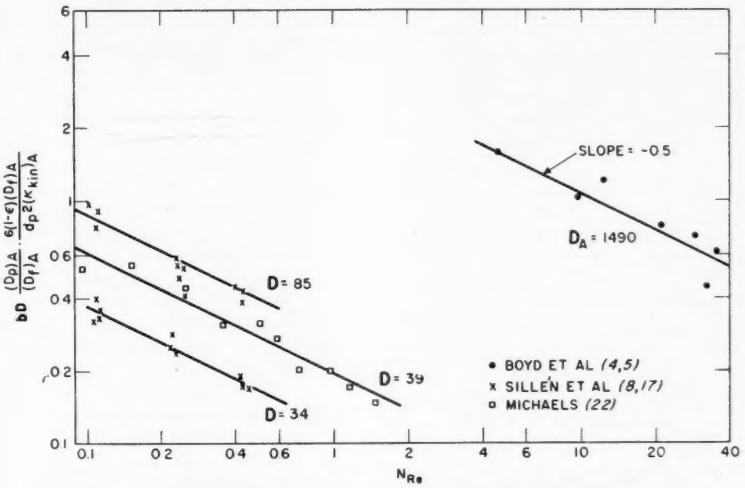

Fig. 6. Determination of Reynolds number exponent.

Diffusivity Ratio. The data available for counterdiffusivities in the resin phase, $(D_p)_{AB}$, are rather limited, both with respect to ions exchanged and resins involved. However, Boyd et al. (*4*) have supplied resin conterdiffusivities for a number of alkali-metal ion pairs. The values that they found for the exchange reaction shown in Equation (3), using Amberlite IR-1 (sulfonated phenol-formaldehyde resin), are given in Table 1.

The ratio $(D_p)_{AB}/(D_f)_{AB}$ was studied with respect to the ionic radii for the exchanging ion pairs, but the data showed no relative trend. Apparently the resin gel can be considered as a viscous medium which reduces the diffusivity uniformly if the ions are univalent and small. For this reason it is assumed that the average ratio is 0.168 ($\sim$ 0.17) for Amberlite IR-1.

The data of Reichenberg (*26*) for sodium-hydrogen exchange on Dowex 50 (sulfonated polystyrene) can be interpolated to obtain a $(D_p)_{AB}/(D_f)_{AB}$ ratio of 0.189 for an 8 to 10% cross-linked resin. For the same type of resin, Bauman and Eichhorn (*2*) measured the diffusion of sodium chloride and hydrochloride into the gel. Averaging their diffusivity values to get $(D_p)_{AB}$ leads to a ratio of 0.185. As this checks Reichenberg's result closely, the diffusivity ratio for Dowex 50 (a sulfonated polystyrene resin) will be taken as 0.187 ($\sim$ 0.19)*.

Typical Experimental Data. Column data for exchange under both trace and gross conditions at ambient temperatures (70° to 80°F,) are available in the literature.

Boyd, Adamson, and Myers (*4, 5*) studied both shallow and deep beds and were the main source of data in the trace region. Work under gross exchange conditions was performed by Sillén and coworkers (*8, 17, 28*), Gilliland and Baddour (*12*), Michaels (*22*), and Nelson (*23*).

The details of the interpretation of data are given in the supplement to this paper.† Typical results from Boyd and coworkers are given in Table 2†.

Table 1. Ratio of Particle Diffusivities to Liquid Diffusivities

Exchanging ions		$(D_p)_{AB}$	$(D_f)_{AB}$	$\frac{(D_p)_{AB}}{(D_f)_{AB}}$	$r^0_A + r^0_B$
A	B	10^{-6} sq. cm./sec.	10^{-5} sq. cm./sec.		10^{-8} cm.
Na	Li	3.0	1.35	0.222	12.1
Na	H	3.7	2.05	0.181	10.8
Na	Na	2.1	1.56	0.135	10.4
Na	NH_4	2.9	1.68	0.173	9.7
Na	K	3.5	1.69	0.207	9.3
Rb	K	2.8	1.84	0.152	7.3
Cs	K	2.0	1.87	0.107	6.7
Average				0.168	

*The present commercial grade of Dowex 50 is more highly crosslinked and has been shown by Boyd and Soldano, *J. Am. Chem. Soc.* **75**, 6091 (1953), to have a substantially lower ratio.

†Complete supplementary data and tabular matter may be obtained as document 4953 from the American Documentation Institute, Photoduplication Service, Library of Congress, Washington 25, D. C., for $3.75 for photoprints or $2.00 for 35-mm. microfilm.

Constants for the Correlation

Reynolds Number Exponent, m. Reference to Equation (23) shows that, if all variables but the flow rate are held constant, the left-hand term less β_2 (the internal-diffusion film ratio) can be plotted against N_{Re} on log-log coordinates, and the slope ($= -m$) determined. Since β_2 is still unknown, the data used must be selected from the external-diffusion controlling region, i.e., at high **D** and low N_{Re} values, where the effect of internal diffusion is negligible. Such data are plotted in Figure 6, and lines of -0.50 slope are drawn through the various groups of points. This slope is comparable to a value of -0.5 used by Hagerty and Bliss (*14*), to -0.4 used by Vermeulen and Hiester (*31*), to -0.6 used by Lapidus and Amundson (*20*), and to exponents in the same range found in general mass transfer studies (*11, 18, 25, 33*).

Schmidt Number Exponent, n. This exponent could normally be determined by plotting the intercepts of Figure 6 (obtained at constant N_{Re}) against N_{Sc} on log-log paper. Because of the limited data, this was not possible in the present study. It is assumed for convenience that the powers of N_{Re} and N_{Sc} are identical; thus, that $n = m = 0.50$. Recent work by Gaffney and Drew (*11*) indicated a value of 0.58 for n. Choosing n and m to be the same permits simplification of the relations, as the product of N_{Re} and N_{Sc} is the N'_{Pe} group in which viscosity and density changes have no effect. This type of simplification is justified by the fact that the correlation is solely to be derived from and is intended to be applied to aqueous solutions.

Slope and Intercept of Correlation Plot. The remaining constants, β_1 and β_2 in Equation (23), are now rather easily found. If the left-hand side of this equation is plotted against the independent variable $\mathbf{D}[(D_p)_A/(D_f)_A](N'_{Pe})^{-0.5}$, the slope of the best line through the data is β_1 and its intercept is β_2. This has been done in Figure 7 and on two similar plots expanding the region near the origin tenfold and hundredfold, the data from the authors previously listed being used. The values of β_1 and β_2 found were 0.29 and 0.060 respectively.

The choice of these constants is confirmed by replotting the data in the same form on logarithmic coordinates, as shown in Figure 8. It is seen that the majority of the points fit the curve well with only a small amount of spread.* A ζ scale, based on Equation (6), has also been indicated on the abscissa of this plot, to facilitate the proper choice of **b** in design problems.

The two diffusional regions are clearly revealed in Figure 8. In the horizontal portion of the curve, at abscissa values less than 0.06, internal diffusion controls; at abscissa values greater than 0.60, the 45° line represents the region where external diffusion controls.

Final Form of Relation. With the constants now determined, the correlation can be written in terms of h/s_A and N'_{Pe}, by use of Equations (14) and (30), as

$$\mathbf{b}\mathbf{D}\frac{(D_p)_A}{(D_f)_A}\cdot\frac{h/(s_A)}{d_p}\cdot\frac{\epsilon}{N'_{Pe}} = 0.29\mathbf{D}\frac{(D_p)_A}{(D_f)_A}(N'_{Pe})^{-0.5} + 0.060 \quad (28)$$

and this is the equation of the solid curve on Figure 8. Rearrangement leads to a simple form relating the Colburn number to other dimensionless parameters:

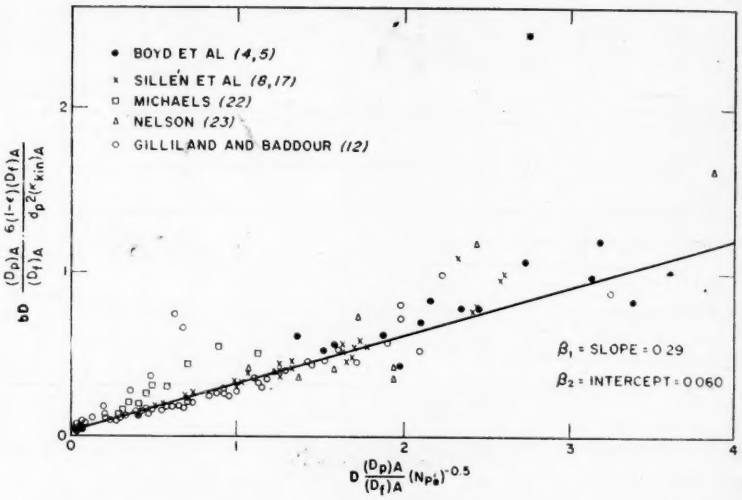

Fig. 7. Linear correlation plot.

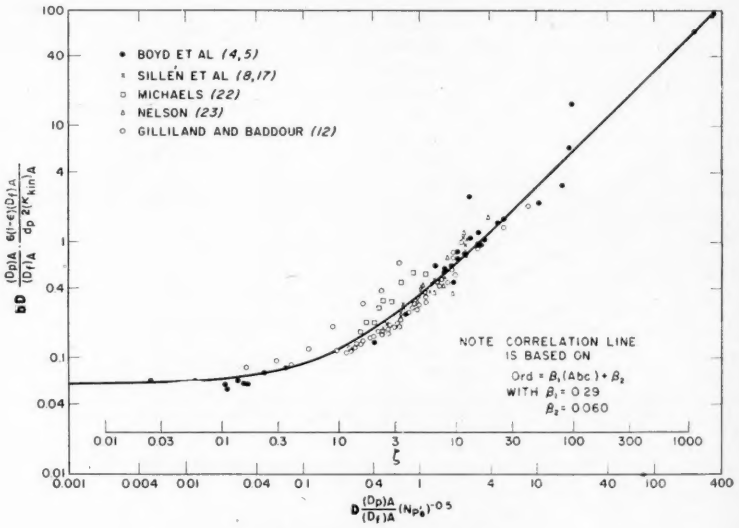

Fig. 8. Logarithmic correlation plot.

Table 2. Range of Experimental Variables in Boyd's Data on Trace Exchange (*4*)

Run	Trace ion	Gross ion	$(1/\kappa_{kin})_A$	N_{Re}	$\mathbf{D}_A$
R-7	Na	K	3.24 sec	11	2.3
R-5	Na	K	0.103	11	344
XV-19	Rb	K	0.0700	11	1,490
M-8	Na	Cs	0.980	440	11.8
M-5	Na	Cs	0.675	0.10	825
M-10	Rb	H	0.492	1190	14,300

*The recent results of Sujata, Banchero, and White, *Ind. Eng. Chem.*, **47**, 2193 (1955), also agree with this correlation to within experimental error.

$$\frac{h}{(s_A)d_p} = \frac{0.29(N'_{Pe})^{0.5}}{\mathbf{b}\epsilon} + \frac{0.060(N'_{Pe})}{\mathbf{b}\epsilon\mathbf{D}_A(D_p)_A/(D_f)_A} \quad (29)^*$$

These data cover a thousandfold range of concentration, a large range of equilibrium constants, a six-hundredfold range of flow velocities, and bed heights varying from 0.04 to 20 in. (0.1 to 50 cm.).

ACKNOWLEDGMENT

The authors wish to express their thanks to John Jost, Jr., and J. Leonard Fick for their assistance in experimental studies at the University of California.

The extensive computations required to prepare Figures 1 through 4 were supported by a grant for institute-sponsored research from Stanford Research Institute.

NOTATION

Dimensions of the variables are indicated by a typical self-consistent set of units.

a_p = effective area for mass transfer, sq. ft./cu. ft.

A, B, etc. = ionic species

$\mathbf{b}$ = correction factor for computing reaction-kinetic coefficients, dimensionless; *see* Equations (20), (21), and (24) to (27).

c_A, c_B, etc. = concentration of ion in the solution phase at a specified point in the column, lb.-equiv./cu. ft.

C_0 = total concentration of ions in the solution entering the column, lb.-equiv./cu. ft.; replaces symbol c_0 used in references *16*, *30*, and *31*.

$\mathbf{D}$ = partition parameter, or ratio of concentrations in resin phase and solution phase at saturation, dimensionless

D = effective ionic diffusivity for counterdiffusion of two components, sq. ft./min.

d_p = mean diameter of resin particles, ft.

G = gross component, in exchange involving trace components

h = height or length of column, ft.

H_t = height of column equivalent to one mass transfer unit, ft.

k = mass transfer coefficient, ft./min.

$K(= K^{II})$ = chemical equilibrium constant for exchange, dimensionless

m, n = exponents

N'_{Pe} = Peclet number for mass transfer, $N_{Re} \cdot N_{Sc}$

N_{Re} = Reynolds number, $d_pR\rho/6(1 - \epsilon)S\mu$, consistent with reference *9*

N_{Sc} = Schmidt number, $\mu/\rho(D_f)_A$

q_A, q_B, etc. = concentration of ion in the resin phase at a specified point in the column, lb.-equiv./lb. dry resin

Q = total ionic concentration in the resin phase (i.e., ultimate capacity), lb.-equiv./lb. dry resin

$r(= 1/K)$ = equilibrium parameter, dimensionless

r^0 = ionic radius, ang.

R = volumetric flow rate, cu. ft./min.

s = column-capacity parameter for the kinetic case, dimensionless

S = cross-sectional area of column, sq. ft.

t = solution-capacity parameter for the kinetic case, dimensionless; $t = (\kappa_{kin})_A(V - v\epsilon)/\mathbf{D}R$

t/s = throughput parameter, dimensionless

u = average linear flow rate through the packed column, ft./min.; $u\epsilon$ is the superficial linear flow rate.

$v(= hS)$ = bulk-packed volume of column, cu. ft.

V = volume of saturating solution fed to column, cu. ft.; $V - v\epsilon$ is the volume that has reached the resin at a bulk volume v downstream from the column inlet

V_{stoic} = volume of saturating fluid which has contained a quantity of solute just equivalent to the exchange capacity of the column, cu. ft.

β_1, β_2 = correlation constants, dimensionless; *see* Equations (6) and (16).

ϵ = ratio of void space outside resin particles to total volume of packed column, dimensionless

θ = solution-capacity parameter for diffusional cases, dimensionless; $(k_fa_p/\mathbf{D})(V - v\epsilon)/R$, or $k_pa_p(V - v\epsilon)/R$

$\theta/\Sigma(= t/s)$ = throughput parameter, dimensionless

κ = general rate coefficient, min.$^{-1}$

μ = viscosity of the solution, lb./(ft.)(min.)

ρ = density of the solution, lb./cu. ft.

ρ_b = bulk density of dry resin, lb./cu. ft. packed volume

Σ = column-capacity parameter for diffusional cases, dimensionless; $k_fa_pv\epsilon/R$, or $k_pa_pDv\epsilon/R$

τ = time, min.

ζ = mechanism parameter, dimensionless; *see* Equation (6).

Subscripts

0 = initial condition

A, B, etc. = ionic species; or process step. A may represent the exchange of species A with species B, etc.

f = fluid (solution) film or phase

i = interface

p = particle (resin) film or phase

Superscripts

$\dagger$ = reverse of reference reaction, i.e., elution

$*$ = value in equilibrium with the actual value for the coexisting phase

LITERATURE CITED

1. Barrow, R. F., C. J. Danby, J. G. Davoud, C. N. Hinshelwood, and L. A. K-Stavely, *J. Chem. Soc.*, 401 (1947).
2. Bauman, W. C., and Jacob Eichhorn, *J. Am. Chem. Soc.*, **69**, 2830 (1947).
3. Beaton, R. H., and C. C. Furnas, *Ind. Eng. Chem.*, **33**, 1500 (1941).
4. Boyd, G. E., A. W. Adamson, and L. S. Myers, Jr., *J. Am. Chem. Soc.*, **69**, 2836 (1947).
5. *Ibid.*, p. 2849.
6. Chilton, T. H., and A. P. Colburn, *Ind. Eng. Chem.*, **27**, 255 (1935).
7. Du Domaine, John, R. L. Swain, and O. A. Hougen, *loc. cit.*, **35**, 546 (1943).
8. Ekedahl, Erik, and L. G. Sillén, *Arkiv. Kemi, Mineral, Geol.*, **25A**, No. 4, 1 (1947).
9. Ergun, S. K., *Chem. Eng. Progr.*, **48**, 227 (1952).
10. Furnas, C. C., *Trans. Amer. Inst. Chem. Engrs.*, **24**, 142 (1930).
11. Gaffney, B. J., and T. B. Drew, *Ind. Eng. Chem.*, **42**, 1120 (1950).
12. Gilliland, E. R., and R. F. Baddour, *loc. cit.*, **45**, 330 (1953).
13. Glueckauf, Eugen, *Trans. Faraday Soc.*, **51**, 1540 (1955).
14. Hagerty, P. F., II, and Harding Bliss, *Ind. Eng. Chem.*, **45**, 1253 (1953).
15. Hiester, N. K., E. F. Fields, Jr., R. C. Phillips, and S. B. Radding, *Chem. Eng. Progr.*, **50**, 139 (1954).
16. Hiester, N. K., and Theodore Vermeulen, *Chem. Eng. Progr.*, **48**, 505 (1952).
17. Hogfeldt, Erik, Erik Ekedahl, and L. G. Sillén, *Acta Chem. Scand.*, **4**, 1471 (1950).
18. Johnson, Frederick, Robert Bentley, and Robert Maurer, Atomic Energy Commission declassified document *MDDC-990* (July 4, 1945).
19. Lapidus, Leon, and N. R. Amundson, *J. Phys. Chem.*, **56**, 984 (1952).
20. *Ibid.*, p. 373.
21. Ledoux, Edward, *J. Phys. Colloid Chem.*, **53**, 960 (1949).
22. Michaels, A. S., *Ind. Eng. Chem.*, **44**, 1922 (1952).
23. Nelson, R. L., Jr., M.S. thesis Univ. California, Berkeley (1951).
24. Opler, Ascher, and N. K. Hiester, "Tables for Predicting the Performance of Fixed Bed Ion Exchange and Similar Mass Transfer Processes," Stanford Research Institute, Stanford, Calif. (1954).
25. Ranz, W. E., *Chem. Eng. Progr.*, **48**, 247 (1952).
26. Reichenberg, D., *J. Am. Chem. Soc.*, **75**, 589 (1953).
27. Selke, W. A., and Harding Bliss, *Chem. Eng. Progr.*, **46**, 509 (1950).
28. Sillén, L. G., *Arkiv. Kemi. Mineral, Geol.*, **22A**, No. 15 (1946).
29. Thomas, H. C., *Ann. N. Y. Acad. Sci.*, **49**, 161 (1948).
30. Vermeulen, Theodore, *Ind. Eng. Chem.*, **45**, 1664 (1953).
31. ———, and N. K. Hiester, *Ind. Eng. Chem.*, **44**, 636 (1952).
32. ———, *J. Chem. Phys.*, **22**, 96 (1954).
33. Wilke, C. R., and O. A. Hougen, *Trans. Am. Inst. Chem. Engrs.*, **41**, 455 (1945).

*When the column feed contains one or more minor trace constituents with respect to a single major component present in both solution and resin ($c_A \ll C_0$, $q_A \ll Q$), each trace constituent exhibits linear-equilibrium behavior (*32*), and therefore $\mathbf{b} = 1$. In applying Equation (29), $\mathbf{D}$ must be used as defined in reference *31*.

Mass Transfer Studies in an Agitated Vessel

A. I. JOHNSON and CHEN-JUNG HUANG

University of Toronto, Toronto, Ontario

A study of rates of dissolution of organic solid from a flat surface into turbulent liquid in a mixing tank of 6 in. I.D. is reported for five systems—benzoic acid–water, salicylic acid–water, salicylic acid–benzene, succinic acid–*n*-butanol, and succinic acid–acetone. Previous theories for the rates of mass transfer are reviewed and compared, and experimental results analyzed and correlated by an equation in terms of dimensionless groups similar to that of Hixson and Baum, Sherwood and Gilliland, and Rushton and Oldshue. The close agreement between the theoretical and experimental values of the exponent of the Schmidt number in this equation may provide new and significant evidence for the applicability of the surface-renewal theory to mass transfer from a flat solid surface into a turbulent liquid.

For free rotational agitation, a local mass transfer coefficient with respect to the position of a cast solid was detected quantitatively. However, the insertion of four baffles into the tank gave a uniform mass transfer coefficient regardless of the position of the cast solid. A decrease in the mass transfer coefficient was observed when baffles were used.

The advantages of the constant and stationary interface, the stability and simplicity of the apparatus, the possibility of duplicating experimental results, and the success of the detection of a local mass transfer coefficient suggest that the present apparatus and procedures could be used for the study of the theory of mass transfer rates from flat surfaces.

Among the basic concepts of mass transfer between phases which have been proposed, the film theory of Whitman and Lewis (*18, 19, 31*) and the Danckwerts surface-renewal theory (*2*) have attracted greater attention from chemical engineers than have others. The first theory pictured a stagnant fluid film at the interface representing the resistance to mass transfer. It was assumed that the solute passed through this film only by molecular diffusion. According to the theory, the mass transfer rate from the interface to the bulk of the phase can be represented by the equation

$$N = \frac{D}{x}(C_i - C)A \qquad (1)$$

Although the film theory has the advantage of supplying a simple picture of a complicated mechanism, it has been doubted whether a stagnant film exists under any turbulent condition, and the usual assumption of a stagnant film at the interface was abandoned by Danckwerts in his surface-renewal theory (*2*). Instead he assumed that the surface was continuously being replaced with fresh fluid. A new term, *surface-renewal rate*, was introduced without specification of the physicochemical properties of the system and the hydrodynamic conditions. Based on this concept, the mass transfer rate equation, similar to Equation (1), can be written as

$$N = \sqrt{Ds}\,(C_i - C)A \qquad (2)$$

Although Danckwerts proposed the surface-renewal theory for gas absorption in a packed tower, a mechanism can be postulated to permit the concept to be applied for solid-liquid or liquid-liquid systems. When the theory was proposed in 1951, Danckwerts made no effort to compare the foregoing equation with published experimental measurements. He regarded the theory as tentative until it was confirmed experimentally. Recently, however, the transient rates of gas absorption by use of a rotating drum for a few systems including a case of mass transfer with chemical reaction were measured by Danckwerts and Kennedy (*3*). Comparing these results with the steady state of gas absorption in the packed tower, they tentatively concluded that none of the present theories by Whitman and Lewis and by Danckwerts gave an adequate description of the absorption process. The recent work of Lynn, Straatemeier, and Kramers (*23*) however shows the applicability of the penetration theory (*11*) of the Higbie

Chen-Jung Huang is at present at the University of Houston, Houston, Texas.

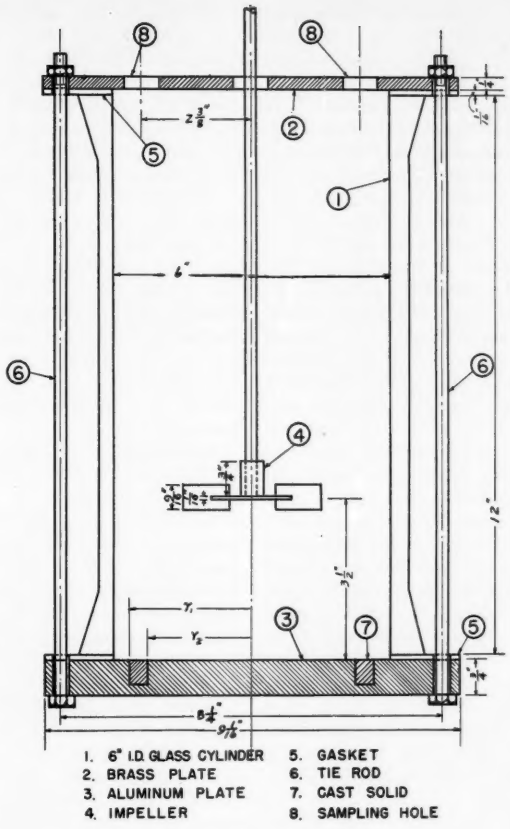

Fig. 1. Agitation tank.

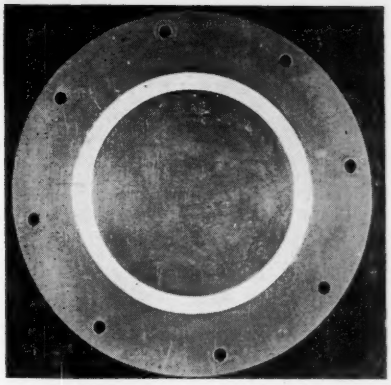

Fig. 2. Bottom plate with cast solid (plate 1).

type to the absorption of sulfur dioxide by water and by aqueous solutions of HCl, $NaHSO_3$, and NaCl in relatively long wetted-wall columns, in short wetted-wall columns, and in wetted spheres singly and in columns. In the presence of small concentrations of a surface-active material the rate of absorption in long wetted-wall columns is very well explained by the penetration theory, which predicts that the rate of absorption is proportional to the diffusivity to the one-half power. It would be premature, therefore, to conclude from these relatively few results that the surface-renewal theory was an unreliable guide. More experimental evidence would be welcomed.

It should be pointed out that both the film and the surface-renewal theories adopted the concentration difference as a driving force; therefore, the equation for rate of mass transfer through a single-phase resistance,

$$N = k(C_i - C)A \qquad (3)$$

is common between the two theories with the different significances attached to the individual mass transfer coefficient k; i.e.,

$$\text{Whitman-Lewis} \qquad k = \frac{D}{x} \qquad (4)$$

$$\text{Danckwerts} \qquad k = \sqrt{Ds} \qquad (5)$$

Up to the present time there have been very few data published which were obtained for the specific purpose of investigating the effect of diffusivity on the mass transfer coefficient. As pointed out by Sherwood and Gordon (*9*), the previous experimental data showed that the effect of diffusivity on the mass transfer coefficient might be represented by the power function $k \propto D^v$ where the exponent v had been reported to be somewhere between 0.15 and unity. A table summarizing these experimental results has been published (*9*). It should be noted that for the study of the additivity of individual mass transfer resistances, Sherwood and Gordon assumed that an individual mass transfer coefficient should vary with molecular diffusivity to the one-half power. Thus it may be concluded that the effect of diffusivity has not been satisfactorily established and that further experimental work for this purpose is desirable.

Besides the two foregoing theories, the kinetic theory of Miyamoto (*24, 25, 26*) and Kishinevskii's surface-renewal theory without penetration (*4, 15, 16, 17*) were also interesting because the existence of a stagnant film at the interface was not assumed. For the process of dissolution of a solid into liquid Miyamoto separated the process into two parts, namely, escape of the solid molecules into the liquid phase and deposition of the dissolved molecules on the solid surface. The further assumption was that, among molecules which made up the solid surface, only those with components of vibration energy at right angles to the interface greater than a threshold value could enter into the liquid phase and, among dissolved molecules, only those which collided with the interface at velocities with components at right angles to the interface greater than a threshold value could deposit on the surface. The mathematical expression for the individual mass transfer coefficient does not include the terms for hydrodynamic conditions of the operations. Thus the application of his theory to equipment design was limited. Kishinevskii's concept was similar to the surface-renewal theory except that the surface became instantaneously saturated with the solute on exposure (*4*). Thus molecular diffusion played very little part in the determination of the rate of absorption. But, as pointed out (*4, 9*), there is strong evidence that the mass transfer coefficient varies with molecular diffusivity.

In chemical engineering research some indirect approaches to evaluating agitation by some measurable quantities have been applied; for example, the studies on the rate of solution of suspended solid pellets were employed for this purpose. The earliest study on the rate at which solids dissolve in their own solution was published by Noyes and Whitney (*27*). The materials (benzoic acid or lead chloride) were cast in the form of cylindrical sticks on glass cores and, after insertion into wide-mouthed bottles containing water, were rotated at a constant rate. The rate of solution was explained on the assumption that a very thin layer of saturated solution was formed at the surface of the solid and that the rate at which the solid dissolved was governed

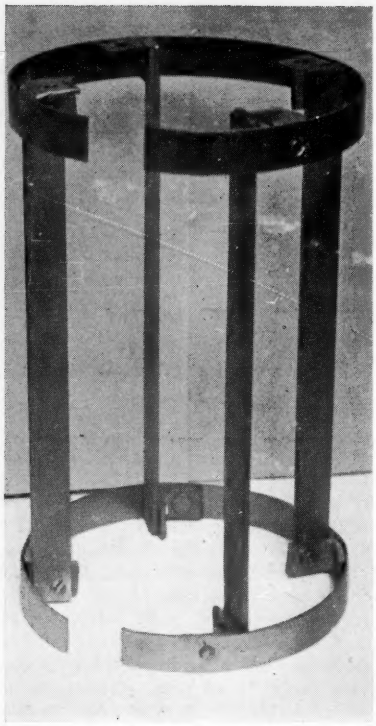

Fig. 3. Baffles.

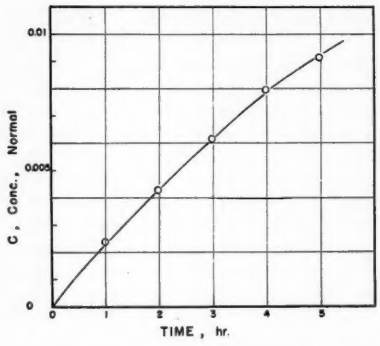

Fig. 4. Concentration of solution.

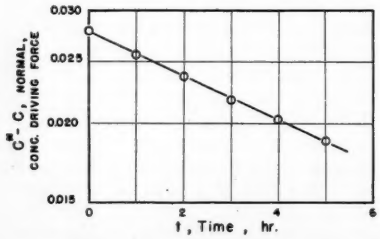

Fig. 5. Determination of mass transfer coefficient k.

by the rate of molecular diffusion from this saturated layer into the main body of the solution. Since then most workers have suspended the solid pellets or particles in the solution for the study of mass transfer between solid and liquid systems in a stirred vessel. For this case Hixson and Crowell (*12*) developed the so-called "cube-root law" for the determination of the mass transfer coefficient on the assumption that the surface area of the solid pellets or particles was proportional to the two-thirds power of the volume or the weight of dissolving solids. Later Hixson and Wilkens (*14*) extended the work, still suspending the benzoic acid tablets in water, to include the effects of stirring speed, size of equipment, and the use of baffles. Since the exact expression of the cube-root law was algebraically complex, Hixson and Baum (*13*) proposed an approximate equation with the simplified assumption that the total area of the surfaces of the suspended solid was constant and that the change of concentration as the dissolution proceeded was small so that the average concentration driving force might be expressed by logarithmic means. Mass transfer data for a series of dimensionally similar agitators in which solids were suspended in liquid were reported. Their experimental results were correlated by the similar equation used by Gilliland and Sherwood (*8*):

$$\left[\frac{kl}{D}\right] = K\left[\frac{\mu}{\rho D}\right]^b\left[\frac{R\,d^2\rho}{\mu}\right]^c \quad (6)$$

The main purpose of the present research was to pursue the Danckwerts type of surface-renewal theory to see whether the theory could be extended to a solid-liquid system. An attempt was made to relate the surface-renewal rate to the operating conditions and physical properties of the agitated system. The present research was limited to the case of mass transfer by physical means only. It was decided to measure rates of solution of organic solid into the turbulent liquid from the flat surface. The operation was made in a mixing tank rather than in a packed tower with its complicated and possibly varying flow patterns or in a wetted-wall column with its rippling or in a mixing tank containing solid particles suspended in agitated liquid with varying surface area. The suspension of the solid particles in the agitated liquid was accompanied by other disadvantages. There was difficulty in obtaining uniform shape of the particles. During agitation the solid particles could be crushed or fractured and the surface area might be changed. A variation in the surface area might also be caused by the agglomeration of the particles. The particles might not have remained suspended in the liquid but have fallen to the bottom of the tank. Thus the advantages of the choice were, first, to have a single fluid resistance to mass transfer and, second, to maintain the interfacial area constant and stationary. An important reason for this system was also that it was intended to be a model of a liquid-liquid system with a fixed interface area.

The second object of the research was to study the method of anticipating the agitator performance by mass transfer data. Specifically, the effects of the position of cast solid, the stirring speed, the position of the impeller, the baffling, and other physicochemical properties on mixing or mass transfer were to be investigated along with the first objective. Since the variation of diffusivities of different organic solids in the same solvent was not great enough for direct determination of its effect on the mass transfer coefficient, several pairs of organic solid-liquid systems were used. If the Danckwerts type of surface-renewal theory could be applied to explain the rate of dissolution, the experimental data could be correlated by Equation (6), in which the exponent to the Schmidt number should be 0.5, as according to Danckwerts's theory k should be proportional to $\sqrt{D}$.

$$\left[\frac{kl}{D}\right] = K\left[\frac{\mu}{\rho D}\right]^{0.5}\left[\frac{R\,d^2\rho}{\mu}\right]^c \quad (7)$$

EXPERIMENT

The experimental runs were made in a mixing tank the dimension of which are shown in Figure 1. The bottom plate was aluminum with a ring depression in which organic solid was cast. Four bottom plates with different rings were used. Figure 2 shows the photograph of a bottom plate and Table 1 lists the radii of the circular depressions for four plates.

The solution was agitated by a turbine-type impeller with six flat blades. The impeller was placed at the center of the

Table 1. Dimensions of the Cast Organic Solid

Plate	Inside radius r_1, cm.	Outside radius r_2, cm.	Surface area A, sq. cm.	Mean radius r_m, cm.
1	6.568	7.620	46.873	7.094
2	5.387	6.317	34.183	5.852
3	3.810	4.666	22.793	4.238
4	0.635	2.009	11.415	1.322

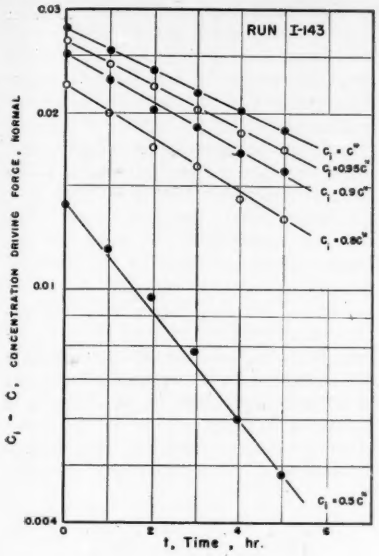

Fig. 6. Effect of interfacial concentration.

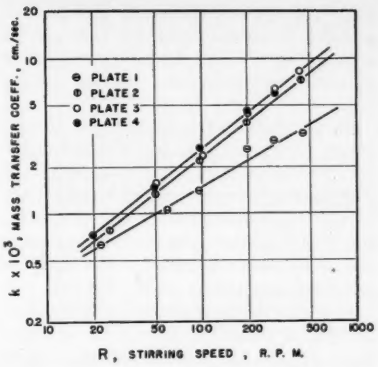

Fig. 7. Effect of stirring speed on rates of dissolution.

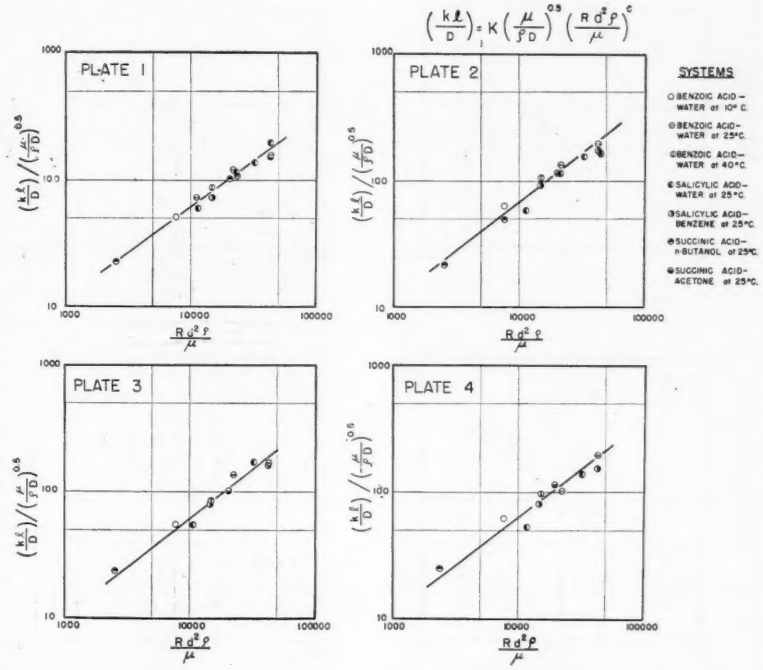

Fig. 8. General correlation for rate of dissolution with baffling.

TABLE 2. RANGE OF EXPERIMENTAL VARIABLES AND PHYSICAL PROPERTIES

Variables	Units	Range
Density	g./cc.	$0.7990 \sim 0.9998$
Viscosity	centipoises	$0.3982 \sim 3.205$
Diffusivity	sq. cm./sec.	$0.2725 \times 10^{-5} \sim 1.850 \times 10^{-5}$
Stirrer speed	rev./min.	$50 \sim 500$
Temperature	°C.	$10 \sim 40$
Stirrer position	in.	$2.5 \sim 5.5$
Mass transfer coefficient	cm./sec.	$0.360 \times 10^{-3} \sim 8.897 \times 10^{-3}$
Sherwood number		$1,070 \sim 13,700$
Schmidt number		$208 \sim 14,800$
Reynolds number		$2,250 \sim 48,760$

tank and was driven by a variable-speed motor. The speed of the stirrer varied within 3% during a run. For the runs with baffling four narrow vertical baffles ¾ in. wide and ⅛ in. thick were inserted. A photograph of the baffles is shown as Figure 3. The agitation tank was placed in either a constant-temperature bath or a constant-temperature room for each run. The temperature fluctuated in the constant-temperature bath by ±0.2°C. and in the constant-temperature room by ±0.5°C. The selection of the system was one of the most difficult problems in this research because the chosen system had to meet several criteria, i.e., no cracking of the cast solid, adherence of the cast solid to the ring depression, wide range of diffusivities, and large variation of the Schmidt number. The following systems were selected on the basis of these conditions: benzoic acid–water at 25°, 10°, and 40°C.; salicylic acid–water at 25°; salicylic acid–benzene at 25°C.; succinic acid–*n*-butanol at 25°C.; and succinic acid–acetone at 25°C.

The main difficulty with the present work was to prepare a flat surface of organic solid without any trace of cracking. The present authors recommend, after trying several methods, slow melting of the solid and gradual cooling of cast solid. The surface of the organic solid was carefully smoothed to the same level as the aluminum plate with a sharp spatula or a razor blade. Finally the surface was rubbed with fine sandpaper, then washed and dried.

When the agitation tank was set ready for a run, the motor was started and allowed to come to speed. The solvent was added from a funnel of which the end tip was close to the tank wall so that the solvent fell along the wall. In this manner 3 liters of solvent could be admitted with very little initial turbulence caused by pouring. As soon as the solvent was added, the funnel was removed and the timer started. A run was then in progress. At a constant interval of time, e.g., 15, 30, or 60 min., depending on the rate of dissolution, a sample of the solution was removed by a 10-cc. pipette and later analyzed. Ten cubic centimeters of fresh solvent was added immediately after the withdrawal of the sample to make up for the amount which had been removed. The sampling point was kept constant during this investigation. The rotating speed of the stirrer was counted every 10 min. by use of a strobotac. The concentration of the samples was readily determined by a straight titration with sodium hydroxide solution of proper concentration with phenolphthalene used as an indicator.

RESULTS

Mass Transfer Coefficient

The concentration change of the solution in the tank with respect to time can be expressed by the following equation:

$$\ln \frac{C_i - C_n}{C_i - C_{n+1}} = k \frac{A}{V} (t_{n+1} - t_n) \qquad (8)$$

which is developed from the following two equations for a batch operation:

$$N = kA(C_i - C) \qquad (9)$$

$$N\,dt = V\,dC \qquad (10)$$

Therefore, when the concentration of liquid phase in the mixing tank is plotted against time, the line should be an exponential curve, as shown in Figure 4. Furthermore, if the run was made for a longer period, the curve would flatten out and become asymptotic to the saturated concentration. Theoretically, the time necessary to reach the saturated concentration is infinite according to Equation (8).

The initial mass transfer coefficient was not measured because the present experimental procedure was not prepared for that purpose. It was observed that except in a few cases out of one hundred fifty runs the mass transfer coefficient for the first interval was usually the same as that observed in the later intervals. A few deviations were most likely due to the hydrodynamic discrepancy caused by the method of pouring solvent into the tank at the beginning of a run.

The removal of dissolved solute owing to intermediate sampling was corrected by the introduction of correction factor ϕ; that is, the true mass transfer coefficient k must be the sum of the apparent mass transfer coefficient k' and the correction factor ϕ.

$$k = k' + \phi \qquad (11)$$

where

$$k' = \frac{\ln \dfrac{C_i - C_n}{C_i - C_{n+p}}}{\dfrac{A}{V}\,p(t_{n+1} - t_n)} \qquad (12)$$

and

$$\phi = \frac{\displaystyle\sum_{m=n+1}^{n+p-1} \ln \frac{C_i - rC_m}{C_i - C_m}}{\dfrac{A}{V}\,p(t_{n+1} - t_n)} \qquad (13)$$

For the determination of correction factor ϕ, a plot of $\ln [(C_i - rC_m)/(C_i - C_m)]$ against C_m will facilitate the calculation. However, the correction was usually very small, i.e., within 3% of the true mass transfer coefficient. Particularly when the solution was dilute and the amount of the solution in an agitation tank was large, the correction was usually not necessary.

During a run the mass transfer coefficient was assumed to be constant. The assumption was sound because the plot of log concentration driving force vs. time was straight through the points as shown in Figure 5. If the assumption did not represent the phenomenon observed, there would not be a single straight line through all the points for a run. A single straight line through the plots also implies that the concentration difference between the saturated solution and the solution was the right driving force for the rate of dissolution. The reproducibility of the experimental results was checked at random and was found to be satisfactory. The deviation in mass transfer coefficient was usually within 6%.

In addition to the advantages of constant interfacial area and the simplicity of the apparatus, the possibility of duplicating the experimental results within the experimental error was encouraging. For this reason the present apparatus would be recommended for the study of mass transfer theory in the future.

Several evidences of the existence of an interfacial resistance have been reported (*3, 6, 11, 30*) for gas-liquid mass transfer studies. However, in these reports the authors stated that for a long period of the exposure, say 10 sec. for the carbon dioxide–water system as reported by Higbie (*11*), the effect was not observed. Emmert and Pigford (*6*) showed that after a very short period of exposure $k/k°$ became asymptotic to unity for the same system; here $k°$ was the mass transfer coefficient if no interfacial resistance was assumed. In the study of rates of dissolution of benzoic or salicylic acid into water under free convection, Wilke and his associates (*32*) concluded that the assumption of interfacial equilibrium was not significantly in error for the organic acids involved. In the study of rate of dissolution of solid from the cylindrical surface, Noyes and Whitney (*27*) explained the action on the assumption that the solution at the interface was saturated. It would appear to be safe to assume that there is no appreciable resistance to mass transfer in this study other than that resulting from hydrodynamic and diffusional considerations.

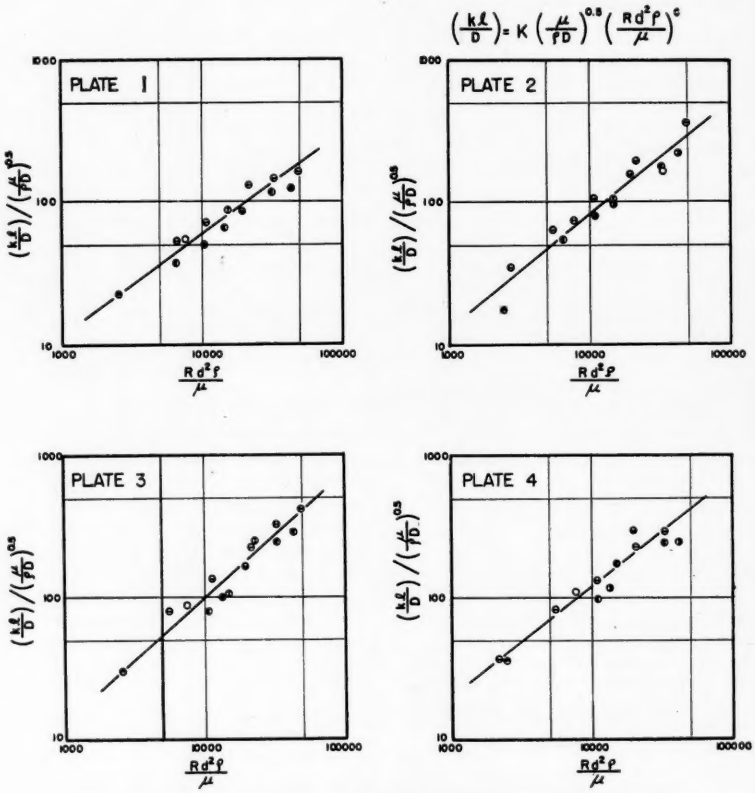

Fig. 9. General correlation for rate of dissolution without baffling.

Table 4. Correlation of Rate of Dissolution

$$[kl/D] = K[\mu/\rho D]^b[(Rd^2\rho)/\mu]^c$$

	Plate	K	b	c
With baffles	1	0.1283	0.475	0.693
	2	0.0722	0.523	0.769
	3	0.0973	0.501	0.702
	4	0.2613	0.467	0.630
Without baffles	1	0.2700	0.499	0.596
	2	0.0431	0.526	0.809
	3	0.0915	0.484	0.865
	4	0.1280	0.422	0.948

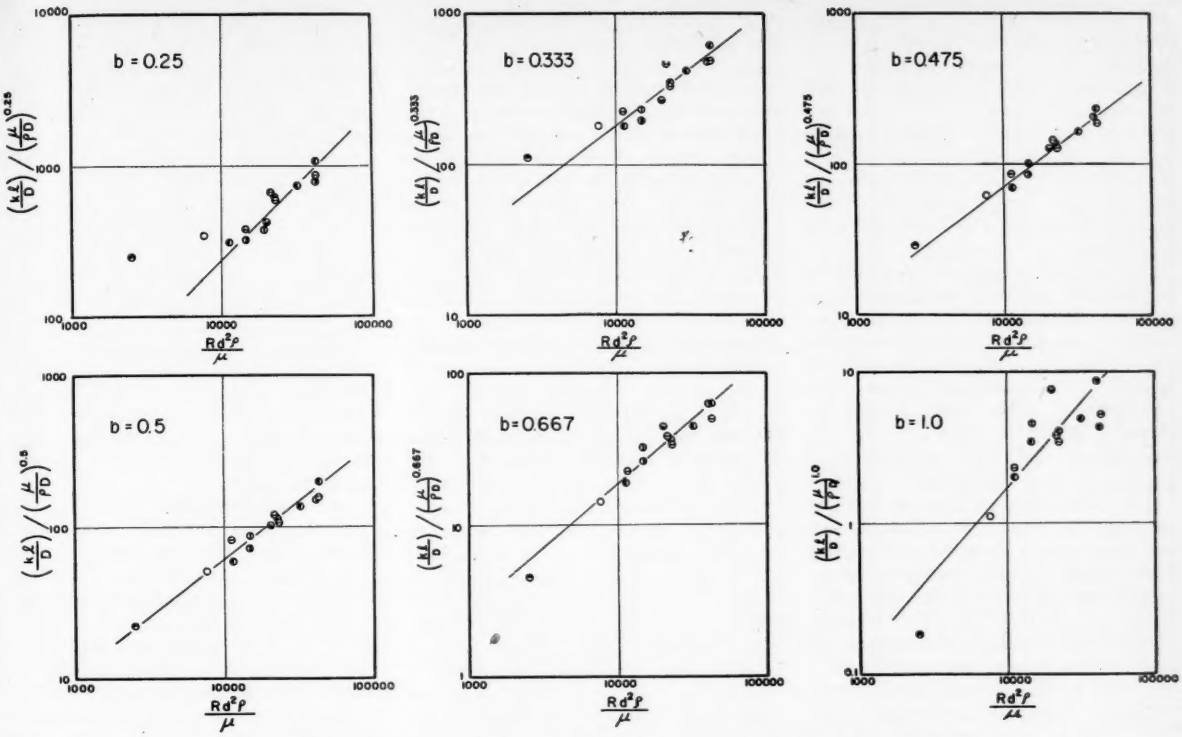

Fig. 10. Comparison of correlations with different exponents of Schmidt number used.

Figure 6 shows the plots of log driving force against time based on the assumption that the interfacial concentration was not at equilibrium. When the solution at the interface was less saturated, the points deviated more from a straight line. As will be shown later, the points for five different systems did not deviate excessively from the general correlation, an implication that the effect of interfacial resistance was negligible in this study or at least that the ratio of k to k° was constant for all the systems.

Effect of the Stirring Speed

Figure 7 shows the effect of the speed of the stirrer on the mass transfer coefficient. For illustration, here the experimental results of the benzoic acid–water system at 25 ± 0.5 °C. without baffling were used. For all runs made, the effect can be generalized that the mass transfer coefficient was proportional to the speed of the stirrer to the βth power.

$$k = \alpha R^\beta$$

The constants α and β depended on the plate and on whether baffling was applied. A similar observation for the power-speed study was reported (*28*) with the exponent β between 2 and 3. However, there was no appreciable distinction in α and β between plates 3 and 4, which were the smaller rings in mean radius. With the use of baffles, the effect of the speed of the stirrer on the coefficient could be represented for each system by a single line regardless of the position of a cast solid.

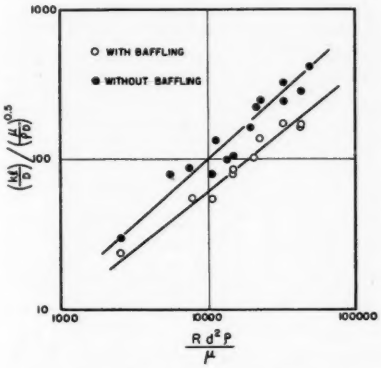

Fig. 11. Effect of baffling (plate 3).

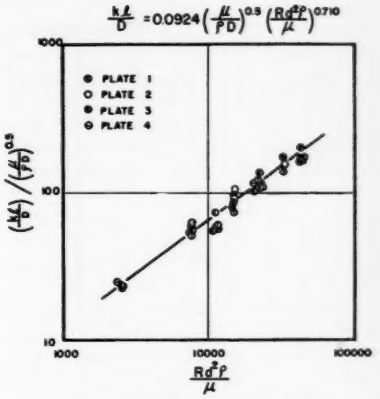

Fig. 12. General correlation for rate of dissolution with baffling.

Figure 7 also shows that higher mass transfer rates were obtained with cast solid rings of small diameter than with the large rings. In an unbaffled tank, with the impeller centrally located and the mixing shaft vertical, the entire tank is set in a rotary flow pattern with the highest linear velocities at the center of the tank. As the ring approaches the wall of the tank, the velocity will be lower and therefore the mass transfer coefficient lower.

The range of experimental variables and the physical properties of the systems studied in the present research are summarized in Table 2. The range of the Schmidt number was rather wide, but the Reynolds number was limited.

Correlation of Data

Equation (6) suggested that when $[kl/D]/[\mu/\rho D]^b$ was plotted against $[(Rd^2\rho)/\mu]$, a correlation would be obtained with a proper choice of the exponent b. Although Danckwerts did not claim that his theory would work for solid-liquid mass transfer, the surface-

renewal theory may be pictured as still applying to solid-liquid interface by the following postulation. A thin liquid layer of saturated concentration was assumed to exist at the interface. Then the controlling mass transfer process between solid and liquid could be pictured as that between the saturated liquid layer and liquid phase. Here the turbulence was assumed to reach the surface of the saturated layer.

The physical properties of the systems for the calculations of the dimensionless groups were obtained from the literature or by measurements. Table 3* tabulates all the experimental results and the calculated dimensionless groups. The experimental results were plotted by $[kl/D]/[\mu/\rho D]^{1/2}$ vs. $[(Rd^2\rho)/\mu]$ on the assumption that the surface-renewal theory might be applicable.

The results seemed to be satisfactory as shown in Figures 8 and 9. For an individual system the previous discussion showed that the mass transfer coefficient varied with the speed of the stirrer to a certain power. This implied the linearity of the plots of the mass transfer coefficient against the stirrer Reynolds number. Then the method of least squares could be applied for the determination of the best values of the exponents b and c of Equation (6). Table 4 lists the constant K and the exponents b and c determined by the method of least squares.

As discussed before, if the mass transfer mechanism follows the surface-renewal theory, the exponent of Schmidt number, b, should be 0.5. The close agreement between the empirical and theoretical values for the exponent b, as tabulated in Table 4, may then support the possible application of the surface-renewal theory to the process of physical dissolution as conducted in the present research. In order to show the differences of the correlation due to different values of the exponent b, Figure 10 was prepared with b equal to 0.25, 0.333, 0.5, 0.475, 0.667, or 1. The experimental data of plate 1 with baffling were taken for comparison.

The mean deviation was 3% for $b = 0.475$, which was determined by the method of least squares, where it was 5.8% when the theoretical value of 0.5 was adopted for b.

For solid-liquid mass transfer the relation between the mass transfer coefficient and the molecular diffusivity has not been established as definitely as for other systems. In order to explore the effect of the Schmidt number on mass transfer in turbulent flow, data were obtained on the rate of solution of cast tubes and cylinders by Linton and Sherwood (*22*). Lin et al. (*20*) measured transfer rates from a flowing electrolyte to the surface of an electrode. These data were correlated with respect to Schmidt number to the two-thirds power. Later Lin, Moulton, and Putnam (*21*) presented a theoretical analysis of mass transfer between a turbulent-fluid system and the wall. The fluid was divided into three layers, namely, the very thin sublaminar layer adjacent to the wall, the turbulent core, and the buffer region between the core and laminar layer. Analysis of these showed that there was no definite laminar film for pure molecular diffusion near the wall. The concept was to introduce into the sublaminar layer a small appropriate amount of eddy which decreases rapidly to zero at the wall. The general mass transfer equation included ϕ_D, which is an involved function of the Schmidt number and the friction factor. Eisenberg, Tobias, and Wilke (*5*) studied the rates of mass transfer at circular cylinders rotating about their axes in the center of stationary cylinders by means of solid dissolution and electrolytic redox reactions. The correlation was in terms of Schmidt number to the 0.644 power. They (*32*) also evaluated the mass transfer coefficient from limiting rates of electrolysis and from rates of dissolution of organic solids where no mechanical agitation was applied. For this case the correlation was made with respect to Schmidt number to the 0.25 power. Gaffney and Drew (*7*) determined the mass transfer coefficient for three organic solvents flowing through the packing of organic acid pellets. The height of the transfer unit increased with the 0.58 power of Schmidt number. Only one previous study, that of Hixson and Baum (*13*), correlated data with the 0.5 power to the Schmidt number.

However, Hixson and Baum did not think that in their study the value of the exponent b to the Schmidt number could be accurately determined because of the narrow range of values for the Schmidt number at a given range of the Reynolds number. They selected 0.5 tentatively because this value gave the best correlation for most points and because it was approximately the same as the value 0.44, which was used by Gilliland and Sherwood (*8*) to correlate their data for mass transfer into turbulent air. Their research was not intended to establish this exponent but was to indicate a method for applying the dissolution constant to the problem of designing and determining the operating characteristics of mixing equipment.

Effect of Baffling

The radial flow, as the result of the application of baffles, has vertical and lateral flow currents that are desired for most mixing operations. But the insertion of the baffles was accompanied by the decrease of mass transfer rate. Apparently the surface-renewal rate for the operation without baffles was higher than that with baffles. The same phenomenon was reported by Hixson and Wilkens (*14*) for the rate of dissolution of suspended solid particles into the liquid in a mixing tank.

The magnitude of the decrease in the rate of dissolution upon insertion of baffles was different for each plate, but the magnitude increased as the cast solid ring became small. When the ring was big enough to get close to the wall of the tank, there was almost no effect. The decrease of the mass transfer coefficient due to baffling is shown in Figure 11, results obtained for plate 3 being used.

Different effects with respect to the number of baffles were not studied. According to Hixson and Wilkens, the introduction of more than four baffles appeared not to influence the dissolution rate further for systems of solids suspended in liquid.

It has been recognized (*3, 10*) that the local value of mass transfer coefficient k would probably vary from one region to another in a packed tower. There are regions in the packing where the surface-renewel rate is high and other parts where the liquid is relatively stationary. This uncertainty and nonuniformity of local k value is the fundamental disadvantage of the use of a packed tower in the study of mass transfer theory. In this research the local k value was detected quantitatively as shown in the correlation of the data.

There was a much greater deviation in the exponent of the Schmidt number for the unbaffled tank than for the baffled tank, as shown in Table 4. With the Reynolds number used as the measure of the hydrodynamic condition in the tank, wider variation in the exponent of the Reynolds number also indicated strongly the variation of hydrodynamic conditions with respect to position. However, when the baffles were inserted, the variation of the local mass transfer coefficient was eliminated, as the experimental results of all four plates could be represented by a single line, as shown in Figure 12. Then a single correlating equation was sufficient to cover all plates if baffling was provided.

$$\left[\frac{kl}{D}\right] = 0.0924\left[\frac{\mu}{\rho D}\right]^{0.500}\left[\frac{R\,d^2\rho}{\mu}\right]^{0.710} \tag{14}$$

As compared with the packed tower, the success of the quantitative detection of the local k value would lead to the recommendation of the use of this apparatus for the study of mass transfer mechanism.

Effect of Surface Structure

The question of the effect of the different crystal structure at the interface was very difficult because of the impossibility of casting exactly the same surface each time. However, if the method of casting

*Table 3 may be obtained as document 4957 from the American Documentation Institute, Photoduplication Service, Library of Congress, Washington, 25, D. C., for $3.75 for photoprints or $2.00 for 35-mm. microfilm.

was repeated in the same manner described in the experimental details, the results could be reproduced, an implication that although the surface might not have the same crystals at any point, its population would be almost the same for each casting. The constant k value during a run and the success of the general correlation for different systems might indicate that minor change in the crystal structure and its population on the surface did not play a dominant role in the present study. Similarly the small deviation of the smoothness of the surface has little effect on the rate of dissolution in the mixing tank, where the hydrodynamic conditions have a greater effect.

Effect of the Position of the Impeller

A change of the flow pattern in the tank caused by the change in the height of the impeller was observed as the change in the dissolution rate. For agitation with baffling, however, the change of the transfer coefficient was insignificant. The application of the baffles masked out the effect of the position of the impeller. Even in the case without baffling, plates 1 and 2 showed insignificant change in the mass transfer coefficient. Near the wall the flow would have greater influence from the wall than would other factors. Appreciable effects of the impeller position were observed for plates 3 and 4 when no baffles were attached. Qualitatively it could be stated that the dissolution rate decreased as the position of the impeller was raised. For power-consumption study (*28*) the effect of the stirring position has been observed but no definite quantitative expressions were obtained. For any quantitative conclusion concerning the effect of the impeller position, more data are needed.

CONCLUSIONS

The following conclusions can be reached from the results of the present investigation.

This study proposed the correlation of the experimental results for mass transfer from a flat solid surface into a turbulent liquid in terms of dimensionless groups with 0.5 used as the exponent of the Schmidt number. The fact of this satisfactory correlation may provide new and significant evidence for the possible applicability of the Danckwerts type of surface-renewal theory to the mass transfer from a flat solid surface into a turbulent liquid in an agitated vessel.

Nonuniformity and instability of local mass transfer coefficient is one of the disadvantages for the use of a packed tower for the study of the theory of mass transfer rates. Furthermore, a local mass transfer coefficient cannot be detected in a packed tower. In this study the local mass transfer coefficient was quantitatively detected with respect to the position of a cast solid; however, insertion of four baffles into the tank gave a uniform mass transfer coefficient regardless of the position of a cast solid. Since the present system can be considered to be a model of a liquid-liquid system, it is concluded that, in order to obtain the uniform mass transfer rate across the liquid-liquid interface in an agitated tank, baffles should be applied.

The advantages of the constant and stationary interface, the stability and simplicity of the apparatus, the possibility of duplicating experimental results, and the success of the detection of the local mass transfer coefficient suggest the use of the present apparatus and procedures for a further study of the mass transfer theory. In particular, a study of the mass transfer rates accompanied by chemical reaction is recommended. The surface-renewal rates obtained in the present work could be compared with the rate obtained for the case accompanied by chemical reaction as a further confirmation of the surface-renewal theory.

NOTATION

A = interfacial area, sq. cm.
C = concentration of solution, g. equivalent/liter or g. equivalent/cc.
C^* = saturated concentration, g. equivalent/liter or g. equivalent/cc.
C_i = interfacial concentration, g. equivalent/liter or g. equivalent/cc.
D = molecular diffusivity, sq. cm./sec.
K = constant
N = rate of mass transfer, g. equivalent/sec.
R = stirring speed, rev./sec. or rev./min.
T = temperature, °C.
V = volume of solution, cc. or liters
a = volume of a sample, cc.
b = exponent of Schmidt number
c = exponent of Reynolds number
d = diameter of impeller
k = mass transfer coefficient, cm./sec.
k' = apparent mass transfer coefficient, defined by Equation (12), cm./sec.
k° = mass transfer coefficient, no interfacial resistance assumed, cm./sec.
l = diameter of the mixing tank, cm.
p = number of sampling
r = constant = $(V - a)/V$
r_1 = inside radius of ring depression for casting solid, cm.
r_2 = outside radius of ring depression for casting solid, cm.
r_m = mean radius of ring depression for casting solid, cm.
s = fractional rate of surface renewal, $(\text{sec.})^{-1}$
t = time, sec.
v = exponent
x = fictitious film thickness, cm.
α = constant
β = constant
ϕ = correction factor defined by Equation (13), cm./sec.
ϕ_D = function of Schmidt number and friction factor, f, proposed by Lin, Moulton, and Putnam (*21*)
ρ = density, g./cc.
μ = viscosity, centipoises or g./(cm.)(sec.)

Subscripts

m = integer
n_1 = an arbitrary integer

LITERATURE CITED

1. Colburn, A. P., *Ind. Eng. Chem.*, **22**, 967 (1930).
2. Danckwerts, P. V., *loc. cit.*, **43**, 1460 (1951).
3. ———, and A. M. Kennedy, *Trans. Inst. Chem. Engrs.*, **32** (Supplement), S49 (1954)
4. Danckwerts, P. V., *A.I.Ch.E. Journal*, **1**, 456 (1955).
5. Eisenberg, Morris, C. W. Tobias, and C. R. Wilke, *Chem. Eng. Progr. Symposium Series* No. 16, **51**, 1 (1955).
6. Emmert, R. E., and R. L. Pigford, paper presented at A.I.Ch.E. New York meeting (1954).
7. Gaffney, B. J., and T. B. Drew, *Ind. Eng. Chem.*, **42**, 1120 (1950).
8. Gilliland, E. R., and T. K. Sherwood, *loc. cit.*, **26**, 516 (1934).
9. Gordon, K. F., and T. K. Sherwood, *Chem. Eng. Progr. Symposium Series* No. 10, **50**, 15 (1954).
10. Hatta, S., *Chem. Eng.* (*Japan*), **18**, 453 (1954).
11. Higbie, R., *Trans. Amer. Inst. Chem. Engrs.*, **31**, 365 (1935).
12. Hixson, A. W., and J. H. Crowell, *Ind. Eng. Chem.*, **23**, 923 (1931).
13. Hixson, A. W., and S. J. Baum, *loc. cit.*, **33**, 478 (1941).
14. Hixson, A. W., and G. A. Wilkens, *loc. cit.*, **25**, 1196 (1933).
15. Kishinevskii, M. K., and A. V. Pamfilov, *Zhur. Priklad. Khim.*, **22**, 1173 (1949).
16. Kishinevskii, M. K., *loc. cit.*, **24**, 542 (1951).
17. *Ibid.*, **27**, 382 (1954).
18. Lewis, W. K., *Ind. Eng. Chem.*, **8**, 825 (1916).
19. ———, and W. G. Whitman, *Ind. Eng. Chem.*, **16**, 1215 (1924).
20. Lin, C. S., E. B. Denton, H. S. Gaskill, and G. L. Putnam, *Ind. Eng. Chem.*, **43**, 2136 (1951).
21. Lin, C. S., R. W. Moulton, and G. L. Putnam, *loc. cit.*, **45**, 636 (1953).
22. Linton, W. H., and T. K. Sherwood, *Chem. Eng. Progr.*, **46**, 258 (1950).
23. Lynn, S., J. R. Straatemeier, and H. Kramers, *Chem. Eng. Sci.*, **4**, 46 (1955).
24. Miyamoto, S., *Bull. Chem. Soc.* (*Japan*), **7**, 8 (1932).
25. *Ibid.*, 388 (1932).
26. ———, *J. Chem. Soc.* (*Japan*), **54**, 410 (1933).
27. Noyes, A. A., and W. R. Whitney, *J. Am. Chem. Soc.*, **19**, 930 (1897).
28. Rushton, J. H., E. W. Costich, and H. J. Everet, *Chem. Eng. Progr.*, **46**, 395 (1950).
29. Rushton, J. H., and J. Y. Oldshue, *Chem. Eng. Progr.*, **49**, 161, 267 (1953).
30. Schrage, R. W., "A Theoretical Study of Interphase Mass Transfer," Columbia University Press, New York (1953).
31. Whitman, W. G., *Chem. Met. Eng.*, **29**, No. 4, 146 (1923).
32. Wilke, C. R., C. W. Tobias, and Morris Eisenberg, *Chem. Eng. Progr.*, **49**, 663 (1953).

Presented at A.I.Ch.E. Detroit meeting

Effect of Wall Proximity on the Rate of Rise of Single Air Bubbles in a Quiescent Liquid

SEIJI UNO and R. C. KINTNER

Illinois Institute of Technology, Chicago, Illinois

. The terminal velocity of air bubbles rising through distilled water, 61% glycerine, diethylene glycol, and a solution of a surface-active agent was measured in vertical cylindrical tubes of 2.09, 3.64, 4.91, 6.90, 9.50, and 15.25 cm. avg. I.D. An equation was developed to express a velocity-correction factor in terms of the ratio of bubble diameter to tube diameter and an empirical constant. The constant was a function of tube diameter and of the surface tension of the liquid. It seemed to be independent of liquid viscosity.

The scientific literature contains the results of many experimenters on the terminal velocity of gas bubbles moving in a stationary liquid field. Except for a few investigations such as those of Bryn (*2*) Rosenberg (*13*), and Haberman and Morton (*4*), the data were taken in tanks or tubes the walls of which were sufficiently close to the moving bubble to cause some doubt as to the absence of boundary effects. The cost of filling a tank of large diameter with pure liquids other than water is usually prohibitive. In order that data taken in tubes of small diameter may be interpreted in terms of the velocity in an infinite medium, an experimental determination of the wall effect was carried out. The results may also be used to arrive at a decision regarding the minimum size of tube or tank in which experimental data may be taken on the movement of single bubbles if wall effects are to be avoided or are to be held below some predetermined value.

PREVIOUS WORK

General Behavior of Bubbles

A number of excellent reviews of the literature on the motion of single air bubbles in a stationary liquid field have been recently published and the entire subject need not be included here. Three general types of shape of the bubble and its resultant behavior in a tank of infinite extent are generally recognized:

1. The bubble is spherical or, if slightly ellipsoidal, acts as if it were a rigid sphere. Bubbles up to about 0.04 cm. equivalent radius are in this class. The equivalent radius is defined as the radius of a sphere having the same volume as the bubble, irrespective of the actual shape of the latter. In this range of sizes the terminal velocity of rise increases with bubble diameter. The curve of drag coefficient

$$C_D = \frac{8}{3}\frac{gr_e}{U_\infty^2} = \Phi\left(\frac{2r_e U_\infty \rho}{\mu}\right) \quad (1)$$

as ordinate vs. Reynolds number as abscissa follows closely that for solid spheres.

2. Increase of bubble size results in a clearly ellipsoidal shape and a deviation from the drag curve for rigid spheres. The terminal velocity increases until a peak is reached at about 0.07 cm. equivalent radius (higher for liquids of high viscosity). Further increase in bubble size results in a decrease in terminal velocity. There is distortion of the interface and, for liquids of ordinary viscosity, the drag coefficient is lower than that for solid spheres. The amount of lowering seems to be a function of surface tension. The peak velocity corresponds to a low point in the curve of C_D vs. Re. As the equivalent radius (or Re) is increased above this value there is an increase of C_D with Re until an equivalent radius of about 0.9 cm. is reached. Bubbles of r_e between 0.35 and 0.9 cm. are unstable in shape although generally ellipsoidal. Above an r_e of 0.5 cm. the instability is marked.

3. At equivalent radii above 0.9 cm. (a little lower in liquids of high viscosity) the shape of the bubble is clearly that of the spherical cap described by many authors. Viscous effects are generally negligible in this region and the drag coefficient reaches a constant value of 2.6 at a Reynolds number of about 4,000.

Other classifications of size, shape, and behavior have been suggested by various authors for some systems under special conditions, but these will suffice for consideration of the wall effect.

Wall Effect on Solid Spheres

Mathematical analysis of the effect of boundary proximity on the rate of fall of solid spheres, negligible inertial effects and a low d/D ratio being assumed, has been carried out by Ladenburg (*6*), Faxen (*3*), Happel and Byrne (*5*), and Wakiya (*15*). The resulting equation is

$$\frac{U}{U_\infty} = \frac{1}{K} = 1 - 2.105\left(\frac{d}{D}\right) + 2.087\left(\frac{d}{D}\right)^3 \quad (2)$$

A binomial expansion of $[1 - (d/D)]^{2.1}$ leads to

$$\frac{1}{K} = 1 - 2.1\left(\frac{d}{D}\right) + 1.155\left(\frac{d}{D}\right)^2 - 0.0385\left(\frac{d}{D}\right)^3 \quad (3)$$

The difference in the two expressions is small in the range over which they may be applied. Hence the correction-factor equation may be expressed in a general form:

$$\frac{1}{K} = \Phi\left(1 - \frac{d}{D}\right)^n \quad (4)$$

McNown, Lee, McPherson, and Engez (*7*) considered that section of the cylindrical boundary near the equator of the falling sphere to approximate a short section of a larger sphere. Treating the problem as one sphere moving inside another permitted the use of spherical coordinates and resulted in the following equation for the range of negligible inertial effects and low values of d/D:

$$K = \frac{1 + \frac{1}{4}\left(\frac{d}{D}\right)^5}{1 - \frac{9}{4}\left(\frac{d}{D}\right) + \frac{5}{2}\left(\frac{d}{D}\right)^3 - \frac{9}{4}\left(\frac{d}{D}\right)^5 + \left(\frac{d}{D}\right)^6} \quad (5)$$

This becomes, to the second approximation,

$$K = 1 + \frac{9}{4}\left(\frac{d}{D}\right) + \left(\frac{9}{4}\cdot\frac{d}{D}\right)^2 \quad (6)$$

A binomial expansion of $[1 - (d/D)]^{-2.25}$ is

$$K = 1 + 2.25\left(\frac{d}{D}\right) + 3.66\left(\frac{d}{D}\right)^2 + 5.18\left(\frac{d}{D}\right)^3 \quad (7)$$

which in the range of variables over which it is applicable does not differ greatly from the analytical expression, and the general form may be said to be approximated by Equation (4).

For large values of (d/D), McNown, et al. (7) assumed that the surface of the falling sphere near its equator and of the near-by cylindrical container approximated two flat plates. This assumption led to the expression

$$K = \frac{3\sqrt{2}\,\pi}{8}\left(1 - \frac{d}{D}\right)^{-5/2} = \frac{1.67}{\left(1 - \frac{d}{D}\right)^{2.5}} \quad (8)$$

for the range of small inertial effects.

Rearranging Equation (8) results in

$$\frac{U}{U_\infty} = \frac{1}{K} = \frac{1}{1.67}\left(1 - \frac{d}{D}\right)^{2.5} = \Phi\left(1 - \frac{d}{D}\right)^n \quad (9)$$

and the form is seen to be the same as the equations for low ranges of d/D.

Newton (*10a*) discussed resistance to a sphere (or cylinder) moving axially in a vertical cylindrical vessel containing a quiescent incompressible fluid. His expression can be translated into a wall-effect correction factor for the case of large inertial effects:

$$\frac{U}{U_\infty} = \frac{1}{K} = \left[1 - \left(\frac{d}{D}\right)^2\right]\left[1 - \frac{1}{2}\left(\frac{d}{D}\right)^2\right]^{1/2} \quad (10)$$

McNown and Newlin (*10*) used the equation of momentum to arrive at an equation for the case of (d/D) nearly equal to unity and negligible viscous shear. Their equation seemed valid for Reynolds numbers above 20,000 and for diameter ratios of 0.75 and higher. Their expression may be converted to the correction-factor form

$$K = \frac{d/D}{(1 - d/D)^2} \quad (11)$$

Interpolation methods were claimed to be reliable for the range of Re of 500 to 20,000 in which both viscous and inertial effects are important.

Each of the equations noted indicates that a plot of log $(1/K)$ vs. log$[1 - (d/D)]$ would result in a straight line. While this is not strictly true for Equation (11), its range of applicability is limited to high values of (d/D) and the plot suggested would be approximately straight.

Frontal Diameter of Bubbles

McNown and Malaika (*8*) and McNown, Malaika and Pramanik (*9*) assumed that the results for solid spheres could be applied to other solid shapes if the diameter ratio were replaced by the ratio of the square root of the projected area of the particle to that of the container cross section. They justified this procedure on the basis of a previous conclusion (*7*) that "the boundary influence was primarily a restriction on the upward flow of the fluid displaced by the settling particle". Since this same phenomenon of backward flow of liquid in the annular space between the moving particle and the container wall must occur upon the upward passage of a gas bubble, it would seem that a length term descriptive of the frontal projected area should be used, rather than the equivalent diameter of the bubble. Such a length term is more difficult and costly to evaluate experimentally. Existing data relating the two are scarce. Rosenberg (*13*) determined the ratio of frontal diameter to equivalent diameter in the range of ellipsoidal bubbles of air in water and found that it varied from 1.0 at r_e of 0.04 cm. to 1.4 at r_e of 0.53 cm. He also presented an idealized conception of the geometry of a spherical cap and plotted data which would indicate that the ratio of frontal diameter to equivalent diameter should be constant at 1.95 for bubbles of equivalent radius between 1.0 and 3.0 cm. The unstable shape of bubbles between r_e of 0.53 and 1.0 cm. precluded any conclusion in regard to the ratio in this range.

Rosenberg's data for the two regions have been plotted on logarithmic paper as shown in Figure 1. The dashed lines result from the best curve drawn through the points on the original plots. The solid curve is a proposed compromise and was used in this work to convert equivalent diameter to frontal diameter. Allawala (*1*) photographed air bubbles rising in water, a 3% isoamyl alcohol solution, and a methyl cellulose solution of viscosity of 31 centipoises. His ratio of frontal diameter to equivalent diameter for ellipsoidal bubbles was lower than that shown in Figure 1, but the values are not considered to be so reliable as those of Rosenberg. In the range of r_e covered in the present work (0.10 to

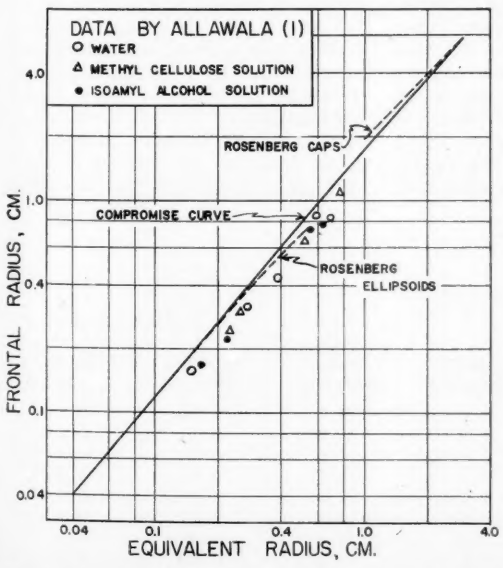

Fig. 1. Conversion of equivalent radius to frontal radius.

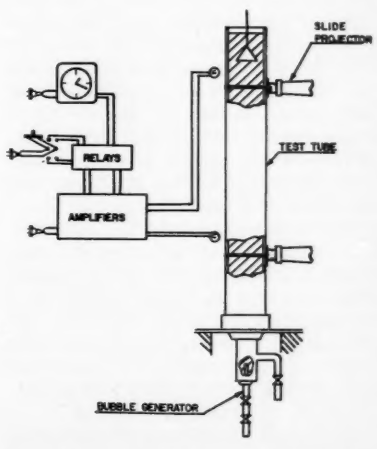

Fig. 2. General arrangement of apparatus.

1.2 cm.) the relationship is approximately linear, and so d_e can replace d in Equation (4).

An examination of the plots of U vs. r_e, C_D vs. Re, and C_D vs. We in the report by Haberman and Morton leads to the generalization that the transition from spheres to ellipsoids occurs at an equivalent radius of 0.03 to 0.08 cm. and that the change to spherical caps is complete at an equivalent radius of 0.9 cm. Values taken from the Haberman and Morton plots are shown in Table 1. If one assumes that the changes from spheres to spheroids to ellipsoids to spherical caps progresses in the same manner in other liquids as in water, the curve for water will serve for all liquids. The assumption seems to be sufficiently valid for liquids of less than 10 centipoises viscosity. The data of Allawala tend to support the assumption that the ratio of frontal diameter to equivalent diameter is independent of the liquid involved although the assumption is questionable for liquids of very high viscosity.

EXPERIMENTS

The terminal-velocity measurements were made in six glass cylinders of 2.09, 3.64, 4.91, 6.90, 9.50, and 15.25 cm. avg. I.D. Each was 4 ft. long and mounted vertically on a metal base plate which was supported in a common frame of pipe and fittings. Figure 2 is a diagram of the apparatus. Velocities were determined by measuring the time for a bubble to rise through a measured distance of about 75 cm. Two photoelectric cell circuits were used to start and to stop an electric timer, which was graduated in 0.01-sec. intervals. Black masking tape was used to provide narrow, horizontal slits at the lower and upper end of the measured vertical distance traveled by the bubble and a strong horizontal beam of light was projected through each slit. On the opposite side of the tube and about 3 in. above each horizontal beam there was placed a type ½-6F8G photoelectric cell. As the bubble passed through the lower light beam, a flicker of bright light reflected from the brilliant mirrorlike frontal surface actuated the photoelectric cell and, through an amplifying circuit and relay, started the electric timer. Upon passing through the upper beam, the bubble was made to actuate a duplicate circuit and to stop the timer, thus recording its time of travel.

Bubble size was determined by "weighing" bubbles under an inverted funnel suspended from one arm of an overhead analytical type of balance as described by Rosenberg (*13*) and by Haberman and Morton (*4*). For very small bubbles the volume of a large number was determined and divided by the number "weighed" to obtain an average bubble size.

In the case of the three smallest tubes the funnel had to touch the wall of the tube to catch relatively large bubbles. A subsidiary device, shown diagrammatically in Figure 3, was installed between the top of the tube and the balance to eliminate the defect of touch and to keep the same accuracy of measurement as in the larger tubes. In this device the bubble was caught under a funnel which touched the tube wall, led into a rubber or Tygon tube, and stopped there by a pinch clamp. The clamp was opened and the bubble permitted to rise in the rubber tube to a second pinch clamp. Closing of the lower and opening of the upper clamp permitted the trapping of the bubble under the upper funnel suspended from the balance arm.

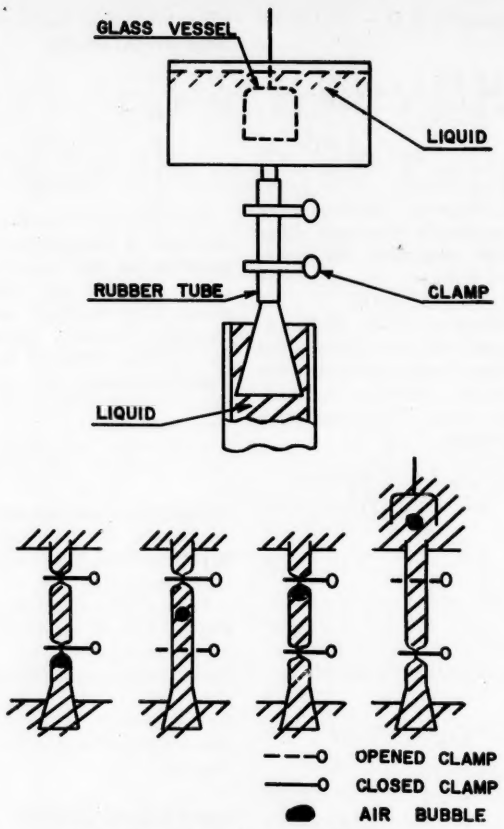

Fig. 3. Mechanism of the subsidiary device.

Bubbles were generated and released by four devices, depending upon the size of the bubble desired and the coalescence property of the system. Properly made glass-capillary nozzles served to produce small bubbles of uniform size. Intermediate sizes were made by orifice-type tubes and the size of such bubbles was determined individually. Very large bubbles were made by the dumping-cup technique described by Rosenberg (*13*), Haberman and Morton (*4*), and Peebles and Garber (*11*). The cup in this device was a 2-in.-diam. copper hemisphere obtained from an old ball check valve. For large bubbles in the TMN (trimethyl nonyl ether of polyethylene glycol pro-

TABLE 1. SHAPE-TRANSITION RADII OF BUBBLES IN LIQUIDS

Liquid	Viscosity, centipoises	Surface tension, dynes/cm.	Transition r_e, cm. Sphere to ellipsoid	Ellipsoid to cap
Corn syrup, 68%	109	79.9	0.05	0.8
Corn syrup, 62%	55	79.2	0.05	0.8
42% glycerine	4.3	71.1	0.07	0.85
Mineral oil	58	20.7	0.07	0.9
Turpentine	1.46	27.8	0.05	0.9
Varsol	0.85	24.5	0.03	0.9
Methyl alcohol	0.52	21.8	0.035	0.9
Cold water	1.47	74.8	0.075	0.85
Distilled water	0.98	72.6	0.04	0.9

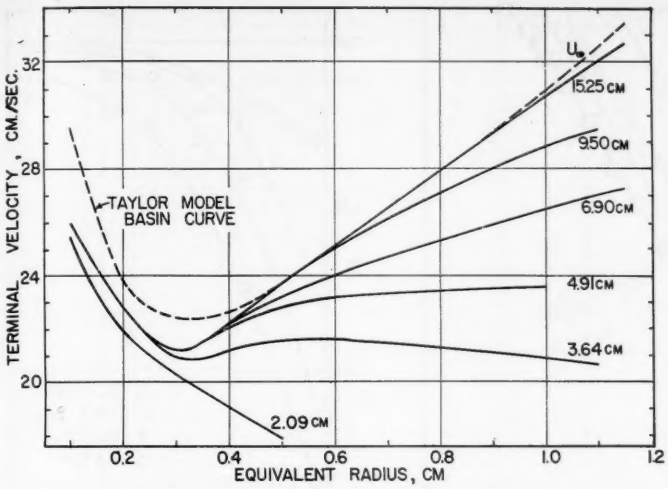

Fig. 4. Velocity curves for water from smoothed data.

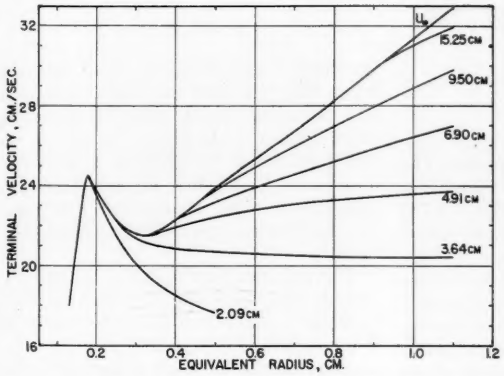

Fig. 5. Velocity curves for glycerine solution from smoothed data.

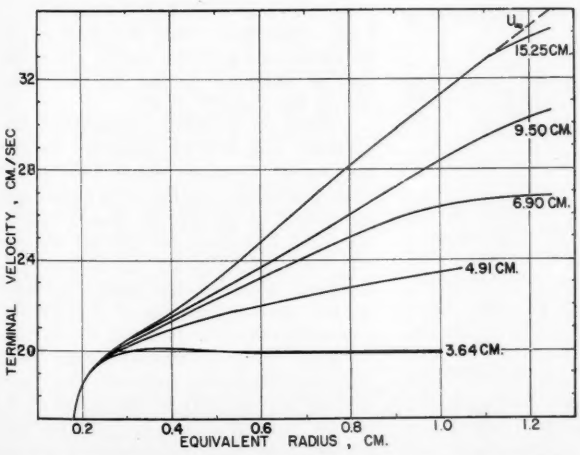

Fig. 7. Velocity curves for diethylene glycol from smoothed data.

duced as a nonionic surface-active agent by the Carbide and Carbon Chemicals Company) solution a device made of pipe fittings, described by Allawala (*1*), was necessary. The bubbles so formed were not uniform and their size was individually measured. The dumping-cup technique was useless, as small bubbles could not be made to coalesce into a single large one under the cup.

Physical properties of the liquids were determined each day of operation. Viscosities were measured with an Ostwald viscometer, densities with a pycnometer, and surface tensions with a Cenco du Nouy tensiometer. Handbook values of the density and viscosity of distilled water were used. The density of the TMN solution was assumed to be the same as that of water, a check determination indicating the validity of the assumption. The 61 wt. % glycerine solution was approximately equivalent to the 56 vol. % solution used by Bryn (*2*). The physical properties of the liquids are summarized in Table 2.

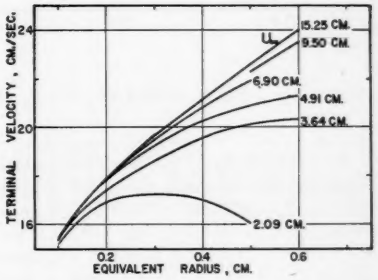

Fig. 6. Velocity curves for TMN solution from smoothed data.

CORRELATION

The effect of tube-wall proximity on the terminal velocity of air bubbles in each of the four liquids is shown graphically in Figures 4 to 7. The plots show smooth curves drawn through the experimental points, which were too numerous to place on these illustrations*. The upper curve is considered to represent the relationship in an infinite medium as the curves for each of the smaller tubes leave it at some point. The data for air bubbles rising in water obtained at the D. W. Taylor Model Basin by Rosenberg (*13*) and by Haberman and Morton (*4*) are shown as a dashed line in Figure 4. Their values were used for U_∞ at r_s of 0.9 to 1.2 cm. In the range of 0.1 to 0.53 cm. the nature of the particular water employed has been shown (*4*) to be highly important, and so the Taylor Model Basin curve could not be used for this range.

*Tables 3 to 9, giving original data on r_s, U, U_∞, and D as well as the data of Greenwood and Allawala, may be obtained as document 4966 from the American Documentation Institute, Photoduplication Service, Library of Congress, Washington 25, D. C., for $1.25 for 35-mm microfilm or photoprints.

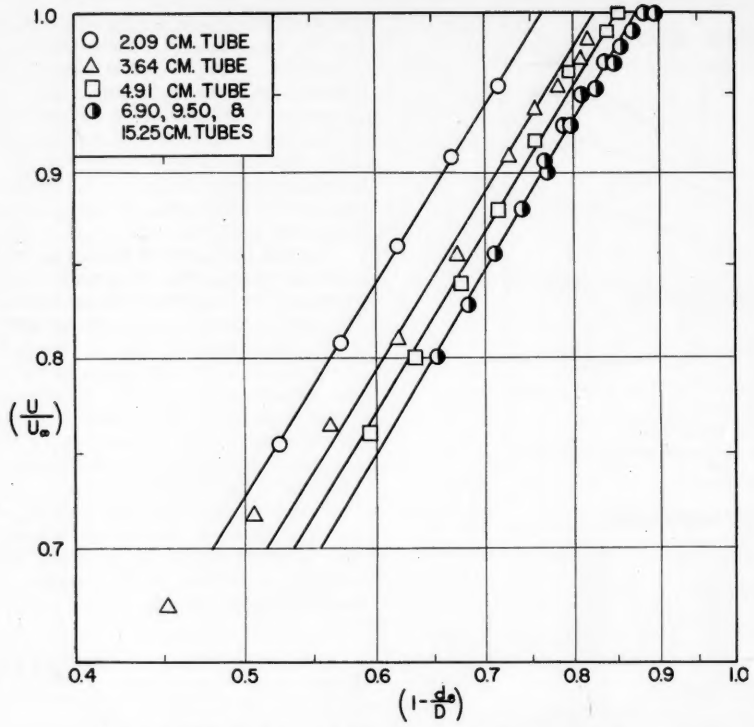

Fig. 8. (U/U_∞) vs. $(1 - d_e/D)$ from smoothed data for water.

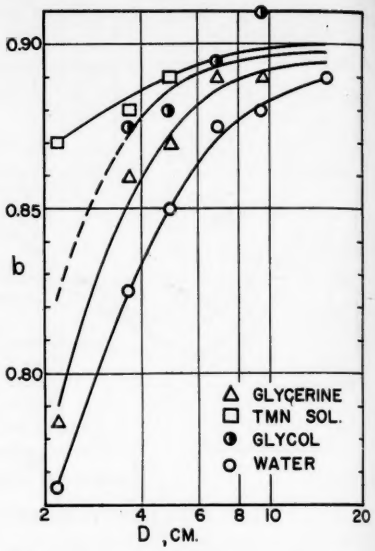

Fig. 9. Values of b as a function of tube size and surface tension.

A consideration of the theoretical analyses of the cases for solid shapes moving in a stationary field liquid indicated that a plot of log (U/U_∞) vs. log $(1 - d/D)$ should result in a unique curve which for low or moderate values of (d/D) should closely approach a straight line. Owing to the approximately linear relationship between frontal and equivalent diameters over the range covered in the experimental work, it was possible to use the latter in making the plots. In order to avoid the natural scattering of experimental points, large plots like Figures 4 to 7 were made from the data for each of the four systems. Points were then taken from the smoothed curves. For water, values of (U/U_∞) and $[1 - (d_e/D)]$ were calculated and plotted as shown in Figure 8. Similar plots were drawn for each of the four systems employed.

Several tendencies were apparent. The data for each system in each tube could be represented by a straight line of 0.765 slope. The intercepts of the lines varied progressively with tube diameter. The lines for a specific tube size and for various systems were parallel, but the intercepts varied inversely with the surface tension of the liquid used. Both slopes and intercepts appeared to be independent of the viscosity of the liquids. An empirical correlation of the data of tube diameter, surface tension, and intercept might result in an algebraic equation which would approximate their relationship. The tendencies are better shown in graphical form in Figure 9. Thus one can express the velocity-correction factor by the equation

$$\frac{1}{K} = \frac{U}{U_\infty} = \left[\frac{1}{b}\left(1 - \frac{d_e}{D}\right)\right]^{0.765} \qquad (12)$$

in which b is a constant which depends upon tube diameter and surface tension. Its numerical value may be obtained from Figure 9, in which the choice of semilogarithmic coordinates is used for convenience and has no mathematical significance. The relationship may also be conveniently expressed in nomographic form.

The minimum ratio of tube diameter to bubble equivalent diameter that must be satisfied if wall effects are to be held to a low magnitude of 1 or 2% may be estimated from the intercept to be $1/(1 - b)$. While the graphs show this value to be about 10, it is recommended that the ratio be at least 15. Not shown on Figure 8 is the series of points having an ordinate of 1.0 and an abscissa greater than b but less than unity. Using Equation (12) with values of (d_e/D) less than $(1 - b)$ would predict a value of U_∞ higher than reality. Such a prediction would obviously be an erroneous one and the use of Equation (12) is therefore limited to values of (d_e/D) less than $(1 - b)$.

Bubbles of a stable ellipsoidal form generally rise in a helical path. Larger bubbles of unstable shape rise in an irregular rocking motion. The horizontal component of the motion cannot exceed the tube diameter and as the helical diameter approaches this value, there is a damping effect on the helical motion. As the frontal diameter of the bubble approaches the tube diameter, the bubble tends to change to the cylindrical form described by many authors. For cap-shaped bubbles this would occur at a (d_e/D) ratio of about ½. This feature places a lower limit of 0.5 for the abscissa of Figure 8.

Table 2. Physical Properties of Test Liquids

Liquid	Temp., (°C.)	Viscosity, centipoises	Density, g./cc.	Surface tension, dynes/cm.
Water	25	0.894	0.997	72.0
	27	0.855	0.997	71.8
	29	0.818	0.996	71.7
61 wt. % glycerine in water	26	7.57	1.15	65.2
	28	7.25	1.15	64.9
0.2% by vol. TMN in water	26	0.866	0.997	28.5
	28	0.828	0.996	28.4
Diethylene glycol	28	24.1	1.111	46.8

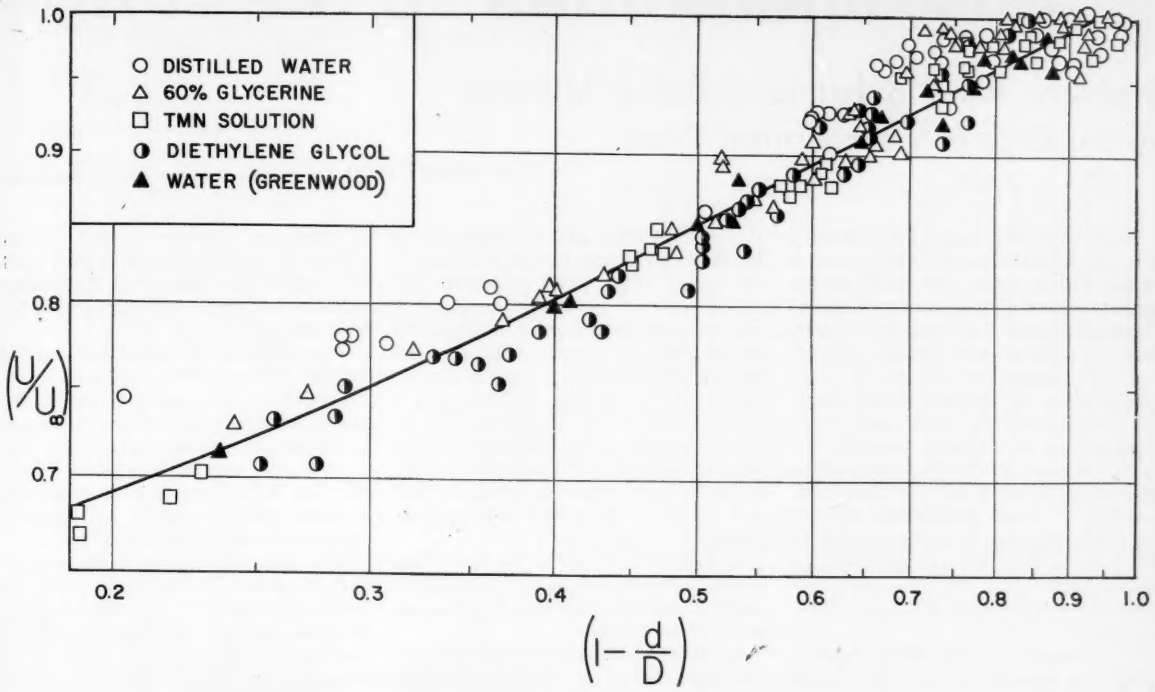

Fig. 10. Plot of original data as (U/U_∞) vs. $(1 - d/D)$.

The use of frontal diameter was tested by plotting the original points as log (U/U_∞) vs. log $[1 - (d/D)]$ as shown in Figure 10. A single curved line can be drawn through the points and will serve to predict the correction factor within a few per cent. The same tendencies may be observed as were shown by the curve using equivalent diameter but are not so pronounced.

SUMMARY

The retarding effect of a near-by cylindrical wall on the terminal velocity of air bubbles rising through the four liquids tested (distilled water, 61% glycerine, diethylene glycol, and a solution of a surface-active agent) can be expressed by Equation (12). The numerical constant b is a function of tube size and of the surface tension of the system. It seems to be independent of the viscosity of the liquid and may be evaluated by means of Figure 9.

The minimum size of the tube in which data may be taken if the wall correction is to be negligible is at least ten (and preferably fifteen) times the equivalent diameter of the largest bubble to be studied.

ACKNOWLEDGMENTS

Thanks are due to H. G. Hempill and M. I. Wernick for assisting with the building of some of the equipment and to J. R. Strom for improving upon some of the apparatus and for helping in the taking of data.

NOTATION

a = constant in Equations (8) and (9)
b = experimental constant in wall-effect correlation
C_D = drag coefficient, dimensionless, defined by Equation (1)
d = frontal diameter of bubble, cm.
d_e = equivalent diameter of bubble, cm.
D = diameter of cylindrical container, cm.
g = acceleration of gravity, cm./sec.^{2}
g_c = units conversion factor, (g.)(cm.)/sec.)^2(g. force)
K = terminal-velocity correction factor, equal to (U_∞/U)
n = exponent in Equations (8) and (9)
r_e = equivalent radius of bubble, equal to $d_e/2$, cm.
r_f = frontal radius of ellipsoid, equal to one-half its major axis
Re = Reynolds number, defined by Equation (1), dimensionless
U = actual terminal velocity of bubble, cm./sec.
U_∞ = terminal velocity at which a bubble would travel in a liquid of infinite extent, cm./sec.
We = Weber number, defined as $(d_e U_\infty^2 \rho/\sigma g_c)$, dimensionless
μ = dynamic viscosity of liquid, g./(cm.)(sec.)
ρ = density of liquid, g./cc.
σ = surface tension of liquid against air, dynes/cm.
Φ = a function
π = 3.1416

LITERATURE CITED

1. Allawala, M. A., M.S. thesis, Illinois Inst. Technol., Chicago (1952).
2. Bryn, T., *Forsch. Gebiete Ingenieurw.*, **4**, 27 (1933).
3. Faxen, H., *Arkiv. Mat. Astron. Fysik*, **19A** (1925).
4. Haberman, W. L., and R. K. Morton, *Rept.* 802, D. W. Taylor Model Basin, Navy Dept., Washington, D. C. (September, 1953).
5. Happel, J. and B. J. Byrne, *Ind. Eng. Chem.*, **46**, 1181 (1954).
6. Ladenburg, *Ann. phys.*, **23**, 447 (1907).
7. McNown, J. S., H. M. Lee, M. B. McPherson, and S. M. Engez, *Proc. VII Internatl. Cong. Appl. Mech.*, London (1948).
8. McNown, J. S., and J. Malaika, *Trans. Am. Geophys. Union*, **31**, 74 (1950).
9. McNown, J. S., J. Malaika, and H. R. Pramanik, *Internatl. Assoc. Hydraulic Res., App.* 25, R. 4, p. 511 (1951).
10. McNown, J. S., and J. T. Newlin, *Proc. First Natl. Conf. Appl. Mech.*, p. 801 (1950).
10a. Newton, I., "Mathematical Principles," p. 348, Univ. Calif. Press, (1934).
11. Peebles, F. N., and H. J. Garber, *Chem. Eng. Progr.*, **49**, 88 (1953).
12. Perry, J. H., "Chemical Engineers Handbook," 3 ed., p. 64, McGraw-Hill Book Company, Inc., New York (1950).
13. Rosenberg, B., *Rept.* 727, D. W. Taylor Model Basin, Navy Dept., Washington, D. C. (September, 1950).
14. Uno, Seiji, M.S. thesis, Illinois Inst. Technol., Chicago (1955).
15. Wakiya, S., *J. Phys. Soc. Japan*, **8**, 254 (1953).

Presented at A.I.Ch.E. Detroit meeting.

Notes on Phase Relations of Binary Mixtures in the Region of the Critical Point

F. H. BARR-DAVID Yale University, New Haven, Connecticut

Many papers have appeared presenting the phase equilibrium of binary mixtures in the critical region, but rarely do the authors present all five common means of representing such data, namely, (1) pressure vs. temperature at constant composition, (2) pressure vs. liquid and vapor compositions at constant temperature, (3) temperature vs. liquid and vapor compositions at constant pressure, (4) vapor composition vs. liquid composition at constant pressure, and (5) vapor composition vs. liquid composition at constant temperature. It is the purpose of this note to show the general interrelationship among the diagrams, useful for comparison of the work of various experimenters.

A P-t diagram for the ethane–heptane system, as reported by Kay (*4*), typical of many binary mixtures, is given in Figure 1, and the other corresponding phase diagrams are shown in Figures 2, 3, 4, and 5. The two phases existing at equilibrium are defined by a horizontal line cutting the isotherm on the P-x, y diagram (Figure 2). For any isotherm the curve to the left is the bubble-point curve, to the right, the dew-point curve. Where these curves meet, and the properties of the liquid and vapor become identical, is the critical point C, by definition. The critical point C is clearly the point of maximum pressure on this isotherm. As shown in the P-t diagram (Figure 1) the locus of points of highest pressure for any composition at specified temperatures is the envelope curve, which then must be the locus of the critical point. The critical point accordingly shifts around the nose of the constant composition loop so that it is always at the point of tangency, as shown.

In Figures 1, 2, and 3 the loci of the critical points C, the maximum pressure points E, and the maximum temperature points F are shown.

In Figure 1, in mixtures with composition loops tangent to the envelope between M, the maximum pressure possible for the two-phase system, and C_b, the critical of pure heptane, the critical point lies between the point of maximum pressure E and the point of maximum temperature (cricondentherm point) F, and the mixture exhibits both types of retrograde condensation. Between M and C_a, the critical of pure ethane, the critical point lies outside this range, and the mixture exhibits retrograde condensation of the first kind only.

Figure 2 shows the cricondentherm F to be the maximum composition point for the isotherm, for clearly at any higher temperature than the isotherm under consideration, two phases do not exist. The locus of maximum pressure points E is the envelope curve, as this is the maximum pressure that can exist for any temperature at a specified composition.

The existence of the three separate singular points for the mixture and the region of retrograde condensation requires that the nose of a constant composition P-t loop be rounded, and similarly the nose of an isotherm on the P-x, y diagram. On an isothermal y-x diagram (Figure 4) and an isobaric y-x diagram (Figure 5) such behavior is shown by the isotherm or isobar approaching the 45° line with a negative slope, as given by FC in Figure 4 and E_1C_1, E_2C_2 in Figure 5.

The t-x, y diagram is represented by

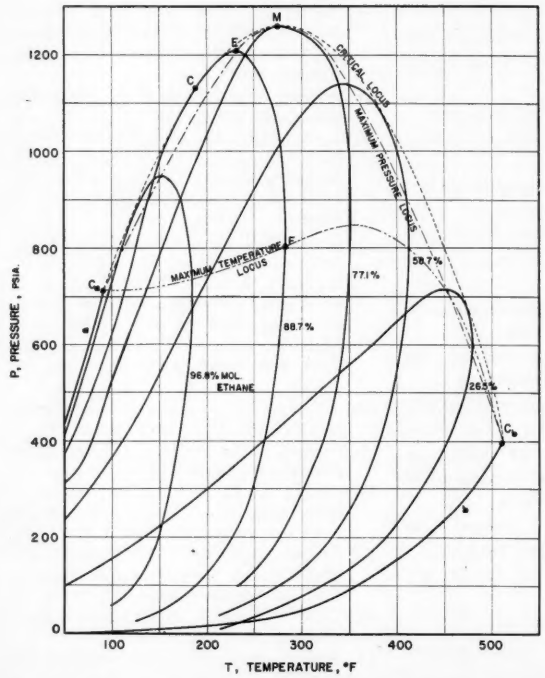

Fig. 1. Pressure-temperature diagram for the ethane-heptane system.

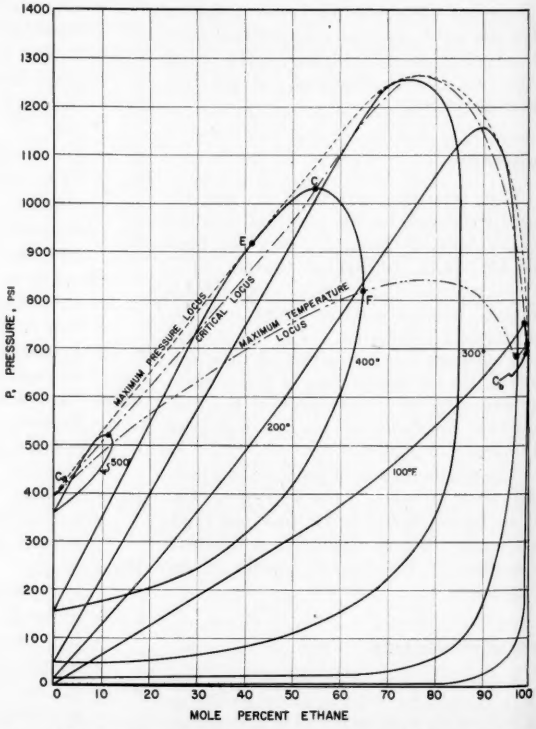

Fig. 2. Pressure-composition diagram for the ethane-heptane system.

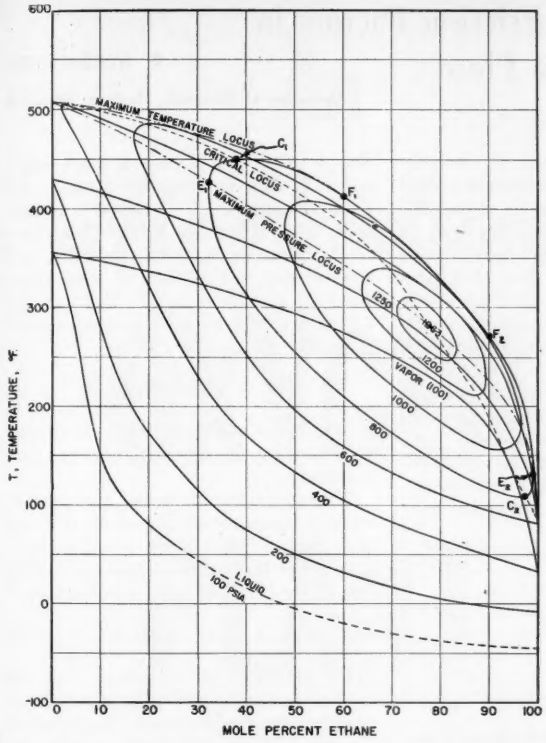

Fig. 3. Temperature-composition diagram for the ethane-heptane system.

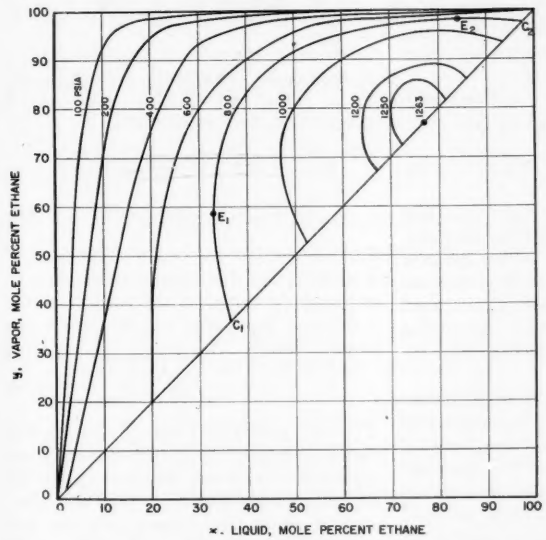

Fig. 5. Isobaric vapor composition-liquid composition diagram for the ethane-heptane system.

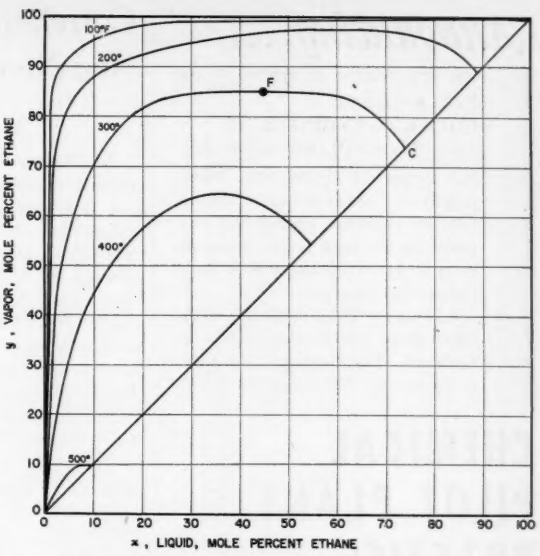

Fig. 4. Isothermal vapor composition-liquid composition diagram for the ethane-heptane system.

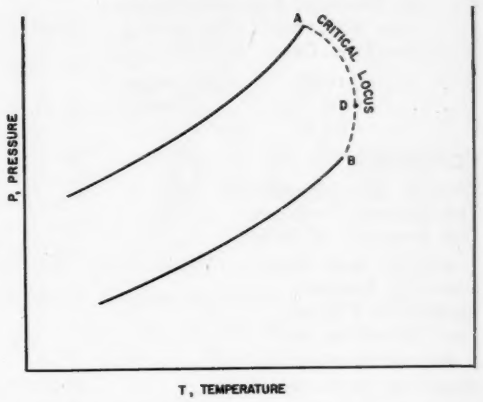

Fig. 6. Pressure-temperature diagram for a system exhibiting two limiting compositions on a pressure-composition diagram.

Figure 3. The condition of the isobars becoming critical at both ends is given by systems that have a critical pressure for the mixture greater than the critical for either component. For the isotherms to become critical at both ends on a P-x, y diagram requires a critical locus as given by the P-t diagram (Figure 6), a more unusual case. Such systems for compositions with critical points lying between B and D then exhibit retrograde condensation of the second kind only. It should be noted, however, that the approximate shape of the t-x, y diagram, in general, is not a mirror image of the P-x, y diagram, as is sometimes stated.

Some systems such as ethanol water, as reported by Griswold et al. (*3*) and Barr-David (*1*), and 2-propanol water, Barr-David (*1*), have sharp-pointed P-t and P-x, y curves. Thus the three singular points coincide and the systems do not exhibit retrograde condensation. Also the critical points of mixtures lie between the critical points of the pure components.

Other shapes of the critical locus exist, and the critical behavior of the mixtures may be deduced in a manner similar to that described above. For example, the N_2O–C_2H_6 system, as reported by Kuenen (*5*), has phase properties such that the center portion of an isotherm on a P-x, y diagram is the first part to become critical. Another characteristic locus is given by the occurrence of gas–gas equilibrium, as reported by Dodge and Lindroos (*2*) and others. Binary systems in which the critical points for the components are widely separated have interesting P-x, y diagrams, in which the isotherms spread out as the temperature is lowered and the critical pressure increases to such a high value that the solidification line may be reached.

LITERATURE CITED

1. Barr-David, F., to be published.
2. Dodge, B. F., and A. E. Lindroos, *Chem. Eng. Progr. Sym. Ser.*, **48**, No. 3, 10 (1952).
3. Griswold, J., J. D. Haney, and V. A. Klein, *Ind. Eng. Chem.*, **35**, 701 (1943).
4. Kay, W. B., *Ind. Eng. Chem.*, **30**, 459 (1938).
5. Kuenen, J. P., "International Critical Tables," 1 ed., vol. 3, p. 381, McGraw-Hill Book Co. Inc., New York (1928).

Announcing...

the first volume to appear of the
INTERSCIENCE
CHEMICAL ENGINEERING
AND TECHNOLOGY LIBRARY

A Series of Texts and Monographs each dealing with a specific field of chemical engineering and outlining the most recent advances, both in plant practice and in basic theoretical principles.

Edited by DR. SHELBY MILLER, *Head of the Department of Chemical Engineering, University of Rochester, Rochester, N. Y.*

CHEMICAL PILOT PLANT PRACTICE

BY DONALD G. JORDAN, Senior Chemical Engineer, American Cyanamid Company, Stamford, Conn.

1955. 160 pages
18 illus., 3 tables
$3.50

CONTENTS:

General Considerations.
The Scale-Up Problem.
The Handling of Solids, Liquids, and Gases.
Chemical Reactors.
Separation Process.
Cost Estimation and Report Writing.
Literature References.

From the Reviews . . .

"Everyone interested in the pilot plant stage of research and development will enjoy reading 'Chemical Pilot Plant Practice'. Donald Jordan's new book is a practical book. It describes pilot plant practice as it is actually being carried out in a large, progressive chemical company. Use of the procedures described may save much time and money for those engaged in pilot plants."—*Chemical and Engineering News.*

"This little book should be read by everyone concerned with the development of new products or processes, whether or not the building of a pilot plant is involved, for the basic philosophy applies to all development work."—*Journal of the Oil and Colour Chemists' Association.*

INTERSCIENCE Publishers, Inc.
250 FIFTH AVENUE
New York 1, N. Y.

Correlation of Friction Factors in Non-Newtonian Flow

R. BYRON BIRD

University of Wisconsin, Madison, Wisconsin

In Metzner and Reed's (*2*) recently published analysis of friction-factor data for non-Newtonian flow in cylindrical tubes the final correlation is based on an analytical solution of the equations of change for the laminar flow of a non-Newtonian fluid obeying the "power-law model." The following dimensional analysis approach gives an alternate method of interpreting the results of Metzner and Reed and may be of interest in connection with flow problems for other geometries and other non-Newtonian models.

The equations of change (*1, 4*) for the steady, isothermal flow of a pure incompressible fluid with no external body forces are

equation of continuity:

$$(\nabla \cdot \mathbf{v}) = 0 \qquad (1)$$

equation of motion:

$$\rho(\mathbf{v} \cdot \nabla)\mathbf{v} = -\nabla p - (\nabla \cdot \boldsymbol{\tau}) \qquad (2)$$

in which $\mathbf{v}$ is the local flow-velocity vector, ρ is the (constant) fluid density, p is the static pressure, and $\boldsymbol{\tau}$ is the shear-stress tensor. These equations are valid in both laminar and turbulent flow, and they may be applied to both Newtonian and non-Newtonian systems.

For the incompressible non-Newtonian power-law model $\boldsymbol{\tau}$ is given by (*3*)

$$| \boldsymbol{\tau} | = \beta \, | \nabla\mathbf{v} + (\nabla\mathbf{v})\dagger |^{\alpha} \qquad (3)$$

in which † indicates the transpose of the dyadic $\nabla\mathbf{v}$, and β and α are the phenomenological constants (the latter denoting the degree of deviation from non-Newtonian behavior). The Newtonian fluid may be regarded as a special case of the empirical relation given in Equation (3) with $\beta = \mu$ and $\alpha = 1$.

The equations of change [with Equation (3) substituted into Equation (2)] may be written in dimensionless form by using two scale quantities: the diameter of the cylindrical tube D and the average linear-flow velocity V. Multiplication of Equation (1) by (D/V) and Equation (2) by $(D/\rho V^2)$ then gives

equation of continuity:

$$(\nabla^* \cdot \mathbf{v}^*) = 0 \qquad (4)$$

equation of motion:

$$(\mathbf{v}^* \cdot \nabla^*)\mathbf{v}^* = -\nabla^* p^* - \left(\nabla^* \cdot \frac{1}{Re_\alpha} \, | \nabla^*\mathbf{v}^* + (\nabla^*\mathbf{v}^*)\dagger \, |^{\alpha}\right) \qquad (5)$$

in which $\mathbf{v}^* = \mathbf{v}/V$, $\nabla^* = D\nabla$, and $p^* = p/\rho V^2$. A modified Reynolds number $Re_\alpha = D^\alpha V^{2-\alpha}\rho/\beta$ also appears quite naturally as a dimensionless group in the reduced equation. If the tube is considered to be of infinite length (this statement is tantamount to neglecting end effects) then the solution of these equations will give the reduced velocity $\mathbf{v}^*$ as a function of the reduced position coordinates $\mathbf{x}^*$

$$\mathbf{v}^* = \mathbf{v}^*(\mathbf{x}^*; Re_\alpha, \alpha) \qquad (6)$$

in which the modified Reynolds number Re_α and the exponent α appear parametrically.

The connection between the reduced velocity distribution [Equation (6)] and the friction factor must now be established. For the cylindrical tube of infinite length the friction factor is defined as

$$(\tau_{rz})_{wall} = (1/2)\rho V^2 \cdot f \qquad (7)$$

[This definition is consistent with the friction factor defined in Equation (9) of Metzner and Reed's paper.] According to Equation (3) the shear stress at the wall is also given by

$$(\tau_{rz})_{wall} = (-\partial v_z/\partial r)^{\alpha}_{wall} \qquad (8)$$

in which r is the radial coordinate and v_z is the component of $\mathbf{v}$ in the axial direction. From these two relations one obtains then:

$$f = -(2\beta/\rho V^2)(\partial v_z/\partial r)^{\alpha}_{wall} = -(2/Re_\alpha)(\partial v^*_z/\partial r^*)^{\alpha}_{wall} \qquad (9)$$

But since $\mathbf{v}$ has the dependence given in Equation (6), the dimensionless velocity gradient evaluated at the wall must depend only upon Re_α and α. Hence one obtains finally

$$f = f(Re_\alpha, \alpha) \qquad (10)$$

That is, one would expect the friction factor to depend upon two dimensionless quantities, Re_α and α. Dimensional analysis alone cannot give any additional information about the manner in which Re_α and α are combined.

For the *laminar region* the exact form for $f(Re_\alpha, \alpha)$ is known. The solution of the equation of motion gives for the velocity distribution (*3*)

$$v(r) = (\Delta p/2\beta L)^{1/\alpha}\left(1 + \frac{1}{\alpha}\right)^{-1} \cdot \left(R^{1+1/\alpha} - r^{1+1/\alpha}\right) \qquad (11)$$

in which $\Delta p/L$ is the pressure gradient through the tube and R is the tube radius. From this expression one may then get

An *Air Products* OXYGEN PLANT

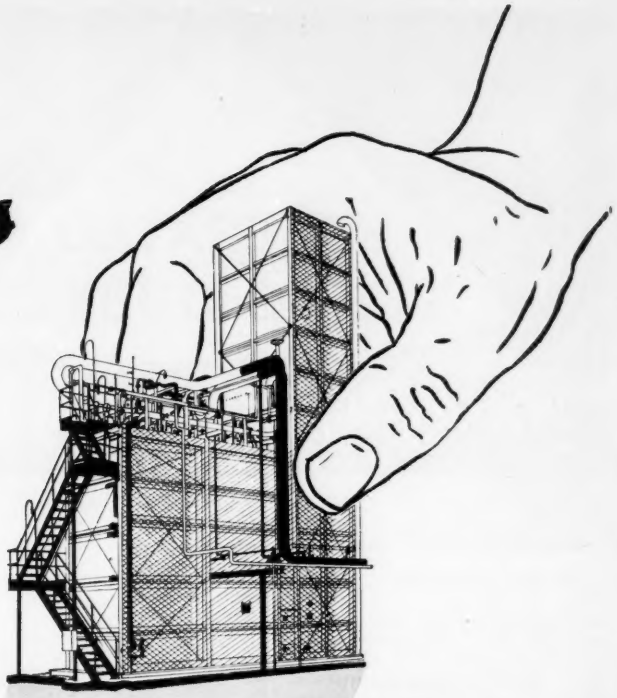

belongs in this picture

Is your Company one of the many concerns in the process industries that are contemplating expansion requiring the use of tonnage or high purity oxygen?

If so, the specialized experience of Air Products in this field (based on more than 700 successful installations) can be of substantial help in formulating your plans. An Air Products Oxygen Plant engineered specifically for your particular requirements can be a real money-maker.

We are equipped to design and build:

Large Capacity Tonnage Generators, regardless of size, purity, high or low pressure cycle, with liquid oxygen pumps, if your oxygen should be under pressure

or

"Packaged" High Purity Generators, producing high purity oxygen and nitrogen simultaneously —oxygen delivered safely under pressure by Air Products patented liquid oxygen pumps.

Send us information regarding your requirements.

Specialists in Low-Temperature Processing

Air Products
INCORPORATED
Dept. M, Box 538 Allentown, Pa.

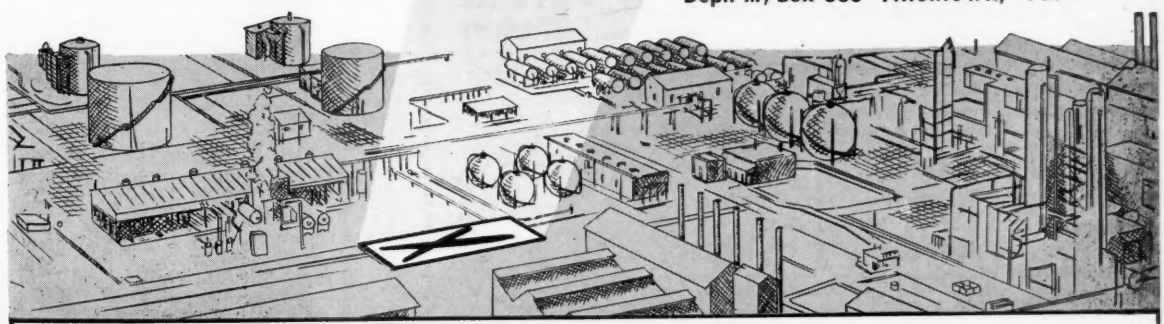

Cost Analyses • Process Design • Apparatus Design • Apparatus Manufacture

FEDERATED ZINC DUST

IS VERSATILE AND LOW IN COST

In many chemical applications and chemical compounds, zinc dust increases efficiency and reduces production costs. It is used . . .

As a reducing agent	**In pipe thread compounds**
As a catalyst	**In coating papers**
As a purifier	**In removing soot**
As a precipitating agent	**In Sherardizing**
In rust-resistant paints	**In pyrotechnics**
In making bleaches	**As a polymerizing agent**

Federated zinc dust is characterized by uniform purity (97 percent metallic zinc); and by fineness (all will pass through a 100-mesh screen; 97% through a 325-mesh screen).

Our complete research and engineering assistance is available to help you find applications for this plentiful, inexpensive product; or to aid you in present application problems. If you want to experiment in the use of zinc dust, we'll be pleased to send you a free half-pint sample. Just fill in the coupon below.

Federated Metals

DIVISION OF AMERICAN SMELTING AND REFINING COMPANY
120 BROADWAY, NEW YORK 5, N. Y.

Federated first in the non ferrous field FMD

☐ Please send me a half-pint sample of Federated Zinc Dust

☐ Please send me a sales engineer to discuss my problem

Name_____ Title_____

Company_____

Address_____

City_____ Zone____ State_____

(*Continued from page 428*)

the power-law analogue of the Hagen-Poiseuille equation

$$Q = \pi R^2 V = 2\pi \int_0^R vr\, dr$$

$$= \pi \left(\frac{\Delta p}{2\beta L}\right)^{1/\alpha} \left(\frac{R^{3+1/\alpha}}{3 + 1/\alpha}\right) \quad (12)$$

The friction factor is defined in terms of the pressure drop and average flow velocity by

$$(\Delta p/L) = (1/2R)(\tfrac{1}{2}\rho V^2)(4f) \quad (13)$$

[which is the same as Metzner and Reed's Equation (9)]. Combination of Equations (12) and (13) gives then directly

$$f(Re_\alpha, \alpha) = 16\, \frac{\frac{1}{8} 2^\alpha (3 + 1/\alpha)^\alpha}{Re_\alpha}$$

$$= \frac{16}{N_{Re}} \quad (14)$$

in which N_{Re} is the Reynolds number of Metzner and Reed. Hence the expression for N_{Re} can be obtained without any reference to the Rabinowitsch equation. It should be noted that N_{Re} is just a special combination of the Re_α and α predicted from dimensional analysis.

For the *turbulent region* the Metzner and Reed method of correlation inherently assumes that in the function $f(Re_\alpha, \alpha)$ the parameters Re_α and α will appear in the same special combination as in laminar flow—that is, f is a function of N_{Re} alone. The data available at the present time are probably not extensive enough to enable one to assess the correctness of the Metzner and Reed assumption. It should, however, be kept in mind that the power-law model is empirical; the fact that the flow curves (throughput vs. pressure drop) for laminar flow are described adequately by the *integrated* form of the power law in Equation (12) does not necessarily imply the correctness of the *differential* statement of the power law in Equation (3). Hence attempts to correlate the turbulent-flow region on the basis of the power-law model may prove impossible because of the inherent inadequacy of the model.

In the preparation of this note the author has had the benefit of correspondence with Professor Metzner and has profited considerably from the interchange of ideas.

LITERATURE CITED

1. Bird, R. B., 'Theory of Diffusion,' in "Advances in Chemical Engineering," Vol. 1, pp. 155–239, Academic Press, Inc., New York (1956).
2. Metzner, A. B., and J. C. Reed, *A.I.Ch.E. Journal*, 1, 434 (1955).
3. Reiner, M., "Deformation and Flow," Lewis, London (1939).
4. Schlichting, H., "Grenzschicht-theorie," G. Braun, Karlsruhe (1951).

(*Dr. Metzner's reply appears on page 10S*)

HIGH CAPACITY CLEAN DISCHARGE WITH EIMCO PAN FILTERS

Detail of Eimco stainless-steel pan-filter showing flexible vacuum and blow connections to each pan. These are exclusive features on the Eimco Pan Filter — particularly advantageous when the slurries filtered require periodic clean-outs of internal parts.

Greater filtering capacity, cleaner discharge and superior washing and drying make the Eimco Pan Filter a highly efficient unit.

Each pan functions as an individual filter with feed, wash, dry and discharge cycles. The pans may be jet washed from the bottom, assuring a clean media during every revolution.

Eimco Pan Filters can be constructed from a wide range of materials to ensure long life and low maintenance when processing corrosive slurries. Materials such as rubber, plastic and many others may be bonded to the surface of the metal construction for protective coating or to prevent product contamination.

Pan filters are available in a variety of sizes from 10 to 500 square feet of filter area.

These and other outstanding features listed below in a comparison with table filters, make the Eimco Pan Filter the most practical and efficient horizontal type vacuum filter available.

	TABLE FILTERS	EIMCO PAN FILTERS
Cake Discharge	Heel of cake remains on media.	Clean, full cake discharge.
Washing	No clear separation of wash. Cake remaining on media carries liquor past cake discharge point, diluting the strong filtrate.	Absolute separation of wash.
Media	Becomes blinded easily. Must stop to remove cake and wash. (Phosphoric acid operation requires considerable downtime.)	Media kept clean through wash during each cycle. Downtime minimum.
Removing, Repairing Media	Difficult repair job.	Media on each pan is easily and quickly changed or repaired.

Let Eimco engineers consult with you on your filtration problem. For years they have made it their business — through research — to offer better liquid-solid separation through filtration.

THE EIMCO CORPORATION

Salt Lake City, Utah—U.S.A. • Export Offices: Eimco Bldg., 52 South St., New York City

New York, N. Y. Chicago, Ill. San Francisco, Calif. El Paso, Tex. Birmingham, Ala. Duluth, Minn. Kellogg, Ida. Baltimore, Md. Pittsburgh, Pa. Seattle, Wash. Pasadena, Calif. Houston, Texas Vancouver, B. C. London, England Gateshead, England Paris, France Milan, Italy Johannesburg, South Africa

B-209

"THE
ELECTRON MICROSCOPE
AT WORK..."

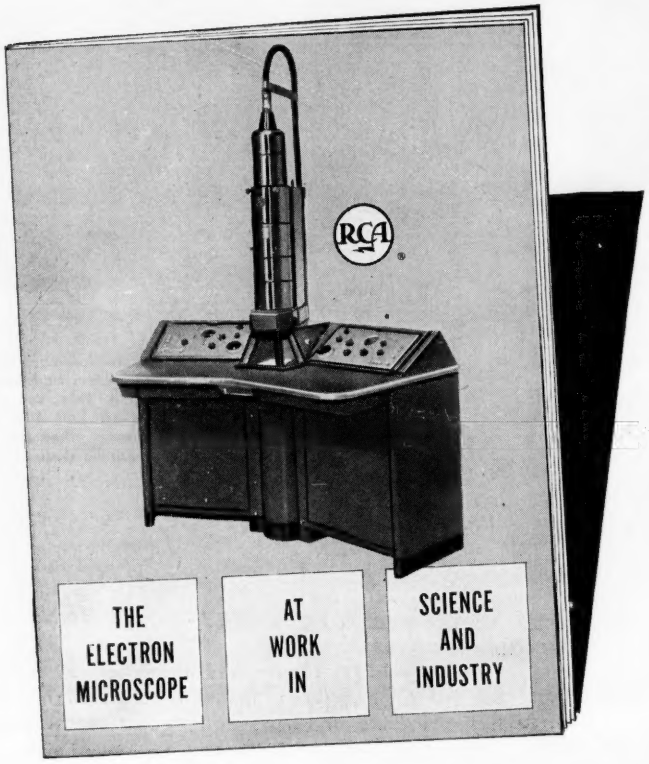

—New Booklet Available

How science and industry use the RCA Electron Microscope to solve problems of quality control, product improvement and new product development including fundamental research, is told in this new booklet, "The Electron Microscope at Work in Science and Industry." Actual case histories are cited, and a variety of micrographs of industrial and medical subjects provide revealing examples of the electron microscope at work. We believe you will find this booklet interesting and helpful. Write for your free copy, or use coupon below.

RCA
RADIO CORPORATION of AMERICA
CAMDEN, N.J.
In Canada: RCA VICTOR Company Limited, Montreal

Radio Corporation of America
Dept. J-288, Building 15-1, Camden, New Jersey

Please send me a copy of your new booklet, "The Electron Microscope at Work in Science and Industry."

NAME_____TITLE_____
COMPANY_____
ADDRESS_____
CITY_____ZONE_____STATE_____

Response

A. B. METZNER

University of Delaware, Newark, Delaware

Professor Bird's mathematical approach to non-Newtonian phenomena appears to represent a fruitful method of attack. Indeed, its only apparent limitation is one which he points out near the end of the paper: viz., his assumption of an empirical relationship between shear stress and shear rate. By contrast, the method of approach used by Metzner and Reed requires *no assumption whatever* as to the specific relationships between these quantities. This statement of fact may be readily verified by reference to the original papers by Rabinowitsch and Mooney, upon which our development was based. (These references have been cited in our paper.) Indeed, the utility and beauty of the clever mathematical work in these two references lies in the fact that the need for any assumption as to the type of fluid behavior is unnecessary, and the results are perfectly applicable to *all* common types of non-Newtonian behavior. This question has been discussed in somewhat greater detail elsewhere (*2*), as well as in the original paper, and need not be repeated here.

It is true that we have implicitly assumed that the grouping of variables in our generalized Reynolds number (α and β in Professor Bird's nomenclature or n' and K' in the Metzner-Reed paper) will be the same outside the laminar region as well as within it. More recent theoretical work at the University of Delaware indicates that the friction factor in turbulent flow may depend on both n' and the generalized Reynolds number when this is done. However, the utility of the generalized Reynolds number in predicting the end of the laminar-flow region suggests retention of this form of the dimensionless group for all flow regimes.

This recent work has progressed to the point of predicting the form of the $f - N_{Re} - n'$ relationships for non-Newtonian fluids in turbulent flow. The assumptions required were substantially identical to those commonly employed by workers dealing with the same problem for Newtonian fluids. However, as the validity of some of these usual assumptions cannot be accepted without question, no publication of these results is planned until experimental confirmation of the theory is obtained. It is relevant to note, on the other hand, that the recommended design procedures given by Metzner and Reed in their summary is supported by this further theoretical work as being conservative in regions where it is not rigorously correct.

It has been pointed out (*1, 2*) that most non-Newtonian fluids approach Newtonian behavior at the extremes of very low

and very high shear rates. The latter situation arises in most work on turbulent flow of non-Newtonians. Accordingly, accurate experimental verification of any theory for the case of fully developed turbulence may prove to be very difficult unless non-Newtonian fluids of exceptional character are employed. Suggestions which readers may have along these lines may well turn out to be a major key to progress in this entire area and are earnestly solicited.

Correspondence with Professor Bird on these problems has been most stimulating and useful to the writer.

LITERATURE CITED

1. Alves, G. E., D. F. Boucher, and R. L. Pigford, *Chem. Eng. Progr.*, **48**, 385 (1952).
2. Metzner, A. B., 'Non-Newtonian Technology-Fluid Mechanics, Mixing and Heat Transfer,' in "Advances in Chemical Engineering," Vol. I, Academic Press, Inc., New York (1956).

BOOKS

The Atomic Nucleus. Robley Evans. McGraw-Hill Book Company, Inc., New York (1955). 972 pp., $14.50.

It is rare that one finds a book that is well suited as a text at an early graduate level and can also be recommended as a reference book for the worker in the field. Evans's is such a book.

As one who has been teaching such a course for several years this reviewer finds that at last he can recommend a text which parallels the material taught and maintains an equivalent level. Further, with its wide and clear coverage and its many references it should provide stimulation and basic understanding and, in addition, sources for a more detailed study.

Emphasis is placed on specific sample experimental procedures and interpretations which then lead into a more general and unifying presentation of a given field. For example, the subject of nuclear reactions is introduced by presenting various experimental studies of the B^{10} (α, p) C^{13} reaction. A study of the fine structure of the protons serves to introduce nuclear-energy levels, whose decay is then discussed. Subsequently, evidence for the neutron, radioactivity, the compound state, and resonances is introduced with historical background, all within the framework of the initial reaction or its competing reactions.

Sufficient theory is presented to provide a basic and qualitative understanding of the various topics. The notation in general corresponds to that in Blatt and Weisskopf's "Theoretical Nuclear Physics." In many ways it can be considered "an experimentalist's guide to Blatt and Weisskopf." The treatment is simpler and more qualitative, places major emphasis on the experimental approach, and assumes less background knowledge on the part of the reader.

Among the subjects covered which are not yet standard are nuclear models, includ-

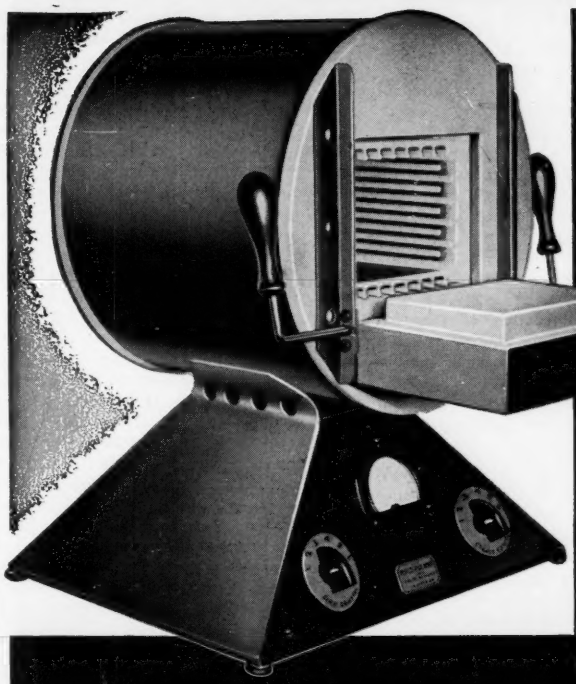

Instruments and Controls operate at approximately room temperature . . . there is no trapped heat.

As a result of correct insulation design, you can shift rapidly to desired operating temperatures.

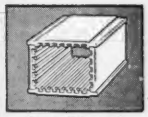

Reversible and easily replaceable Multiple Units, time-tested for 30 years, have been retained.

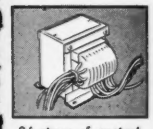

36 steps of control through a Hevi Duty Tap-Changing Transformer allows maximum flexibility of control.

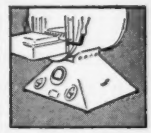

Controls are mounted in a recessed position for safety and at correct angle for proper vision.

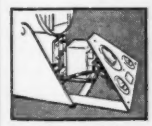

Rear panel is removable for access to terminal board. Release of front panel permits control assembly to slide forward.

HEVI DUTY
"MULTIPLE UNIT"
MUFFLE FURNACE
For Temperatures To 2000° F.

This furnace has been designed for general laboratory requirements such as drying of precipitates, ash determinations, fusions, ignitions, heating metals and alloys, enameling, heat treating, and experimental test work.

The efficient Hevi Duty Muffle Furnace shown is housed in a cylindrical shell mounted on a pyramidal type base with practicaly line contact between them . . . allowing for free circulation of air and eliminating trapped heat in the base. Available in four standard sizes.

For complete details, construction, and specifications, see your Laboratory Supply Dealer, or write for Bulletin LAB-849.

"MULTIPLE UNIT"

HEVI DUTY ELECTRIC COMPANY
MILWAUKEE 1, WISCONSIN
Heat Treating Furnaces... Electric Exclusively
Dry Type Transformers *Constant Current Regulators*

(*Continued from page 11S*)

ing brief discussion of the collective model; stripping reactions, but only briefly; and a rather more-than-average-detailed discussion of the radiations associated with moderate energy synchrotrons, such as bremsstrahlung, interactions of electromagnetic radiations with matter, and the stopping of electrons. Among the subjects not included are coulomb excitation, reactor physics, and meson physics.

WALDO RALL

Estimation of Critical Properties of Organic Compounds by the Method of Group Contributions. A. L. Lydersen. Engineering Experiment Station Report 3. College of Engineering, University of Wisconsin, Madison, Wisconsin (1955). 22 pages.

This short report is a very appropriate companion to Report 4, reviewed below. Tables of incremental values for various atoms and atomic groups, to be used with equations revised by the author, are presented by which the critical temperature, pressure, and volume of a compound may be estimated. The only experimental value required is the normal boiling point, when T_r is calculated. Comparison of calculated and experimental results with a large number of compounds shows an arithmetic average deviation of less than 1 and 3.8% for T_r and p_r respectively. An equation is also presented by which z_c may be estimated from the molal latent heat of vaporization at the normal boiling point. This is a very useful and easily understood empirical study.

R. H. M. SIMON

Chemical Engineering, Volume II: Unit Operations. J. M. Coulson and J. F. Richardson. McGraw-Hill Book Company, Inc., New York (1955). 588 pages, $9.00.

The second volume of this work comes up to the promise of the first. The first volume was devoted to the fundamentals of transfer of momentum, heat, and mass, with specific attention to engineering factors in flow of fluids, heat transfer, and humidification. The second volume deals with subject matter organized in the following interesting fashion: flow of fluids past particles (flow through granular beds and packed columns, filtration, the centrifuge); systems involving relative motion between a fluid and particles (sedimentation, fluidization, conveying, gas cleaning); applications of mass transfer (leaching, distillation, absorption of gases, liquid-liquid extraction); evaporation, crystallization, and drying; size reduction and classification of solids; mixing.

The work as a whole may be characterized as a well-coordinated presentation, somewhat broader in scope than other works covering the same kind of material and well-balanced in the division between theory and practice. It is understandable by virtue of good composition and the effective use of line drawings and photographs.

As a reference book we should suppose that many practicing engineers would like to consider this volume for addition to personal libraries. Granted that much of the subject matter is well presented in other sources, the somewhat different viewpoint of these authors will be interesting and helpful.

As a textbook for undergraduate students the book has limitations imposed by its breadth. The instructor choosing this as a text must realize that only a fraction of the material in it can be covered in undergraduate work. The student will be confused at times by the wealth of material available but he will at the same time develop some familiarity with a work of broad scope. Whether this is a better approach to undergraduate instruction than using texts of more limited scope depends largely on the instructor.

The volume seems well suited to serve as a basis for graduate instruction in the unit operations. Much of the basic material for such courses is here in well-organized form.

CHARLES A. WALKER

Generalized Thermodynamic Properties of Pure Fluids. A. L. Lydersen, R. A. Greenkorn, and O. A. Hougen. Engineering Experiment Station Report 4. College of Engineering, University of Wisconsin, Madison, Wisconsin (1955). 99 pages, $3.50.

This work represents an important step in refining the law of corresponding states so that it may be used to predict the pVT behavior and thermodynamic properties of fluids more accurately than was heretofore possible.

The authors introduce the critical compressibility factor, z_c, which in addition to reduced temperature, T_r, and reduced pressure, p_r, defines the compressibility factor, z. This additional parameter helps to account for variations in chemical structure and thereby improves the correlations based on the law of corresponding states.

The experimentally observed properties of up to eighty-two elements and compounds of varied structure and composition were

You can turn to the experience and extensive facilities of Stearns-Roger for engineering, construction or for the complete turn-key job, wherever processing is involved. When America's basic industries have a plant problem—metallurgical, chemical processing, oil and gas, power, sugar—they take it up with
Stearns-Roger
DENVER • HOUSTON • EL PASO • SALT LAKE CITY
Stearns-Roger Engineering Company, Ltd., Calgary, Alberta
when you make tomorrow's plant decisions
ENGINEERS · · · CONSTRUCTORS · · · MANUFACTURERS

used to construct tables of z as a function of p_r and T_r for values of z_c of 0.23, 0.25, 0.27, and 0.29. In addition, other tables of considerable utility were compiled on the basis of these values of z_c over suitable ranges of p_r and T_r. Among these are the thermodynamic properties of saturated liquids and gases, reduced densities of gases and liquids, deviations of enthalpy, entropy, and internal energy of gases and liquids from ideal-gas behavior, fugacity coefficients, and vaporization-equilibrium constants.

The entire development, from the choice of the third parameter to the methods of obtaining the tabulated values, is carried out with admirable clarity and verbal economy. The use of the tables for constructing thermodynamic charts and for solving problems involving the Joule-Thomson effect is effectively explained. The text contains many helpful figures and illustrative problems which should make it particularly attractive to those not continually in touch with thermodynamics.

The authors present an extensive bibliography and a large quantity of data comparing experimentally determined with calculated generalized values of various properties. The use of the added parameter, z_c, is shown to improve the correlation significantly, particularly around the critical point and in the regions of saturated liquid and vapor. At higher values of p_r and T_r the beneficial effect of this added parameter diminishes.

An errata sheet is included which accounts for almost (but not quite) all the errors in the text. The editing leaves something to be desired, but this deficiency becomes insignificant when the value of the work is considered.

This report should definitely be on the bookshelves of our teachers and students, and anyone in the field whose work is concerned with the application of the law of corresponding states.

R. H. M. Simon

Distillation Literature, Index and Abstracts, 1953–54. Arthur and Elizabeth Rose. Applied Science Laboratories, Inc., State College, Pennsylvania (1955). 412 pages, $12.50.

The 1953–54 volume has been preceded by similar volumes, the first covering 1941–45 and the second 1946–52. Arthur and Elizabeth Rose also contributed Chapters I and IV to "Distillation" (published by Interscience Publishers, Inc., in 1951), which includes bibliographies and a wealth of references on distillation from the earliest reports to 1950. Taken together, this is a unique accomplishment by the Rose team as well as a tremendous job, similar to Hercules' labors, in so completely and exhaustively abstracting all the reports in the technical literature of many languages on the important subject of distillation. In fact, there is nothing else available even remotely approaching the completeness and precision of the distillation abstracts by Arthur and Elizabeth Rose. It is noted that the 1946–52 volume of this series was judged by the American Library Association to be the best bibliography on sciences related to agriculture published in 1953–54 and was the basis for the presentation of the Oberly Award to the authors.

The present 1953–54 volume is nearly two-thirds the size of the 1946–52 volume,

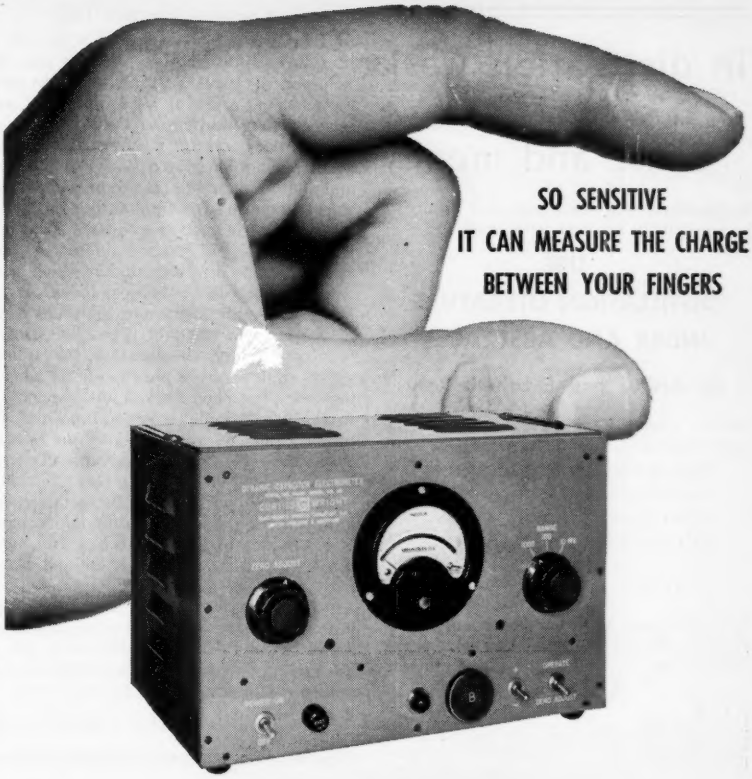

CURTISS-WRIGHT

DYNAMIC CAPACITOR ELECTROMETER

FOR STABLE AMPLIFICATION OF LOW-LEVEL DC SIGNALS

Measures currents as low as 10^{-16} amp. • Extremely high input impedance . . . 10^{15} ohms. • Low drift — less than ± 1 mv per 24 hours. • Uses dependable, durable dynamic capacitor. • Accuracy of ± ½ % full scale. • Only 14" x 10" x 9"

The Curtiss-Wright Dynamic Capacitor Electrometer is ideal for measuring minute currents or voltages from high impedance sources. There is no 60 cps interference since the Dynamic Capacitor Electrometer operates at 1,000 cps. The instrument can be used to measure static charges, potentials of floating grids, insulation leakage currents, capacitor dielectric leakages; and to study transistors and diodes. Its ruggedness, reliability, and high sensitivity make it especially suited for use in the nuclear field as a component in reactor control systems and in industrial control systems employing radioisotopes as energy sources. It can be used for pH determination, and in mass spectrometry. In biophysics and medicine it may be used to measure cell potentials, skin potentials, streaming potentials, injury potentials, and nerve impulses. Besides providing an indication on its own meter, it will operate any standard recorder. For details, write Nuclear Equipment Sales Dept., Curtiss-Wright Corporation, Electronics Division, Carlstadt, N. J.

ELECTRONICS DIVISION
CURTISS-WRIGHT
CORPORATION • CARLSTADT, N. J.

In distillation work it's easy to save time and money

to stimulate new ideas and new profits, to catch up on your back reading—

USE

DISTILLATION LITERATURE INDEX AND ABSTRACTS

by Arthur and Elizabeth Rose

Covers years 1946-54 inclusive. Sections on such important subjects as

VAPOR-LIQUID EQUILIBRIUM
AZEOTROPES
AZEOTROPIC DISTILLATION
EXTRACTIVE DISTILLATION
CALCULATIONS AND THEORY
ANALYSIS

Includes Data, Theory, Experimental Procedures, Plant Processes, Patents, Books, Advertising

* * * * * *

Complete Author Indexes. 780 Subject Headings, Including Names of Substances. Informative Abstracts. Hundreds of Pages. Thousands of Entries. Exact Journal References. All abstracts on each subject are in one easily accessible place. You get in a minute what takes hours to dig from regular sources.

* * * * * *

☐ Complete DISTILLATION LITERATURE volume. Covers all subjects and authors for years 1946-52 inclusive. Contains 595 pages fine print; hard cover binding. Price $25.00

☐ Complete DISTILLATION LITERATURE volume. Same as above for years 1953-54. 412 pages; hard cover binding. Price $12.50

Important sections of the above are also available in convenient and economical forms for specialists:

☐ Section on VAPOR-LIQUID EQUILIBRIUM, AZEOTROPES, EXTRACTIVE DISTILLATION. Spiral bound; contains 155 pages fine print. Covers period 1946-54. Includes all references and abstracts, and especially complete and convenient indexes to substances. Price $5.00

☐ Section on ANALYSIS BY DISTILLATION. Covers period 1946-54. Spiral bound; 67 pages fine print. Price $2.00

☐ Section on CALCULATIONS AND THEORY. Covers period 1946-54. Includes subjects such as theory of batch distillation, calculations, computers, design, diffusion, nomographs, throughput. Spiral bound; 125 pages fine print. Price $4.00

* * * * * *

Order postpaid direct from

APPLIED SCIENCE LABORATORIES, INC.

140 N. Barnard Street
State College, Pa.

(*Continued from page 13S*)

evidencing the increasing rate of growth of literature on distillation. Like the previous volumes, the present volume contains three sections: (1) a list of all subject and substance index headings and cross references used in the book, (2) a main subject index section comprising the majority of the book and containing abstracts grouped according to subject, and (3) a final author index section giving the authors and their locations, titles of articles, journal references, and subject index headings under which each entry is found in the subject index.

The book contains more than 400 pages of abstracts in compact type. The general plan of indexing, classification, selection of appropriate words or phrases of index headings, etc., has been worked out logically. It would be a formidable job to proofread the present 1953–54 volume, but spot reading throughout the book has not yet disclosed typographical or factual errors. The language used in writing the abstracts appears uniformly clear and adequately informative. It is obvious to anyone reading and using the abstracts that both Arthur and Elizabeth Rose are not just abstractors, but authorities in the field of distillation, and that they have conscientiously digested, correlated and edited suitably every one of the great number of pieces of information reduced to abstract form in their book.

WALTER J. PODBIELNIAK

INDEX OF ADVERTISERS

Air Products, Inc.	7S
Applied Science Laboratories, Inc.	14S
Bowen Engineering, Inc.	282
Curtiss-Wright Corp.	13S
Du Mont Laboratories, Inc., Allen B.	6S
Eimco Corp., The	9S
Federated Metals Div., American Smelting & Refining Co.	8S
Foote Mineral Co.	Inside Front Cover
Harshaw Chemical Co., The	4S
Hevi Duty Electric Co.	11S
Interscience Publishers, Inc.	428
Librascope, Inc.	5S
Mixing Equipment Co., Inc.	Back Cover
Philbrick Researches, Inc., George A.	14S
Radio Corp. of America	10S
Stearns-Roger Mfg. Co.	12S
York Process Equipment Corp.	Inside Back Cover

Advertising Offices

New York 36—Lansing T. Dupree, Adv. Mgr.; John M. Gaede, Asst. Adv. Mgr.; Paul A. Jolcuvar, Dist. Mgr.; Donald J. Stroop, Dist. Mgr.; Hale H. Carey, Dist. Mgr.; 25 W. 45th St., Columbus 5-7330.

Chicago 11—Richard R. Quinn, Dist. Mgr., 612 North Michigan Ave., Room 507, Superior 7-0385.

Cleveland 15—Eugene B. Pritchard, Dist. Mgr., 1836 Euclid Ave., Superior 1-3315.

Pasadena 1—Richard P. McKey, Dist. Mgr., 465 East Union St., Ryan 1-8779.

Analog Computing for One and All

with GAP/R modular components

The Model K2-X Operational Amplifier is an octal-based plug-in unit which nobly serves as nucleus for accurate feed-back computing.

With an output of ±100V the K2-X is priced at $28. The K2-W at $24, puts out an ample ±50V with less power needed.

Model K2-P is a Stabilizing Amplifier used in tandem with the K2-W or K2-X. It provides long term DC Stability measured in microvolts. All plug directly into the HK (shown below) or other environments. The K2-P having inherent stability below 0.1 MV is priced at $60.

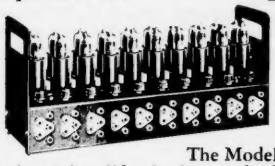

The Model HK Operational Amplifier in the standard version offers 10 K2-W Amplifiers for analog calculations of infinite variety. A stabilized HK using K2-X and K2-P *"paired"* plug-ins provides greater output plus stability. The *standard* HK with 10 K2-Ws is $425. The *stabilized* HK with 5 of above "pairs" is $625.

Supplied also in a self-powered version as the compact Model HKR Operational Tenfold, all manifolds can be purchased in either *standard* or *stabilized* forms or in other combinations.

For rapid utilization of the HK or HKR, Model K- Modular Assembly units are offered either in kit form or assembled as Adder, Coefficient, Differentiator, Integrator or Unit-lag Passive Operational Plug-ins. Prices furnished on request.

One of the many "power packages" from GAP/R is the Model R-100 Regulated Power Supply, conservatively rated at 100 ma, ±300VDC, and modestly priced at $165.

Indicated below are two possible arrangements whereby your laboratory or engineering office can obtain a basic computing facility at minimum cost.

20 OPERATIONAL AMPLIFIERS Plus Regulated Power		10 STABILIZED AMPLIFIERS Plus Regulated Power	
2 HKs (with 20 K2-Ws)	$850.	2 HKs (10X's + 10 P's)	$1250.
1 R-100 Power Supply	165.	2 R-100 Power Supplies	330.
	$1015.		$1580.

For more details and other information please write to:

George A. Philbrick Researches, Inc.
230 Congress Street, Boston 10, Massachusetts

GAP/R

ents

onal
ased
obly
rate

ut of
2-X
$28.
$24.
mple
less

HK
ver-
log
zed
ug-
ity.
25.
rs"

as
en-
in
or

he
es"
00
ely
tly

ge-
gi-
ng

c.
ts

56